Physics of the Solid State, Vol. 42, No. 9, 2000, pp. 1579–1583. Translated from Fizika Tverdogo Tela, Vol. 42, No. 9, 2000, pp. 1537–1541.

METALS AND SUPERCONDUCTORS

Inelastic Neutron-Scattering Study of the Phonon Spectrum of $Bi_2Sr_2CaCu_2O_8$-Based Nd-Containing Solid Solutions

A. V. Knot'ko*, A. V. Garshev, V. I. Putlyaev*, and S. I. Morozov*****

** Moscow State University, Vorob'evy gory, Moscow, 119899 Russia*

e-mail: knotko@inorg.chem.msu.ru

*** Moscow State University, Materials Science Department, Vorob'evy gory, Moscow, 119899 Russia*

**** Institute of Physics and Power Engineering, pl. Bondarenko 1, Obninsk, Kaluga oblast, 249020 Russia*

Received January 13, 2000

Abstract—A study of the phonon spectra of $Bi_2Sr_2Ca_{1-x}Nd_xCu_2O_\delta$ solid solutions (x = 0.1, 0.25, 0.75) by inelastic neutron scattering on a DIN-2PI forward-scattering spectrometer is reported. As the Nd content increases, the frequency of the Cu–O stretching vibrational modes increases (by about 70 meV), an effect caused by a change in carrier concentration in the CuO_2 sheet and not depending on the "internal pressure." An analysis of the displacement of the peak near 11 meV (assigned to cation vibrations in the SrO sheet of the $Bi_2Sr_2CaCu_2O_8$ structure) suggests that a sizable part of the Nd atoms occupy Sr positions. © *2000 MAIK "Nauka/Interperiodica".*

$Bi_2Sr_2CaCu_2O_8$-based high-temperature superconductors (Bi2212) belong to materials that are most promising from the viewpoint of possible applications. Investigations of the microscopic properties of such superconductors with heterovalent substitution at various sites greatly contribute to our understanding of the mechanism of superconductivity and of the modification of their electrophysical properties (such as T_c, J_c, room-temperature electrical conductivity, etc.). Of considerable interest is the substitution of various rare-earth elements for Ca and Sr. This substitution can be carried out within a very broad range and results in the reduction of copper [1, 2], which is accompanied by a decrease in the superconducting transition temperature and the metal–semiconductor transition.

The part played by electron–phonon coupling in the HTSC mechanism remains an open issue. Therefore, an investigation of the variation of the phonon density of states in HTSC compounds, more specifically, in Bi2212, in the course of varying their electrophysical properties appears to be promising. Presently, there are very few studies of the changes in the phonon spectrum incurred by heterovalent substitution in Bi2212 compounds [3, 4]. Only $Bi_2Sr_2Ca_{1-x}Y_xCu_2O_\delta$ solid solutions have been investigated up until recently. The observed changes in the phonon spectrum are associated [4] with the simultaneous action of the change in carrier concentration caused by copper reduction and the "internal pressure" arising from the difference between the ionic radii of Ca and Y. We believe that an attempt at separating the impacts of these two factors on phonon spectrum modification would be of interest. The "internal pressure" effect can be excluded by using a RE element with an ionic radius close to that of calcium, for instance, Nd, for Ca replacement. Thus, the purpose of this study is to reveal the key factor in the phonon spectrum variation by investigating the lattice dynamics of $Bi_2Sr_2Ca_{1-x}Nd_xCu_2O_\delta$ solid solutions while varying the Nd content.

1. EXPERIMENTAL TECHNIQUE AND DATA TREATMENT

$Bi_2Sr_2Ca_{1-x}Nd_xCu_2O_\delta$ samples (x = 0.1, 0.25, 0.75) were prepared from nitrate–oxynitrate mixtures obtained by dissolving ChDA-grade Bi_2O_3, $SrCO_3$, and CuO, and OSCh-grade $CaCO_3$ and Nd_2O_3 in 20% nitric acid, with subsequent evaporation of the solution. The sample preparation included decomposition of the salt mixture at 750°C and several (two or three) subsequent stages of annealing at 860°C for 24 h each, with intermediate grinding. All the anneals were performed in air.

X-ray diffraction analysis of the samples on a DRON-3M diffractometer (CuK_α radiation, with silicon used as the internal standard to determine the cell parameters) showed that they are similar in composition to $Bi_2Sr_2CaCu_2O_8$-based solid solutions. The unit cell parameters refined by least-squares fitting are listed in Table 1. The figures demonstrate a monotonic variation of the parameters that is in accordance with the literature data [5, 6], which is evidence in favor of the formation of solid solutions.

The inelastic neutron-scattering experiments were performed on a DIN-2PI forward-scattering spectrometer installed at the IBR-2 reactor (JINR, Dubna) [7]. The spectra were measured at room temperature in the time-of-flight regime at energy E within a scattering

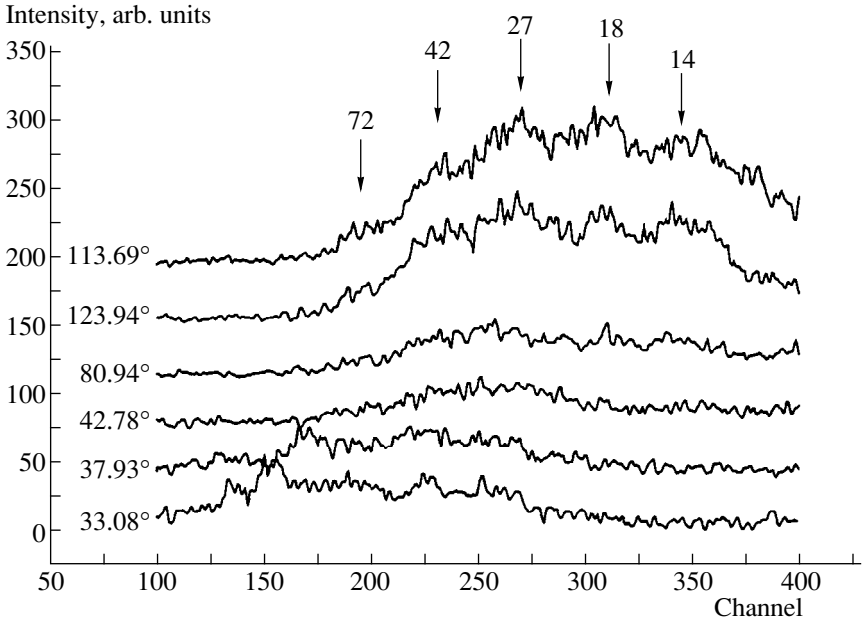

Fig. 1. Inelastic neutron scattering spectra obtained on a $Bi_2Sr_2Ca_{0.9}Nd_{0.1}Cu_2O_y$ sample for different scattering angles. The arrows identify the main spectral features and the corresponding values of E (meV).

angle range of 10–134°, the initial neutron energy being E_0 = 8.15 meV. The spectrometer resolution in the energy transfer region $\varepsilon = E - E_0$ = 0–80 meV was $\Delta E/E \approx$ 5–8%. The spectra were normalized against the vanadium elastic peak.

Because the samples studied contained a paramagnetic ion (Nd^{3+}), an estimate was made of the contributions due to magnetic and phonon inelastic neutron scattering from the angular dependence of the scattered intensity. Figure 1 presents spectra of an x = 0.1 sample obtained by detectors probing different scattering angles. For scattering angles less than 42°, one observes a considerable neutron flux with energies E = 65–1980 meV (channels 100–200), which corresponds to the thermal background, and therefore, subsequent analysis was done using data obtained at scattering angles above 42°. For scattering angles θ from 42 to 134°, the momentum transferred to a neutron lies within the range Q = 1.8–4.2 Å^{-1} for ε = 6 meV and Q = 5.2–8 Å^{-1} for ε = 80 meV. It can be expected that the magnetic form factor is already small for $Q \approx 2$ Å^{-1}, so that magnetic scattering should not noticeably contribute to the spectrum of inelastically scattered neutrons (ISN) for $\theta > 40°$. Indeed, as seen from Fig. 1, for angles above 40°, one observes a monotonic growth of the ISN intensity with an increasing scattering angle in the energy transfer region ε = 1.5–100 meV (channels 175–400), which is evidence of the nonmagnetic character of the scattering. This angular dependence of the inelastically scattered intensity shows that the spectra obtained for $\theta > 40°$ are primarily due to scattering from phonons.

Table 1. Parameters of the orthorhombic unit cell of $Bi_2Sr_2Ca_{1-x}Nd_xCu_2O_\delta$ solid solutions (x = 0.1, 0.25, 0.75) (Å)

Composition	x = 0.1	x = 0.25	x = 0.75
a	5.418(3)	5.425(3)	5.465(3)
b	5.418(3)	5.425(3)	5.465(3)
c	30.75(4)	30.68(4)	30.46(2)

After introducing standard corrections for detector efficiency and neutron flux attenuation by the sample, the ISN spectra taken in the 42–134° scattering-angle range were treated to obtain a generalized frequency spectrum $G(\varepsilon)$ in the incoherent approximation [8]. The generalized spectrum is the lattice frequency spectrum weighted by the factor $\sum \sigma_i \langle |\xi_i(\varepsilon)|^2 \rangle / m_i$, where σ_i, m_i, and $\langle |\xi_i(\varepsilon)|^2 \rangle$ are the scattering cross section, mass, and mean squared polarization vectors of the ith atom, respectively. Multiphonon scattering was taken into account in Sjolandar's approximation [9]. Multiple scattering was neglected, because sample transmission for scattered neutrons did not exceed 10%.

The generalized frequency spectra averaged over measurements on all detectors within the 42–134° scattering angle range are shown in Fig. 2 for samples with x = 0.1, 0.25, and 0.75; also presented for comparison is a spectrum of unsubstituted Bi2212 obtained in [3]. To make a numerical estimation of the differences in phonon density-of-states spectra among the samples with different Nd concentrations, the low-frequency

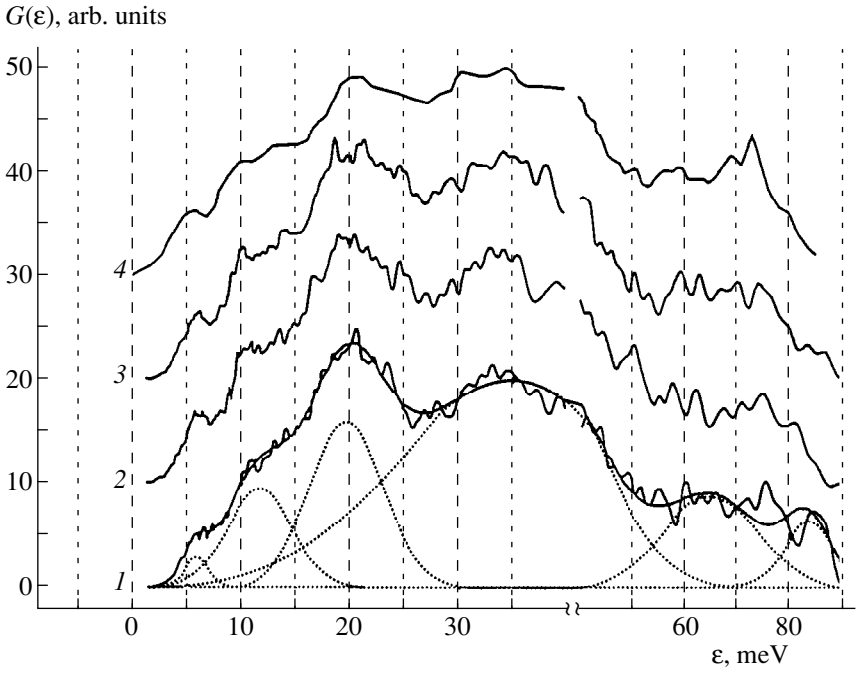

Fig. 2. Generalized frequency spectra $G(\varepsilon)$ of the $Bi_2Sr_2Ca_{1-x}Nd_xCu_2O_\delta$ solid solutions (x: *1*—0.75, *2*—0.25, *3*—0.1) obtained for this experiment, and (*4*) for $Bi_2Sr_2CaCu_2O_\delta$ [3]. Shown below spectrum *1* for $x = 0.75$ are the Gaussians of Eq. (1), whose superposition fits the spectrum obtained.

($\varepsilon < 50$ meV) part of these spectra was approximated by a superposition of Gaussians:

$$I = A/(w(\pi/2)^{1/2})\exp(-2(\varepsilon-\varepsilon_c)/w)^2, \qquad (1)$$

where I is the intensity; ε is the energy; and A, w, and ε_c are the parameters. After subtraction of the sum of the functions describing the low-frequency part, the functions of Eq. (1) were used to fit the high-frequency part of the spectra. The parameters of the Gaussians are listed in Table 2 for all samples, and the functions describing the generalized frequency spectrum of the $x = 0.75$ sample are plotted in Fig. 2.

2. RESULTS AND DISCUSSION

A comparison of our spectra with the results quoted in [3, 10–12] for the solid solutions of $Bi_2Sr_2Ca_{1-x}Y_xCu_2O_\delta$ and unsubstituted $Bi_2Sr_2CaCu_2O_8$ shows that peak *1* relates to vibrations of Bi atoms; peak *4*, to those of Cu and cations in the Ca sheet; peak *5* is a superposition of Cu vibrations and several types of oxygen vibrations; peak *6* is due to oxygen vibrations in the SrO sheet; and peak *7* originates from those in the CuO_2 sheet (peaks *6* and *7* were assigned according to [3]; the authors of [10] attributed the peak near 60 meV to O vibrations in the CuO_2 sheet and that near 75 meV, to those in the SrO sheet). While peaks *2* and *3* are assigned in [3] to Sr and Cu vibrations, experimental determination of the partial spectrum of Cu vibrations [12] in $Bi_{1.8}Pb_{0.2}Sr_2Ca_{1.1}Cu_{2.1}O_\delta$ made by the isotope contrast technique (^{63}Cu and ^{65}Cu) showed that copper vibrations lie higher in frequency (the two broad peaks near 20 and 35 meV). One can conclude that peaks *2* and *3* are related to the vibrations of cations (Sr, Nd, and Ca) in the SrO sheet, while the Cu vibrations contribute to peaks *4* and *5*. As seen from Table 2, as the Nd content increases from $x = 0.1$ to 0.75, peak *6* increases in integrated intensity compared to peak *7*, with the centroids of these peaks shifting toward higher frequencies. Substitution of Y for Ca in this structure was observed [3] to shift the 60-meV peak toward lower energies and the 75-meV peak, toward higher energies, with these changes happening due to a metal–semiconductor transition occurring with increasing Y concentration. Note that, in the case of Y being substituted for Ca, the observed shifts could be assigned to a change in the charge of the CuO_2 sheet, because both the copper reduction and the internal pressure are due to the difference between the ionic radii of Ca^{2+} and Y^{3+} [4] (1.26 and 1.10 Å, respectively [13]); but when Nd substitutes for Ca (the ionic radius of Nd^{3+} is 1.25 Å), there is practically a zero internal pressure effect and hence, the observed changes in the spectrum are accounted for by the change in the state of copper oxidation, which is responsible for the metal–semiconductor transition. A comparison of the changes in the phonon spectrum observed with increasing Y [3] and Nd contents suggests that the main reason for the change of the part of the spectrum associated with O vibrations in the CuO_2 sheet in the case of Y being substituted for Ca is

Table 2. Parameters of the Gaussians of Eq. (1) whose superposition fits the generalized frequency spectra obtained for the compounds under study

Composition	Parameters	1	2	3	4	5	6	7
$x = 0.1$	ε_c (meV)	6.25	9.91	12.7	19.4	34.8	59.0	74.5
	w (meV)	2.87	2.30	3.37	8.27	19.4	13.6	14.8
	A (a.u.)	20.7	23.3	27.0	164	512	120	162
$x = 0.25$	ε_c (meV)	5.93	10.8		19.0	34.3	53.2	70.4
	w (meV)	2.35	4.48		7.89	21.2	8.93	16.7
	A (a.u.)	14.2	51.2		153	557	50.7	176
$x = 0.75$	ε_c (meV)	5.93	11.7		19.7	34.8	65.2	83.3
	w (meV)	2.27	6.05		6.83	21.1	17.9	8.87
	A (a.u.)	8.38	71.5		136	522	196	71.1

Table 3. Estimates of the Sr, Ca, and Nd distributions over the sites of the alkaline-earth elements in the $Bi_2Sr_2Ca_{1-x}Nd_xCu_2O_\delta$ solid solutions [6]

Substitution	Sr(1)	Ca(1)	Nd(1)	Sr(2)	Ca(2)	Nd(2)
$x = 0.1$	1.66	0.26	0.08	0.34	0.64	0.02
$x = 0.75$	1.52	0.10	0.38	0.48	0.15	0.37

Note: $E(1)$ corresponds to the occupancy of Sr sites, $E(2)$ corresponds to that of Ca sites, and the data presented for the $x = 0.75$ composition were obtained based on the conclusion [6] that Nd is equally distributed over Ca and Sr sites at high Nd concentrations.

also the change in the copper oxidation state. The differences in the shift of the peak responsible for the O vibrations in the SrO sheet can be due to a sizable amount of Nd being present in this sheet, while in the case of Y substitution, it is observed to localize in the Ca sheet, which is caused by the difference between the Nd^{3+} and Y^{3+} ionic radii. The observed changes in the relative peak intensities can be discussed using the estimates of cation distribution over crystallographic sites made in [6] from Rietveld analysis (Table 3) and the values of σ/m for Ca, Sr, and Nd, namely, 0.073, 0.070, and 0.111 barn/amu, respectively. An increase in the Nd content gives rise to a certain decrease (from 16 to 14% for $x = 0.1$ and 0.75) in the relative integrated intensity of peak *4*. At the same time, according to a calculation, there is a slight increase in the scattering intensity in the Ca sheet (by 3.0% for $x = 0.1$ and 3.5% for $x = 0.75$), and one can conclude that the dominant contribution to the observed effect comes from the change in the state of copper oxidation.

A similar calculation made for peaks *2* and *3* yields an increase in integrated intensity with increasing Nd content (by 5.9% for $x = 0.1$, and 6.3% for $x = 0.75$); this change in intensity agrees with the one observed experimentally, although the latter is slightly larger in magnitude than the calculated value. As the copper oxidation state decreases without the occurrence of the metal–semiconductor transition (with the Nd content increasing from $x = 0.1$ to $x = 0.25$), the observed changes in the positions of the peaks associated with atomic vibrations in the CuO_2 sheet are seen to be opposite in sign to those obtained as x is increased from 0.1 to 0.75, which also suggests a change in the fraction of metallic bonding with variation of the carrier concentration in the CuO_2 sheet as the major reason for the observed changes in the vibration frequencies of the above atoms.

We also note with interest the change in the position of peaks *2* and *3*. With Y substituted for Ca, no change in the position of this peak was observed [3], whereas substitution of Nd for Ca in the $x = 0.1$ composition produced two peaks, which merged with increasing Nd content into one peak with a substantially larger width (Table 2). Fitting the sum of peaks *2* and *3* with the Gaussian of Eq. (1) for the $x = 0.1$ sample yields $\varepsilon_c = 11.2$ meV, $w = 4.18$ meV, and $A = 50.3$. The change in the vibrational frequency in the SrO sheet can be associated with the substantial replacement of Sr by Nd here, whereas substitution of an RE for an alkaline-earth element in the $Bi_2Sr_2CaCu_2O_8$ structure was found in most publications to be crystallographically selective (see, e.g., [5, 14]), with the actual location of the RE ion in the structure being determined on the basis of its ionic radius. The Rietveld refinement procedure applied to x-ray diffraction profiles [6] provided a qualitative estimate for the site distribution of Ca, Sr, and Nd ions in these solid solutions, with Nd found in considerable amounts in the SrO sheet. However, the applicability of x-ray diffraction for this purpose is very limited, because the atomic scattering factors for the

Sr atom and the 0.45Nd + 0.55Ca system are similar. The cation distributions (Table 3) obtained in [6] were used to make an approximate calculation of the vibration frequency ratio of cations in the SrO sheet for the Nd contents $x = 0.1$ (ω_1) and $x = 0.75$ (ω_2) from the expression

$$\omega_1/\omega_2 = ((Z_1\mu_2)/(Z_2\mu_1))^{1/2}, \quad (2)$$

where ω is the vibration frequency; $Z = Z(\mathrm{Nd})\alpha + Z(\mathrm{Sr})(1-\alpha)$, with $Z(\mathrm{Nd})$ and $Z(\mathrm{Sr})$ being the charges of the Nd^{3+} and Sr^{2+} ions, respectively; $\mu = \alpha m(\mathrm{Nd}) + \beta m(\mathrm{Ca}) + (1-\alpha-\beta)m(\mathrm{Sr})$; α is the fraction of Nd atoms occupying Sr sites; β is that of Ca atoms at the Sr sites; and $m(\mathrm{Nd})$, $m(\mathrm{Sr})$, and $m(\mathrm{Ca})$ are the atomic masses of Nd, Sr, and Ca, respectively. This expression was derived within the model of atoms vibrating in a rigid-crystal field under the assumption that the interatomic interaction force in a predominantly ionic crystal is proportional to the average cation charge ($(1-\alpha-\beta)Sr^{2+} + \beta Ca^{2+} + \alpha Nd^{3+}$) at a constant anion charge (O^{2-}). For $x_1 = 0.1$ and $x_2 = 0.75$, the ω_1/ω_2 ratio was calculated to be 0.967, while the value extracted from the $G(\varepsilon)$ spectra obtained is 0.951, which, considering the inaccuracies present in both the calculational model employed and the Nd distribution data, can be regarded as a satisfactory agreement in support of the assumption that a substantial fraction of Nd is present in the SrO sheet.

To sum up, phonon spectra of the $Bi_2Sr_2Ca_{1-x}Nd_xCu_2O_\delta$ solid solutions have been measured by inelastic neutron scattering.

The neutron diffraction data were found not to contradict the assumption that a considerable fraction of the Nd introduced in large concentrations in $Bi_2Sr_2CaCu_2O_8$ occupies Sr sites.

It has been shown that the part of the phonon spectrum associated with Cu–O vibrations ($\varepsilon \geq 50$ meV) reveals a shift toward higher frequencies with increasing Nd content accompanied by an increase in the spectrum cutoff (from 74 to 85 meV for the Nd content per formula unit increasing from 0.1 to 0.75) because of the ionic radii of Ca^{2+} and Nd^{3+} being similar. The observed changes may be considered as being due to a change in the copper oxidation state rather than resulting from the internal pressure effect. Because there was a similar change in the high-frequency part of the spectrum in the case of Y substituted for Ca [3], the conclusion was drawn that the observed changes are also accounted for here by a change in the state of copper oxidation.

ACKNOWLEDGMENTS

The authors are indebted to A. V. Puchkov (Physics and Power Institute, Russia) for preliminary calculations made in the course of preparation of the experiment and to O. V. Sobolev (Physics and Power Institute, Russia) for assistance in performing the neutron diffraction measurements.

Support of the Russian State Program "Topical Problems in Condensed Matter Physics" in the field "Neutron Studies of Matter" is gratefully acknowledged.

REFERENCES

1. A. Manthiram and J. B. Goodenough, Appl. Phys. Lett. **53**, 420 (1988).
2. N. A. Babushkina, M. V. Dobrotvorskaya, N. A. Kasatkina, *et al.*, Physica C (Amsterdam) **197**, 299 (1992).
3. B. Renker, F. Gompf, D. Ewert, *et al.*, Z. Phys. B **77**, 65 (1989).
4. M. Kakihana, M. Osada, M. Kall, *et al.*, Phys. Rev. B **53**, 11 796 (1996).
5. N. G. Naumov, P. N. Samoĭlov, and V. E. Fedorov, Zh. Neorg. Khim. **37**, 1203 (1992).
6. A. V. Knotko, A. V. Garshev, A. G. Veresov, *et al.*, in *Materials of MRS 1998 Fall Meeting, Boston, 1998*, p. 357.
7. V. A. Parfenov, P. S. Klemyshev, I. G. Morozov, and A. F. Pavlov, in *Proceedings of the Symposium on Neutron Inelastic Scattering, 1977* (IAEA, Vienna, 1978), Vol. 1, p. 81.
8. V. F. Turchin, *Slow Neutrons* (Atomizdat, Moscow, 1963; Israel Program for Scientific Translations, Jerusalem, 1965).
9. A. Sjolandar, Ark. Fys. **14**, 315 (1958).
10. D. Shimada, N. Tsuda, U. Paltzer, and F. W. de Wette, Physica C (Amsterdam) **298**, 195 (1998).
11. P. P. Parshin, M. G. Zemlyanov, and A. V. Irodova, Fiz. Nizk. Temp. **22** (5), 564 (1996) [Low Temp. Phys. **22**, 435 (1996)].
12. P. P. Parshin, M. G. Zemlyanov, A. V. Irodova, *et al.*, Fiz. Tverd. Tela (St. Petersburg) **38** (6), 1665 (1996) [Phys. Solid State **38**, 919 (1996)].
13. R. D. Shannon and C. T. Prewitt, Acta Crystallogr. Sect. B **25**, 935 (1969).
14. J. Fujikami, M. Akamatsu, R. Yoshizaki, *et al.*, Physica C (Amsterdam) **174**, 359 (1991).

Translated by G. Skrebtsov

Physics of the Solid State, Vol. 42, No. 9, 2000, pp. 1584–1589. Translated from Fizika Tverdogo Tela, Vol. 42, No. 9, 2000, pp. 1542–1546.

METALS AND SUPERCONDUCTORS

Inverted Forerunning and Wake of the Solitary Oscillating Abrikosov Vortex in a Magnetic Superconductor

A. I. Lomtev

Donetsk Physicotechnical Institute, National Academy of Sciences of Ukraine, Donetsk, 340114 Ukraine

e-mail: lomtev@kinetic.ac.donetsk.ua

Received November 18, 1999; in final form, February 25, 2000

Abstract—The magnetic structure of a solitary oscillating Abrikosov vortex in a magnetic superconductor is investigated. It is shown that the process of the vortex motion in the presence of the magnetic subsystem substantially modifies the shape of the vortex, with the result that there appears an "inverted forerunning" in front of the vortex and an "inverted wake" behind it that is far from its center. *© 2000 MAIK "Nauka/Interperiodica".*

1. There is a wide range of magnetic superconductors exhibiting new unique properties [1–3]. In addition to triple compounds [4], magnetism and superconductivity were found to coexist in HTSC compounds such as REBaCuO, RECuO, and others, where RE signifies a rare-earth ion. A strong antiferromagnetic correlation of copper spins in CuO_2 planes in the superconducting state is one of the main features of HTSC materials [5].

An external magnetic field penetrates into magnetic superconductors of the second kind in the form of Abrikosov vortices [6] and causes the magnetic-subsystem magnetization around the normal core of a vortex over distances on the order of at least the London field-penetration depth λ. A sufficiently large alternating current flowing through a superconductor in the mixed state provokes oscillations of Abrikosov vortices [7]. Moreover, microwave radiation of a sufficiently large power can also cause harmonic oscillations of a set of Abrikosov vortices.

In [8], the magnetic structure of an isolated Abrikosov vortex moving slowly and uniformly in a bulk magnetic superconductor was investigated and the phenomenon of the "inverted wake" far behind the vortex was predicted.

It is of interest to examine the magnetic field distribution of a vortex for other kinds of motion that differ from slow and uniform motions. We note that an analysis of the magnetic structure of a solitary Abrikosov vortex that executes harmonic oscillations in a magnetic superconductor had not yet performed.

In this paper, we investigate the magnetic field of an oscillating solitary Abrikosov vortex in a bulk magnetic superconductor, whose thickness d_0 in the direction of the vortex magnetic field is much larger than the London penetration depth λ It is shown that, within the thickness of the superconductor (far from its surface), the process of oscillations in the presence of the magnetic subsystem substantially deforms the vortex, causing new effects—the "inverted forerunning" in front of the vortex and (predicted in [8]) the "inverted wake" behind it that is far from its center.

We note the essential difference in the behavior of the magnetic field of the Abrikosov vortex in uniform motion [8] and in harmonic oscillations. In the first case, the field distribution, featured with the inverted wake, is stationary and does not depend on time, while in the second case the structure of both the inverted forerunning and the inverted wake is nonstationary and its variations during a period of oscillations are essential.

2. We will assume the interaction between conduction electrons and the magnetic subsystem to be of an electromagnetic (dipole) nature and neglect the spin–spin exchange interaction. In the London approximation, where the condition $\lambda \gg \xi$ is fulfilled (ξ is the correlation length), the structure of the vortex core can be ignored. We will consider the interval of magnetic fields $H_{c1} < B \ll H_{c2}$, where H_{c1} and H_{c2} are the lower and upper critical fields of the superconductor, respectively. Therefore, considering isolated vortices, we actually assume that, in a very sparse mixed state, the distance between them is subject to the inequality $d \gg \lambda$.

As in [9, 10], in order to describe an isolated vortex, we will start from the Maxwell equations for the electric field $\mathbf{E}(\mathbf{r}, t)$ and magnetic induction $\mathbf{B}(\mathbf{r}, t) = \operatorname{curl} \mathbf{A}(\mathbf{r}, t)$ [$\mathbf{A}(\mathbf{r}, t)$ is the vector potential]. The magnetic induction equals the sum of the magnetic field $\mathbf{H}(\mathbf{r}, t)$ produced by the persistent current $\mathbf{j}(\mathbf{r}, t)$ and

1063-7834/00/4209-1584$20.00

of the magnetization $\mathbf{M}(\mathbf{r}, t)$,

$$\begin{aligned} \mathrm{curl}\mathbf{B}(\mathbf{r}, t) &= 4\pi c^{-1}\mathbf{j}(\mathbf{r}, t) \\ &+ 4\pi\mathrm{curl}\mathbf{M}(\mathbf{r}, t) + c^{-1}\partial\mathbf{E}(\mathbf{r}, t)/\partial t, \\ \mathrm{curl}\mathbf{E}(\mathbf{r}, t) &= -c^{1}\partial\mathbf{B}(\mathbf{r}, t)/\partial t. \end{aligned} \quad (1)$$

A relation between the current, potential, and the phase of the order parameter $\Theta(\mathbf{r}, t)$ (with London's gauge of the potential $\mathrm{div}\mathbf{A}(\mathbf{r}, t) = 0$) is given by the expression [9]

$$\mathbf{j}(\mathbf{r}, t) = (c/4\pi\lambda^2)[(\Phi_0/2\pi)\nabla\Theta(\mathbf{r}, t) - \mathbf{A}(\mathbf{r}, t)], \quad (2)$$

where Φ_0 is the magnetic flux quantum. The phase of the order parameter is subject to the condition

$$\mathrm{curl}\nabla\Theta(\mathbf{r}, t) = 2\pi\mathbf{z}_0\delta(\mathbf{r} - \mathbf{r}_0(t)), \quad (3)$$

where $\mathbf{z}_0$ is the unit vector (along the Z axis) of the magnetic field of the vortex located at the point $\mathbf{r}_0(t)$ and $\delta(\mathbf{r})$ is the Dirac delta function. Using Eq. (2) for the current and Eq. (3) for the source and eliminating the electric field $\mathbf{E}(\mathbf{r}, t)$ between Eqs. (1), we obtain the specific equation describing the distribution of the magnetic field of an isolated Abrikosov vortex in a magnetic superconductor

$$\begin{aligned} \lambda^2\mathrm{curl}\,\mathrm{curl}\mathbf{H}(\mathbf{r}, t) + (\lambda^2 c^{-2}\partial^2/\partial t^2 + 1)\mathbf{B}(\mathbf{r}, t) \\ = \mathbf{z}_0\Phi_0\delta(\mathbf{r} - \mathbf{a}_0\sin\Omega_0 t), \end{aligned} \quad (4)$$

where, for the oscillating vortex, we have taken $\mathbf{r}_0(t) = \mathbf{a}_0\sin\Omega_0 t$, with $\mathbf{a}_0$ and Ω_0 being the amplitude and frequency of the harmonic oscillations, respectively.

The only difference in Eq. (4) from the corresponding equation for an isotropic nonmagnetic superconductor [11, 12] lies in the substitution $\mathbf{B}(\mathbf{r}, t) \longrightarrow \mathbf{B}(\mathbf{r}, t) - 4\pi\mathbf{M}(\mathbf{r}, t) = \mathbf{H}(\mathbf{r}, t)$ for the curl argument. We note that, for fields of the class $\mathbf{H}(\mathbf{r}, t) = \mathbf{z}_0 H(x, y, t)$, not only does $\mathrm{div}\mathbf{B}(\mathbf{r}, t) = 0$, but $\mathrm{div}\mathbf{H}(\mathbf{r}, t) = 0$.

In the kinematic approach used here, it is assumed that, for the Abrikosov vortex, the dynamic equations have already been solved, and we deal with the class of solutions that describe the forced harmonic oscillations of the isolated vortex filament about the equilibrium position.

As it was first noted in [13], the vortex motion is caused by the Lorentz force exerted by the superfluid component of the current. When studying the dynamics of the moving vortex, account must be taken of dissipative processes such as (1) the mechanism of the Joule heating of normal excitations near the filament center [7]; (2) the mechanism associated with nonuniformity of the order parameter of the vortex, namely, the mechanism of the parameter relaxation, when the vortex passes a given point in the superconductor [7]; and (3) the magnetic mechanism of dissipation due to magnetic polarization of the medium by the field of the moving vortex [14].

In real superconductors, the situation is much more complex due to pinning forces; therefore, pure harmonic oscillations of the very sparse vortex lattice would be realized only at a sufficiently large value of the alternating (oscillating) current flowing through the specimen, when the influence of pinning centers can be neglected.

In the very sparse mixed state, the density of vortices is small and the spacing between them, as we have already noted, satisfies the inequality $d \gg \lambda$. In this case, there is no transport current in the bulk of the superconductor (due to the Meissner effect), and all current flows only through skin layers near the boundaries. It is in these skin layers that the vortex experiences the Lorentz force. Because of the continuity of the vortex filament along the Z axis far from the boundaries in the bulk of the superconductor, the vortex will oscillate harmonically and its motion can be considered as two dimensional.

It should be noted that in principle, the vortex deformation in the mixed state of the superconductor is also of importance [15]. However, in the very sparse mixed state under consideration, this deformation is small because of a low vortex concentration and it will have only slight effects, both qualitative and quantitative, on the phenomena of the inverted forerunning and the wake of the oscillating Abrikosov vortex.

3. Taking the two-dimensional Fourier transform in the XY-plane, orthogonal to the vortex, Eq. (4) for the magnetic field is reduced to the form

$$\begin{aligned} k^2\lambda^2\mathbf{H}(\mathbf{k}, t) + (\lambda^2 c^{-2}\partial^2/\partial t^2 + 1)\mathbf{B}(\mathbf{k}, t) \\ = \mathbf{z}_0\Phi_0\exp(-i\mathbf{k}\mathbf{a}_0\sin\Omega_0 t), \end{aligned} \quad (5)$$

where $\mathbf{k} = (k_x, k_y)$ and $\mathbf{k} = (k_x^2 + k_y^2)^{1/2}$.

Using the expansion of the exponential function in terms of the Bessel functions of the integer order $J_n(x)$ [16]

$$\begin{aligned} \exp(-i\mathbf{k}\mathbf{a}_0\sin\Omega_0 t) &= \cos(\mathbf{k}\mathbf{a}_0\sin\Omega_0 t) - i\sin(\mathbf{k}\mathbf{a}_0\Omega_0 t) \\ &= J_0(\mathbf{k}\mathbf{a}_0) + 2\sum_{m=1}^{\infty} J_{2m}(\mathbf{k}\mathbf{a}_0)\cos(2m\Omega_0 t) \\ &- i2\sum_{m=0}^{\infty} J_{2m+1}(\mathbf{k}\mathbf{a}_0)\sin[(2m+1)\Omega_0 t] \end{aligned} \quad (6)$$

and taking the Fourier transform in time, Eq. (5) is reduced to an algebraic equation which has the following solution:

$$\mathbf{H}(\mathbf{r}, \omega) = \frac{\mathbf{z}_0\Phi_0 I(\mathbf{k}, \omega)}{k^2\lambda^2 + (1 - \lambda^2\omega^2 c^{-2})[1 + 4\pi\chi(\mathbf{k}, \omega)]}, \quad (7)$$

where the source spectral density has the form

$$I(\mathbf{k}, \omega) = 2\pi\Big\{J_0(\mathbf{ka}_0)\delta(\omega) + \sum_{m=1}^{\infty} J_{2m}(\mathbf{ka}_0) \times [\delta(\omega + 2m\Omega_0) + \delta(\omega - 2m\Omega_0)] - \sum_{m=0}^{\infty} J_{2m+1}(\mathbf{ka}_0) \times [\delta(\omega + (2m+1)\Omega_0) - \delta(\omega - (2m+1)\Omega_0)]\Big\} \quad (8)$$

and the magnetic susceptibility $\chi(\mathbf{k}, \omega)$ is defined by the standard equation

$$\mathbf{B}(\mathbf{k}, \omega) = [1 + 4\pi\chi(\mathbf{k}, \omega)]\mathbf{H}(\mathbf{k}, \omega). \quad (9)$$

Since $\lambda \gg a$ (a is the lattice constant of the crystal), it is natural to describe the magnetic subsystem in the hydrodynamic approximation. For the paramagnetic temperature region, we have the following expression for the susceptibility [17]:

$$\chi(\mathbf{k}, \omega) = \chi_1(\mathbf{k}, \omega) + i\chi_2(\mathbf{k}, \omega) = i\frac{\chi_0 Dk^2}{\omega + iDk^2}, \quad (10)$$

where χ_0 is the static magnetic susceptibility and the spin diffusion coefficient for two-dimensional Heisenberg magnets is equal to $D = (1/3)(2\pi)^{1/2}Ja^2[s(s+1)]^{1/2}$ (J is the intralayer exchange parameter, s is the spin) [18].

In the strict sense, a superconducting current screens the long-wavelength part of the exchange and electromagnetic interactions, renormalizing the parameters of the magnetic subsystem [19]. However, we will not take this circumstance into account, restricting our consideration to the paramagnetic temperature interval and making only order-of-magnitude estimates of the phenomenon.

From Eqs. (7) and (8), taking the inverse Fourier transform in frequency, we find the time dependence of the Fourier components of the vortex magnetic field:

$$\mathbf{H}(\mathbf{q}, t) = \mathbf{H}_0(\mathbf{q}, t) + \mathbf{H}_1(\mathbf{q}, t),$$

$$\mathbf{H}_0(\mathbf{q}, t) = \mathbf{z}_0\Phi_0(1 + 4\pi\chi_0 + q^2)^{-1} \times \exp(-iq_x a_0\lambda^{-1}\sin\Omega\tau), \quad (11)$$

$$\mathbf{H}_1(\mathbf{q}, t) = \mathbf{H}_{1\mathrm{Re}}(\mathbf{q}, t) - i\mathbf{H}_{1\mathrm{Im}}(\mathbf{q}, t), \quad (12)$$

$$\mathbf{H}_{1\mathrm{Re}}(\mathbf{q}, t) = 2\mathbf{z}_0\Phi_0\sum_{m=1}^{\infty} J_{2m}(q_x a_0/\lambda) \times \left[\frac{F_1(\mathbf{q}, \tau, m)}{F_2(\mathbf{q}, m)} - \frac{\cos(2m\Omega\tau)}{1 + 4\pi\chi_0 + q^2}\right], \quad (13)$$

$$\mathbf{H}_{1\mathrm{Im}}(\mathbf{q}, t) = 2\mathbf{z}_0\Phi_0\sum_{m=1}^{\infty} J_{2m+1}(q_x a_0/\lambda) \times \left[\frac{F_3(\mathbf{q}, \tau, m)}{F_4(\mathbf{q}, m)} - \frac{\sin((2m+1)\Omega\tau)}{1 + 4\pi\chi_0 + q^2}\right], \quad (14)$$

where the functions F_1, F_2, F_3, and F_4 have the form

$$\mathbf{F}_1(\mathbf{q}, \tau, m) = \{[1 - \beta(2m\Omega)^2] \times [1 + 4\pi\chi_1(\mathbf{q}, 2m\Omega)] + q^2\}\cos(2m\Omega\tau) - 4\pi[1 - \beta(2m\Omega)^2]\chi_2(\mathbf{q}, 2m\Omega)\sin(2m\Omega\tau),$$

$$\mathbf{F}_2(\mathbf{q}, m) = \{[1 - \beta(2m\Omega)^2][1 + 4\pi\chi_1(\mathbf{q}, 2m\Omega)] + q^2\}^2 + 4\pi[1 - \beta(2m\Omega)^2]\chi_2(\mathbf{q}, 2m\Omega)\}^2,$$

$$\mathbf{F}_3(\mathbf{q}, \tau, m) = \{[1 - \beta(2m+1)^2\Omega^2] \times [1 + 4\pi\chi_1(\mathbf{q}, (2m+1)\Omega)] + q^2\}\sin((2m+1)\Omega\tau) + 4\pi[1 - \beta(2m+1)^2\Omega^2]\chi_2(\mathbf{q}, (2m+1)\Omega) \times \cos((2m+1)\Omega\tau), \quad (15)$$

$$\mathbf{F}_4(\mathbf{q}, m) = \{[1 - \beta(2m+1)^2\Omega^2] \times [1 + 4\pi\chi_1(\mathbf{q}, (2m+1)\Omega)] + q^2\}^2 + \{4\pi[1 - \beta(2m+1)^2\Omega^2]\chi_2(\mathbf{q}, (2m+1)\Omega)\}^2.$$

Here, the dimensionless quantities $q = \lambda k$, $\Omega = \Omega_0\lambda/v_0$, $\tau = tv_0/\lambda$, and $\beta = (v_0/c)^2$ have been introduced, with the $v_0 = D/\lambda$ being the characteristic velocity; the X axis is taken as the direction of the vortex oscillations.

Using Eqs. (11)–(15), we obtain an integral representation for the distribution of the magnetic field of the oscillating solitary Abrikosov vortex in the magnetic superconductor

$$\mathbf{H}(\mathbf{r}, t) = \frac{\mathbf{z}_0\Phi_0}{2\pi\lambda^2}K_0(\sqrt{(x - a_0\sin\Omega_0 t)^2 + y^2}/\lambda_m) + \mathbf{H}_1(\mathbf{r}, t), \quad (16)$$

where K_0 is the MacDonald function of the zeroth order, $\lambda_m = \lambda/\sqrt{(1 + 4\pi\chi_0)}$ is the field penetration depth renormalized by the magnetic subsystem, and $\mathbf{H}_1(\mathbf{r}, t)$ is given by the expression

$$\mathbf{H}_1(\mathbf{r}, t) = \mathbf{H}_{1S}(\mathbf{r}, t) + \mathbf{H}_{1A}(\mathbf{r}, t)$$

$$= 4\int_0^\infty\int_0^\infty \frac{dq_x dq_y}{(2\pi\lambda)^2}\cos(q_x x/\lambda)\cos(q_y y/\lambda)\mathbf{H}_{1\mathrm{Re}}(\mathbf{q}, t) \quad (17)$$

$$+ 4\int_0^\infty\int_0^\infty \frac{dq_x dq_y}{(2\pi\lambda)^2}\sin(q_x x/\lambda)\cos(q_y y/\lambda)\mathbf{H}_{1\mathrm{Im}}(\mathbf{q}, t).$$

According to Eqs. (16) and (17), the dominant positive contribution to the magnetic field of the oscillating Abrikosov vortex is determined by the MacDonald function K_0 centered at the variable point $x_C(t) = a_0\sin\Omega_0 t$. However, the entire information about the inverted forerunning and wake is contained in the integrals of Eq. (17) $\mathbf{H}_{1S}(\mathbf{r}, t)$ and $\mathbf{H}_{1A}(\mathbf{r}, t)$, which are centered at the origin of the XY plane. The function $\mathbf{H}_{1S}(\mathbf{r}, t)$ is symmetrical with respect to both variables, x and y, while the function $\mathbf{H}_{1A}(\mathbf{r}, t)$ is symmetrical with respect to y and antisymmetrical with respect to x. We are now in a position to elucidate how the inverted regions of the magnetic field are formed on the X axis (the direction of oscillations). This effect is most pronounced at the time points $t_n \approx \pm n\pi\Omega_0^{-1}$ ($n = 0, 1, \ldots$), when the centering point $x_C(t_n)$ of the function K_0 is close to the origin. At these instants, the well-localized function K_0, being positive, falls off to zero rapidly. At the same time, the functions $\mathbf{H}_{1S}(\mathbf{r}, t)$ and $\mathbf{H}_{1A}(\mathbf{r}, t)$, being less localized than the function K_0, can have both positive and negative values. The inverted forerunning is the superposition of the negative minimum of $\mathbf{H}_{1S}(\mathbf{r}, t)$ and of the positive maximum of $\mathbf{H}_{1A}(\mathbf{r}, t)$, whereas the inverted wake is the superposition of two negative minima of these functions.

4. The typical value of χ_0 for antiferromagnets is 10^{-3}–10^{-5}. The characteristic velocity $v_0 \propto Jsa(a/\lambda)$ is $(\lambda/a) \propto (10^2$–$10^3)$ times lower than the spin-wave velocity v_s. For CuO_2 layers, because of strong intralayer exchange, the velocity of spin waves is rather high, $v_s \propto (0.5$–$1.3) \times 10^7$ cm/s [3], i.e., $v_0 \propto 10^4$–10^5 cm/s. We note that the experimentally observed maximal velocity of vortices is significantly lower, $v_A \approx 6.6 \times 10^3$ cm/s [20]. The maximum velocity of vortex oscillations $V_0 = a_0\Omega_0$ is much lower than the relaxation rate of the magnetic subsystem, which is of the order of v_s. Consequently, in our case, the magnetic subsystem adjusts to the field of the oscillating vortex instantaneously for all practical purposes, with the result that the vortex field is renormalized because of time and spatial dispersion of the magnetic susceptibility, which leads to new phenomena—the inverted foregoing in front of the vortex and the inverted wake behind it far apart from its center.

Let us list the main features of the magnetic field of the oscillating solitary Abrikosov vortex following from the analytical and numerical calculations.

(1) At $a_0 = 0$ or $\Omega_0 = 0$, the field coincides with the standard one with an accuracy to the "magnetic" renormalization of the penetration depth.

(2) At $\chi_0 = 0$, the field is similar to that of the oscillating isolated vortex in a nonmagnetic superconductor, where there is no forerunning or wake.

(3) As a rule, the vortex field is asymmetrical relative to the plane orthogonal to the direction of oscillations.

(4) The oscillating vortex has a shape flattened along the Y axis.

(5) In the direction of the axis of oscillations X, there is an inverted forerunning in front of the vortex and an inverted wake behind it. Inside them, $H < 0$; i.e., the magnetic field is oppositely directed to the total magnetic flux in the vortex $\mathbf{z}_0\Phi_0$.

(6) Inside the regions where $H < 0$, the field reaches its minimal values.

(7) The value and the structure of the magnetic field of the vortex as a whole and, particularly, of its inverted forerunning and inverted wake vary markedly in time during a period of oscillations.

(8) The stationary distribution of the vortex field averaged over a period essentially differs from the standard one and is given by the integral

$$\mathbf{H}_{\mathrm{mean}}(x, y) = \frac{\mathbf{z}_0\Phi_0}{2(\pi\lambda)^2} \times \int_{-\pi/2}^{\pi/2} d\varphi K_0\left(\sqrt{(x - a_0\sin\varphi)^2 + y^2}/\lambda_m\right). \quad (18)$$

5. The numerical analysis showed that, at values of $\chi_0 \propto 10^{-3}$–10^{-4} (which is comparable to the susceptibility of the copper subsystem of HTSC materials), the frequency $\Omega \propto 10^3$, amplitude $a_0 = 5\lambda$, and the parameter $\beta \propto 10^{-10}$–10^{-12}; the minima of the inverted-forerunning and inverted-wake fields are symmetric about the vortex center and are separated from it by the distance $r_{01,2} \approx 10\lambda$ at $\tau_0 = \pi$, with $H_{\min 1,2} = H(r_{01,2}, \tau_0)2\pi\lambda^2/\Phi_0 \propto 10^{-5}$–$10^{-6}$. For $\chi_0 \propto 10^{-2}$ (such values of the magnetic susceptibility are typical of triple compounds, as well as HTSC ones containing rare-earth ions, near the temperature of the magnetic ordering $T_N \propto 1$ K), $\Omega = 1$, $a_0 = 5\lambda$, and $\tau = \pi$; the distribution of the reduced instantaneous magnetic vortex field $H = 2\pi\lambda^2 H(x, 0, \tau = \pi)/\Phi_0$ along the X axis (with respect to the variable x/λ) has two minima at $y = 0$: at $r_{01} \propto 7\lambda$, we have the field $H_{\min 1} \propto -2 \times 10^{-3}$, which corresponds to the inverted forerunning and, at $r_{02} \propto 5\lambda$, we have $H_{\min 2} \propto -10^{-2}$, which corresponds to the inverted wake, as shown in Fig.1. We note that, at $\Omega_0\tau = \Omega\tau = \pi$, the vortex moves to the left, and the maximum of its field

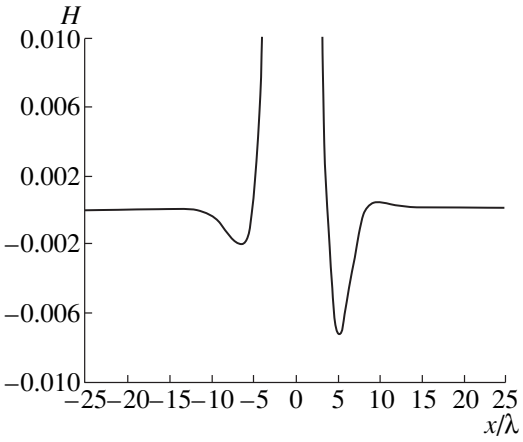

Fig. 1. Distribution of the reduced instantaneous magnetic vortex field $H = 2\pi\lambda^2 H(x, 0, \tau = \pi)/\Phi_0$ along the X axis with respect to the variable x/λ at $y = 0$, with the minima corresponding to the inverted forerunning on the left and to the inverted wake on the right of its center.

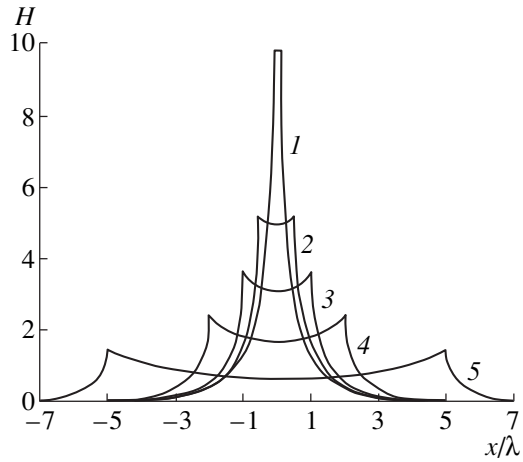

Fig. 2. Distribution of the reduced magnetic vortex field $H = 2(\pi\lambda)^2 H_{\text{mean}}(x, 0)/\Phi_0$, averaged over a period of oscillations, along the X axis with respect to the variable x/λ at $y = 0$ for five values of the amplitude of oscillations $a_0 = 0.1\lambda$ (*1*); 0.5λ (*2*); λ (*3*); 2λ (*4*); and 5λ (*5*).

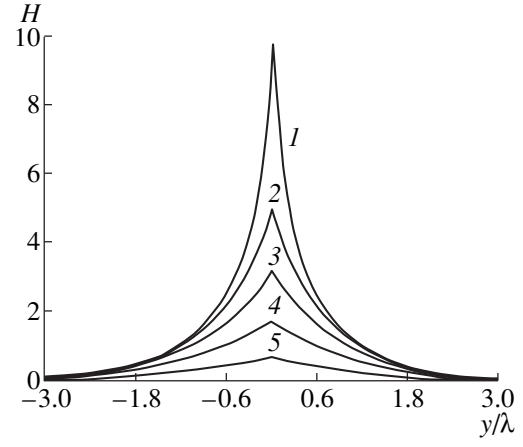

Fig. 3. Distribution of the reduced magnetic vortex field $H = 2(\pi\lambda)^2 H_{\text{mean}}(0, y)/\Phi_0$, averaged over a period of oscillations, along Y axis with respect to the variable y/λ at $x = 0$ for the same values of the amplitude of oscillations, as in Fig. 2.

passes the point $x = 0$ at this instant. The maximum dimensionless field is of the order of 40 at this point.

According to Eq. (18), the distribution of the vortex magnetic field, averaged over a period of oscillations, depends on the amplitude a_0; it is positive everywhere, and essentially differs from the standard distribution of the magnetic field of the motionless Abrikosov vortex. Figures 2 and 3 show the stationary distribution of the reduced magnetic vortex field $\mathbf{H}_{\text{mean}}(x, 0)2(\pi\lambda)^2/\Phi_0$ averaged over a period of oscillations along the X axis (with respect to the variable x/λ) at $y = 0$, and $\mathbf{H}_{\text{mean}}(0, y)2(\pi\lambda)^2/\Phi_0$ along the Y axis (with respect to the variable y/λ) at $x = 0$, respectively, for five different values of the amplitude of oscillations.

As is well known [21, 22], the inversion of the longitudinal component of the magnetic field results in the attraction of the vortices to one another. Therefore, because of the new phenomena of the inverted forerunning and inverted wake, the oscillating vortices will be aligned in chains, which can substantially affect the operation of the memory devices based on the Abrikosov vortices.

ACKNOWLEDGMENTS

The author is grateful to Yu.E. Kuzovlev for useful advice and help in numerical calculations and to A.I. D'yachenko, V.N. Krivoruchko, and Yu.V. Medvedev for critiques and encouragement.

REFERENCES

1. A. I. Buzdin, L. N. Bulaevskiĭ, M. L. Kulich, and S. V. Panyukov, Usp. Fiz. Nauk **144**, 597 (1984) [Sov. Phys. Usp. **27**, 927 (1984)].
2. A. I. Buzdin and L. N. Bulaevskiĭ, Usp. Fiz. Nauk **149**, 45 (1986) [Sov. Phys. Usp. **29**, 412 (1986)].
3. Yu. A. Izyumov, N. M. Plakida, and Yu. N. Skryabin, Usp. Fiz. Nauk **159**, 621 (1989) [Sov. Phys. Usp. **32**, 1060 (1989)].
4. *Superconductivity in Ternary Compounds*, Vol. 2: *Superconductivity and Magnetism*, ed. by E. Fisher and M. Maple (Springer, Heidelberg, 1982; Mir, Moscow, 1985).
5. *Physical Properties of High Temperature Superconductors*, ed. by D. M. Ginzberg (World Scientific, Singapore, 1989; Mir, Moscow, 1990), Chaps. 4, 6.
6. A. A. Abrikosov, Zh. Éksp. Teor. Fiz. **32**, 1442 (1957) [Sov. Phys. JETP **5**, 1174 (1957)].
7. L. P. Gor'kov and N. B. Kopnin, Usp. Fiz. Nauk **116**, 413 (1975) [Sov. Phys. Usp. **18**, 496 (1975)].
8. V. N. Krivoruchko, Pis'ma Zh. Éksp. Teor. Fiz. **55**, 285 (1992) [JETP Lett. **55**, 284 (1992)].
9. E. M. Lifshitz and L. P. Pitaevskiĭ, in *Course of Theoretical Physics*, Vol. 5: *Statistical Physics* (Nauka, Moscow, 1978; Pergamon, New York, 1980), Part 2, Chap. 5.
10. H. Umezawa, H. Matsumoto, and M. Tachiki, in *Thermo Field Dynamics and Condensed States* (North-Holland, Amsterdam, 1982; Mir, Moscow, 1985), Chap. 11.

11. P. G. de Gennes, in *Superconductivity of Metals and Alloys* (Benjamin, New York, 1966; Mir, Moscow, 1968), Chap. 3.
12. M. Tinkham, in *Introduction to Superconductivity* (McGraw-Hill, New York, 1975; Atomizdat, Moscow, 1980), Chap. 5.
13. P. G. de Gennes and J. Matrikon, Rev. Mod. Phys. **36**, 45 (1964).
14. V. N. Krivoruchko and Yu. A. Dimashko, Sverkhprovodimost': Fiz., Khim., Tekh. **5**, 967 (1992).
15. E. B. Sonin, A. K. Tagantsev, and K. B. Traito, Phys. Rev. B **46**, 5830 (1992).
16. *Handbook of Mathematical Functions*, ed. by M. Abramowitz and I. A. Stegun (Dover, New York, 1971; Nauka, Moscow, 1979).
17. B. I. Halperin and P. C. Hohenberg, Phys. Rev. **188**, 898 (1969).
18. P. M. Richards and M. B. Salamon, Phys. Rev. B **9**, 32 (1974).
19. A. I. Buzdin, Pis'ma Zh. Éksp. Teor. Fiz. **40**, 193 (1984) [JETP Lett. **40**, 956 (1984)].
20. A. N. Samus', A. F. Popkov, V. I. Makhov, *et al.*, Sverkhprovodimost': Fiz., Khim., Tekh. **4**, 1324 (1991).
21. A. M. Grishin, A. Yu. Martynovich, and S. V. Yampol'skiĭ, Zh. Éksp. Teor. Fiz. **97**, 1930 (1990) [Sov. Phys. JETP **70**, 1089 (1990)].
22. A. I. Buzdin and A. Yu. Simonov, Zh. Éksp. Teor. Fiz. **98**, 2074 (1990) [Sov. Phys. JETP **71**, 1165 (1990)].

Translated by N. Ostrovskaya

Physics of the Solid State, Vol. 42, No. 9, 2000, pp. 1590–1595. Translated from Fizika Tverdogo Tela, Vol. 42, No. 9, 2000, pp. 1547–1552.

METALS AND SUPERCONDUCTORS

Substitutions in the Nd/Ba Cation Subsystem in Thin Films of the $NdBa_2Cu_3O_y$ High-Temperature Superconductor

P. B. Mozhaev*, **, F. V. Komissinskiĭ*, **, Z. G. Ivanov*, and G. A. Ovsyannikov**

**Chalmers Technological University, Gothenburg, S-41296 Sweden*

***Institute of Radio Engineering and Electronics, Russian Academy of Sciences, Mokhovaya ul. 11, Moscow, 103907 Russia*

e-mail: pbmozh@hitech.cplire.ru

Received February 28, 2000

Abstract—Thin films of the $Nd_{1+x}Ba_{2-x}Cu_3O_y$ high-T_c superconductor (NBCO) with different neodymium/barium ratios have been obtained by laser ablative cosputtering of targets with different elemental compositions. The films with excess neodymium ($x > 0$) had a low surface particle density and were rough, but their critical temperature decreased with increasing x. Conversely, barium-rich films ($x < 0$) exhibited independence of the superconducting properties of the film composition, with an appreciable number of particles observed on the surface. Substitution of Ba for Nd in NBCO thin films is apparently impeded, so that excess barium precipitates in the form of $(Ba,Cu)O_z$ particles. The structure and superconducting properties of NBCO reveal a strong dependence on the conditions of film saturation by oxygen. © *2000 MAIK "Nauka/Interperiodica".*

$NdBa_2Cu_3O_x$ (NBCO) is a metal-oxide high-temperature superconductor (HTSC) with a $ReBa_2Cu_3O_x$ structure (ReBCO), where Re stands for a rare-earth element. This material has recently become a subject of intensive studies as a substitute for the most widespread compound of this structure, $YBa_2Cu_3O_x$ (YBCO). The critical temperature of NBCO is the highest recorded among materials of the ReBCO structure and is 98 K [1], with a value of 94 K having been reached in thin films [2].

An essential role in the formation of the structure in ReBCO materials is played by the ionic radius of the rare-earth element, whose magnitude determines the probability of Ba being replaced (ionic radius 0.142 nm) by a rare-earth element with the formation of a $Re_{1+x}Ba_{2-x}Cu_3O_y$ solid solution or the exchange of Ba and Re atoms giving rise to disorder in the Re/Ba cation subsystem [3]. The yttrium ion, which has a relatively small ionic radius (0.089 nm), does not form a solid solution and disorder in the cation subsystem becomes manifest only at high temperatures [4]. The neodymium ion has the largest ionic radius among the rare-earth elements forming ReBCO superconducting compounds (0.0995 nm), which makes possible solid-solution formation up to $x = 0.7$ [3].

Substitutions in the Nd/Ba cation subsystem have been intensively studied from the time of the report on the NBCO preparation [5–10]. Incorporation of a Nd^{3+} ion into the Ba^{2+} site results in the appearance in the Cu–O chain plane of an additional oxygen ion, the destruction of the chain order around it, and the formation of a tetragonal modification with an attendant increase in the lattice constant c. The increase in the number of oxygen ions per unit cell reduces the hole concentration and lowers the critical temperature. These phenomena were observed to occur both in Nd substitution for Ba [5–8] and in mutual rearrangement (disorder) in the Nd/Ba cation subsystem [8–10]. However, optimization of the conditions of preparation of Nd-rich films ($x > 0$) permitted a critical temperature close to that obtained in films with $x = 0$ [11]. The NBCO films had a remarkably smooth surface, which is accounted for by the smaller effect of deviations from stoichiometry, with the excess material becoming incorporated into the solid solution rather than precipitating in the form of foreign-phase particles. The crystal structure of the films obtained also revealed an extremely high quality, which is due to layer-by-layer growth persisting up to thicknesses above 200 nm [11]. The effect of increasing the barium content in NBCO thin films was studied [6–8], but the results obtained were contradictory. This can apparently be attributed to these studies not having been systematic enough; in particular, no independent optimization of the deposition parameters for films of different elemental composition was carried out.

The purpose of this work was to investigate the effect of substitutions in the Nd/Ba cation subsystem on the properties of films with different neodymium and barium contents obtained by laser ablation sputtering.

1. TECHNIQUES

Thin $Nd_{1+x}Ba_{2-x}Cu_3O_y$ films ($x = -0.15,\ldots, 0.15$) were prepared by pulsed laser ablation cosputtering (a KrF excimer laser and an energy density at the target of 1.7 J/cm^2) of two ceramic targets of different elemental

composition [12]. The targets were mounted on a rotating holder, and a laser pulse was directed on the target to be sputtered by a computer-controlled synchronizing system. The number of sputtering pulses directed on each target were in an integer ratio. The relative amounts of the elements in the films thus prepared were found from the compositions of the sputtered targets using the measurements made with an x-ray microprobe analyzer.

The material was sputtered on $LaAlO_3$(001) and $SrTiO_3$(001) substrates and on sapphire(1102) with a 250-Å thick CeO_2(001) buffer layer, which were heated to a high temperature T_D (about 800°C) [13]. Silver paste was used to improve the thermal contact of the substrate with the heater. The pressure during the deposition was 0.3–1.0 mbar. After the deposition, the films were saturated with oxygen, a procedure including rapid cooling to a temperature T_a, admission of oxygen to atmospheric pressure, and cooling at a rate r_a for a time t_a (inset in Fig. 2). Some samples were maintained after the completion of deposition at the deposition temperature and pressure for a time t_h. The parameters of this procedure were typically t_h = 0 min, T_a = 450°C, r_a = 10°C/min, and t_a = 1 h.

The superconducting properties (the critical transition temperature T_c and the transition width ΔT_c) were derived from the measured dependences of the magnetic susceptibility of the films on temperature. The crystal structure parameters of the films were determined by x-ray θ/2θ scanning. The lattice parameters were calculated with due account of all diffraction peaks of the (*h*00), (0*k*0), and (00*l*) families observed [14], and the stresses in the films were estimated from the dependence of peak broadening on the diffraction angle [15]. The volume ratios of the domains with *a*, *b*, and *c* orientation were estimated from integrated-intensity ratios of the (200), (020), and (006) peaks, respectively, taking into account the standard intensities obtained by θ/2θ scanning of powder samples and available from the literature. The particle density on the surface was determined from photomicrographs made with an optical microscope, which permitted one to take into account particles greater than 0.3 μm in size. The surface roughness R_a was calculated automatically during surface profile measurements with an AlfaStep profilometer as the arithmetic mean of the deviation from the mean height of the relief. The needle advance velocity was 2 μm/s; the measurement frequency, 50 Hz; the vertical resolution, better than 5 Å; and the measured trace length, 50 μm. The substrate surface roughness measured in these conditions before the film deposition was 10–15 Å.

2. RESULTS AND DISCUSSION

The superconducting properties of the NBCO films with $x \approx 0$ depended strongly on the deposition regime; and for films obtained on $LaAlO_3$ substrates, T_c = 85–86 K and ΔT_c was less than 2 K. Such films were oriented with the *c* axis perpendicular to the substrate plane (*c*-oriented films), the lattice parameter *c* varied from 11.740 to 11.755 Å, and the stresses in the films did not exceed 0.15%. The lattice parameters of the films saturated with oxygen by the standard procedure are listed in Table 1, and typical diffraction patterns of the NBCO films are presented in Fig. 1. In some films, besides the *c*-oriented domains, *a*- and *b*-oriented domains were also present (Figs. 1a, 1b). The lattice constants *a* and *b* estimated from the θ/2θ x-ray scans of such films were 3.864–3.876 and 3.905–3.907 Å, respectively. The *a* or *b* domain orientation perpendicular to the substrate plane depended on the material of the substrate. On $LaAlO_3$ and the CeO_2 buffer layer, one observed the formation of *a*-oriented parts of NBCO films; however, the films on $SrTiO_3$ always contained domains oriented with the *b* axis perpendicular to the substrate plane, irrespective of the deposition conditions. This orientation is not typical of ReBCO-family materials, although when NBCO films were deposited by laser sputtering on a $SrTiO_3$ film, one also observed [16] the growth of a *b*-oriented film (peak *3* in the inset to Fig. 2 in [16]). This could be due to the parameter of the $SrTiO_3$ cubic lattice (3.905 Å) being close to the *b* parameter of the NBCO films. The x-ray diffraction peaks of a *b*-oriented NBCO film and a $SrTiO_3$ film practically coincide, which required the deconvolution of the observed diffraction peak into the constituent peaks (see inset to Fig. 1b). Lowering the deposition temperature to 740°C produced films predominantly of the *a* orientation with the lattice constants $c^* = 11.83$ Å, and $a^* = 3.91 \pm 0.001$ Å. Such films were not superconducting, which, besides the lattice constants, implies the formation of a tetragonal NBCO structure.

The oxygen saturation regime strongly affected the structure and properties of $NdBa_2Cu_3O_y$ films. Increasing T_a and t_a compared to the standard procedure resulted in an increase in the lattice constant *c* to 11.77–11.81 Å and a decrease in T_c (Fig. 2). These phenomena are probably associated with the disorder in the Nd/Ba cation subsystem which sets in during oxygen saturation at a high temperature [9, 10]. It was shown [9, 17] that maintaining NBCO at a high temperature (800–900°C) and low oxygen pressure favors ordering in the Nd/Ba subsystem. Subsequent saturation with oxygen at a low temperature (340°C) does not bring about substantial disorder and degradation of the superconducting properties [17]. The saturation of NBCO films with oxygen in accordance with these recommendations allowed us to reach T_c and ΔT_c on the level of the best parameters attained with the standard oxygen-saturation procedure (curve *1* in Fig. 2).

In order to systematically investigate the effect of the composition of films on their properties, the oxygen pressure during sputtering, in accordance with the literature data [2], was chosen equal to 0.3 mbar and the films were deposited on $LaAlO_3$(001) substrates. For

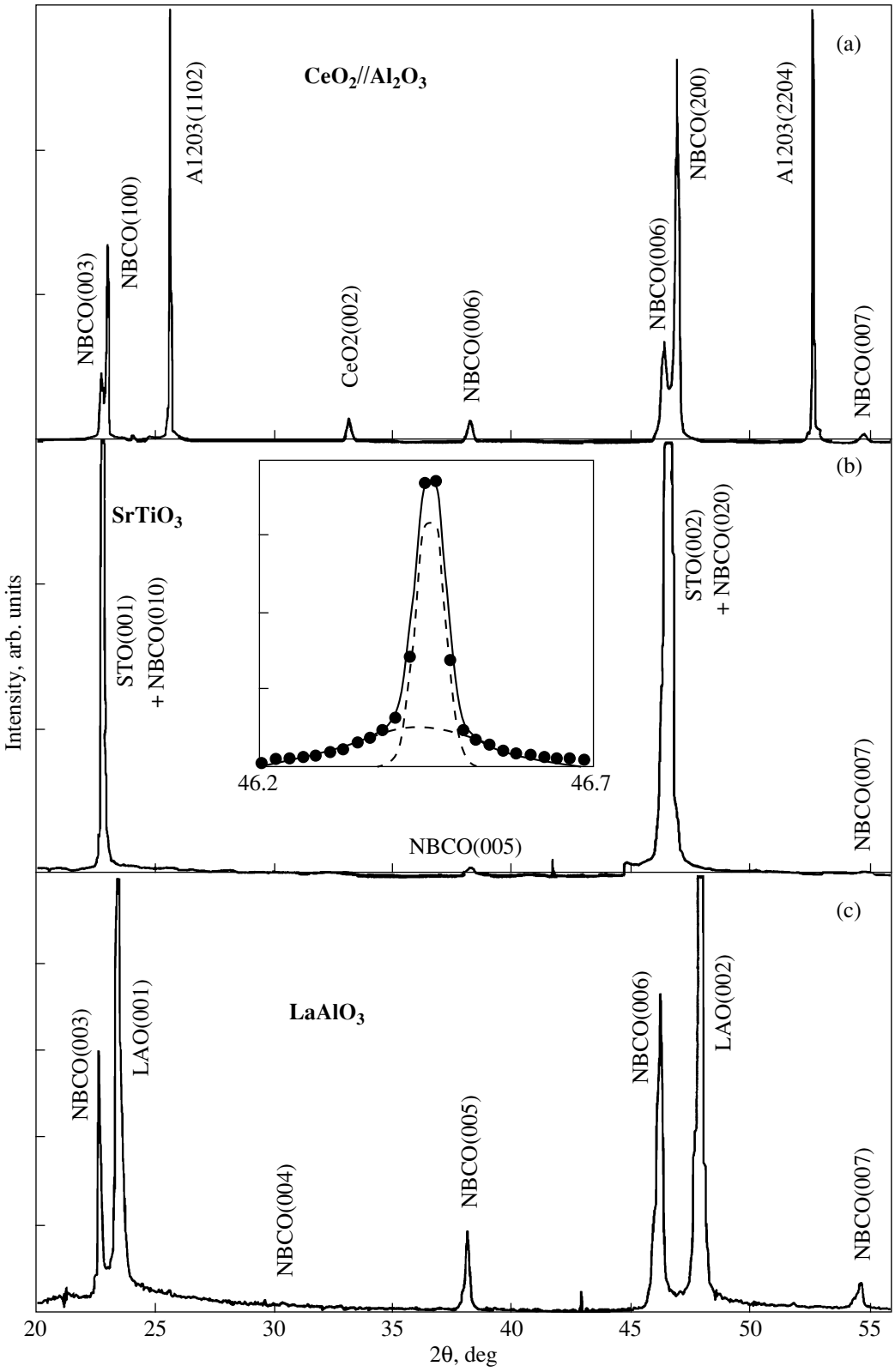

Fig. 1. X-ray θ/2θ diffractograms of $Nd_1Ba_2Cu_3O_y$ films (a) of the mixed *a* and *c* orientations on $CeO_2(001)//Al_2O_3(1\underline{1}02)$ substrate, (b) of the mixed *b* and c orientations on $SrTiO_3(001)$ substrate, and (c) of the *c* orientation on $LaAlO_3(001)$ substrate. Inset to (b): decomposition of the x-ray diffraction peak into the constituent peaks due to $SrTiO_3(002)$ (46.467°, half-width 0.058°) and NBCO(020) (46.44°, half-width 0.235°); dashed lines show calculated peaks, and the solid line is their sum.

Table 1. Lattice parameters of $NdBa_2Cu_3O_y$ films deposited by laser ablation sputtering

Substrate	p_{02}, mbar	T_D, °C	*c* orientation			*a*(*b*) orientation		
			fraction, %	lattice constant, Å	stresses, %	fraction, %	lattice constant, Å	stresses, %
$LaAlO_3$ $CeO_2//Al_2O_3$	0.6–1.0	770–790	100	c = 11.74–11.755	0.13–0.5	0	Not determined	Not determined
$SrTiO_3$	0.75–1.0	760–830	37–54	c = 11.74–11.77	0.11–0.17	46–63	b = 3.906	Same
$CeO_2//Al_2O_3$	0.4–0.6	780	17–50	c = 11.725–11.76	0.4–0.9	50–83	a = 3.867–3.876	0.5–1.0
$SrTiO_3$	0.3–0.6	750–770	2–6	c = 11.76–11.765	Not determined	94–98	b = 3.906	0.34–0.74
$LaAlO_3$, $SrTiO_3$	0.4–0.75	680–730	<1	c = 11.83–11.85	Same	100	a = 3.91	0.36–0.42
$LaAlO_3^*$	1.0	750–790	65–100	c = 11.77–11.78	0.47–0.6	0–38	a = 3.872; b = 3.907	2.7–3.0
$LaAlO_3^{**}$	0.3–1.0	780	1–2	c = 11.80–11.805	0.8	98–99	a = 3.89–3.91	0.55

* Oxygen admitted at a high temperature.
** Prolonged oxidation.

Table 2. Properties of $Nd_{1+x}Ba_{2-x}Cu_3O_y$ films with different elemental compositions deposited on $LaAlO_3$(001) substrates at a pressure of 0.3 mbar

x	Deposition temperature providing the highest T_c, °C	Critical temperature T_c, K	Surface roughness, Å	Surface particle density, 10^6 cm^{-2}
0.14	795	73	14	2
0.06	800	81	12	3
0	810	85.95	11	2
–0.06	No optimization		16	2.5
–0.08	810	85.5	52	20
–0.13	810	86.2	360	30
–0.14	No optimization		600	70

each elemental composition of NBCO films, the deposition temperature providing the highest T_c was determined. The film parameters obtained at these temperatures are listed in Table 2. The dependence of T_c on the relative content of barium and neodymium is plotted in Fig. 3. A decrease in the barium content below two atoms per unit cell reduces the attainable critical temperature, which agrees with the literature. At the same time, an increase in the barium content does not entail a further increase or decrease in T_c within the range covered. The film surface morphology also underwent changes as one crossed over from barium-deficient to barium-rich films (Fig. 3). The former had a smooth surface with a low particle density (less than 10^6 cm^{-2}) and a roughness comparable with that of the original substrates (10–20 Å). An increase in the barium content above the stoichiometric level produced fast growth of both the particle density on the film surface and the film roughness (Table 2). A similar effect was observed in [6–8] for $x < -0.10$. X-ray diffractometric measurements allowed one to identify the forming particles as BaO and Ba_2CuO_3 [6, 7]. In contrast to the dependences of T_c on the composition of the films under study obtained by us, a maximum in T_c was observed at $x = -0.03$ in [6, 7] and at $x = 0$ in [8]. This is possibly due to the fact that in none of the works cited above were the deposition conditions optimized for each elemental composition studied.

The observed behavior of T_c and of the film morphology under variation of the elemental composition can be attributed to a different character of substitutions in the Ba/Nd subsystem. The neodymium ion apparently enters the barium site quite easily, and the deficiency of barium in a film is compensated by neodymium. This results in the formation of a smooth film with high lattice perfection, but T_c of such a film decreases with increasing Nd content. The corresponding chemical reaction of NBCO formation can be written as $(1 + x)NdO_{1.5} + (2 - x)BaO + 3CuO \longrightarrow Nd_{1+x}Ba_{2-x}Cu_3O_y$ for $x > 0$. In contrast, the excess barium is only incorporated into the lattice in small

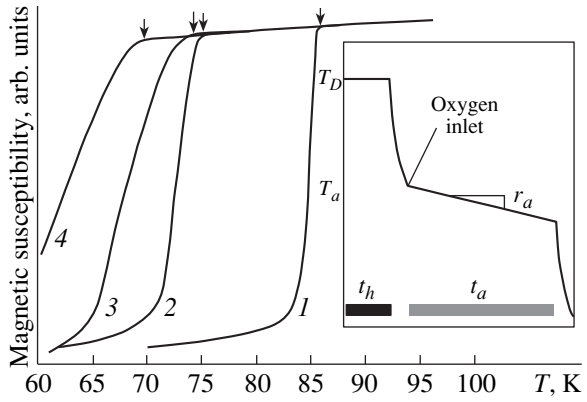

Fig. 2. Dependence of the magnetic susceptibility on temperature for $NdBa_2Cu_3O_y$ films deposited on a $LaAlO_3(001)$ substrate at 780°C and subjected to various oxygen saturation procedures: (*1*) t_h = 15 min, T_a = 350°C, r_a = 0, t_a = 1 h; (*2*) t_h = 0, T_a = 450°C, r_a = 0, t_a = 1 h; (*3*) t_h = 0, T_a = 750°C, r_a = 10°C/min, t_a = 1 h; and (*4*) t_h = 0, T_a = 450°C, r_a = 0, t_a = 2.5 h. The critical temperatures are identified by arrows. Inset: schematic of oxygen saturation procedure. See text for explanation of the notation.

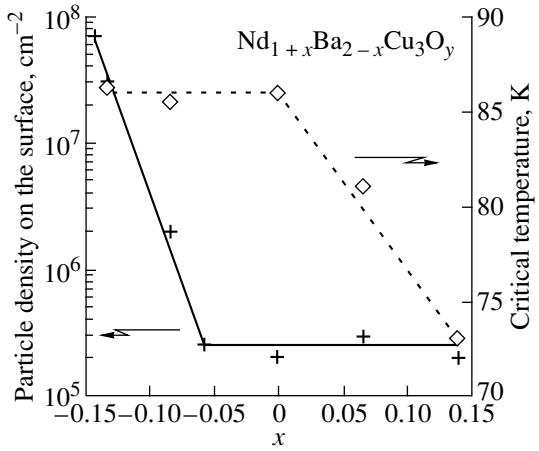

Fig. 3. Dependence of the critical temperature and particle density on the surface of $Nd_{1+x}Ba_{2-x}Cu_3O_y$ films on a $LaAlO_3(001)$ substrate on their elemental composition. The deposition temperature was optimized for each elemental composition (see Table 2). The lines are drawn to aid the eye.

amounts and precipitates in the form of foreign phases. Therefore, the NBCO film has a close-to-stoichiometric composition ($x = 0$) and exhibits the corresponding superconducting properties, but particles appear on its surface. The reaction of NBCO formation assumes the form $(1 + x)NdO_{1.5} + (2 - x)BaO + 3CuO \longrightarrow (1 + x)Nd_1Ba_2Cu_3Cu_3O_y + (-3x)(Ba,Cu)O_z$ for $x < 0$. The proposed mechanism finds support in the observation that the optimum film deposition temperature remains constant with increasing barium content, whereas when x decreases, the optimum deposition temperature decreases (Table 2). The optimum temperatures for the formation of phases with excess neodymium are known to decrease with increasing Nd content [11].

The relatively low critical temperature of 86 K reached in the optimization of the deposition process may be due to one of two possible reasons. First, the critical temperature of the films thus prepared can decrease as a result of the destruction of the chain order in the Cu–O sheets due to the disorder in the Nd/Ba subsystem. However, an increase in disorder results in an increase in the lattice parameter c, while the values measured by us agree with those for standard films with $T_c > 90$ K. A more probable reason is the presence of impurities in the sputtered target; indeed, the high sensitivity of NBCO to impurities [18, 19] can bring about a sharp drop of T_c even at a very low impurity concentration.

It should be pointed out that some authors ([16, 20–23]), despite comprehensive optimization of the deposition conditions, did not succeed in reaching critical temperatures in NBCO films above 86–88.5 K, whereas others ([6–8, 11]) report repeatedly obtaining critical temperatures above 91 K. In both groups, the same techniques and similar deposition parameters were used. This discrepancy suggests the existence of some overlooked factor, which results in a T_c drop by 5–8 K. There is a report [20] of the formation of a "high-temperature" NBCO phase with T_c = 95 K, which the authors did not, however, succeed in isolating from the "low-temperature" ($T_c < 90$ K) phase.

Thus, we have studied the effect of substitutions in the Nd/Ba cation subsystem on the properties of $Nd_{1+x}Ba_{2-x}Cu_3O_y$ films obtained by laser ablation sputtering. NBCO films prepared on $SrTiO_3(001)$ substrates exhibited the orientation of a substantial part of the film with the b axis perpendicular to the substrate plane. The structure and superconducting properties of $Nd_{1+x}Ba_{2-x}Cu_3O_y$ reveal a strong dependence on the conditions of film saturation with oxygen, which is probably associated with disorder appearing in the Nd/Ba subsystem during film saturation with oxygen. The investigation of the deposition of NBCO films with different barium and neodymium contents indicates the incorporation of excess neodymium into the barium sites on the superconductor lattice, whereas excess barium precipitates in the form of particles observed on the film surface.

ACKNOWLEDGMENTS

The authors are grateful to Prof. T. Claeson and V. B. Kravchenko for fruitful discussions.

Partial support of the ESPRIT program (Contract no. 23429 HTS-RSFQ), Swedish Materials Consortium, of the RF State Program "Modern Problems in the Physics of Condensed State" (Superconductivity section), of the Russian Foundation for Basic Research, and of the INTAS program of the European Community is gratefully acknowledged.

REFERENCES

1. J. G. Lin, C. Y. Huang, Y. Y. Xue, *et al.*, Phys. Rev. B **51**, 12 900 (1995).
2. M. Badaye, J. G. Wen, K. Fukushima, *et al.*, Supercond. Sci. Technol. **10** (11), 825 (1997).
3. H. Wu, M. J. Kramer, K. W. Dennis, and R. W. McCallum, Physica C (Amsterdam) **290**, 252 (1997).
4. J. Ye and K. Nakamura, Phys. Rev. B **50** (10), 7099 (1994).
5. C. Le Paver-Thivet, B. Leibold, and H.-U. Habermeier, in *Proceedings of the 2nd European Conference on Applied Semiconductivity, Edinburg, 1995*, ed. by D. Dew-Hughes (Inst. of Physics, Bristol, 1995), Inst. Phys. Conf. Ser. **148**, 863 (1995).
6. Y. Li and K. Tanabe, J. Appl. Phys. **83** (12), 7744 (1998).
7. Y. Li and K. Tanabe, IEEE Trans. Appl. Supercond. **9** (2), 1586 (1999).
8. Z. Mori, T. Inoue, N. Yokoyama, *et al.*, LT22 CDROM (1999).
9. T. Puig, X. Obradors, B. Martinez, *et al.*, IEEE Trans. Appl. Supercond. **9** (2), 2054 (1999).
10. I. Zelenay, A. Nafidi, C. Greaves, and R. Suryanarayanan, Physica C (Amsterdam) **231**, 207 (1994).
11. M. Saluzzo, I. Maggio-Aprile, and O. Fischer, Appl. Phys. Lett. **73** (5), 683 (1998).
12. P. B. Mozhaev, F. Rönnung, P. V. Komissinskii, *et al.*, Physica C (in press).
13. P. B. Mozhaev, G. A. Ovsyannikov, and Ĭ. L. Skov, Zh. Tekh. Fiz. **69** (2), 119 (1999) [Tech. Phys. **44**, 242 (1999)].
14. M. S. Raven, E. E. Inametti, Y. M. Wan, and B. G. Murray, Supercond. Sci. Technol. **7**, 462 (1994).
15. J. P. Gong, M. Kawasaki, K. Fujito, *et al.*, Phys. Rev. B **50** (5), 3280 (1994).
16. Yu. A. Boĭkov, V. A. Danilov, T. Claeson, and D. Erts, Fiz. Tverd. Tela (St. Petersburg) **41** (3), 395 (1999) [Phys. Solid State **41**, 355 (1999)].
17. T. Kimura, T. Goto, and K. Watanabe, IEEE Trans. Appl. Supercond. **9** (2), 2101 (1999).
18. Y. Xu, W. Guan, Y. F. Chen, *et al.*, Phys. Rev. B **50** (2), 1223 (1994).
19. S. S. Ata-Allah, Y. Xu, and Ch. Heiden, Physica C (Amsterdam) **221**, 39 (1994).
20. W. H. Tang and J. Gao, Physica C (Amsterdam) **313**, 115 (1999).
21. A. Eulenberg, E. J. Romans, Y. C. Fan, and C. M. Pegrum, Physica C (Amsterdam) **312**, 91 (1999).
22. I. S. Kim, K. W. Lee, Y. K. Park, and J. Ch. Park, Appl. Phys. Lett. **68** (13), 1859 (1996).
23. Y. Hakuraku, S. Miyata, T. Inoue, and S. Nozoe, Supercond. Sci. Technol. **11** (2), 179 (1998).

Translated by G. Skrebtsov

Physics of the Solid State, Vol. 42, No. 9, 2000, pp. 1596–1601. Translated from Fizika Tverdogo Tela, Vol. 42, No. 9, 2000, pp. 1553–1558.

METALS AND SUPERCONDUCTORS

Transition from Thermally Activated to Regular Flow of Magnetic Flux Vortices in HTSC

V. N. Kushnir, A. Yu. Petrov, and S. L. Prischepa

Belarussian State University of Information Science and Radio Engineering, ul. Brovka 6, Minsk, 220027 Belarus

e-mail: aleks@gw.bsuir.unibel.by

Received March 17, 2000

Abstract—The effect of structural inhomogeneities in a superconductor on a vortex medium flow in weak magnetic fields at temperatures varying from 78 to 83 K for various bias current densities is investigated by using transport measurements of $Bi_2Sr_2CaCu_2O_{8+x}$ thin-film microbridges. The results obtained are analyzed on the basis of the theories of flux creep and the regular flow of vortices. It is shown that the current dependences of the effective potential for vortex pinning can be satisfactorily described in the framework of two statistical models, one of which was proposed earlier by the authors. Both models cover the regimes of thermally activated and regular flow of vortices as limiting cases. The wide transition region in which the creep and regular vortex flow processes simultaneously occur due to a large dispersion in the pinning energy distribution. It is found that when the magnetic field exceeds a certain value, the average value and dispersion of the pinning potential decrease sharply, so that the conditions of regular flow set in even for small values of the bias current. This fact is attributed to the destruction of vortex lines into two-dimensional segments. © *2000 MAIK "Nauka/Interperiodica".*

The difference between high-temperature and traditional superconductors is most clearly pronounced in the vicinity of the superconducting transition temperature T_c [1]. Transport measurements are among the main tools of experimental investigations of HTSC near T_c [2, 3]. In spite of their differences, numerous theoretical models proposed for quantitative interpretation of the results of transport measurements [resistive and current–voltage characteristics (IVC)] [4] are based on analysis of the motion of the Abrikosov vortex lattice. The mechanisms of motion of the vortex lattice (VL) in a HTSC are found to be much more complicated than in traditional superconductors in view of a high degree of anisotropy, a layered structure, and large values of T_c. "Static" disorder (e.g., large dispersion in the pinning energy distribution) strongly affects the H–T phase diagrams [5]. For example, the vortex creep–flow crossover caused by "static" disorder [6–8] leads to a strong broadening of the nonlinear segment of the IVC.

Apart from elastic vibrations of the VL and transport motion associated with the transport current, bends (including kinks) and "twists" of vortex lines become significant. Vortex filaments themselves in HTSC possess a structure owing to which two-dimensional vortices can be observed for certain magnetic fields H and temperatures T (e.g., with the help of neutron diffraction [9]). Consequently, in the case of HTSC, we can speak of a "vortex medium" rather than a vortex lattice. High values of T_c combined with the layered structure of HTSC lead to complex fluctuational movements of vortices, which is manifested in the presence of a large number of phase transitions and crossovers in the vortex medium reflected in the phase diagram. For example, "melting" of the vortex lattice (i.e., a transition from the state with a regular structure to the state of a "vortex liquid") takes place at a certain temperature $T_m(H)$ [4, 10]; at higher temperatures $T_m^*(H)$, the destruction ("evaporation") of vortex lines takes place: $2D$ segments of vortex lines start showing independent fluctuational movement [4, 11].

The present work aims at studying the peculiarities of the crossover from creep to a regular flux flow (RFF) in thin HTSC films. We analyzed the experimental dependences $\rho(T, H, J)$ (ρ is the resistivity and J is the current density) for $Bi_2Sr_2CaCu_2O_{8+x}$ thin-film microbridges near the superconducting transition temperature for low values of the applied magnetic field ($H \ll H_{c2}$).

Films of $Bi_2Sr_2CaCu_2O_{8+x}$ of thickness $d_f = 0.1$ μm were formed by molecular beam epitaxy on a Riber setup at Salerno University (Italy). The deposition technology is described in detail in [12]. The superconducting transition temperature T_c ($R = 0$) exceeded 85 K. The films were highly textured, with the c axis perpendicular to the MgO(100) substrate. Transport measurements were made according to the standard four-probe technique with a constant displacement current. The data were recorded on a PC. The measuring procedure was described in detail in [13]. A magnetic field up to 1100 Oe was created by a copper solenoid. All the measurements were made using liquid nitrogen as a coolant. The microbridges were formed by the standard

1063-7834/00/4209-1596$20.00

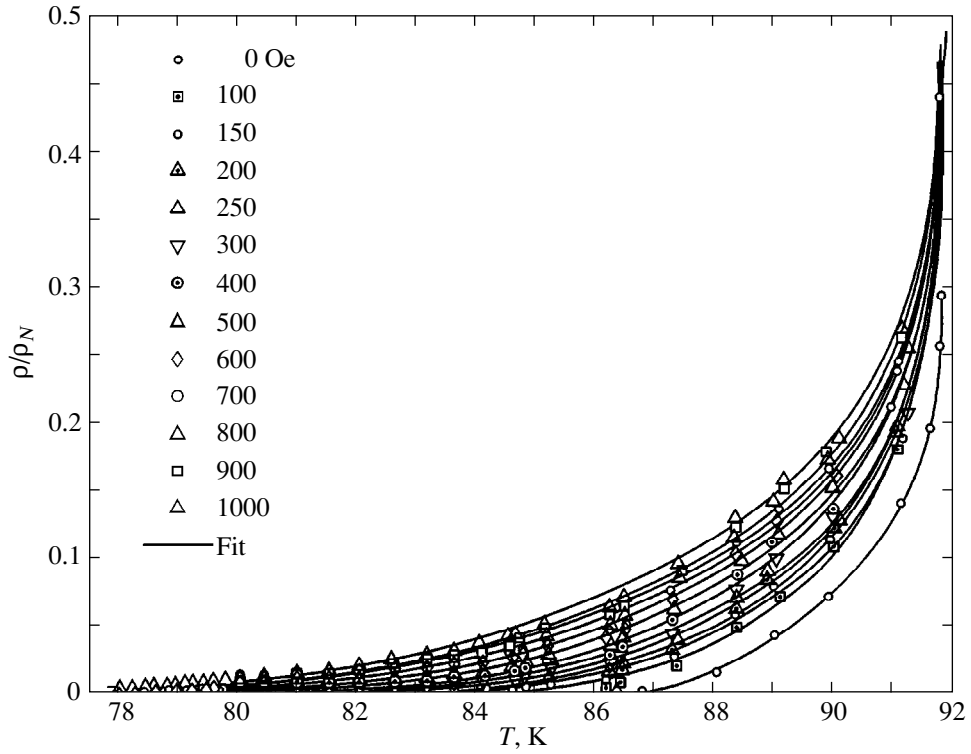

Fig. 1. Temperature dependence of the resistivity (low-resistivity region) for various values of applied magnetic field for $J = 111$ A/cm^2.

photolithographic technique. The length of the bridges was 50 μm, and the width was 30 μm.

We obtained the resistivity $\rho(T)$ curves for a number of values of H and J. By way of an example, Fig. 1 shows the $\rho(T, H)$ dependences for the transport current density $J = 111$ A/cm^2. Obviously, the transition width increases with the magnetic field. For HTSC, such a broadening at temperatures not very close to T_c (the meaning of this expression will be clarified below) is attributed to the thermal activation of vortex motion in the field of pinning centers. In this case [14], the resistivity can be presented in the form

$$\rho(T, H, J) = \rho_0 \exp\left(-\frac{U_\rho(T, H, J)}{k_B T}\right). \quad (1)$$

Here, ρ_0 is the preexponential factor of the order of the resistivity ρ_N in the normal state, k_B is the Boltzmann constant, and U_ρ is the effective pinning potential. We will henceforth analyze resistive characteristics through the magnitude of the effective pinning potential:

$$U_\rho(T, H, J) = k_B T \ln\left(\frac{\rho_0}{\rho(T, H, J)}\right). \quad (2)$$

Let us now clarify the meaning of the expression "temperatures not very close to T_c." Plotting the $U_\rho(T)$ dependences in accordance with Eq. (2) (Fig. 2), we see that they are linear at $T \le T^* \sim T_c$ ($T^* \sim 83$–84 K in our case). In the region of linearity of $U_\rho(T)$, we can state with confidence that the main contribution to the resistive characteristics comes from thermal excitations of vortices in the field of pinning centers.

It should be noted that, since it is difficult to determine the exact value of the preexponential factor ρ_0, the value of $U_\rho(T)$ is also determined with a certain background $\sim k_B T$. For this reason, it is more convenient to use, instead of $U_\rho(T)$, its linear extrapolation $U_{\rho 0}$ to zero temperature.

Let us analyze the current dependences $U_{\rho 0}(\log J)$ for various values of the magnetic field, which were obtained from resistive characteristics (for the sake of clarity of presentation, the values of current are plotted on a logarithmic scale) (Fig. 3).

It can be seen that the dependence $U_{\rho 0}(\log J)$ has the shape of a step. The left and right "shelves" of the dependence $U_{\rho 0}(\log J)$ actually correspond to two modes of the behavior of the vortex lattice with ρ = const (linear, or ohmic IVC) divided by the crossover region.

The interpretation of the right "shelf" of the dependence $U_{\rho 0}(\log J)$ in terms of RFF (for $J > J^* \sim (2$–$4) \times 10^4$ A/cm^2) is quite trivial [15]. Indeed, the work W^* done by the Lorentz force F_L^* on the extraction of a vortex line with a length equal to the film thickness d_f

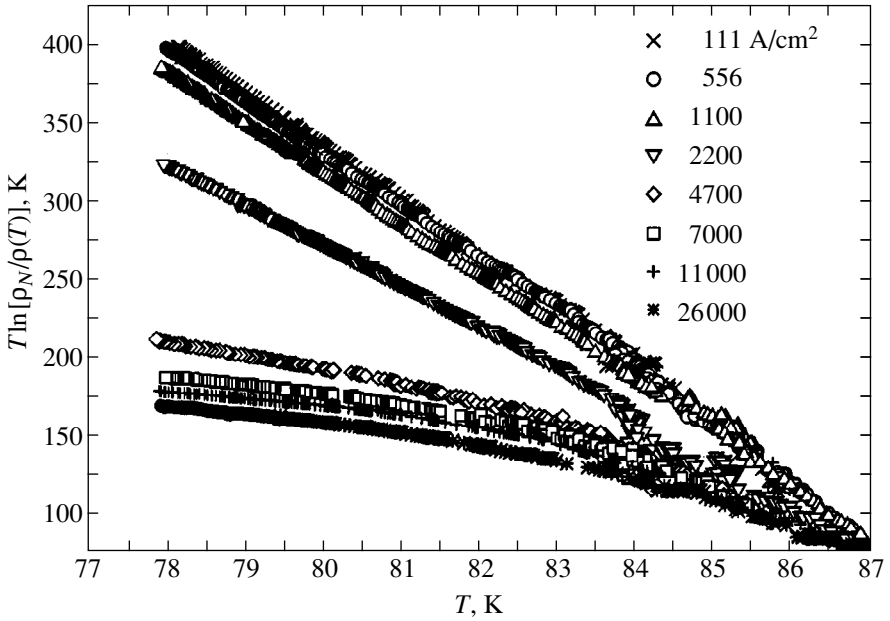

Fig. 2. Dependence $U_\rho(T)$ obtained from the experimental data by using Eq. (3) for various values of J for H = 100 Oe.

from a potential well of width $r_p \geq \xi_{ab}$ (ξ_{ab} = 15 Å is the correlation length in the *ab* plane [16]) for $J = J^*$ is a quantity of the order of $F_L^* r_p \approx J^* \Phi_0 d_f \xi_{ab}$ (Φ_0 is the magnetic flux quantum). The substitution of the values of J^*, d_f, ξ_{ab}, and Φ_0 into the last equality gives a value of $W^* \sim k_B T$ of the order of the pinning energy $U_\rho(T, J^*)$ at $T \sim 80$ K.

The left "shelf" of the dependence $U_{\rho 0}(\log J)$ ($0 < J < 10^3$) A/cm^2 $\sim 0.1 J^*$), which also corresponds to a linear IVC, is not at all typical of superconductors and, strictly speaking, contradicts the concept of the superconducting state: for superconductors, the condition $\rho(J \longrightarrow 0) \longrightarrow 0$ (or, which is the same, $U_\rho(T, H, J) \longrightarrow \infty$) holds. In our case, $U_\rho(T, H, J \longrightarrow 0)$ is a finite quantity: $U_\rho(T, H, J \longrightarrow 0) \sim (5\text{–}6) k_B T$. It was noted in [17, 18] that this is a typical value for a thermally activated flux flow (TAFF) regime for which the relatively low potential barrier is overcome by a vortex with a rather high probability in view of large thermal fluctuations. This makes the mode observable. According to Blatter *et al.* [4], the TAFF regime can exist if the vortex lattice is in the "melted state" observed at temperatures $T > T_m(H)$. Glazman and Koshelev [11] obtained the following estimate of the melting point $T_m(H)$ of a vortex lattice (which is also valid for small values of the field H):

$$T_m(H) = \frac{\varepsilon_0 c_L^2}{\gamma}\left[\frac{\pi}{2}\ln\left(\frac{H_{c2}(T)}{H}\right)\right]^{1/2}\left(\frac{\Phi_0}{H}\right)^{1/2}, \qquad (3)$$

where $\varepsilon_0 = (\Phi_0/4\pi\lambda_{ab})^2$ is the energy per unit length of a vortex line, γ is the anisotropy factor, c_L is the Lindemann number, λ_{ab} is the magnetic field penetration depth in the *ab* plane, and $H_{c2}(T)$ is the upper critical field. Substituting into Eq. (3) the values $c_L = 0.2$, $H_{c2}(0) \approx 23$ T, $\gamma \approx 70$, and $\lambda_{ab}(0) \approx 0.21$ μm typical of $Bi_2Sr_2CaCu_2O_{8+x}$ [16], we obtain $T_m \leq 80$ K for $H \gtrsim$ (50–100) Oe. Thus, the relation $T_m(H) \leq T$ holds in the ranges of fields and temperatures under investigation. It is appropriate to note here the possibility of one more "phase transition" following from the experimental results. Figure 3 shows that the values of $U_{\rho 0}(J)$ for TAFF regimes and flux flows differ insignificantly for H = 1100 Oe. One of the reasons for such a disappearance of pinning is the destruction ("evaporation") of vortex lines [10]. The essence of this phenomenon is that, as a result of thermal fluctuations, the coupling between 2*D*-segments of a vortex lines becomes very weak. Glazman and Koshelev [11] give the following estimate of the temperature $T_m^*(H)$ corresponding to the destruction of a vortex lines:

$$T_m^*(H) \approx T_m(H)\left[\frac{\pi\Phi_0}{H\Lambda^2}\ln\left(\frac{\Lambda}{\pi\xi_{ab}}\right)\right]^{1/2}, \qquad (4)$$

where $\Lambda = \gamma s$ is the Josephson length and s = 15 Å is the separation between the superconducting layers. In accordance with Eq. (4), the value of the field H_d corresponding to the destruction of the lines at $T \approx 80$ K is approximately equal to 2000 Oe. The dependences $T_m^*(H)$ and $T_m(H)$ calculated from Eqs. (3) and (4) are shown in the inset to Fig. 3. The experimentally obtained values [9] are slightly lower: $H_d \sim$ (600–1000) Oe. The exaggerated value obtained in [11] can be explained

with a high degree of confidence by the fact that the estimate of Eq. (4) was obtained disregarding the effect of point defects in the CuO planes. However, point defects enhance the bending deformations of vortex lines, facilitating their destruction. As a result of the decomposition of vortex lines into $2D$ segments, any small transport current for $H \geq H_d$ causes a free flow of two-dimensional vortices.

The most probable reason behind the relatively broad current crossover region ($0.1J^* \leq J \leq J^*$) is the large value of dispersion σ in the pinning energy distribution: $\sigma \sim U(T, H, J) \sim k_B T$. This means that creep and RFF occur simultaneously in a vortex system for a current density $J \in (0.1J^*, J^*)$. In order to quantitatively describe the experimental data and to demonstrate the effect of statistical disorder on the vortex dynamics, let us consider two theoretical models [19, 20]. In the Griessen model [19] (known as the parallel resistor model), a solitary vortex (or a "bundle," "cluster" of vortices) is considered, for which the average time of residence in the creep state and the average time of settlement in the state of regular flow are determined. Then we use a certain averaging procedure to determine the mean velocity of a vortex, after which the electric field strength induced by the transport current is calculated. In the second model [20], we consider an ensemble of vortices each of which overcomes a potential barrier whose height and width are random quantities. When the transport current is switched on, one part of the vortices performs a motion over the barrier; i.e., it is in the state of flow, while the other part moves through the barrier owing to thermal fluctuations; i.e., it is in the state of creep. The common feature of these two models is that they both contain TAFF for small J and RFF for large J as limiting cases. It is interesting to note that the experimental data are successfully described by the simplest versions of these models.

We will not give the details of the Griessen model here and only present the final formula of its "one-domain" version for logarithmic resistive characteristics:

$$U_\rho(J) = k_B T \ln\left(\frac{\rho_N}{\rho}\right) = k_B T \ln\left(\frac{\rho_N}{\rho_{ff}}\right) + k_B T \ln\left\{1 + C(H, T)\frac{J/J_l}{\sinh\left[\frac{A(H, T)}{k_B T}\frac{J}{J_l}\right]}\right\}. \quad (5)$$

Here, $A(H, T)$ is the change in the energy of a vortex line (bundle of vortices) associated with the Lorentz force and J_l is the local critical current (the critical current for the bundle of vortices). The parameter $C(H, T)$ can be expressed in terms of the characteristic lengths

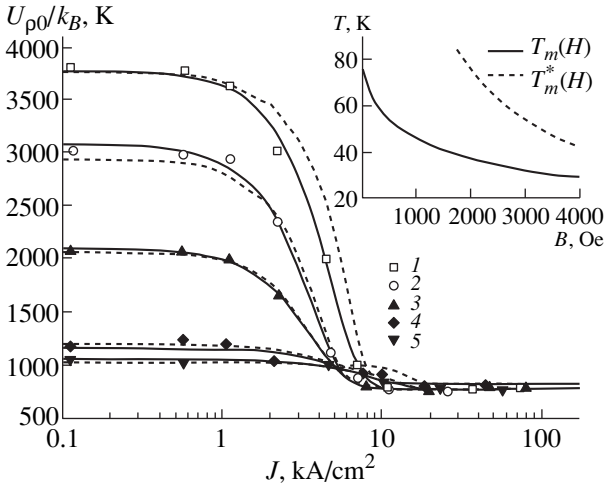

Fig. 3. Dependence $U_{\rho 0}(J)$ for various values of magnetic field. The data were obtained for different values of magnetic field H, Oe: 50 (*1*), 150 (*2*), 600 (*3*), 800 (*4*), and 1100 (*5*). The inset shows the calculated dependences $T_m^*(H)$ (curve *1*) and $T_m(H)$ (curve *2*).

of creep (L_c) and of free flow (L_f) and through the resistivity ρ_{ff} in the regular flow mode. It should be noted that, in the limit of large J, we have

$$U_\rho(J) \approx k_B T \ln\left(\frac{\rho_N}{\rho_{ff}}\right) + k_B T C(H, T)\frac{J}{J_l}\exp\left(-\frac{A}{kT}\frac{J}{J_l}\right),$$

which means that the resistivity of the sample asymptotically approaches ρ_{ff} for $J \gg J_l$. The solid curves in Fig. 3 correspond to the $U_\rho(J)$ dependences calculated by Eq. (5) using A and C as fitting parameters.

According to the second model [20], the electric field strength is given by

$$E = n_{cr}(J)E_c \exp\left(-\frac{\overline{U(J)}}{k_B T}\right) + n_f(J)\rho_{ff} J. \quad (6)$$

Here, $n_f(J)$ and $n_{cr}(J) = 1 - n_f(J)$ are the fractions of vortices participating in RFF and the creep of vortices, respectively; E_c is the preexponential factor, $\exp(-\overline{U(J)}/k_B T) \equiv \langle \exp(-U(J, J_c)/k_B T)\rangle_{J_c \geq J}$, where $U(J, J_c)$ is the height of the potential barrier overcome by a vortex in creep; J_c is the local critical current (the current for which the potential barrier for a vortex disappears); and the symbol $\langle \ldots \rangle$ indicates averaging over the distribution of potential-barrier heights and widths such that $J_c \geq J$.

The simplest special case of the $E(J)$ dependence of Eq. (6) is realized for an exponential distribution

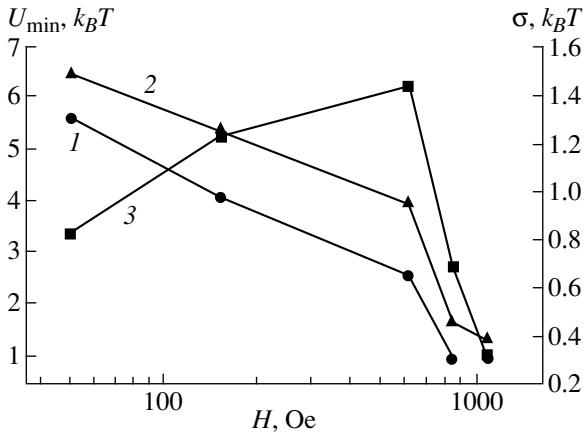

Fig. 4. Dependence of the fitting parameters $U_{\min}$, σ and the average value $\bar{U}$ on the applied magnetic field plotted by using the fitting procedure described by Eqs. (7).

of pinning potential and a linear dependence $U(J) = U_0 - Ja \equiv U_0(1 - J/J_c)$, where a is a constant and $U_0 \in [U_{\min}, \infty)$ [20]:

$$\begin{cases} E = E_c \dfrac{1}{1+\dfrac{\sigma}{k_BT}} 2\sinh\left[\dfrac{U_{\min}}{k_BT}\dfrac{J}{J_{\min}}\right]\exp\left(-\dfrac{U_{\min}}{k_BT}\right) \\ \text{at } J < \dfrac{U_{\min}}{a} \equiv J_{\min} \\ n_f = 0, \end{cases} \tag{7a}$$

$$\begin{cases} E = \dfrac{2E_c}{1+\dfrac{\sigma}{k_BT}}\sinh\left[\dfrac{U_{min}}{k_BT}\dfrac{J}{J_{min}}\right]\exp\left(-\dfrac{U_{\min}}{k_BT}\right) \\ \times \exp\left\{-\dfrac{U_{\min}}{\sigma}\left[1+\dfrac{\sigma}{k_BT}\right]\left[\dfrac{J}{J_{\min}}-1\right]\right\} + n_f(J)\rho_{ff}J \\ n_f = 1 - \exp\left\{-\dfrac{U_{\min}}{U}\left[\dfrac{J}{J_{\min}}-1\right]\right\} \text{ at } J > J_{\min}. \end{cases} \tag{7b}$$

For $J \ll J_{\min}$, Eq. (7a) describes the TAFF mode with a logarithmic characteristic:

$$k_BT\ln\left(\frac{\rho_N}{\rho}\right) \approx U_{\min} + k_BT\ln\left[\frac{\rho_N J_{\min}}{E_c}\frac{k_BT+\sigma}{2U_{\min}}\right].$$

For $J \gg J_{\min}$, we obtain

$$E \approx \rho_{ff}J + \frac{E_c(1-n_f(J))}{1+\dfrac{\sigma}{k_BT}}$$

$$= \rho_{ff}J + \frac{E_c}{1+\dfrac{\sigma}{k_BT}}\exp\left\{-\frac{U_{\min}}{\sigma}\left(\frac{J}{J_{\min}}-1\right)\right\};$$

i.e., the IVC exponentially approaches the IVC of an RFF in accordance with the experimentally observed type of transition to this mode. The $U_\rho(J)$ dependences plotted in accordance with Eq. (7) are presented in Fig. 3 by dashed curves. While processing the experimental data, we used $U_{\min}$ and σ as fitting parameters. The values of $U_{\min}$ and σ obtained for various values of H are presented in Fig. 4. The behavior of $U_{\min}$ and σ as functions of the magnetic field is quite typical at $H \in$ (50, 600 Oe). As the value of H increases from 50 to 600 Oe, the value of $U_{\min}(H)$ decreases, while $\sigma(H)$ increases, which is not surprising, since the "additional" vortices occupy "weaker" pinning centers. It can be seen from Fig. 4 that the average value of the pinning potential $\bar{U}(H) = U_{\min}(H) + \sigma(H)$ is a linear function of $\ln(H)$ for $H \in [50, 600]$ Oe, which confirms the correctness of the choice of the exponential distribution of the pinning energy [12]. As the value of H increases from 600 to 850 Oe, the value of $U_{\min}(H)$ decreases quite sharply down to the background value of k_BT and the dispersion σ also decreases. In this case, the mode of regular flow of 2*D* vortices starts being dominant. It should be noted that, for $U_{\min} = k_BT$, the fraction of vortices settled into the state of regular flow exist even for current densities close to zero.

Thus, we have obtained the following main results. Transport measurements for thin-film microbridges of $Bi_2Sr_2CaCu_2O_{8+x}$ have been made in weak magnetic fields for various values of the bias current. It is shown that the experimental data can be explained both qualitatively and quantitatively on the basis of statistical models [19, 20] containing TAFF and RFF regimes as limiting cases.

The magnetic-field dependences of the parameters of the model of [20] are found, which characterize the effect of microscopic inhomogeneities in the sample on the motion of vortices, viz., the dispersion $\sigma(H)$ of the pinning potential distribution and the mean value of the pinning potential $\bar{U}(H) = U_{\min}(H) + \sigma(H)$. It is shown that the rapid decrease in $\sigma(H)$ and $U(H)$ for $H > H_d \sim$ 800 Oe is associated with the transition to a regular vortex flow. In addition, the destruction of vortex lines into 2*D* segments can also affect the dynamics of vortices for $H \geq 1000$ Oe.

REFERENCES

1. A. S. Aleksandrov and N. F. Mott, *High Temperature Superconductors and Other Superfluid* (Taylor and Francis, Bristol, 1994).
2. A. N. Lykov, Physica C (Amsterdam) **218**, 485 (1993).
3. S. V. Meriakri, Zarubezh. Radioélektron. Usp. Sovrem. Radioélektron. **10**, 3 (1999).
4. G. Blatter, M. V. Feigel'man, V. B. Geshkenbein, *et al.*, Rev. Mod. Phys. **66** (4), 1125 (1994).
5. V. Vinokur, B. Khaykovich, E. Zeldov, *et al.*, Physica C (Amsterdam) **295** (3–4), 209 (1998).

6. R. Griessen, Phys. Rev. Lett. **64** (14), 1674 (1990).
7. J. Chen, D. L. Yin, C. Y. Li, and J. Tan, Solid State Commun. **89** (9), 775 (1994).
8. T. Kisu, T. Nakamura, M. Takeo, *et al.*, IEEE Trans. Appl. Supercond. **5**, 1363 (1995).
9. E. M. Forgan, R. Cubbit, M. T. Wylie, *et al.*, in *Proceedings of the 1994 International Workshop on Superconductivity, Kyoto, Japan, 1994*, p. 151.
10. D. Feinberg, J. Phys. III **4** (2), 169 (1994).
11. L. I. Glazman and A. E. Koshelev, Phys. Rev B **43** (4), 2835 (1991); Appl. Supercond. **5** (2), 1363 (1995).
12. C. Attanasio, C. Coccorese, V. N. Kushnir, *et al.*, Physica C (Amsterdam) **255** (3/4), 239 (1995).
13. I. L. Seleznev, S. V. Zhdanovich, V. A. Popov, and S. L. Prischepa, Prib. Tekh. Éksp. **6**, 210 (1992).
14. M. Tinkham, Phys. Rev. Lett. **61** (14), 1658 (1988).
15. J. Bardeen and M. J. Stephen, Phys. Rev. A **140**, 1197 (1965).
16. S. L. Cooper and K. E. Gray, in *Physical Properties of High Temperature Superconductors*, ed. by D. M. Ginzberg (World Scientific, Singapore, 1994), p. 63.
17. P. H. Kes, J. Aarts, J. van den Berg, *et al.*, Supercond. Sci. Technol. **1** (1), 242 (1989).
18. D. Dew-Hughes, Cryogenics **28** (10), 674 (1988).
19. R. Griessen, Physica C (Amsterdam) **175** (3/4), 315 (1991).
20. V. N. Kushnir, C. Coccorese, S. L. Prischepa, and M. Salvato, Physica C (Amsterdam) **275** (3/4), 211 (1997).

Translated by N. Wadhwa

Physics of the Solid State, Vol. 42, No. 9, 2000, pp. 1602–1605. Translated from Fizika Tverdogo Tela, Vol. 42, No. 9, 2000, pp. 1559–1562.

SEMICONDUCTORS AND DIELECTRICS

Criterion for Formation of the First Bound State of an Optical Polaron

V. K. Mukhomorov

Research Institute of Agrophysics, Russian Academy of Agricultural Sciences, Grazhdanskiĭ pr. 14, St. Petersburg, 195220 Russia

Received December 21, 1999

Abstract—The ground state of an optical polaron has been analyzed for an arbitrary force of the electron–phonon coupling. The eigenvalue differential equation is transformed into the Fredholm integral equation. With the trace method applied to the kernel of integral equation, it is found that the first bound state of the optical polaron appears only provided that the dimensionless coupling constant obeys the inequality $\alpha_c \geq 2.8$. © *2000 MAIK "Nauka/Interperiodica".*

The dependence of polaron states on the electron–phonon coupling constant (α_c) was discussed repeatedly [1–6]. The extreme cases of strong and weak coupling were investigated in detail. In the former case, the polaron clusters had an inherent internal structure, and the number of electronic eigenstates became infinite at $\alpha_c \gg 1$ [7]. In the latter case, the interaction between an electron and crystal lattice vibrations was accounted for by the methods of perturbation theory [8, 9]. However, up to now, the exact electron–phonon coupling constant at which the optical polaron occurs in the first quasi-discrete bound state remains unknown. The perturbation theory makes incorrect predictions for the variation in the effective mass of the slow electron even at $\alpha_c \approx 6$ [2]. The resulting large changes in the mass are contradictory to observations. The general problem of determining the number of bound states for Hamiltonians with smooth potentials was treated repeatedly [10–18].

In the present work, a mathematical approach based on the analysis of solutions of the integral equation for the polaron problem is applied to determine the critical value of the coupling constant at which the first bound state appears in the polaron potential well.

In order to determine the dependence of the polaron potential on the electron–phonon coupling constant, let us apply the Buĭmistrov–Pekar method [1] describing the quantum states of electrons, which interact with the harmonically oscillating polarization field at arbitrary α_c. At $\alpha_c \longrightarrow 0$, this approach duplicates the results of the perturbation theory, and at $\alpha_c \gg 1$, it reproduces the extreme case of the strong electron autolocalization [7]. At intermediate values of the coupling constant ($\alpha_c \approx 1$), according to the method [1], the total energy of the optical polaron is almost 5% less than that found within the often used alternative Feynman approach based on path integrals [4].

In the continuous approximation, the Hamiltonian for the electron–phonon system can be written as

$$H = -(\hbar^2/2m^*)\Delta + \sum_k (\hbar\omega_k/2)(q_k^2 - \partial^2/\partial q_k^3) + \sum_k c_k q_k \chi_{-k}(r). \quad (1)$$

Hamiltonian (1) holds for the spherical equipotential surface and minimum energy at the point $k = 0$. Here, m^* is the effective mass of the band electron, $\mathbf{r}$ is the radius vector of the electron, q_k are the normal coordinates for the longitudinal optical vibration with the frequency ω_k and the wave vector $\mathbf{k}$, and c_k is the coupling coefficient for the kth lattice vibration and the electron. For the longitudinal optical vibrations, the coupling coefficient c_k can be represented in the form

$$c_k = -\frac{\hbar\omega_k}{|k|}(4\pi\alpha_c)^{1/2}\left(\frac{\hbar}{2m^*\omega_k}\right)^{1/4}, \quad \alpha_c = \frac{e^2}{\varepsilon^*\hbar\omega_k}\left(\frac{m^*\omega_k}{2\hbar}\right)^{1/2}, \quad \frac{1}{\varepsilon^*} = \frac{1}{\varepsilon_\infty} - \frac{1}{\varepsilon_s}, \quad (2)$$

where ε_∞ and ε_s are the high-frequency and static permittivities of the medium. The functions

$$\chi_k(r) = (2/V)^{1/2}\sin(\mathbf{kr} + \pi/4) \quad (3)$$

form the complete set of functions, which are orthonormalized to the cube of volume V. In the method [1], it is assumed that the equilibrium positions q_k^0 of harmonic oscillators of the phonon field change in response to the electron field, and this displacement depends on the electron wave function $\varphi(r)$ and, thus, on the electron coordinates. Taking into account this dependence, let us replace the variables $\mathbf{r}$, q_k in Hamiltonian (1) with

new coordinates $\mathbf{r}$, $q_k' = q_k - q_k^0(r)$ and write the Hamiltonian in the form

$$H = -\frac{\hbar^2}{2m^*}\Bigg[\Delta - 2\sum_r(\nabla q_k^0\nabla)\frac{\partial}{\partial q_k'} + \sum_{k,k_1}(\nabla q_k^0, \nabla q_{k1}^0)\frac{\partial^2}{\partial q_k'\partial q_{k1}'} - \sum_k(\Delta q_k^0)\frac{\partial}{\partial q_k'}\Bigg] \quad (4)$$

$$+ \sum_k\frac{\hbar\omega_k}{2}\Bigg[(q_k^0 + q_k')^2 - \frac{\partial^2}{\partial q_k^2}\Bigg] + \sum_k c_k(q_k^0 + q_k')\chi_{-k}(r).$$

Within the adiabatic approximation, the full wave function of the system can be written as the product $\psi = \varphi(r)\prod_k\Phi_k(q_k')$, where Φ_k is the wave eigenfunction of lattice vibrations. The functional of the total energy of the polaron is represented by

$$\bar{H} = (\hbar^2/2m^*)\int|\nabla\varphi|^2 d\tau - \sum_k(c_k^2/2\hbar\omega_k)\langle\varphi|\chi_{-k}(r)|\varphi\rangle^2 + \sum_k\hbar\omega_k(n_k + 1/2)$$

$$+ \sum_k c_k[\langle\varphi|q_k^0\chi_{-k}(r)|\varphi\rangle - \langle\varphi|\chi_{-k}(r)|\varphi\rangle\langle\varphi|q_k^0|\varphi\rangle] + \sum_k(\hbar^2/2m^*)(n_k + 1/2)\langle\varphi|(\nabla q_k^0)^2|\varphi\rangle. \quad (5)$$

Extremalizing functional (5) for q_k^0, we can derive the Euler equation whose solutions define q_k^0. However, it was demonstrated [1] that this solution can be replaced by the linear approximation $q_k^0 = a_k\chi_{-k}(r)$, where a_k is the variational parameter, which is determinable from the minimum condition for functional (4). The extreme value of the parameter a_k obtained from functional (4) is given by

$$a_k = -\frac{c_k(1 - \langle\varphi|\cos(\mathbf{kr})|\varphi\rangle^2)}{\frac{\hbar^2k^2}{2m^*} + \hbar\omega_k(1 - \langle\varphi|\cos(\mathbf{kr})|\varphi\rangle)^2}. \quad (6)$$

It is assumed that the electron wave function of the ground state is a Gaussian, $\varphi(r) = (2\beta/\pi)^{3/4}\exp(-\beta r^2)$, and, consequently, the matrix element in relationship (6) can be written as $\langle\varphi|\cos(\mathbf{kr})|\varphi\rangle = \exp(-k^2/8\beta)$, where β is the variational parameter. In order to solve the eigenvalue problem, let us vary functional (5) for the function $\varphi(r)$. As a result, we obtain the equation

$$-(\hbar^2/2m^*)\Delta\varphi + \sum_k(\hbar\omega_k/2)(2q_k^0\langle\varphi|q_k^0|\varphi\rangle\varphi - q_k^{02}\varphi) - \sum_k(c_k^2/\hbar\omega_k)\chi_{-k}(r)\langle\varphi|\chi_{-k}(r)|\varphi\rangle$$

$$+ \sum_k[q_k^0\chi_{-k}(r)\varphi - \langle\varphi|\chi_{-k}(r)|\varphi\rangle q_k^0\varphi - \chi_{-k}(r)\langle\varphi|q_k^0|\varphi\rangle\varphi] - \sum_k(\hbar^2/2m^*)(2n_k + 1)(\nabla q_k^0)^2\varphi = \lambda\varphi. \quad (7)$$

Retaining the terms in the differential equation (7), which depend on the coordinate $\mathbf{r}$, we derive the following eigenvalue differential equation:

$$\Delta\varphi + (2m^*/\hbar^2)\Bigg[\sum_k\chi_{-k}(r)\langle\varphi|\chi_{-k}(r)|\varphi\rangle \times(\hbar\omega a_k^2 + 2c_k a_k + (c_k^2/\hbar\omega_k))\varphi + \lambda\varphi\Bigg] = 0. \quad (8)$$

We substitute the parameter a_k in the form (6) and the function $\chi_{-k}(r)$ into Eq. (8) and pass on from the summation over $\mathbf{k}$ to integration. As a result, we have the equation

$$\Delta\varphi + \Bigg[\frac{4e^2\alpha_c^2}{\hbar\pi\varepsilon^*\omega}\times\int_0^\infty\frac{k^3\sin(kr)\exp(-k^2/8\beta)}{r[a_c^2k^2 + 1 - \exp(-k^2/4\beta)]}dk + \lambda\frac{2m^*}{\hbar^2}\Bigg]\varphi = 0. \quad (9)$$

Equation (9) was derived within the zero-variance approximation $\omega_k = \omega$.

Then, according to [11, 17], the differential equation can be transformed to the integral equation. Let us preliminarily replace the radial function of the ground state $\varphi(r) = u(r)/r$. In this case, Eq. (9) can be rewritten as

$$\frac{d^2u(r)}{dr^2} + \Bigg[\frac{4e^2\alpha_c^2}{\hbar\pi\varepsilon^*\omega}\times\int_0^\infty\frac{k^3\sin(kr)\exp(-k^2/8\beta)}{r[a_c^2k^2 + 1 - \exp(-k^2/4\beta)]}dk + \lambda\frac{2m^*}{\hbar^2}\Bigg]u(r) = 0. \quad (10)$$

It is impossible to calculate the integral in Eq. (10) in a closed form. However, its dependence on the radius vector r for the ground electronic state can be approximated by the analytical form $V_0\exp(-\gamma r^2)$ with a high accuracy. The parameters of the potential V_0 and γ can

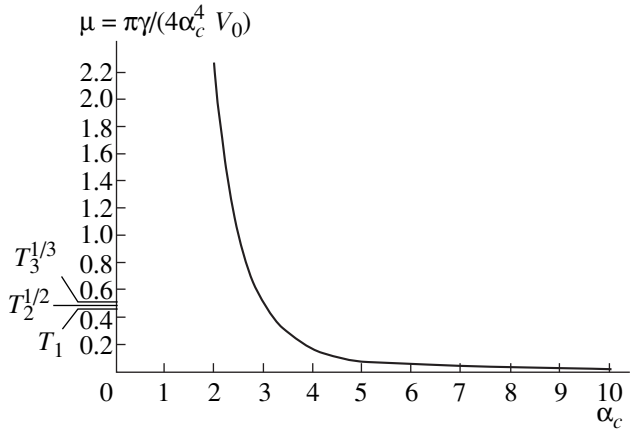

Dependence of the parameter μ on the dimensionless constant of the electron–phonon coupling α_c. T_1, T_2, and T_3 are the iterative values of the kernel trace of the integral equation.

be found numerically at given values of the coupling constant and the variational parameter β, which is determined from the extreme properties of functional (5). Taking into account the boundary conditions $u(0) = u(\infty) = 0$, we recast Eq. (10) into the Fredholm integral equation

$$u(r) = \int_0^r zu(z)((4\alpha_c^4 V_0/\pi\gamma)\exp(-z^2) + 2\lambda m^*/\hbar^2)dz + \int_r^\infty ru(z)((4\alpha_c^4 V_0/\pi\gamma)\exp(-z^2) + 2\lambda m^*/\hbar^2)dz. \quad (11)$$

When deriving Eq. (11), we used the integral relationship

$$\int_{x_0}^x dx \int_{x_0}^x dx \ldots \int_{x_0}^x f(x)dx = [1/(n-1)!]\int_{x_0}^x (x-z)^{n-1} f(z)dz, \quad (12)$$

and passed on to the new variable $z = r\sqrt{\gamma}$. By using the substitution $u(z) = w(z)\exp(z^2/2)$ and taking into account that the critical value of the α_c parameter corresponds to the potential at which λ becomes zero, the integral equation (11) can be rearranged to the form

$$w(z) = (4\alpha_c^4 V_0/\pi\gamma)\int_0^\infty K(z, t)w(t)dt, \quad (13)$$

where the equation kernel now has

$$K(z, t) = \begin{cases} t\exp[-(z^2 + t^2/2)], & t < z \\ z\exp[-(z^2 + t^2)/2], & t > z. \end{cases}$$

According to the Mercer theorem [19], Eq. (13) with a symmetric degenerate and continuous kernel has a limited number of nontrivial solutions. As the potential increases, the first eigenvalue appears only when the kernel trace $T_j = \int_0^\infty K_j(x, x)dx$, which is obtained in the jth iteration cycle of the method of successive approximations, satisfies the inequality

$$T_j^{1/j} \geq \pi\gamma/4\alpha_c^4 V_0 = \mu. \quad (14)$$

For the jth iterated kernel $K_j(z, t)$, the following relationship holds:

$$K_j(z, t) = \int_0^\infty K_{j-1}(z, t)K(y, t)dy, \quad K_1(z, t) = K(z, t). \quad (15)$$

For the integrated kernel $K_j(x, x)$ in the third-order iteration, we have

$$T_3 = \frac{1}{4}\left(\frac{3\pi}{4\sqrt{2}} - \sum_{k=1}^\infty \sum_{n=0}^\infty \left(\frac{2}{3}\right)^{n+k+1} \frac{(n+k+1)!2^{n+k} n!k!}{(2n+1)!(2k+1)!}\right). \quad (16)$$

Requirement (14) enables one to calculate the critical value of α_c at which it will be met. The transition from the state $T_j^{1/j} < \mu$ to the state $T_j^{1/j} > \mu$ can be treated as the formation region of the first bound state of the optical polaron. The trace method was applied earlier [17] in order to determine the number of bound states for different-type smooth potentials. The deviation from the results of the direct numerical calculations [20] does not exceed 4%.

The dependence of the parameter μ on the electron–phonon coupling constant is shown in the figure. The inequality for $T_j^{1/j}$ holds at $\alpha_c \geq 2.8$. This value corresponds to the appearance of the first bound state. For the coupling constant $\alpha_c < 2.8$, the optical polaron has no inherent internal structure. The critical value of the coupling constant is close to the approximate estimate $\alpha_c > 2$ [2]. The iterative convergence for T_j, as is seen from the figure, is rather rapid and enables one to restrict the estimation of μ to the third iteration cycle.

REFERENCES

1. V. M. Buĭmistrov and S. I. Pekar, Zh. Éksp. Teor. Fiz. **32** (5), 1193 (1957) [Sov. Phys. JETP **5**, 970 (1957)].
2. D. Pines, *Polarons and Excitions*, ed. by C. C. Kuper and C. D. Whitfield (New York, 1962), p. 321.
3. V. M. Buĭmistrov, Fiz. Tverd. Tela (Leningrad) **5** (10), 3264 (1963) [Sov. Phys. Solid State **5**, 2387 (1963)].

4. R. P. Feynman, Phys. Rev. **97** (2), 660 (1965).
5. W. J. Huybrechts, J. Phys. C: Solid State Phys. **10** (17), 3761 (1977).
6. N. Tokuda, J. Phys. C: Solid State Phys. **13** (3), L851 (1980).
7. S. I. Pekar, *Investigation on the Electron Theory of Crystals* (Gostekhizdat, Moscow, 1951).
8. T. Lee, F. Low, and D. Pines, Phys. Rev. **90** (1), 297 (1953).
9. M. Gurari, Philos. Mag. **44**, 329 (1953).
10. J. M. Blatt and J. D. Jackson, Phys. Rev. **26**, 18 (1949).
11. V. Bargmann, Proc. Natl. Acad. Sci. USA **38**, 961 (1952).
12. J. Schwinger, Proc. Natl. Acad. Sci. USA **47**, 122 (1961).
13. K. Chadan, Nuovo Cimento Soc. Ital. Fis. A **33**, 191 (1968).
14. D. Simon, J. Math. Phys. **10**, 1123 (1969).
15. F. Martin, Helv. Phys. Acta **45** (1), 140 (1972).
16. M. L. Baeteman and K. Chadan, Nucl. Phys. A **255** (1), 35 (1975).
17. R. Dutt and R. S. Gangopadhyay, Phys. Lett. A **109** (1/2), 4 (1985).
18. F. M. Fernandez, Q. Ma, and R. H. Tipping, Phys. Rev. A **39** (4), 1605 (1989).
19. V. I. Smirnov, in *A Course of Higher Mathematics* (GITTL, Moscow, 1957; Addison-Wesley, Reading, 1964), Vol. 4.
20. J. M. Blatt and V. F. Weisskopf, *Theoretical Nuclear Physics* (Wiley, New York, 1952; Inostrannaya Literatura, Moscow, 1954).

Translated by N. Korovin

Physics of the Solid State, Vol. 42, No. 9, 2000, pp. 1606–1609. Translated from Fizika Tverdogo Tela, Vol. 42, No. 9, 2000, pp. 1563–1566.

SEMICONDUCTORS AND DIELECTRICS

Microstructure of Bulk GaN Layer Grown on Sapphire Substrates with Amorphous Buffer

V. V. Bel'kov, Yu. V. Zhilyaev, G. N. Mosina, S. D. Raevskiĭ, L. M. Sorokin, and M. P. Shcheglov

Ioffe Physicotechnical Institute, Russian Academy of Sciences, Politekhnicheskaya ul. 26, St. Petersburg, 194021 Russia
e-mail: zhilyaev@jyuv.ioffe.rssi.ru

Received January 24, 2000

Abstract—The structure of bulk GaN layers grown on (0001) sapphire substrates by vapor-phase epitaxy has been studied by x-ray diffraction and transmission electron microscopy (TEM). It is found that these layers contain grown-in and screw dislocations. The dislocation density decreases away from the interface. The effect of an amorphous buffer layer on the formation of the initial GaN layer and, thus, on the degree of perfection of gallium nitride layers is elucidated. A model of generating grown-in dislocations and the relaxation mechanism of misfit stresses are proposed. © *2000 MAIK "Nauka/Interperiodica".*

1. INTRODUCTION

Gallium nitride—a most abundant wide-gap semiconductor—has been extensively used in optoelectronics in the short-wavelength range. It is known that the efficiency and reliability of emitting GaN-based devices depend on the type and the density of defects in the material.

According to recent papers [1–4], the GaN layers (from 0.5 to 5 μm thick) on sapphire and SiC substrates can be prepared by different techniques, such as metalloorganic chemical vapor deposition (MOCVD), molecular beam epitaxy (MBE), and CVP. The structural perfection of these layers was examined by different diffraction methods: x-ray diffraction, transmission electron microscopy (TEM), high-resolution electron microscopy (HREM), and low-angle convergent beam electron diffraction (LACBED). It was found the studied materials are characterized by a high density of dislocations, dislocation boundaries, and staking faults [5–7]. The application of the vapor-phase epitaxy method made possible growing "bulk" GaN layers of thickness more than 100 μm [8–11], which can be used as substrates for homoepitaxy. The microstructure of these materials was investigated by the TEM technique [10, 11]. Melnik *et al.* [10] studied a defect layer in the immediate vicinity (within 3 μm) of the GaN/SiC interface [10]. Defects in GaN deposited onto a sapphire substrate preliminarily coated with a layer of zinc oxide were described in [11].

In the present work, we studied the GaN layers grown by vapor-phase epitaxy on the (0001) sapphire substrates with a low-temperature amorphous GaN buffer layer (note that the gallium nitride layers thus prepared are easily separated from the substrates [12]). Moreover, consideration was given to the mechanisms of formation of crystal defects in gallium nitride films.

2. SAMPLES AND EXPERIMENTAL TECHNIQUE

The gallium nitride layers 100–800 μm thick were investigated by double-crystal x-ray diffractometry and transmission electron microscopy (including different diffraction techniques: electron diffraction, examination of diffraction contrast images of linear and planar defects, and analysis of dislocations on the basis of invisibility criterion).

Planar GaN(0001) and cross-sectional GaN$(10\bar{1}0)$ samples were prepared for the TEM investigations. After mechanical grinding, the samples were thinned (to a thickness transparent for electrons) by conventional ion etching in an argon ion flow. The planar samples for the TEM observations were produced both on the side of the interface and on the side of the surface.

3. RESULTS

A region of the planar sample near the interface is displayed in Fig. 1a. This region is a buffer layer. The diffraction pattern of this layer exhibits wide diffuse rings, which are typical of an amorphous material (Fig. 1b). Figure 2a shows the image of the layer at the initial growth stage when a continuous layer starts to grow from single nuclei. Particles have both curvilinear contours and crystallographic faceting. The particle size ranges from 10 to 30 nm. The coalescence texture, which is formed in the presence of the azimuthal orientation of nuclei, is clearly seen in the microdiffraction pattern of this region (Fig. 2b). The texture axis is directed along [0001]. It should be noted that nuclei

1063-7834/00/4209-1606$20.00

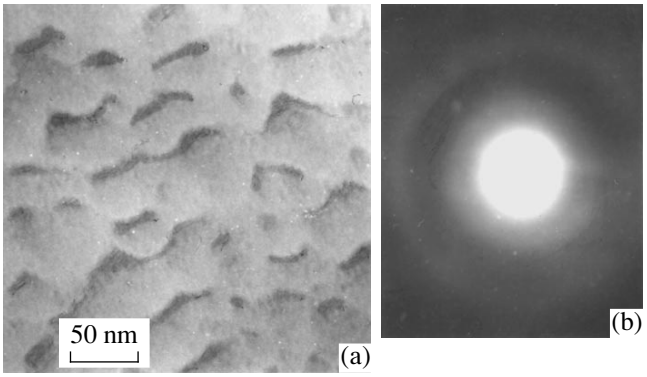

Fig. 1. (a) Planar TEM image and (b) diffraction pattern of an amorphous buffer layer.

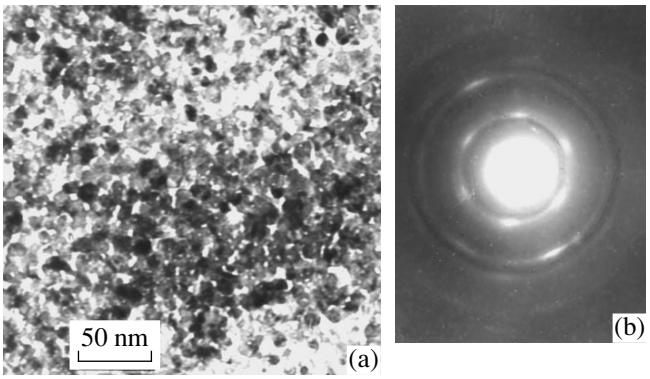

Fig. 2. (a) Planar TEM image and (b) microdiffraction pattern of the GaN layer near the interface (coalescence texture is seen).

already arise during the growth of the low-temperature buffer layer. The TEM observation of the buffer layer prior to the growth of the main layer of gallium nitride has revealed that the upper part of the buffer layer contains small particles whose size does not exceed 5 nm. No coalescence texture is observed in this case.

A further growth of the layer is accompanied by the formation of crystal defects due to a considerable difference in the lattice parameters of sapphire and GaN.

As can be seen from the TEM image of the GaN layer cross-section near the interface (Fig. 3a), the dislocation density in this region is rather high. Closer examination of Fig. 3a reveals cross-sections of several grains adjacent to each other by lateral faces. The grains involve different dislocations, most of which grow from the layer–substrate interface. The dislocations can be conventionally separated into three types: D_1, D_2, and D_3. The D_1 dislocations are located in the grain boundaries in parallel to the growth axis. The grown-in dislocations D_2 are directed toward the surface almost along the C axis. They often close on vertical grain boundaries. These dislocations sometimes form narrow half-loops whose branches lie in different planes [13]. At the same time, the D_2 dislocations generate a large number of the D_3 dislocations, which are aligned parallel to the interface in the (0001) basal

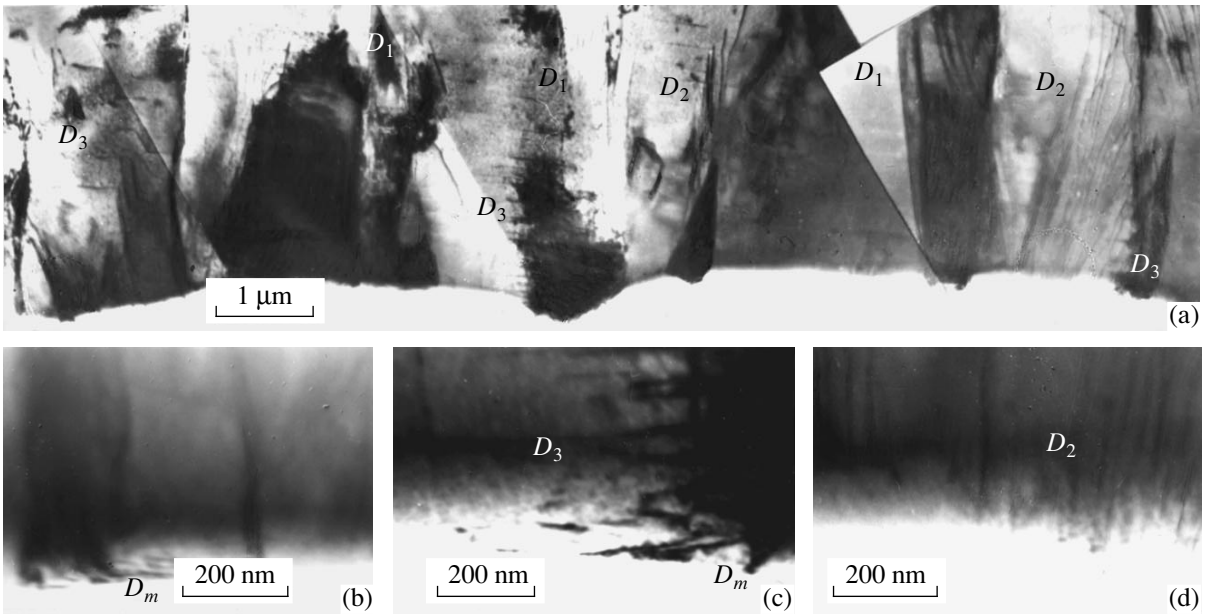

Fig. 3. TEM images of (a) the cross-section of the GaN layer near the interface and (b), (c), and (d) regions (marked by circles) at the layer–substrate interface at a larger magnification. Designations: D_1 = grown-in dislocations in the grain boundaries, D_2 = dislocations growing from the interface within grains, and D_3 = dislocations running parallel to the interface in the (0001) basal plane.

planes. The highest concentration of D_3 dislocations is observed near the interface (Figs. 3b–3d). It is clearly seen that the dislocations are formed at the layer–substrate interface. A portion of dislocations lie in the interface plane and can play the role of misfit dislocations D_m.

In the GaN layer located at a distance of more than 100 μm from the interface, the dislocation density is considerably less. The grains grown up to several tens of microns contain single dislocations whose density is estimated at 10^7 cm^{-2}. The total density of dislocations (including grain boundary dislocations) in the near-surface layer of gallium nitride is of the order of 10^9 cm^{-2}.

The Burgers vectors of the observed dislocations were determined from the invisibility criterion $gb = 0$, where g is the operating reflection for the image of dislocations with the Burgers vector b [13].

An analysis shows that the D_1 dislocations arise on the interface at points of contact between island nuclei (crystallites) and, then, grow toward the film surface in parallel to the growth axis. These dislocations form tilt low-angle grain boundaries and are arranged in the $(10\bar{1}0)$ prismatic planes. The Burgers vector of the dislocations is equal to $1/3[11\bar{2}0]$ and is directed across the dislocation line; i.e., these are edge dislocations.

The D_2 dislocations, like the D_1 dislocations, arise at the interface (Fig. 3c). They are arranged in the $\{10\bar{1}0\}$ prismatic and $\{10\bar{1}1\}$ pyramidal planes. The Burgers vectors b of these dislocations are equal to $[0001]$ and $1/3[11\bar{2}3]$, respectively. For the most part, the lines of dislocations with $b = [0001]$ are parallel to the C axis, and, hence, these are screw dislocations. The dislocations with vector $b = 1/3[11\bar{2}3]$ also can possess the screw component. The lines of these dislocations lie along the $[01\bar{1}2]$ and $[01\bar{1}1]$ directions. They are seen for the reflections $g = 0002$ and are not seen for the reflections $g = \bar{1}100$.

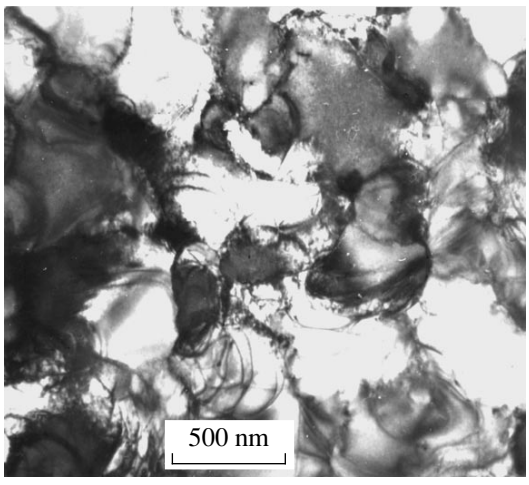

Fig. 4. TEM image of the planar sample at a distance of ~1 μm from the interface. The D_3 dislocations are seen.

The D_3 dislocations in the planar image of the region located at a distance of 1 μm from the interface appear as curved lines (Fig. 4). The Burgers vector of these dislocations is equal to $1/3[11\bar{2}0]$. A curvilinear shape of dislocation lines suggests a mixed character of the dislocations.

The Burgers vector of the D_m dislocations, most likely, is also equal to $1/3[11\bar{2}0]$. As the distance from the layer–substrate interface increases, these dislocations undergo bending and are displaced into the low-angle grain boundaries.

The dislocation structure described above was also observed for the gallium nitride layers grown on silicon substrates.

4. DISCUSSION

Under conditions of heteroepitaxial GaN growth, there occurs bulk nucleation of dislocations, resulting in their island-type growth. The nuclei coalesce to form a continuous layer and often give rise to growth facets in low-energy planes. These are the (0001) and $\{10\bar{1}0\}$ planes in the case of wurtzite crystals, among which is GaN. A perfect nucleus shape is a hexagonal-base pyramid. When growing islands come in contact, the dislocation walls (the D_1 dislocations) are formed between these islands from low-angle boundaries, which relieve stresses arising from their azimuthal misorientation. The boundaries comprise rows of edge-type rectilinear dislocations. The distance between dislocations in the boundaries is inversely proportional to the misorientation angle. In the case of island-type growth, the misfit dislocations are generated within each of the islands, which grow virtually independent of one another to their coalescence upon the formation of a continuous layer. If the layer–substrate interface coincides with the glide plane, the generation of misfit dislocations likely occurs through the mechanism of gliding dislocations from island edges along the interface [14]. In hexagonal crystals, the (0001) basal plane is the most closely packed one. Therefore, the easiest glide should proceed in the basal plane; however, when the glide in the basal plane is hindered by stress fields or other factors, the dislocation glide is of the prismatic type in the $(10\bar{1}0)$ $[\bar{1}2\bar{1}0]$ system and the pyramidal type in the $(10\bar{1}1)$ $[\bar{1}2\bar{1}0]$ system [15].

The relaxation of misfit stresses under growth conditions can be retarded by different factors such as the barrier to nucleation of misfit dislocation, high Peierls

stresses hindering the dislocation glide, and the interaction of dislocations with one another and other defects that impede the motion and multiplication of dislocations.

The D_m dislocations that are formed at the layer–substrates interface glide in the (0001) basal plane and, thus, bring about the relaxation of shear stresses. However, the motion and multiplication of dislocations in the interface is likely hindered by vertical dislocation boundaries, which are responsible for the formation of a columnar structure in the GaN layer. Hence, the misfit stresses do not relax completely, and the residual elastic stresses arise in the layer. This results in the elastic strain and the bending of the epitaxial layer (Fig. 3a). The elastic stresses in the bulk of the layer are partially compensated for by the D_3 dislocations, which are generated by the D_2 dislocations located in the prismatic and pyramidal planes.

Therefore, already at the initial stage of growth, the layers growing on the amorphous buffer layer form a perfect coalescence texture with the texture axis along the [0001] direction. The dislocation density in the layer near the surface is of the order of 10^9 cm^{-2}. In the case when the buffer layer has a polycrystalline structure with crystallite sizes up to 300 nm, the defect density in the films grown on this layer is considerably higher.

The x-ray diffraction analysis revealed that the half-widths of the x-ray rocking curves are equal to 6–8 arcmin for the layers grown on the amorphous buffer layer and 45–90 arcmin for the layers on the polycrystalline buffer layer.

5. CONCLUSION

Thus, it was found that the dislocation structure of the bulk GaN layers is determined, for the most part, by the formation of the initial nucleus layer. The initial layer grown on the amorphous buffer layer exhibits a perfect texture. The majority of the dislocations in the layer are of the grow-in type. The edge-type dislocations form the low-angle grain boundaries and cross the layer from the interface to the surface. The density of these dislocations varies only slightly with an increase in the layer thickness and is equal to 10^9 cm^{-2}. During the growth, a portion of the grown-in dislocations of the screw type undergo bending and close on the grain boundaries. They generate the dislocations arranged in the (0001) basal planes. These dislocations are predominantly located near the layer–substrate interface and very rarely occur near the surface. Consequently, the grown-in dislocations of the edge type that arise from the island coalescence at the initial growth stage make a decisive contribution to the dislocation structure of the GaN films grown on the amorphous buffer layer.

ACKNOWLEDGMENTS

This work was supported by the Russian Foundation for Basic Research, project no. 97-02-18088.

REFERENCES

1. T. Sasaki and S. Zembutsu, J. Appl. Phys. **61**, 2533 (1987).
2. T. W. Weeks, Jr., M. D. Bremser, K. S. Ailey, *et al.*, Appl. Phys. Lett. **67**, 401 (1995).
3. X. J. Ning, F. R. Chien, P. Pirouz, *et al.*, J. Mater. Res. **11**, 580 (1996).
4. R. Molnar, W. Goetz, L. T. Romano, and N. M. Johnson, J. Cryst. Growth **178**, 147 (1997).
5. P. Vermaut, P. Ruternana, G. Nouct, *et al.*, Inst. Phys. Conf. Ser. **146**, 289 (1995).
6. W. Qian, M. Skowronski, M. de Graef, *et al.*, Appl. Phys. Lett. **66**, 1252 (1995).
7. F. A. Ponce, MRS Bull. **23** (2), 51 (1997).
8. G. Jacob, M. Boulon, and M. Futado, J. Cryst. Growth **42**, 136 (1977).
9. T. Detchprohm, K. Hiramatsu, H. Amano, and I. Akasaki, Appl. Phys. Lett. **61**, 2688 (1992).
10. Y. V. Melnik, I. P. Nikitina, A. S. Zubrilov, *et al.*, Inst. Phys. Conf. Ser. **142**, 863 (1996).
11. L. T. Romano, B. S. Krusor, and R. J. Molnar, Appl. Phys. Lett. **71**, 2283 (1997).
12. V. V. Bel'kov, V. M. Botnaryuk, L. M. Fedorov, *et al.*, in *Proceedings of the MRS Fall Meeting, Boston, USA, 1996*, Mater. Res. Soc. Symp. Proc. **449**, 343 (1996).
13. P. B. Hirsch, A. Howie, R. B. Nicholson, D. W. Pashley, and M. J. Whelan, *Electron Microscopy of Thin Crystals* (Butterworths, London, 1965).
14. J. W. Matthews, in *Epitaxial Growth*, ed. by J. W. Matthews (Academic, New York, 1975), Part B, p. 560.
15. J. P. Hirth and J. L. Dothe, *Theory of Dislocations* (John Wiley & Sons, New York, 1970).

Translated by O. Borovik-Romanova

Physics of the Solid State, Vol. 42, No. 9, 2000, pp. 1610–1612. Translated from Fizika Tverdogo Tela, Vol. 42, No. 9, 2000, pp. 1567–1569.

SEMICONDUCTORS AND DIELECTRICS

Determination of the Polaron Shift in Titanium Diselenide-Based Intercalation Compounds

A. N. Titov*, A. V. Dolgoshein*, I. K. Bdikin, and S. G. Titova*****

**Ural State University, pr. Lenina 51, Yekaterinburg, 620083 Russia*

e-mail: alexander.titov@usu.ru

***Institute of Solid State Physics, Russian Academy of Sciences, Chernogolovka, Moscow oblast, 142432 Russia*

****Institute of Metallurgy, Ural Division of the Russian Academy of Sciences, Yekaterinburg, 620016 Russia*

Received February 8, 2000

Abstract—A study is reported of the dependence of the $TiSe_2$ lattice constants on the concentration of an intercalated metal in various valence states and external pressure. The strain energy and the polaron shift created in the intercalation of $TiSe_2$ with metals in various valence states have been determined. The position of the polaron band is shown to decrease linearly with the increasing intercalant ionization potential. © *2000 MAIK "Nauka/Interperiodica".*

In many cases, the intercalation of layered titanium dichalcogenides results in carrier localization in the form of small-radius polarons [1]. The effect of this factor on the phase diagram reduces to limiting the region of single-phase stability to meeting the condition [2] $(E_d - \mu) < 0$, where E_d is the energy corresponding to the center of the polaron band and μ is the electron chemical potential (the Fermi level). In titanium dichalcogenides intercalated with silver, the single-phase state forms only when the concentration of the donor impurity reaches a certain critical level at which the polaron-band center drops below the Fermi level. By contrast, when the intercalants are metals with a higher valence, the single-phase state is stable at arbitrarily low intercalant concentrations. This implies that the polaron band in such materials lies below the Fermi level of the starting compound. This is corroborated by x-ray spectroscopy data available for some of the above compounds [3]. It can thus be suggested that the position of the polaron band is determined by the Coulomb interaction of conduction electrons with the ionized impurity. Therefore, it appears reasonable to choose as a parameter determining the polaron band position the ionization potential of the impurity in the experimentally established valence state for the same starting host matrix. In this case, the polaron shift can be estimated from the experimentally determined lattice distortions induced by the polaron formation [4], provided the elastic constants are known.

The $TiSe_2$ structure belongs to the CdI_2 type, the space group is $P3m1$, and the unit cell contains one formula unit. Titanium atoms make up plane hexagonal networks and occupy one half of the octahedral voids in the hcp array formed by selenium atoms. The intercalated atoms are located in free octahedral voids lying midway between the two titanium atoms along the normal to the titanium network plane. Intercalation of transition metals into titanium diselenide intercalant concentrations that [5, 6] are not too high corresponding to the region of a dilute solid solution, where impurity atoms can be considered as isolated, results in the unit cell parameters becoming linearly dependent on the impurity concentration, without any change in the space group. Such a dependence may be treated as a result of substitution of Ti–*M*–Ti (where *M* stands for the intercalant) for Ti–*V*–Ti (*V* is the vacancy) centers, which have different characteristic dimensions. The deviation from linearity observed for $x > 0.25$, where x is the intercalant concentration, is due to the strain fields in the host matrix around the impurity-containing centers reaching the percolation threshold [7]. Thus, the size of a center strained by intercalation can be derived from the concentration dependence of the lattice constants within the intercalant content range $0 < x < 0.25$.

This work deals with the determination of the polaron shift in titanium diselenide intercalated by different metals. Using the same starting material permits one to reckon the position of the polaron band from its Fermi level. To find the energy associated with the intercalation-induced strain, we invoked the pressure dependence of the lattice constants obtained by x-ray diffraction.

The samples for the x-ray studies were prepared by the standard technique of elemental synthesis in an ampoule. The details of preparation and characterization of the material can be found elsewhere [8]. After the synthesis and the characterization, the M_xTiSe_2 materials (here *M* stands for Cr, Fe, Co) were quenched from 850°C to prevent intercalant ordering and to eliminate a possible effect of this factor on the lattice constants. The x-ray diffraction measurements were car-

1063-7834/00/4209-1610$20.00

ried out on a DRON-3M setup with Cu$K_\alpha$radiation. The lattice parameters were calculated with an error Δa_0 = 0.001 Å and Δc_0 = 0.002 Å. The results are displayed in Fig. 1 together with the available literature data. The x-ray diffraction study of the compressibility of $TiSe_2$ was performed in a quasi-hydrostatic regime in a diamond-anvil high-pressure chamber (the diameter of the working surface 0.6 mm) capable of delivering pressures of up to 20 GPa [10]. The diffractometer used was RIGACU R200 (MoK_α, graphite monochromator, rotating-anode tube). Ruby and NaCl crystals were employed for the calibration of the pressures applied to a sample. The pressure was determined to within ±0.2 GPa, and the lattice constants, to within Δa_0 = 0.005 Å and Δc_0 = 0.01 Å.

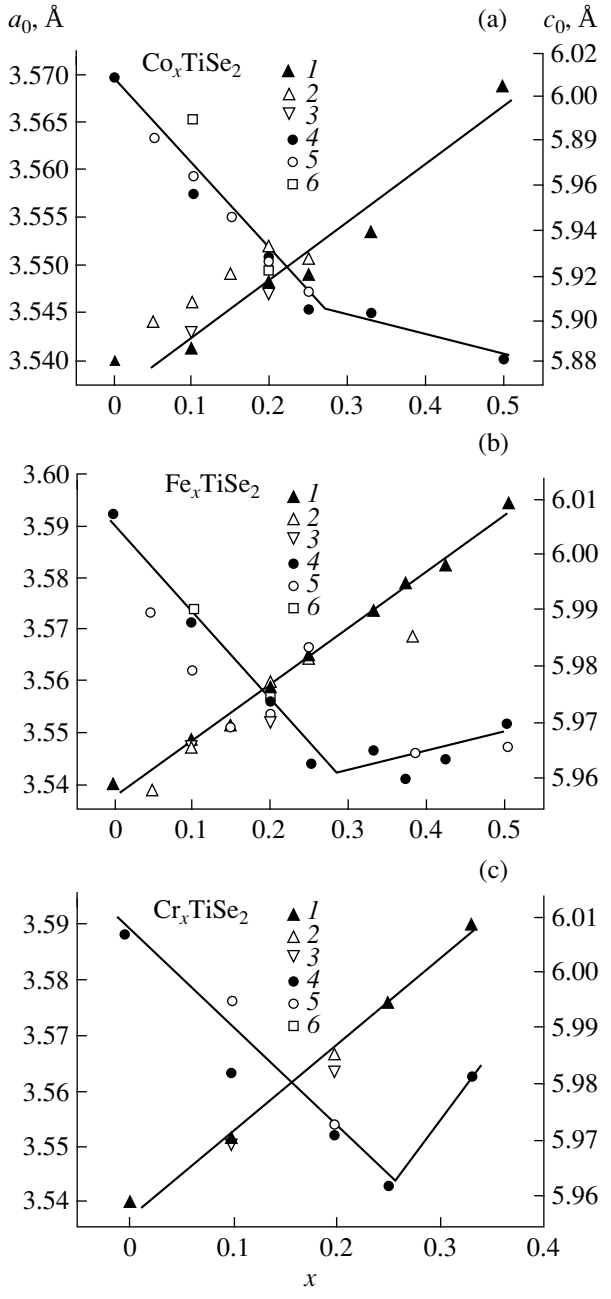

Fig. 1. Concentration dependences of the crystallographic parameters a_0 (*1–3*) and c_0 (*4–6*) for (a) Co_xTiSe_2, (b) Fe_xTiSe_2, and (c) Cr_xTiSe_2. *1* and *4* are the data of this work, *2* and *5* are the data from [6] and *3* and *6* are the data from [9].

The good agreement of our with literature data (Fig. 1) on the Co_xTiSe_2 and Fe_xTiSe_2 systems apparently implies that the impurity ordering affects the lattice constant only insignificantly. The characteristic dimensions of the centers calculated from the data in Fig. 1 for the intercalant concentrations $x < 0.25$ are listed in the table.

The pressure dependences of the $TiSe_2$ lattice parameters are displayed in Fig. 2. The compressibilities in the a_0 and c_0 directions derived from these data are 2.51×10^{-12} and 1.53×10^{-11} Pa^{-1}, respectively. These values are close to those calculated for the isostructural TiS_2, for which the corresponding quantities calculated from the data of [12] are, respectively, 4.07×10^{-12} and 1.46×10^{-11} Pa^{-1}in the semiconducting pressure region, and 3.32×10^{-12} and 0.632×10^{-11} Pa^{-1} in the semimetallic region. A certain growth of the compressibility in the direction normal to the basal plane in $TiSe_2$ compared to $TiSe_2$ can apparently be attributed to the increased width of the van der Waals gap of the first material.

The lattice strain energy induced by polaron formation is $\gamma_c(\Delta c_0)^2$, where Δc_0 is the strain created in the formation of the Ti–*M*–Ti center, and γ_c is the inverse compressibility in the c_0 direction. The strain energy (polaron shift) calculated in this way for the case of various metals intercalated into $TiSe_2$ is displayed in Fig. 3 as a function of the impurity ionization potential in the experimentally established (for Ag, Cr, Fe, Co, Ti) or the most probable (for Ni) valence state.

Intercalation with alkali metals, which do not form covalent bonds with the host lattice, results in an

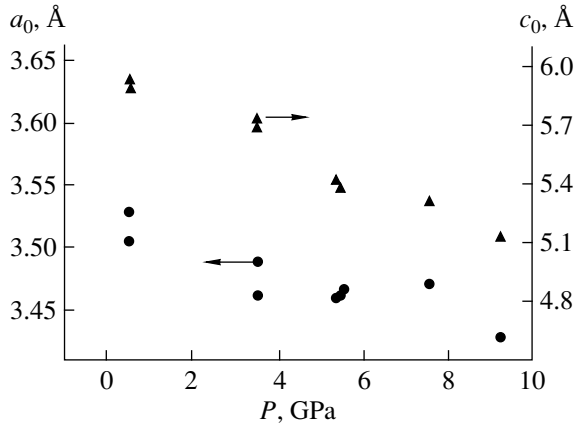

Fig. 2. Pressure dependences of the $TiSe_2$ lattice constants.

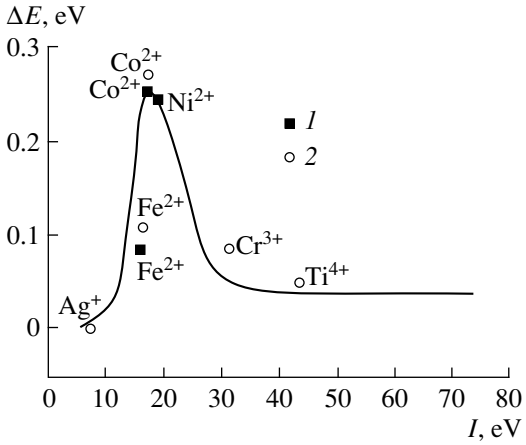

Fig. 3. Dependence of the polaron shift on the intercalant ionization potential. *1* is the data calculated from [6], *2* is this work, and solid line is the result of optimization by model [2].

increase in the lattice constant c_0 through the increase in the interlayer separation. It was shown [13] that an increase in c_0 is directly proportional to the ionic radius of the intercalant ion for the given host lattice. This suggests the conclusion that this effect is associated with the interaction of the filled shells of the intercalant atom and the host lattice. Obviously, in the case of intercalation with transition metals and silver, this effect will be masked by the observed decrease in c_0. While considering this factor presently appears impossible due to the lack of data on the effect of covalent bonding on the intercalant coordination by chalcogen atoms, it is clear that suppressing an increase in c_0 should bring about an increase in the real work expended in straining the lattice. Thus, the numerical values of the polaron shift in M_xTiSe_2 obtained in this work should be considered as a lower estimate.

One can readily see that the dependence of the polaron shift on the impurity ionization potential (Fig. 3) coincides in shape with the one calculated in [2]. This provides support for the starting assumption that it is the Coulomb interaction of conduction electrons with the intercalant that determines the position of the polaron band relative to the Fermi level of the starting material and, hence, the magnitude of the polaron shift. Optimization of the obtained dependence of the polaron shift on the ionization potential I with respect to the theoretical relation [2] shows that a fit can be reached if one replaces I with I/α, where $\alpha = 33$ is the proportionality coefficient which has the meaning of the ionization-potential screening constant (the static dielectric permittivity).

This model can be tested using information on the Mn_xTiSe_2 compound that has not been studied to date. These data will be obtained by our group and published in the near future.

Characteristic dimensions of the Ti–*M*–Ti cluster calculated from the linear portion ($x < 0.25$, where x is the intercalant content) of the concentration dependence of the lattice parameters

Clusters	c_0	a_0
Ti–V–Ti (TiS_2)	6.008	3.540
Ti–Ag–Ti (Ag_xTiSe_2) [11]	6.008	3.540
Ti–Ti–Ti (Ti_xTiSe_2) [5]	5.953	3.552
Ti–Cr–Ti (Cr_xTiSe_2)	5.875	3.598
Ti–Fe–Ti (Fe_xTiSe_2) [6]	5.876	3.663
Ti–Fe–Ti (Fe_xTiSe_2)	5.837	3.638
Ti–Ni–Ti (Ni_xTiSe_2) [6]	5.611	3.584
Ti–Co–Ti (Co_xTiSe_2) [6]	5.583	3.594
Ti–Co–Ti (Co_xTiSe_2)	5.608	3.579

ACKNOWLEDGMENTS

Support of the Russian Foundation for Basic Research (Grant no. 98-03-3265a) and of the Ministry of Education of the RF (Grant no. 97-0-7.1-169) is gratefully acknowledged.

REFERENCES

1. A. N. Titov and A. V. Dolgoshein, Fiz. Tverd. Tela (St. Petersburg) **40**, 1187 (1998) [Phys. Solid State **40**, 1081 (1998)].
2. A. N. Titov and A.V. Dolgoshein, Fiz. Tverd. Tela (St. Petersburg) **42**, 425 (2000) [Phys. Solid State **42**, 434 (2000)].
3. A. Titov, S. Titova, M. Neumann, *et al.*, Mol. Cryst. Liq. Cryst. **311**, 161 (1998).
4. N. F. Mott and E. A. Davis, in *Electron Processes in Non-Crystalline Materials* (Clarendon, Oxford, 1979), p. 427.
5. O. Yu. Pankratova, L. I. Grigor'eva, R. A. Zvinchuk, and A. V. Suvorov, Zh. Neorg. Khim. **38** (3), 410 (1993).
6. Y. Arnaud, M. Chevreton, A. Ahouanjiou, *et al.*, J. Solid State Chem. **17**, 9 (1976).
7. A. N. Titov, Fiz. Tverd. Tela (St. Petersburg) **38** (10), 3126 (1996) [Phys. Solid State **38**, 1709 (1996)].
8. V. G. Pleshchev, A. N. Titov, and A. V. Kuranov, Fiz. Tverd. Tela (St. Petersburg) **39** (9), 1618 (1997) [Phys. Solid State **39**, 1442 (1997)].
9. Y. Tazuke and T. Takeyama, J. Phys. Soc. Jpn. **66**, 827 (1997).
10. V. F. Degtyareva, I. Bdikin, and S. Khasanov, Solid State Commun. **99**, 907 (1996).
11. L. S. Krasavin, A. N. Titov, and V. M. Antropov, Fiz. Tverd. Tela (St. Petersburg) **40** (12), 2165 (1998) [Phys. Solid State **40**, 1962 (1998)].
12. D. R. Allan, A. A. Kelsey, S. J. Clark, *et al.*, Phys. Rev. B **57** (9), 5106 (1998).
13. J. Rouxel and R. Brec, Annu. Rev. Mater. Sci. **16**, 137 (1986).

Translated by G. Skrebtsov

Physics of the Solid State, Vol. 42, No. 9, 2000, pp. 1613–1621. Translated from Fizika Tverdogo Tela, Vol. 42, No. 9, 2000, pp. 1570–1578.

SEMICONDUCTORS AND DIELECTRICS

X-ray Diffraction and Optical Studies of $CdS_{1-x}Se_x$ Solid Solutions with Stacking Faults

N. R. Grigor'eva*, R. V. Grigor'ev*, E. P. Denisov, B. A. Kazennov*, B. V. Novikov*, and D. L. Fedorov****

**Institute of Physics (Petrodvorets Branch), St. Petersburg State University, ul. Ul'yanovskaya 1, Petrodvorets, St. Petersburg, 198504 Russia*

e-mail: grigor@snoopy.phys.spbu.ru

***Baltic State Technical University, St. Petersburg, 198005 Russia*

Received February 7, 2000; in final form, February 28, 2000

Abstract—The existence in $CdS_{1-x}Se_x$ crystals (with $x = 0.10$–0.50) of crystalline regions with stacking faults (SF) was first demonstrated by x-ray diffraction and optical methods. X-ray diffraction studies showed SF to be present in all the samples investigated, but in different concentrations. The effect of SF present in $CdS_{1-x}Se_x$ solid solutions of different compositions on their exciton reflectance and photoluminescence (PL) spectra has been studied. Crystals with high SF concentrations were found to exhibit new exciton bands, which are manifested in reflectance and PL spectra. In the $CdS_{1-x}Se_x$ phase with SF, resonant emission due to free excitons and the corresponding phonon replicas have been observed. The effect of reabsorption, which can bring about a change in the zero-phonon emission line shape (doublet formation), as well as affect the intensity ratios of the zero-phonon line to the phonon replicas, has been analyzed. It is pointed out that the variation with temperature of the shape of the SF-induced PL exciton line indicates its complex structure, with the constituents of this structure varying in intensity with increasing temperature. © *2000 MAIK "Nauka/Interperiodica".*

Solid solutions (SS) of semiconductors enjoy wide application, because their parameters, namely, the gap width, effective carrier mass, crystal structure, and lattice constant can be varied within a broad range by properly varying their composition. SS based on II–VI compounds are employed to develop tunable lasers, light-emitting diodes, photodiodes, and other optoelectronic devices. At the same time, such SS as $CdS_{1-x}Se_x$, $Zn_xCd_{1-x}Se$, and $Zn_{1-x}Mg_xS$ are model objects for investigating the effect of structural and compositional disorder on their properties.

$CdS_{1-x}Se_x$ solid solutions were studied most comprehensively [1–6]. It was established that localized states make up a smooth exciton-band tail, whose density of states decreases as one moves into the band gap [3–6]. According to [1, 2], radiative recombination in $CdS_{1-x}Se_x$ at helium temperatures is dominated by excitons localized at compositional fluctuations. The photoluminescence (PL) spectrum represents a system of equidistant lines due to exciton interaction with phonons. The linewidth is determined by the involvement of excitons with different localization energies. A mobility edge for excitons [7] was experimentally found to exist in the $CdS_{1-x}Se_x$ system. Some authors found that the exciton reflectance (ER) and PL spectra in $CdS_{1-x}Se_x$ solid solutions with a low concentration of one of the components ($x \sim 0.01$) can have a completely different shape. These changes originate from exciton localization processes in near-surface potential wells created in SS with a band gap narrower than that in the bulk [8–10].

The II–VI compounds and their SS are known to crystallize in two modifications, more specifically, the cubic (ZB), with space group T_d^2, and the hexagonal (W), with space group C_{6v}^4. A characteristic feature of II–VI compound crystals is their ability to form stacking faults (SF). The effects of SF on the optical properties of II–VI compounds and of their SS were studied for ZnS [11, 12] and ZnS : (Ag, Cu, Mg) [13]. In $CdS_{1-x}Se_x$, no SF have yet been observed, and to our knowledge, their contribution to the optical properties has not been studied. This may possibly be attributed to the fact that their constituent compounds CdS and CdSe do not form bulk cubic single crystals in usual conditions. The $CdS_{1-x}Se_x$ solid solutions were always assumed to form a hexagonal lattice.

This publication reports on a study of the effect of SF in $CdS_{1-x}Se_x$ solid solutions of various compositions on their ER and PL spectra. X-ray diffraction measurements showed the presence of SF in all the samples studied, but in different concentrations (Figs. 1, 2). Crystals with high SF contents have revealed new exciton bands, which manifest themselves in reflectance and PL spectra (Figs. 3–9). A brief account of these results has already been given in [14, 15].

1063-7834/00/4209-1613$20.00

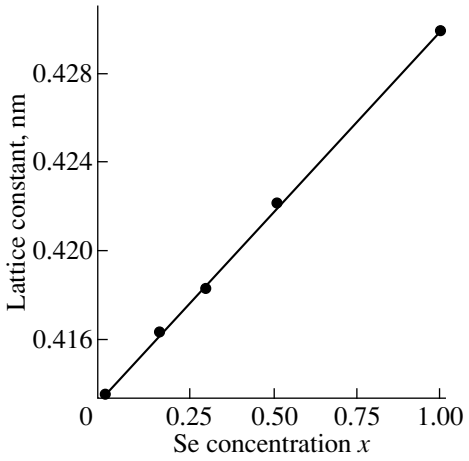

Fig. 1. Dependence of the hexagonal-lattice parameter on the Se content in $CdS_{1-x}Se_x$.

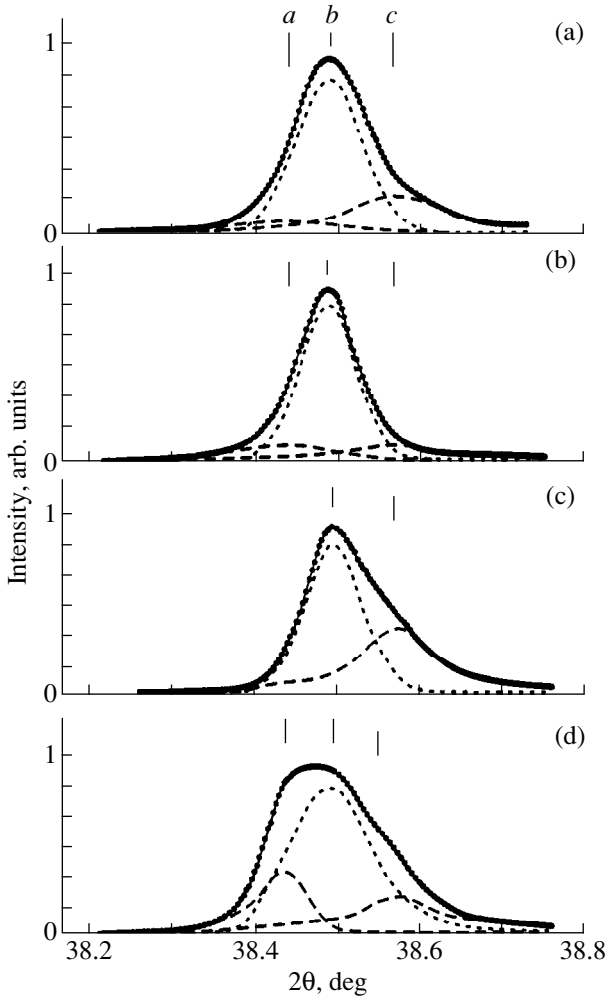

Fig. 2. (220) reflection profiles obtained with CuK_α radiation on $CdS_{1-x}Se_x$ samples. Se concentration (x): (a) 0.15, (b) 0.30, (c) 0.50, and (d) 0.50.

1. EXPERIMENTAL TECHNIQUES

For our study we grew $CdS_{1-x}Se_x$ single crystals with $x \approx 0.10$, 0.15, 0.30, and 0.50 (0.51) by sublimation at 950°C. The starting mixture was preliminarily homogenized by multiple sublimation. The samples were shaped like platelets and hexahedral pins (needles). The largest single-crystal faces were about 2 × 5 mm at a sample thickness from 0.1 to 1 mm. The crystals were not intentionally doped during growth. ER and PL spectra were measured from both natural faces and surfaces polished in an etch.

We studied the angular position and profiles of the diffraction lines from (110) hexagonal planes, which are natural faces of the needlelike single crystals. The x-ray diffraction measurements were performed on a Rigaku D/max RX diffractometer (St. Petersburg United Research Center) with CuK_β radiation. The calculated probing depth is ~10 μm for normal x-ray incidence and is proportional to sinθ for other grazing-incidence angles θ. The crystallographic axes of the needlelike crystals were set parallel to the goniometer axis. They were of sixfold symmetry in all samples, and the sample surface thus coincided with a (110)-type hexagonal plane.

The ER and PL spectra, as well as the temperature dependences, were investigated on an automated setup making possible coordinated measurements and permitting one to obtain, in one measurement, enough information to allow a comparative analysis. The setup included a DFS-24 monochromator with a dispersion of 0.45 nm/mm. When making polarization measurements, a polarizer with a depolarizing wedge used to eliminate the polarizing action of the monochromator was set in front of the entrance slit of the latter. A sample was CW pumped in the fundamental absorption region by a DRSh-250 mercury lamp provided by the corresponding filters and an argon laser. A halogen incandescent lamp was employed to obtain reflectance spectra. To measure the temperature dependences, a sample was immersed in liquid helium or maintained in its vapor. To ensure a constant temperature, the thermostatted chamber with the samples was provided with a thermal sensor and a controlled heater making up a servo-drive. The temperature-setting accuracy was not worse than ±1 K.

2. X-RAY DIFFRACTION STUDIES

Considered in terms of the closest packing model [16], the sphalerite and wurtzite lattices differ only in the way their atomic layers are stacked along the body diagonal of the cubic unit cell. As a result of a change in the atomic interaction energy, the ZB–W phase transition produces a small change in the internuclear distances and, accordingly, in the interplanar separations $d(hkl)$, where h, k, l are the crystallographic plane indices. This phase transition also gives rise to an angular displacement of the x-ray diffraction peak or to its split-

ting if both phases are present. The relative peak displacement is usually ~0.2–0.6%.

As follows from an analysis of the diffractograms, all samples are single-phase SS without separate precipitation of the CdS or CdSe components. The samples studied are single crystals consisting of crystallites differing in structure. There is no stress between the crystallites, and the crystallographic axes of all crystallites are oriented in the same direction. The misorientation of the crystallite crystallographic axes is ~0.1–2°. The absence of a diffuse background indicates that the samples have practically no point defects and an amorphous component. Figure 1 shows the variation of the *a* parameter of the hexagonal cell of the samples under study vs. Se content. One readily sees that this dependence is practically linear, i.e., that the *a* parameter varies proportionally to the compositional variation.

A comprehensive x-ray diffraction investigation of $CdS_{1-x}Se_x$ solid solutions of variable composition (x = 0.15, 0.30, 0.50) was carried out. The second-order diffraction-line profiles obtained from the (110) planes, which correspond to the (220) reflections, are compared in Fig. 2, where the profiles are normalized to the maximum intensity and matched horizontally. The profiles are decomposed into elementary constituents, shown in Fig. 2 by dashed lines. Taking into account that each crystallographic phase in a sample may contain coherent-scattering regions of different size, the diffraction-line profiles were fitted by Gaussian-based functions. This fitting approach allowed us to attain an rms deviation, no more than 1.5×10^{-3}.

As seen from the asymmetry of the profiles, all of them can be considered to consist of two or three peaks, *a*, *b*, and *c*. A similar pattern of profile decomposition in peaks *a*, *b*, and *c* was also found by us to be valid for ZnS single crystals [13]. Peak *a* corresponding to large internuclear distances was assigned [13] to the high-temperature hexagonal phase; peak *c*, to the cubic phase; and the intermediate peak *b* was due to crystallites with SF, i.e., to crystallites made up of layers of hexagonal and cubic phases. A conclusion was drawn [13] that the existence of a separate peak *b* suggests that the crystallites with SF can be considered an independent crystalline phase. The position of peak *b* varied in our samples within a certain range, depending on the volume ratio of the cubic and hexagonal phases. For example, in Fig. 2, peak *b* is displaced toward peak *a* from the midpoint of the *ac* segment, which implies that the crystallites with SF responsible for peak *b* are enriched in hexagonal layers. It is also seen that the x = 0.50 sample, whose profile is depicted in Fig. 2d, contains a large amount of pure hexagonal crystallites compared with the sample of the same composition (x = 0.50), whose profile is given in Fig. 2c. Because peak *b* has the maximum intensity in each profile, it can be maintained that most of the crystallites in all samples contain SF.

3. REFLECTANCE SPECTRA

The $CdS_{1-x}Se_x$ crystals with different compositions studied here revealed three characteristic groups of exciton reflectance spectra. The first group exhibits two known features corresponding to the formation of *A* and *B* excitons in the hexagonal modification of the SS (Figs. 3a and 3d). The spectra shift to lower energies with increasing Se concentration.

In the second group of crystals one can observe, besides the above-mentioned *A* and *B* exciton lines, additional long-wavelength features denoted by us as A_{SF} and B_{SF}. They also have the shape of dispersion curves, and their intensity is comparable to that of the *A* and *B* lines (Figs. 3b and 3d). The A_{SF} line is seen in the $E \perp C$ component, and B_{SF} is in the $E \parallel C$ component. The distance between the A_{SF} and B_{SF} lines varies in samples of different compositions from 5 to 15 meV. The A–A_{SF} distance in crystals with x = 0.30 was found to be ~35 meV. In some cases, spectra of the first or second group could be observed in different parts of the same sample.

Finally, some crystals exhibited only A_{SF} and B_{SF} features, which were polarized as specified above. Sometimes, one could see in the spectra of these samples weak, shorter wavelength features (Fig. 3c). The reflectance spectra of crystals belonging to the third group are also presented in Figs. 6–8. Note that spectra of each type could be observed in the samples studied, irrespective of the value of x.

Thus, the reflectance spectra of a number of single-crystal $CdS_{1-x}Se_x$ samples revealed a previously unknown additional structure resembling a doublet with oppositely polarized components. We associate the formation of this structure (A_{SF}, B_{SF}) with the existence of SF in these samples. As shown in the specific example of ZnS crystals [11, 12], it is the formation of SF in the sphalerite structure that results in a polarized splitting of the exciton ground state and a change in the gap width. The magnitude of the splitting is directly related to the anisotropic field parameter. The effect of SF on the excitonic states was also studied in considerable detail in $Zn_{1-x}Mg_xS$ solid solutions [17].

As already mentioned, a characteristic feature of the II–VI compound crystals is their trend to SF formation. By stacking faults, a wrong layer sequence is understood. It gives rise to an intermediate structure with a variable anisotropy. CdS and CdSe usually crystallize in the wurtzite structure. However, epitaxial layers grown on an oriented GaAs substrate may possess a sphalerite structure. In these conditions, the exciton resonance in the cubic CdS modification is downshifted by 15 meV [18, 19]. In CdSe crystals, this shift is about 70 meV [17]. In other words, $E_g^{ZB} < E_g^{W}$ for both CdS and CdSe. An analysis of exciton reflectance spectra gives one grounds to maintain that the appearance of the additional long-wavelength doublet structure in

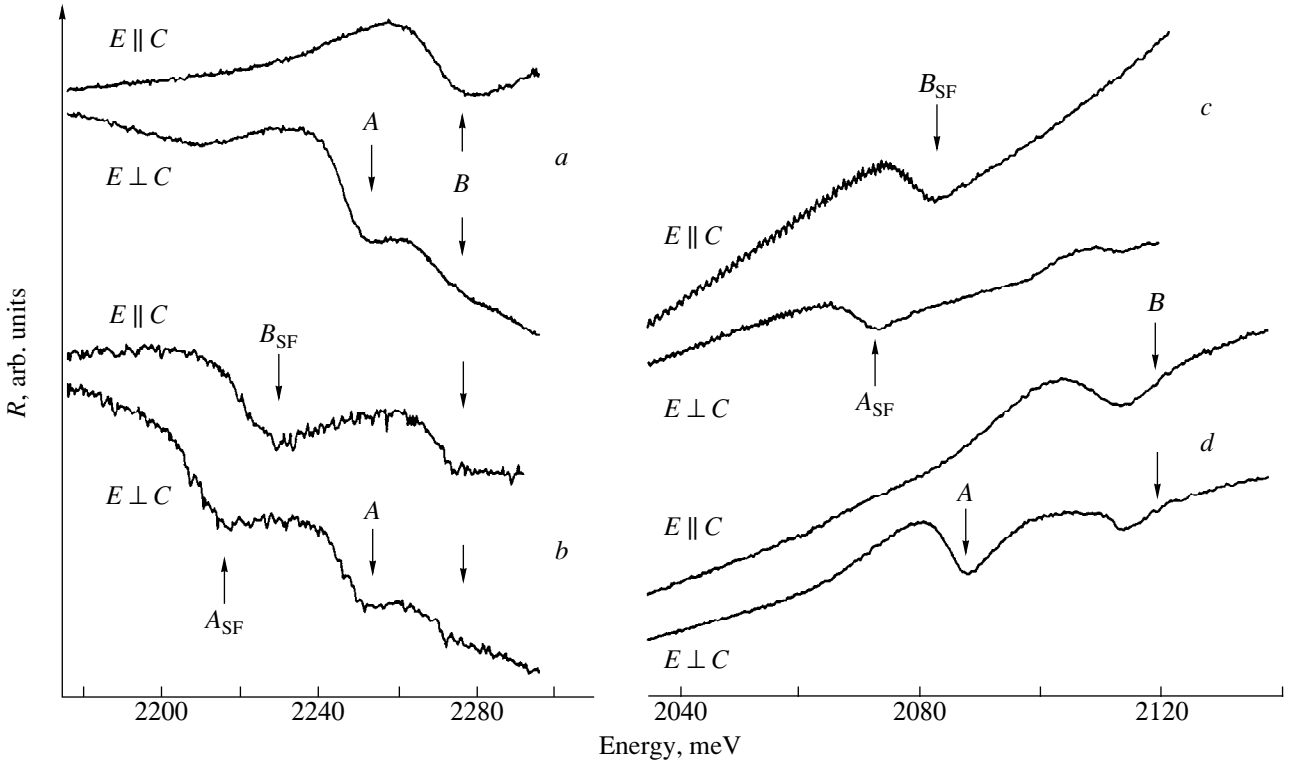

Fig. 3. Reflectance spectra of $CdS_{1-x}Se_x$ crystals. Se concentration (x): (*a*) 0.15, (*b*) 0.30, (*c*) 0.50, (*d*) 0.51.

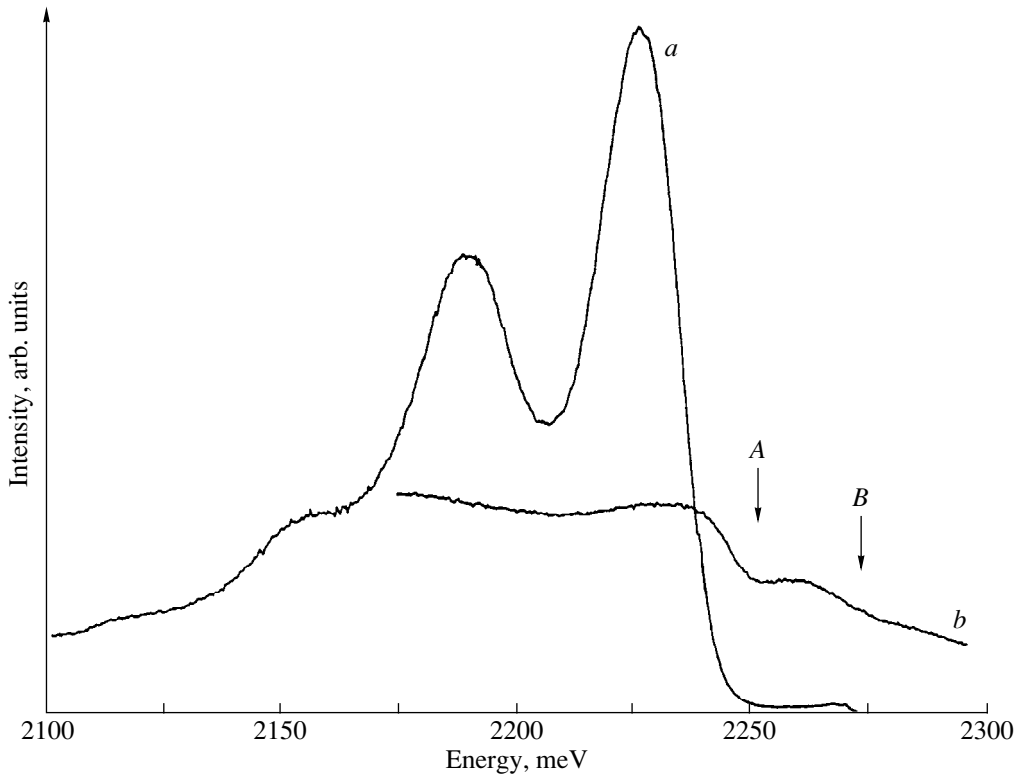

Fig. 4. Spectra of (*a*) photoluminescence and (*b*) reflectance of a $CdS_{1-x}Se_x$ crystal (x = 0.30).

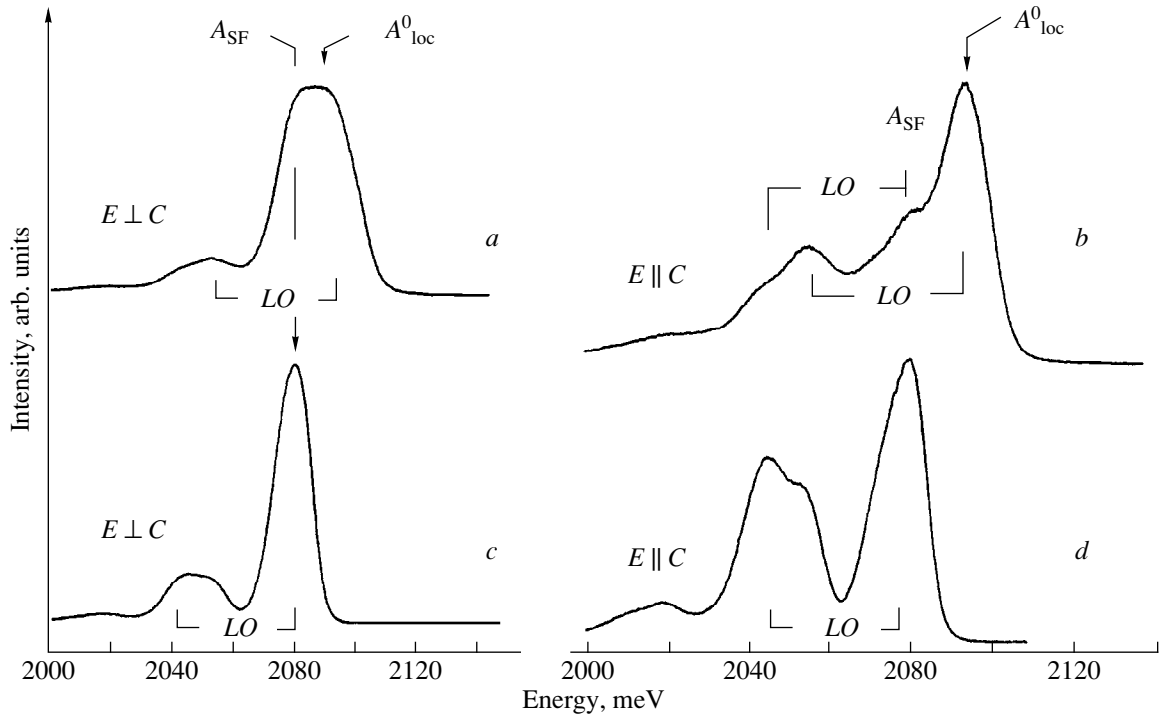

Fig. 5. Photoluminescence spectra of a $CdS_{1-x}Se_x$ crystal ($x = 0.50$) obtained (*a*, *b*) from natural faces and (*c*, *d*) from a surface treated with a polishing etchant.

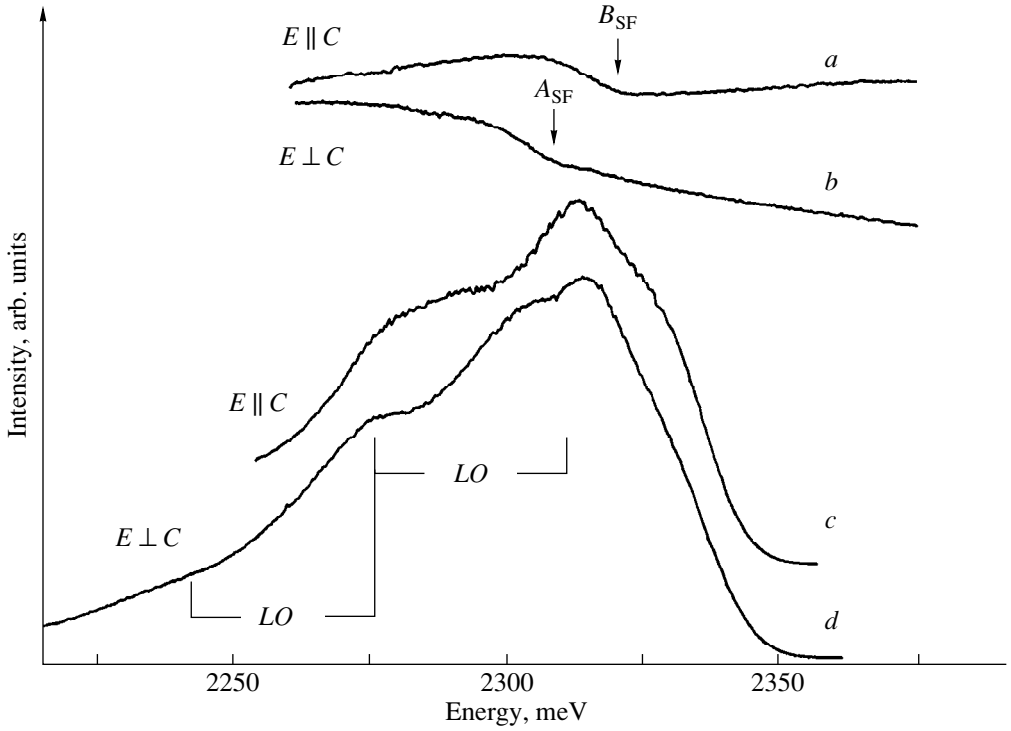

Fig. 6. Spectra of (*a*, *b*) reflectance and (*c*, *d*) photoluminescence of a $CdS_{1-x}Se_x$ crystal ($x = 0.15$).

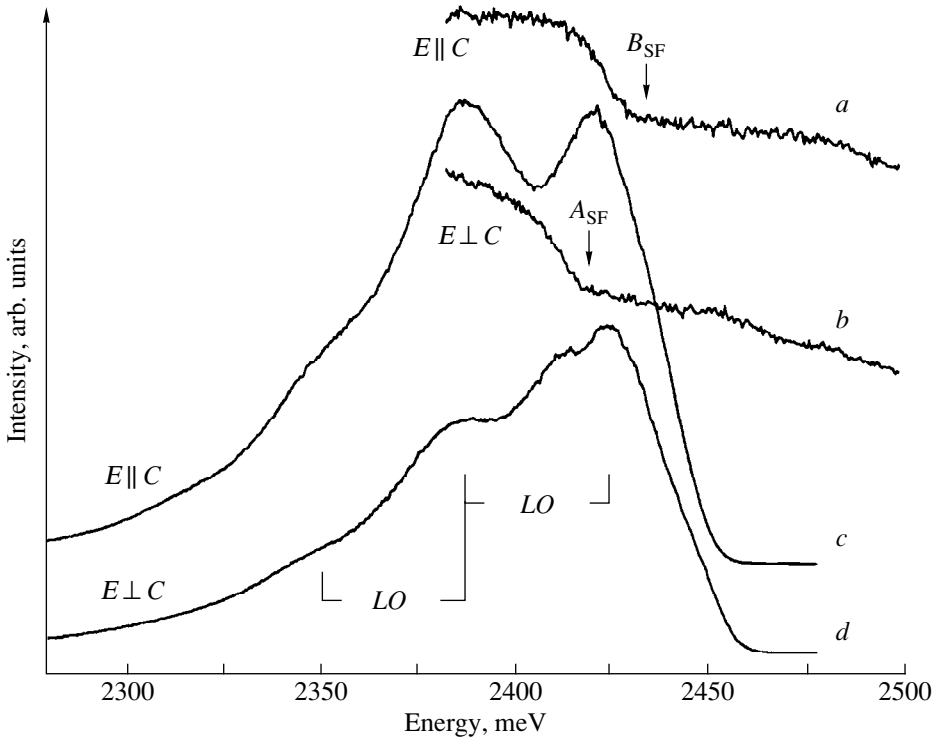

Fig. 7. Spectra of (*a*, *b*) reflectance and (*c*, *d*) photoluminescence of a $CdS_{1-x}Se_x$ crystal ($x = 0.10$).

$CdS_{1-x}Se_x$ samples is due to the formation of crystallites with SF.

4. PHOTOLUMINESCENCE SPECTRA

As in the reflectance spectra, in the photoluminescence of the samples studied one can identify three main types of spectra. One of them is the well-known emission due to localized excitons in the hexagonal phase (Fig. 4) and is observed at low temperatures. It is shifted approximately by the *A* exciton localization energy and has a series of phonon replicas. Spectra of the second type are observed when crystals of the hexagonal phase have regions with SF. In this case, the PL spectrum exhibits the well-known emission of the hexagonal phase, as well as a new emission line, which is shifted to lower energies with respect to the hexagonal-phase radiation and is resonant with the A_{SF} reflectance line (Figs. 5a and 5b). The PL line A_{SF} also has a system of replicas with a phonon of slightly lower energy. As seen from Figs. 5a and 5b, in the $E \perp C$ component, both lines merge to form one maximum, while for $E \parallel C$ they are well separated. It should be stressed that, in crystals of this type, phonon replicas make up a doublet in which the component intensity ratio can vary. The intensity ratio of the zero-phonon components A^0_{loc} and A_{SF} can also vary (Fig. 5b). We shall return to this point later.

In the third group of crystals, where the emission of crystallites with SF dominates, only the A_{SF} line and its phonon replicas are observed (Figs. 6–8). The intensity of the zero-phonon line in samples of this group may be lower than that of the first phonon replica, which we believe to be due to the resonant character of emission in the A_{SF} line.

As is well known, in crystals with a surface layer of thickness *d*, where excitons annihilate mainly nonradiatively, one may observe a drop in emission intensity and the formation of a doublet (the self-absorption effect). This phenomenon was first observed experimentally in CdS crystals [20], later on CdTe [21] and ZnSe [22], and was described in considerable detail in [23, 24]. Taking into account self-absorption yields the following expression for the intensity of a zero-phonon emission line [24, 25]:

$$I_{PL} = I^0_{PL}(\nu)\exp[-k(\nu)d],$$

where $k(\nu)$ is the absorption coefficient and *d* is the diffusion length. Substituting the free-exciton diffusion length in the expression for $I^0_{PL}(\nu)$, it can be shown that, as *d* increases, one first observes a broadening of the emission line accompanied by a drop in its intensity, followed by the formation and deepening of a dip, i.e., the appearance of a doublet. Figure 5b demonstrates the formation of a doublet structure in the $E \perp C$ component. The dip is particularly clearly pronounced in the

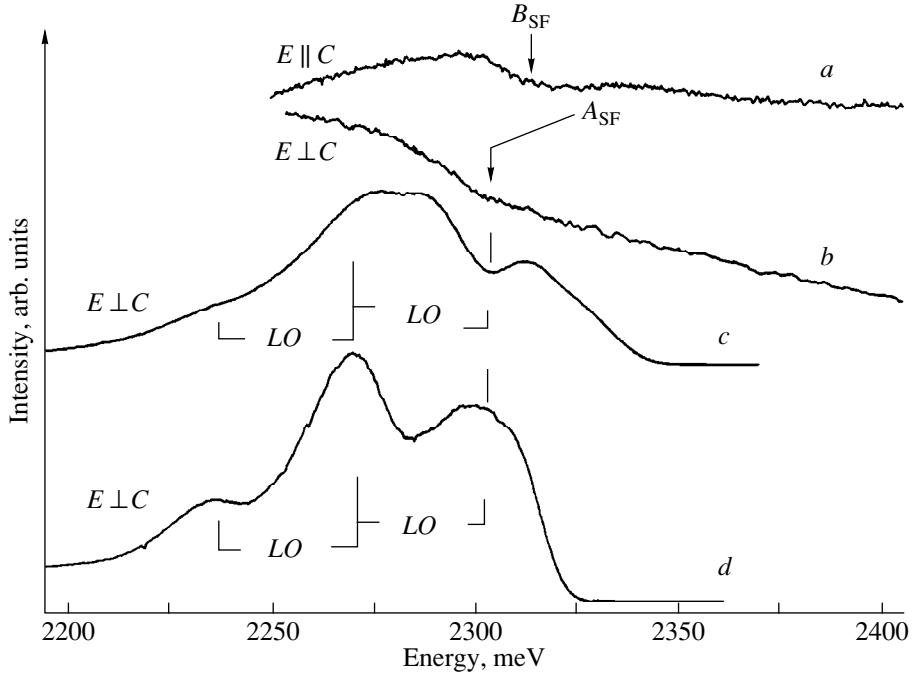

Fig. 8. Spectra of reflectance (*a*, *b*) and photoluminescence from a natural face (*c*) and after polishing with an etchant (*d*) of a $CdS_{1-x}Se_x$ crystal ($x = 0.15$).

sample illustrated by Fig. 8c. On polishing the sample in an etch, a maximum appeared in place of the dip and the PL intensity increased (Fig. 8d).

We believe that $CdS_{1-x}Se_x$ crystals with SF exhibit resonant emission of free excitons and their phonon replicas. Reabsorption may change the shape of the zero-phonon emission line (doublet formation), as well as affect the intensity ratio of the zero-phonon line and its replicas.

The self-absorption effect can manifest itself in a peculiar way in samples of the second group, where regions with SF and the W structure coexist. While PL spectra from the regions with SF and the W structure have a similar shape, the intensity ratio of the zero-phonon line to its first phonon replica in the spectra are different. It is natural to assume that this is due to the existence in the near-surface region of a nonluminescing layer with SF. Because $E_g^{ZB} < E_g^{W}$, the zero-phonon line emission of localized excitons (in the region with the W structure) is absorbed in this layer, which entails a change of the A_{loc}^0/A_{loc}^{LO} ratio.

The spatial inhomogeneity of the distribution of regions with SF and the W structure was confirmed experimentally by etching the surface (curves *c* and *d* in Fig. 5). After the treatment in a polishing etch, the A_{loc}^0 PL line, associated with the W structure, disappeared in both the $E \perp C$ and $E \parallel C$ components. This proves that the layer adjoining the surface was dominated by the W structure before the etching.

Note that, after removal of the layer with the dominant W structure and disappearance of the A_{loc}^0 line, its phonon replica persisted, although its intensity fell markedly. After the etching, the layer containing mostly crystallites with SF became closest to the surface. As a result, the A_{loc}^0 emission did not escape from the crystal (due to absorption by the long-wavelength edge of the SF layer). The phonon replica A_{loc}^{LO} lies on the low-energy side of the absorption edge of the SF crystallites and can be observed in the spectrum; its low intensity is apparently associated with the low intensity of localized-exciton emission in the bulk of this sample.

5. TEMPERATURE DEPENDENCE

An analysis of the temperature dependences of the PL spectra obtained on our samples shows that, as the temperature increases, the intensity of the A_{loc} and A_{SF} lines decreases, their shape changes, and one also observes a considerable decrease in the intensity of phonon replicas of both the A_{loc} and A_{SF} lines. The phonon replicas in the spectrum disappear at 34 K.

In this communication, we first note specific features in the behavior of the A_{SF} line (Fig. 9). The variation of the shape of this line with temperature implies

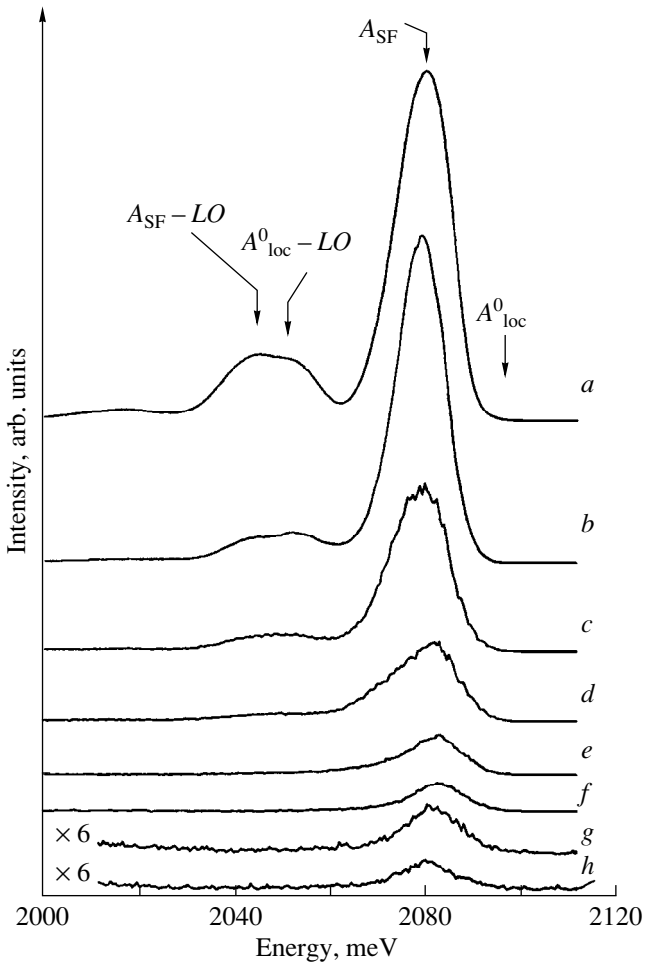

Fig. 9. Temperature dependence of the photoluminescence spectra ($E \perp C$) of a $CdS_{1-x}Se_x$ crystal ($x = 0.50$). Temperature (K): (*a*) 4.2, (*b*) 11.5, (*c*) 18, (*d*) 27, (*e*) 34, (*f*) 43, (*g*) 53, and (*h*) 63. The A_{loc} arrow specifies the localized-exciton PL line for the W phase.

its complex structure. The constituents of this structure vary in intensity with increasing temperature. As a result, one can observe the A_{SF} profile acquiring an asymmetric shape with a distinct long-wavelength tail. As the temperature is further increased, the emission line shape again becomes practically symmetric.

We followed the temperature behavior of the A_{loc} and A_{SF} emission lines in different parts of the sample whose A_{loc} line exhibited properties similar to those of the A_{SF} (the weakening of the phonon replicas and a change in the shape). The temperature behavior of A_{loc} and A_{SF} will be considered in more detail in another publication.

6. RESULTS AND DISCUSSION

The above results of x-ray-diffraction and optical studies permit a conclusion that a crystalline phase with SF has been detected in $CdS_{1-x}Se_x$ crystals. The (220) reflection profiles obtained for different compositions are characteristic of crystals with SF. In all samples, the strong peak *b* produced by crystallites with SF lies between the positions of *a* and *c* corresponding to the hexagonal and cubic phases, respectively. In different crystals, the maximum of *b* may shift toward *a* or *c*. This suggests that the regions formed predominantly in all samples are those with the SF, as well as with hexagonal and cubic structures in various relative amounts. The largest relative number of regions with SF is observed for $x = 0.30$.

The $CdS_{1-x}Se_x$ crystals studied revealed splitting and polarization of exciton lines in reflectance spectra differing from those in the hexagonal phase. This observation can be compared with the theoretical [25, 26] and experimental [11, 12] data, by which the existence of SF in the cubic phase manifests itself as a splitting of the degenerate valence band, with the magnitude of the splitting proportional to the disorder parameter α [1, 12].

One can roughly estimate the extent of disorder in the crystals studied. For $\alpha = 0.33$, the "induced" crystal field in ZnS crystals was found [11] to be ~11.7 meV (~36% with respect to crystal-field splitting in the W phase of ZnS). In the $CdS_{1-x}Se_x$ crystals with $x = 0.50$ studied by us, the crystal-field splitting in the W phase is ~30 meV and the "induced" splitting is ~8 meV; i.e., this ratio is about 25%. According to our data, in $x = 0.30$ crystals it is about 40%. Thus, the crystal-field splitting effect in $CdS_{1-x}Se_x$ crystals observed by us is comparable with that in ZnS crystals, and the "induced" splitting is comparable with the crystal-field splitting in the W phase.

Exciton PL spectra of the phase with SF exhibit a new line, which is resonant with the long-wavelength reflectance line. Simultaneously, PL spectra may also contain emission lines belonging to the phase with SF and the W phase. This shows that each phase exists independently and occupies definite geometrical regions. This point is also stressed by the experiment on local excitation of the surface and its treatment with a polishing etchant.

In crystals, or parts of crystals, with SF, exciton emission differs little from that in the W phase. It also has a zero-phonon line and several phonon replicas, which fall off in intensity toward lower energies. In order to make a more accurate assignment of an emission line to a crystalline phase, one has to use both reflectance spectra and x-ray diffraction measurements.

The observed self-reversal of the A_{SF} line shows it to be related to free excitons. It is hardly likely, however, that only free excitons produce emission in solid solutions with SF. Indeed, as seen from the temperature dependences, the A_{SF} line profile is made up of independently varying components. The longer wavelength component already disappears at approximately 34 K. We relate this component to both exciton localization at

compositional fluctuations and that associated with structural disorder. A further increase in temperature delocalizes the excitons. Note the fairly quick disappearance of the phonon replicas with increasing temperature, a phenomenon possibly caused by a change in the character of exciton–phonon interaction.

Although optical manifestation of SF in $CdS_{1-x}Se_x$ solid solutions has not yet been reported, these materials had earlier exhibited features which we believe could be associated with the SF. For instance, in some $CdS_{1-x}Se_x$ samples with $x = 0.15$, Agekyan *et al.* observed [27] a doublet structure in the localized-exciton emission line (O_1 and O_2) which was, however, related [27] to specific features of exciton diffusion in the density-of-states tail. The frequently observed doublet structure in the phonon replicas of localized excitons can also possibly be assigned to SF-related effects.

A manifestation of structural disorder was recently observed in $Zn_{1-x}Mg_xSe$ mixed crystals at the sphalerite–wurtzite phase transition, which takes place in this compound at $x = 0.19$. It was shown [28, 29] that at this concentration one observes the coexistence of the ZB and W structures, two polytypes (8H and 4H), and stacking faults.

Thus, we have demonstrated by x-ray diffraction and optical methods that $CdS_{1-x}Se_x$ crystals (for $x = 0.10$–0.50) contain crystalline regions with stacking faults.

ACKNOWLEDGMENTS

This work was supported by the Russian Foundation for Basic Research, project no. 00-15-96756.

REFERENCES

1. E. Cohen and M. D. Sturge, Phys. Rev. B **25**, 3828 (1982).
2. S. Permogorov, A. Reznitsky, S. Verbin, *et al.*, Phys. Status Solidi B **113**, 589 (1982).
3. J. A. Kash, A. Ron, and E. Cohen, Phys. Rev. B **28**, 6147 (1983).
4. S. A. Permogorov, A. N. Reznitskiĭ, S. Yu. Verbin, and V. A. Bonch-Bruevich, Pis'ma Zh. Éksp. Teor. Fiz. **38**, 22 (1983) [JETP Lett. **38**, 25 (1983)].
5. S. Yu. Verbin, S. A. Permogorov, A. N. Reznitskiĭ, *et al.*, Fiz. Tverd. Tela (Leningrad) **31** (1), 84 (1989) [Sov. Phys. Solid State **31**, 46 (1989)].
6. A. A. Klochihin, S. A. Permogorov, and A. N. Reznitsky, J. Cryst. Growth **159**, 848 (1996).
7. S. Permogorov, A. Reznitsky, S. Verbin, and V. Lysenko, Solid State Commun. **47**, 5 (1983).
8. V. A. Kiselev, B. V. Novikov, and A. E. Cherednichenko, *Exciton Spectroscopy of a Near-Surface Region of Semiconductors* (Leningrad, 1987).
9. A. S. Batyrev, N. V. Karasenko, B. V. Novikov, *et al.*, Pis'ma Zh. Éksp. Teor. Fiz. **62**, 397 (1995) [JETP Lett. **62**, 408 (1995)].
10. N. R. Grigor'eva, B. A. Kazennov, B. V. Novikov, *et al.*, Fiz. Tverd. Tela (St. Petersburg) **41**, 1568 (1999) [Phys. Solid State **41**, 1437 (1999)].
11. A. N. Ryvkin, L. G. Suslina, G. N. Khil'ko, and E. B. Shadrin, Pis'ma Zh. Éksp. Teor. Fiz. **7**, 335 (1968) [JETP Lett. **7**, 262 (1968)].
12. G. L. Bir, G. E. Pikus, L. G. Suslina, *et al.*, Fiz. Tverd. Tela (Leningrad) **13**, 3551 (1972) [Sov. Phys. Solid State **13**, 3000 (1971)].
13. E. P. Denisov, A. G. Areshkin, D. L. Fedorov, and S. G. Konnikov, Fiz. Tverd. Tela (St. Petersburg) **39**, 49 (1997) [Phys. Solid State **39**, 41 (1997)].
14. B. V. Novikov, N. R. Grigor'eva, R. V. Grigor'ev, *et al.*, Pis'ma Zh. Éksp. Teor. Fiz. **70**, 221 (1999) [JETP Lett. **70**, 222 (1999)].
15. N. R. Grigorieva, R. V. Grigoriev, E. P. Denisov, *et al.*, in *Abstracts of Ninth Int. Conf. on II–VI Compounds, 1999.*
16. T. Penkala, *Zarys krystalochemii* (Pánstwowe Wydawn. Naukowe, 1972; Khimiya, Leningrad, 1974).
17. L. S. Markov and D. L. Fedorov, Kristallografiya **38**, 179 (1993) [Crystallogr. Rep. **38**, 229 (1993)].
18. T. Yodo and Sh. Tanaka, J. Appl. Phys. **72** (7), 2781 (1992).
19. Y. Endoh, Y. Kawakami, and T. Taguchi, Jpn. J. Appl. Phys. **27**, L2199 (1988).
20. K. F. Lider and B. V. Novikov, Opt. Spektrosk. **23**, 611 (1967).
21. V. S. Vavilov, A. A. Gippius, and Zh. R. Panosyan, *Cadmium Telluride* (Moscow, 1968).
22. B. V. Novikov, A. B. Pavlov, and V. G. Talalaev, Fiz. Tverd. Tela (Leningrad) **23**, 207 (1981) [Sov. Phys. Solid State **23**, 116 (1981)].
23. V. V. Travnikov and V. V. Krivolapchuk, Fiz. Tverd. Tela (Leningrad) **24**, 961 (1982) [Sov. Phys. Solid State **24**, 547 (1982)].
24. G. P. Yablon'skiĭ, Yu. P. Rakovich, A. A. Gladyshchuk, and V. V. Dolin, Zh. Prikl. Spektrosk. **60**, 248 (1994).
25. J. I. Pankov, *Optical Processes in Semiconductors* (Prentice-Hall, Englewood Cliffs, 1971; Mir, Moscow, 1973).
26. J. L. Birman, Phys. Rev. **115**, 1493 (1959).
27. V. Agekyan, R. Bindeman, R. Schwabe, *et al.*, Phys. Status Solidi B **116**, K43 (1983).
28. A. Cichos, F. Firszt, U. Falke, *et al.*, Acta Phys. Pol. A **95**, 269 (1999).
29. F. Firszt, A. Cichos, P. Dluzevski, *et al.*, Solid State Commun. **108**, 367 (1998).

Translated by G. Skrebtsov

Physics of the Solid State, Vol. 42, No. 9, 2000, pp. 1622–1624. Translated from Fizika Tverdogo Tela, Vol. 42, No. 9, 2000, pp. 1579–1581.

SEMICONDUCTORS AND DIELECTRICS

Discovery of Hyperbolic Excitons in Layered Semiconductor BiI_3

S. V. Virko, M. P. Lisitsa, and F. V. Motsnyĭ

Institute of Semiconductor Physics, National Academy of Sciences of Ukraine, Kiev, 252028 Ukraine

e-mail: motsnyi@sun.semicond.kiev.ua

Received January 13, 2000; in final form, March 2, 2000

Abstract—Hyperbolic excitons have been detected in layered semiconductor BiI_3. Their main parameters have been evaluated. © *2000 MAIK "Nauka/Interperiodica".*

Excitons existing near van Hove critical saddle points of the M_1 type and called hyperbolic have been predicted theoretically in [1, 2], and observed experimentally in the optical spectra of single crystals of GaSe [3–5], InSe [6], TlSe [7], and GaP [8]. The absorption and photoluminescence bands corresponding to them are located in an energy region far above the forbidden gap E_G. Due to the absence of detailed calculations of the energy band structure for most compounds, a search for hyperbolic excitons presents difficulties and, as a result, they are poorly studied.

The present work is dedicated to an investigation of the temperature dependences of the reflection spectra (RS) of layered BiI_3 single crystals for photon energies $h\nu > E_G$ with the aim of revealing hyperbolic excitons.

The single crystals of BiI_3 were grown by the Bridgman technique. The samples were in the form of rectangular plates, with the optical C axis being perpendicular to the plane of cleaving. An atomically clean surface was used as a precautionary measure against the influence of the surface condition. The surface was produced by cleaving the samples with a knife in liquid helium or peeling them off with scotch tape in cold helium gas. The surface was mirrorlike, and much care was taken to prevent the samples from deforming.

The light of a stabilized filament lamp was directed at a sample at an angle that was less than 5° with respect to the C axis. The reflection spectra were recorded for the polarization $\mathbf{E} \perp \mathbf{C}$ by using a PSG-2 spectrometer with a resolution of 0.15 meV at temperatures of 5–300 K. The temperature was measured with a precision of ±0.5 K.

The data on the dispersion of the indices of refraction $n(h\nu)$ and absorption $\kappa(h\nu)$ for the polarization $\mathbf{E} \perp \mathbf{C}$ at 4.2 K are derived by the classical Kramers–Kronig relations, as the effects of spatial dispersion are not essential in BiI_3 [9, 10].

The typical reflection spectra of the BiI_3 single crystals with an atomically clean surface, as well as the $n(h\nu)$ and $\kappa(h\nu)$ dependences, for the polarization $\mathbf{E} \perp \mathbf{C}$ and an energy range 1.5–5.5 eV at 5 K are shown in Fig. 1. Alongside known bands at 2.098, 2.206, and at 2.124 eV, caused by free [10, 11] and quasi-surface [10, 12] excitons, respectively, a clearly pronounced band appears at 3.804 eV. The latter is also observed in the RS of samples with a natural surface; therefore, it cannot be associated with the surface condition. The maximum absorption coefficient in this band is 5×10^5 cm^{-1}, which is sufficiently large and cannot be caused by the presence of an impurity or other defects of the crystal lattice.

The influence of temperature on the band at 3.804 eV is illustrated in Figs. 2 and 3. As can be seen, the band undergoes essential variations with a temperature rise: the maximum of reflection shifts to lower energies by 4.6×10^{-2} eV, the reflection coefficient decreases from 30 to 23%, and the half-width of the band more than doubles. The temperature dependence of the last quantity is described well by the empirical relationship:

$$\Gamma(T) = (\Gamma_0^2 + AT^2)^{1/2}, \quad (1)$$

where $\Gamma_0 = 85$ meV and $A = 150$ meV^2/T^2 (curve *1* in Fig. 3). It should be noted that the maximum of this band remains steady to $T \approx 45$ K, but it shifts to lower energies with a rate of $dE_{max}/dT = -3.6 \times 10^{-4}$ eV/T at temperatures $T > 45$ K (curve *2* in Fig. 3). The band maximum obeys the empirically determined temperature dependence of the form

$$E_{max}(T) = 3.804 - 6.2 \times 10^{-4} T^2/(T + 240\ \text{K})\ \ (\text{eV}), \quad (2)$$

which was found to be valid for hyperbolic excitons in GaSe [3].

Thus, the large value of the absorption coefficient, together with its strong temperature dependence, conclusively indicates that the band at 3.804 eV is of excitonic origin.

Taking $E_G = 2.242$ eV for BiI_3 at $T = 4.2$ K [10, 11], we notice that the exciton level corresponding to this band is 1.6 eV above the fundamental absorption edge. This level can be associated with both parabolic excitons of deeper subbands of the conduction and valence bands and hyperbolic excitons. However, it is known

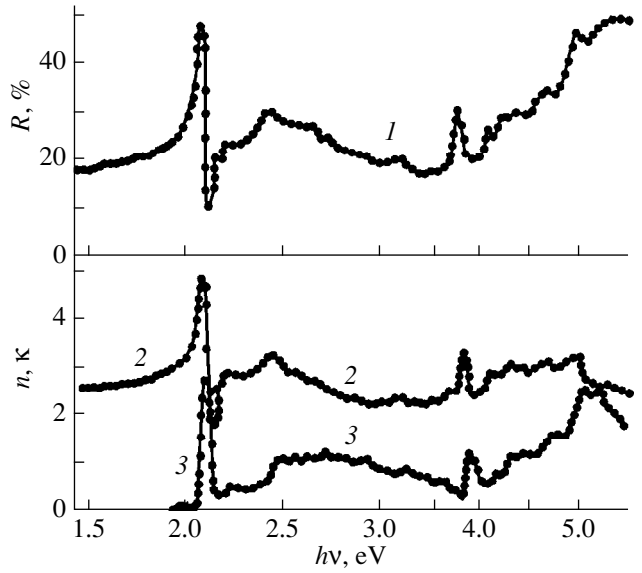

Fig. 1. Reflection spectra (*1*) and dispersion of the indices of refraction $n(h\nu)$ (*2*) and absorption $\kappa(h\nu)$ (*3*) in layered BiI_3 single crystals with atomically clean surface at $T = 4.2$ K and $\mathbf{E} \perp \mathbf{C}$.

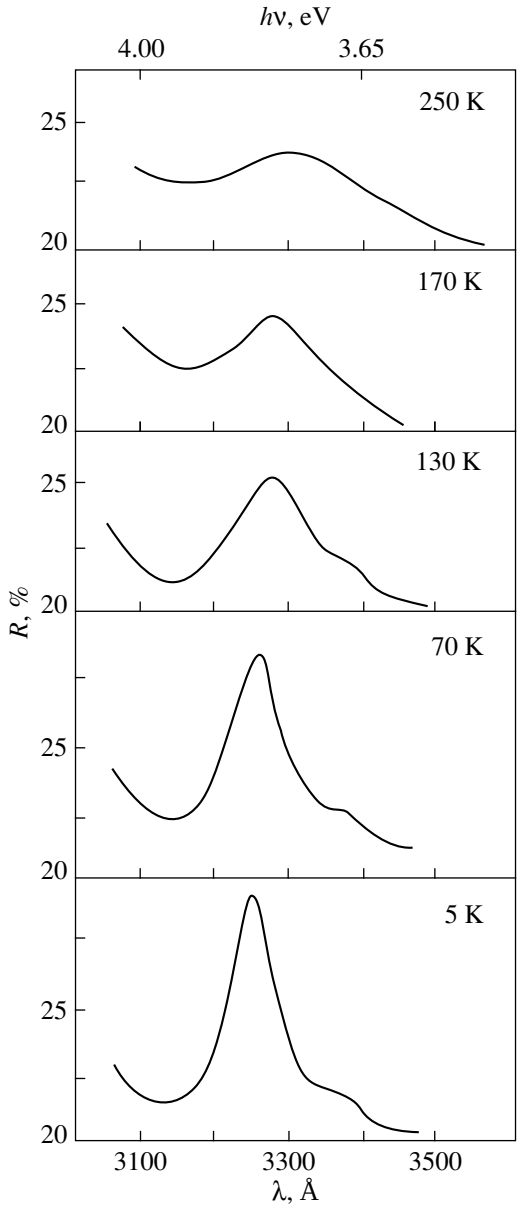

Fig. 2. Temperature dependence of the reflection band at 3.804 eV in layered BiI_3 single crystals at $\mathbf{E} \perp \mathbf{C}$.

[1] that the variation of the density of states is of the form $dN/dE \sim (E - E_G)^{1/2}$ for the interband transitions at the van Hove M_0 point, whereas it has the form of $dN/dE \sim [C - b(E_C - E)]^{1/2}$ and $dN/dE \sim C$ for the transitions near the critical saddle point of the M_1 type for $E \le E_C$ and $E > E_C$, respectively (E_C is the energy at the van Hove M_1 saddle point and C and b are constants). On the other hand, we have $K \sim \kappa \sim dN/dE$; therefore, the characteristic feature of the hyperbolic excitons, distinct from the parabolic excitons, is, for example, the existence of a plateau on a $K(E)$ or a $\kappa(E)$ curve on the short-wave side of the exciton resonance. Such a plateau was, in reality, observed earlier in the absorption spectra of the hyperbolic excitons in a layered GaSe [3]. A plateau is also on a $\kappa(E)$ curve of the layered BiI_3 at energy $h\nu = 4.4$ eV (curve *3* in Fig. 1). The validity of the conclusion drawn is also supported by the following arguments.

(1) For all known semiconductors, the coefficient of the temperature shift of deeper subbands of the valence band and higher subbands of the conduction band is less than that of the subbands responsible for the fundamental absorption edge. In the case of BiI_3, we have $dE_G/dT = +8 \times 10^{-5}$ eV/T at $T \le 45$ K and -1.3×10^{-4} eV/T at $T > 45$ K [10]. Therefore, the different temperature behavior of $E_{max}(T)$ and $E_G(T)$ at $T \le 45$ K and the fact that the rate of the long-wave shift of E_{max} is 1.7 times higher than that of E_G at $T > 45$ K cannot be explained by the involvement of the above-mentioned subbands in the occurrence of the 3.804-eV band.

(2) The temperature broadening of the 3.804-eV band is extremely strong at $T = 270$ K. It exceeds the initial half-width at $T = 5$ K by 153 meV, which is considerably greater than the corresponding broadening of the exciton absorption band with $n = 1$ [10, 11].

(3) The temperature shift of the maximum of the band in question is consistent with that for the hyperbolic excitons in GaSe [3].

Consequently, all of the above allows us to conclude that the 3.804-eV band belongs to a van Hove singularity of the M_1 type rather than to that of the M_0 type.

We have estimated the binding energy of the hyperbolic excitons by analogy with the binding energy of the M_0-point excitons, accepting that $E_{ex}^{hyp} = E_{M1} - E_{max}$.

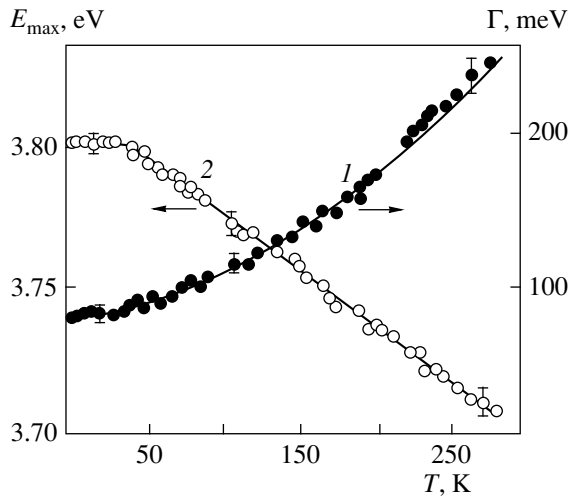

Fig. 3. Temperature dependence of the half-width (*1*) and energy position of the maximum (*2*) of the reflection band at 3.804 eV in the layered BiI_3 single crystals at $\mathbf{E} \perp \mathbf{C}$.

Taking $E_{M1} = 4.4$ eV at $T = 4.2$ K, we have derived that $E_{ex}^{hyp} = 0.6$ eV.

(4) The half-width of the absorption band at 3.804 eV is equal to 85 meV at 5 K, which is 2.4 times as large as the half-width of the main exciton band with $n = 1$. Accepting $\tau \sim 1/\Gamma$, we find that, for BiI_3, the lifetime of the hyperbolic excitons τ_{ex}^{hyp} is 2.4 times shorter than that of the parabolic excitons, τ_{ex}^{par}. This seems likely to be caused by the dynamical instability of the hyperbolic excitons near the critical saddle point of the M_1 type. Unfortunately, the available calculation of the energy band structure of BiI_3 [13] does not allow this point to be identified with a specific point of the Brillouin zone.

Thus, we conclude that hyperbolic excitons have been detected in a layered semiconductor BiI_3 by investigating the reflection spectra of samples with atomically clean and natural surface's in the energy region $h\nu > E_G$.

ACKNOWLEDGMENTS

The authors are grateful to O.S. Sergeev for assistance in performing the reflection spectra measurements.

The work was partly supported by the International Soros Science Educational Program (ISSEP), grant no. EPU052023.

REFERENCES

1. J. P. Phillips, *Spectra-Structure Correlation* (Academic, New York, 1964; Mir, Moscow, 1968).
2. J. P. Phillips, in *Semiconductors and Semimetals*, Vol. 3: *Optical Properties of III–V Compounds*, ed. by R. K. Willardson and A. C. Beer (Academic, New York, 1967; Mir, Moscow, 1970).
3. V. K. Subashiev, Solid State Commun. **9** (5), 369 (1971).
4. V. I. Sokolov and V. K. Subashiev, Phys. Status Solidi B **65** (1), K74 (1974).
5. V. T. Agekyan, Yu. F. Solomonov, Yu. A. Stepanov, and V. K. Subashiev, Fiz. Tekh. Poluprovodn. (Leningrad) **10** (9), 1776 (1976) [Sov. Phys. Semicond. **10**, 1058 (1976)].
6. A. I. Savchuk, N. L. Govaleshko, G. D. Dalevskiĭ, and Z. D. Kovalyuk, Ukr. Fiz. Zh. **17** (9), 1548 (1972).
7. G. I. Abutalybov and M. L. Belle, Fiz. Tekh. Poluprovodn. (Leningrad) **9** (7), 1330 (1975) [Sov. Phys. Semicond. **9**, 878 (1975)].
8. G. F. Glinskiĭ, A. A. Kopylov, and A. A. Pikhtin, Fiz. Tekh. Poluprovodn. (Leningrad) **12** (7), 1237 (1978) [Sov. Phys. Semicond. **12**, 785 (1978)].
9. S. V. Virko, M. P. Lisitsa, F. V. Motsnyĭ, and O. S. Sergeev, Fiz. Tverd. Tela (St. Petersburg) **35** (4), 974 (1993) [Phys. Solid State **35**, 500 (1993)].
10. F. V. Motsnyĭ, Author's Abstract of Doctoral Dissertation in Mathematical Physics (IFP NAN, Kiev, 1993).
11. M. P. Lisitsa, F. V. Motsnyĭ, and S. F. Terekhova, Ukr. Fiz. Zh. **22** (9), 1484 (1977).
12. M. P. Lisitsa and F. V. Motsnyĭ, Pis'ma Zh. Éksp. Teor. Fiz. **40** (10), 434 (1984) [JETP Lett. **40**, 1258 (1984)].
13. M. Schlüter, M. L. Cohen, S. E. Kohn, and C. Y. Fong, Phys. Status Solidi B **78** (2), 737 (1976).

Translated by N. Kovaleva

Physics of the Solid State, Vol. 42, No. 9, 2000, pp. 1625–1633. Translated from Fizika Tverdogo Tela, Vol. 42, No. 9, 2000, pp. 1582–1589.

SEMICONDUCTORS AND DIELECTRICS

Excitons in Monoclinic Zinc Diphosphide: Orthoexciton and Polariton Effects at $n = 1$ Resonance

I. S. Gorban'†, A. P. Krokhmal', and Z. Z. Yanchuk

Shevchenko National University, Vladimirskaya ul. 64, Kiev, 252033 Ukraine

e-mail: expdept@expphys.ups.kiev.ua

Received September 20, 1999; in final form, March 6, 2000

Abstract—Quantitative investigations of the hydrogen-like exciton B series in the absorption spectra of the β-ZnP_2 crystal for various wave vector directions and polarization states of radiation are conducted. It is shown that the B spectrum constitutes a single orthoexciton series with *S*-type envelope functions, and low-energy components in doublet lines belong to the *S*-type for lines in the series with $n \geq 3$. Polariton effects are clearly manifested at the $B_{n=1}$ exciton resonance, and Bouguer's law is violated. The oscillator strength tensor components are determined for transitions to the exciton states of the B series, and the polariton parameters at the $B_{n=1}$ exciton resonance are calculated. © *2000 MAIK "Nauka/Interperiodica".*

An analysis of low-temperature absorption in crystals near the $n = 1$ exciton resonances must include the exciton–photon interaction (mixing) [1–3] not only for electric dipole excitons [4–8], but also for dipole-forbidden (quadrupole) excitons with very low oscillator strength, which lead to weak spatial dispersion [9, 10].

In addition to the hydrogen-like C series of a singlet electric-dipole exciton [11–14] and its mixed mode [15], the optical spectra of monoclinic zinc diphosphide β-ZnP_2 display at least two relatively weak dipole-forbidden hydrogen-like exciton series, A and B in the vicinity of the fundamental absorption band [11–13, 15]. It is significant that, although the exciton Rydberg constant Ry for each absorption series has different values, all the series converge to virtually the same limit $E_\infty = (1.6026 \pm 0.0002)$ eV upon an increase in the principal quantum number n [13, 15, 16]. This indicates that the series C, B, and A are exciton states formed from the wave functions of the same pair of electron bands [15, 16].

It is generally accepted that the B series, whose magnetic properties were investigated in [17, 18], is due to the *nS* states of a triplet exciton split by the short-range exchange interaction [11, 17–19]. It is assumed that the doublet lines for the terms in this series with $n \geq 3$ emerge due to mixing the wave-function envelopes of an orthoexciton in the *nS* states of symmetry Γ_1^+ with an appropriate, completely symmetric function from the envelopes of the functions $3\Gamma_1^+ + 2\Gamma_2^+$ of the *nD* states. In this case, the low-energy components of the doublet lines belong to *D* states [17–19]. It was assumed in [13, 16] that the B series starts from $n \geq 2$ and is due to transitions to the *nP* states of a singlet exciton. The origin of the principal line (the so-called B line) of this series remained unclear. The properties of the A series, which is also the exciton series of β-ZnP_2 [15], will be described in our next publication.

In this paper, a quantitative analysis of exciton absorption spectra taking into account polariton effects is carried out for the first time for the B series with a view to ascertaining its origin.

1. EXPERIMENT

The exciton absorption spectra of β-ZnP_2 crystals at temperatures of 1.7 K and above were determined from the transmission spectra and investigated for various directions of the radiation wave vector $\mathbf{s} = \mathbf{q}/q$ and for various polarization states of the vector **E**. The spectra were measured with a spectral resolution of 0.05 meV on a device described in [15, 20] with a ±0.00003 eV error in measuring the photon energies (reduced to wavelengths in vacuum). The samples were cut from single crystals grown in our laboratory [15] by a diamond cutting wheel along the normal to the principal directions defined in crystallography or crystal physics. The cut planes of the samples were disoriented by not more than 0.5° relative to the crystallographic axes. We also used the plates cut and ground parallel to the natural faces of the (100), (110), and (102) types. It should be recalled that the crystallographic axes are arranged in the standard manner for the monoclinic system: the monoclinic axis $C_2 \parallel \mathbf{b} \parallel Y$, $\mathbf{c} \parallel Z$, and the axis **a** lies in the *XZ* mirror plane at an angle $\beta = 102.3°$ to the **c** axis [15, 21]. In our experiments, we used 0.8 to 0.04 mm-thick plates. After mechanical grinding by the diamond

† Deceased.

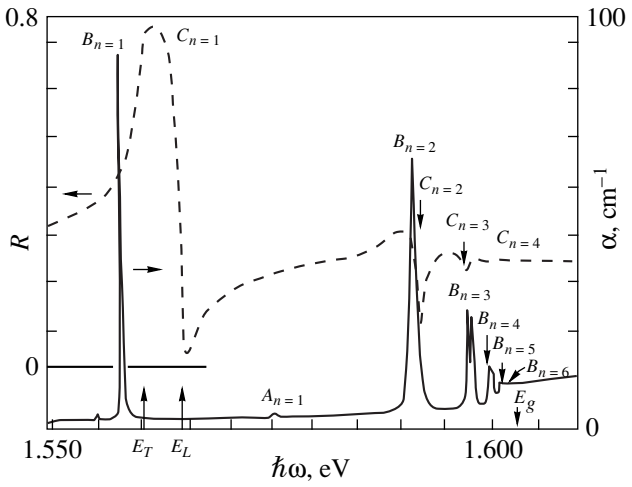

Fig. 1. Exciton absorption spectra of a β-ZnP_2 crystal for **s** ⊥ (100) and **E** ∥ **b** (solid curve) and reflection spectra for **E** ∥ **c** (dashed curve) for T = 1.7 K and d = 0.445 mm.

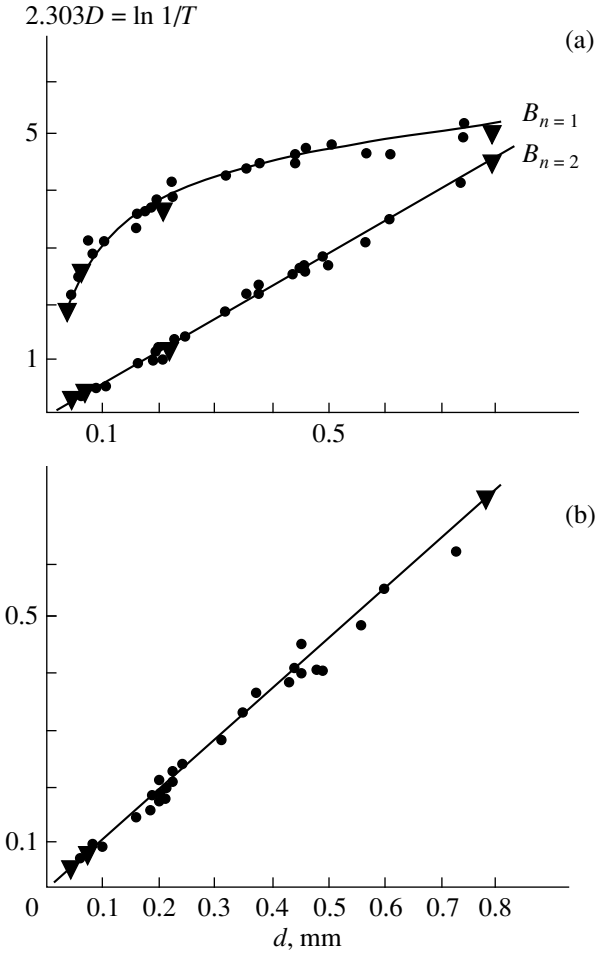

Fig. 2. (a) Dependence of the optical density D at the $B_{n=1}$ and $B_{n=2}$ lines for **s** ⊥ (100) and **E** ∥ **b** on the sample thickness. (b) Dependence of D on d in the region of band-to-band transitions; T = 1.7 K.

pastes ASM-100, the samples were subjected to a soft chemical etching in a dilute solution of bromine in methanol. We also studied the exciton reflection and transmission spectra for β-ZnP_2 crystals under uniaxial compression. The force for axial deformation of the samples was created in a special device with the help of a lever.

2. DISCUSSION OF EXPERIMENTAL RESULTS

2.1. Spectroscopic Properties of the B Spectrum

Figure 1 shows the exciton spectrum of a high-quality [15] β-ZnP_2 sample in a traditional geometry, i.e., for **s** ⊥ (100). For the **E** ∥ **b** polarization, the absorption spectra contain a hydrogen-like B series of lines clearly manifested up to n = 6, while for **E** ∥ **e**, the reflection spectrum is the C spectrum of a singlet exciton. The table presents the experimentally observed energies of lines corresponding to the B spectrum, as well as the energies calculated in the hydrogen-like approximation from the terms of the series with n = 3 and 4 for both low-energy and high-energy components of doublets and their difference. It should be noted that the energies for the B series are given only in [18] and agree with our data.

It was mentioned in our previous publication [15] that, at helium temperatures, the absorption coefficient α at the peak of the $B_{n=1}$ line, as well as its integrated absorption (IA), varies for different crystals, with the α value increasing markedly for thinner samples (see Fig. 1 in [15]). For example, the value of α is as high as 685 cm^{-1} for a sample of thickness d = 0.038 mm. The comparatively strong absorption (α ~ 700 cm^{-1}) observed for the $B_{n=1}$ line in thin samples led the authors of [17–19] to conclude that the B series is associated with weak allowed dipole transitions. Figure 2a shows the optical density at the transmission minimum of the $B_{n=1}$ and $B_{n=2}$ lines as a function of the sample thickness for 30 samples. The triangles in this figure indicate the optical density of the same sample upon a gradual decrease of its thickness. The nonexponential dependence, $2.303D = \ln T^{-1} = f(d)$, for the $B_{n=1}$ line indicates the violation of Bouguer's law, which is typical of the absorption at the n = 1 exciton resonances [4–8, 22]. The $\ln T^{-1}(d)$ dependence for the $B_{n=2}$ line, as well as in the region of the band-to-band transitions ($\hbar\omega$ = 1.609 eV), is found to be linear in accordance with Bouguer's law (Fig. 2b). Henceforth, we will define the "absorption coefficient" for the $B_{n=1}$ line at low temperatures in the conventional manner and use this term without inverted commas, bearing in mind that only transmission has a physical meaning. It should be observed that the transmission at the $B_{n=1}$ line amounts to $T \le 0.4\%$ for the sample thickness $d \approx$ 0.4 mm, and the error in the measurements of D thus increases significantly with the sample thickness.

Energies of the lines of the B spectrum experimentally observed and calculated in the hydrogen-like approximation, as well as their difference

n	E_{exp} (eV)	E_H^{low} (eV)	$E_H^{\text{low}} - E_{\text{exp}}$ (eV)	E_H^{high} (eV)	$E_H^{\text{high}} - E_{\text{exp}}$ (eV)
1	1.55775	1.55388	−0.00388	1.55764	−0.00011
2	1.59108	1.59044	−0.00064	1.59143	0.00035
3	1.59721	1.59721	0	–	–
3	1.59768	–	–	1.59768	0
4	1.59958	1.59958	0	–	–
4	1.59987	–	–	1.59987	0
5	1.60070	1.60068	−0.00002	–	–
5	1.60090	–	–	1.60089	−0.00001
6	1.60137	1.60128	−0.00009	1.60144	0.00007
		E_∞ = 1.60263 eV		E_∞ = 1.60269 eV	
		R_y^{low} = 0.04875 eV		R_y^{high} = 0.04505 eV	

Note: The energies of the lines in doublets were refined by separating contours.

The half-width of the $B_{n=1}$ line varies with the direction of the wave vector and the polarization state of the radiation. For $\mathbf{s} \perp (100)$ and $\mathbf{E} \parallel \mathbf{b}$, it amounts to $H \leq 0.2$ meV for a sample thickness $d \approx 0.20$ mm (when the dependence of absorption on thickness is not manifested strongly). For other directions of the wave vectors and for polarizations with a nonzero component of the vector $\mathbf{E}$ along the axis $X \parallel (100) \parallel [\mathbf{b} \times \mathbf{c}]$, the half-width of the $B_{n=1}$ line is larger. For example, $H \approx 0.28$ meV in the geometry $\mathbf{s} \perp (100)$ for $\mathbf{E} \perp \mathbf{c}$, when the angle between the electric induction $\mathbf{D}$ and the X axis in the XY plane ($[\mathbf{b} \times \mathbf{c}]\mathbf{b}$) is equal to $\varepsilon = 40.1°$, while $H \approx 0.32$ meV in the geometry $\mathbf{s} \perp (010)$ and $\mathbf{E} \parallel X$. When the vector $\mathbf{s}$ is directed along the axis $\mathbf{c} \parallel Z$, $H \approx 0.20$ meV for the polarization $\mathbf{E} \parallel \mathbf{b}$, and $H \approx 0.32$ meV for $\mathbf{E} \parallel X$. An increase in the half-width of the $B_{n=1}$ line can be explained by the fact that accidental spin degeneracy is preserved in the Abelian group (crystallographic class C_{2h}) for the nS states of an orthoexciton in zero external magnetic field, and only the states of the orthoexciton of symmetry $2\Gamma_1^-(y)$ are probably manifested spectroscopically for $\mathbf{E} \parallel \mathbf{b}$, while for $\mathbf{E} \parallel X$, the state $\Gamma_2^-(x)$ is also manifested [15]. Such anisotropy apparently reflects the manifestation of spatial dispersion at the $B_{n=1}$ orthoexciton resonance.

The $B_{n=2}$ line has a rather large half-width $H \cong 0.82$ meV with a weak negative asymmetry [23] $\delta = (H^+ - H^-)/H = -0.02$. However, the half-width of the low-energy component of a doublet with $n = 3$ is $H \approx 0.28$ meV, while the half-width of the high-energy component is $H \approx 0.32$ meV without any noticeable asymmetry. The components for terms with $n \geq 4$ have approximately the same half-widths. The considerable broadening and the low-energy asymmetry of the $B_{n=2}$ line are probably associated with interband scattering of an orthoexciton from the exciton band with $n = 2$ to the ground state, accompanied by the emission of longitudinal optical phonons with a nonzero wave vector [23, 24]. The energy difference between the $n = 2$ and $n = 1$ bands of an orthoexciton for $\mathbf{k} = 0$ is 34.33 meV, which is slightly larger than the energy $\hbar\Omega = 31.5$ – 33.7 meV of an actual phonon [19, 25, 26]. The weak negative asymmetry of the $B_{n=2}$ line indicates the low intensity of the exciton–phonon interaction. A similar energy difference for the $n = 3$ band amounts to 39.5 meV. There are no suitable phonons for this energy gap [25, 26] (or their density of states is quite low), meaning that the lines remain relatively narrow and symmetric. It should be noted that, in the geometry $\mathbf{s} \perp (102)$ and $\mathbf{E} \parallel \mathbf{b}$, all the lines of the B spectrum become narrower by ≈0.06 meV, and the line resolution in doublets increases accordingly.

The table shows that the series formed by high-energy components of doublets obeys the hydrogen-like regularities better than the series consisting of low-energy components. This can be explained by assuming that low-energy states from those with $n \geq 3$ in the case of the (s–d) splitting are the nS states, while high-energy states are the nD states, for which $|\Phi(\mathbf{r})|^2_{r=0} = 0$ and, hence, the "central-cell corrections" are negligibly small for them.

If the C and B series originate from the same pair of electron and hole bands, being nS states of a $\Gamma_2^-(z)$ singlet exciton and of a $2\Gamma_1^-(y) + \Gamma_2^-(y)$ triplet exciton [15], these series must be shifted identically during crystal deformation with increasing stress. The orthos-

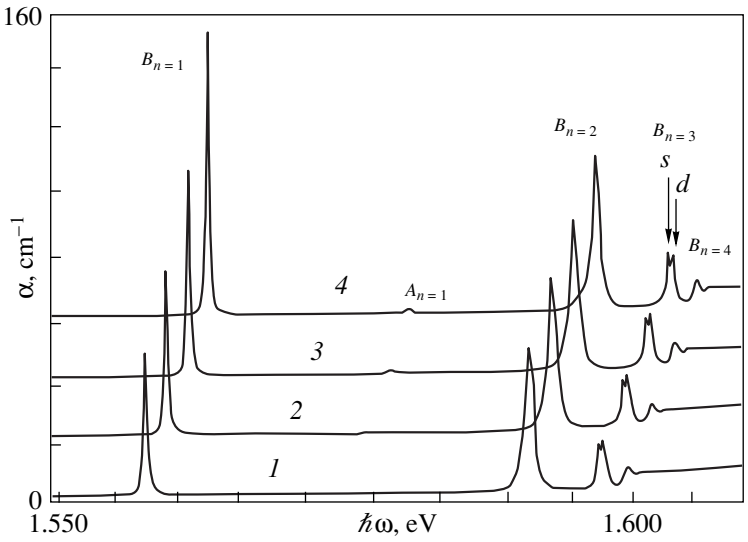

Fig. 3. Transformation of the B spectrum under uniaxial compression along the *b* axis of a β-ZnP_2 crystal following its "quasiplastic" deformation at room temperature. **P**, MPa: 0 (*1*), 120 (*2*), 240 (*3*), and 360 (*4*). **s** ⊥ (100) and **E** ‖ **b**, T = 4.5 K. Spectra *2–4* are shifted consecutively by 20 cm^{-1} along the ordinate axis.

tates with different symmetries must generally be shifted with different rates as a result of the axial deformation of the crystal. In the case of the axial compression of a β-ZnP_2 crystal along the axes **c**(*Z*) and **b**(*Y*), it was found that C and B series are shifted linearly towards higher energies as the stress changes from "zero"[1] to ~300 MPa.[2] For **P** ‖ **c** and **s** ⊥ (010), the C series for **E** ‖ **c** and the B series for **E** ‖ *X* are shifted at approximately the same "rate" $\partial E/\partial P \approx 9.93 \times 10^{-6}$ eV/MPa. For **P** ‖ **b** and **s** ⊥ (100), the bands the C series for **E** ‖ **c** and the lines of the B series for **E** ‖ **b** are shifted at a higher rate than for **P** ‖ **c**. The rates of displacement for lines with $n = 1$ are slightly different: $C_{n=1}$—$\partial E/\partial P \approx 1.70 \times 10^{-5}$ eV/MPa for $C_{n=1}$ and $\partial E/\partial P \approx 1.48 \times 10^{-5}$ eV/MPa for $B_{n=1}$.

For **s** ⊥ (010) and **E** ‖ **c**, the $\Gamma_2^-(z)$ states of a singlet exciton are observed, while for **E** ‖ *X*, the *nS* states of a $\Gamma_2^-(x)$ orthoexciton are probably manifested, and the series are displaced at the same rate. For **s** ⊥ (100) and **E** ‖ **c**, the *nS* states of the $\Gamma_2^-(z)$ singlet exciton are observed, while for **E** ‖ **b**, only the states $2\Gamma_1^-(y)$ are likely to be manifested in the 1*S* orthoexciton. Consequently, these lines are shifted at slightly different rates, which obviously reflects the exchange–deformation splitting of the orthoexciton [27].

While analyzing the effect of axial deformation along the **b** axis on the exciton spectra of β-ZnP_2, we obtained one more relatively important result. As usual, a sample having a size of 4.0 × 2.80 × 0.432 mm was indented by a load **P** ≈ 240 MPa into the POS-40 solder "pads" for ~1 min at room temperature prior to measurements in order to deform the crystal uniformly [28]. Then the device with the sample was unloaded, placed in a cryostat, and cooled to 4.5 K. The recording of transmission spectra revealed that under "zero" loading, the transmission at the $B_{n=2}$ line increased considerably and amounted to $T \approx 5.85\%$ as compared to $T \approx 0.35\%$ for the free sample. The transmission at the $B_{n=3}$ line and at low-energy components of doublet lines with $n \geq 3$ (they will be denoted by the index *s*) also increased (approximately twofold). As the stress increases, apart from the shift of the spectrum to higher energies, the absorption started increasing at $B_{n=1}$ and $B_{n=2}$ lines, as well as at the "*s*" components of doublet lines with $n \geq 3$ (Fig. 3). At the stress σ ≈ 360 MPa, the absorption spectrum of the B series again acquired the usual ratio of intensities (cf. Fig. 1). Leaving aside the mechanism of selective increase in the transparency at the resonances of the B-exciton spectrum (following the "quasiplastic" deformation of the crystal at room temperature), we note the identical behavior of the $B_{n=1}$ line and the low-energy components of doublet lines for $n \geq 3$. This indicates their genetic relationship; consequently, the "*s*" lines for $n \geq 3$ are due not to *nD* states [18, 19], but, like the $B_{n=1}$ line, to the *nS* states of an orthoexciton [17]. The "accidental" orbital degeneracy

[1] "Zero" stress does not rule out low residual uniaxial stress due to friction in the system of the lever and the punch, as well as that due to possible quasi-plastic deformation emerging when the sample is indented into a "pad" made of a POS-40 solder at room temperature.

[2] The positions of the bands in the C series were determined from the minima in the dispersion contours of reflection spectra.

in the hydrogen-like system can be removed by violating the central symmetry of the Coulomb field and by the spin–orbit interaction [29]. As the axial deformation of the crystal increases, the splitting in doublets with $n \geq 3$ does not change. Consequently, this splitting is associated not with the crystal field, but with relativistic effects. Considering that the spin–orbit splitting of the valence band is insignificant [15, 17], the doublet splitting is apparently associated with the **j**–**j** interaction, since the orbital angular momenta and their components in low-symmetry crystals are not conserved, and the magnetic moments associated with the orbital motion are equal to zero in the first approximation ("quenching" of orbital angular momenta by the crystal field [30]).

2.2. Energy Dissipation for Exciton Polaritons

Photoexcitons or exciton polaritons are absorbed in a crystal if the dissipation of their mechanical energy (characterized by the attenuation factor γ) occurs at the dissipative subsystem (at phonons, crystal structure defects, and also near the surface) [1]. The fraction of the electromagnetic energy of an exciton polariton, or the intensity of the exciton–photon interaction, is associated with the "delay" effect and is characterized by the magnitude of the longitudinal–transverse splitting, which is directly determined by the oscillator strength of the exciton transition. The attenuation factor γ can be smoothly varied by increasing the temperature of the crystal. At a certain temperature T_c, it attains the critical value $\gamma \geq \gamma_c$, for which the interaction between excitons and photons is negligible, and the crystal loses spatial dispersion. This is confirmed by the loss of transparency at $n = 1$ exciton resonances [4–7, 9]. The area bounded by the curve becomes proportional to the oscillator strength F of the exciton transition [31, 32] and no longer depends on the temperature and thickness of the sample in accordance with the semiclassical theory of exciton absorption [33].

Figure 4 shows the temperature dependence of the integrated absorption A in eV cm^{-1} at the $B_{n=1}$ and $B_{n=2}$ lines for $\mathbf{s} \perp (100)$ and $\mathbf{E} \parallel \mathbf{b}$ for two samples. In a sample of thickness $d = 0.205$ mm, the IA for the $B_{n=1}$ line increases with T by more than an order of magnitude and attains saturation at $T_c \approx 110$ K. For the $n = 2$ line, the temperature increase of IA is insignificant. In a thinner sample ($d = 0.076$ mm), the saturation for the $B_{n=1}$ line is attained at a lower value of $T_c \approx 90$ K in accordance with the general tendency of IA variation at $n = 1$ exciton resonances in other semiconductors due to an increase in absorption in the surface layers [5, 6].

In the region of IA saturation, the values of A_{sat} for the $B_{n=1}$ line are determined by the semiclassical formula [33] for the tensor component of the oscillator strength for the exciton transition to a molecule (the unit cell of β-ZnP_2 contains eight structural units [21]) for three crystallographic directions. For the direction

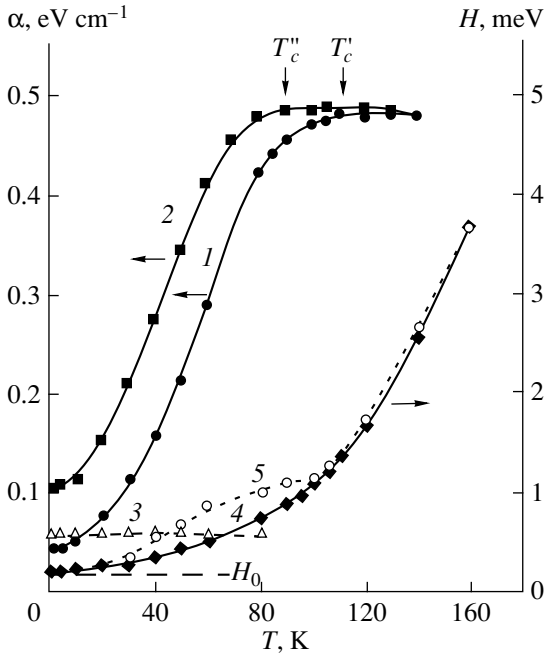

Fig. 4. Temperature dependence of integrated absorption at $B_{n=1}$ lines [$d = 0.205$ (curve *1*) and 0.076 mm (curve *2*)] and at $B_{n=2}$ lines (curve *3*) and the half-width H of the $B_{n=1}$ line for a chemically polished sample with $d = 0.076$ mm (curve *4*) and a mechanically polished sample (curve *5*).

$\mathbf{s} \parallel X \parallel [\mathbf{b} \times \mathbf{c}]$, or $\mathbf{s} \perp (100)$, it amounts to $F^X_{n=1} = (8.2 \pm 0.3) \times 10^{-7}$ for $\varepsilon_b = 10$ in for the polarization $\mathbf{E} \parallel \mathbf{b}$ [18], while $F^Y_{n=1} = 2.6 \times 10^{-6}$ for $\mathbf{s} \parallel Y \parallel \mathbf{b}$ when $\mathbf{E} \parallel X$ and $\varepsilon_a = 7.8$ [18]. For $\mathbf{s} \parallel Z \parallel \mathbf{c}$, $F^Z_{n=1} = 8.2 \times 10^{-7}$ when $\mathbf{E} \parallel \mathbf{b}$, and $F^Z_{n=1} = 2.3 \times 10^{-6}$ when $\mathbf{E} \parallel X$. It was found that the ratio of the oscillator strengths for the terms of the B series in the direction $\mathbf{s} \parallel X$ obeys the relation $F_n \propto 1/n^3$ $F_{n=1}/F_{n=2} \cong 7.8$; $F_{n=2}/F_{n=3} \cong 3.24$, and $F_{n=3}/F_{n=4} \cong 2.35$) if we assume that the doublet lines with $n \geq 3$ are due to the "*s*–*d*" splitting [17–19]. In this case, a fraction of the oscillator strength is pumped from the *nS* states to the *nD* states due to the mixing, by the anisotropic component of the Hamiltonian, of the envelopes of the functions of the *nS* states of an orthoexciton of symmetry $\Gamma_1^+(xz)$ with one of the three functions of the *nD* states having the same symmetry [19, 34, 35]. The above relationship is a typical feature of a *S* type exciton series [36]. The obtained value of $F^X_{n=1}$ proved to be four orders of magnitude smaller than the oscillator strength $F^X_{C_{n=1}} = 6.0 \times 10^{-3}$ for a 1*S* singlet exciton (having the same direction). This oscillator strength was calculated from the longitudinal–transverse splitting $\delta_{LT} = 4.56 \times 10^{-3}$ eV that we obtained by analyzing the mixed mode [15] for the background permittivity

$\varepsilon_c = 9.7$ [18]. If the B series comprises the states of a singlet exciton with envelope functions of the *P* type [13, 16], in which dipole transitions are parity forbidden, the oscillator strength must obey the law $F_n \propto (n^2 - 1)/n^5$ and lead to other ratios of the lines in the series: $F_{n=1}/F_{n=2} = 0$; $F_{n=2}/F_{n=3} = 2.848$, and $F_{n=3}/F_{n=4} \cong 2.247$ [36]. In this case, the discrepancy between the theory and the experiment can hardly be explained by anisotropy of effective masses and permittivity. Moreover, transitions to the *nP* states are only allowed in the quadrupole approximation [15] and must be characterized by an oscillator strength much smaller than the obtained values,[3] which follows from the results of experiments on two-photon absorption [37].

The assumption concerning the surface origin of the $B_{n=1}$ line [16] was not confirmed in our experiments. The IA for the $B_{n=1}$ line remains constant within the experimental error upon an order-of-magnitude change in the area of the aperture of the calibrated diaphragm limiting the radiation flux incident on the sample. It is also virtually independent of the quality of the illuminated surface (natural or mechanically polished).

Figure 4 also shows the temperature variation in the half-width H for the $B_{n=1}$ line. As the temperature T increases from 1.7 to ~10 K, the half-width of the $B_{n=1}$ line remains virtually unchanged (curves *4* and *5*). The dashed curve corresponds to the value of H_0 including the constant components γ_0 and γ_s associated with the scattering of polaritons from crystal structure defects and in the surface layers, respectively. A further increase in T leads to a superlinear dependence $H(T)$, which reflects the polariton scattering first from acoustic phonons and then from longitudinal optical phonons [7]. Curve *5* describes the variation o H for the $B_{n=1}$ line in a sample with a mechanically polished face (d = 0.205 mm), the opposite face remaining natural. The $\gamma(T)$ dependence for the given sample has an inflection in the polariton temperature region $T \leq T_c$. The same dependence $\gamma(T)$ was also observed for thinner mechanically polished samples. The deviation of the $\gamma(T)$ dependence from the smooth curve *4* observed for chemically polished samples in the form of the inflection in the temperature range $T \leq T_c$ can be explained by surface effects. Chemical etching removes the mechanically damaged surface layer, along with the oxide layer and the adsorbed molecular ions. These results agree with the assumption made by Aliev *et al.* [7] concerning the effect of the field of the surface charge on a similar behavior of the $\gamma(T)$ curve observed for ZnTe.

In [15], we assumed that the broadening and asymmetry on the high-energy wing of the $B_{n=1}$ line contour in low-quality β-ZnP_2 crystals at helium temperatures are mainly due to the scattering of exciton polaritons from lattice defects, rather than due to intraband scattering of excitons from phonons [18]. This assumption is confirmed by our present studies. The broadening and asymmetry of the $B_{n=1}$ line contour agree with the theoretical predictions for the exciton absorption in the presence of exciton scattering from charged defects (without regard for the screening effects) [38, 39]. According to Skaitys *et al.* [39], the scattering of exciton polaritons from positively charged defects will be more intense.

The experimental data described above indicate that the B spectrum is a single series of an orthopolariton split off by the exchange interaction. It is well known that the exchange splitting of a degenerate exciton state is equal to the doubled exchange integral, which is approximately proportional to $A \propto (e^2/d)(d/a_{ex})^3$ for *nS* states, where d is the atomic spacing in the lattice and a_{ex} is the Bohr radius of the exciton. The separation d between the nearest P and Zn atoms in β-ZnP_2 is equal to 0.239 nm [21], while the Bohr radius a_{ex} of a 1*S* singlet exciton is ~1.8 nm; consequently, $2A \sim 2.8 \times 10^{-3}$ eV. The difference between the energy of a $B_{n=1}$ exciton and the energy $E_T = 1.5603$ eV of a transverse $C_{n=1}$ exciton [12, 15] is 2.6×10^{-3} eV, which almost coincides with the theoretical estimate. Moreover, the short-range exchange interaction leads to an exciton energy that is independent of the direction of the wave vector [40], which is observed in actual practice for the B series [15].

When photoexcitons are the eigenstates of a crystal, Bouguer's law is violated at $n = 1$ exciton resonances at low temperatures: the absorption coefficient increases when the sample thickness decreases below a certain value of d [4–8]. This is associated with an increase in γ due to an increase in the scattering of exciton polaritons in the surface layers of thickness d_s as compared to the interior region d_i of the crystals, in which $\gamma = \gamma_0$ and is determined only by the dissipation of photoexciton energy at crystal structure defects [1, 5, 7, 8]. The attenuation of exciton polaritons depends considerably on the quality of the surface. For example, the half-width H of the $B_{n=1}$ line of a mechanically polished sample with $d = 0.077$ mm at $T = 1.7$ K is approximately equal to 0.35 meV, whereas after polishing etching of this sample in a dilute solution of bromine in methanol (d = 0.076 mm), its value decreases by half ($H \cong 0.18$ meV). The decrease in polariton attenuation also reduces the integrated absorption approximately twofold.

Aliev *et al.* [8] analyzed the thickness dependence of absorption at the $n = 1$ resonance of a dipole exciton in GaAs and proposed the following empirical formula describing the IA variation as a function of the sample thickness:

$$A(d) = A_i + 2\frac{d_s}{d}A_s\left(1 - \frac{A_i}{A_s}\right), \qquad (1)$$

where A_i is the IA in the interior layer of thickness d_i, which is not perturbed by surface effects, d_s is the thick-

[3] For example, $F_{2y} = 2.8 \times 10^{-6}$ for a line with $n = 2$ in the dipole-allowed *P* series for Cu_2O [33].

ness of the surface layer, and A_s is the absorption in the surface layer. We assume that, as the crystal thickness decreases to $d \le 2d_s$ (the conditions at both surfaces are identical), IA attains saturation determined by the critical attenuation γ_s^c of polaritons in the surface layers. We also assume that the values of A_s and γ_s^c must coincide with the values of A_{sat} and γ_c determining the loss of polariton properties and of spatial dispersion of the crystal at an exciton resonance at $T \ge T_c$. Aliev *et al.* [8] also assume that the thickness d_s in GaAs is determined by the nonuniform field F_s of the surface charge.

The fitting of the $A(d)$ dependence to the experimental data obtained for the $B_{n=1}$ line by using Eq. (1) (Fig. 5) gives the following fitting parameters: d_s = 9.2 μm, A_s = 0.46 eV cm^{-1}, and A_i= 0.024 eV cm^{-1}. The latter virtually coincide with the experimental data (A_{sat} = 0.48 eV cm^{-1}, as well as with A = 0.0025 eV cm^{-1} for thick samples. If we replace d by $d = d_i + 2d_s$ in Eq. (1) and calculate $A(d_i)$, saturation $A(d \le 2d_s) = A_s$ also takes place for $d_i = 0$, in accordance with formula (14) for IA for $\gamma = \gamma_s$ obtained in [32]. It should be noted that the obtained estimate of the value of d_s at a $B_{n=1}$-orthoexciton resonance in β-ZnP_2 is two orders of magnitude higher than the value of d_s = 0.11 μm obtained for an n = 1 dipole exciton in GaAs [8]. Consequently, such a large value of d_s in β-ZnP_2 can hardly be explained only by the field F_s of the surface charge and by the band bending associated with it, since the background permittivity ε_b = 10 in β-ZnP_2 [18] is comparable with ε_0 = 12.6 in GaAs [41]. If we assume that the concentration of the majority carriers (holes) in the β-ZnP_2 crystals under investigation is two orders of magnitude higher than $n < 5 \times 10^{14}$ cm^{-3} in epitaxial GaAs [8], this will lead to values of the field F_{0s} at the surface that are only one order of magnitude higher than in GaAs. However, the increase in the screening length (radius) with the charge carrier concentration will exponentially decrease the surface field $F_s(d) \sim F_{0s}\exp(-z/r_D)$ [42]. It appears that the thickness d_s is mainly determined by polariton effects or, to be more precise, by the conversion rate f of the electromagnetic fraction of the photoexciton energy into the mechanical energy, which is determined by the oscillator strength F of the exciton transition or by the longitudinal–transverse splitting Δ_{LT} [1, 31].

It was found that the absorption increases significantly when the sample thickness becomes smaller than a definite value typical of a given crystal. It was mentioned above that this characteristic dimensional thickness for a $B_{n=1}$ orthoexciton in β-ZnP_2 is $d_{dim} \sim 0.2$mm, while d_{dim} for an orthoexciton (Γ_6) in GaSe is approximately equal to 0.02 mm [22]. However, $d_{dim} \sim 0.002$ mm for a dipole exciton in GaAs [8]. The latter value is also two orders of magnitude smaller than that for β-ZnP_2.

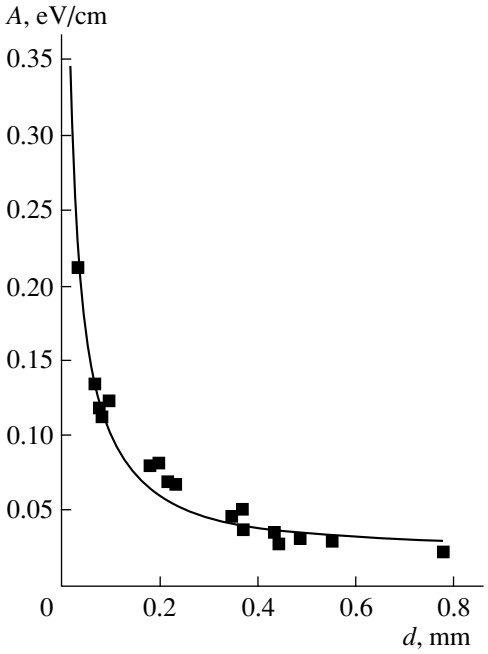

Fig. 5. Dependence of integrated absorption in the $B_{n=1}$ line on the sample thickness (symbols correspond to experimental results obtained at T = 1.7 K). The solid curve was obtained theoretically by formula (1) with the fitting parameters A_s = 0.46, A_i = 0.024 eV cm^{-1}, and d = 0.092 mm.

It is essential that the oscillator strengths for the transitions in question also consecutively differ by approximately one order of magnitude: $F_m^X = 8.2 \times 10^{-7}$ in β-ZnP_2, $F_m = 1.9 \times 10^{-5}$ in GaSe, and $F = 4.98 \times 10^{-4}$ in GaAs.[4] The frequencies of the corresponding photoexciton oscillations for β-ZnP_2 and GaSe amount to 6.6×10^{12} and 4.9×10^{13} s^{-1} (these values were obtained from IA by the formula $A_{sat} = \pi\hbar f^2/2c\sqrt{\varepsilon_0}$ [31]), while the frequency for GaAs is 9.4×10^{13} s^{-1} (it was calculated from Δ_{LT} = 0.1 meV). If IA attains saturation in the region of d_s [8], this thickness can be estimated as $d_s \approx v_g/2f$ (v_g is the group velocity) since a photoexciton performing an oscillation is transformed into a mechanical exciton in the surface layer, where $\gamma = \gamma_c^s \ge f$. Consequently, the smaller the value of F for an exciton transition, the larger is d_s, and vice versa. The inverse proportionality cannot be strictly observed (especially for larger values of F), since the refractive index of the additional wave increases manifold in the exciton resonance region, and the group velocity of the photoexciton will decrease. For a large oscillator strength, the field of the surface charge can only increase d_s if its

[4] The values of F_m for GaSe were calculated using A_{sat} = 29.8 eV cm^{-1} [5] and ε_0 = 7.6 [36], while the value of F for GaAs was calculated using Δ_{LT} = 0.1 meV [41], which is the average of the experimental values 0.08 and 0.13 meV [42].

penetration depth $z_s > d_s$. If we assume that the refractive index for the ordinary and the additional waves in β-ZnP_2 for **s** ⊥ (100) and **E** || **b** at the resonance of a $B_{n=1}$ orthoexciton differs insignificantly from $\sqrt{\varepsilon_b}$ and roughly put $v_g \approx c/\sqrt{\varepsilon_b}$, we obtain $d_s \approx v_g/2f = 7.2$ μm, which agrees with the value obtained from the thickness dependence. Such an estimate for a dipole exciton in GaAs gives the value of $d_s \approx 0.45$ μm, which is four times as high as that obtained in [8]. This is not surprising, given that the value of n increases considerably at a dipole resonance for the additional wave.

The available experimental data can be used to estimate the characteristic, or dimensional thickness d_{dim} (below which a strong thickness dependence is observed) from the relation $2d_s/d_i \approx 0.1$ (under identical conditions at the two surfaces). This gives $d_{\text{dim}} \approx 2d_s + d_i = 22d_s = 0.202$ mm for β-ZnP_2 and $d_{\text{dim}} \approx 22d_s = 2.42$ μm for GaAs, which virtually coincides with the experimental estimates.[5] For $2d_s/d_i \ll 0.1$, the integrated absorption tends to the absorption in an infinitely large crystal and is determined only by the attenuation γ_0. Obviously, $\gamma_0 \le \gamma \le \gamma_s^c$ in the region $d_i \le 20d_s$, where a strong thickness dependence $A(d)$ is observed.

Thus, it was found that the "nonclassical" behavior of absorption upon a decrease in temperature and thickness of the crystal at the resonance of an $n = 1$ orthoexciton in β-ZnP_2 is similar in all respects to the effects observed for dipole and quadrupole resonances in many semiconductors. All of these phenomena are due to polariton effects and spatial dispersion [5–10]. Consequently, the polariton effects observed for a triplet $n = 1$ exciton in β-ZnP_2 are common for excitons in semiconductors and indicate that the photoexciton interaction at the lowermost $n = 1$ exciton resonances in crystals cannot be disregarded even for transitions with a low oscillator strength.

ACKNOWLEDGMENTS

This research was partially supported by the Ukrainian State Foundation for Basic Research (grant no. 2.4/311).

REFERENCES

1. J. J. Hopfield, Phys. Rev. **112** (5), 1555 (1958).
2. S. I. Pekar, *Crystal Optics and Additional Light Waves* (Naukova Dumka, Kiev, 1982).
3. V. M. Agranovich and V. L. Ginzburg, *Crystal Optics with Spatial Dispersion, and Excitons* (Nauka, Moscow, 1979; Springer-Verlag, New York, 1984).
4. J. Voigt, Phys. Status Solidi B **64** (2), 549 (1974).
5. A. Bosacchi, B. Bosacchi, and S. Franchi, Phys. Rev. Lett. **36** (18), 1086 (1976).
6. N. N. Akhmediev, G. P. Golubev, V. S. Dneprovskiĭ, and E. A. Zhukov, Fiz. Tverd. Tela (Leningrad) **25** (7), 2225 (1983) [Sov. Phys. Solid State **25**, 1284 (1983)].
7. G. N. Aliev, O. S. Koshchug, and R. P. Seĭsyan, Fiz. Tverd. Tela (St. Petersburg) **36** (2), 373 (1994) [Phys. Solid State **36**, 203 (1994)].
8. G. N. Aliev, N. V. Luk'yanova, and R. P. Seĭsyan, Fiz. Tverd. Tela (St. Petersburg) **40** (5), 869 (1998) [Phys. Solid State **40**, 800 (1998)].
9. F. I. Kreĭngol'd and V. L. Makarov, Pis'ma Zh. Éksp. Teor. Fiz. **20** (7), 441 (1974) [JETP Lett. **20**, 201 (1974)].
10. D. Fröhlich, A. Kulik, B. Uebbing, *et al.*, Phys. Rev. Lett. **67** (17), 2343 (1991).
11. A. B. Pevtsov, S. A. Permogorov, A. V. Sel'kin, and N. N. Syrbu, Fiz. Tekh. Poluprovodn. (Leningrad) **16** (8), 1399 (1982) [Sov. Phys. Semicond. **16**, 897 (1982)].
12. R. S. Berg, P. Y. Yu, and Th. Mowles, Solid State Commun. **46** (2), 101 (1983).
13. I. S. Gorban', N. M. Belyĭ, V. A. Borbat, *et al.*, Dokl. Akad. Nauk Ukr. SSR, Ser. A, No. 4, 48 (1988).
14. O. Arimoto, M. Tachiki, and K. Nakamura, J. Phys. Soc. Jpn. **60** (12), 4351 (1991).
15. I. S. Gorban', A. P. Krokhmal', and Z. Z. Yanchuk, Fiz. Tverd. Tela (St. Petersburg) **41** (2), 193 (1999) [Phys. Solid State **41**, 170 (1999)].
16. I. S. Gorban', M. M. Bilyi, I. M. Dmitruk, and O. A. Yeschenko, Phys. Status Solidi B **207**, 171 (1998).
17. T. Goto, S. Taguchi, K. Cho, *et al.*, J. Phys. Soc. Jpn. **59** (2), 773 (1990); **58** (10), 3822 (1989).
18. S. Taguchi, T. Goto, M. Takeda, and G. Kido, J. Phys. Soc. Jpn. **57** (9), 3256 (1988).
19. M. Sugisaki, O. Arimoto, and K. Nakamura, J. Phys. Soc. Jpn. **65** (1), 23 (1996).
20. S. I. Boĭko, I. S. Gorban', A. P. Krokhmal', *et al.*, Fiz. Tekh. Poluprovodn. (St. Petersburg) **27** (5), 815 (1993) [Semiconductors **27**, 447 (1993)].
21. M. E. Flett and Th. A. Mowles, Acta Crystallogr. C **40**, 1778 (1984).
22. M. S. Brodin and Yu. P. Gnatenko, Ukr. Fiz. Zh. **11** (7), 759 (1966).
23. Y. Toyozawa, J. Phys. Chem. Solids **25** (1), 59 (1964).
24. K. Shindo, T. Goto, and T. Anzai, J. Phys. Soc. Jpn. **36** (3), 753 (1974).
25. I. M. Dmitruk, M. M. Bilyi, I. S. Gorban', and Z. Z. Janchuk, in *Proceedings of the 5th International Conference on Raman Spectroscopy, Pittsburgh, 1996*, p. 874.
26. N. N. Syrbu, Fiz. Tekh. Poluprovodn. (St. Petersburg) **26** (6), 1069 (1992) [Sov. Phys. Semicond. **26**, 599 (1992)].
27. V. A. Kiselev and A. G. Zhilich, Fiz. Tverd. Tela (Leningrad) **13** (8), 2398 (1971) [Sov. Phys. Solid State **13**, 2008 (1971)].
28. V. D. Kulakovskiĭ, V. B. Timofeev, and V. M. Édel'shteĭn, Zh. Éksp. Teor. Fiz. **74** (1), 372 (1978) [Sov. Phys. JETP **47**, 193 (1978)].
29. L. D. Landau and E. M. Lifshitz, *Course of Theoretical Physics*, Vol. 3: *Quantum Mechanics: Non-Relativistic Theory* (Nauka, Moscow, 1989; Pergamon, New York, 1987).

[5] Unfortunately, the thickness dependences of integrated absorption for GaSe are not presented in [5] and [22].

30. R. M. White, *The Quantum Theory of Magnetism* (Springer-Verlag, Berlin, 1983; Mir, Moscow, 1985).
31. A. S. Davydov, *The Theory of Solid State* (Nauka, Moscow, 1976).
32. N. N. Akhmediev, Zh. Éksp. Teor. Fiz. **79** (4), 1534 (1980) [Sov. Phys. JETP **52**, 773 (1980)].
33. R. Knox, *Theory of Excitons* (Academic, New York, 1963; Mir, Moscow, 1966).
34. J.-A. Deverin, Nuovo Cimento B **63** (1), 1 (1969).
35. E. Mooser and M. Schlüter, Nuovo Cimento B **18** (1), 164 (1973).
36. R. J. Elliott, Phys. Rev. **108** (6), 1384 (1957).
37. D. Fröhlich, M. Schierkamp, J. Schubert, *et al.*, Phys. Rev. B **49** (15), 10337 (1994).
38. V. N. Ermakov, V. M. Nitsovich, and N. V. Tkach, Ukr. Fiz. Zh. **22** (4), 653 (1977).
39. E. Skaitys, V. I. Sugakov, and O. S. Zinets, Phys. Status Solidi B **58** (1), 415 (1973).
40. G. L. Bir and G. E. Pikus, *Symmetry and Stain-Induced Effects in Semiconductors* (Nauka, Moscow, 1972; Wiley, New York, 1975).
41. D. D. Sell, S. E. Stokowski, R. Dingle, and J. V. Di Lorenzo, Phys. Rev. B **7** (10), 4568 (1973).
42. L. Schultheis and I. Balslew, Phys. Rev. B **28** (4), 2292 (1983).

Translated by N. Wadhwa

Physics of the Solid State, Vol. 42, No. 9, 2000, pp. 1634–1639. Translated from Fizika Tverdogo Tela, Vol. 42, No. 9, 2000, pp. 1590–1594.

SEMICONDUCTORS AND DIELECTRICS

Configuration Vibronic Mixing for a Neutral Vacancy in Silicon and Diamond

S. S. Moliver

Ul'yanovsk State University, ul. L'va Tolstogo 42, Ul'yanovsk, 432700 Russia

e-mail: moliver@sv.uven.ru

Received March 9, 2000

Abstract—Configuration vibronic mixing is considered for a fully symmetric Jahn–Teller electronic term with orientation-degenerate terms (due to the distortion direction) including a correlation correction in a single-open-shell approximation. The approach is nonempirical and involves only linear vibronic coupling. The adiabatic potential is a multiwell one, because the different configurations involved in the exact Jahn–Teller term have different vibronic coupling with a lattice distortion. The stabilization energy, the frequencies of local lattice vibrations, the vibronic coupling parameter, and the energy barriers to migration and to distortion-axis reorientation are estimated for a neutral vacancy in silicon and diamond with allowance made for configuration vibronic coupling. The estimates agree with the results obtained by different experimental and theoretical methods for a wide range of properties associated with the Jahn–Teller effect. © *2000 MAIK "Nauka/Interperiodica".*

INTRODUCTION

An adequate description of properties of a vacancy in silicon, diamond, and other covalent semiconductors should be based on calculations of multiplet structures of high-symmetry atomic configurations with an open electron shell, because electron correlation and the vibronic coupling are of critical importance in these systems [1, 2].

At the present time, there are two competing methods for treating the electron correlation in a defect crystal: the local approximation to the electron density functional (LDA) and the configuration interaction approximation based on the molecular-orbital method. Although the LDA has been used very successfully in the theory of defect crystals [2], it is not universal, because the results obtained by this method depend heavily on the model employed and the computational procedure. As an illustration, we refer to the analysis of the convergence of the LDA performed in [3] with respect to the size of the supercell (characterizing the model) and the discretization cell size of the Brillouin zone (which specifies the computational procedure) for different crystalline systems, specifically, for a vacancy in silicon. As the convergence was reached in the calculations, the energy for the vacancy formation rose to 10 eV, which is much higher than the experimental value 3.6 ± 0.2 eV [4].

Even if the electronic structure of a defect, including electron correlation corrections, is supposed to be exactly calculated for a given configuration of the nuclei, it is questionable whether the vibronic-effect problem for this defect becomes less difficult to solve. In this paper, we also suppose that the electron state is adiabatic and that its wave function can be represented by its expansion due to configuration interaction and that the different molecular-orbitals determinants of this expansion have different linear vibronic coupling with the Jahn–Teller (JT) mode.

In [5], the multiplet structure of a neutral vacancy in silicon and diamond was calculated for different distortions, as well as for the saddle point of a barrier to migration, by using the restricted open-shell Hartree–Fock–Roothaan molecular orbital (ROHF) method. This method leads to an intraconfiguration interaction correction to an electron correlation when a self-consistent determinant combination is found. Therefore, the correlation energies and other energy parameters characterizing the JT effect and determined by the ROHF method can be referred to as the single-open-shell approximation values; these values agree with a great deal of theoretical and experimental data for silicon and diamond [5].

The ROHF correlation corrections for the intraconfiguration interaction are of a different order of magnitude, depending on the filling of the molecular orbitals of the open shell. If the JT effect leads to the splitting of a high-symmetry term and an electron configuration arises whose filling is different in character, then there appears a discontinuity in the behavior of the ROHF multiplet structure: the adiabatic energy of a split-off term does not tend to the energy of the full-symmetry term as the lattice distortion vanishes. The amount of the discontinuity equals the correlation energy in the single-open-shell approximation [5] (the method can also be extended to the case of a larger number of open shells). The objective of this paper is to treat the vibronic mixing problem for the JT effect by a quan-

1063-7834/00/4209-1634$20.00

tum-chemical method that does not involve any empirical vibronic coupling parameters. In this treatment, the standard quadratic vibronic coupling arises due to the configuration mixing in the full-symmetry electron state.

1. RESULTS OBTAINED BY THE OPEN-SHELL METHOD

The method of molecular orbitals (MOs), as applied to a neutral vacancy, came under criticism. The configuration interaction corrections to the Hartree–Fock MOs were found [6] to be so large that the valence bond method is more adequate. However, this result was obtained in a cluster model of a fully symmetric monovacancy, with a cluster not being large enough for the model to be realistic. Furthermore, it is overlooked that, if a lattice distortion is taken into account in the MO scheme, there will appear terms for which the correlation corrections can be smaller than for fully symmetric states (of course, one should apply the open-shell method in order to see this). The terms with different correlation corrections arise, for example, in the case of a tetragonally distorted neutral monovacancy.

In this case, the displacements of atoms (distortions) lowering the symmetry of an atomic configuration belong to representations of the $\mathbf{T}_d$ group for a monovacancy and to representations of the $\mathbf{D}_{3d}$ group for a semivacancy (which is a vacancy situated at the saddle point of a barrier to migration). An arbitrary shift of the vacancy nearest neighbor with a position vector of $\left[\frac{1}{4}\frac{1}{4}\frac{1}{4}\right]$ can be expanded in terms of the normal modes [2]

$$\begin{aligned}&(A_1)[111] + (E, 1)[\bar{1}\bar{1}2] + (E, 2)[1\bar{1}0]\\ &+ (T_2, 1)[101] + (T_2, 2)[0\bar{1}\bar{1}] + (T_2, 3)[\bar{1}\bar{1}0],\end{aligned} \quad (1)$$

where the dimensionless (not normalized) distortions are indicated in parentheses. The first distortion in Eq. (1) is relaxation, i.e., the normal mode that does not lower the symmetry and in which all the nearest neighbor atoms are shifted along the ⟨111⟩ directions by the same amount. In modeling, we represented the relaxation (A_1) of a monovacancy as a shift of its four nearest neighbors toward the empty lattice site, while the relaxation (A_{1g}) of a semivacancy was represented by a shift of the six nearest neighbors toward the two empty sites [5].

According to the theory of vibronic coupling of the orbital triplet of electronic MOs with modes belonging to the twofold irreducible representation [2], the adiabatic electron energy is minimal for any of the three tetragonal distortions along an axis of the ⟨001⟩ type,

$$\begin{aligned}&q = (E, 1) \neq 0,\\ &(E, 2) = (T_2, 1) = (T_2, 2) = (T_2, 3) = 0,\\ &\mathbf{T}_d \longrightarrow \mathbf{D}_{2d}, \quad t_2 \longrightarrow e + b_2.\end{aligned} \quad (2)$$

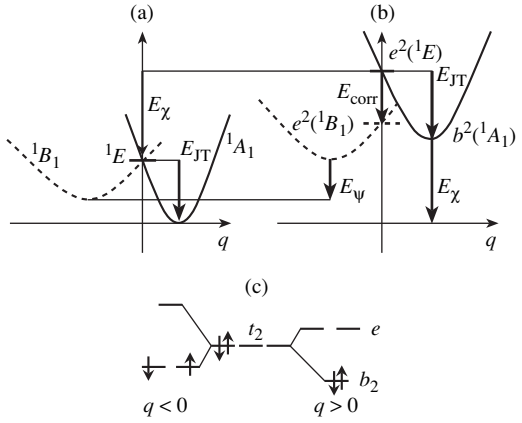

Fig. 1. Scheme of configuration vibronic mixing for a neutral vacancy with tetragonal distortion: (a) "true" many-electron adiabatic terms, (b) adiabatic terms in the single-open-shell approximation calculated by the ROHF method [5], and (c) splitting and filling of molecular orbitals of a vacancy at different amounts of tetragonal distortion defined by Eq. (2). Correlation corrections differ in value, depending on the term type: E_χ is the correction for terms with covalent filling of molecular orbitals (by pairs), E_ψ is that for terms with exchange filling, and E_{corr} is the correction in the single-open-shell approximation.

Figure 1a schematically shows the "true" adiabatic energies of the JT many-electron terms as if they could be calculated with all correlation corrections, while Fig. 1b (also schematically) presents these terms as calculated by the ROHF method [5]. When stabilized, the degenerate ^1E term of a fully symmetric monovacancy reduces to the b_2^2 configuration with a closed shell and a single $^1A_1$ term. This term is represented by the solid adiabatic parabola, which tends to the $t_2^2(^1E)$ energy level as the distortion vanishes. However, in the ROHF approximation, the adiabatic parabola of the $^1B_1$ term of the e^2 configuration with an open shell (dashed line) is shifted downward with respect to its JT partner b_2^2 ($^1A_1$) and does not tend to the $t_2^2(^1E)$ energy level as the distortion vanishes.

This discontinuous behavior of the energies of the terms into which the ^1E doublet is split is a many-electron effect (revealed by the ROHF method), rather than the result of an inexact calculation. Indeed, in the independent-electron approximation, the amount of splitting-off of the e doublet of MOs from the t_2 triplet is half that of the b_2 singlet and both vary continuously

with distortion. Hence, the b_2^2 configuration is energetically more favorable [2], and the distortion will have a direction at which the b_2 level is lower than e. This is illustrated in Fig. 1c, which also describes many-electron states; in this case, the levels represent not the contributions to the total energy of the system, but the orbital energies (the eigenvalues of the Fock matrices, the physical interpretation of which is given by Koopman's and Brillouin's theorems), and the filling of these levels shows that the terms are of the covalent (χ) and exchange (ψ) types. The discontinuous behavior of the splitting-off amount signifies that the correlation energies E_χ of the $t_2^2({}^1E)$ and $b_2^2({}^1A_1)$ covalent terms are approximately equal, but they are higher than the correlation energy E_ψ of the $e^2({}^1B_1)$ exchange term. In addition to the ground-state configuration t_2^2, the "true," fully symmetric ground state ${}^1E$ contains other electron configurations (they are indicated by another dashed line in Fig. 1b). These configurations have two or more open shells and are no longer of a pure covalent character, as is the ground-state configuration. If the configuration interaction with them were taken into account, this would lead to a correlation correction such that the JT splitting would vary continuously with distortion. Thus, the difference in energy between the covalent full-symmetry term and its JT exchange component at zero distortion is, in the ROHF approximation, the correlation energy $E_{\rm corr}$ calculated in the single-open-shell approximation.

In the ROHF approximation, the exchange terms, both triplets and singlets (similar to $e^2({}^1B_1)$ in the case of a neutral monovacancy), have smaller correlation energies than the terms of a covalent character have. Therefore, the ROHF approximation allows one not only to self-consistently calculate individual terms of a multiplet structure, but also to evaluate the correlation corrections from the response of the terms to a lowering of symmetry. Using the difference in energy of the covalent and exchange JT partners, the correlation energy of the ${}^1E$ ground state of a fully symmetric neutral monovacancy in the single-open-shell approximation was found to be [5] $E_{\rm corr} \approx 0.5$ eV (in silicon) and 0.7 eV (in diamond). For diamond, this estimate agrees with the configuration interaction correction experimentally found to be [7] 0.63 eV for the ${}^1E$ term.

2. CONFIGURATION VIBRONIC MIXING

Usually, when the JT effect is considered, the exact adiabatic electron states (including electron correlations) of a fully symmetric nuclear configuration are assumed to be known [2]. In the case of a monovacancy, these are two degenerate ${}^1(E, i)$ states, $i = 1, 2$. In order to obtain them by the configuration interaction (CI) method, for example, in the defect molecule approximation [1], the ground-state $t_2^2({}^1E)$ electron configuration is mixed with configurations $a_1^{2-m}t_2^{2+m}$ (i.e., the wave function is represented as the sum of determinants with unknown coefficients), where $m = 1$ and 2 correspond to one- and two-electron excitations, respectively. Calculations show [5] that $E_{\rm corr}$ is not small in comparison to the JT stabilization energy E_{JT}; on the other hand, the MOs of the a_1 type all lie deep in the valence band and, hence, cannot be responsible for a CI correction as large as this. Therefore, the defect molecule model is inadequate, and the CI predominantly involves configurations corresponding to the excitation of shallow triplet and doublet levels, $t^{6-m}t_2^{2+m}$ and $e^{4-m}t_2^{2+m}$, associated with the crystalline surrounding. Calculations of the mixing with these configurations should be based on group-theoretical analysis and present a considerable problem. In this paper, a configuration vibronic mixing (CVM) method is proposed in which we do not perform the CI procedure for the fully symmetric electron state, which, in itself, is of no importance and is auxiliary in constructing the wave function of the system of electrons and nuclei. Instead, in order to include the CI, the Born–Oppenheimer adiabatic electronic function is expanded in terms of the five Hartree–Fock functions of the ROHF approximation: two of the covalent, $t_2^2[{}^1(E, i)]$ type, belonging to the full-symmetry orbital doublet, and three of the exchange, $e^2[{}^1(B_1, j)]$ type, where the index $j = x, y, z$ specifies the axis of tetragonal distortion.

A standard procedure, which is formulated as a "vibronic $E \times e$ problem" for determining an adiabatic multiwell potential corresponding to the experimental data, involves empirical vibronic coupling parameters [2]: $I = \langle E, 1|(E, 2)|E, 2\rangle$ for linear coupling and $\langle E, 1|(E, 1)(E, 2)|E, 2\rangle$ for quadratic coupling. These parameters are matrix elements of the derivatives of the adiabatic electron Hamiltonian with respect to distortion normal modes, where, for brevity, the derivatives are denoted by the index specifying the variable with respect to which the derivative is taken. In the CVM approximation, the quadratic coupling parameters turn out to be unnecessary, because in the problem with a dimensionality as large as five the adiabatic potential automatically becomes a multiwell one, depending on two distortion modes (E, i). Group-theoretical analysis shows that, in addition to I, there are six independent linear vibronic coupling parameters

$$J_i = \langle z|(E, i)|z\rangle,$$

$$F_i = \langle z|(E, i)|x\rangle = \langle z|(E, i)|y\rangle, \quad (i = 1, 2),$$

$$G_1 = \langle E, 1|(E, 1)|z\rangle = -\langle E, 2|(E, 2)|z\rangle,$$

$$G_2 = \langle E, 1|(E, 2)|z\rangle = \langle E, 2|(E, 1)|z\rangle,$$

where, instead of the notation $e^2[^1(B_1, j)]$ denoting a state, we have written, for brevity, only the index $j = x, y, z$, specifying the axis of tetragonal distortion. The parameters indicated above are divided into pairs; the other pairs of the matrix elements are obtained from them by the cyclic permutation of x, y, and z and are not independent, but are related to those presented above by 2×2 matrices of the irreducible representation E of the $\mathbf{T}_d$ group. All independent vibronic parameters can be calculated by a quantum-chemical method in the ROHF approximation. Therefore, the method we propose here for calculating the JT effect is totally nonempirical, and the adiabatic multiwell potential as obtained by this method is not expressed in terms of the empirical quadratic vibronic coupling, but is determined by linear couplings (of different strengths) with different electron configurations forming a fully symmetric orbital doublet. The JT problem being treated in the CVM approximation can be referred to as a $(E + B_1') \times e$ problem by analogy with the standard notation.

On the whole, the quantum-chemical modeling of the JT effect in the CVM approximation holds much promise. This statement can be supported by a comparison, made below, between the parameters of the $b_2^2(^1A_1)$ and $e^2(^1B_1)$ adiabatic terms as calculated by this method (their behavior is shown schematically in Fig. 1b, while the numerical results are presented in [5]) and those obtained from a wide range of vacancy properties associated with the JT effect and investigated by various experimental and theoretical methods.

From the adiabatic parabola of the former term (solid curve), an upper estimate can be obtained for the JT stabilization energy of a neutral vacancy; from the normalized amounts of the equilibrium distortion for both terms $\|(E, 1)\|$ and their stabilization energies, one can immediately determine the linear vibronic parameters I and J_1 and make an upper estimate of the frequency characterizing the lattice elastic energy near the vacancy [2],

$$I, J_1 = \frac{2E_{JT}}{\|(E, 1)\|}, \quad \omega^2 = \frac{2E_{JT}}{M\|(E, 1)\|^2}.$$

For diamond, we obtain $E_{JT} \leq 0.40$ eV. This agrees with nonempirical [8] and empirical [7] calculations of the electronic structure, which give 0.25 eV, with an empirical estimate of 0.2 eV [9] from the optical spectra, as well as with two independent empirical theories of the JT effect for a vacancy that are believed to be the most adequate (630 and 270 meV [10]; these values of the stabilization energy of a monovacancy in diamond are empirically fitted to the frequency and the vibronic coupling parameter, which are indicated below in parentheses after the values obtained in this paper): $\hbar\omega \leq 160$ meV (81, 131 [10]; the optical phonon frequency in diamond is 165 meV), $I = 7.6$ (3.2, 7.9 [10]), and $J_1 = 3.5$ eV Å^{-1}.

In silicon, we have $E_{JT} \leq 0.27$ eV, which agrees with a nonempirical calculation (0.2 eV [11]) in a model (consistent with the experimental data) of a vacancy as a negative-U center [2]. The other quantities are found to be $\hbar\omega \leq 60$ meV (the optical phonon frequency in silicon is 64 meV), $I = 3.7$ (1.12 [11]), and $J_1 = 2.2$ eV Å^{-1}.

3. BARRIERS TO MIGRATION AND REORIENTATION

The height of a barrier to migration can be estimated from the energy of the singlet state at the full-symmetry saddle point, i.e., from the energy of the ^1E_g term of a semivacancy [5]. This term is of an exchange–covalent character; hence, the correlation correction to it is of the same order of magnitude as those to the $^3T_1(\mathbf{T}_d)$, $^3A_2(\mathbf{D}_{2d})$, and $^3A_2(\mathbf{C}_{3v})$ terms of a monovacancy, and an indirect comparison can be drawn. The true energy of the singlet state of a monovacancy with tetragonal distortion (including the configuration vibronic mixing) should be lower than that of the lowest triplet term calculated in the ROHF approximation, which is the $^3A_2(\mathbf{C}_{3v})$ state, stabilized by a trigonal distortion, according to calculations in [5]. Thus, we obtain a lower ROHF estimate to be

$$E_m[V^0] \geq {}^1E_g(\mathbf{D}_{3d}) - {}^3A_2(\mathbf{C}_{3v}). \quad (3)$$

Because the ^1E_g term is orbitally degenerate, the state of a vacancy at the saddle point to migration is stabilized by the JT effect, which is interpreted in [12] as the migrating atom switching from its covalent bonding to the pair of neighbors of the vacancy at the initial site to its bonding to the pair of neighbors of the vacancy at the final site. (The notion of a migrating vacancy is self-contradictory; the vacancy is best considered as being at lattice sites, whereas the atom continuously transfers or migrates. At the saddle point of the barrier to migration, the atom is between two empty sites, the initial and the final one, and it is this atomic configuration that is called a semivacancy, or a split vacancy.) Let an atom migrate from site $\left[\frac{1}{4}\frac{1}{4}\frac{1}{4}\right]$, to which a monovacancy hops, to site [000], where the monovacancy was before. The lowering of symmetry (stabilization due to the JT effect) occurs when the migrating atom at the saddle point is displaced along the $[11\bar{2}]$ direction from the center of the $\mathbf{D}_{3d}$ symmetry, i.e., from the full-symmetry saddle point $\left[\frac{1}{8}\frac{1}{8}\frac{1}{8}\right]$. The symmetry of the stabilized semivacancy is lowered to $\mathbf{C}_{1h}$, and the orbital degeneracy is completely lifted; therefore, the restricted Hartree–Fock–Roothaan approximation to a closed electron shell (RHF method) can be used to calculate the adiabatic parabola, i.e., the displacement dependence of the total energy. This refinement of the ROHF estimate given by Eq. (3) is worth making after a calcula-

tion by the CVM method for a monovacancy. Without the correction for the JT effect, Eq. (3) gives [5]

$$E_m[V^0] \geq \begin{cases} 0.4\ \text{eV}(0.45 \pm 0.04\ [13]) & \text{in silicon} \\ 1.3\ \text{eV}(2.3 \pm 0.3\ [14]) & \text{in diamond.} \end{cases}$$

The experimental values are indicated in parentheses. For diamond, the results that agree with the experiment best of all have been obtained to date by the electron density functional method: $2.8 = (3.3 - 0.5_{JT})$ eV for the cluster model [12] and 1.7–1.9 eV for the supercell model [8].

The height of the barrier to the reorientation of the axis of tetragonal distortion of a monovacancy E_r can be determined in the same way as that of the barrier to migration, namely, by comparing adiabatic parabolas of two closed-shell terms calculated by the RHF method. One of them, represented by the solid curve in Fig. 1b, was discussed above. In the RHF approximation, this term gives the energy of the atomic monovacancy configuration with tetragonal distortion. The saddle point of a barrier to the reorientation of the axis of this distortion arises because of atomic displacements corresponding to the (E, 2) normal mode of tetragonal distortion in Eq. (1). The symmetry of such a monovacancy is lowered to $\mathbf{D}_2$, the degeneracy is completely lifted, and the corresponding closed-electron-shell calculation [5] gives the following results.

For silicon, we obtain $E_r[V^0] = 0.09$ eV, which is far less than an experimental value of 0.23 eV [13] and, hence, should be refined by the CVM method. At the same time, in the cluster model, the height of a barrier to reorientation calculated even by the nonempirical Hartree–Fock method with correlation corrections is found to be 0.33 eV [15], which exceeds the experimental values of both the height of a barrier to reorientation and the stabilization energy E_{JT}. Because the agreement between the barrier to migration calculated in the same paper [15], 1.1 eV, and the experimental value (0.45 ± 0.04 eV) is still poorer, the conclusion suggests itself that the quasi-molecular large-unit-cell model [5] is more adequate than the cluster model to describe the effect of the crystalline surrounding on low energy barriers in silicon.

For diamond, we have $E_r[V^0] = 0.14$ eV. Although there are no direct experimental data on the height of a barrier to reorientation in diamond, this quantity is known to be small, because in diamond, unlike silicon, the JT effect for a monovacancy is of a dynamical, rather than static, nature [2]. An "empirical" theory of the dynamical JT effect allows one to relate the barrier to reorientation to the experimentally measured splitting (8 meV) of the optical spectrum band $GR1$, but the relation involves the linear and quadratic vibronic coupling parameters, and, hence, the quantities are not uniquely determined (for example, the equilibrium distortion and relaxation are not determined at all). There are two best sets of values of adjustable parameters, and the values of $E_r[V^0]$ for them are approximately the same (24 and 26 meV [10]). Using the CVM method, which involves only linear vibronic coupling, will refine the large value of the barrier to reorientation given by the RHF method and allow one to relate it to the ground-state vibronic splitting of 8 meV for a neutral vacancy in diamond.

CONCLUSION

Thus, the open-shell molecular-orbital method (ROHF) allows one to calculate the multiplet structures of high-symmetry atomic configurations of a neutral vacancy in silicon and diamond [5] and to analyze the relationship between electron correlation and vibronic coupling in terms of the configuration interaction. If a high-symmetry term is split because of the JT effect and an electron configuration arises whose filling is of a different type than that of the original configuration, a discontinuity appears in the behavior of the ROHF multiplet structure: the adiabatic energy of the split-off term does not tend to the energy of the full-symmetry term as the lattice distortion vanishes. The amount of the discontinuity equals the correlation energy in the single-open-shell approximation.

The energy barriers to relevant processes can be estimated on the basis of adiabatic energy curves for the states with closed shells. For this purpose, a method is proposed in which configuration vibronic mixing of the fully symmetric Jahn–Teller term in the ROHF approximation is introduced with orientation-degenerate terms (due to the distortion direction) including a correlation correction in the single-open-shell approximation. This method is nonempirical and involves only linear vibronic coupling. The adiabatic potential is a multiwell one in this method, because different configurations involved in the exact Jahn–Teller term have different vibronic coupling with a lattice distortion.

Estimates including configuration vibronic mixing are made of the stabilization energy, the frequency of local lattice vibrations, the vibronic coupling parameter, the energy of a phononless dipole-allowed optical electron transition [5], and the energy barriers to migration and to distortion-axis reorientation. The calculations agree with the results obtained by different experimental and theoretical methods for a wide range of vacancy properties associated with the Jahn–Teller effect.

ACKNOWLEDGMENTS

The author is grateful to S.V. Bulyarskiĭ for his encouragement.

This work was supported by the Russian Foundation for Basic Research, project no. 98-02-03327.

REFERENCES

1. M. Lanno and J. Bourgoin, *Point Defects in Semiconductors I* (Springer-Verlag, New York, 1981; Mir, Moscow, 1984).
2. J. Bourgoin and M. Lanno, *Point Defects in Semiconductors* (Springer-Verlag, New York, 1983; Mir, Moscow, 1985).
3. G. Makov, R. Shah, and M. C. Payne, Phys. Rev. B **53** (23), 15513 (1996).
4. S. Dannefaer, P. Masher, and D. Kerr, Phys. Rev. Lett. **56** (20), 2195 (1986).
5. S. S. Moliver, Fiz. Tverd. Tela (S.-Peterburg) **42** (4), 655 (2000) [Phys. Solid State **42**, 673 (2000)].
6. G. T. Surratt and W. A. Goddard III, Solid State Commun. **22** (7), 413 (1977); Phys. Rev. B **18** (6), 2831 (1978).
7. A. Mainwood and A. M. Stoneham, J. Phys.: Condens. Matter **9** (11), 2453 (1997).
8. J. Bernholc, A. Antonelli, T. M. Del Sole, *et al.*, Phys. Rev. Lett. **61** (23), 2689 (1988).
9. G. Davies, J. Phys. C **15**, L149 (1982).
10. G. Davies, Rep. Prog. Phys. **44** (7), 787 (1981).
11. M. Lannoo, G. A. Baraff, and M. Schlüter, Phys. Rev. B **24** (2), 943 (1981).
12. S. J. Breuer and P. R. Briddon, Phys. Rev. B **51** (11), 6984 (1995).
13. G. D. Watkins and R. P. Messmer, Phys. Rev. Lett. **32**, 1244 (1974).
14. G. Davies, S. C. Lawson, A. T. Collins, *et al.*, Phys. Rev. B **46** (20), 13157 (1992).
15. M. A. Roberson and K. Estreicher, Phys. Rev. B **49** (24), 17040 (1994).

Translated by Yu. Epifanov

Physics of the Solid State, Vol. 42, No. 9, 2000, pp. 1640–1642. Translated from Fizika Tverdogo Tela, Vol. 42, No. 9, 2000, pp. 1595–1597.

SEMICONDUCTORS AND DIELECTRICS

Electric-Field-Induced Orientation of Iron Tetragonal Centers in $KTaO_3$

L. S. Sochava, V. É. Bursian, and A. G. Razdobarin

Ioffe Physicotechnical Institute, Russian Academy of Sciences, Politekhnicheskaya ul. 26, St. Petersburg, 194021 Russia
e-mail: Lev.Sochava@pop.ioffe.rssi.ru

Received March 14, 2000

Abstract—$Fe_K^{3+}-O_i^{2-}$ impurity centers in a $KTaO_3$ sample to which a dc electric field E = 75 kV/cm is applied are shown to be oriented at temperatures $T \geq 120$ K. In these conditions, the effective local field acting on the electric dipole moment of a center exceeds the applied field by a factor 7.6. © *2000 MAIK "Nauka/Interperiodica".*

1. The orientation of defect centers in a lattice can be ordered by exerting an anisotropic action on the crystal. The alignment of $Fe_K^{3+}-O_i^{2-}$ tetragonal centers in a $KTaO_3$ cubic crystal by polarized light was discovered [1] and studied in considerable detail [2]. The mechanism of this alignment was shown [2] to consist in anisotropic recharging of the centers by polarized light, which does not involve their real reorientation.

By a universally accepted model [3, 4], the center being discussed here represents a complex of an impurity ion Fe^{3+} at a K^+ site and an O^{2-} ion occupying an interstitial site located near Fe_K^{3+} along one of the ⟨100⟩ crystallographic directions. Thus, the $KTaO_3$ lattice allows six possible center orientations (Fig. 1).

Because the center being discussed has an electric dipole moment (Fig. 1), one may attempt to order the orientation of the $Fe_K^{3+}-O_i^{2-}$ centers by a method different from the one employed in [1, 2], namely, by applying a dc electric field to the sample. It is known that, for a dipole center to be oriented by an external electric field, it must have a possibility to undergo spontaneous (thermal) reorientation at the temperature of the experiment. Recent publications [5] suggested the existence of such reorientations of this center at the temperature T = 117–120 K and reported determination of the barrier separating the interstitial positions of the O_i^{2-} ion (0.34 ± 0.02 eV).

This work reports on the orientation of the $Fe_K^{3+}-O_i^{2-}$ complexes in $KTaO_3$ by an external electric field.

2. The study was made on $KTaO_3$: Fe single crystals grown from a batch containing 20000 ppm iron at the Physical Department of the Osnabrück University, Germany. Rectangular samples with the edges aligned with ⟨100⟩ and measuring typically $0.7 \times 2 \times 3$ mm were cut from a single-crystal boule and studied in the as-grown state. Silver-paste electrodes were applied to 2×3-mm faces.

EPR spectra were measured with a standard SE/X 2544 X-range spectrometer, with the samples held in liquid nitrogen or in a jet of its vapor. In the latter case, the temperature was stabilized to within ±1 K.

The electric fields used in experiments in both liquid and gaseous nitrogen were up to 150 kV/cm.

3. The optical alignment of $Fe_K^{3+}-O_i^{2-}$ centers by polarized light was observed to set in at T = 78 K [1, 2]. This method of ordering of the center orientation is obviously more efficient, the lower the probability of thermal reorientation of the center at the temperature of

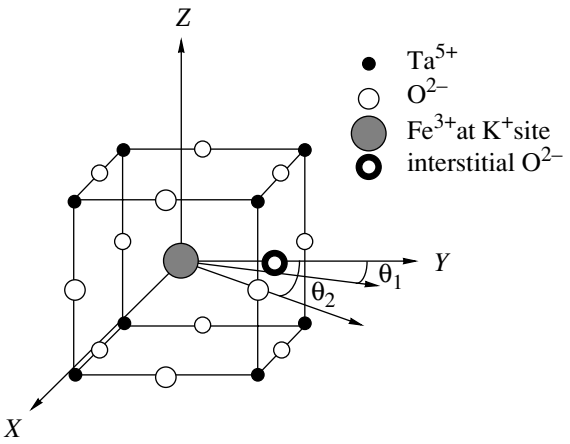

Fig. 1. $Fe_K^{3+}-O_i^{2-}$ center in a $KTaO_3$ lattice (in one of its six possible orientations). In Figs. 2 and 3, the field E is applied along [010], and the field H is canted from [010] by angles θ_1 and θ_2, respectively.

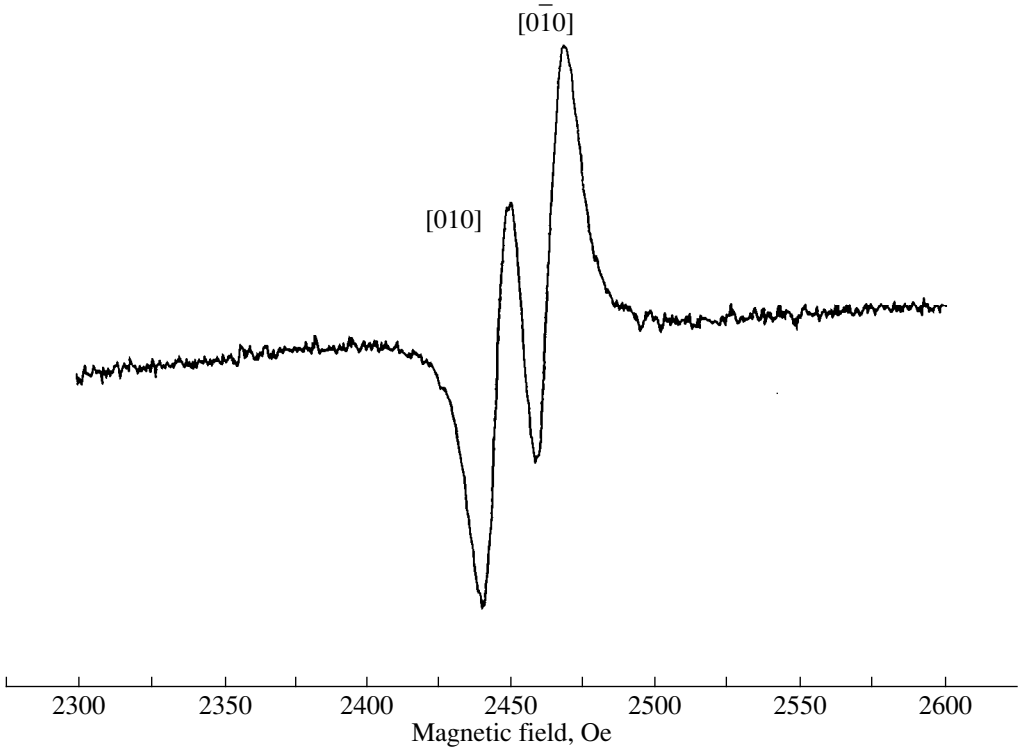

Fig. 2. Electric-field-induced splitting of the EPR line at $T = 78$ K. The two components correspond to centers with dipole moments along and counter to the field, respectively. $\mathbf{E} \parallel [010]$, $E = 92$ kV/cm. $\mathbf{H} \perp [001]$, $\angle(\mathbf{H}, \mathbf{E}) = \theta_1 = 18°$.

the experiment. At $T = 78$ K, the degree of the light-induced center alignment persists indefinitely in the dark; that is, thermal reorientation does not occur at this temperature at all. On the other hand, as already mentioned, in order for an external electric field to be capable of orienting a center, thermal reorientation must be allowed. It thus becomes clear that no orientation of the $Fe_K^{3+}-O_i^{2-}$ centers in an external electric field should take place at $T = 78$ K, and that higher temperatures are required for it to be observable.

The experiments carried out confirmed these arguments. Figure 2 shows an EPR line corresponding to centers with the tetragonal axis aligned with ⟨010⟩; the line was obtained at $T = 78$ K in a field $E = 92$ kV/cm applied along the axis of the above centers. (The **H** field made an angle $\theta_1 = 18°$ with the tetragonal axis of the centers, an orientation corresponding to the maximum line splitting of this center [6].) The line is seen to split in two equal components, with the splitting (19 Oe) being as large as twice the original linewidth. Thus, at $T = 78$ K, the number of the centers with the dipole moment directed along the field is equal to that of the centers with the dipole moment oriented opposite to the field, and it persists indefinitely. This means that, at $T = 78$ K, an external electric field does not orient the centers (although, as this will be shown in Section 4, in these conditions $pE_{loc}/kT > 4$, where E_{loc} is the effective local field acting on the center dipole); i.e., the centers do not undergo thermal reorientation at this temperature.

Experiments with an electric field performed at higher temperatures revealed reorientation of the centers starting from $T \approx 120$ K. It was found that quantitative measurements of the extent of orientation can be more conveniently carried out by comparing the intensities not of the components of the field-split line, but rather those of the lines corresponding to the center orientation along different ⟨100⟩ axes. We used the magnetic-field orientation with **H** canted by 1–2° in the (001) plane from the ⟨110⟩ direction; in this case, one observes two lines near $H = 1500$ Oe (Fig. 3a): one of the lines corresponds to two centers with the tetragonal axis along ⟨110⟩, parallel to **E**, and the other is associated with two other centers with their axis along ⟨100⟩, perpendicular to **E**.

Figure 3 shows characteristic recordings of these two lines obtained at $T = 122$ K in zero field and in fields of 47 and 75 kV/cm after having kept the sample in the field for a long time. The integrated-intensity ratio of these two lines obtained at 75 kV/cm differs by about four times from that measured in zero field. Estimation of the degree of alignment as $\eta = (I_\parallel - I_\perp)/(I_\parallel + I_\perp)$, where $I_\parallel$ and $I_\perp$ are the intensities of the two lines, yields $\eta = 0.6$. Thus, the existence of thermal reorientation of the center under study at $T = 122$ K cannot be questioned.

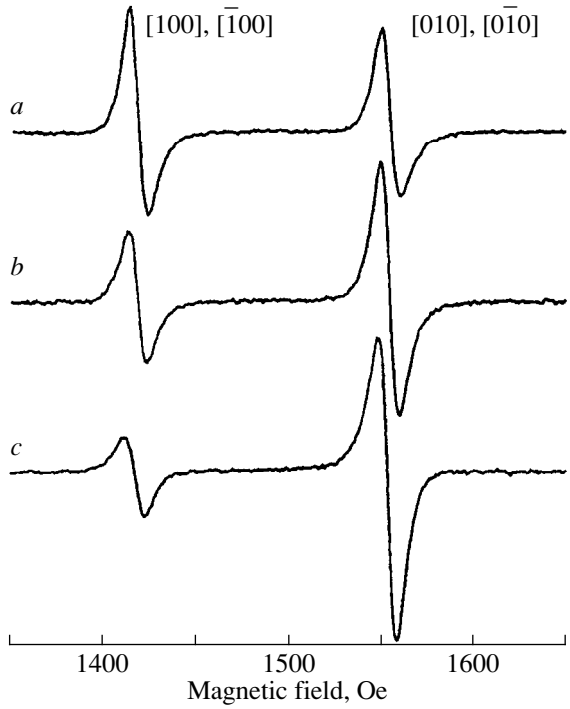

Fig. 3. Variation with electric field **E** ∥ [010] of the intensity of the two EPR lines corresponding to different orientations of the $Fe_K^{3+}-O_i^{2-}$ center measured at $T = 122$ K. E (kV/cm): (*a*) 0, (*b*) 47, and (*c*) 75. $\angle(\mathbf{H}, \mathbf{E}) = \theta_2 = 43.5°$. Adjoining the lines are the center orientations contributing to the given line (see Fig. 1).

4. The experimental data obtained permit the determination of the product $p_{\text{eff}}E$ (p_{eff} is the effective dipole moment corresponding to the observed degree of dipole orientation in an external electric field E) and, hence, of p_{eff},

$$p_{\text{eff}} = 30.4\ e\text{Å} = 146D.$$

On the other hand, the known structure of the center under study makes it possible to directly estimate its dipole moment p_c (assuming, in accordance with theoretical calculations [7], that the distance between the Fe_K^{3+} and O_i^{2-} ions is close to 2 Å):

$$p_c \cong 2e \times 2\ \text{Å} = 4\ e\text{Å} = 19.2D.$$

A comparison of the values of p_{eff} and p_c shows that the effective local field E_{loc} acting on the center dipole is substantially in excess of the applied field E

$$E_{\text{loc}} = (7.6 \pm 0.8)E.$$

The dipole of the center cannot obviously be considered as a point type (its arm is one half the lattice constant), and therefore, it does not appear strange that the E_{loc} found here significantly differs from the calculated local field at a point in the $KTaO_3$ lattice with a cubic environment [8]

$$E_{\text{loc}}^{(\text{cub})} = \frac{\varepsilon + 2}{3}E \cong 170E$$

(the dielectric constant ε is about 500 for $KTaO_3$ at $T =$ 122 K).

Thus, it is clear that the experimentally observed high degree of center orientation in a comparatively weak external field is due to both the large E_{loc}/E ratio and the appreciable dipole moment of the center.

ACKNOWLEDGMENTS

The authors are indebted to Dr. H. Hesse and Prof. S. Kapphan (Osnabrück Universität, Germany) for providing high-quality $KTaO_3$: Fe crystals, to S. A. Basun for fruitful discussions, and to A. A. Kaplyanskiĭ for interest in the work and support.

Support of the Russian Foundation for Basic Research (grant no. 99-02-18319) is gratefully acknowledged.

REFERENCES

1. H.–J. Reyher, B. Faust, M. Käding, *et al.*, Phys. Rev. B **51**, 6707 (1995).
2. S. A. Basum, L. S. Sochava, V. E. Bursian, *et al.*, in *Proceedings of the XIII International Conference on Defects in Insulating Materials, Wake Forest University, USA, 1996*; Mater. Sci. Forum **239**–**241**, 345 (1997).
3. I. P. Bykov, M. D. Glinchuk, A. A. Karmazin, and V. V. Laguta, Fiz. Tverd. Tela (Leningrad) **25** (12), 3586 (1983) [Sov. Phys. Solid State **25**, 2063 (1983)].
4. V. V. Laguta, M. D. Glinchuk, I. P. Bykov, *et al.*, Fiz. Tverd. Tela (Leningrad) **29** (8), 2473 (1987) [Sov. Phys. Solid State **29**, 1422 (1987)].
5. V. S. Vikhnin, A. S. Polkovnikov, H.-J. Reyher, *et al.*, in *Proceedings of the 9th International Meeting of Ferroelectricity, Seoul, Korea, 1997*; J. Korean Phys. Soc. **32**, S486 (1998); H.-J. Reyher, in *Proceedings of the VI Russian–German Seminar on Point Defects in Insulators and Deep-Level Centers in Semiconductors, St. Petersburg, 1997* (unpublished).
6. I. N. Geĭfman, M. D. Glinchuk, and B. K. Krulikovskiĭ, Zh. Éksp. Teor. Fiz. **75** (4), 1468 (1978) [Sov. Phys. JETP **48**, 741 (1978)].
7. H. Donnerberg, M. Exner, and C. R. A. Catlow, Phys. Rev. B **47** (1), 14 (1993).
8. C. Kittel, *Introduction to Solid State Physics* (Wiley, New York, 1976; Nauka, Moscow, 1978).

Translated by G. Skrebtsov

Physics of the Solid State, Vol. 42, No. 9, 2000, pp. 1643–1647. Translated from Fizika Tverdogo Tela, Vol. 42, No. 9, 2000, pp. 1598–1601.

DEFECTS, DISLOCATIONS, AND PHYSICS OF STRENGTH

Molecular Static Model of $CuInSe_2$ Crystal: Energy Properties of Some Structural Defects

A. N. Varaksin*, **, A. V. Postnikov*, A. B. Sobolev**, M. V. Yakushev****, and R. D. Thomlinson******

**Institute of Industrial Ecology, Ural Division, Russian Academy of Sciences, Yekaterinburg, 620219 Russia*
e-mail: varaksin@ecko.uran.ru
***Ural State Technical University, ul. Mira 19, Yekaterinburg, 620002 Russia*
****Universität Osnabruck, FB Physik, 49069 Osnabruck, Deutschland*
*****University of Salford, Physics Department, Salford M5 4WT, UK*
Received December 7, 1999; in final form, February 21, 2000

Abstract—A molecular static model of a $CuInSe_2$ crystal is constructed, and the energies of formation of isolated defects are calculated. An analysis of the interaction between defects shows that, for a high defect concentration (exceeding 1%), the energies of interaction between defects can considerably exceed the values obtained in the continuous medium approximation. It is found that the role of interaction between defects in quantum-chemistry calculations using the model of supercells (periodic defect) is considerably underestimated.

$CuInSe_2$ (CIS) is one of the most promising materials used as the absorbing layer of solar batteries [1]. The efficiency and radiation stability of this material makes it a leader among thin-film transducers of solar energy. The efficiency of transformation attained under laboratory conditions is as high as 18.8% [2]. In recent years, considerable attention was paid to an analysis of the relation of defect formation to the observed properties of $CuInSe_2$ [3–6]. The main problems encountered in investigations include the clarification of the mechanisms of defect passivation during the implantation of ions and the determination of the origin of radiation stability of $CuInSe_2$ crystals. The essential stage in the solution of such problems is the determination of the energies of formation E_f and interaction E_{int} of the main defects. The knowledge of these energies makes it possible to determine the concentration of defects in the initial crystal (if the crystal growth conditions are known). The values of E_f and E_{int} also determine the crystal state as a result of defect redistribution, such as during the thermal annealing following irradiation.

1. MOLECULAR STATIC QUASI-IONIC MODEL OF $CuInSe_2$ CRYSTAL

The molecular static model of the $CuInSe_2$ crystal is based on the concept of pairwise ion–ion interactions (potentials). The $CuInSe_2$ crystal is a semiconductor, and hence, the description of its properties using ionic potentials is approximate. The accuracy of the description is different for different properties of the crystal. It was proven in a number of publications that the quasi-ionic model can be used for estimating the energies of formation and interaction of defects in semiconducting materials [7].

The pair potential is constructed from the Coulomb and short-range components. The Coulomb component is determined by ionic charges, which are chosen to be +1 for the copper ion, +3 for the indium ion, and –2 for the selenium ion (in electron charge units). These values of the charges have been confirmed both theoretically and experimentally [8].

When concurrence on the magnitudes of ionic charges is reached, the construction of the molecular static model boils down to determining the parameters of the short-range component Φ_{sh} of the pair potential, which is usually presented in the Born–Mayer–Van der Waals form

$$\Phi_{sh}(r) = B\exp(-r/r_0) - C/r^6.$$

The required parameters B, r_0, and C for the $CuInSe_2$ crystal must ensure

(1) the reproducibility of the structure of a perfect crystal (ionic coordinates in a unit cell);

(2) zero pressure in the crystal (or the minimum total energy of the crystal for a given size of a unit cell);

(3) the reproducibility of experimental values of the bulk compression modulus and dielectric constants of the crystal; and

(4) the reproducibility of the changes in the total energy of the crystal upon a change in the parameter Δ (displacement of selenium ions from the symmetric position), which are obtained by the total-potential band method of linear combination of muffin-tin orbitals (LMTO); we used the version of the method described in [9].

1063-7834/00/4209-1643$20.00 © 2000 MAIK "Nauka/Interperiodica"

Table 1. Parameters of the short-range component of the pair potential

Ion pairs	B, eV	r_0, Å	C, eV Å^6
Se–Se	0.0	0.0	341.0
Se–Cu	1.078×10^4	0.220	0.0
Se–In	1.848×10^3	0.390	0.0

Table 2. Energies of formation of solitary defects in $CuInSe_2$

Defect	Energy of formation, eV		
	our results	data obtained in [11]	data obtained in [5]
Cu vacancy	2.3	2.9	0.63
Se vacancy	4.6	2.6	–
In vacancy	7.4	2.8	4.29
Cu–Frenkel defect	3.1	7.3*	2.67*
Se–Frenkel defect	10.1	25.0*	–
In–Frenkel defect	10.9	11.9*	–
In–Cu antisite defect	3.6	2.9*	4.26*
2V(Cu) + In(Cu)	–9.63	–	–
Cu–Frenkel pair	1.24	–	–
In–Cu antisite pair	0.25	–	–

* These values were obtained by the summation of energies of formation of components constituting the given defect, presented in [11] and [5].

When parametrizing the molecular static model, we assumed that the interaction potentials between cations (Cu–Cu, Cu–In, and In–In) are equal to zero in view of the large separation between them (which is much larger than the separation between the unlike ions Se–Cu and Se–In) and that these potentials abruptly decrease with increasing distance between the ions (much more sharply than for Se–Cu and Se–In). The van der Waals component of the Se–Se interaction potential was borrowed from research [10] carried out for a ZnSe crystal. In this way, the Se–Se, Se–Cu, and Se–In potentials were fitted to satisfy the requirements formulated above. The results are presented in Table 1.

These parameters of pair potentials ensure the stability of the structure for a perfect crystal; satisfy the condition of zero pressure; give the value of the bulk compression modulus $G = 0.69 \times 10^{+12}$ erg/cm^3, which is close to the experimental value ($G = 0.71 \times 10^{+12}$ erg/cm^3 [3]); and make it possible to reproduce the LMTO data in the molecular static model to a high degree of accuracy (the error is below 2% for all values of the parameter Δ).

The dielectric properties of the crystal were reproduced by using the Dick–Overhauser shell model of an ion. Using the shell parameters for a selenium ion that were obtained by Harding [10] for the ZnSe crystal (the shell charge q^s equal to –3.0 and the "core–shell" coupling constant K_{sc} = 11.3 eV/Å^2), we obtain the following values for the dielectric constants: $\varepsilon_0 = 8.6$ and $\varepsilon_\infty = 4.6$.

We can easily reproduce in our calculations the experimental values of ε_0 of the order of 13.6 and of ε_∞ of the order of 8 by varying the shell parameters of the indium ion (the copper ions are usually assumed to be nonpolarizable). For example, for the shell charge q^s of the indium ion equal to –1.0 and for the "core–shell" coupling constant equal to 45.0 eV/Å^2, we obtain ε_0 = 16.1 and $\varepsilon_\infty = 8.0$.

It turns out, however, that the shell parameters of the indium ion reproducing the experimental values of dielectric constants lead to a "polarization catastrophe": the cores of indium ions are "torn" from the shells when a charged defect (e.g., a vacancy) is formed in the crystal. Thus, the copper and indium ions in the proposed model are assumed to be nonpolarizable; the values of dielectric constants are underestimated and the calculated values of the energy of the defect formation are exaggerated in this case.

2. ENERGY OF FORMATION OF ISOLATED DEFECTS

Using the parameters given in Table 1, we calculated the energies of formation of isolated (solitary) structural defects in $CuInSe_2$ (Table 2). We considered traditional defects such as vacancies and Frenkel defects, as well as the In–Cu antisite defect (in which the indium and copper ions have changed places, and the separation between them is equal to infinity) and the defect 2V(Cu) + In(Cu) proposed in [4, 5], which is a compact group of two copper vacancies and an indium ion at a copper site. The term "Cu–Frenkel pair" in Table 2 denotes the complex formed by a copper vacancy and an interstitial copper ion being at the distance of next-to-nearest neighbors (at the nearest neighbor distance, the Frenkel pair is unstable and is annihilated), while the term "In–Cu antisite pair" stands for an In–Cu antisite defect at the nearest distance between In and Cu. In view of the interaction between the components of a defect complex, the energy of formation of a Cu–Frenkel pair is considerably lower than the energy of formation of a Cu–Frenkel defect (the same is true of an In–Cu antisite pair).

A comparison of the results of our calculations made by the molecular static method (the Mott–Littleton approach) using the MOLSTAT program [12] with the results of Neumann's calculations [11] made in the two-band dielectric model of the crystal shows a satisfactory coincidence for defects with a low energy of formation, such as a copper vacancy and an In–Cu antisite defect. The energy of formation of a Frenkel defect in a copper sublattice in the scheme of [11] appears to be unexpectedly high.

The negative value of the energy of formation of the defect $2V$(Cu) + In(Cu) obtained by the molecular static (MS) method is worth noting. In the MS method, this is the energy required for the removal of three copper ions to infinity plus the gain in energy in the case when a trivalent indium ion occupies the copper site. In actual practice, the energy of formation of such a defect must also include the energy of ionization of an indium atom to a trivalent ion, which cannot be calculated by the MS method. Thus, the value of the energy of the formation of the defect $2V$(Cu) + In(Cu) given in Table 2 is conditional and will be used only for estimating the interaction between defects (see below).

It is interesting to compare the energies of defect formation as calculated in the molecular static model with the results of quantum-chemistry calculations [4–6]. A good agreement is observed for electrically neutral defect complexes (Cu–Frenkel defect and In–Cu-antisite defect). For charged defects (copper and indium vacancies), a quantitative agreement is not observed, but quantum-chemistry calculations confirm a much higher energy of formation of an indium vacancy as compared to a copper vacancy (for example, the energies of formation of all vacancies in the model of [11] are approximately equal).

Table 2 provides an answer to the question concerning the dominating type of defects in $CuInSe_2$ crystal. According to our results, an In–Cu antisite pair possessing the lowest energy of formation and preserving the stoichiometry of the crystal must be the main defect in the case of thermally activated disordering. According to the results obtained in [4, 5], a $2V$(Cu) + In(Cu) complex can be another defect with a low energy of formation; however, it violates the crystal stoichiometry (the absolute value of the energy of formation of this defect cannot be calculated by the MS method; see above).

The results described above lead to the conclusion that the parametrization of the molecular static model carried out by us is successful. We will apply this parametrization to solve the problem of the interaction between defects in $CuInSe_2$.

3. INTERACTION BETWEEN DEFECTS

In order to estimate the interaction between defects in the molecular static method, we used the model of a periodic defect, in which a defect is placed in a large unit cell (LUC) containing N ions of the lattice and is translated periodically in space. The calculations were made for N = 16, 32, 64, and 128 ions. For large values of N, such calculations can be made only by the molecular static method.

Since a LUC in the MS method must be electrically neutral, the calculations were made for three types of defects: a Cu–Frenkel pair, $2V$(Cu) + In(Cu), and an In–Cu antisite pair. Table 3 contains the results of calculation of the interaction energy between defects located in different LUCs, i.e., the variation of energy of defect formation with the number N. As $N \longrightarrow \infty$, the interaction energy between defect complexes tends to zero, while the energy of formation of a defect complex calculated in the model of a periodic defect tends to the energy of the formation of a solitary defect (see Table 2).

Columns 2, 4, and 6 of Table 3 contain the energies of interaction between periodically repeated defects calculated by Eq. (1) in the continuous-medium approximation:

$$E_{\text{int}} = \sum_{ij} Q_i Q_j / \varepsilon_0 R_{ij}, \qquad (1)$$

where Q_i and Q_j are the charges of the defect complex components, ε_0 = 13.6 is the static permittivity of $CuInSe_2$, and R_{ij} is the separation between the components of the defect complex in different calculated cells. Since all of the defects are neutral complexes, the energy of their interaction is small (does not exceed 0.17 eV). The negative values of E_{int} of Eq. (1) indicate that the energy of formation of a periodic defect in the continuous-medium approximation is lower than the energy of formation of a solitary defect.

However, the calculation of the energies by the molecular static method (columns 1, 3, and 5 in Table 3) with an exact microscopic inclusion of all the interactions leads to a different result: as a result of the over-

Table 3. Variation of the energy of formation (eV) of defect complexes in $CuInSe_2$ upon a change in the number N of ions in the large unit cell

Number N of ions in LUC	Cu–Frenkel pair		$2V$(Cu) + In(Cu)		In–Cu antisite pair	
	MS method	Coulomb formula of Eq. (1)	MS method	Coulomb formula of Eq. (1)	MS method	Coulomb formula of Eq. (1)
	1	2	3	4	5	6
16	+0.36	−0.0476	+1.04	−0.0884	+0.01	−0.1670
32	+0.04	−0.0213	+0.13	−0.0531	+0.04	−0.0562
64	+0.07	−0.0315	+0.07	−0.0330	+0.02	−0.0239
128	−0.06	−0.0142	−0.06	−0.0122	−0.02	−0.0048

lapping of the deformation fields for neighboring defects, the energy of their interaction is positive and quite significant as compared to the energy of formation of a solitary defect. For example, the energy of interaction E_{int} = + 0.36 eV for a Cu–Frenkel pair for N = 16 (the minimum size of a LUC) is not negligibly small as compared to the energy of formation of a solitary defect (1.24 eV). The energy of interaction calculated by the MS method is negative and close to the value given by Eq. (1) only for a very large unit cell (N = 128 ions). Approximately the same situation is observed for the defect 2V(Cu) + In(Cu), the increase in the energy of formation upon a decrease in the separation between the defects being still stronger (+1.04 eV for N = 16; see column 3 in Table 3).

The situation with an In–Cu antisite pair is quite different. Even the results presented in Table 2 for the energy of the formation of solitary defects indicate a sharp decrease (by 3.35 eV) in the formation energy upon a transition from an In–Cu antisite defect (E_f = 3.60 eV) to an In–Cu antisite pair (E_f = 0.25 eV). Note for comparison that the change in the energy upon a transition from a Cu–Frenkel defect to a Cu–Frenkel pair amounts to only 1.86 eV (from E_f = 3.10 to 1.24 eV). In principle, the physical reason behind such a difference is clear: the components of a Frenkel pair are singly charged against the background of a perfect lattice, while, in the case of an antisite pair, the components are doubly charged. At the same time, the separation between the components in an antisite pair is considerably smaller than for a Frenkel pair. Consequently, the interaction "within" an In–Cu antisite pair is much stronger than in a Cu–Frenkel pair, which explains such a low energy of formation of an In–Cu antisite pair.

Table 3 also illustrates the peculiar behavior of an In–Cu antisite pair in the formation of a periodic defect. For example, for the minimum size N = 16 of the large unit cell, i.e., for the maximum overlapping of deformation fields for neighboring defects, the energy of formation of a given defect increases only by 0.01 eV; note for comparison that the corresponding increase in the energy is 0.36 eV for a Cu–Frenkel pair and 1.04 eV for a 2V(Cu) + In(Cu) defect. The change in the energy of formation of an In–Cu antisite pair for other values of N is also insignificant (column 5 in Table 3).

According to the data contained in Table 3, we can conclude that the interaction between the defects under investigation does not facilitate the formation of defects with a concentration higher than 1% (one defect in a large unit cell comprised of 100 ions) since the energy of interaction between defects for $N < 100$ becomes positive and increases with the defect concentration.

The results obtained in this section also allow us to make the following remarks concerning the quantum-chemistry analysis of the properties of defects in $CuInSe_2$. In quantum-chemistry approaches [4–6], calculations were made for a unit cell of a fixed size, which makes it impossible to estimate the contribution of interaction to the energy of the defect formation. Moreover, computational difficulties encountered in quantum-chemistry methods only permit an analysis of small-size unit cells (as a rule, 32 ions for a $CuInSe_2$ crystal in the model with periodic boundary conditions [4–6]), whereas the interaction between defects can be estimated only by varying the separation between them (e.g., by changing the unit cell size), preferably over a wide range. In the quantum-chemistry approach, the energy of interaction E_{int} is usually estimated on the basis of the Coulomb formula of Eq. (1), which gives low values of the energy E_{int}. Our results show that this is not always the case: if the theoretical unit cell is small, the effects of interaction can be strong and can vary significantly upon a transition from one type of defect to another.

Thus, we have constructed the molecular static quasi-ionic model of the $CuInSe_2$ crystal. The analysis of the energies of formation of solitary defects carried out in this model and their comparison with the results obtained by other authors (with the results of calculations by other methods) substantiate the constructed model.

The model was used for an analysis of the interaction between defects in $CuInSe_2$. The results show that, when the defect concentration exceeds 1%, the interaction energies between defects become positive and can considerably exceed the values obtained in the continuous-medium approximation. It was noted that the authors of quantum-chemistry calculations of the properties of defects in crystals (calculations, which are the most correct at the moment) considerably underestimate the role of the interactions between defects. Our results show that a symbiosis of quantum-chemistry and molecular static models is possible: some quantum-chemistry results (e.g., the data on the variation of the crystal energy upon a change in the lattice geometry) are used in the parametrization of the molecular static model, after which the model can be used for analyzing those properties of defects that cannot be calculated using the quantum-chemistry method as of yet (e.g., for calculating the interaction energies between defects for various defect concentrations).

ACKNOWLEDGMENTS

This work was supported by the INTAS Foundation (grant no. 96-0634) and the Russian Foundation for Basic Research (grant no. 98-03-33195a).

REFERENCES

1. U. Rau and H. W. Schock, Appl. Phys. A **69** (2), 131 (1999).
2. M. A. Contreras, B. Egaas, K. Ramanathan, *et al.*, Prog. Photovoltaics **7**, 311 (1999).

3. A. Rockett and R. W. Birkmire, J. Appl. Phys. **70** (7), R81 (1991).
4. S. B. Zhang, Su-Huai Wei, and A. Zunger, Phys. Rev. Lett. **78** (21), 4059 (1997).
5. S. B. Zhang, Su-Huai Wei, and A. Zunger, Phys. Rev. B **57** (16), 9642 (1998).
6. T. Yamamoto and H. Katayama-Yoshida, in *Proceedings of the 11th International Conference on Ternary and Multinary Compounds, Salford, 1997*, p. 37.
7. C. R. A. Catlow and A. M. Stoneham, J. Phys. C: Solid State Phys. **16** (22), 4321 (1983).
8. J. E. Jaffe and A. Zunger, Phys. Rev. B **28** (10), 5822 (1983).
9. A. V. Postnikov, T. Neumann, G. Borstel, and M. Methfessel, Phys. Rev. B **48** (9), 5910 (1993).
10. J. H. Harding, J. Phys. C: Solid State Phys. **14** (20), 5049 (1981).
11. H. Neumann, Cryst. Res. Technol. **18**, 901 (1983).
12. Yu. N. Kolmogorov and A. N. Varaksin, Zh. Strukt. Khim. **32** (4), 162 (1991).

Translated by N. Wadhwa

Physics of the Solid State, Vol. 42, No. 9, 2000, pp. 1648–1651. Translated from Fizika Tverdogo Tela, Vol. 42, No. 9, 2000, pp. 1602–1605.

DEFECTS, DISLOCATIONS, AND PHYSICS OF STRENGTH

Effect of Cascade Gamma-Radiation Summation Processes on the Precision of Calculating the Probability of Three-Photon Annihilation of Positronium

S. K. Andrukhovich, N. M. Antovich, and A. V. Berestov

Institute of Physics, Belarussian Academy of Sciences, ul. F. Skoriny 70, Minsk, 220072 Belarus

e-mail: berestov@dragon.bas-net.by

Received February 25, 2000

Abstract—The processes of cascade gamma-quanta summation, disregarded when measuring the energy spectrum of ^{22}Na in samples by a one-detector spectrometer, are studied, along with the effect of these processes on the change in the area bounded by the 511-keV annihilation line in the calculation of the probability $P_{3\gamma}$ of three-photon annihilation of positronium. An increase in the number of annihilation quanta in "positronium-forming" samples and their redistribution to the low-energy spectral region are responsible for the difference between the areas of the photopeak of the accompanying nuclear quantum, with respect to which the spectra are normalized, and of the corresponding peak in the aluminum standard. The departure of the real value of $P_{3\gamma}$ from its value, determined without taking into account the summation processes on a highly effective scintillation NaI(T1) detector and a semiconducting Ge detector, amounts to 56 and 25%, respectively, for a distance of 3 cm between the positronium source and the detector surface. © *2000 MAIK "Nauka/Interperiodica".*

The positron diagnostic methods are widely used in contactless and nondestructive control, as well as for investigating physicochemical and technological properties of various materials and media.

It is well known (see, for example, [1]) that positronium has two ground states: a triplet, or orthopositronium *o*-Ps [^{t}Ps($^3S_1$)] with parallel spins of the electron and the positron, and a singlet, or parapositronium *p*-Ps [^{s}Ps($^1S_0$)], in which the electron and positron spins are antiparallel. The total angular momentum of orthopositronium is $J_t = 1$, and three substates differing in the magnetic quantum number ($m = +1, 0, -1$) are possible in this case. For parapositronium, $J_s = 0$ and $m = 0$. Consequently, the statistical weight of the triplet state is three times as great as that of the singlet state: the ortho-state is formed in 75% and the parastate occurs in 25% of the cases involving the formation of positronium. The *o*-Ps experiences 3γ annihilation (the energy spectrum of gamma quanta is continuous from 0 to 511 keV), while *p*-Ps experiences 2γ annihilation (discrete quanta with an energy of 511 keV flying apart at an angle of 180°). The lifetime τ_s^0 of a *p*-Ps atom equals 1.25×10^{-10} s, while the lifetime τ_t^0 of a free *o*-Ps atom prior to annihilation is 1.4×10^{-7} s.

As a rule, the quenching processes (pick-off annihilation, ortho–para conversion, and chemical interaction) lead to a considerable decrease (by an order of magnitude or even larger) in the lifetime τ_t of *o*-Ps in condensed matter.

The three-photon annihilation probability $P_{3\gamma}$ is one of the important parameters characterizing the decay of positronium atoms in a substance; the knowledge of the exact value of this probability is essential for ultimately obtaining information on the structure and features of the substances under investigation [1, 2].

1. EXISTING METHODS OF DETERMINING $P_{3\gamma}$

The positronium formation probability P is connected with the probability $P_{3\gamma}$ of 3γ annihilation through the familiar expression [1]

$$P_{3\gamma} \cong 0.75P\tau_t/\tau_t^0 + (1 - P)/372. \quad (1)$$

The value of $P_{3\gamma}$ can be obtained directly by comparing the experimental energy spectra measured in the sample under investigation and in a substance in which positronium is definitely not formed (e.g., aluminum), and the three-photon decay during the annihilation of a free positronium occurs with the probability $P_{3\gamma} = 1/372$. This phenomenon forms the basis of one of the existing methods of determining $P_{3\gamma}$, which is described in [1] and in greater detail, for example, in [2] and widely used in experimental investigations.

This method can be briefly described as follows. The emission of a positron during the decay of the nucleus of the ^{22}Na isotope is accompanied by the emission of a nuclear gamma quantum with an energy of 1275 keV. Let ε_1 be the efficiency of detection of a 511-keV annihilation quantum in a photopeak and ε_2 be the efficiency of detection of a nuclear quantum in the

corresponding photopeak. Considering that the probability of the three-photon annihilation of a free positron is negligible (1/372), we can write the following expressions in the case of aluminum as a reference:

$$(S_{511})_{\mathrm{Al}} = 2\varepsilon_1 Q, \quad (2)$$

$$(S_{1275})_{\mathrm{Al}} = \varepsilon_2 Q, \quad (3)$$

where $(S_{511})_{\mathrm{Al}}$ and $(S_{1275})_{\mathrm{Al}}$ are the count rates for annihilation and nuclear gamma-quanta, respectively, and Q is the activity of the positron source. The analogous quantities for the sample under investigation are related through the formula

$$(S_{511})_{\mathrm{Ps}} = 2\varepsilon_1(1 - P_{3\gamma})Q, \quad (4)$$

while the intensity of the 1275-keV line remains unchanged, since it does not depend on the structure of the sample, i.e.,

$$(S_{1275})_{\mathrm{Ps}} = \varepsilon_2 Q. \quad (5)$$

In order to determine the probability of the three-phonon annihilation experimentally, one must compare two energy spectra—for the aluminum reference sample and for the sample under investigation—under the assumption that the number of positrons emitted in the two cases is the same. Since we cannot ensure exactly the same geometry of measurements for the two samples and since the positron sources used in the experiments have different activities, the following normalization procedure is usually employed: after the subtraction of the background count rate, the energy spectra must contain the peaks of nuclear gamma radiation of the same area, i.e.,

$$(S_{1275})_{\mathrm{Al}} = (S_{1275})_{\mathrm{Ps}}. \quad (6)$$

Accordingly, the spectra are normalized to equal areas of the nuclear radiation peak, and the experimentally observed quantity in this case is given by

$$\Delta = (S_{511})_{\mathrm{Al}} - (S_{511})_{\mathrm{Ps}} = 2\varepsilon_{3\gamma} Q, \quad (7)$$

whence

$$P_{3\gamma} = \Delta / 2\varepsilon_1 Q. \quad (8)$$

Another method used for determining the three-photon annihilation probability, which is similar to the above method, involves the application of strong magnetic fields (>2.5 T) in which magnetic quenching of positronium takes place; as a result, the probability of three-phonon annihilation in the sample becomes two-thirds of its value in zero magnetic field [1].

It should be noted that, while presenting the results of investigations of elastomer samples of various grade using the above-described technique, the authors of monograph [2] noted that the absolute values of the three-photon annihilation probability are much larger than those calculated by Eq. (1) using data on the positronium lifetime in these samples. The noted difference in the absolute values is attributed by the authors of [2] to a lack of precision in the procedure of determining the level of external background radiation, although, in our opinion, the factors described below can be responsible for this difference.

2. INCLUSION OF SUMMATION PROCESSES OF CASCADE GAMMA RADIATION IN DETERMINING THE PROBABILITY $P_{3\gamma}$

We will not discuss the processes relevant to an incorrect determination of the background nor the events corresponding to the accidental coincidence of quanta from different decays (which have different origins) and their contributions to the energy spectra under investigation. We will consider the physical effects emerging during the detection of the cascade gamma radiation emitted upon the decays described above.

Let ε_1^c be the efficiency of the detection of a Compton-scattered 511-keV annihilation gamma quantum by the detector, $d\varepsilon_2^c$ be the efficiency of detection of the Compton-scattered 1275-keV nuclear quantum, and ε_3^t be the total efficiency of detection of a quantum emitted as a result of the decay of an orthopositronium atom.

In this case, taking into account that a positron and a 1275-keV gamma quantum are emitted in a cascade in the case of an aluminum reference, the following processes, which are associated with the summation of quanta emitted in the same decay of a nucleus and simultaneously reaching the sensing element, occur in the detector, in addition to the processes considered above:

(1) the detection of a Compton-scattered annihilation quantum coinciding with the Compton-scattered nuclear quantum (the count rate of this process is $2\varepsilon_1^c \varepsilon_2^c Q$);

(2) the detection of a Compton-scattered annihilation quantum together with the completely absorbed nuclear quantum ($2\varepsilon_1^c \varepsilon_2 Q$);

(3) the detection of a completely absorbed annihilation quantum together with the Compton-scattered nuclear quantum ($2\varepsilon_1 \varepsilon_2^c Q$);

(4) the detection of a completely absorbed annihilation quantum with the completely absorbed nuclear quantum ($2\varepsilon_1 \varepsilon_2 Q$).

In principle, the sum of the Compton-scattered annihilation and nuclear quanta can fall within the region of the photopeaks under investigation. However, process (1) barely affects the areas of the 511- and 1275-keV photopeaks, since it contributes to the continuous Compton distribution in all regions of the energy spectrum, which is subtracted during line processing by conventional spectroscopic methods (e.g., the "trapezoid" method). Apart from this, one of the consequences of the high energy resolution of a semiconducting detector

Table 1. Values of detection efficiency and coefficient κ for scintillation and semiconducting detectors as functions of the separation R of the positronium source and sample from the detector surface

NaI(Tl) ∅150 × 100 mm						
R, cm	ε_1	ε_1^t	ε_2	ε_2^c	ε_3^t	κ
3	0.11	0.046	0.07	0.083	0.16	1.56
10	0.037	0.015	0.023	0.028	0.052	1.12
20	0.013	0.005	0.008	0.0095	0.017	1.035
Ge 200 cm^3						
3	0.036	0.072	0.019	0.069	0.103	1.25
10	0.009	0.017	0.005	0.015	0.026	1.05
20	0.0025	0.0065	0.0016	0.006	1.010	1.02

is that the probability of the sum of two Compton-scattered quanta falling within the region of the photopeaks under investigation is negligible as compared to the probability of all possible combinations of quanta summation processes.

Processes (3) and (4) lead to a change in the area of the 511-keV photopeak, while processes (2) and (4) lead to a change in the area of the 1275-keV photopeak. It should also be noted that, in contrast to processes (2) and (3) leading to a change in the area of only one (corresponding) photopeak, process (4) lowers both the annihilation photopeak and the nuclear photopeak simultaneously. Taking the above arguments into account, we can write for the 511-keV line

$$(S_{511})^*_{\mathrm{Al}} = 2\varepsilon_1 Q(1-\varepsilon_2^t), \tag{9}$$

where $\varepsilon_2^* = (\varepsilon_2 + \varepsilon_2^c)$ is the total efficiency of detecting the nuclear quantum and

$$(S_{1275})^*_{\mathrm{Al}} = \varepsilon_2 Q(1-2\varepsilon_1^t), \tag{10}$$

where $\varepsilon_1^t = (\varepsilon_1 + \varepsilon_1^c)$ is the total efficiency of detecting a 511-keV annihilation quantum.

In the case of the "positronium-forming" sample under investigation, annihilation quanta of orthopositronium have an energy lower than 511 keV and are detected not in the photopeak, but in the Compton region of the spectrum. Also considering the fact that three gamma quanta are emitted simultaneously during the decay of an orthopositronium atom, we have the following processes of the same origin as those listed above:

(1) $[2\varepsilon_1^c(1-P_{3\gamma}) + 3\varepsilon_3^t P_{3\gamma}]\varepsilon_2^c Q$,

(2) $[2\varepsilon_1^c(1-P_{3\gamma}) + 3\varepsilon_3^t P_{3\gamma}]\varepsilon_2 Q$,

(3) $2\varepsilon_1(1-P_{3\gamma})\varepsilon_2^c Q$,

(4) $2\varepsilon_1(1-P_{3\gamma})\varepsilon_2 Q$.

This gives

$$(S_{511})^*_{\mathrm{Ps}} = 2\varepsilon_1 Q(1-\varepsilon_2^t)(1-P_{3\gamma}), \tag{11}$$

$$(S_{1275})^*_{\mathrm{Ps}} = \varepsilon_2 Q[1-2\varepsilon_1^t + P_{3\gamma}(2\varepsilon_1^t - 3\varepsilon_3^t)]. \tag{12}$$

Let us analyze the consequences of the requirement of the equality for the areas of the photopeaks corresponding to the nuclear gamma-quantum, which is used as a criterion for the comparison of spectra. For this purpose, we multiply the spectrum of the aluminum reference sample by the normalization coefficient

$$\begin{aligned}(S_{1275})^*_{\mathrm{Ps}}/(S_{1275})^*_{\mathrm{Al}} \\ = [1-2\varepsilon_1^t + P_{3\gamma}(2\varepsilon_1^t - 3\varepsilon_3^t)]/(1-2\varepsilon_1^t).\end{aligned} \tag{13}$$

This gives

$$P^*_{3\gamma} = \Delta^*(1-2\varepsilon_1^t)/2Q\varepsilon_1(1-\varepsilon_2^t)(1-3\varepsilon_3^t). \tag{14}$$

Thus, the probability $P_{3\gamma}$ determined in this way differs from that calculated by Eq. (8) by a factor of

$$\kappa = (1-2\varepsilon_1^t)/(1-\varepsilon_2^t)(1-3\varepsilon_3^t). \tag{15}$$

The values of the coefficient κ for some types of the detector used are given in Table 1. In our calculations, we used the experimental data obtained with a Na(T1) detector with a size of ∅150 × 100 mm and a high efficiency Ge detector GC8021 having a volume of 200 cm^3 [3] in the energy range 0.03–2.0 MeV.

It should be noted that we did not seek to obtain an exact analytical expression for the correction coefficient, since this procedure requires a meticulous inclusion of the energy dependence of the efficiency of detecting the three-photon annihilation quanta, as well as the angular distribution of the quanta emitted as a result of the decay of *o*-Ps. The aim of this publication is to attract the attention of experimenters to the existing processes of summation of cascade gamma radiation, to estimate these processes, and to propose mea-

sures for eliminating their effect on the results of measurements.

In order to simplify the estimation, we assumed that the value of ε_3^t is equal to the total efficiency of detecting a 392-keV quantum. According to Vartanov and Samoilov [4], the deviation of the value of the total efficiency of gamma-quantum detection from the average value in the energy range 0.1–0.5 MeV does not exceed 12% for a scintillation detector based on a ∅150 × 100 mm Na(T1) crystal.

Table 1 shows that disregarding the summation processes described above leads to a considerable overestimation of the true $P_{3\gamma}$ at a distance ≤10 cm to the detector surface. It should be noted that the investigated summation processes are manifested irrespective of the lower energy threshold (whose maximum value cannot obviously exceed 0.5 MeV) set for the detection of the spectra.

The results of calculations made here were verified by us experimentally. For this purpose, we investigated the probability $P_{3\gamma}$ in the initial silica gel using a scintillation spectrometer with a detector based on a 150 × 100 mm Na(T1) crystal and a ^{22}Na positron source with an activity of 3.2×10^5 Bq by the technique described in Section 1 (disregarding the processes of summation described in this work). The results of the investigation are presented in Table 2, which shows, among other things, that the value of the three-photon annihilation probability for positronium with the positron source and the samples in the immediate vicinity of the detector is about four times as high as the true value of $P_{3\gamma}$.

The results presented in Table 2 confirm the considerable effect of the summation of cascade gamma radiation on the value of the three-photon annihilation probability being determined and agree with the data in Table 1.

Thus, in order to determine the exact value of the three-photon annihilation probability for positronium using the method described in [2], one must take into account the processes of summation of cascade gamma radiation considered in this work. It should be observed that the error in determining the probability P of the positron formation and the three-photon annihilation probability $P_{3\gamma}$ by magnetic quenching can lead to considerable errors caused by a disregard of the processes of summation of cascade radiation.

Table 2. Experimental values of $P_{3\gamma}$ measured on a spectrometer with a NaI(T1) detector having a size ∅150 × 100 mm

Separation R of source and sample from detector surface, cm	$P_{3\gamma}$, %
0	14.65 ± 0.12
3	4.71 ± 0.12
5	4.03 ± 0.12
10	3.65 ± 0.12

It should be noted, in conclusion, that the correction of the spectra taking into account the processes of summation is not required when the solid angle of incidence on the detector is ≤2% of 4π steradians.

ACKNOWLEDGMENTS

The authors are grateful to O.N. Metelitsa, I.V. Bondarev, and B.A. Martsynkevich for fruitful discussions.

This research was supported in part by the Belarus Foundation for Basic Research (grant no. F97-055).

REFERENCES

1. V. I. Gol'danskiĭ, *Physical Chemistry of Positron and Positronium* (Nauka, Moscow, 1968).
2. Z. R. Abdurasulev, P. U. Arifov, N. Yu. Arutyunov, *et al.*, *Methods of Positron Diagnostics and Interpretation of Positron Annihilation Spectra* (Fan, Tashkent, 1985).
3. S. F. Bulyga, V. G. Gulo, I. V. Zhuk, *et al.*, Preprint No. 21, IRFKhP Nats. Akad. Navuk Belarusi (Minsk, 1998).
4. N. A. Vartanov and P. S. Samoĭlov, *Applied Scintillation Gamma Spectroscopy* (Atomizdat, Moscow, 1975).

Translated by N. Wadhwa

Physics of the Solid State, Vol. 42, No. 9, 2000, pp. 1652–1658. Translated from Fizika Tverdogo Tela, Vol. 42, No. 9, 2000, pp. 1606–1612.

DEFECTS, DISLOCATIONS, AND PHYSICS OF STRENGTH

Behavior of Screw Dislocations near Phase Boundaries in the Gradient Theory of Elasticity

M. Yu. Gutkin*, K. N. Mikaelyan*, and E. C. Aifantis**

**Institute of Problems in Machine Science, Russian Academy of Sciences, Vasil'yevskiĭ ostrov, Bol'shoi pr. 61, St. Petersburg, 199178 Russia*

e-mail: gutkin@def.ipme.ru

***Aristotle University of Thessaloniki, Thessaloniki 54006, Greece*

Michigan Technological University, Houghton, MI 49931, USA

Received February 16, 2000

Abstract—The solution of the boundary-value problem on a rectilinear screw dislocation parallel to the interface between phases with different elastic moduli and gradient coefficients is obtained in one of the versions of the gradient theory of elasticity. The stress field of the dislocation and the force of its interaction with the interface (image force) are presented in integral form. Peculiarities of the short-range interaction between the dislocation and the interface are described, which is impossible in the classical linear theory of elasticity. It is shown that neither component of the stress field has singularities on the dislocation line and remains continuous at the interface in contrast to the classical solution, which has a singularity on the dislocation line and permits a discontinuity of one of the stress components at the interface. This results in the removal of the classical singularity of the image force for the dislocation at the interface. An additional elastic image force associated with the difference in the gradient coefficients of contacting phases is also determined. It is found that this force, which has a short range and a maximum value at the interface, expels a screw dislocation into the material with a larger gradient coefficient. At the same time, new gradient solutions for the stress field and the image force coincide with the classical solutions at distances from the dislocation line and the interface, which exceed several atomic spacings. © *2000 MAIK "Nauka/Interperiodica".*

1. The description of the elastic interaction of dislocations with interfaces is one of the main problems in the theory of defects in heterogeneous materials. The models of such an interaction are widely used in the physics of strength and plasticity of poly- and nanocrystals, composites, and thin-film solid-state structures [1–4]. The traditional description of the behavior of dislocations at interfaces is based on solving the boundary-value problems in the classical linear theory of elasticity. The corresponding solutions successfully describe the elastic field of dislocations at distances of several atomic spacings from the interfaces or dislocation lines. Consequently, these solutions are valid in the cases where the long-range interaction between dislocations and interfaces plays the leading role. However, classical solutions do not apply when the inclusion of short-range interactions is essential. This mainly concerns the singularity of elastic fields of the dislocation on its line and the singularity of the force of interaction between the dislocation and the interface (image force) in the case where the dislocation is at the interface. In addition, some components of the elastic stress field of the dislocation have discontinuities at the interfaces. This is admissible in a classical macroscopic description, but is physically unsubstantiated in the case of a nano- or microscopic analysis. In order to avoid the above difficulties in the theoretical description of the behavior of dislocations at the interfaces, we will henceforth apply the gradient theory of elasticity to formulate and solve the boundary-value problem on a linear screw dislocation parallel to the phase boundary.

This work is a natural continuation of our systematic investigations [5–10] of defects (dislocations [5–10] and disclinations [8–10]) in the gradient theory of elasticity. The main results of such a description are the removal of singularities in the fields of displacements [5–8, 10], deformations [5–10], and stresses [7, 9, 10] and in the energies [7, 8, 10] on the lines of defects. Using a simple gradient modification [5, 6, 8] of the linear theory of elasticity proposed in [11] and tested in problems on cracks [11–15], we obtained new nonsingular solutions for fields of displacements and deformations from dislocations, for the energies of dislocations, and fields of deformations from disclinations. However, the solutions for elastic stresses in this gradient theory remained singular as in the classical theory of elasticity. In order to obtain new nonsingular solutions, a more general gradient theory proposed in [16, 17] was used in [7, 9, 10]. The basic equation in this theory has the form

$$(1 - c_1\nabla^2)\sigma = (1 - c_2\nabla^2)[\lambda(\mathrm{tr}\epsilon)I + 2\mu\epsilon], \qquad (1)$$

where λ and μ are the Lamé elastic constants; σ and ϵ are the tensors of elastic stresses and strains, respectively; I is a unit tensor; ∇^2 denotes the Laplacian; and c_1 nd c_2 are two different gradient coefficients. Following the simple procedure of solution of Eq. (1) proposed in [16] in analogy with that presented earlier in [12], we obtained solutions for rectilinear dislocations [7, 10] and disclinations [9, 10] in an infinite isotropic elastic medium. These new solutions lead to nonsingular expressions for strains, as well as for stresses.

For example, the field of stresses for a rectilinear screw dislocation whose line coincides with the z axis of the Cartesian system of coordinates has the form [7, 10]

$$\sigma_{xz} = \frac{\mu b_z}{2\pi}\left[-\frac{y}{r^2} + \frac{y}{\sqrt{c_1}r}K_1\left(\frac{r}{\sqrt{c_1}}\right)\right],$$
$$\sigma_{yz} = \frac{\mu b_z}{2\pi}\left[\frac{x}{r^2} - \frac{x}{\sqrt{c_1}r}K_1\left(\frac{r}{\sqrt{c_1}}\right)\right], \quad (2)$$

where b_z is the Burgers vector of the dislocation, $r^2 = x^2 + y^2$, and $K_n(r/\sqrt{c_1})$ is an nth-order modified Bessel function of the second kind (MacDonalds function), $n = 0, 1, \ldots$. The first terms in the brackets are the classical solution [18], while the second terms are additional gradient terms. Such a structure of the solution, which is also typical for other elastic fields and defects in [7, 9, 10], perfectly agrees with the Ru–Aifantis theorem [12], which states that the solution of the boundary-value problem in the gradient elasticity theory can be written as the sum of the classical solution of the same boundary-value problem and additional gradient terms defined by the solution of the corresponding Helmholtz equation. It is interesting to note that the field of stresses of Eq. (2) exactly coincides with the solution obtained by Eringen [19–21] in his version of the nonlocal theory of elasticity. For $r \longrightarrow 0$, we have $K_1(r/\sqrt{c_1}) \longrightarrow \sqrt{c_1}/r$ and $\sigma_{iz} \longrightarrow 0$ $(i = x, y)$. The same result was obtained in [16] from the asymptotic solution for a screw dislocation, as well as for the tip of an antiplane shear crack. It was proved in [7] that the elastic stresses of Eq. (2) attain their peak values $\approx\mu/4$ at a distance $\approx\sqrt{c_1}$ (which can be estimated as $\approx a/4$ [11], where a is the lattice constant) from the dislocation line.

All the results described above were obtained for defects in an infinite isotropic elastic medium characterized by the Lamé elastic constants λ and μ, as well as the gradient coefficients c_1 and c_2 (or by only one gradient coefficient c in the special gradient theory of elasticity [11]). In the present work, we consider a screw dislocation parallel to the planar interface between two elastic isotropic media with different Lamé constants and gradient coefficients. We will derive, in an integral form, the stress field of a dislocation and the force of its interaction with the interface (image force), and describe the peculiarities of the short-range interaction of the dislocation with the interface at the nanoscopic level.

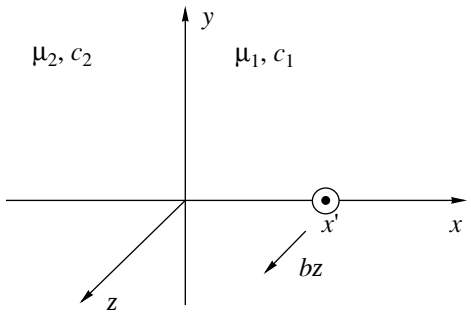

Fig. 1. Screw dislocation at a planar interface.

2. Let us consider plane interface between two elastic isotropic media 1 ($x > 0$) and 2 ($x < 0$) with shear moduli μ_i and the gradient coefficients c_{1i} and c_{2i}, where $i = 1, 2$, respectively (Fig. 1). Let us suppose that the line of a rectilinear screw dislocation with the Burgers vector b_z passes through the point $(x = x', y = 0)$ parallel to the z axis of the Cartesian system of coordinates.

2.1. Classical Solution

In the classical theory of elasticity ($c_{1i} = c_{2i} \equiv 0$) for $x' \geq 0$, the stress field of the dislocation is determined (in the units of $\mu_1 b_z/(2\pi)$ by the expressions [22]

$$\sigma_{xz}^{0(1)} = -\frac{y}{r_-^2} + \frac{\Gamma - 1}{\Gamma + 1}\frac{y}{r_+^2},$$
$$\sigma_{yz}^{0(1)} = \frac{x - x'}{r_-^2} + \frac{\Gamma - 1}{\Gamma + 1}\frac{x + x'}{r_+^2} \quad (3)$$

for medium 1 and by the expressions

$$\sigma_{xz}^{0(2)} = -\frac{2\Gamma}{\Gamma + 1}\frac{y}{r_-^2}, \quad \sigma_{yz}^{0(2)} = \frac{2\Gamma}{\Gamma + 1}\frac{x - x'}{r_1^2} \quad (4)$$

for medium 2, where $r_\pm^2 = (x \pm x')^2 + y^2$ and $\Gamma = \mu_2/\mu_1$.

It can be easily verified that the component σ_{xz}^0 is continuous at the interface ($x = 0$), while the component σ_{yz}^0 experiences a jump,

$$([\sigma_{yz}^0]_{x=0} = \sigma_{yz}^{0(1)}(x = 0) - \sigma_{yx}^{0(2)}(x = 0))$$
$$= \frac{\mu_1 b_z}{\pi}\frac{\Gamma - 1}{\Gamma + 1}\frac{x'}{x'^2 + y^2}, \quad (5)$$

in this region. In the classical theory of elasticity, such a jump can be easily explained from the macroscopic point of view since this yz component does not make any contribution to the x component of the elastic force,

which must be balanced at the interface. On the other hand, if we consider the stressed state at a perfectly conjugate interface from the nanoscopic point of view, the origin of this jump becomes unclear. Indeed, atomic forces on both sides of the interface elastically interact not only with atoms of their own medium, but also with atoms from the other medium. Consequently, we must assume the existence of a transient region of a thickness of several atomic layers, in which elastic interactions between atoms vary smoothly from a strong interaction in a more rigid medium to a weak interaction in the softer medium. Such an assumption immediately leads to the conclusion that the stress jump of Eq. (5) is just a consequence of the approximation of the classical model of a continuous medium, whose properties often differ from reality in the description of nanoscopic phenomena.

In order to illustrate what has been said above, note that the magnitude of the stress jump of Eq. (5) tends to infinity in the *xz* plane when the dislocation comes in contact with the interface. Thus, the stress jump at the interface should obviously be eliminated if possible while solving the given problem in any generalized theory of elasticity aimed at describing phenomena on a nanoscopic level.

2.2. Gradient Solution

Let us now consider the same problem in the gradient theory of elasticity with the basic relation (1). It was proposed in [16] and also described in [7, 9, 10] that the solution of Eq. (1) boils down to the independent solution of the following nonhomogeneous Helmholtz equations for the fields of stresses σ and strains ϵ:

$$(1 - c_1\nabla^2)\sigma = \sigma^0, \quad (1 - c_2\nabla^2)\epsilon = \epsilon^0, \tag{6}$$

where the fields of stresses σ^0 and strains ε^0 are solutions of the same boundary-value problem in the classical theory of elasticity. We will consider here only the solution of the first of Eqs. (6) for the field of stresses since it is most interesting for various applications.

The first of Eqs. (6) can be solved by the Fourier integral transformation method [6–10]. We first write this equation in the form

$$(1 - c_{1i}\nabla^2)\sigma^{(i)} = \sigma^{0(i)}, \tag{7}$$

where $\sigma^{0(i)}$ are defined by the equalities (3) and (4). For the sake of simplicity, we will henceforth omit the first index "1" in the notation of the gradient coefficients c_{1i}, so that c_1 now belongs to material 1 and c_2, to material 2. On the basis of conclusions drawn in Sec. 2.1, as well as the results obtained in [12, 16], we use the classical boundary conditions

$$[\sigma_{xz}]_{x=0} = \sigma_{xz}^{(1)}(x=0) - \sigma_{xz}^{(2)}(x=0) = 0 \tag{8}$$

and three additional boundary conditions

$$[\sigma_{yz}]_{x=0} = \sigma_{yz}^{(1)}(x=0) - \sigma_{yz}^{(2)}(x=0) = 0,$$
$$\left[\frac{\partial\sigma_{jz}}{\partial x}\right]_{x=0} = \left.\frac{\partial\sigma_{jz}^{(1)}}{\partial x}\right|_{x=0} - \left.\frac{\partial\sigma_{jz}^{(2)}}{\partial x}\right|_{x=0} = 0, \quad j = x, y. \tag{9}$$

The first of Eqs. (9) eliminates the jump of the *yz* component of the stress field at the interface, while the second ensures the smooth variation of both components upon a transition through the boundary.

Omitting cumbersome intermediate calculations, we give only the final results here. The gradient solution can be presented (in the units of $\mu_1 b_z/2\pi$) in the form

$$\sigma_{xz}^{(1)} = \sigma_{xz}^{0(1)} + \frac{y}{\sqrt{c_1}r_-}K_1\left(\frac{r_-}{\sqrt{c_1}}\right) + \int_0^{+\infty}\frac{s\sin(sy)}{\lambda_1+\lambda_2}e^{-x\lambda_1} \times\left(\frac{\lambda_1-\lambda_2}{\lambda_1}e^{-x'\lambda_1} + 2\frac{\Gamma-1}{\Gamma+1}e^{-x's}\right)ds, \tag{10}$$

$$\sigma_{yz}^{(1)} = \sigma_{yz}^{0(1)} + \frac{x-x'}{\sqrt{c_1}r_-}K_1\left(\frac{r_-}{\sqrt{c_1}}\right) + \int_0^{+\infty}\frac{\lambda_1\cos(sy)}{\lambda_1+\lambda_2}e^{-x\lambda_1} \times\left(\frac{\lambda_1-\lambda_2}{\lambda_1}e^{-x'\lambda_1} + 2\frac{\Gamma-1}{\Gamma+1}e^{-x's}\right)ds \tag{11}$$

for medium 1, where $\lambda_i = \sqrt{1/c_i + s^2}$, $i = 1, 2$, and

$$\sigma_{xz}^{(2)} = \sigma_{xz}^{0(2)} + 2\int_0^{+\infty}\frac{s\sin(sy)}{\lambda_1+\lambda_2}e^{x\lambda_2}\left(e^{-x'\lambda_1} + \frac{\Gamma-1}{\Gamma+1}e^{-x's}\right)ds, \tag{12}$$

$$\sigma_{yz}^{(2)} = \sigma_{yz}^{0(2)} + 2\int_0^{+\infty}\frac{\lambda_2\cos(sy)}{\lambda_1+\lambda_2}e^{x\lambda_2}\left(e^{-x'\lambda_1} + \frac{\Gamma-1}{\Gamma+1}e^{-x's}\right)ds \tag{13}$$

for medium 2.

Let us briefly consider the structure of the gradient solution of Eqs. (10)–(13). First, all the stress field components contain the classical solution of Eqs. (3), (4), as well as the additional gradient terms, in accordance with the Ru–Aifantis theorem [12, 16] (see Sec. 2.1). Second, they contain the gradient solution of Eqs. (2) obtained in [7] for an infinite homogeneous medium ($\Gamma = 1$, $c_1 = c_2 = c$), which is presented in Eqs. (10), (11) in an explicit analytic form and in Eqs. (10)–(13) in an integral form. For $\Gamma = 1$ and $c_1 = c_2 = c$, expressions (10)–(13) are transformed into Eq. (2). Third, the stress field components of Eqs. (10)–(13) contain specific terms that are only due to the difference in the gradient coefficients c_1 and c_2. These terms

are presented in an integral form by the last terms in Eqs. (10)–(13) for $\Gamma = 1$.

3. The structure of the gradient solution of Eqs. (10)–(13) allows us to consider the following three typical situations separately: a "purely elastic" interface ($\Gamma \neq 1$, $c_1 = c_2 = c$), a "purely gradient" interface ($\Gamma = 1$, $c_1 \neq c_2$), and a general "mixed gradient–elastic" interface ($\Gamma \neq 1$, $c_1 \neq c_2$).

3.1. Purely Elastic Interface ($\Gamma \neq 1$, $c_1 = c_2 = c$)

In this case, the gradient solution (in the units of $m_1 b_z/2\pi$) has the form

$$\sigma_{xz}^{(1,2)} = \sigma_{xz}^{0(1,2)} + \frac{y}{\sqrt{c}r_-}K_1\left(\frac{r_-}{\sqrt{c}}\right) + \frac{\Gamma-1}{\Gamma+1}\int_0^{+\infty}\frac{s}{\lambda}\sin(sy)e^{-|x|\lambda - x's}ds, \quad (14)$$

$$\sigma_{yz}^{(1,2)} = \sigma_{yz}^{0(1,2)} - \frac{x-x'}{\sqrt{c}r_-}K_1\left(\frac{r_-}{\sqrt{c}}\right) + \frac{\Gamma-1}{\Gamma+1}\mathrm{sgn}(x)\int_0^{+\infty}\cos(sy)e^{-|x|\lambda - x's}ds, \quad (15)$$

where $\sigma_{iz}^{0(1,2)}$ are defined by equalities (3) and (4) and $\lambda = \sqrt{1/c + s^2}$. Unlike the classical solution of Eqs. (3) and (4), in which the component σ_{yz}^0 suffers the discontinuity of Eq. (5) at the interface, both components are continuous at the interface. This difference is clearly seen in Figs. 2 and 3. The magnitude of the classical jump increases as the dislocation approaches the interface. Figure 3 also shows clearly that the gradient solution gives finite values of stresses on the dislocation line, while the classical solution has a singularity in this region. The classical and gradient solutions coincide away from the interface ($r > 5\sqrt{c}$) and from the dislocation line, but differ considerably at nanoscopic distances ($r < 5\sqrt{c}$) from them.

When the dislocation is just at the interface ($x' = 0$), the integrals in Eqs. (14) and (15) can be evaluated explicitly, which gives (in the units of $\mu_1\mu_2 b_z/[\pi(\mu_1 + \mu_2)]$)

$$\sigma_{xz} = -\frac{y}{r^2} + \frac{y}{\sqrt{c}r}K_1\left(\frac{r}{\sqrt{c}}\right), \qquad \sigma_{yz} = \frac{x}{r^2} - \frac{x}{\sqrt{c}r}K_1\left(\frac{r}{\sqrt{c}}\right), \quad (16)$$

where $r^2 = x^2 + y^2$. It should be noted that the gradient solutions of Eq. (16) for such an interface dislocation differ from the gradient solutions of Eq. (2) for a dislocation in an infinite homogeneous medium only in the constant factor $2\mu_2/(\mu_1 + \mu_2)$. The same also applies to the classical solutions.

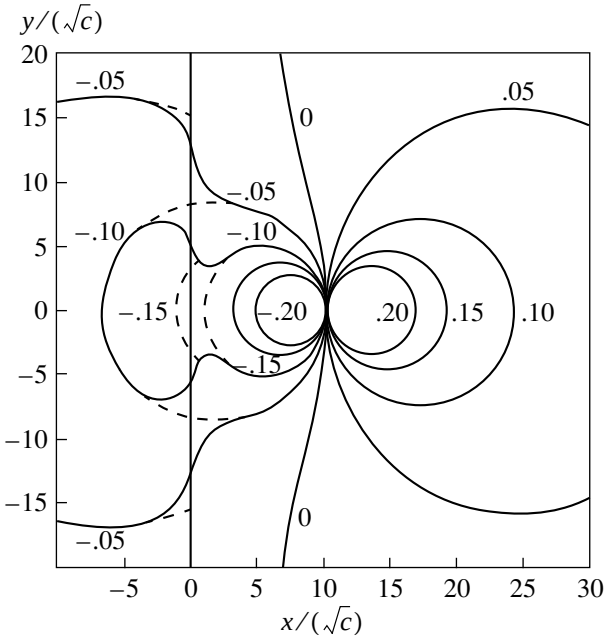

Fig. 2. Map of the stress field σ_{yz} of a screw dislocation located at the point (10, 0) at a planar interface ($x = 0$) for $\mu_2 = 2\mu_1$ and $c_1 = c_2 = c$. The stresses are given in the units of $\mu_1 b_z/(2\pi\sqrt{c})$. The dashed curves are isolines for the classical solution σ_{yz}^0.

Let us now consider the image force F_x^{el} exerted by the interface per unit length of the dislocation {see Fig. 1). The gradient solution (in the units of $\mu_1 b_z^2/2\pi$ has the form

$$F_x^{\mathrm{el}}(x') = b_z\sigma_{yz}^{(1)}(x = x', y = 0) = \frac{\Gamma-1}{\Gamma+1}\left\{\frac{1}{2x'} - \int_0^{+\infty}e^{-x'(\lambda+s)}ds\right\}, \quad (17)$$

where the first term in the braces is the classical singular solution, and the second is the additional gradient term. A numerical analysis of this expression is presented in Fig. 4, which also shows a similar solution for a dislocation located in medium 2 ($x' < 0$). It can be seen that a classical singularity can be eliminated from gradient solutions for the image force attaining its maximum values at distances c from the interface and vanishes at it.

This result is of special importance for a dislocation at the free surface, when $\Gamma = 0$ (see the solid and dashed curves in Fig. 4 in the regions of negative values of the force F_x^{el}). Indeed, it is natural to assume that, as long

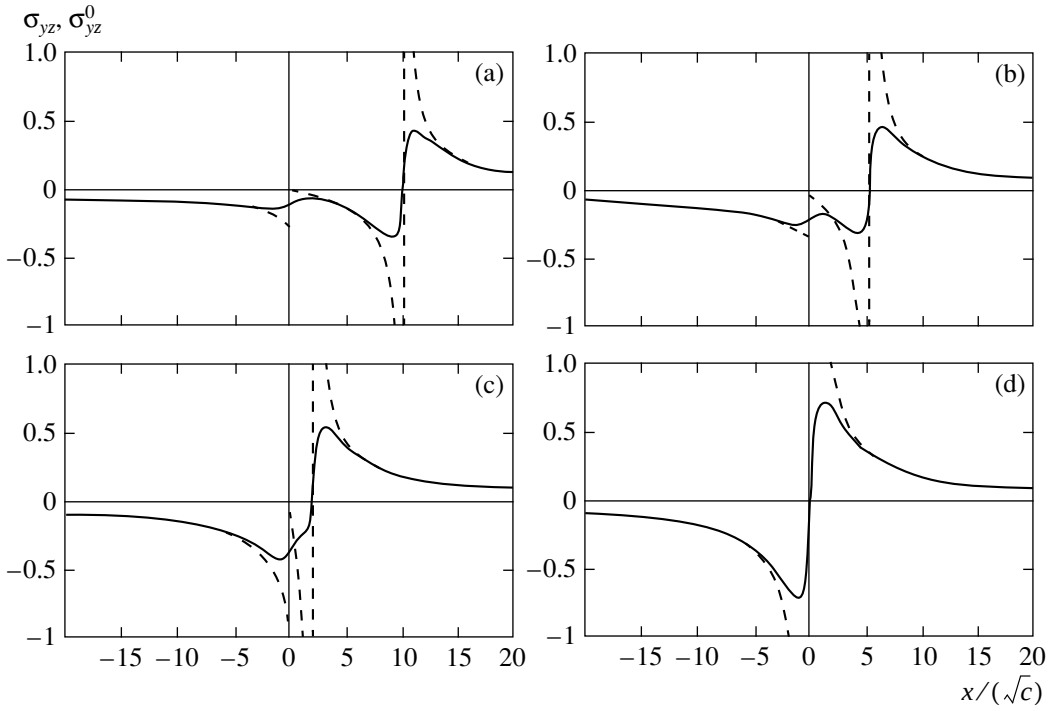

Fig. 3. Distribution of the stress component σ_{yz} (x, y = 0) near the screw dislocation line located at a distance $x'/\sqrt{c}$ = 10 (a), 5 (b), 2 (c), and 0 (d) from the interface (x = 0) for $\mu_2 = 10\mu_1$ and $c_1 = c_2 = c$. The stresses are given in the units of $\mu_1 b_z^2/(2\pi\sqrt{c})$. The dashed curves describe distributions for the classical solution σ^0_{yz}.

as a dislocation is at the free surface, it does not experience the action of any force. The image force appears and increases as the dislocation core starts penetrating the material (the core radius naturally appears in the gradient theory and is estimated as $\approx 4\sqrt{c}$ [5]), attains its peak value, and then decreases with increasing distance from the free surface towards the bulk of the material. This last stage is correctly described by the classical solution {see Fig. 4}, which, however, cannot explain the previous stages. The maximum cleavage stress $\tau_{max} = |F_x^{el}|_{max}/b_z$ that must be overcome by a screw dislocation penetrating the material can be estimated in the gradient theory of elasticity with the basic relation (1). The curve in Fig. 4 gives an estimate $\tau_{max} \approx \mu/2\pi$, i.e., the value of the order of the theoretical shear strength [18].

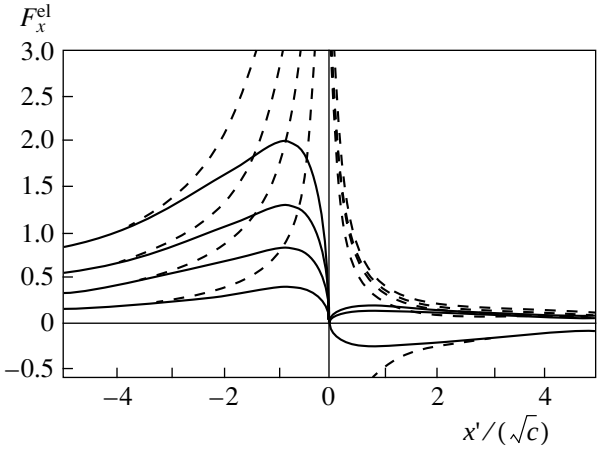

Fig. 4. Dependence of the image force F_x^{el} on the position $x'/\sqrt{c}$ of a dislocation at a "purely elastic" interface (x' = 0) for $c_1 = c_2 = c$ and μ_2/μ_1 = 10, 7, 5, 3, and 0 (from top to bottom). The values of force are in the units of $\mu_1 b_z^2/(2\pi\sqrt{c})$. The dashed curves describe the dependences for the classical solution.

As regards the interior phase boundary, the vanishing of the image force at the interface (the existence of an unstable equilibrium) has not yet been explained.

3.2. Purely Gradient Interface ($\Gamma = 1$, $c_1 \neq c_2$)

In this case, the gradient solution is defined by formulas (10)–(13) for $\Gamma = 1$. We only consider the corresponding image force F_x^{gr} exerted on a dislocation by the interface due to the difference in the gradient coef-

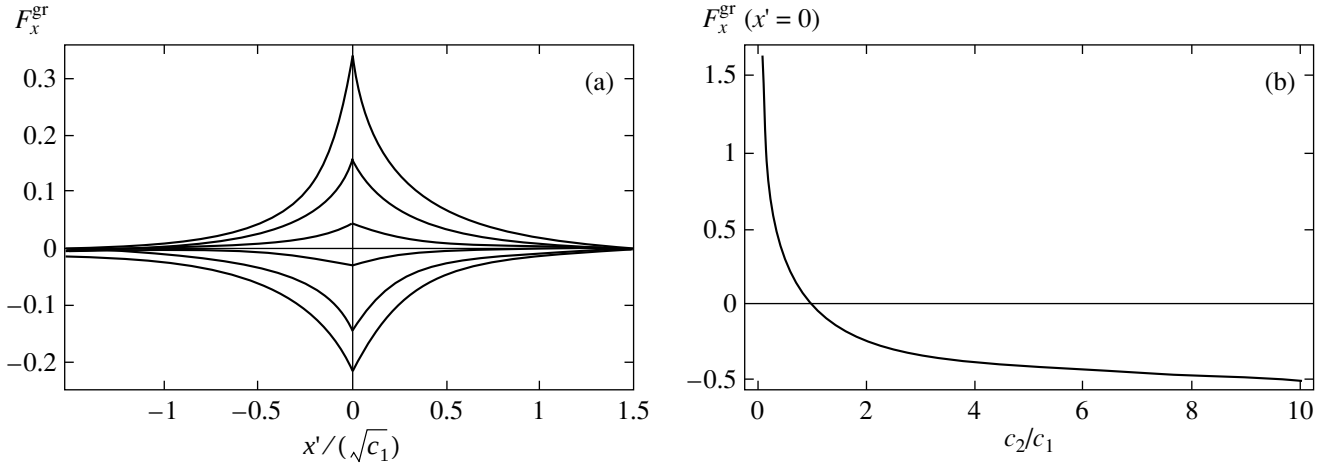

Fig. 5. Dependence of the image force F_x^{gr} on the position $x'/\sqrt{c_1}$ of a dislocation at a "purely gradient" interface ($x' = 0$) for $\mu_2 = \mu_1$ and $c_2/c_1 = 0.5$, 0.7, 0.9, 1.1, 1.5, and 2 (from top to bottom) (a) and dependence of the image force F_x^{gr} at the interface ($x' = 0$) on the ratio c_2/c_1 (b). The values of the force are in the units of $\mu_1 b_z^2/(2\pi\sqrt{c_1})$.

ficients c_1 and c_2. This force is defined (in the units of $\mu_1 b_z^2/2\pi$ as

$$F_x^{gr}(x') = b_z\sigma_{yz}^{(1)}(x = x', y = 0) = -\int_0^{+\infty}\frac{\lambda_1 - \lambda_2}{\lambda_1 + \lambda_2}e^{-2x'\lambda_1}ds. \quad (18)$$

For $c_1 > c_2$, i.e., for $\lambda_1 < \lambda_2$, the integral in Eq. (18) is negative, and the force F_x^{gr} is positive. This means that the dislocation is repelled from the interface to the bulk of material 1, which has a larger gradient coefficient. This effect agrees with the gradient solution for the elastic energy $W = \mu b_z^2/(4\pi)\{\gamma + \ln(R/2\sqrt{c_1})\}$ of a screw dislocation [7, 8, 10], where $\gamma = 0.577\ldots$ is the Euler constant and R is the characteristic size of the solid. Obviously, the greater the value of c_1, the smaller the energy W. The curves in Fig. 5 show that $F_x^{gr}(x')$ is a short-range force that differs from zero only in the immediate vicinity of the interface. At the interface itself, the force assumes a maximum value which strongly depends on the ratio c_2/c_1 (see Fig. 5).

3.3. Mixed Gradient–Elastic Interface ($\Gamma \neq 1$, $c_1 \neq c_2$)

In this case, the gradient solution is given by relations (10)–(13), and the image force F_x assumes the form [in the units of $\mu_1 b_z^2/2\pi$

$$F_x(x) = \frac{\Gamma - 1}{\Gamma + 1}\frac{1}{2x'} - \int_0^{+\infty}\frac{\lambda_1}{\lambda_1 + \lambda_2}\left\{\frac{\lambda_1 - \lambda_2}{\lambda_1}e^{-2x'\lambda_1} + 2\frac{\Gamma - 1}{\Gamma + 1}e^{-x'(\lambda_1 + s)}\right\}ds. \quad (19)$$

It should be noted that the force F_x is not just a superposition of the forces F_x^{el} and F_x^{gr} defined by formulas (17) and (18), respectively. Nevertheless, it possesses some typical features of these forces (Fig. 6). Like F_x^{el}, the image force of Eq. (19) is a long-range nonsingular force coinciding with the classical image force away from the interface ($|x'| > 5\sqrt{c_1}$). In analogy with the force F_x^{gr}, at the interface, it assumes finite values which depend on the ratios μ_2/μ_1 and c_2/c_1. The sign and the qualitative behavior of the force F_x near the

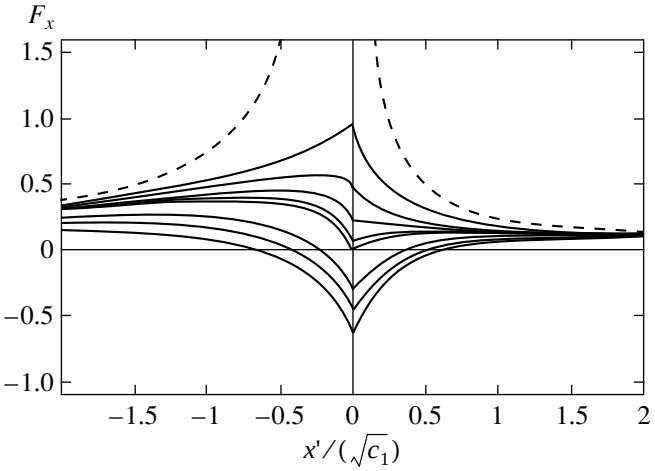

Fig. 6. Dependence of the image force F_x on the position $x'/\sqrt{c_1}$ of a dislocation at a "mixed gradient–elastic" interface ($x' = 0$) for $\mu_2 = 3\mu_1$ and $c_1/c_2 = 0.3$, 0.5, 0.7, 0.9, 1, 2, 3, and 5 (from top to bottom). The values of the force are in the units of $\mu_1 b_z^2/(2\pi\sqrt{c_1})$. The dashed curves describe the dependences for the classical solution.

interface is completely determined by the ratio of the gradient coefficients c_2/c_1. For example, for $\mu_2 > \mu_1$, three different modes of the behavior of F_x are observed (Fig. 6). If $c_2 < c_1$, $F_x > 0$ for any x' and it attains its maximum value at or near the interface. For $c_2 = c_1$, $F_x \equiv F_x^{el}$ and it vanishes at the interface (see Subsection 3.1). If $c_2 > c_1$, we have $F_x > 0$ for any x' except the small region near the interface. The size of this region, which depends on the ratio c_2/c_1, is approximately equal to $\sqrt{c_1}$, and $F_x < 0$ within this region, attaining its minimum value at the interface. Accordingly, we can single out three typical modes of the behavior of a dislocation at the interface for $\mu_2 > \mu_1$. If $c_2 < c_1$, the dislocation is expelled from material 2 into material 1 and has no equilibrium positions near the interface. For $c_2 = c_1$, the dislocation behaves similarly, but has an unstable equilibrium position at the interface. For $c_2 > c_1$, a dislocation located in material 2 is drawn towards the interface and is "trapped" near the interface in a position of stable equilibrium $x' \approx -(0.2\text{–}0.8)\sqrt{c_1}$. In turn, a dislocation located in material 1 has a position of unstable equilibrium $x' \approx (0.4\text{–}0.7)\sqrt{c_1}$ near the interface. It is attracted to it within a small region $x' < (0.4\text{–}0.7)\sqrt{c_1}$ and repelled from it outside this region.

4. Thus, we have obtained a solution of the boundary-value problem on a rectilinear screw dislocation parallel to the planar interface between two elastic isotropic media with different elastic constants and different gradient coefficients in the gradient theory of elasticity with the basic relation (1). The elastic stress field of the dislocation and the image force exerted on it by the interface are presented in a general integral form. It is shown that both components of the stress field have no singularities on the dislocation line and remain continuous at the interface in contrast to the classical solution [22] having a singularity on the dislocation line and permitting a jump in one of the two components at the interface. The gradient and the classical solution coincide away from the interface and from the dislocation line (at distances much greater than $10\sqrt{c_1}$). The continuity of stresses at the interface made it possible to eliminate the classical singularity [22] of the image force for a dislocation emerging at the interface. An additional elastic image force that emerges due to the difference in the gradient coefficients of the contacting phases is also determined. It is shown that this force, which has a short range and attains its maximum value at the interface, expels a screw dislocation to the material with a larger gradient coefficient. In the general case, when the shear moduli μ_1 and the gradient coefficients c_i for the contacting phases are different, the overall image force may act differently at the interface, depending on the ratios μ_2/μ_1 and c_2/c_1, although its long-range component remains the same as in the classical theory of elasticity.

ACKNOWLEDGMENTS

This research was carried out within the framework of the INTAS (grant no. INTAS-93-3213-Ext) and TMR (contract no. ERBFMRX CT 960062) programs, as well as under partial support of the Scientific Council of the Russian Ministry of Science and Technology program "Physics of Solid-State Nanostructures" (grant no. 97-3006).

REFERENCES

1. J. D. Eshelby, in *Dislocations in Solids*, ed. by F. R. N. Nabarro (North-Holland, Amsterdam, 1979), Vol. 1, p. 167.
2. M. Yu. Gutkin and A. E. Romanov, Phys. Status Solidi A **125** (1), 107 (1991).
3. R. Bonnet, Phys. Rev. B **53** (16), 10978 (1996).
4. A. E. Romanov, in *Nanostructured Materials: Science and Technology*, ed. by G. M. Chow and N. I. Noskova (Kluwer, Dordrecht, 1998), p. 207.
5. M. Yu. Gutkin and E. C. Aifantis, Scr. Mater. **35** (11), 1353 (1996).
6. M. Yu. Gutkin and E. C. Aifantis, Scr. Mater. **36** (1), 129 (1997).
7. M. Yu. Gutkin and E. C. Aifantis, Scr. Mater. **40** (5), 559 (1999).
8. M. Yu. Gutkin and E. C. Aifantis, Phys. Status Solidi B **214** (2), 245 (1999).
9. M. Yu. Gutkin and E. C. Aĭfantis, Fiz. Tverd. Tela (St. Petersburg) **41** (12), 2158 (1999) [Phys. Solid State **41**, 1980 (1999)].
10. M. Yu. Gutkin and A. E. Aifantis, in *Nanostructured Films and Coatings*, NATO ARW Series, High Technology, Vol. 78, ed. by G.-M. Chow, I. A. Ovid'ko, and T. Tsakalakos (Kluwer, Dordrecht, 2000), p. 247.
11. B. S. Altan and E. C. Aifantis, Scr. Metall. Mater. **26** (2), 319 (1992).
12. C. Q. Ru and E. C. Aifantis, Acta Mech. **101** (1), 59 (1993).
13. E. C. Aifantis, J. Mech. Behav. Mater. **5** (3), 355 (1994).
14. D. J. Unger and E. C. Aifantis, Int. J. Fract. **71**, R27 (1995).
15. B. S. Altan and E. C. Aifantis, J. Mech. Behav. Mater. **8** (3), 231 (1997).
16. C. Q. Ru and E. C. Aifantis, Preprint MTY Report (Houghton, MI, 1993).
17. W. W. Milligan, S. A. Hackney, and E. C. Aifantis, in *Continuum Models for Materials with Microstructure*, ed. by H. Mühlhaus (Wiley, New York, 1995), p. 379.
18. J. P. Hirth and J. Lothe, *Theory of Dislocations* (McGraw-Hill, New York, 1967; Atomizdat, Moscow, 1972).
19. A. C. Eringen, J. Phys. D: Appl. Phys. **10**, 671 (1977).
20. A. C. Eringen, J. Appl. Phys. **54** (9), 4703 (1983).
21. A. C. Eringen, in *The Mechanics of Dislocations*, ed. by E. C. Aifantis and J. P. Hirth (American Society for Metals, Metals Park, 1985), p. 101.
22. T. Mura, in *Advances in Materials Research*, ed. by H. Herman (Interscience, New York, 1968), Vol. 3, p. 1.

Translated by N. Wadhwa

Physics of the Solid State, Vol. 42, No. 9, 2000, pp. 1659–1667. Translated from Fizika Tverdogo Tela, Vol. 42, No. 9, 2000, pp. 1613–1620.

DEFECTS, DISLOCATIONS, AND PHYSICS OF STRENGTH

Edge Dislocations near Phase Boundaries in the Gradient Theory of Elasticity

K. N. Mikaelyan*, M. Yu. Gutkin*, and E. C. Aifantis**

**Institute of Problems in Machine Science, Russian Academy of Sciences, Vasil'evskiĭ ostrov, Bol'shoi pr. 61, St. Petersburg, 199178 Russia*
e-mail: gutkin@def.ipme.ru
***Aristotle University of Thessaloniki, Thessaloniki 54006, Greece*
Michigan Technological University, Houghton, MI 49931, USA
Received February 25, 2000; in final form, March 6, 2000

Abstract—A solution of the boundary-value problem in the gradient theory of elasticity concerning a rectilinear edge dislocation parallel to the interface between phases with different elastic moduli and gradient coefficients is obtained. The interaction between the dislocation and the interface is considered on a nanoscopic level. It is shown that the stress field has no singularities on the dislocation line and remains continuous at the interface, unlike the classical solution, which is singular at the dislocation line and allows a discontinuity of two stress components at the interface. The gradient solution also removes the classical singularity of the image force for the dislocation on the interface. An additional elastic image force associated with the difference in the gradient coefficients of contacting phases is also determined. It is found that this force, which has a short range and a maximum at the interface, expels the edge dislocation into the material with a smaller gradient coefficient.

1. In our previous publication [1], we analyzed the behavior of a rectilinear screw dislocation at the interface by using a version of the gradient theory of elasticity proposed earlier for an analysis of asymptotic elastic fields at the mouth of an antiplanar shear crack and on a screw dislocation line [2, 3]. The basic equation in the gradient theory has the form

$$(1 - c_1\nabla^2)\sigma = (1 - c_2\nabla^2)[\lambda(\mathrm{tr}\boldsymbol{\varepsilon})\mathbf{I} + 2\mu\boldsymbol{\varepsilon}], \quad (1)$$

where λ and μ are Lamé elastic constants, σ and $\boldsymbol{\varepsilon}$ are the tensors of elastic stresses and strains, $\mathbf{I}$ is a unit tensor, ∇^2 denotes the Laplacian, and c_1 and c_2 are two different gradient coefficients. This theory is a generalization of the special theory of gradient elasticity with $c_1 \equiv 0$ and $c_2 \equiv c$ proposed in [4] and subsequently used for eliminating singularities in the fields of displacements and strains at the mouths of cracks [4–8] and on dislocation lines [9–11], as well as in the deformation fields on disclination lines [11]. Solving the same problems on the basis of the relation (1) also enabled us to get rid of singularities in the fields of elastic stresses of cracks [2], dislocations [2, 12, 13], and disclinations [13, 14].

For example, the field of stresses for a rectilinear edge dislocation whose line coincides with the z axis and whose Burgers vector b_x is directed along the x axis of the Cartesian reference frame can be presented (in the units of $\mu b_x/[2\pi(1-\nu)]$) in the form [12, 13]

$$\sigma_{xx} = -y(r^2 + 2x^2)/r^4 + 2y[y^2\Phi_1 + (3x^2 - y^2)\Phi_2], \quad (2)$$

$$\sigma_{yy} = -y(r^2 - 2x^2)/r^4 + 2y[x^2\Phi_1 - (3x^2 - y^2)\Phi_2], \quad (3)$$

$$\sigma_{xy} = x(r^2 - 2y^2)/r^4 + 2x[y^2\Phi_1 + (x^2 - 3y^2)\Phi_2], \quad (4)$$

$$\sigma_{zz} = \nu(\sigma_{xx} + \sigma_{yy}), \quad (5)$$

where ν is the Poisson ratio, $r^2 = x^2 + y^2$, $\Phi_1 = K_1(r/\sqrt{c_1})/(\sqrt{c_1}\,r^3)$, $\Phi_2 = [2c_1/r^2 - K_2(r/\sqrt{c_1})]/r^4$, and $K_n(r/\sqrt{c_1})$ is an nth-order modified Bessel function of the second type (a MacDonald function), $n = 0, 1, \ldots$. The first terms in Eqs. (2)–(4) are the classic solution [15], while the remaining terms are additional gradient terms. Such a division of the total solution into the classical and gradient components corresponds to the Ru–Aifantis theorem [5], which proved that the solution of the boundary-value problem in the gradient theory of elasticity can be written as the sum of the classical solution of the same boundary-value problem and additional gradient terms defined by the solution of the corresponding Helmholtz equation. It should be noted that the field of stresses of Eqs. (2)–(5) was obtained in an explicit analytic form, in contrast to the analogous solution in the Eringen nonlocal theory of elasticity [16], which is presented exclusively in the integral form. For $r \longrightarrow 0$, we have $K_1(r/\sqrt{c_1}) \longrightarrow \sqrt{c_1}/r$, $K_2(r/\sqrt{c_1}) \longrightarrow 2c_1/r^2 - 1/2$, and $\sigma_{ij} \longrightarrow 0$ ($i, j = x, y$). It was proved in [12] that the stresses of Eqs. (2)–(5) attain their peak

values ($|\sigma_{xx}| \approx 0.45\mu$ and $|\sigma_{yy}| \approx |\sigma_{xy}| \approx 0.27\mu$ for $b_x = a = 4\sqrt{c_1}$ and $\nu = 0.3$) at distances $\approx a/4$ (where a is the lattice constant) from the dislocation line. Beyond the limits of the dislocation core ($r \geq r_0 \approx 4\sqrt{c_k}$ [10]), the gradient solution coincides with the classical solution.

Taking advantage of the possibility of eliminating singularities from the stress fields of defects [12–14] by using the gradient theory of elasticity with the basic relation (1), we analyzed the behavior of dislocations at the interface. In [1], we used relation (1) to solve the problem on a rectilinear screw dislocation near a planar interface between elastically isotropic media with different elastic constants and gradient coefficients. We obtained the gradient solutions for the stress field of the dislocation and the force of its interaction with the interface (image force) in integral form. It was proved that neither one of the components of the stress field has singularities at the dislocation line, and they remain continuous at the interface, unlike the classical solution [17], which has a singularity on the dislocation line and permits a jump of one of the components at the interface. Away from the boundary and from the dislocation line (at distances $\gg 10\sqrt{c_1}$), the gradient and classical solutions coincided. The continuity of stresses at the interface led to the removal of the classical singularity [17] of the image force on the emergence of a dislocation at the interface. Also, we obtained an additional elastic image force associated with the difference in the gradient coefficients of the phases in contact. It was found that this force, which has a short range and a maximum at the interface, expels a screw dislocation to the material with a larger gradient coefficient. In the general case, when the elastic moduli μ_i and the gradient coefficients c_i of the contacting phases were different (we used the simplified notation $c_{1i} \equiv c_i$, where the index $i = 1, 2$ indicates phase 1 or 2), the overall image force demonstrated different behavior at the interface, depending on the ratio μ_2/μ_1 and c_2/c_1, although its long-range component remained the same as in the classical theory of elasticity.

In the present work, we consider a similar problem for an edge dislocation. The integral form of gradient solutions is obtained for the field of elastic stresses of the dislocation and for the image force acting on it. The behavior of the dislocation at the interface is considered in detail.

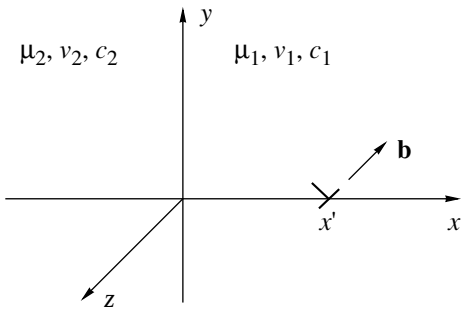

Fig. 1. Edge dislocation at a planar interface.

2. Let us consider the plane interface between two elastic isotropic media 1 ($x > 0$) and 2 ($x < 0$) with shear moduli μ_i, the Poisson ratios ν_i, and the gradient coefficients c_{1i} and c_{2i}, where $i = 1, 2$, respectively (Fig. 1). Let us suppose that the line of a rectilinear edge dislocation with the Burgers vector $\mathbf{b} = b_x\mathbf{e}_x + b_y\mathbf{e}_y$ passes through the point ($x = x'$, $y = 0$) parallel to the z axis of the Cartesian system of coordinates.

2.1. Classical Solution

In the classical theory of elasticity ($c_{1i} = c_{2i} \equiv 0$) for $x' \geq 0$, the stress field of dislocations is determined (in the units of $\mu_1/[\pi(k_1 + 1)]$) by the expressions [17]

$$\sigma_{xx}^{0(1)} = b_x\left\{-\frac{2y}{r_-^2} - \frac{4yx_-^2}{r_-^4} + \frac{(A+B)y}{r_+^2} + \frac{4Ay(x'^2 + x^2)}{r_+^4} + \frac{32Ayxx'x_+^2}{r_+^6}\right\} + b_y\left\{-\frac{2x_-}{r_-^2} + \frac{4x_-^3}{r_-^4} + \frac{(A+B)x - (3A-B)x'}{r_+^2} + \frac{4Ax_+(x'^2 - 6x'x - x^2)}{r_+^4} + \frac{32Axx'x_+^3}{r_+^6}\right\}, \quad (6)$$

$$\sigma_{yy}^{0(1)} = b_x\left\{-\frac{2y}{r_-^2} + \frac{4yx_-^2}{r_-^4} + \frac{(3A-B)y}{r_+^2} + \frac{4Ay(3x'^2 + 4x'x - x^2)}{r_+^4} - \frac{32Ayxx'x_+^2}{r_+^6}\right\} + b_y\left\{\frac{6x_-}{r_-^2} - \frac{4x^3}{r_-^4} - \frac{(5A+B)x + (9A+B)x'}{r_+^2} + \frac{4Ax_+(3x'^2 + 10x'x + x^2)}{r_+^4} - \frac{32Axx'x_+^3}{r_+^6}\right\}, \quad (7)$$

$$\sigma_{xy}^{0(1)} = b_x\left\{-\frac{2x_-}{r_-^2} - \frac{4x_-^3}{r_-^4} + \frac{(3A-B)x - (A+B)x'}{r_+^2}\right.$$

$$+\frac{4Ax_+(x'^2+6x'x-x^2)}{r_+^4}-\frac{32Axx'x_+^3}{r_+^6}\Bigg\}$$

$$+b_y\Bigg\{-\frac{2y}{r_-^2}+\frac{4yx_-^2}{r_-^4}+\frac{(A+B)y}{r_+^2}$$

$$-\frac{4Ay(x'^2+4x'x+x^2)}{r_+^4}+\frac{32Ayxx'x_+^2}{r_+^6}\Bigg\}, \quad (8)$$

$$\sigma_{zz}^{0(1)} = \nu_1(\sigma_{xx}^{0(1)}+\sigma_{yy}^{0(1)}) \quad (9)$$

for medium 1 and by the expressions

$$\sigma_{xx}^{0(2)} = b_x\Bigg\{\frac{(A+B-2)y}{r_-^2}-\frac{4yx_-[(1-B)x-(1-A)x']}{r_-^4}\Bigg\}$$

$$+b_y\Bigg\{\frac{(A+B-2)x+(B-3A+2)x'}{r_-^2} \quad (10)$$

$$+\frac{4x_-^2[(1-B)x-(1-A)x']}{r_-^4}\Bigg\},$$

$$\sigma_{yy}^{0(2)} = b_x$$

$$\times\Bigg\{\frac{(3B-A-2)y}{r_-^2}+\frac{4yx_-[(1-B)x-(1-A)x']}{r_-^4}\Bigg\}$$

$$+b_y\Bigg\{\frac{(6-5B-A)x+3(B+A-2)x'}{r_-^2} \quad (11)$$

$$-\frac{4x_-^2[(1-B)x-(1-A)x']}{r_-^4}\Bigg\},$$

$$\sigma_{xy}^{0(2)} = b_x\Bigg\{\frac{(3B-A-2)x+(2-A-B)x'}{r_-^2}$$

$$+\frac{4x_-^2[(1-B)x-(1-A)x']}{r_-^4}\Bigg\}+b_y\Bigg\{\frac{(A+B-2)y}{r_-^2} \quad (12)$$

$$+\frac{4yx_-[(1-B)x-(1-x)x']}{r_-^4}\Bigg\},$$

$$\sigma_{zz}^{0(2)} = \nu_2(\sigma_{xx}^{0(2)}+\sigma_{yy}^{0(2)}) \quad (13)$$

for medium 2, where $x_\pm = x \pm x'$, $r_\pm^2 = x_\pm^2 + y^2$, $A = (1-\Gamma)/(1+k_1\Gamma)$, $B = (k_2 - k_1\Gamma)/(k_2+\Gamma)$, $\Gamma = \mu_2/\mu_1$, $k_i = 3 - 4\nu_i$, $i = 1, 2$.

It can easily be verified that the components σ_{xx}^0 and σ_{xy}^0 are continuous at the interface ($x = 0$), while the components σ_{yy}^0 and σ_{zz}^0 experience jumps $[\sigma_{kl}^0] = \sigma_{kl}^{0(1)} - \sigma_{kl}^{0(2)}$ in this region, which are given by

$$[\sigma_{yy}^0]_{x=0} = \frac{(A-B)b_xy-(3A+B)b_yx'}{x'^2+y^2}+\frac{4A(b_xy+b_yx')x'^2}{(x'^2+y^2)^2}, \quad (14)$$

$$[\sigma_{zz}^0]_{x=0} = \frac{\nu_1[(A-1)b_xy-(3A+1)b_yx']-\nu_2(B-1)(b_xy+b_yx')}{x'^2+y^2}+\frac{4\nu_1A(b_xy+b_yx')x'^2-2\nu_2(A-1)b_yx'^3}{(x'^2+y^2)^2} \quad (15)$$

(in the units of $\mu_1/[\pi(1-\nu_1)]$). It was discussed in detail in [1] that, in the classical theory of elasticity, such jumps are quite natural from macroscopic point of view, but cannot be explained by nanoscopic analysis. They are just consequences of the approximation of the classical model of a continuous medium, whose properties often differ from reality in describing nanoscopic phenomena.

2.2. Gradient Solution

Let us now consider the same problem in the gradient theory of elasticity with the basic relation (1). It was proposed in [2] and also mentioned in [1, 12–14] that the solution of Eq. (1) boils down to the independent solution of the following nonhomogeneous Helmholtz equations for the fields of stresses σ and strains $\boldsymbol{\varepsilon}$:

$$(1-c_1\nabla^2)\boldsymbol{\sigma} = \boldsymbol{\sigma}^0, \quad (1-c_2\nabla^2)\boldsymbol{\varepsilon} = \boldsymbol{\varepsilon}^0, \quad (16)$$

where the fields of stresses $\boldsymbol{\sigma}^0$ and strains $\boldsymbol{\varepsilon}^0$ are solutions of the same boundary-value problem in the classical theory of elasticity. We will consider here only the solution of the first of Eqs. (16) for the field of stresses, since it is most interesting for various applications.

Equation (16) can be solved by the Fourier integral transformation method [1, 10–14]. We first write this equation in the form

$$(1-c_{1i}\nabla^2)\boldsymbol{\sigma}^{(i)} = \boldsymbol{\sigma}^{0(i)}, \quad (17)$$

where $\boldsymbol{\sigma}^{0(i)}$ are defined by the equalities (6)–(13). For the sake of simplicity, we omit the first index "1" in the notation of the gradient coefficients c_{1i}, so that c_1 now belongs to material 1 and c_2, to material 2. On the basis of the conclusions drawn in Sec. 2.1, as well as the results obtained in [2, 5], we use the classical boundary conditions

$$[\sigma_{xx}]_{x=0} = [\sigma_{xy}]_{x=0} = 0 \tag{18}$$

and six additional boundary conditions

$$[\sigma_{yy}]_{x=0} = [\sigma_{zz}]_{x=0} = \left[\frac{\partial\sigma_{xx}}{\partial x}\right]_{x=0} = \left[\frac{\partial\sigma_{yy}}{\partial x}\right]_{x=0} = \left[\frac{\partial\sigma_{xy}}{\partial x}\right]_{x=0} = \left[\frac{\partial\sigma_{zz}}{\partial x}\right]_{x=0} = 0. \tag{19}$$

The last four of Eqs. (19) ensure a smooth variation of all components of the stress field upon a transition through the boundary in analogy with [1].

Omitting cumbersome intermediate calculations, we give only the final results here. The gradient solution can be presented as the sum $\sigma_{kl}^{(i)} = \sigma_{kl}^{0(i)} + \sigma_{kl}^{gr(i)}$, where the classical solution $\sigma_{kl}^{0(i)}$ is defined by expressions (6)–(13), while the additional gradient terms $\sigma_{kl}^{gr(i)}$ can be presented (in the units of $\mu_1/[\pi(k_1+1)]$) in the form

$$\begin{aligned}
\sigma_{xx}^{gr(1)} &= 4b_x\Big\{y^3\Phi_1(r_-) + y(3x_-^2 - y^2)\Phi_2(r_-) \\
&\quad - \frac{2Ac_1y}{r_+^6}\left[3x_+^2 - y^2 + 24x'x_+\frac{x_+^2 - y^2}{r_+^2}\right] \\
&\quad + \int_0^\infty \frac{s^2\sin(sy)}{\lambda_1+\lambda_2}e^{-x\lambda_1}\Big[c_1s\frac{\lambda_2-\lambda_1}{\lambda_1}e^{-x'\lambda_1} \\
&\quad + \{Ac_1(\lambda_2+s)(1+2x's) - c'(\lambda_2-s)\}e^{-x's}\Big]ds\Big\} \\
&\quad + 4b_y\Big\{-x_-y^2\Phi_1(r_-) - x_-(x_-^2 - 3y^2)\Phi_2(r_-) \\
&\quad + \frac{2Ac_1}{r_+^6}\left[x_+(x_+^2 - 3y^2) - 6x'\frac{x_+^4 - 6x_+^2y^2 + y^4}{r_+^2}\right] \\
&\quad + \int_0^\infty \frac{s^2\cos(sy)}{\lambda_1+\lambda_2}e^{-x\lambda_1}[c_1(\lambda_2-\lambda_1)e^{-x'\lambda_1}
\end{aligned} \tag{20}$$

$$\begin{aligned}
&\quad - \{Ac_1(\lambda_2+s)(1-2x's) + c'(\lambda_2-s)\}e^{-x's}]ds\Big\}, \\
\sigma_{yy}^{gr(1)} &= 4b_x\Big\{x_-^3y\Phi_1(r_-) - y(3x_-^2 - y^2)\Phi_2(r_-) \\
&\quad + \frac{2Ac_1y}{r_+^6}\left[3x_+^2 - y^2 + 24x'x_+\frac{x_+^2 - y^2}{r_+^2}\right] \\
&\quad - \int_0^\infty \frac{\lambda_1^2\sin(sy)}{\lambda_1+\lambda_2}e^{-x\lambda_1}\Big[c_1s\frac{\lambda_2-\lambda_1}{\lambda_1}e^{-x'\lambda_1} \\
&\quad + \{Ac_1(\lambda_2+s)(1+2x's) - c''(\lambda_2-s)\}e^{-x's}\Big]ds\Big\} \\
&\quad + 4b_y\Big\{-x_-^3\Phi_1(r_-) + x_-(x_-^2 - 3y^2)\Phi_2(r_-) \\
&\quad - \frac{2Ac_1}{r_+^6}\left[x_+(x_+^2 - 3y^2) - 6x'\frac{x_+^4 - 6x_+^2y^2 + y^4}{r_+^2}\right] \\
&\quad - \int_0^\infty \frac{\lambda_1^2\cos(sy)}{\lambda_1+\lambda_2}e^{-x\lambda_1}[c_1(\lambda_2-\lambda_1)e^{-x'\lambda_1} \\
&\quad - \{Ac_1(\lambda_2+s)(1-2x's) \\
&\quad + (B + c's^2)(\lambda_2-s)/\lambda_1^2\}e^{-x's}]ds\Big\},
\end{aligned} \tag{21}$$

$$\begin{aligned}
\sigma_{xy}^{gr(1)} &= 4b_x\Big\{-x_-y^2\Phi_1(r_-) - x_-(x_-^2 - 3y^2)\Phi_2(r_-) \\
&\quad + \frac{2Ac_1}{r_+^6}\left[x_+(x_+^2 - 3y^2) + 6x'\frac{x_+^4 - 6x_+^2y^2 + y^2}{r_+^2}\right] \\
&\quad + \int_0^\infty \frac{s\cos(sy)}{\lambda_1+\lambda_2}e^{-x\lambda_1}[c_1s(\lambda_2-\lambda_1)e^{-x'\lambda_1} \\
&\quad + \{B - Ac_1(\lambda_1^2 + \lambda_2 s)(1+2x's) - c's(\lambda_2-s)\}e^{-x's}]ds\Big\} \\
&\quad + 4b_y\Big\{x_-^2y\Phi_1(r_-) - y(3x_-^2 - y^2)\Phi_2(r_-)
\end{aligned} \tag{22}$$

$$+\frac{2Ac_1y}{r_+^6}\left[3x_+^2-y^2-24x'x_+\frac{x_+^2-y^2}{r_+^2}\right]$$

$$-\int_0^\infty\frac{s\sin(sy)}{\lambda_1+\lambda_2}e^{-x'\lambda_1}[c_1\lambda_1(\lambda_1-\lambda_1)e^{-x'\lambda_1}$$

$$+\{B+Ac_1(\lambda_1^2+\lambda_2 s)(1-2x's)-c's(\lambda_2-s)\}e^{-x's}]ds\Bigg\},$$

$$\sigma_{zz}^{gr(1)} = 4\nu_1\Bigg\{(b_xy-b_yx_-)r_-^2\Phi_1(r_-)$$

$$-b_x\int_0^\infty\frac{\sin(sy)}{\lambda_1+\lambda_2}e^{-x\lambda_1}\Bigg[s\frac{\lambda_2-\lambda_1}{\lambda_1}e^{-x'\lambda_1}+\{A(\lambda_2+s)(1+2x's)$$

$$-[(B-1)\nu_2/\nu_1+1](\lambda_2-s)\}e^{-x's}\Bigg]ds$$

$$-b_y\int_0^\infty\frac{\cos(sy)}{\lambda_1+\lambda_2}e^{-x\lambda_1}[(\lambda_2-\lambda_1)e^{-x'\lambda_1}$$

$$-\{A[s+\lambda_2(1-2x's)]$$

$$+[(B-1)\nu_2/\nu_1+1](\lambda_2-s)\}e^{-x's}]ds\Bigg\} \quad (23)$$

for medium 1 and

$$\sigma_{xx}^{gr(2)} = 8(B-1)c_2\{-b_xy(3x_-^2-y^2)$$

$$+b_yx_-(x_-^2-3y^2)\}/r_-^6$$

$$-4b_x\int_0^\infty\frac{s^2\sin(sy)}{\lambda_1+\lambda_2}e^{x\lambda_2}[2c_1se^{-x'\lambda_1}$$

$$+\{Ac_1(\lambda_1-s)(1+2x's)-c'(\lambda_1+s)\}e^{-x's}]ds$$

$$-4b_y\int_0^\infty\frac{s^2\cos(sy)}{\lambda_1+\lambda_2}e^{x\lambda_2}[2c_1\lambda_1e^{-x\lambda_1}$$

$$-\{Ac_1(\lambda_1-s)(1-2x's)+c'(\lambda_1+s)\}e^{-x's}]ds,$$

$$\sigma_{yy}^{gr(2)} = 8(B-1)c_2\{b_xy(3x_-^2-y^2)$$

$$-b_yx_-(x_-^2-3y^2)\}/r_-^6$$

$$+4b_x\int_0^\infty\frac{\lambda_1^2\sin(sy)}{\lambda_1+\lambda_2}e^{x\lambda_2}[2c_1se^{-x'\lambda_1}$$

$$+\{Ac_1(\lambda_1-s)(1+2x's)-c''(\lambda_1+s)\}e^{-x's}]ds \quad (25)$$

$$+4b_y\int_0^\infty\frac{\lambda_1^2\cos(sy)}{\lambda_1+\lambda_2}e^{x\lambda_2}[2c_1\lambda_1e^{-x\lambda_1}$$

$$-\{Ac_1(\lambda_1-s)(1-2x's)$$

$$+(B+c's^2)(\lambda_1+s)/\lambda_1^2\}e^{-x's}]ds,$$

$$\sigma_{xy}^{gr(2)} = 8(B-1)c_2\{b_xx_-(x_-^2-3y^2)$$

$$+b_yy(3x_-^2-y^2)\}/r_-^6$$

$$+4b_x\int_0^\infty\frac{s\cos(sy)}{\lambda_1+\lambda_2}e^{x\lambda_2}[-2c_1\lambda_1se^{-x'\lambda_1}$$

$$+\{B-Ac_1\lambda_1(\lambda_1-s)(1+2x's)+c's(\lambda_1+s)\}e^{-x's}]ds \quad (26)$$

$$+4b_y\int_0^\infty\frac{s\sin(sy)}{\lambda_1+\lambda_2}e^{x\lambda_2}[2c_1\lambda_1^2e^{-x'\lambda_1}$$

$$-\{B+Ac_1\lambda_1(\lambda_1-s)(1-2x's)+c's(\lambda_1+s)\}e^{-x's}]ds,$$

$$\sigma_{zz}^{gr(2)} = 4b_x\nu_1\int_0^\infty\frac{\sin(sy)}{\lambda_1+\lambda_2}e^{x\lambda_2}[2se^{-x'\lambda_1}$$

$$+\{A(\lambda_1-s)(1+2x's)$$

$$-[(B-1)\nu_2/\nu_1+1](\lambda_1+s)\}e^{-x's}]ds$$

$$+4b_y\nu_1\int_0^\infty\frac{\cos(sy)}{\lambda_1+\lambda_2}e^{x\lambda_2}[2\lambda_1e^{-x'\lambda_1}$$

$$+\{A[s-\lambda_1(1-2x's)]$$

$$-[(B-1)\nu_2/\nu_1+1](\lambda_1+s)\}e^{-x's}]ds \quad (27)$$

for medium 2, where the functions $\Phi_j(r_-)$ are defined in the remarks to formulas (2)–(4), $c' = c_1 + c_2(B-1)$, $c'' = c_1 + c_2(B-1)\lambda_2^2/\lambda_1^2$, and $\lambda_i = \sqrt{1/(c_i+s^2)}$, $i = 1, 2$.

The stress field components $\sigma_{kl}^{(i)}$ obtained in the form of a superposition of classical expressions (6)–(13) and the additional gradient components (20)–(27) are continuous at the interface ($x = 0$). For $\mu_1 = \mu_2 = \mu$, $\nu_1 = \nu_2 = \nu$, and $c_1 = c_2 = c$ (the limiting transition to the case of a homogeneous medium), these expressions are transformed into Eqs. (2)–(5). As $c_1 = c_2 \longrightarrow 0$ (the limiting transition to the classical theory of elasticity), the additional gradient components in Eqs. (20)–(27) vanish. It should be noted that, as in the case of a screw dislocation [1], expressions (20)–(27) contain specific terms that are due only to the difference in the gradient

coefficients c_1 and c_2 (e.g., the first terms in the integrand).

3. Let us consider separately the following three typical situations: a purely elastic interface ($\mu_1 \neq \mu_2$, $\nu_1 \neq \nu_2$, $c_1 = c_2 = c$), a purely gradient interface ($\mu_1 = \mu_2$, $\nu_1 = \nu_2$, $c_1 \neq c_2$), and a general mixed gradient–elastic interface ($\mu_1 \neq \mu_2$, $\nu_1 \neq \nu_2$, $c_1 \neq c_2$).

3.1. Purely Elastic Interface ($\mu_1 \neq \mu_2$, $\nu_1 \neq \nu_2$, $c_1 = c_2 = c$)

In this case, we consider only the effects associated with the difference in the elastic constants of contacting media. Two big advantages in the gradient theory of elasticity over the classical theory are worth noting here: first, the absence of singularities in the stress fields $\sigma_{kl}^{(i)}$ on the dislocation line, and second, the absence of nonphysical jumps in the stresses $\sigma_{yy}^{(i)}$ and $\sigma_{zz}^{(i)}$ of the type of Eqs. (14), (15) at the interface. This allows us to consider nanoscopic short-range elastic interactions between dislocations and phase boundaries, which is impossible in the classical theory of elasticity leading to the singular solution of Eqs. (6)–(13) with the components $\sigma_{yy}^{0(i)}$ and $\sigma_{zz}^{0(i)}$ discontinuous at the interface. Figure 2 shows, by way of an example, the distribution of the stress field $\sigma_{yy}^{(i)}(x, 0)$ of a dislocation with the Burgers vector b_y near the interface. It can be seen that the classical and gradient solutions coincide away from the boundary ($r > 10\sqrt{c}$) and from the dislocation line, but these solutions are quite different in their vicinity (in the nanoscopic region $r < 10\sqrt{c}$).

Let us now consider the image force F_x^{el} exerted per unit length of a dislocation by the interface (see Fig. 1). For the dislocation with the Burgers vector b_x, the gradient solution $F_x^{\text{el}}(x') = b_x\sigma_{xy}^{(1)}(x = x', 0)$ (in the units of $\mu_1 b_x^2/[\pi(k_1 + 1)]$) has the form

$$F_x^{\text{el}}(x') = -\frac{A+B}{2x'} + \frac{4Ac}{x'^3} + 2c\int_0^{+\infty} s[B(\lambda - s) - A(\lambda + s)(1 + 2x's)]e^{-x'(\lambda+s)}ds, \quad (28)$$

where $\lambda = \sqrt{1/c + s^2}$. The first term in Eq. (28) is a classical singular solution [17], while the remaining are additional gradient terms. The results of a numerical analysis of Eq. (28) are presented in Fig. 3, which also shows analogous solutions for a dislocation in medium 2 ($x' < 0$). It can be seen that the gradient solution has lost the classical singularity and that it is continuous at

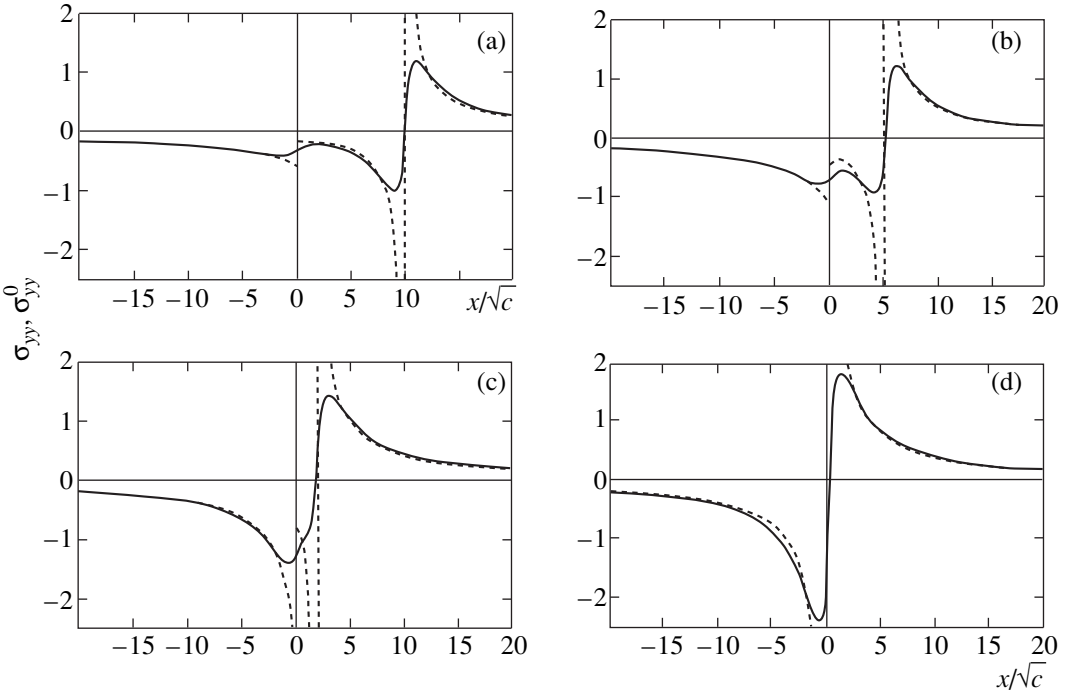

Fig. 2. Distribution of the stress component $\sigma_{xy}(x, y = 0)$ near the edge dislocation line with the Burgers vector b_y, located at a distance $x'/\sqrt{c} = 10$ (a), 5 (b), 2 (c), and 0 (d) from the interface ($x = 0$) for $\mu_2 = 10\mu_1$, $\nu_1 = \nu_2 = 0.3$, and $c_1 = c_2 = c$. The stresses are given in the units of $\mu_1 b_y/[\pi(k_1 + 1)\sqrt{c}]$. The dashed curves describe distributions for the classical solution σ_{yy}^0.

the interface and attains its maximum value at a distance $\approx\sqrt{c}$ from it.

In the special case of a free surface ($\mu_2 = \nu_2 = 0$; see the curves in Fig. 3 in the region of negative values of F_x^{el}), the image force vanishes at the interface. This force emerges and grows as the dislocation core penetrates the material (the core radius naturally emerges in the gradient theory of elasticity and is estimated as $\approx 4\sqrt{c}$ [9, 10]), attains its maximum value, and then decreases as the dislocation moves from the free surface to the bulk of the material. This last stage (for $x' > 5\sqrt{c}$) is correctly described by a classical solution (see Fig. 3) which, however, cannot describe the previous stages. Using the gradient solution of Eq. (28), we can estimate the maximum cleavage stress $\tau_{max} = |F_x^{el}|_{max}/b_x$, which must be overcome by an edge dislocation penetrating the material. The curve in Fig. 3 leads to the estimate $\tau_{max} \approx \mu/2.8\pi$ (for $\nu = 0.3$), i.e., the value of the order of the theoretical shear strength [15].

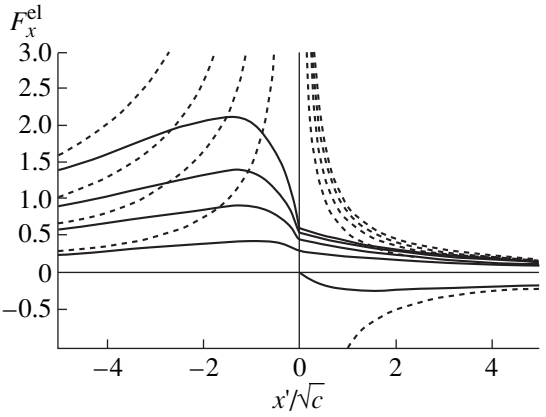

Fig. 3. Dependence of the image force F_x^{el} on the position $x'/\sqrt{c}$ of an edge dislocation with the Burgers vector b_x at a "purely elastic" interface ($x' = 0$) for $c_1 = c_2 = c$, $\nu_1 = \nu_2 = 0.3$, and $\mu_2/\mu_1 = 10$, 7, 5, 3, and 0 (from top to bottom). The values of force are in the units of $\mu_1 b_x^2/[\pi(k_1 + 1)\sqrt{c}]$. The dashed curves describe the dependences for the classical solution.

3.2. Purely Gradient Interface ($\mu_1 = \mu_2$, $\nu_1 = \nu_2$, $c_1 \neq c_2$)

In this case, we only consider the effects associated with the difference in the gradient coefficients of contacting media. We confine our analysis to the image force F_x^{gr} exerted on a dislocation by the interface due to the difference c_1 and c_2. For a dislocation with the Burgers vector b_x, this force is defined (in the units of $\mu_1 b_x^2/[\pi(k_1 + 1)]$) as

$$F_x^{gr}(x') = 4\int_0^{+\infty} \frac{s^2}{\lambda_1 + \lambda_2}\{c_1(\lambda_2 - \lambda_1)e^{-2x'\lambda_1} + (c_2 - c_1)(\lambda_2 - s)e^{-x'(\lambda_1 + s)}\}ds. \quad (29)$$

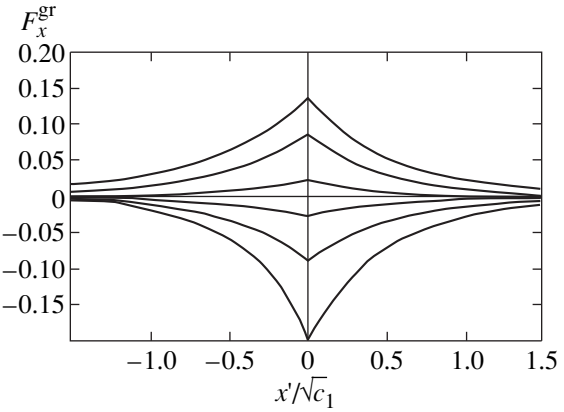

Fig. 4. Dependence of the image force F_x^{gr} on the position $x'/\sqrt{c}$ of an edge dislocation with the Burgers vector b_x at a "purely gradient" interface ($x' = 0$) for $\mu_2 = \mu_1$, $\nu_1 = \nu_2 = 0.3$, and $c_2/c_1 = 2$, 1.5, 1.1, 0.9, 0.7, and 0.5 (from top to bottom). The values of force are in the units of $\mu_1 b_x^2/[\pi(k_1 + 1)\sqrt{c_1}]$.

A numerical analysis of this integral proved that F_x^{gr} is positive for $c_2 > c_1$ and negative for $c_2 < c_1$ (Fig. 4). This means that the edge dislocation is repelled by the interface to the bulk of the material with a smaller gradient coefficient. Such edge dislocation behavior differs qualitatively from the behavior of a screw dislocation, which is expelled to the material with a larger gradient coefficient [1]. The reasons behind such a difference remain unclear. Figure 4 shows that F_x^{gr} is a short-range force and is manifested in the immediate vicinity of the interface. At the interface itself, the force assumes a maximum value that depends heavily on the ratio c_2/c_1.

3.3. Mixed Gradient–Elastic Interface ($\mu_1 \neq \mu_2$, $\nu_1 \neq \nu_2$, $c_1 \neq c_2$)

In this case, the image force F_x assumes the form (in the units of $\mu_1 b_x^2/[\pi(k_1 + 1)]$)

$$F_x(x') = -\frac{A + B}{2x'} + \frac{4Ac_1}{x'^3} + 4\int_0^{+\infty} \frac{s}{\lambda_1 + \lambda_2} \times [c_1 s(\lambda_2 - \lambda_1)e^{-2x'\lambda_1} + [B - Ac_1(\lambda_1^2 + \lambda_2 s) \times (1 + 2x's) - c's(\lambda_2 - s)\}e^{-x'(\lambda_1 + s)}]ds. \quad (30)$$

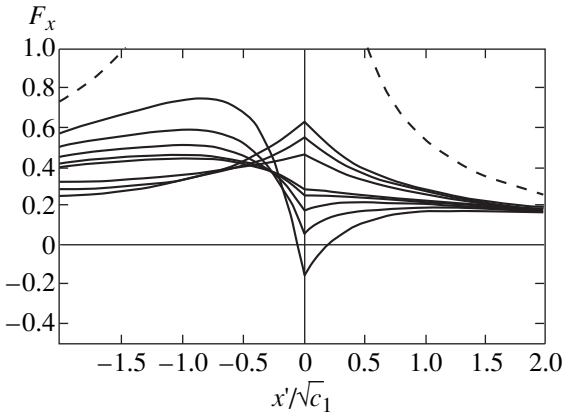

Fig. 5. Dependence of the image force F_x on the position $x'/\sqrt{c_1}$ of an edge dislocation with the Burgers vector b_x at a "mixed gradient–elastic" interface ($x' = 0$) for $\mu_2 = \mu_1$, $\nu_1 = \nu_2 = 0.3$, and $c_2/c_1 = 5, 3, 2, 1, 0.9, 0.7, 0.5$ and 0.3 (from top to bottom). The values of force are in the units of $\mu_1 b_x^2/[\pi(k_1 + 1)\sqrt{c_1}]$. The dashed curves describe the dependences for the classical solution.

It should be noted that the force F_x is not just a superposition of the forces F_x^{el} and F_x^{gr} defined by formulas (28) and (29), respectively. This can be seen clearly from Fig. 5. The image force of Eq. (30) is a long-range nonsingular force coinciding with the classical image force away from the interface ($|x'| > 5\sqrt{c_1}$). Its magnitude at the interface depends heavily on the ratios μ_2/μ_1 and c_2/c_1. The sign and the qualitative behavior of the force F_x near the interface is determined to a considerable extent by the ratio of the gradient coefficients c_2/c_1. For example, for $\mu_2/\mu_1 = 3$, three different modes of the behavior of F_x are observed (Fig. 5). If $c_2 > c_1$, we have $F_x > 0$ for any x' and it attains its maximum value at the interface or near it. If $c_2 = c_1$, we have $F_x \equiv F_x^{el}$ (see Sec. 3.1). If $c_2 < c_1$, we have $F_x > 0$ for any x' except in the small region near the interface. The size of this region is determined by the ratio c_2/c_1. For $c_2/c_1 = 0.3$, it is approximately equal to $0.3\sqrt{c_1}$, and $F_x < 0$ within this region, attaining the minimum value at the interface. Accordingly, we can single out three typical modes of the behavior of a dislocation at the interface for $\mu_2/\mu_1 = 3$. If $c_2 \geq c_2$, the dislocation is expelled from material 2 into material 1 and has no equilibrium positions near the interface. For $c_2 < c_1$ (e.g., for $c_2/c_1 = 0.3$), a dislocation located in material 2 is drawn towards the interface and can be "trapped" near it in the stable equilibrium position $x' \approx -0.1\sqrt{c_1}$. In turn, a dislocation located in material 1 has a position of unstable equilibrium $x' \approx 0.2\sqrt{c_1}$ near the interface. It is attracted to it within a small region $x' < 0.2\sqrt{c_1}$ and repelled from it outside this region.

4. Thus, we have obtained a solution of the boundary-value problem on a rectilinear edge dislocation parallel to the planar interface between two elastic isotropic media with different elastic constants and different gradient coefficients in the gradient theory of elasticity with the basic relation (1). The elastic stress field of the dislocation and the image force exerted on it by the interface are presented in a general integral form. It is shown that all the components of the stress field have no singularities on the dislocation line and remain continuous at the interface in contrast to the classical solution [17] having a singularity on the dislocation line and permitting a jump in the two normal components at the interface. The gradient and the classical solution coincide away from the interface and from the dislocation line (at distances much longer than $\geqslant 10\sqrt{c_1}$). The classical singularity [17] of the image force for a dislocation emerging at the interface is eliminated in the gradient solution. In this case, the force remains finite and continuous everywhere. Besides, an additional elastic image force emerging due to the difference in the gradient coefficients of the contacting media is determined. It is shown that this force, which has a short range and attains the maximum value at the interface, expels an edge dislocation to the material with a smaller gradient coefficient. In the general case, when the shear moduli μ_i and the gradient coefficients c_i are different for the contacting media, the overall image force may behave at the interface in different ways, depending on the ratios μ_2/μ_1 and c_2/c_1, although its long-range component remains the same as in the classical theory of elasticity.

ACKNOWLEDGMENTS

This research was carried out within the framework of the INTAS (grant no. INTAS-93-3213-Ext) and TMR (contract no. ERBFMRX CT 960062) programs, as well as with the partial support of the Scientific Council on the Russian Ministry of Science and Technology program "Physics of Solid-State Nanostructures" (grant no. 97-3006).

REFERENCES

1. M. Yu. Gutkin, K. N. Mikaelyan, and E. S. Aĭfantis, Fiz. Tverd. Tela (St. Petersburg) **42** (9), 1606 (2000) [Phys. Solid State **42** (2000) (in press)].
2. C. Q. Ru and E. C. Aifantis, Preprint MTU Report (Houghton, MI, 1993).
3. W. W. Milligan, S. A. Hackney, and E. C. Aifantis, in *Continuum Models for Materials with Microstructure*, ed. by H. Mühlhaus (Wiley, New York, 1995), p. 379.
4. B. S. Altan and E. C. Aifantis, Scr. Metall. Mater. **26** (2), 319 (1992).

5. C. Q. Ru and E. C. Aifantis, Acta Mech. **101** (1), 59 (1993).
6. E. C. Aifantis, J. Mech. Behav. Mater. **5** (3), 355 (1994).
7. D. J. Unger and E. C. Aifantis, Int. J. Fract. **71**, R27 (1995).
8. B. S. Altan and E. C. Aifantis, J. Mech. Behav. Mater. **8** (3), 231 (1997).
9. M. Yu. Gutkin and E. C. Aifantis, Scr. Mater. **35** (11), 1353 (1996).
10. M. Yu. Gutkin and E. C. Aifantis, Scr. Mater. **36** (1), 129 (1997).
11. M. Yu. Gutkin and E. C. Aifantis, Phys. Status Solidi B **214** (2), 245 (1999).
12. M. Yu. Gutkin and E. C. Aifantis, Scr. Mater. **40** (5), 559 (1999).
13. M. Yu. Gutkin and A. E. Aifantis, in *Nanostructured Films and Coatings*, NATO ARW Series, High Technology, Vol. 78, ed. by G.-M. Chow, I. A. Ovid'ko, and T. Tsakalakos (Kluwer, Dordrecht, 2000), p. 247.
14. M. Yu. Gutkin and E. C. Aifantis, Fiz. Tverd. Tela (St. Petersburg) **41** (12), 2158 (1999) [Phys. Solid State **41**, 1980 (1999)].
15. J. P. Hirth and J. Lothe, *Theory of Dislocations* (McGraw-Hill, New York, 1967; Atomizdat, Moscow, 1972).
16. A. C. Eringen, in *The Mechanics of Dislocations*, ed. by E. C. Aifantis and J. P. Hirth (American Society for Metals, Metals Park, 1985), p. 101.
17. T. Mura, in *Advances in Materials Research*, ed. by H. Herman (Interscience, New York, 1968), Vol. 3, p. 1.

Translated by N. Wadhwa

Physics of the Solid State, Vol. 42, No. 9, 2000, pp. 1668–1670. Translated from Fizika Tverdogo Tela, Vol. 42, No. 9, 2000, pp. 1621–1623.

DEFECTS, DISLOCATIONS, AND PHYSICS OF STRENGTH

Thermal Activation Analysis of Superplastic Deformation of Bi_2O_3 Ceramics

N. G. Zaripov

Institute of Problems of Metal Superplasticity, Russian Academy of Sciences, ul. Khalturina 39, Ufa, 450001 Bashkortostan, Russia

e-mail: zaripov@anrb.ru

Received February 11, 2000

Abstract—Activation energies for the conventional hot and superplastic deformations of Bi_2O_3 ceramics have been determined. It is shown that different deformation mechanisms are responsible for significant changes in the activation energy of plastic flow. *© 2000 MAIK "Nauka/Interperiodica".*

1. INTRODUCTION

It is known [1–3] that the transition of different materials into the superplasticity state actuates specific deformation mechanisms which provide the attainment of large plastic strains without fracture. As a rule, a particular mechanism of deformation can be elucidated using a combination of investigation techniques: microstructural observations, studies of the deformation relief and fine structure of the material, and a number of integral methods (e.g., on the change in the crystallographic texture). In some cases, the thermal activation analysis of plastic deformation has considerable advantages. This method is widely applied in analyzing plastic deformations of ceramic materials [4–8], since the complex microstructural studies, especially with the use of transmission electron microscopy, usually involve considerable difficulties. Therefore, the experimental determination of the activation energy for plastic deformation can provide important information on the atomic mechanisms and processes responsible for the diffusion of ions in ceramic materials.

However, comparitive studies of the actual deformation mechanisms determined for any ceramic materials by direct methods and from the results of thermal activation analysis are absent in the literature. The experimental revelation of a pronounced correlation between the mechanisms and the activation energy of plastic deformation would allow us to restrict ourselves, in many cases, only to the analysis of mechanical properties for treating the actual deformation mechanisms.

The present paper reports the results of the evaluation of the apparent activation energy for conventional hot and superplastic deformations of Bi_2O_3 ceramics and their correlation with the experimentally determined deformation mechanisms.

Earlier [9, 10], it was shown that the model Bi_2O_3 ceramics exhibits all indications of superplastic flow under certain temperature–rate conditions. It was experimentally found that, under conditions of superplasticity, the grain boundary sliding is a dominating deformation mechanism whose contribution to the total strain is about 80% [9]. Such a specific mechanism of deformation should result in substantial changes in the thermal activation parameters; however, up to date, these data for Bi_2O_3 ceramics are unavailable.

2. MATERIALS AND EXPERIMENTAL TECHNIQUES

The samples were obtained from the polycrystalline Bi_2O_3 powder with a particle size of 10–100 μm by hot pressing at a temperature of 650°C and a pressure of 500 MPa. Compression mechanical experiments were carried out at temperatures of 600, 625, and 650°C in the strain rate range 10^{-2}–10^{-5} s^{-1}. The phase composition was determined by the differential thermal and x-ray diffraction analyses in the temperature range 20–800°C.

The apparent activation energy was determined from the analysis of phenomenological equations of superplastic strain. As a rule, the rate of superplastic strain $\dot{\varepsilon}$ at the steady-state stage of flow is described by the known equation [1–4]

$$\dot{\varepsilon} = \frac{AD_0Gb}{kT}\left(\frac{b}{d}\right)^p\left(\frac{\sigma}{G}\right)^n \exp\left(-\frac{Q}{kT}\right), \qquad (1)$$

where σ is the applied stress; G is the shear modulus; D_0 is the preexponential factor of the diffusion coefficient; Q is the apparent activation energy; b is the Burgers vector; d is the grain size; and A, p, and n are the constant dimensionless coefficients. If one assumes that, in a considerably narrow temperature range, the shear modulus changes within very restricted limits and the ceramic materials have a stable grain size, the equa-

tion of strain rate is simplified and has the form

$$\dot{\varepsilon} = K\sigma^n \exp\left(-\frac{Q}{kT}\right), \quad (2)$$

where K is the coefficient accounting for the constant parameters. From this equation, the apparent activation energy for the constant applied load (in the case of creep) can be determined as follows:

$$Q = -kn\partial \ln\dot{\varepsilon}/\partial(1/T). \quad (3)$$

Under conditions of active loading for the identical strain rates, the formula takes the form

$$Q = -kn\partial \ln\sigma/\partial(1/T). \quad (4)$$

Thus, the experimental determination of the apparent activation energy under the above assumptions can be carried out according to the following formula:

$$Q = kn\ln\left(\frac{\sigma_1}{\sigma_2}\right)\frac{T_1T_2}{T_1 - T_2}. \quad (5)$$

3. RESULTS AND DISCUSSION

The microstructure of the Bi_2O_3 ceramics in the initial hot-pressed state consists of equiaxial grains with a mean size of 8–10 μm. After deformation under conditions of superplasticity (T = 650°C, $\dot{\varepsilon} = 10^{-4}$ s^{-1}) [9], when the rate sensitivity of flow stress m reaches a value of 0.4, even at $\varepsilon > 75\%$, the grains virtually retain their equiaxiality, and their size does not change substantially (Fig. 1). This allows us to put the coefficient $p = 1$ in Eq. (1) and describe the strain process by Eq. (2).

Differential thermal and high-temperature x-ray powder diffraction analyses have shown that, upon heating up to the melting temperature and cooling, the Bi_2O_3 ceramics undergoes several phase transformations. However, upon heating and cooling in the temperature range 20–715°C (below the melting point and the $\alpha \longrightarrow \delta$ transition temperature), only a single-phase region occurs (the low-temperature monoclinic α modification [9]). Thus, the temperature range of the performance of the experiments corresponds to only one region.

The dependence of the flow stress on the degree of strain (the σ–ε curves) of the Bi_2O_3 ceramics at T = 650°C strongly depends on the strain rate. As is seen from Fig. 2, the peak flow stress decreases with a decrease in the strain rate. At strain rates higher than 10^{-4} s^{-1}, the flow stress passes through a peak, abruptly decreases, and reaches the steady-state stage of deformation at which the flow stress is virtually independent of the degree of strain. At strain rates of 10^{-4} s^{-1} and less, the initial peak of the flow stress disappears, the σ–ε curves have the shape characteristic of superplastic deformations of metals and intermetallides [2, 3]. In general, the degree of strain ε = 25–30% (practically for all the strain rates) can be taken as the onset of the steady-state stage, and the flow stresses for all these degrees of strain can be used to determine the activation energy.

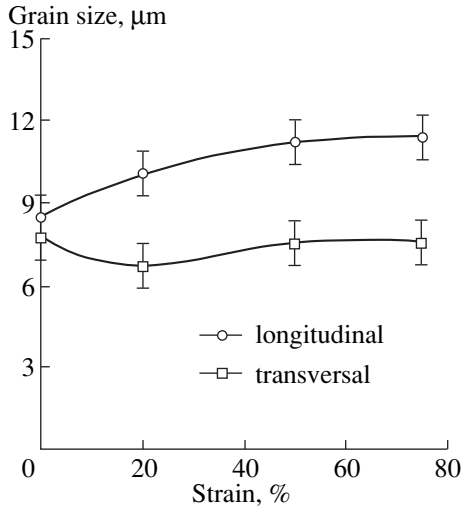

Fig. 1. Dependences of the grain size of Bi_2O_3 ceramics on the strain upon superplastic deformation (T = 650°C, $\dot{\varepsilon} = 10^{-4}$ s^{-1}).

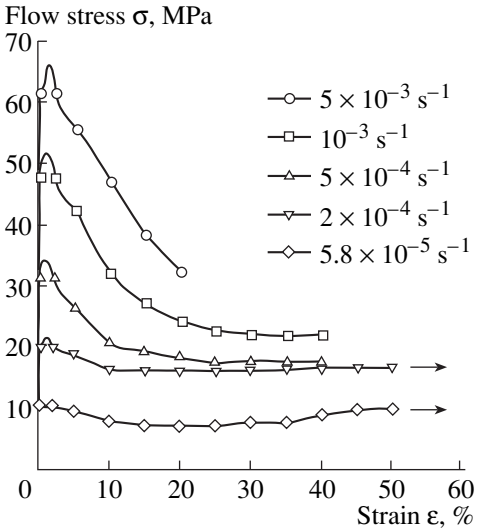

Fig. 2. Stress–strain curves for Bi_2O_3 ceramics at different strain rates (T = 650°C).

The rate dependence of the flow stress at the steady-state stage (at $\varepsilon > 30\%$) exhibits different behavior depending on temperature (Fig. 3). It is seen that, at temperatures of 600 and 652°C in the entire range of strain rates studied, the index of flow stress n is nearly constant and equal to four or five. As the temperature increases up to 650°C in the range of strain rates $\dot{\varepsilon} = 5 \times 10^{-5}$–$2 \times 10^{-4}$ s^{-1}, the coefficient n decreases down to 2.5 (i.e., coefficient $m = 1/n$ increases up to 0.4); however, at higher rates ($\dot{\varepsilon} = 10^{-3}$–$10^{-2}$ s^{-1}), its value

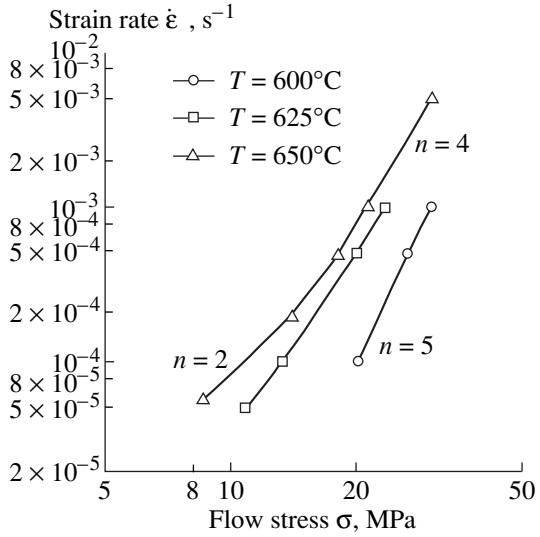

Fig. 3. Curves of the strain rate plotted against the flow stress for Bi_2O_3 ceramics.

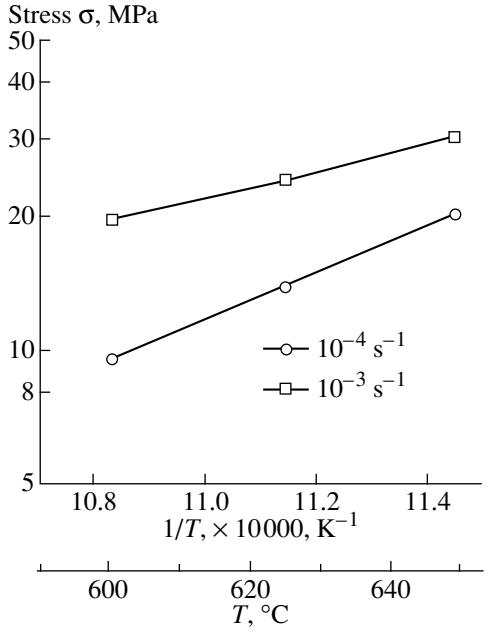

Fig. 4. The $\ln\sigma$–$1/T$ curves for Bi_2O_3 ceramics at different strain rates.

remains also high ($n \cong 4$). The activation energy Q, which is determined from the slopes of the $\ln\sigma$–$1/T$ curves (Fig. 4), significantly differs for superplastic and hot deformations. For the superplastic deformation, the activation energy is 228 kJ/mol, and for the hot deformation, its value is 415 kJ/mol.

The difference in the activation energies can be associated with the difference in the mechanisms operating under the conditions of conventional hot and superplastic deformations. The conventional hot deformation [high strain rates and (or) low temperatures] mainly occurs by means of transcrystalline dislocation slip. This is evidenced by the microstructural studies and investigations into the fine structure of ceramics [10]. At these strain rates, the formation of the subgrain structure and dislocation walls takes place, and the refinement of a microstructure occurs.

Under conditions of superplastic deformation, the grain boundary sliding is the main mechanism of deformation [1–3, 9, 10]. In this case, even at the strain $\varepsilon > 75\%$, the grains retain their equiaxiality, the grain sizes virtually do not change, the preliminary drawn marks at the grain boundaries are displaced, and a low density of dislocations is observed.

Thus, the large differences between the activation energies for the conventional hot and superplastic deformations can be connected with different mechanisms of deformation in the Bi_2O_3 ceramics. The processes responsible for the deformation can be reliably established with the available data on the diffusion parameters of the elements.

ACKNOWLEDGMENTS

This work was supported by the Russian Foundation for Basic Research (project no. 99-03-33077) and the Federal Program “Integratsiya” (project no. A0004).

REFERENCES

1. M. V. Grabskiĭ, *Structural Superplasticity of Metals* (Metallurgiya, Moscow, 1975).
2. O. A. Kaĭbyshev, *Superplasticity of Commercial Alloys* (Metallurgiya, Moscow, 1984).
3. O. A. Kaibyshev, *Superplasticity of Alloys: Intermetallides and Ceramics* (Springer-Verlag, Berlin, 1992).
4. A. H. Chokshi, Mater. Sci. Technol. **7** (7), 469 (1991).
5. P. C. Panda, R. Raj, and P. E. D. Morgan, J. Am. Ceram. Soc. **68** (10), 522 (1985).
6. F. Wakai, S. Sakaguchi, and Y. Matsuno, Adv. Ceram. Mater. **1** (3), 259 (1986).
7. K. R. Venkatachari and R. J. Raj, J. Am. Ceram. Soc. **69** (2), 135 (1986).
8. Y. Maehara and T. G. Langdon, J. Mater. Sci. **25**, 2275 (1990).
9. N. G. Zaripov, O. A. Kaĭbyshev, and O. M. Kolnogorov, Fiz. Tverd. Tela (S.-Peterburg) **35** (8), 2114 (1993) [Phys. Solid State **35**, 1051 (1993)].
10. N. G. Zaripov, O. M. Kolnogorov, and L. V. Petrova, Mater. Sci. Forum **170**–**172**, 397 (1994).

Translated by T. Galkina

Physics of the Solid State, Vol. 42, No. 9, 2000, pp. 1671–1674. Translated from Fizika Tverdogo Tela, Vol. 42, No. 9, 2000, pp. 1624–1627.

DEFECTS, DISLOCATIONS, AND PHYSICS OF STRENGTH

Nanoindentation and Strain Characteristics of Nanostructured Boride/Nitride Films

R. A. Andrievskiĭ*, G. V. Kalinnikov*, N. Hellgren, P. Sandstrom**, and D. V. Shtanskiĭ*****

** Institute of Problems in Chemical Physics, Russian Academy of Sciences, Chernogolovka, Noginskiĭ raĭon, Moscow oblast, 142432 Russia*

*** Thin Films Division, Department of Physics, Linköping University, S-581 836 Linköping, Sweden*

**** Bardin Central Research Institute of Ferrous Metallurgy, State Scientific Center, Vtoraya Baumanskaya ul. 9/23, Moscow, 107005 Russia*

e-mail: ara@icp.ac.ru

Received February 11, 2000

Abstract—The hardness, elastic modulus, and elastic recovery of nanostructured boride/nitride films 1–2 μm thick have been investigated by the nanoindentation technique under the maximum loads over a wide range (from 5 to 100 mN). It is demonstrated that only the hardness parameters remain constant at small loads (5–30 mN). The data obtained are discussed and compared with the parameters determined by other methods.

The basic ideas of investigating strain characteristics upon continuous indentation of an indenter were formulated in the mid-1970s (see, for example, [1–5]). This method has been extensively used in studies of films and surface layers, specifically upon nanoindentation under small loads (see, for example, [6–9]). A great body of data on the hardness H and the elastic modulus E was obtained by the indentation technique. In particular, valuable information on films based on interstitial phases (transition metal carbides, nitrides, and borides) was generalized in the review [10]. Interesting techniques of examining the microindentation kinetics were proposed by Golovin and Tyurin [11]. However, the observed dependences of H and E on the indentation load P have yet to be unambiguously interpreted, and the reliability of the strain parameters is not universally obvious and is not necessarily discussed. The sole exception is the work of Menchik *et al.* [9], who attempted to unify the techniques of determining E in nanoindentation experiments with ball diamond indenters. From general considerations and in relation to the study of size effects in nanostructured materials (specifically in films) [12], it is important to reveal the degree of absolute reliability of the data obtained from nanoindentation measurements.

As a continuation of our earlier work concerned with the determination of the hardness and elastic properties of Ti(B,N) films by conventional methods [13], it was of interest to investigate the same films by the nanoindentation method. The conditions of magnetron sputtering and the characteristics of the $Ti(B_{0.73}N_{0.2}O_{0.05}C_{0.02})_{1.56}$ film (**I**) with a hexagonal structure of the AlB_2 type and the $Ti(N_{0.49}B_{0.34}O_{0.12}C_{0.05})_{1.49}$ film (**II**) with a cubic structure of the NaCl type were given in [13]. Single-crystal silicon wafers were used as substrates. The film thicknesses were $\delta_I = 1.7–1.8$ μm and $\delta_{II} = 1.2–1.3$ μm.

The structural features were examined by the high-resolution transmission electron microscopy (JEM-3010). The crystallite sizes (L) were estimated on the basis of dark-field images as $L_I = 4–8$ nm for film **I** and $L_{II} = 3–6$ nm for film **II**. Figure 1 shows a micrograph obtained in the direct resolution mode. One can clearly see a characteristic fringe structure and the crystalline character of intercrystalline boundaries. These features were described in detail in our previous work [14].

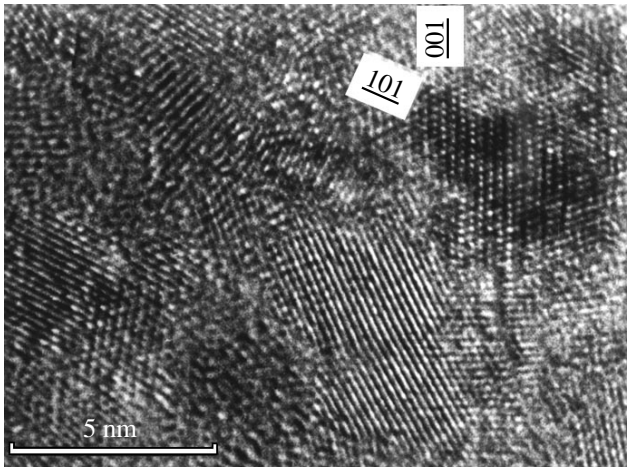

Fig. 1. An image of the structure of film **I** in the direct resolution mode.

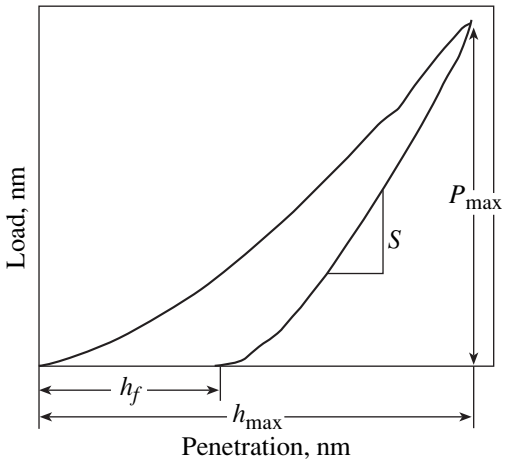

Fig. 2. Schematic representation of the dependences of the load on the penetration of an indenter under loading and unloading.

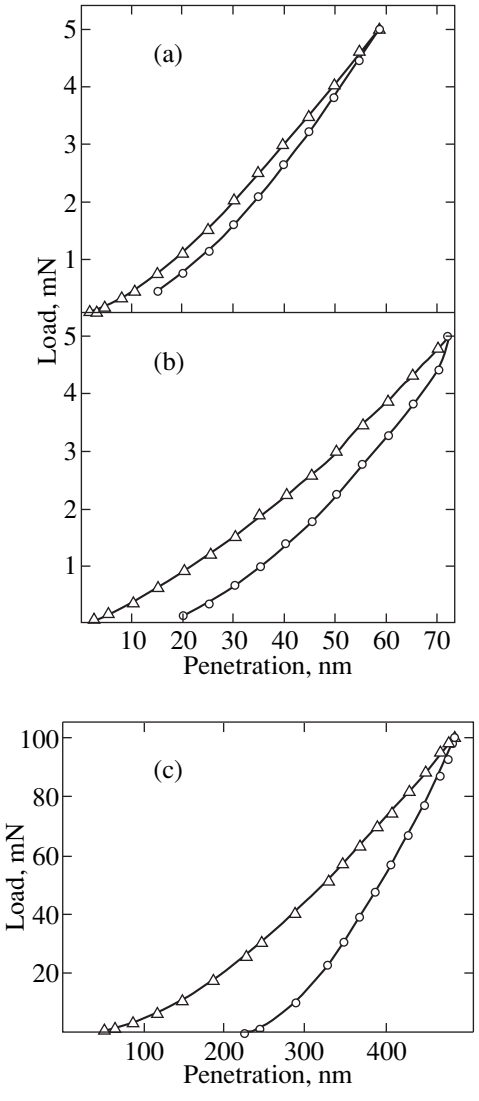

Fig. 3. Experimental loading–unloading curves at (a, b) P_{max} = 5 mN and (c) P_{max} = 100 mN for films (a, c) **I** and (b) **II**.

The nanoindentation measurements were carried out on a Nano Indentor TM II instrument [15] with the use of Berkovich trihedral diamond indenters. The maximum loads P_{max} were equal to 5, 10, 30, and 100 mN. As before (see, for example, [16]), the loading–unloading procedure consisted in loading up to P_{max}, unloading down to $0.1P_{max}$, holding for 50 s, repeated loading to P_{max}, holding for 200 s, and final unloading. At least ten indentations were made for each P_{max} load.

Figure 2 illustrates the loading–unloading scheme and the estimation with the use of the measured parameters. According to the known technique [7], these parameters were used to evaluate $H = P_{max}/A$, $S = dP/dh$, the elastic modulus of the "film + indenter" system $E^* = S/2(\pi/A)^{0.5}$, and the so-called elastic recovery $R = (h_{max} - h_f)/h_{max}$, where A is the indenter projection area determined from the maximum depth of indenter penetration h_{max}. In turn, the elastic modulus of the film E_{film} was calculated from the relationship $1/E^* = (1 - \nu_{ind^2})/E_{ind} + (1 - \nu_{film^2})/E_{film}$, where ν_{ind} and ν_{film} are the Poisson ratios of the indenter and the film ($\nu_{film} \sim 0.2$), respectively; and E_{ind} is the elastic modulus of the indenter (for diamond, E = 1141 GPa and ν = 0.07 [7]).

The experimental loading–unloading curves for the studied films are depicted in Fig. 3. The dependences of the strain characteristics on P are displayed in Fig. 4. As follows from the results obtained, only the hardness H is independent of P at small loads (P = 5–30 mN). The R and E quantities in the studied P range increase with a decrease in the load. Note that brittle films **I** and **II** are almost identical in the elastic recovery, i.e., the very conventional parameter of brittleness (the perfect plasticity and the perfect elastic recovery correspond to R = 0 and 1, respectively), whereas the hardnesses H and the elastic moduli E of the films differ considerably.

In this respect, it is of interest to compare the H and E quantities determined from the nanoindentation measurements with the experimental data obtained by conventional methods. According to [13], $H_I \sim 49$ and E_I = 460 ± 50 GPa for film **I** and $H_{II} \sim 49$ and E_{II} = 480 ± 100 GPa for film **II**. The data on the hardness were obtained with a PMT-3 microhardness tester at a load of 0.3 N and were processed according to the procedure described in [17], which made it possible to eliminate the effect of a softer substrate and differences in film thicknesses on the results of measurements. The Young moduli were determined by the contactless technique of measuring the elastic properties. A comparison of these data with the results demonstrated in Fig. 4 led to the conclusion that different techniques of determining H and E furnish the comparable results for film **I**, whereas the nanoindentation measurements for film **II** give the smaller parameters.

However, this inference requires certain comments. It should be kept in mind that the hardness characteristics obtained in traditional measurements can be larger

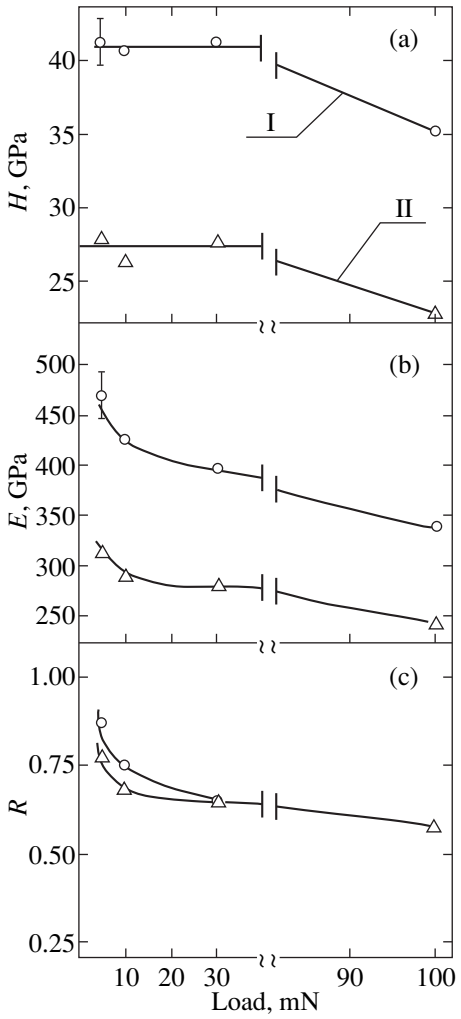

Fig. 4. Effect of the maximum load on (a) hardness, (b) elastic modulus, and (c) elastic recovery.

than those determined by the nanoindentation technique due to the known relaxation effect (the so-called recovered and unrecovered hardnesses). Moreover, it is worth noting that the thicknesses of the studied samples differ, and, hence, the relative depths of indenter penetration h/δ are also different. For example, this ratio at $P = 5$ mN is equal to 0.034 for film **I** and 0.057 for film **II**. At larger loads, this difference becomes all the more evident, and the effect of the substrate should be taken into account. In the general case, the scale effect, i.e., the effect of the indentation load on the strain characteristics, can be due to the scaling violation [18] and the inhomogeneity of the surface layers in the studied objects. As follows from recent publications (see, for example, [19–21]), the surface topography also plays an important part at very small loads (~10 mN and less). The investigation of the Ti(B,N) film surface by the atomic-force microscopy [20] revealed that the relief of films **II** is more developed than that of films **I**, which can be partly responsible for a decrease in the estimates of H and E. Finally, the elastic modulus E evaluated from the nanoindentation data characterizes the strained state under conditions of nonuniform bulk compression. All these factors can affect the measured parameters, but this effect is difficult, if not impossible, to consider them quantitatively

It should be noted that, unlike the results shown in Fig. 4, our earlier nanoindentation experiments [22] made on films **I** with the use of the first nanoindenter model [6] demonstrated a drastic increase in the hardness with a decrease in the load P_{max} from 50 to 10 mN. On the other hand, the errors in measurements of the parameters, specifically of the hardness, sharply increased at small loads (less than 10–20 mN) [20, 23]. On this basis, it is clear that the reliability of strain parameters obtained from the nanoindentation data is rather conventional, and the contribution of possible effects should be considered in detail in each particular case.

ACKNOWLEDGMENTS

We would like to thank Prof. J.-E. Sundgren and Prof. L. Hultman of the Linköping University (Sweden) for their kind attention to the present study.

This work was supported by the International Association of Assistance for the promotion of cooperation with scientists from the New Independent States of the former Soviet Union (project INTAS no. 96-2232), the Program “Integration” (project no. 855), and the Program of the cooperation of the Russian Academy of Sciences and the Royal Swedish Academy of Sciences.

REFERENCES

1. A. P. Ternovskiĭ, V. P. Alekhin, M. Kh. Shorshorov, *et al.*, Zavod. Lab. **39**, 1242 (1973).
2. S. I. Bulychev, V. P. Alekhin, M. Kh. Shorshorov, *et al.*, Zavod. Lab. **41**, 1137 (1975).
3. S. I. Bulychev, V. P. Alekhin, M. Kh. Shorshorov, and A. P. Ternovskiĭ, Probl. Prochn., No. 9, 79 (1976).
4. Yu. S. Boyarskaya, D. Z. Grabko, and M. S. Kats, *Physics of Microindentation Processes* (Shtiintsa, Kishinev, 1986).
5. S. I. Bulychev and V. P. Alekhin, *Material Testing by Continuous Indentation of an Indenter* (Mashinostroenie, Moscow, 1990).
6. M. F. Doerner and W. D. Nix, J. Mater. Res. **1**, 601 (1986).
7. W. C. Oliver and G. M. Pharr, J. Mater. Res. **7**, 1564 (1992).
8. E. Soderlund and D. J. Rowcliffe, J. Hard Mater. **5**, 149 (1994).
9. J. Menchik, D. Munz, E. Quandt, *et al.*, J. Mater. Res. **12**, 2475 (1997).
10. R. A. Andrievskiĭ, Usp. Khim. **66**, 57 (1997) [Russ. Chem. Rev. **66**, 53 (1997)].
11. Yu. I. Golovin and A. I. Tyurin, Kristallografiya **40**, 884 (1995) [Crystallogr. Rep. **40**, 818 (1995)].

12. R. A. Andrievskiĭ and A. M. Glezer, Fiz. Met. Metallogr. **88**, 50 (1999) [Phys. Met. Metallogr. **88**, 45 (1999)].
13. R. A. Andrievskiĭ, G. V. Kalinnikov, N. P. Kobelev, *et al.*, Fiz. Tverd. Tela (S.-Peterburg) **39**, 1859 (1997) [Phys. Solid State **39**, 1661 (1997)].
14. R. A. Andrievskiĭ, G. V. Kalinnikov, and D. V. Shtanskiĭ, Fiz. Tverd. Tela (S.-Peterburg) **42** (4), 741 (2000) [Phys. Solid State **42**, 760 (2000)].
15. G. M. Pharr, W. C. Oliver, and F. R. Brotzen, J. Mater. Res. **7**, 613 (1992).
16. H. Liungcrantz, C. Engstrom, L. Hultman, *et al.*, J. Vac. Sci. Technol. A **16**, 3104 (1998).
17. B. Jonsson and S. Hogmark, Thin Solid Films **114**, 257 (1984).
18. Yu. V. Mil'man, Probl. Prochn., No. 6, 52 (1990).
19. X. Wang, A. K. Kolitsch, and W. Moller, Appl. Phys. Lett. **71**, 1951 (1997).
20. R. A. Andrievski, in *Surface-Controlled Nanoscale Materials for High-Added-Value Applications*, ed. by K. E. Gonsalves, M.-E. Baraton, R. Singh, H. Hofmann, J. Chen, and J. Akkara (MRS, Warrendale, 1998), Mater. Res. Soc. Symp. Proc. **501**, 149 (1998).
21. R. A. Andrievski, J. Solid State Chem. **133**, 249 (1997).
22. R. A. Andrievskiĭ, S. A. Amanulla, E. J. Brookes, *et al.*, Neorg. Mater. **31**, 1600 (1995) [Inorg. Mater. **31**, 1456 (1995)].
23. G. Shafirstein, M. Gee, S. Osgerby, and S. Saunders, in *Thin Films—Stresses and Mechanical Properties V*, ed. by Sh. Baker, C. Ross, P. Townsend, C. Volkert, and P. Borgesen (MRS, Warrendale, 1995), Mater. Res. Soc. Symp. Proc. **356**, 717 (1995).

Translated by O. Borovik-Romanova

Physics of the Solid State, Vol. 42, No. 9, 2000, pp. 1675–1679. Translated from Fizika Tverdogo Tela, Vol. 42, No. 9, 2000, pp. 1628–1632.

MAGNETISM AND FERROELECTRICITY

Spectra of Multiquantum Echo Signals from Quadrupole Nuclei with Half-Integral Spin in Magnetically Ordered Materials

S. N. Polulyakh*, N. A. Sergeev, and A. A. Shemyakov*****

**Simferopol State University, ul. Yaltinskaya 4, Simferopol, 320625 Ukraine*

e-mail: roton@ccssu.crimea.ua

***Szczecin University, 70-451 Szczecin, Poland*

****Donetsk Physicotechnical Institute, National Academy of Sciences of Ukraine, Donetsk, 340114 Ukraine*

Received October 5, 1999

Abstract—The numerical simulation of two-pulse echo signals at times 2τ, 4τ, and 6τ for the $I = 5/2$ spin and at time 2τ, 4τ, and 8τ for the $I = 7/2$ spin (τ is the time interval between exciting pulses) is carried out. It is shown that a delay by 2τ in the moment of formation of the echo results in the disappearance of extreme quadrupole satellites in the NMR spectrum obtained by recording the frequency dependence of the echo amplitude. The echoes at the maximum possible time of formation $(2I + 1)\tau$ are only observed at the frequency of the purely magnetic spectroscopic transition $\pm\frac{1}{2} \rightleftarrows \mp\frac{1}{2}$; no such echoes are observed at the quadrupole satellite frequencies. The computations are compared with the experimental results obtained for the ^{55}Mn nuclei (spin $I = 5/2$) in the perovskite $GdCu_3Mn_4O_{12}$ and the spinel $Li_{0.5}Fe_{2.5}O_4$: Mn. © *2000 MAIK "Nauka/Interperiodica".*

The main peculiarities of NMR in magnetically ordered materials are determined by the hyperfine interactions between the exchange-coupled electronic spin subsystem and the nuclear spin subsystem in the paramagnetic state [1, 2]. Moreover, the NMR in magnetically ordered materials is characterized by the inhomogeneous broadening of spectral lines, which ensures the formation of nuclear-spin echoes [1, 2]. Quadrupole electric interactions in a spin system with inhomogeneous broadening of spectral lines lead to the formation of additional responses that are known as multiquantum echoes [3].

Multiquantum signals of a nuclear-spin echo from quadrupole nuclei in magnetically ordered materials were first observed in the case of NMR for ^{53}Cr nuclei having a spin $I = 3/2$ [4]. In order to generate echo signals, Abelyashev *et al.* [4] used a sequence of two exciting pulses separated by a time interval τ. A multiquantum echo was observed at the instant of time 4τ. The main peculiarity of the 4τ echo is that this signal is formed only at frequencies corresponding to purely magnetic spectroscopic transitions $\left(\left(\pm\frac{1}{2} \rightleftarrows \mp\frac{1}{2}\right)\right)$, and no such signals are observed at the quadrupole satellite frequencies. On the other hand, the ordinary 2τ echo from the quadrupole nuclei is observed at the frequencies of all spectral lines. Thus, the quadrupole electric interactions are suppressed completely in NMR spectra recorded from the frequency dependence of the amplitude of multiquantum echo 4τ.

Experimental and theoretical studies of the peculiarities of the formation of multiquantum echo signals were undertaken in [5] by considering the example of the NMR for ^{53}Cr nuclei in a single crystal of ferromagnetic $CdCr_2Se_4$. In particular, it was shown [5] that the peak of the multiquantum 4τ echo signal is formed when the amplitude of the varying magnetic field[1] during the action of the exciting pulses is comparable with the quadrupole splitting of the NMR spectrum. Besides, the duration of the first exciting pulse must be about double the duration of the second pulse. Such a ratio of the durations of exciting pulses ensuring the optimal formation of the multiquantum echo is inverse to the ratio of durations of pulses ensuring the maximal amplitude of the ordinary 2τ echo.

Multiquantum 4τ echoes were also observed experimentally in the case of NMR for ^{63}Cu and ^{65}Cu nuclei in ferromagnetic copper sulfochromite [6]. Each copper isotope has a spin of $I = 3/2$. However, ordinary echo signals from nuclei with a larger spin are also observed experimentally in magnetically ordered materials. Among others, the nuclei ^{55}Mn (spin $I = 5/2$) and ^{59}Co (spin $I = 7/2$) belong to this category.

The aim of the present work is to study the conditions of formation and the frequency spectra of multichannel echo signals from quadrupole nuclei with the half-integral spin $I > 3/2$.

[1] The amplitude is measured in the frequency units.

1. THEORY

In the absence of a varying magnetic field, the Hamiltonian of the nuclear quadrupole spin system in a rotating system of coordinates can be presented in the form [2]

$$H = -\Delta\omega I_z + \omega_q\left(I_z^2 - \frac{I(I+1)}{3}\right), \quad (1)$$

where $\Delta\omega$ is the detuning, I is the nuclear spin, and ω_q is the quadrupole interaction energy. During the action of the exciting pulses, we must take the interaction with the varying magnetic field into account in the Hamiltonian:

$$H_1 = H - \omega_1 I_x. \quad (2)$$

While writing this expression, we assumed that the x axis of the rotating system of coordinates is chosen along the varying magnetic field.

In the case of inhomogeneous broadening of the spectral line, the detuning $\Delta\omega$ and the quadrupole interaction energy ω_q can be presented in the form

$$\Delta\omega = \Delta\omega_0 + \delta\omega, \quad (3)$$

$$\omega_q = \omega_{q0} + \delta\omega_q. \quad (4)$$

Here, the quantities $\Delta\omega_0$ and ω_{q0} characterize the spin system as a whole, while $\delta\omega$ and $\delta\omega_q$ describe an individual isochromatic group of spins [7].

In order to calculate the transverse component $M_+ = M_x + iM_y$ of the nuclear magnetization, we use the density matrix operator. Following [3, 7, 8], we obtain an expression for the time at which the echo signal is formed in the case of two exciting pulses separated by the time interval τ:

$$t = \left(1 + \frac{\delta\omega(m' - m'') - \delta\omega_q(m'^2 - m''^2)}{\delta\omega - \delta\omega_q(2m+1)}\right)\tau. \quad (5)$$

Moments of formation of echo signals for quadrupole nuclei with spin $I = 5/2$

Serial no.	Magnetic quantum number			Moment of formation
	m	m'	m''	
1	3/2	5/2	3/2	$t = 2\tau$
2	1/2	3/2	1/2	
3	–1/2	1/2	–1/2	
4	–3/2	–1/2	–3/2	
5	–5/2	–3/2	–5/2	
6	1/2	5/2	–1/2	$t = 4\tau$
7	–3/2	1/2	–5/2	
8	–1/2	3/2	–3/2	
9	–1/2	5/2	–5/2	$t = 6\tau$

Here, m, m' and m'' are the magnetic quantum numbers. Formula (5) only determines the moment of formation of the echo signal for values of the magnetic quantum numbers for which t depends neither on $\delta\omega$ nor on $\delta\omega_q$. The amplitude of the corresponding echo signal is described by the expression

$$V_+ = m'''\sqrt{I(I+1) + m(m+1)}\langle m|\varphi_{j1}\rangle\langle\varphi_{j1}|m'\rangle$$
$$\times\langle m'|\varphi_{j2}\rangle\langle\varphi_{j2}|m'''\rangle\langle m'''|\varphi_{j3}\rangle\langle\varphi_{j3}|m''\rangle\langle m''|\varphi_{j4}\rangle \quad (6)$$
$$\times\langle\varphi_{j4}|m+1\rangle\exp(it_1(\varepsilon_{j3} - \varepsilon_{j2}) + it_2(\varepsilon_{j4} - \varepsilon_{j1})).$$

Here, t_1 and t_2 are the durations of the first and second exciting pulses, $|\varphi_j\rangle$ are the eigenfunctions, and ε_j are the eigenvalues of the Hamiltonian H_1, given by Eq. (2), of the spin system during the action of the varying magnetic field

$$H_1|\varphi_j\rangle = \varepsilon_j|\varphi_j\rangle. \quad (7)$$

In accordance with Eq. (6), the main problem in calculating the echo signal amplitude is in evaluating the eigenfunctions and eigenvalues of the Hamiltonian H_1. A numerical procedure was used in [5] for solving this problem. The eigenfunctions of the Hamiltonian H_1 were presented there in the form of a linear combination of the eigenfunctions of the operator I_z:

$$|\varphi_j\rangle = C_{jm}|m\rangle. \quad (8)$$

The constant coefficients C_{jm} and the eigenvalues ε_j were obtained by the numerical diagonalization of the matrix $\langle m|H_1|m'\rangle$.

2. NUMERICAL SIMULATION

We consider multiquantum echoes whose moments of formation do not depend on the nature of inhomogeneous broadening of the spectral line [7, 8]. In other words, we consider signals whose moments of formation, given by Eq. (5), are independent of $\delta\omega$ and $\delta\omega_q$.

For the $I = 5/2$ spin, the sets of magnetic quantum numbers describing the formation of echoes are presented in the table. Signals 1–5 are ordinary echoes, while 6–9 are multiquantum echo signals. In order to study the spectral properties of each echo, we calculated the dependence of the amplitude of Eq. (6) on the detuning $\delta\omega$ for the corresponding values of the magnetic quantum numbers. The matrix $\langle m|H_1|m'\rangle$ was constructed under the assumption that the quantities $\delta\omega$ and $\delta\omega_q$ are equal to zero [5].

It was found as a result of computations that the maxima of multiquantum echo signals 8 and 9 (see table) are observed for a detuning $\delta\omega = 0$, while the maxima of echo signals 6 and 7 correspond to $\delta\omega = 2\omega_{q0}$ and $\Delta\omega = -2\omega_{q0}$, respectively. It was also found that the theoretical dependences $V = V(\Delta\omega)$ are expanded by an amount determined by the amplitude of the varying field ω_1 in the same way as for nonquadru-

pole nuclei (see Chapter 2 in [9]) and quadrupole nuclei with spin $I = 3/2$ [5]. Omitting the detailed analysis of such a broadening, which is beyond the scope of the present work, we note that the broadening determined by ω_1 is considerably suppressed in the NMR experiments on magnetic materials. The departure of the shape of real exciting pulses from squareness may be one of the possible reasons behind the suppression of the broadening.

The detuning $\Delta\omega = 0$ in the rotating system of coordinates corresponds to the frequency of the spectroscopic transition $\left(\pm\frac{1}{2} \rightleftarrows \mp\frac{1}{2}\right)$, i.e., to the frequency $\omega_0 = \gamma B$ in the laboratory reference frame (here, γ is the gyromagnetic ratio and B is the induction of the constant magnetic field). Figure 1 schematically shows the frequency position of the theoretical maxima of echo signals formed at different instants of time for quadrupole nuclei with half-integral spins.

It follows from the data presented in Fig. 1 that a delay in the moment of formation of the signal by 2τ leads to the disappearance of two extreme quadrupole satellites in the spectrum of this signal. The quadrupole satellites are suppressed completely for the spectra of multiquantum echo signals with the largest possible time of formation $t = (2I + 1)\tau$. In particular, the complete suppression of the quadrupole satellites for quadrupole nuclei with spin $I = 3/2$ is observed for the 4τ echo.

In order to analyze the optimal conditions for the formation of multiquantum echoes, we calculated the dependences of the echo signal amplitudes on the parameters of the exciting pulses. The theoretical dependences of the echo signal amplitude V on the variable field ω_1 are shown in Fig. 2 for a fixed value of $\omega_{q0} = 1$ in the case of the spin $I = 5/2$. The values presented in Fig. 2 were obtained as follows: the durations t_1 and t_2 of the first and second exciting pulse, respectively, were varied for each fixed value of ω_1. Each of the values presented in Fig. 2 corresponds to the first maximum of the relevant echo signal amplitude.

It follows from the data presented in Fig. 2 that the peaks of the amplitudes of multiquantum echo signals are formed when the amplitude of the varying magnetic field is comparable with the magnitude of the quadrupole interaction. Supplementary computations carried out by us show that condition $\omega_1 \approx \omega_{q0}$ is also observed when the multiquantum echo signals are excited for the spin $I = 7/2$. The peak of the multiquantum echo amplitude was formed under the condition that the duration of the first exciting pulse exceeded the duration of the second pulse: $t_1 = (2.25 \pm 0.75)t_2$. Man [10] carried out a more detailed theoretical analysis of the dependences of the echo signal amplitudes on the durations of the exciting pulses.

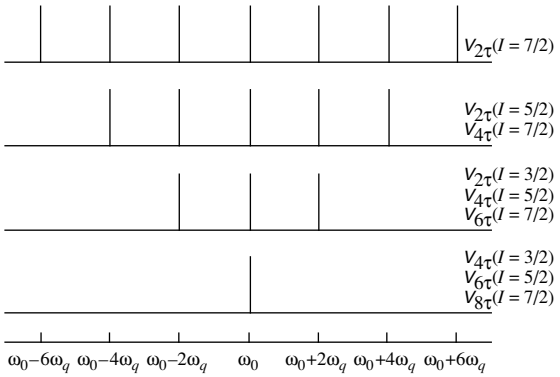

Fig. 1. Theoretical values of the frequencies corresponding to the maxima of the amplitudes $V_{n\tau}$ of the echo signals at times $n\tau$ ($n = 2, 4, 6, 8$) for quadrupole nuclei with half-integral spin I.

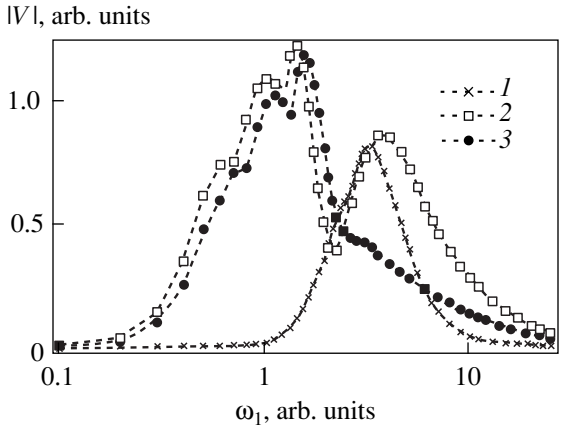

Fig. 2. Theoretical dependences of the amplitudes V of the multiquantum echo signals on the varying magnetic field ω_1 for nuclei with spin $I = 5/2$ for $\omega_q = 1$. Curve *1* is the 6τ echo for $\Delta\omega_0 = 0$; curve *2* is the 4τ echo for $\Delta\omega_0 = 0$, and curve *3* is the 4τ echo for $\Delta\omega_0 = \pm 2\omega_{q0}$.

3. EXPERIMENT

In order to experimentally verify the theoretical results, we investigated the multiquantum echo signals from the quadrupole nuclei ^{55}Mn (spin $I = 5/2$) in magnetically ordered materials. Experiments were carried out on an incoherent pulse NMR spectrometer. The spectra were recorded by registering the dependence of the echo signal amplitude on the frequency of oscillations of the varying magnetic field during the action of the exciting pulses.

The experiments were carried out on a polycrystalline sample of $GdCu_3Mn_4O_{12}$. According to the data of the x-ray diffraction analysis, this compound is a cubic perovskite (space group $Im3$) [11]. Figure 3 shows the experimentally recorded NMR spectra of the ^{55}Mn nuclei of Mn^{4+} ions at a temperature $T = 77$ K. Curve *1* in Fig. 3 is the NMR spectrum recorded from the 2τ

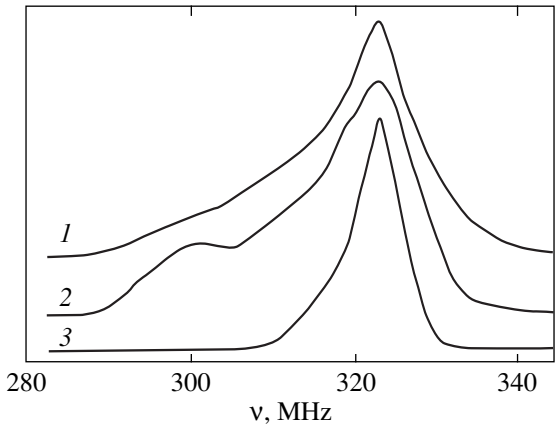

Fig. 3. NMR spectra of ^{55}Mn nuclei of Mn^{4+} ions in $GdCu_3Mn_4O_{12}$ at $T = 77$ K, recorded from the 2τ (curve *1*), 4τ (curve *2*), and 6τ (curve *3*) echo signals.

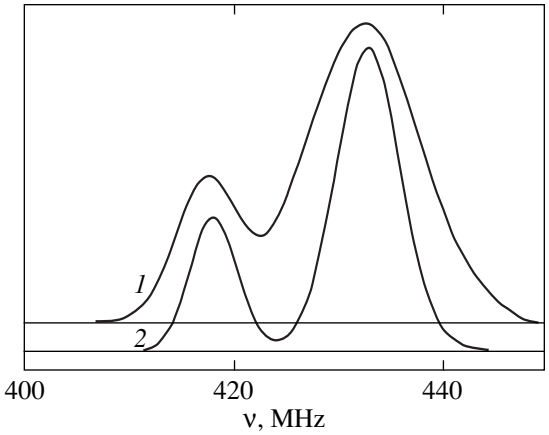

Fig. 4. NMR spectra of ^{55}Mn nuclei of Mn^{3+} ions in $Li_{0.5}Fe_{2.5}O_{12}$: Mn at $T = 77$ K, recorded from the 2τ (curve *1*) and 4τ (curve *2*) echo signals.

echo signal at $t_1 = t_2 = 0.7$ μs. In addition to the ordinary 2τ echo signal, echo signals 4τ and 6τ were also observed experimentally. The formation of additional echo signals was observed for $t_1 > t_2$, which agrees with the theoretical peculiarities of the formation of multiquantum echoes. Curves *2* and *3* in Fig. 3 are the NMR spectra recorded from the 4τ and 6τ echo signals at $t_1 = 1.1$ μs and $t_2 = 0.6$ μs. Each of the spectra presented in Fig. 3 was normalized to the maximum value of its amplitude.

At present, data on the local symmetry of the surroundings of the Mn^{4+} ions in the perovskite $GdCu_3Mn_4O_{12}$ are not available in the literature. The presence of experimentally observed multichannel echo signals is an indication of the quadrupole splitting of the NMR specturm and, by extension, of the local symmetry of the positions of Mn^{4+} ions being lower than cubic. A possible interpretation of the experimentally observed NMR spectra may be based on the facts that (i) the local fields are anisotropic on the ^{55}Mn nuclei, i.e., the magnetic field B and the quadrupole interaction energy ω_q are functions of the angle θ between the electron magnetization vector and the local crystallographic axis;[2] (ii) the sample is inhomogeneous in angle θ.

According to the theoretical results (Fig. 1), the 4τ echo spectrum must not contain extreme quadrupole satellites. This is manifested experimentally in the form of a decrease in the relative intensity of the spectrum in the high-frequency region and in the formation of a resolved spectral structure (curve 2 in Fig. 3). The 6τ echo spectrum must not contain any quadrupole satellites. This is observed experimentally as a narrowing of the spectral line with an increase in the time at which the echo signal is formed (Fig. 3). Thus, the experimentally observed properties of multiquantum echo signals on ^{55}Mn nuclei in $GdCu_3Mn_4O_{12}$ qualitatively confirm the theoretical results.

Experiments on the formation of spin echo signals from the ^{55}Mn nuclei were also carried out on a sample of the spinel $Li_{0.5}Fe_{2.5}O_4$: Mn at a temperature $T = 77$ K. The NMR spectra presented in Fig. 4 correspond to the resonance of the ^{55}Mn nuclei of Jahn–Teller ions Mn^{3+} occupying B positions in the investigated spinel. The NMR spectrum recorded from the 2τ echo reflects the inhomogeneous broadening of the spectral line caused by the anisotropy of local fields at Mn nuclei [12].

In addition to the 2τ echo signal, we also observed experimentally an additional 4τ echo signal. A comparison of the conditions of formation of this signal with the theoretical results (dependence of the echo amplitude on the duration of exciting pulses and the amplitude of the varying magnetic field) indicates that the 4τ echo is a multiquantum echo signal from a quadrupole nucleus. In the NMR spectrum recorded from the 4τ echo, a narrowing of the spectral lines caused by the disappearance of extreme quadrupole satellites is observed experimentally (Fig. 4). This agrees with the theoretical results. Experiments aimed at recording the NMR spectra from the 6τ echo in $Li_{0.5}Fe_{2.5}O_4$: Mn were not successful, apparently due to a more rapid attenuation of this signal compared to the 2τ and 4τ echo signals.

Thus, numerical simulation of the processes of formation of multiquantum echo signals from quadrupole nuclei with half-integral spin in spin systems with nonuniform broadening of the spectral line shows that the formation of multiquantum echo signals is only possible in the case of a nonzero quadrupole interaction ω_q. For the optimal formation of two-pulse multiquantum

[2] In the general case, when the local symmetry of a position is lower than the uniaxial symmetry, the description of the anisotropy under consideration requires two angles, viz., θ and φ [2].

echo signals, the first exciting pulse must be longer than the second: $t_1 = (2.25 \pm 0.75)t_2$. In contrast to the ordinary 2τ echo signal, the amplitude of the multiquantum echo signals depends not only on the duration of the exciting pulses, but also on the ratio of the amplitude ω_1 of the varying magnetic field to the quadrupole interaction ω_q. The maximum amplitude of the multiquantum echo signals is realized under the condition $\omega_1 \approx \omega_q$.

For nuclei with a half-integral spin, echo signals are formed at the instants of time $t = n\tau$, where $n = 2, 4, \ldots, (2I + 1)$, irrespective of the nature of inhomogeneous broadening. Spectral lines corresponding to the frequency ω_0 of a purely magnetic spectroscopic transition, as well as the frequencies $\omega_0 \pm k\omega_q$ [$k = 2, 4, \ldots, (2I - 1)$] of quadrupole satellites, are recorded in the 2τ echo spectrum. A delay of 2τ in the formation of the echo signal leads to the disappearance of two extreme quadrupole satellites in the spectrum of this echo signal. A complete disappearance of quadrupole satellites takes place in the spectra of multiquantum echo signals formed at the instant of time $t = (2I + 1)\tau$.

The theoretical results for quadrupole nuclei with spins $I = 5/2$ and $7/2$ agree with the results obtained earlier for quadrupole nuclei with spin $I = 3/2$ [5]. The experimental data on multiquantum echoes from ^{55}Mn nuclei with spin $I = 5/2$ in the perovskite $GdCu_3Mn_4O_{12}$ and the spinel $Li_{0.5}Fe_{2.5}O_4$: Mn qualitatively confirm the theoretical results. Supplementary echo signals in the NMR of quadrupole nuclei ^{59}Co with spin $I = 7/2$ in magnetically ordered materials were also observed in experiments [13]. However, the authors of [13] focused on the kinetics of echo attenuation, rather than the spectral properties of the echo signals.

ACKNOWLEDGMENTS

The authors are grateful to V.K. Prokopenko for his help in recording the NMR spectra, to I.O. Troyanchuk for synthesizing the perovskite samples, and to V.N. Berzhanskiĭ for fruitful discussions of the results of this research.

REFERENCES

1. M. I. Kurkin and E. A. Turov, *NMR in Magnetically Ordered Materials and Its Applications* (Nauka, Moscow, 1990).
2. A. Abragam, *The Principles of Nuclear Magnetism* (Clarendon Press, Oxford, 1961; Inostrannaya Literatura, Moscow, 1963).
3. I. Solomon, Phys. Rev. **110** (1), 61 (1958).
4. G. N. Abelyashev, V. N. Berzhanskiĭ, N. A. Sergeev, and Yu. V. Fedotov, Zh. Éksp. Teor. Fiz. **94** (1), 227 (1988) [Sov. Phys. JETP **67**, 127 (1988)].
5. G. N. Abelyashev, V. N. Berzhanskiĭ, *et al.*, Zh. Éksp. Teor. Fiz. **100** (6), 1981 (1991) [Sov. Phys. JETP **73**, 1096 (1991)].
6. V. N. Berzhanskiĭ, A. I. Gorbovanov, and S. N. Polulyakh, Zh. Éksp. Teor. Fiz. **115** (6), 2106 (1999) [JETP **88**, 1151 (1999)].
7. G. N. Abelyashev, V. N. Berzhanskiĭ, S. N. Polulyakh, *et al.*, Zh. Éksp. Teor. Fiz. **100** (4), 1255 (1991) [Sov. Phys. JETP **73**, 693 (1991)].
8. V. I. Tsifrinovich, Zh. Éksp. Teor. Fiz. **94** (7), 208 (1988) [Sov. Phys. JETP **67**, 1413 (1988)].
9. A. Losche, *Kerninduktion* (Deutsche Verlag der Wissenschaften, Berlin, 1957; Inostrannaya Literatura, Moscow, 1963).
10. P. P. Man, Phys. Rev. B **52** (13), 9418 (1995).
11. F. P. Korshikov, I. O. Troyanchuk, L. A. Bashkirov, *et al.*, Fiz. Tverd. Tela (St. Petersburg) **29** (1), 210 (1987) [Sov. Phys. Solid State **29**, 117 (1987)].
12. V. Ya. Mitrofanov, A. Ya. Fishman, and A. A. Shemyakov, Pis'ma Zh. Éksp. Teor. Fiz. **61** (7), 570 (1995) [JETP Lett. **61**, 581 (1995)].
13. V. O. Golub, V. V. Kotov, A. N. Pogorelyĭ, and Yu. A. Pod'elets, Fiz. Tverd. Tela (Leningrad) **31** (11), 48 (1989) [Sov. Phys. Solid State **31**, 1864 (1989)].

Translated by N. Wadhwa

Physics of the Solid State, Vol. 42, No. 9, 2000, pp. 1680–1687. Translated from Fizika Tverdogo Tela, Vol. 42, No. 9, 2000, pp. 1633–1640.

MAGNETISM AND FERROELECTRICITY

Calculation of the Field of a Lattice of Point Magnetic Dipoles

E. V. Rozenfel'd

Institute of Metal Physics, Ural Division, Russian Academy of Sciences, ul. S. Kovalevskoĭ 18, Yekaterinburg, 620219 Russia
e-mail: rosenfeld@imp.uran.ru

Received in final form February 16, 2000

Abstract—The magnetic field **H** produced by a spatially periodic distribution of point magnetic dipoles is expanded in a Fourier series. Because of a rapid (exponential) falloff of its harmonic amplitudes, the field **H** at an arbitrary point is the sum of the fields of only several nearest layers (or chains) of dipoles. The method is applied to calculate the magnetic fields at interstitial sites of Sm in different antiferromagnetic states. © *2000 MAIK "Nauka/Interperiodica".*

INTRODUCTION

The problem of calculating the magnetic field at different points of a unit cell of a crystalline magnet arises rather frequently in solid state physics. In particular, this problem is central in interpreting the results of muon experiments, which allow one to determine local magnetic fields at interstitial sites. There are several contributions to the local field in a crystal: the demagnetizing field, the Lorentz field, the Fermi field, and the field of the lattice of point magnetic dipoles. The methods of calculating the first three contributions and some of the problems that arise in this case are discussed in [1–3]. The last contribution, i.e., the field produced at an arbitrary point **r** by the system of dipoles $\mathbf{m}_\nu$ localized at points $\mathbf{R}_\nu$, is given by the expression

$$\mathbf{H}_{\text{dip}}(\mathbf{r}) = \sum_\nu \frac{3\mathcal{R}_\nu(\mathcal{R}_\nu\mathbf{m}_\nu) - \mathbf{m}_\nu\mathcal{R}_\nu^2}{\mathcal{R}_\nu^5}, \quad (1)$$
$$\mathcal{R}_\nu = \mathbf{r} - \mathbf{R}_\nu,$$

and usually no problems arise in calculating this field. The only complication is posed by the fact that the terms in Eq. (1) decrease slowly with increasing $\mathcal{R}$ and, therefore, the summation should be performed over a very large number of coordination shells.

The situation becomes far less clear when one not only calculates the field of a lattice of point dipoles by Eq. (1) at a specific point, but also analyzes the contributions to this field from different groups of dipoles. This analysis is too difficult to be practical, especially in the case of complex magnetic structures, because only in exceptional cases may the contribution from the nearest dipoles be dominant over that from distant coordination shells. In this regard, the experimental data reported in [4] are suggestive. According to those data, the field acting on a muon in a sample was virtually unaffected when the sample underwent the phase transition from the ferromagnetic to an antiferromagnetic state. To our knowledge, this result still remains unexplained. In general, when the dipole fields are analyzed, the situation is clear only for points of a high (cubic or higher) symmetry; according to a well-known theorem, the field equals zero at these points.

Thus, it is of interest to separate a few parts of the lattice that make dominant contributions to the field at a given point. Of course, there are virtually an infinitely large number of ways in which a variety of terms in the sum in Eq. (1) can be grouped together so that the fields produced by some groups cancel each other. However, it seems natural to consider the partitions for which the parts of the lattice producing dominant contributions to the field have a rather simple geometrical form and are closer to the point at which the field is calculated than for other partitions.

The objective of this paper is to develop a technique that allows one to reduce the problem of calculating the dipole field at an arbitrary point to a calculation of the field produced at this point by a few atomic planes or chains nearest to the point. The contributions from the remaining atoms of the lattice are determined in the continuum approximation with any preset degree of accuracy. It is important that the calculation of the field of atomic planes or chains does not also involve sums of a large number of terms. In order to calculate $\mathbf{H}_{\text{dip}}(\mathbf{r})$to the required precision, it is sufficient to take into account only several Fourier harmonics of the field of an atomic plane or a chain (the number of these harmonics depends on the position of the point **r**).

The existence of such a convenient representation of the dipole field is due to the fact that the field of a one-dimensional (chain) or a two-dimensional (atomic plane) periodic dipole array falls off rapidly (exponentially) with distance from it. At a distance equal to three or four lattice parameters, the field of an atomic plane virtually vanishes, while the field of a chain becomes identical to that of a uniformly magnetized line. The corresponding formulas and estimates of their accuracy are presented in Section 1.

1063-7834/00/4209-1680$20.00

Usually, Eq. (1) is used to calculate $\mathbf{H}_{dip}(\mathbf{r})$ in a finite volume (sphere, as a rule). Outside this volume, the magnetization distribution is assumed to be continuous, which leads to an additional contribution, namely, the Lorentz field. The distinctive feature of the technique proposed in this paper is that the volume in which the discrete structure of the lattice is explicitly taken into account is infinite in one or two dimensions. The problem of calculating the Lorentz field in this case is discussed in Section 2. The results obtained are illustrated in Section 3 by the example of calculating the magnetic field at interstitial sites of different types in samarium in two different antiferromagnetic states.

1. FOURIER TRANSFORM OF THE FIELD OF SIMPLEST LATTICES

The Fourier transform is given by the standard formulas

$$f(x) = \frac{A_0}{2} + \sum_{k=1}^{\infty}\left\{A_k\cos\left(2\pi k\frac{x}{a}\right) + B_k\sin\left(2\pi k\frac{x}{a}\right)\right\},$$

$$A_k = \frac{2}{a}\int_0^a f(x)\cos\left(2\pi k\frac{x}{a}\right)dx, \qquad (2)$$

$$B_k = \frac{2}{a}\int_0^a f(x)\sin\left(2\pi k\frac{x}{a}\right)dx.$$

In the case of a periodic function of two or more variables, these formulas are written for each of its arguments.

1.1. Linear Chain

Let us consider a chain of identical dipoles $\mathbf{m}(m_\parallel, 0, m_\perp)$ located along the x axis at regular intervals equal to a (Fig. 1). The field of this chain is given by

$$\mathbf{H}^{\text{line}}(\mathbf{r}) = \sum_{n=-\infty}^{\infty}\frac{3\mathcal{R}_n(\mathcal{R}_n\mathbf{m}) - \mathbf{m}\mathcal{R}_n^2}{\mathcal{R}_n^5}, \qquad (3)$$
$$\mathcal{R}_n = (x - na, y, z).$$

This field is a periodic function of x with a period a and can be expanded in a Fourier series of Eq. (2). The integral over a period in Eq. (2) and the sum over sites in Eq. (3) are combined to give an integral with respect to x between infinite limits, which is easily reduced to MacDonald functions. As a result, the components of the field of Eq. (3) are found to be

$$H_x^{\text{line}} = h_x^{\text{line}} + \frac{2q^3}{\pi}\sum_{k=1}^{\infty}k^2\{-m_\parallel K_0(qk\rho)\cos(qkx) + m_\perp K_1(qk\rho)\cos(\varphi)\sin(qkx)\},$$

$$H_y^{\text{line}} = h_y^{\text{line}} + \frac{2q^3}{\pi}\sum_{k=1}^{\infty}k^2\{m_\perp K_2(qk\rho)\cos(\varphi)\cos(qkx) + m_\parallel K_1(qk\rho)\sin(qkx)\}\sin(\varphi), \qquad (4)$$

$$H_z^{\text{line}} = h_z^{\text{line}} + \frac{q^3}{\pi}\sum_{k=1}^{\infty}k^2\{m_\perp[K_0(qk\rho) + K_2(qk\rho)\cos(2\varphi)]\cos(qkx) + 2m_\parallel K_1(qk\rho)\cos(\varphi)\sin(qkx)\}.$$

Here, $q = 2\pi/a$; $\mathbf{m}_\parallel$ and $\mathbf{m}_\perp$ are the components of $\mathbf{m}$ parallel to the x axis and to the yz plane, respectively; ρ is the projection of $\mathbf{r}$ onto the yz plane; and φ is the angle between $\mathbf{m}_\perp$ and ρ. In Fig. 1, which illustrates this notation, and in Eq. (4), the vector $\mathbf{m}_\perp$ is assumed to be parallel to the z axis.

The theory of Bessel functions gives the following expression for the Macdonald functions for large values of u:

$$K_\mu(u) \approx \sqrt{\frac{\pi}{2u}}\exp(-u)[1 + O(1/u)]. \qquad (5)$$

In particular, at $\mu = 0$, 1, and 2, the values $u > 10$ can be considered to be large. In this case, we have $K_\mu(2\pi) \approx 10^{-3}$, $K_\mu(4\pi) \approx 10^{-6}$, and $K_\mu(8\pi) \approx 10^{-12}$. Therefore, if the distance of the point $\mathbf{r}$ from the chain is $\rho > 3$–$4a$, the contributions from higher Fourier harmonics virtually vanish and the field of the chain becomes identical to the field of a uniformly magnetized line with a linear magnetic moment density $\mathbf{m}/a$,

$$h_x^{\text{line}} = 0,$$
$$h_y^{\text{line}} = \frac{2m_\perp}{a\rho^2}\sin(2\varphi), \quad h_z^{\text{line}} = \frac{2m_\perp}{a\rho^2}\cos(2\varphi). \qquad (6)$$

Thus, the field of a chain magnetized along its axis is practically zero at distances larger than 2–3 times its

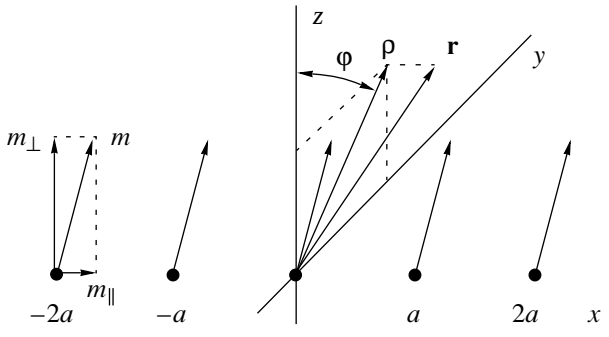

Fig. 1. Chain of magnetic dipoles $\mathbf{m}(m_\parallel, 0, m_\perp)$: φ is the angle that the projection ρ of the position vector $\mathbf{r}$ onto the yz plane makes with the z axis.

period. From Eq. (6), it also follows that, if the lateral surface of a cylinder is uniformly covered with magnetized chains, the magnetic field on the axis of the cylinder is also zero.

At small ρ, however, higher harmonics become more important. The reason for this will become clear if we consider the x dependence of the field of the chain at a distance $\rho \approx a$ from its axis. According to Eq. (3), the field near any site is produced, for the most part, by the magnetic moment localized on this site. Therefore, the x dependence of the field is a set of peaks localized near each site. The peaks become progressively narrower and higher with decreasing ρ, and their shape is adequately described by the function $((x - na)^2 + \rho^2)^{-3/2}$; hence, their width is of the order of ρ and their height is proportional to ρ^{-3}. This "comb" can be adequately represented by a Fourier series with a finite number of terms if the wavelength of the Fourier harmonic with the maximum index $k_{\max}$ is fairly small in comparison to the peak width. For instance, if $k_{\max} = 5a/\rho$, the relative accuracy of the approximation in the region $\rho > a/1000$ will be $\delta < 10^{-5}$, quite sufficient for practical purposes.

1.2. Planar Rectangular and Hexagonal Lattices

Let the xy plane be uniformly covered with such chains, with the separation between them being b. If there is no shift of the chains along the x axis, this system can be considered as a set of chains with a period b, which are parallel to the y axis and spaced at regular intervals equal to a. Using the expansion into a Fourier series in x and y as in Eq. (2), we obtain[1]

$$\begin{aligned}\mathbf{H}^{\text{plane}}(\mathbf{r}) = \frac{8\pi^2}{ab}\sum_{k,l=0}^{\infty}\Bigg\{&\mathbf{A}_{l,k}\cos\left(\frac{2\pi}{a}kx\right)\cos\left(\frac{2\pi}{b}ly\right)\\ &+\mathbf{B}_{l,k}\cos\left(\frac{2\pi}{a}kx\right)\sin\left(\frac{2\pi}{b}ly\right)\\ &+\mathbf{C}_{l,k}\sin\left(\frac{2\pi}{a}kx\right)\cos\left(\frac{2\pi}{b}ly\right)\\ &+\mathbf{D}_{l,k}\sin\left(\frac{2\pi}{a}kx\right)\sin\left(\frac{2\pi}{b}ly\right)\Bigg\}\exp\{-2\pi Q_{l,k}|z|\},\end{aligned} \tag{7}$$

where the term with $k = l = 0$ is absent and the following notation has been introduced:

$$Q_{l,k} = \sqrt{\left(\frac{k}{a}\right)^2 + \left(\frac{l}{b}\right)^2},$$

$$\begin{Bmatrix}A^{(x)}_{l,k}\\ A^{(y)}_{l,k}\\ A^{(z)}_{l,k}\end{Bmatrix} = \frac{2-\delta_{l,k,0}}{Q_{l,k}}\begin{Bmatrix}-Q^2_{0,k}m_x\\ -Q^2_{l,0}m_y\\ +Q^2_{l,k}m_z\end{Bmatrix},$$

$$\begin{Bmatrix}D^{(x)}_{l,k}\\ D^{(y)}_{l,k}\\ D^{(z)}_{l,k}\end{Bmatrix} = \frac{2Q_{l,0}Q_{0,k}}{Q_{l,k}}\begin{Bmatrix}m_y\\ m_x\\ 0\end{Bmatrix}, \tag{8}$$

$$\begin{Bmatrix}B^{(x)}_{l,k}\\ B^{(y)}_{l,k}\\ B^{(z)}_{l,k}\end{Bmatrix} = \operatorname{sgn}(z)(2-\delta_{k,0})Q_{l,0}\begin{Bmatrix}0\\ m_z\\ m_y\end{Bmatrix},$$

$$\begin{Bmatrix}C^{(x)}_{l,k}\\ C^{(y)}_{l,k}\\ C^{(z)}_{l,k}\end{Bmatrix} = \operatorname{sgn}(z)(2-\delta_{l,0})Q_{0,k}\begin{Bmatrix}m_z\\ 0\\ m_y\end{Bmatrix}.$$

It is seen that the field falls off exponentially with distance from the plane. In fact, this means that the field at any point is determined fundamentally by the two or three atomic planes nearest to this point and the contributions from the other atomic planes can be neglected.

As in the case of a linear chain, at small $|z|$, there are peaks in the x and y dependences of the field given by Eq. (7); the peaks are positioned at sites, and their width is of the order of $|z|$. Hence, in this case, too, the maximum indices $k_{\max}$ and $l_{\max}$ of the harmonics kept in the Fourier series are determined by the value of $|z|$ and the required precision.

The field of a planar hexagonal lattice is also easily calculated using Eqs. (7) and (8). This lattice with an interatomic spacing a can be considered as a combination of two identical planar rectangular sublattices with unit-cell parameters a and $a\sqrt{3}$ along the x and y axes, respectively. The sublattices are shifted relative to each other in such a way that the sites of one of them are at the centers of unit cells of the other. Therefore, the x and y coordinates of an arbitrary point defined relative to the central sites (origins of coordinates) of the sublattices differ by exactly half the periods along the x and y axes, respectively. Furthermore, in the sum of the contributions with arbitrary indices l and k to the field produced by these two sublattices, the factor $[1 + (-1)^{k+l}]$ appears, and we obtain formulas identical to Eqs. (7) and (8) with the following two changes: (i) the parameter b is replaced by $a\sqrt{3}$, and (ii) only the terms with $l + k$ even are kept in the sum in Eq. (7), and the sum is doubled.

[1] At first glance, it may appear that the part of Eq. (7) that is an odd function of z does not vanish when $z \to 0$. However, this is not the case, which can be shown using identities such as $\lim_{a\to 0}\sum_{\nu=1}^{\infty}\nu e^{-\nu a}\sin(\nu t) = 0$, and $\lim_{a\to 0}\sum_{\nu=1}^{\infty}e^{-\nu a}\cos(\nu t) = -1/2$.

1.3. Three-Dimensional Lattices

The formulas obtained above are very convenient for computations and analysis of contributions to the field. Equation (7) for **H** can be transformed into a translationally invariant expression when needed (say, when calculating the electronic spectrum). For this purpose, Eq. (7) should also be expanded into a Fourier series in *z*, which is easily performed using the well-known identities

$$\int_0^\infty e^{-px}\begin{Bmatrix}\sin(Qx)\\ \cos(Qx)\end{Bmatrix}dx = \frac{1}{Q^2+p^2}\begin{Bmatrix}Q\\ p\end{Bmatrix}. \qquad (9)$$

If all the magnetized planes perpendicular to the *z* axis are identical and located at regular intervals *c* along *z*, Eq. (9) can be applied immediately to the field in Eq. (7) by putting $Q = 2\pi/c$. In the case of more complex lattices, these can always be represented as a combination of the simplest sublattices and the total field can be obtained by adding the fields of the sublattices.

For reasons of space, we do not present here the simple, but rather cumbersome, formulas for three-dimensional lattices. We merely note that those expressions appear asymmetrical with respect to *x*, *y*, and *z*, as well as to *a*, *b*, and *c*, although the symmetry actually takes place. The reason for this is the order of priority of expansions into a Fourier series in *x*, *y*, and *z*, but the symmetrization can be easily performed when needed (see also footnote 1).

2. THE LORENTZ FIELD

Local fields in crystals are generally calculated by the Lorentz method. According to this method, a relatively large volume $\mathcal{V}$ is separated around the point at which the field is to be found, and the contribution to the field from this volume is calculated with regard to the discrete structure of the lattice. Outside this volume, the continuum approximation is used and the magnetic dipoles are assumed to be uniformly "smeared" over their unit cell rather than localized at the lattice sites. The contribution from the continuous dipole distribution to the field at a point **r** is [1]

$$\mathbf{H}_{\text{cont}}(\mathbf{r}) = \mathbf{H}_\text{L}(\mathbf{r}) + \mathbf{H}'(\mathbf{r}), \quad \mathbf{H}_\text{L}(\mathbf{r}) = \int_{S(\mathcal{V})}\frac{\overline{\mathcal{R}}}{\mathcal{R}^3}(\mathbf{I}(\mathbf{r}')d\mathbf{s}),$$

$$\mathbf{H}'(\mathbf{r}) = -\int_{\mathbf{r}'\notin\mathcal{V}}\frac{\overline{\mathcal{R}}}{\mathcal{R}^3}\rho_m(\mathbf{r}')d\mathbf{r}' + \int_S\frac{\overline{\mathcal{R}}}{\mathcal{R}^3}(\delta\mathbf{I}(\mathbf{r}')d\mathbf{s}), \qquad (10)$$

$$\rho_m(\mathbf{r}) = -\text{div}(\mathbf{I}(\mathbf{r})), \quad \delta\mathbf{I}(\mathbf{r}) = \mathbf{I}_2(\mathbf{r}) - \mathbf{I}_1(\mathbf{r}),$$

$$\overline{\mathcal{R}} = \mathbf{r}' - \mathbf{r}.$$

Here, $\mathbf{I}(\mathbf{r})$ is the magnetization (total magnetic moment density) at the point **r** and $\delta\mathbf{I}(\mathbf{r})$ is the discontinuous change in magnetization at the point **r** on the interface *S* of two magnetic media (*1* and *2*), specifically, on the surface of the body. The field is produced both by inhomogeneities of the magnetization inside the body (their contribution is proportional to the volume magnetic charge density ρ_m) and by the discontinuity in magnetization $\delta\mathbf{I}$, giving rise to a surface magnetic charge density proportional to it.

The field arising from the discontinuity in magnetization on the surface $S(\mathcal{V})$ of the volume $\mathcal{V}$ is the Lorentz field $\mathbf{H}_\text{L}$. Assuming the magnetization to be the same everywhere over this surface and equal to $\mathbf{I}(\mathbf{r})$, we obtain that the Lorentz field is proportional to $\mathbf{I}(\mathbf{r})$, with the coefficient of proportionality being dependent only on the shape of the surface $S(\mathcal{V})$,

$$\mathbf{H}_\text{L} = 4\pi\mathcal{N}\mathbf{I}(\mathbf{r}), \quad \mathcal{N} = \frac{1}{4\pi}\int_{S(\mathcal{V})}\frac{\overline{\mathcal{R}}}{\mathcal{R}^3}(\mathbf{n}d\mathbf{S}). \qquad (11)$$

Here, **n** is the unit vector along the direction of $\mathbf{I}(\mathbf{r})$ and $\mathcal{N}$ is the demagnetizing factor of the volume $\mathcal{V}$. Specifically, if the surface $S(\mathcal{V})$ is a sphere, $\mathcal{N} = 1/3$ and we obtain a standard expression $\mathbf{H}_\text{L} = 4\pi\mathbf{I}(\mathbf{r})/3$. The contribution $\mathbf{H}'$ from other inhomogeneities and discontinuities in magnetization is generally called the demagnetizing field.

Formulas (10) are obtained immediately from Eq. (1) by converting the sum to an integral (for more details, see [2, 3]). The surface integrals in Eqs. (10) arise when the space integral over the region outside the volume $\mathcal{V}$ is transformed using standard formulas of vector analysis, specifically, the Ostrogradskiĭ–Gauss theorem. Therefore, the surface integrals of this type, proportional to the normal component of the magnetization, have no physical interpretation. This is an explanation of why, in the continuum approximation, there appear additional contributions from discontinuities in magnetization at surfaces that are absent in the sum of the fields of point dipoles.

With the expressions for Fourier series derived in the preceding section, the field at an arbitrary point in the crystal can be written as

$$\begin{aligned}\mathbf{H}(\mathbf{r}) &= \mathbf{H}^{(\text{F})}(\mathbf{r}) + \mathbf{H}_{\text{cont}}(\mathbf{r})\\ &= \mathbf{H}^{(\text{F})}(\mathbf{r}) + \mathbf{H}_\text{L}(\mathbf{r}) + \mathbf{H}'(\mathbf{r}).\end{aligned} \qquad (12)$$

Here, $\mathbf{H}^{(\text{F})}$ is the contribution from dipoles whose field is included in the Fourier series and $\mathbf{H}_{\text{cont}}$ is the contribution from the remainder of the dipole lattice whose magnetization is considered as being continuously distributed. It remains to be seen why the lattice sites cannot all be taken into account in the field $\mathbf{H}^{(\text{F})}$ and how the Lorentz field can be calculated in the case where the volume $\mathcal{V}$ is infinite in one or two dimensions.

Let us first consider the simplest case where $\mathbf{H}^{(\text{F})}$ is the sum of the fields produced by several nearest atomic planes and described by Eq. (7). This sum can include

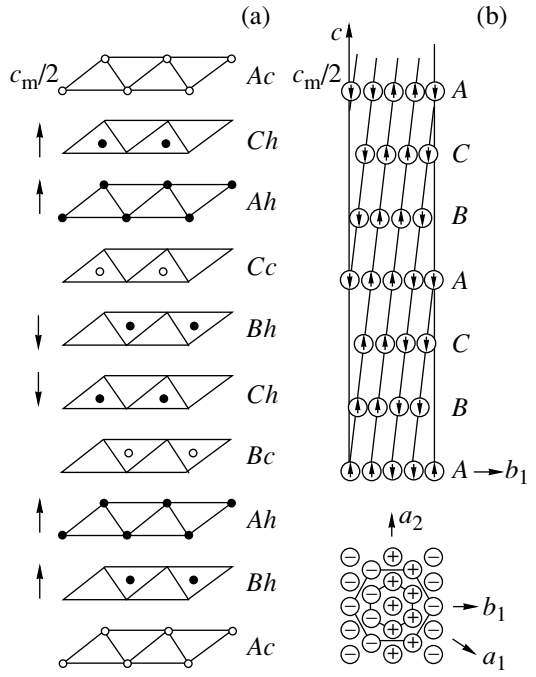

Fig. 2. Ordering of magnetic moments in hexagonal layers in Sm (the figure is taken from [5]): (a) at high temperatures $T_2 < T < T_1$, the magnetic moments are ordered (in the directions indicated by arrows) in *h* layers, in which the first coordination shell of an atom has hexagonal symmetry, but the moments are disordered in *c* layers, in which the coordination shells have cubic symmetry; and (b) at low temperatures $T < T_2$, the moments are ordered in *c* layers (only these layers are shown at the top of the figure, while at the bottom, the distribution of magnetic moments is presented for atoms in a *c* layer).

more distant planes, but the result will be virtually the same, because the field of a plane falls off exponentially with distance from the plane. However, only the total field of the entire infinite plane falls off exponentially; this is due to the fact that the contributions from the "central" (nearest to the point of observation) and the "peripheral" parts of the plane almost completely cancel each other. If a body of an arbitrary shape is divided into plane-parallel layers, only the layers that are nearest to the point of observation can be considered "infinite." For layers more distant from this point, the peripheral parts are smaller and the contribution from such a layer to the field at the point of observation becomes nonzero.

In this case, the "Lorentz volume" is a planar, infinitely thin (macroscopically) layer parallel to a chosen atomic plane. If the component of the magnetization at the point **r** along the direction perpendicular to this plane is $\mathbf{I}_\perp(\mathbf{r})$, then the Lorentz field is $\mathbf{H}_L(\mathbf{r}) = 4\pi\mathbf{I}_\perp(\mathbf{r})$, because the demagnetizing factor of a planar disk in the direction perpendicular to its plane equals unity.

The case where $\mathbf{H}^{(F)}$ is the sum of the fields of several parallel atomic chains described by Eq. (4) can be treated in much the same way. It is convenient to consider the chains that lie within a cylinder of a radius *R* whose axis passes through the point **r**. As was indicated above, the sum of the fields of chains evenly distributed over the surface of a cylinder equals zero at its axis [see Eqs. (4), (6)]. Because the distribution of chains over the cylinder becomes much more uniform as its radius increases, it will suffice to take into account only the chains within an infinitely thin (macroscopically) cylinder. Again, this is true only for infinitely long chains, for which the contributions from the central and peripheral regions cancel each other. Therefore, the Lorentz field equals the field of the cylinder, and we obtain $\mathbf{H}_L(\mathbf{r}) = 2\pi\mathbf{I}_\perp(\mathbf{r})$, where $\mathbf{I}_\perp(\mathbf{r})$ is the projection of $\mathbf{I}(\mathbf{r})$ onto the plane perpendicular to the chains.

In both cases, according to Eq. (12), the demagnetizing field must be added to the Lorentz field. In a sample in the form of a thin planar disk, the fields $\mathbf{H}_L$ and $\mathbf{H}'$ cancel each other if $\mathbf{H}^{(F)}$ is calculated for the planes parallel to the disk plane. For a thin cylindrical sample, we have $\mathbf{H}_{cont} = 0$, if $\mathbf{H}^{(F)}$ is calculated as the sum of the fields of chains parallel to the axis of the cylinder. Thus, the contributions can be redistributed between the different terms in Eq. (12), but the final result is, naturally, independent of the way of calculating $\mathbf{H}^{(F)}$.

3. LOCAL FIELDS IN SAMARIUM

A rhombohedral lattice of samarium consists of nine periodically repeated hexagonal layers *ABABCBCAC*… (see Fig. 2 taken from [5]). Within a period, the pairs of atomic layers in which the symmetry of the first coordination shell of an atom is identical to that of an *hcp* lattice are separated by layers of atoms whose first coordination shell has cubic symmetry. In Fig. 2a, these layers are marked with indices *h* and *c*, respectively. The lattice parameters are $a = 3.631$ and $c = 26.035$ Å and, hence, the separation *d* between hexagonal layers is 2.893 Å.

Studies by different methods revealed (see [5, 6] and the references therein) that samarium undergoes two antiferromagnetic phase transitions at temperatures $T_1 \approx 106$ and $T_2 \approx 14$ K. The high-temperature phase transition is accompanied by ferromagnetic ordering of magnetic moments in *h* layers along the *z* axis. In this case, in a pair of adjacent *h* layers, the ordering is ferromagnetic, while pairs of *h* layers separated by a *c* layer are ordered antiferromagnetically (Fig. 2a). The magnetic moments in *c* layers are not ordered at high temperatures $T_2 < T < T_1$. In these layers, the chains of atomic dipoles parallel to the *a* axis are ordered ferromagnetically along the *z* axis only at $T < T_2$. In this case, the chains, as well as the layers, are divided into pairs, in each of which the moments of dipoles are parallel to each other, while the moments in adjacent pairs of chains, as well as in pairs of *h* layers, are antiparallel to each other, but there is no nonmagnetic spacer between the pairs of chains (Fig. 2b). The magnetic moment at any site is $m = (5/7)\mu_B$ [5].

Muon experiments revealed [6] that, in the $T_2 < T < T_1$ temperature range, the magnitude of the magnetic field acting on a muon in a Sm crystal can have two different values. Figure 3 shows the temperature dependences of the magnetic inductions of these fields, B_1 and B_2, taken from [6]. The presence of only two magnetically nonequivalent positions was interpreted in [6] as the presence of only two crystallographic positions, and the inference was drawn that muons occupy only octahedral, but not tetrahedral, interstitial sites. The authors of [6] also pointed out that the ratio between the magnitudes of the magnetic field acting on muons at these two nonequivalent positions was indirect evidence in favor of this conclusion. The fields in octahedral interstices between two *h* layers and between *h* and *c* layers (*hh* and *hc* interstices, respectively) as calculated in [6] are 1.75 and 0.88 kOe, respectively; that is, they differ by a factor of two. The experimental values of the ratio between these fields are also about two at temperatures in the vicinity of T_1. However, it should be noted that, when B_2 reaches saturation (Fig. 3), its experimental value is about three times larger than the calculated one.

The growth in the field B_1 with decreasing temperature is explained in [6] by the magnetization of itinerant electrons in the regions between *h* and *c* layers, which is heavily temperature-dependent. Assuming that the field acting on these electrons is proportional to B_2 and that the temperature dependence of their paramagnetic susceptibility follows the Curie–Weiss law, the authors of [6] arrived at the formula

$$B_1(T) = 47\left(1 + \frac{18}{T + 6.7}\right)B_2(T), \qquad (13)$$

which is in excellent agreement with the experimental data (Fig. 3). However, this explanation assumes the presence of antiferromagnetic exchange characterized by a Néel temperature that is of the same order of magnitude as the paramagnetic temperature in Eq. (13), namely, 6.7 K. The exchange with $T_N = T_2$ does exist in *c* layers (as pointed out in [6]), but the physical meaning of this exchange is not clear in the case of itinerant electrons. At the same time, it is obvious that the total field (no matter whether it is magnetic or molecular) exerted on *c* layers by *h* layers is zero. For this reason, the possible ordering of atomic moments in *c* layers at $T > T_2$ was not considered in [6].

In our opinion, the discussion of experimental data in [6] did not answer the following three critical questions: (a) Why do the experiment and calculations give the same value for the ratio between the fields at *hh* and *hc* interstitial sites but essentially different values for the magnitudes of these fields? (b) Does the fact that the experimentally measured field acting on muons in a crystal has only two different values signify that the muons cannot occupy tetrahedral interstitial sites? (c) Which are the precise magnetic moments

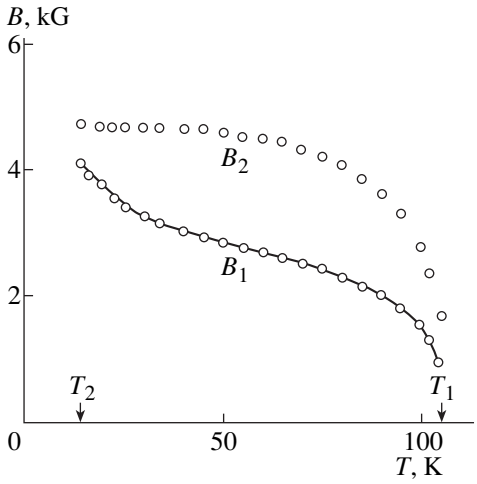

Fig. 3. Experimental values of the fields acting on a muon in Sm (the figure is taken from [6]); the smooth curve is a plot of Eq. (13).

when the ordering causes B_1 to sharply increase with decreasing temperature?

In order to answer these questions, we calculated the field at interstitial sites of different types in Sm. Assuming that the atomic moments in *c* layers are disordered in the temperature range $T_2 < T < T_1$, these fields can be found by adding up the fields $\mathbf{H}_{ferro}$ of the ferromagnetic *h* layers (see table).[2] From the table, it is seen that the field of an *h* layer very sharply decreases with distance from it. Therefore, when calculating the field at *hc* interstices, it suffices to take into account only one, the nearest *h* layer, and the two nearest layers should be considered in the case of *hh* interstices. That is why the fields at nonequivalent octahedral interstitial sites differ by a factor of two. It is also seen that, in the plane $z = \text{const} \approx d$, parallel to the *h* layer, the field of this layer rapidly oscillates in both magnitude and direction. For instance, near the sites, at points with (*x*, *y*) coordinates equal to (0, 0), ($a/2$, $\pm(a\sqrt{3})/2$), etc., the direction of the field coincides with that of the magnetic moments of the sites, whereas between the sites, at the points ($a/2$, $\pm(a\sqrt{3})/6$), etc., the magnetic field reverses its direction.

The calculated fields listed in the table coincide with the experimental values obtained in [6] for octahedral interstices, but significantly differ from those for tetrahedral interstices. At either of the two *hh* interstices, the field equals –1.60 kOe, while at two *hc* interstices, the field is –2.23 and +0.63 kOe, respectively.[3] The three fields are all parallel to the *z* axis, and the sign indicates

[2] The origin of the coordinates can coincide with any atom of the layer.

[3] In [6], the fields were found to be 2.27, 1.72, and 0.60 kOe, respectively.

Fields produced by a ferromagnetically ordered *h* layer ($\mathbf{H}_{ferro}$) and by a *c* layer ordered as shown in Fig. 2b ($\mathbf{H}_{antiferro}$) at octahedral and tetrahedral interstitial sites whose (*x*, *y*, *z*) coordinates are listed in the first column

Coordinates	$\mathbf{H}_{ferro}$	$\mathbf{H}_{antiferro}$
$\mathrm{oct}\left(\frac{a}{2}, \frac{a\sqrt{3}}{6}, \frac{d}{2}\right)$	(0, 0, –.88)	(0, –.12, .02)
$\mathrm{oct}\left(\frac{a}{2}, \frac{a\sqrt{3}}{6}, \frac{3d}{2}\right)$	(0, 0, 0)	(0, –.07, .27)
$\mathrm{oct}\left(\frac{a}{2}, \frac{a\sqrt{3}}{6}, \frac{5d}{2}\right)$	(0, 0, 0)	(0, –.02, .07)
$\mathrm{oct}\left(\frac{a}{2}, \frac{a\sqrt{3}}{6}, \frac{7d}{2}\right)$	(0, 0, 0)	(0, 0, .0.2)
$\mathrm{oct}\left(\frac{a}{2}, \frac{a\sqrt{3}}{6}, -\frac{d}{2}\right)$	(0, 0, –.88)	(0, 1.34, .0.2)
$\mathrm{oct}\left(\frac{a}{2}, \frac{a\sqrt{3}}{6}, -\frac{3d}{2}\right)$	(0, 0, 0)	(0, .29, .0.8)
$\mathrm{oct}\left(\frac{a}{2}, \frac{a\sqrt{3}}{6}, -\frac{5d}{2}\right)$	(0, 0, 0)	(0, .07, .0.2)
$\mathrm{oct}\left(\frac{a}{2}, \frac{a\sqrt{3}}{6}, -\frac{7d}{2}\right)$	(0, 0, 0)	(0, .02, 0)
$\mathrm{tet}\left(\frac{a}{2}, \frac{a\sqrt{3}}{6}, \frac{d}{4}\right)$	(0, 0, –2.23)	(0, –.11, –1.11)
$\mathrm{tet}\left(\frac{a}{2}, \frac{a\sqrt{3}}{6}, \frac{7d}{4}\right)$	(0, 0, 0)	(0, –.05, .2)
$\mathrm{tet}\left(\frac{a}{2}, -\frac{a\sqrt{3}}{6}, \frac{d}{4}\right)$	(0, 0, –2.23)	(0, –1.28, –.44)
$\mathrm{tet}\left(\frac{a}{2}, -\frac{a\sqrt{3}}{6}, \frac{7d}{4}\right)$	(0, 0, 0)	(0, –.2, .05)
$\mathrm{tet}\left(\frac{a}{2}, \pm\frac{a\sqrt{3}}{2}, \frac{3d}{4}\right)$	(0, 0, .63)	(0, ±.42, ±1.32)
$\mathrm{tet}\left(\frac{a}{2}, \pm\frac{a\sqrt{3}}{2}, \frac{5d}{4}\right)$	(0, 0, .03)	(0, ±.27, ±.34)

Note: The origin of the coordinates coincides with the center of the hexagon shown at the bottom of Fig. 2b, the *y* axis is along the b_1 axis in Fig. 2b, the *z* axis is normal to the plane of the layer, and (*x*, *y*, *z*) are the components of the magnetic field in kOe (or kG).

their orientation with respect to the magnetization of the nearest *h* layers.

In this situation, without additional experimental data, it is impossible to decisively answer the first two of the questions formulated above. Indeed, it is reasonable to suppose that, in the $T_2 < T < T_1$ range, the magnetization of itinerant electrons vanishes in *c* layers but reaches its maxima and minima in the middle between *h* layers. Then, the field exerted on a muon at different interstitial sites by itinerant electrons should be of a similar nature.[4] For the sake of simplicity, let us assume that this dependence is sinusoidal,

$$H(z) = H_0 \sin\left(\frac{\pi z}{3d}\right), \qquad (14)$$

where the $z = 0$ plane coincides with the *c* layer. Putting the amplitude H_0 equal to 6.5 kOe, we obtain the total field $H_{hc} \approx 2.4$ kOe in both tetrahedral *hc* interstices and $H_{hh} \approx 4.7$ kOe in tetrahedral *hh* interstices (Fig. 3). However, we by no means advocate that this explanation of the existence of two different fields acting on a muon in Sm is preferable to that proposed in [6]. In Eq. (14), one can put $H_0 = -2.9$ kOe and obtain the same values, close to the experimental ones, $H_{hc} \approx -2.4$ and $H_{hh} \approx -4.7$ kOe, for octahedral *hc* and *hh* interstices, respectively. It should be emphasized that now the fields $\mathbf{H}_{hc}$ and $\mathbf{H}_{hh}$, as well as $\mathbf{H}_0$, are opposite in direction to the magnetization of the nearest *h* layers.

Thus, the situation is rather complicated and is determined fundamentally by the spin density distribution function $\boldsymbol{\mu}_s(\mathbf{r})$ of itinerant electrons in a unit cell. Furthermore, one should take into account that muons can cause a redistribution of the charge and, hence, spin density of these electrons [7] and distortions of the initial magnetic lattice [8]. For this reason, it is very likely that none of the interpretations given above will prove to be true.

An even more complicated situation occurs in the low temperature range $T < T_2$, where the magnetic moments of *c* layers are ordered. The fields $\mathbf{H}_{antiferro}$ produced by a *c* layer at different points are listed in the last column of the table. Dipoles with $m > 0$ are assumed to be at the origin of coordinates and at points $(\pm a/2, (a\sqrt{3})/2, 0)$, while dipoles with $m < 0$ are at points $(\pm a/2, -(a\sqrt{3})/2, 0)$. It is seen that the field generated by a *c* layer at an octahedral interstitial site is weak when the three *c*-layer atoms nearest to the site are magnetized in one direction. However, if the interstitial site is between chains whose magnetic moments are oppositely directed, the field increases sharply and its *y* component reaches a value of 1.34 kOe. Adding up this field and the field produced at an *hc* interstice by the nearest *h* layer (directed along the *z* axis and equal to 0.88 kOe), we obtain 1.6 kOe, a value that is insignificantly different from the value of the field at an octahedral *hh* interstice (1.75 kOe).

Clearly, the presence of a muon at an *hc* interstitial site somewhat upsets the balance of the fields exerted on a *c* layer by its neighbor *h* layers. The field arising

[4] We do not identify this field with the Fermi field for reasons pointed out in [2, 3].

because of this is most likely to be of an exchange nature, and if this field is high enough, it can lead to a partial ordering in the *c* layer in accordance with Eq. (13). Of course, the ordering will not occur at large distances at $T > T_2$, but even if the three atoms nearest to the *hc* interstice are ordered (two atoms having a magnetic moment up and one atom, down), the field component perpendicular to the *z* axis will be equal to 1.13 kOe. Therefore, the total field at the octahedral *hc* interstitial site will be 1.43 kOe (cf. 1.75 kOe at an *hh* interstice). However, this explanation of the growth in B_1 with decreasing temperature is not infallible. It would be valid if the atoms of the *c* layer were antiferromagnetically ordered near the muon; that is, if the exchange integral for nearest neighbor atoms were negative. However, this is inconsistent with the results of [5], according to which this integral is positive, and it is not clear how a muon can affect the magnitudes and signs of the exchange integrals.

As is seen from the table, the fields produced by the ordered magnetic moments of a *c* layer at tetrahedral interstitial sites have an even wider spread in magnitude and direction than at octahedral interstices. This offers strong possibilities for constructing an analogous scheme to explain the temperature dependence of B_1 under the assumption that muons occupy only tetrahedral interstitial sites. However, the emergence of a nonzero magnetization in *c* layers leads to a change in the polarization of itinerant electrons. Because this polarization is of crucial importance [see Eq. (14)], the possibilities for speculations are almost limitless in this case. For this reason, the simplest qualitative estimates similar to those made above are invalid here. In order to solve the problem of the two fields acting on a muon in Sm, it seems likely that one should calculate $\boldsymbol{\mu}_s(\mathbf{r})$ in the initial lattice and consider the distortions caused by the presence of the muon. Further experimental investigations are also of considerable interest especially the measurements of the directions of local fields at low temperatures.

4. CONCLUSIONS

The formulas derived in Section 1 show that the Fourier harmonics of the field of a chain or an atomic plane composed of identical magnetic dipoles fall off very rapidly (exponentially) with distance from them. Therefore, in actuality, the field at any point of a magnet is produced only by two or three atomic planes nearest to the point. This explains, in particular, the absence of any change in the field acting on a muon when the ferromagnet–spiral-antiferromagnet phase transition occurs [4].

This fact also makes the much-simplified analysis of the contributions to the field at interstitial sites of a ferromagnet possible. Such analysis performed for samarium allows the following inferences to be drawn:

(1) If the field exerted on a muon by itinerant electrons is taken into account, the fields at two of the three inequivalent tetrahedral interstitial sites can be approximately the same. For this reason, it is not improbable that muons occupy tetrahedral, rather than octahedral, interstitial sites in Sm.

(2) The presence of a muon at any of the *hc* interstitial sites causes a change in the electron density distribution and, hence, in the exchange integral between *h* and *c* layers. As a result, the total exchange field acting on a *c* layer becomes nonzero. Therefore, the growth in one of the two fields acting on a muon [6] can be due to the local ordering of magnetic moments in the *c* layer.

ACKNOWLEDGMENTS

The author is grateful to Yu.P. Irkhin for the statement of the problem of calculating local fields in complex magnetic lattices and for helpful discussions.

REFERENCES

1. I. E. Tamm, *The Fundamentals of the Theory of Electricity* (Nauka, Moscow, 1976).
2. E. V. Rozenfel'd and Yu. P. Irkhin, Fiz. Met. Metalloved. **86** (4), 35 (1998).
3. E. V. Rozenfel'd and Yu. P. Irkhin, Izv. Akad. Nauk (in press).
4. W. Hofmann, W. Kundig, P. F. Meier, *et al.*, Phys. Lett. A **65** (4), 343 (1978).
5. W. C. Koehler and R. M. Moon, Phys. Rev. Lett. **29** (21), 1468 (1972).
6. I. I. Gurevich, I. G. Ivanter, B. F. Kirillov, *et al.*, Zh. Éksp. Teor. Fiz. **100** (4), 1353 (1991) [Sov. Phys. JETP **73**, 749 (1991)].
7. V. Yu. Irkhin and Yu. P. Irkhin, Phys. Rev. B **57** (3), 2697 (1998).
8. Yu. P. Irkhin and V. Yu. Irkhin, Fiz. Tverd. Tela (S.-Peterburg) **40** (7), 1298 (1998) [Phys. Solid State **40**, 1182 (1998)].

Translated by Yu. Epifanov

Physics of the Solid State, Vol. 42, No. 9, 2000, pp. 1688–1690. Translated from Fizika Tverdogo Tela, Vol. 42, No. 9, 2000, pp. 1641–1643.

MAGNETISM AND FERROELECTRICITY

Anomalous Temperature Dependence of the Magnetoresistance in Co/Cu Multilayers

P. D. Kim, D. L. Khalyapin, I. A. Turpanov, L. A. Li, A. Ya. Beten'kova, and S. V. Kan

Kirenskiĭ Institute of Physics, Siberian Division, Russian Academy of Sciences, Akademgorodok, Krasnoyarsk, 660036 Russia

e-mail: kim@post.krascience.rssi.ru

Received February 18, 2000

Abstract—An anomalous temperature dependence of magnetoresistance (MR) of Co/Cu multilayer films with a ~3 Å thick magnetic layer has been established experimentally. The temperature of the MR maximum T_{max} is shown to coincide with the Néel temperature. The variation of T_{max} with the Cu layer thickness follows an oscillatory pattern. *© 2000 MAIK "Nauka/Interperiodica".*

Multilayer films with alternating ferromagnetic and nonmagnetic layers have been among the most intensely studied magnetic systems in recent years. The mounting interest in magnetic multilayers stems primarily from the application potential of these systems (in particular, the possibility of using them in magnetic information storage devices). At the same time, such structures represent a good model system for studying fundamental physical relations.

We have studied magnetic and magnetoresistance properties of Co/Cu multilayer films with ultrathin (about 3 Å-thick) Co layers. As was shown earlier [1, 2], this thickness of a magnetic layer is a limit at which magnetic ordering is still possible. We studied the temperature dependences of the magnetoresistance of Co/Cu multilayered films. All the samples were prepared by magnetron sputtering with the successive deposition of Co and Cu layers on glass substrates at room temperature in an argon environment. Each sample was made up of 120 Co/Cu bilayers. The Co layer thickness and the Cu modulation period of the multilayer system were calculated from x-ray fluorescence data. All the samples had a polycrystalline structure.

The temperature dependence of the MR was studied by the technique described in [2]; a dc current I was passed through the sample whose magnetization was reversed by a varying magnetic field $H = H_a\cos(\omega t)$ normal to the film plane with a frequency $f = \omega/2\pi$ = 37 Hz. The magnetization M generated in this way is proportional to H within a broad range of fields, and the domain structure of the sample does not affect the value of being MR measured. It was shown earlier that $\Delta R \sim M^2$ [2], and therefore,

$$\Delta R \sim H_a^2\cos^2(\omega t) = \frac{1}{2}H_a^2(1 + \cos(2\omega t)).$$

Since the current through the sample is constant, an ac voltage of frequency $2f$ = 74 Hz is induced across the sample with an amplitude proportional to the MR: $U_a = \Delta RI/2$, where $\Delta R = R_0 - R_{min}$, R_0 being the sample resistance in zero field, and R_{min}, in a field H_a. The voltage was amplified by a selective amplifier. The temperature dependence of R_0 was measured separately. The magnetoresistance was determined from the relation $MR = \Delta R/R_0$. The investigation was carried out in the 77–300 K temperature range under heating and in magnetic fields of up to 500 kOe.

We found that the temperature dependences of the magnetoresistance of films with ultrathin Co layers behave anomalously; namely, each curve exhibits a clearly pronounced maximum (a magnetoresistance peak) below room temperature (Fig. 1). The absence of

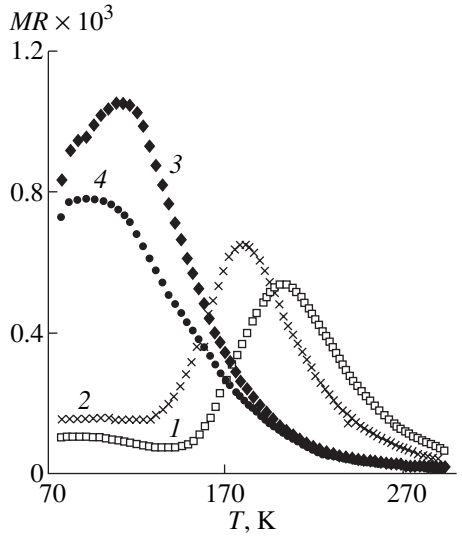

Fig. 1. Typical temperature dependences of the MR of Co/Cu multilayer films obtained for various thicknesses of the Cu layer in a field of 500 Oe. d_{Cu} (Å): (*1*) 14, (*2*) 15, (*3*) 18.5, and (*4*) 21.5.

1063-7834/00/4209-1688$20.00 © 2000 MAIK "Nauka/Interperiodica"

an MR peak for some samples is apparently due to a shift in the temperature T_{max} of the peak towards a region below 77 K.

This method of magnetoresistance determination was proposed by us [2] to estimate the Curie temperature Θ_C directly from magnetoresistance measurements. The magnetoresistance curve for Co/Cu multilayer films contains a linear segment at temperatures above T_{max}. Within this region, the $M \sim (\Theta_C - T)^{1/2}$ relation holds, because $\Delta R \sim M^2$ [3]. Extrapolation of the linear segment makes it possible to determine the Curie temperature Θ_C of the film for a given applied magnetic field H (Fig. 2). Knowing the dependence of Θ_C on H, one can determine the zero-field value of Θ_C.

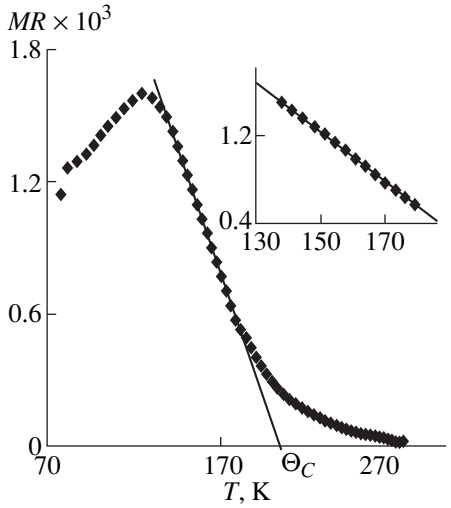

Fig. 2. Determination of the Curie temperature Θ_C (for the sample with d_{Cu} = 16 Å).

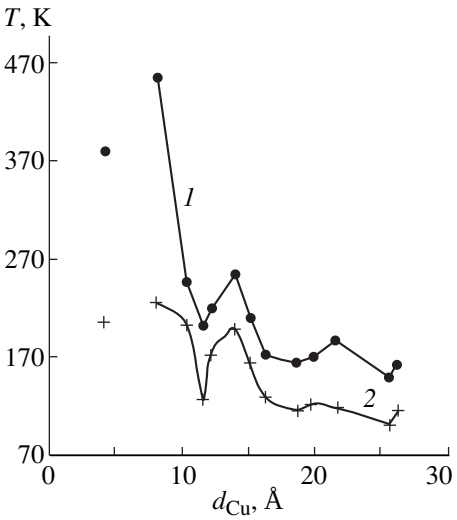

Fig. 3. Dependences of the Curie temperature Θ_C (*1*) and T_{max} (*2*) on d_{Cu}.

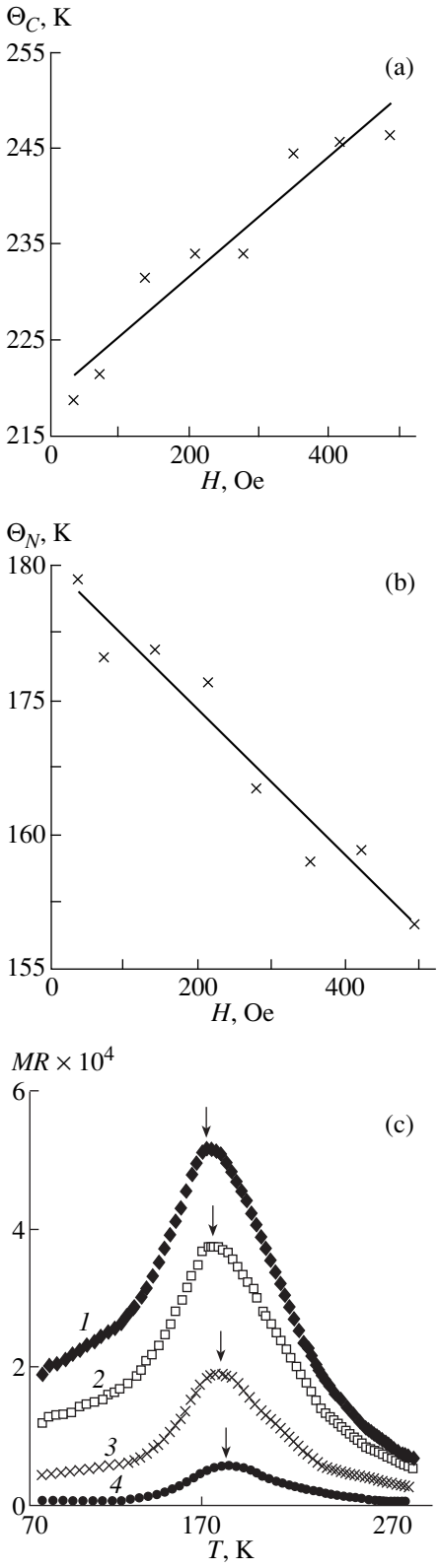

Fig. 4. Dependences of the Curie (a) and Néel (b) temperatures on the applied magnetic field H obtained for the sample with d_{Cu} = 12 Å; and (c) magnetoresistance curves measured in different fields. The arrows identify the MR peak. H (Oe): (*1*) 490, (*2*) 420, (*3*) 280, and (*4*) 140.

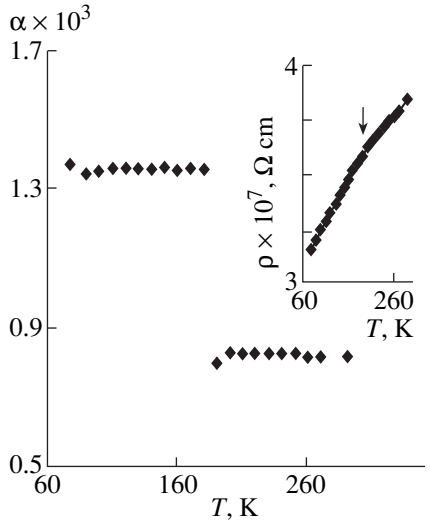

Fig. 5. Dependence of the temperature coefficient of resistivity α for a sample with d_{Cu} = 14 Å on temperature *T*. The inset shows the temperature behavior of the resistivity ρ. The arrow identifies T_{max} for this sample.

Thus, there exists a critical temperature T_{max} for multilayer Co/Cu films, at which the magnetoresistance is maximal. This temperature depends substantially on the thickness of the Cu nonmagnetic layer, and this dependence, as well as the dependence of Θ_C on d_{Cu}, exhibits an oscillatory character (Fig. 3).

The magnitude of the applied magnetic field also noticeably affects the measured values of Θ_C and T_{max}; namely, an increase of the field amplitude generally brings about a decrease of T_{max} and an increase of Θ_C (Fig. 4).

The interaction of magnetic atoms through a nonmagnetic layer in the multilayer films studied may be both ferromagnetic and antiferromagnetic [2]. The observed experimental results can be interpreted if we take into account the existence of antiferromagnetic coupling in these films.

It is known that the existence of a susceptibility maximum at the Néel point Θ_N is a feature of antiferromagnetic ordering [3]. The film structure can be represented in the following way: the Co magnetic layer consists of a large number of ferromagnetic spin clusters ordered antiferromagnetically or in a mixed manner, part of the clusters ordered ferromagnetically, and the remainder, antiferromagnetically. The magnetoresistance peak corresponds to the maximum in the film susceptibility at $T_{max} = \Theta_N$. Such a temperature dependence of susceptibility was theoretically considered by Landau in 1933 [4] for materials made up of ferromagnetically ordered layers.

This model finds confirmation in the character of Θ_C and Θ_N variation with an increasing external magnetic field. The magnetic field orients the spins in one direction, which favors the ferromagnetic and hinders the antiferromagnetic ordering. Therefore, the destruction of antiferromagnetic order in the presence of a field occurs at lower, and that of the ferromagnetic order, at higher temperatures.

Antiferromagnetic systems exhibit anomalies of nonmagnetic properties, for instance, the conductivity, at the Néel point. Figure 5 presents the dependence of the temperature coefficient of resistivity α on temperature (for a sample with d_{Cu} = 14 Å). Within the temperature interval from 180 to 190 K, α undergoes a jump. The Néel temperature Θ_N for a given sample, which is determined by extrapolating the T_{max} to a zero field, is ~180 K. This observation can be treated as an indirect confirmation of the proposed model.

The temperature dependences of magnetoresistance of the films with d_{Cu} varying from 8 to 12 Å have a more complex pattern and contain two or three peaks, which can be attributed to the more complex structure of these samples. Most likely, they represent a multi-phase system, with each phase having its own Curie and Néel temperatures.

Such temperature anomalies characterized by a magnetoresistance peak were observed earlier in Ni/Cu films with thicker magnetic layers (~15 Å) in an in-plane magnetic field [4, 5]. This effect, however, is less clearly pronounced in them with the MR varying smoothly, and the peak not observed in all samples. We believe that the anomalies in the temperature dependence of MR are due to a substantial increase in the magnetic anisotropy at lower (below T_{max}) temperatures.

Thus, we have experimentally discovered an anomalous peak in the magnetoresistance of Co/Cu multilayer films with ultrathin Co layers, which is due to the existence of an antiferromagnetic ordering and corresponds to the Néel point. The dependence of the position of the peak on d_{Cu} exhibits an oscillatory character.

ACKNOWLEDGMENTS

Support of the Russian Foundation for Basic Research (grant no. 99-02-17816) is gratefully acknowledged.

REFERENCES

1. E. S. Mushailov, V. K. Maltsev, I. A. Turpanov, and P. D. Kim, J. Magn. Magn. Mater. **138**, 207 (1994).
2. P. D. Kim, Y. H. Jeong, I. A. Turpanov, *et al.*, Pis'ma Zh. Éksp. Teor. Fiz. **64** (5), 341 (1996) [JETP Lett. **64**, 370 (1996)].
3. S. V. Vonsovskiĭ, *Magnetism* (Nauka, Moscow, 1971; Wiley, New York, 1974).
4. L. D. Landau, Phys. Z. Sowjetunion **4**, 675 (1933).
5. H. Kubota, M. Sato, and T. Miyazaki, J. Magn. Magn. Mater. **167** (1), 12 (1997).

Translated by G. Skrebtsov

Physics of the Solid State, Vol. 42, No. 9, 2000, pp. 1691–1695. Translated from Fizika Tverdogo Tela, Vol. 42, No. 9, 2000, pp. 1644–1648.

MAGNETISM AND FERROELECTRICITY

Influence of Surface on the Effective Magnetic Fields in α-Fe_2O_3 and $FeBO_3$

A. S. Kamzin*, B. Stahl, R. Gellert***, M. Müller**, E. Kankeleit***, and D. B. Vcherashniĭ***

**Ioffe Physicotechnical Institute, Russian Academy of Sciences, ul. Politekhnicheskaya 26, St. Petersburg, 194021 Russia*
***Materials Sciences Department, Technical University, Darmstadt, 64287 Germany*
****Institute of Nuclear Physics, Technical University, Darmstadt, 64289 Germany*
Received January 17, 2000; in final form, February 24, 2000

Abstract—First measurements of the effective magnetic fields as a function of the depth at which the iron ions are in the surface layer of α-Fe_2O_3 and $FeBO_3$ single crystals are reported. The method used is the depth-selective conversion-electron Mössbauer spectroscopy. An analysis of experimental spectra revealed that the magnetic properties of the crystal surface vary smoothly from the bulk to surface characteristics within a layer ~100 nm thick. The layers lying below ~100 nm from the surface are similar in properties to the bulk of the crystal, and their spectra consist of narrow lines. The spectral linewidths increase smoothly as one approaches the crystal surface. The spectra obtained from a ~10-nm thick surface layer consist of broad lines indicating a broad distribution of effective magnetic fields. Calculations show that the field distribution width in this layer is δ = 2.1(3) T, for an average value H_{eff} = 32.2(4) T. It has been experimentally established that, at room temperature (291 K), the effective magnetic fields smoothly decrease as one approaches the crystal surface. The effective fields in a 2.4(9)-nm surface layer of α-Fe_2O_3 crystals are lower by 0.7(2)% than the fields at the ion nuclei in the bulk of the sample. In the case of $FeBO_3$, the effective fields decrease by 1.2(3)% in a surface layer 4.9(9) nm thick. © *2000 MAIK "Nauka/Interperiodica".*

INTRODUCTION

The development of new experimental methods to study the properties of thin surface layers, which made a comparison of the results of an experiment with predictions of current theories of surface magnetism possible, has stimulated an explosive growth of publications reporting on investigations of the magnetic properties of surfaces.

An important parameter characterizing the magnetic properties of a surface is the magnetic moment both in the ground state (at T = 0 K) and at nonzero temperatures. Theoretical calculations showed that, at zero temperature, the average magnetic moment is larger in the outermost layer of Ni(001) by 20%, and in that of Fe(001), by 34% compared to its bulk value, at a depth of four monolayers from the surface [1].

The data obtained by Mössbauer spectroscopy (MS) stand out amongst the other experimental results. The broad use of MS in studies of both bulk and surface magnetic properties is due to the fact that it permits one to carry out investigations on the microscopic or local scale, because the effective magnetic field at iron ion nuclei (H_{eff}) measured by MS is directly related to the local moment and is determined without the application of an external magnetic field and irrespective of the orientation of the local spin moment. For instance, the MS was employed to obtain the dependence of the effective magnetic field on the distance of Fe^{57} atoms from the surface [2, 3]. These studies were performed on films made up of a certain number of Fe^{56} layers and a layer of Fe^{57} atoms, the latter being deposited at a distance d from the surface. Using a series of such films in which d varied within the $0 < d < d_n$ interval, where n is the number of layers in the sample, it was found [2, 3] that, at $T \approx 0$ K, the effective magnetic field increases as one approaches the surface. At room temperature, a reverse effect was observed, namely, the magnitude of H_{eff} decreases as one comes closer to the surface. Studies of a thin α-Fe_2O_3 film by the depth-selective conversion-electron Mössbauer spectroscopy (DSCEMS) showed that, at room temperature, the magnitude of H_{eff} in a thin surface layer is less by 2% than that in the bulk of a sample [3]. H_{eff} at the surface at T = 4.2 K was experimentally found to be less than that in the bulk [4]. Assuming the $H_{\text{eff}}(T)$ relation to be proportional to $M_s(T)$ both in the bulk and at the sample surface, the results of [4] agree with theory [5]. At the same time, the experimental data obtained for other materials are in a much poorer agreement with the theory.

Measurements of the spin moment of polarized electrons scattered from the Fe(100) surface showed that, at room temperature, the magnetic moment at the surface of a sample is larger by 30% than that in the bulk [6]. These data are in substantial disagreement with the theoretical predictions that the room tempera-

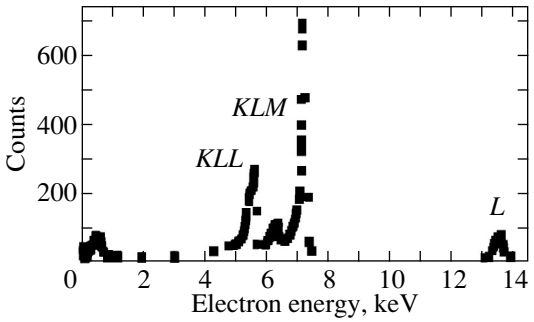

Fig. 1. Energy spectrum of electrons emerging from the surface of a 10-monolayer thick Fe^{57} film obtained with a DSCEMS spectrometer.

ture magnetization should decrease as one approaches the surface because of the surface spin waves.

Thus, by far, not all experimental and theoretical data are in agreement, and, therefore, further studies of the effect of the surface on the magnetic properties of the surface layer are needed. The most efficient methods in this respect are those that permit a direct comparison of experimental data on the surface and the bulk properties, as is possible, for instance, with Mössbauer spectroscopy. Besides, practically all surface property studies were performed on metallic films, whose surfaces may readily become oxidized, and this introduces errors in experimental data. Therefore, one should make measurements on samples whose surface is not subject to oxidation.

These considerations stimulated the present experimental study of the surface properties of α-Fe_2O_3 and $FeBO_3$ single crystals using the DSCEMS method. The layer-by-layer investigation of the surface layer was performed by the DSCEMS method, first proposed and developed in [7]. This method is based on measuring Mössbauer spectra by detecting electrons escaping from the crystal under study within a narrow interval of their energy spread. To improve the precision of electron selection in energy and to increase the spectrometer collecting power, a magnetostatic electron analyzer was calculated by computer simulation. The spectrometer thus constructed had the following characteristics: transmission 21% of 4π and energy resolution 0.2–2%, depending on sample size [8, 9]. As shown on calibration samples representing films deposited in Fe^{56}–Fe^{57}–Fe^{56} layers, such spectrometers permit an investigation of a surface layer 5–10 Å thick [3]. The thickness of the layer under study and its distance from the surface were calculated by the Monte Carlo method [9, 10].

1. EXPERIMENTAL

Figure 2 presents an electron energy spectrum obtained from a Fe^{57} film ten monolayers thick by the DSCEMS method. In order to perform layer-by-layer analysis of the surface properties of a layer up to 200 nm thick, a narrow part of the *K* line has to be isolated with the magnetostatic analyzer. The thickness of the layer under study is determined by the width of the isolated *K*-line part. The higher the analyzer resolution, the thinner is the layer from which the information can be extracted. The distance of the layer to be studied from the sample surface is determined by the position of the discriminator window within the *K* line. When detecting electrons in the 6.7-keV energy region, one obtains information on the layers lying at ~100 nm from the crystal surface. If the energy of the detected electrons is 7.29 keV, one studies the properties of a surface layer not more than 2–4 nm thick. By further increasing the energy of the detected electrons, one obtains data on layers lying deeper than 100 nm from the surface. The reason for this lies in that, in this case, one also detects the *L* electrons, which were produced with an initial energy of ~14 keV (Fig. 1) and, hence, escaped from larger depths, because their range in the material is larger than that of the *K* electrons.

2. RESULTS OF THE EXPERIMENTS AND DISCUSSION

We chose to study α-Fe_2O_3 and $FeBO_3$ crystals, which are ordered antiferromagnetically below the Néel temperatures of ~961 and ~348 K, respectively, and possess a weak ferromagnetic moment. The choice of these compounds was stimulated by the following considerations. Iron ions in α-Fe_2O_3 and $FeBO_3$ occupy the same crystallographic position, and their room-temperature Mössbauer spectra consist of one well–resolved Zeeman sextuplet with close-to-natural linewidths. Besides, the bulk properties of these crystals are studied fairly well (see [11, 12] and references therein), thus permitting a comparison between our experimental data on the bulk properties and the published figures. Finally, the surface of these crystals is not subject to corrosion or any other changes in its properties. This is evidenced by the absence of visible changes in the Mössbauer spectra measured from a thin surface layer with an interval of one year.

The α-Fe_2O_3 and $FeBO_3$ single crystals were prepared from a melt solution. The Fe^{57} isotope content in the compounds was 100%. Plates ~5 mm in diameter were cut from the single crystals. X-ray diffraction measurements showed the *C* crystallographic axis to be perpendicular to the plate plane. In the course of crystal preparation, particular attention was directed at the quality of the surface to be studied. Previous experiments [12] demonstrated that a high-quality surface is obtained when chemically etched in orthophosphoric acid at 90°C for one minute. It should be pointed out that, in order to check the quality of crystal surface preparation, Mössbauer spectra were measured of a layer ~3 nm thick at temperatures above the Néel point. The spectra obtained consisted only of quadrupole splitting lines, and an analysis showed them to be fully

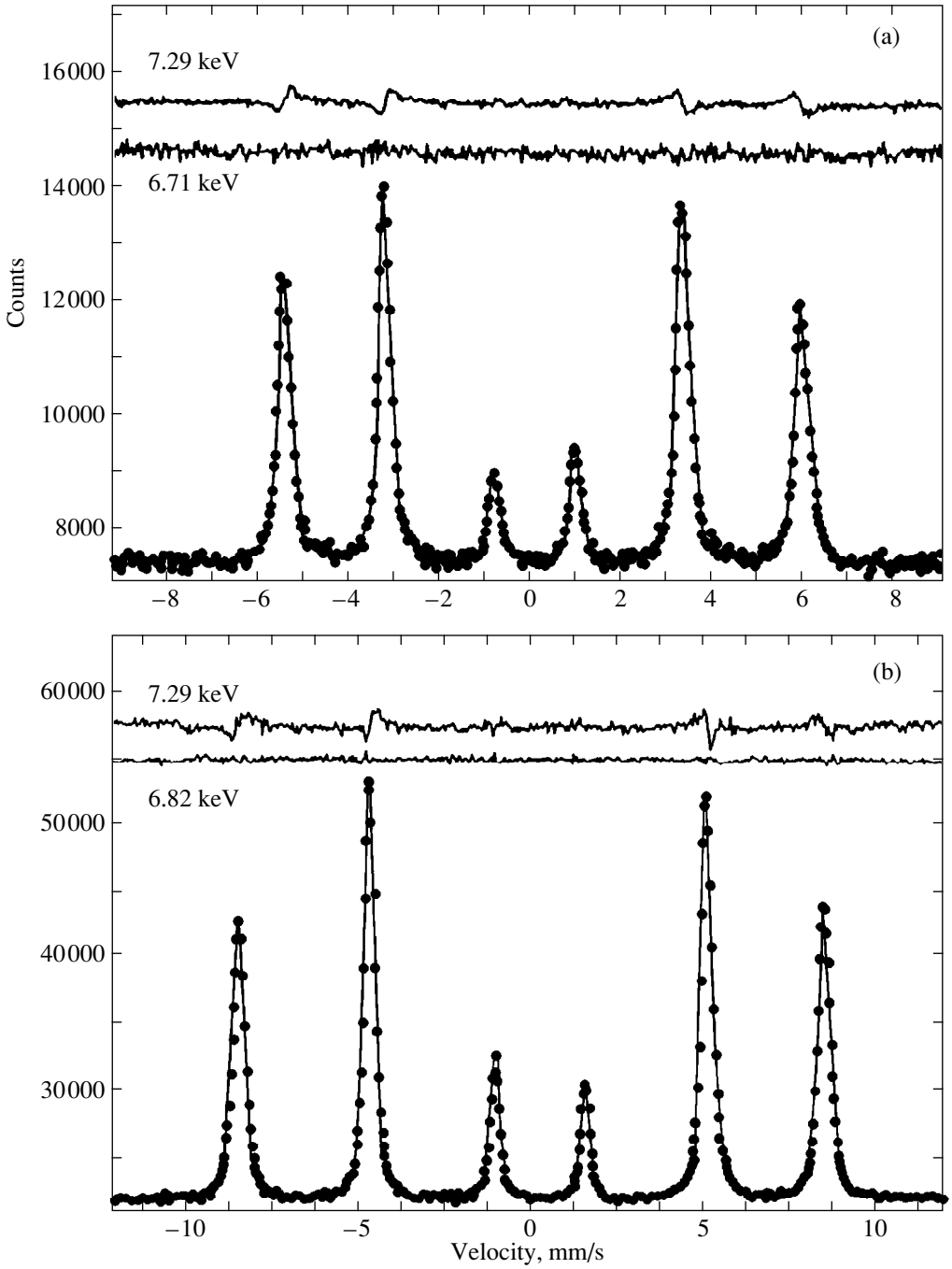

Fig. 2. Mössbauer spectra of (a) $FeBO_3$ and (b) α-Fe_2O_3 single crystals obtained at 291 K by detecting electrons 6.71 and 6.82 keV in energy, respectively. The gamma-ray wave vector is parallel to the *C* crystallographic axis. The experimental spectra are shown with dots, while the theoretical ones are represented by solid lines. Displayed above the spectra are the difference curves between the bulk spectra and those measured with electrons of energy 7.29 and 6.71 keV for α-Fe_2O_3, and of 7.29 and 6.82 keV for $FeBO_3$.

identical to those from the layers lying deeper than 200 nm from the surface.

The DSCEMS method was employed to obtain room-temperature experimental spectra of α-Fe_2O_3 and $FeBO_3$ in the 6.6–7.8-keV energy interval. The gamma-ray beam was parallel to the *C* crystallographic axis. The experimental spectra of $FeBO_3$ and α-Fe_2O_3 measured by detecting electrons with energies of 6.71 and 6.82 keV are shown in Fig. 2 by dots. Also shown there are the results of a mathematical treatment of these data in the form of a theoretical spectrum (solid line) and difference curves. The widths of the spectral lines presented in Fig. 2 coincide within experimental error with the natural widths of spectral lines for Fe^{57}. This indi-

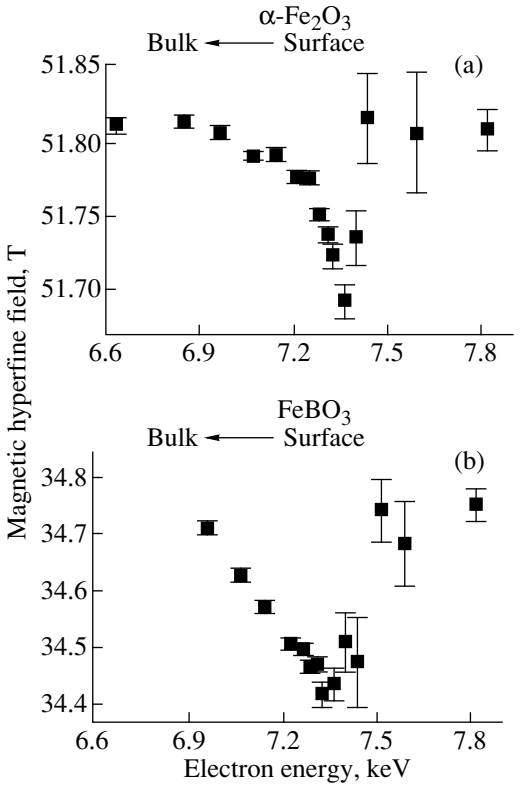

Fig. 3. Effective magnetic fields in (a) α-Fe_2O_3 and (b) $FeBO_3$ vs. the energy of the electrons being detected. The change in the position from 6.71 to 7.29 keV corresponds to a change in depth of the layer under study from 100 to 2.4(9) nm in α-Fe_2O_3 and from 100 to 4.9(9) nm in $FeBO_3$.

cates a high quality of the spectrometer employed and of the crystals under study, as well as permits a high-precision calculation of the hyperfine interaction parameters.

A mathematical analysis of the spectra obtained by detecting 6.71-keV electrons showed that they fit the parameters obtained for the bulk of the sample well. This is displayed by the difference curve in Fig. 2a. However, when one uses the same parameters for the mathematical description of the spectrum obtained with 7.29-keV electrons, the difference between the theoretical and experimental spectra becomes clearly visible. This manifests itself clearly in the difference curve derived for the 7.29-keV energy in $FeBO_3$. As evident from the difference curves presented in Fig. 2b, similar results were obtained for α-Fe_2O_3. As the energy of detected electrons increases, i.e., as one approaches the crystal surface, the spectral lines smoothly broaden. The spectra measured from a ~10-nm thick surface layer of $FeBO_3$ consist of broad lines, which implies a broad distribution of the effective magnetic fields. As follows from calculations, the field distribution width in this layer is $\delta = 2.1(3)$ T for an average value $H_{\text{eff}} = 32.2(4)$ T.

Note a specific feature of the experimental spectra of the α-Fe_2O_3 and $FeBO_3$ crystals studied here, namely, the spectral lines of these crystals are not strictly symmetrical relative to zero velocity (Fig. 2). The intensities of the outer and inner line pairs corresponding to the transitions with $\Delta m = 1$ are noticeably asymmetric. Similar spectra of α-Fe_2O_3 and $FeBO_3$ single crystals were also obtained by other authors, but the nature of this line asymmetry was not discussed by them. Our analysis of this phenomenon has led us to the following conclusion. The principal axis of the electric-field gradient in the crystals studied is directed along the *C* axis, whereas the effective magnetic field is perpendicular to the latter. We believe [13] that, when these hyperfine fields interact, the absorption line intensities depend on the angle of their mutual orientation. When they are orthogonal, as is the case with α-Fe_2O_3 and $FeBO_3$, the resonance lines are asymmetric, exactly as in the spectra of Fig. 2. Note that the total line intensity ratio remains unchanged.

The experimental spectra were used to calculate the intensity ratio of the Zeeman sextuplet lines, which was found to be 3 : 4 : 1. This is an additional argument in favor of the x-ray diffraction measurements, which indicate that the magnetic moments of Fe atoms are oriented parallel to the crystal surface plane and perpendicular to the *C* axis. The effective magnetic fields derived from experimental spectra, which were obtained by detecting electrons with energies from 6.6 to 7.8 keV, are displayed in Fig. 3 as a function of the electron energy.

To interpret the effective magnetic field relations in Fig. 3, the electron escape functions were analyzed. It was found that electrons with energies below 6.9 keV emerge from layers located further than 100 nm from the surface, whereas the 7.25-keV electrons carry information from a surface layer 2–4 nm thick. Mössbauer spectra measured with electrons having energies from 6.9 to 7.25 keV provide data on the properties of layers lying from 100 to ~2 nm from the sample surface.

An analysis of Mössbauer spectra obtained by detecting electrons with energies above 7.3 keV showed the spectral lines to be substantially broader than those measured with electrons below 7.21 keV in energy. The effective magnetic fields derived from a mathematical treatment of the spectra are plotted in Fig. 3; one readily sees that, as the electron energy increases above 7.3 keV, the effective magnetic fields increase and the accuracy of their determination decreases. The reason for this, as already pointed out, lies in that this region also includes *L* electrons, which have lost most of their energy because they escape from depths substantially in excess of 100 nm.

As seen from Fig. 3, the effective magnetic fields at iron nuclei located further than 100 nm from the crystal surface (in Fig. 3, this corresponds to electron energies of 6.9 keV and less) are 518.3 kOe for α-Fe_2O_3 and 347.2 kOe for $FeBO_3$. These values coincide with the

figures obtained in studies of the bulk properties [11, 12]. As seen from Fig. 3, the effective magnetic fields decrease as the energy of the detected electrons increases (i.e., as one approaches the crystal surface). For the electron energy of 7.29 keV, the effective magnetic fields assume the values of 516.9 kOe for α-Fe_2O_3 and 344.2 kOe for $FeBO_3$. Thus, the effective fields at the iron nuclei located in a surface layer 2.4(9) nm thick decrease compared to those in the bulk of the sample by 1.4 kOe in the case of α-Fe_2O_3. For $FeBO_3$, as shown by the calculations of the electron escape functions, the effective fields decrease by 3.0 kOe as the surface layer becomes 4.9(9) nm thick. Considered on a percentage basis, the decrease of the effective fields is 0.7% in the surface layers of α-Fe_2O_3 and 1.2% in those of $FeBO_3$. The difference between the magnitudes of this effective magnetic-field decrease may be accounted for by the measurements that were performed at $T = 291$ K. This corresponds to reduced temperatures (T/T_N) of 0.30 for α-Fe_2O_3 and 0.84 for $FeBO_3$. It may be conjectured that the effective magnetic fields determined at the surface of α-Fe_2O_3 crystals are less subject to thermal perturbations because the corresponding measurements are performed further away from the Néel point on the temperature scale.

For comparison, we present experimental data on the properties of a surface layer of an epitaxial α-Fe_2O_3 film [3] and of a film produced by depositing iron ions [4]. In the case of α-Fe_2O_3, the effective magnetic fields decrease at room temperature from 51.761 ± 0.008 to 50.6 ± 0.8 T within a surface layer 18 ± 3 Å thick [3]. Measurements performed on a film consisting of 30 monolayers of Fe ions showed that the effective fields fall off from 33.2 ± 1 to 32.8 ± 1 T as one approaches the film surface from its bulk [4].

The surfaces of α-Fe_2O_3 and $FeBO_3$ crystals were also studied by conversion-electron Mössbauer spectroscopy. In this case, one detects both the conversion and Auger electrons escaping from the sample, and the spectra can be used to derive information on the state of a surface layer ~200 nm thick. As follows from calculations, the best fit to experimental data for α-Fe_2O_3 and $FeBO_3$ crystals can be attained only within a model representing a set of spectra with the effective fields taken from the plots in Fig. 3.

Thus, we have reported on the first experimental studies of the effect of the surface on the properties of a near-surface layer in macroscopic crystals. It has been found that the effective magnetic fields at iron ion nuclei in a surface layer ~100 nm thick (and the magnetization) decrease smoothly as one approaches the sample surface.

ACKNOWLEDGMENTS

Support of the German Science Foundation and of the Russian Foundation for Basic Research (Grants nos. 96-02-10038 and 98-02-18279) is gratefully acknowledged.

The Russian authors are indebted to the PROMT Company (http://www.promt.ru) for the software provided.

REFERENCES

1. A. J. Freeman, J. Magn. Magn. Mater. **35**, 31 (1983); S. Ohnishi, A. J. Freeman, and M. Wienert, J. Magn. Magn. Mater. **31**–**34**, 889 (1983).
2. A. H. Ovens, C. L. Chien, and J. C. Walker, J. Phys. (Paris) **40**, C2–74 (1978); G. Bayreuter, J. Vac. Sci. Technol. A **1**, 19 (1983).
3. T. Yang, A. Krishnan, N. Benczer-Koller, and G. Bayreuther, Phys. Rev. Lett. **48**, 1292 (1982); T. Yang, J. Trooster, T. Kachnovski, and R. Benczer-Koller, Hyperfine Interactions **10**, 795 (1981).
4. A. J. Tyson, H. Ovens, and J. C. Walker, J. Magn. Magn. Mater. **35**, 126 (1983); A. J. Tyson, H. Ovens, J. C. Walker, and G. Bayreuter, J. Appl. Phys. **52**, 2487 (1981).
5. D. L. Mills and A. A. Maradudin, J. Phys. Chem. Solids **28**, 1855 (1967).
6. U. Gradmann, J. Walker, R. Feder, and E. Tamura, J. Magn. Magn. Mater. **31**–**34**, 1 (1983).
7. E. Moll and E. Kankeleit, Nukleonik **7**, 180 (1965).
8. B. Stahl and E. Kankeleit, Nucl. Instrum. Methods Phys. Res. B **122**, 149 (1997).
9. B. Stahl, R. Gellert, O. Geiss, *et al.*, *GSI Scientific Report, Darmstadt, Germany (1994)*, p. 180; R. Gellert, O. Geiss, G. Klingelhofer, *et al.*, Nucl. Instrum. Methods Phys. Res. B **76**, 381 (1993).
10. D. Liljequist, T. Ekdahl, and L. Baverstam, Nucl. Instrum. Methods **155**, 5292 (1978).
11. M. Eibschutz and M. E. Lines, Phys. Rev. B **7**, 4907 (1973).
12. A. S. Kamzin and L. A. Grigor'ev, Fiz. Tverd. Tela (St. Petersburg) **36**, 1271 (1994) [Phys. Solid State **36**, 694 (1994)]; Zh. Éksp. Teor. Fiz. **104**, 3489 (1993) [JETP **77**, 658 (1993)].

Translated by G. Skrebtsov

Physics of the Solid State, Vol. 42, No. 9, 2000, pp. 1696–1704. Translated from Fizika Tverdogo Tela, Vol. 42, No. 9, 2000, pp. 1649–1656.

MAGNETISM AND FERROELECTRICITY

Relation of Magnetic and Structural Factors in the Course of Phase Transitions in MnAs-Based Alloys

S. K. Asadov*, É. A. Zavadskiĭ*, V. I. Kamenev*, E. P. Stefanovskiĭ, A. L. Sukstanskiĭ*, and B. M. Todris***

** Donetsk Physicotechnical Institute, National Academy of Sciences of Ukraine, Donetsk, 83114 Ukraine*

*** Department of Physics, Ben-Gurion University of the Negev, POB 653, Beer-Sheva, 84105 Israel*

e-mail: asadov@host.dipt.donetsk.ua

Received February 25, 2000

Abstract—A phenomenological analysis of the magnetic and structural phase states observed in the manganese arsenide–based alloys over a wide range of temperatures and pressures has been performed. The unique first-order phase transitions from the paramagnetic and metamagnetic states to the ferromagnetic state are studied experimentally. It is found that these transitions exhibit characteristic features associated with the magnetostriction suppression of nucleation when the lability boundary of the paramagnetic phase is absent and the transition from the metamagnetic state is not thermodynamically "forbidden." The phase behavior of manganese arsenide–based alloys is interpreted within the proposed model. This model accounts for the interrelation of the magnetic, structural, and elastic properties of alloys and also the specific features of phase transformations in real crystals. *© 2000 MAIK "Nauka/Interperiodica".*

1. INTRODUCTION

The results obtained in numerous experimental investigations of manganese arsenide MnAs over a wide range of temperatures T and pressures P [1–4] are generalized in the P–T phase diagram shown in Fig. 1. As is seen from the figure, three phases with different magnetic and structural characteristics are observed at atmospheric pressure: the paramagnetic hexagonal phase $PM(B8_1)$, the paramagnetic orthorhombic phase $PM(B31)$, and the hexagonal ferromagnetic phase $FM(B8_1)$. The hydrostatic pressure considerably affects the stability of these phases, and its increase gives rise to three new states with an orthorhombic symmetry of crystal lattice: the ferromagnetic phase $FM(B31)$ and two metamagnetic modulated long-period structures $MMS(B31)$ and $MMS'(B31)$.

A number of theoretical models were proposed for interpreting magnetic and structural transformations realized in MnAs [5–9]. The concept of the decisive role of competing interaction between two order parameters—the magnetic parameter describing the appearance of ferromagnetic ordering and the structure parameter characterizing orthorhombic distortions of the crystal lattice—turned out to be most consistent and fruitful [9]. The concept proposed in [9] and advanced in subsequent publications [10, 11] provided answers to three very important (from the viewpoint of the physics of magnetic phenomena) questions regarding the unique behavior of MnAs upon the $FM(B8_1) \rightleftharpoons PM(B31)$ phase transition. First, why is the order–disorder magnetic transition treated as the first-order phase transition? Second, why is a rise in the magnetic symmetry from ferromagnetic to paramagnetic upon this transition, contrary to the reasons for the relativistic magnetostriction, accompanied by a lowering in the symmetry of the crystal lattice from hexagonal to orthorhombic? Finally, why do the lines of this phase transition in the P–T diagram (Fig. 1, lines *cdf*, *klm*) have a specific shape? However, the possibility of forming phases with a different magnetic ordering in MnAs was not discussed.

The aim of the present work was to perform a thermodynamic analysis of all phases (including the phases with a modulated long-period magnetic structure *MMS*)

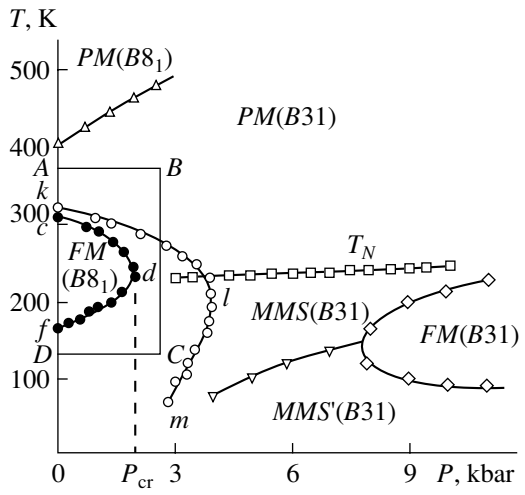

Fig. 1. Experimental P–T phase diagram of magnetic and structural states for manganese arsenide.

1063-7834/00/4209-1696$20.00 © 2000 MAIK "Nauka/Interperiodica"

observed in manganese arsenide. The generalized phase diagram of magnetic and structural equilibrium states was constructed; moreover, the specific features of the phase transitions due to the occurrence of metastable states were revealed experimentally. The results of the thermodynamic analysis were compared with the experimental data. On this basis, we proposed the consistent model of phase transitions observed in MnAs.

2. MODEL

Let us give a phenomenological description of the observed structural and magnetic states and the phase transitions between these states. According to [9–11], the thermodynamic potential of the MnAs system can be constructed with two (structural and magnetic) order parameters. These parameters describe the appearance of orthorhombic distortions and magnetic ordering, respectively. The nonzero component of the three-dimensional order parameter φ, which corresponds to one out of three prongs of the star of wave vector $k = b_1/2$, is chosen as the parameter of structural distortions. This is explained by the fact that, upon the $PM(B8_1) \rightleftharpoons PM(B31)$ second-order phase transition, the change in the space symmetry $P6_3/mmc \longrightarrow P_{nma}$ as a result of the displacement of Mn and As ions from symmetric positions [3, 12] is realized through one out of three branches of the irreducible representation i_4 ($k = b_1/2$) of the $P6_3/mmc$ group [13]. The lowering in the symmetry is attended by the formation of domains, which are rotated with respect to each other through an angle of 120° in the plane of a hexagonal basis [3] and differ in the sign of the φ parameter. Consequently, there exist the transition regions between domains, i.e., the domain boundaries in which the φ parameter varies.

Considering the possible description of a nonuniform spatial distribution of the φ parameter (the case of small gradients), the density of the thermodynamic potential of structural distortions is given by

$$\Phi_\varphi = \frac{1}{2}\alpha_\varphi(\partial\varphi/\partial x_i)^2 + \frac{1}{2}a''_\varphi\varphi^2 + \frac{1}{4}b''_\varphi\varphi^4. \quad (1)$$

Here, α_φ, a''_φ, and b''_φ are the phenomenological parameters of the theory.

The irreducible magnetic vectors $\mathbf{m} = \mathbf{M}_1 + \mathbf{M}_2 + \mathbf{M}_3 + \mathbf{M}_4$ and $\mathbf{l} = \mathbf{M}_1 - \mathbf{M}_2 - \mathbf{M}_3 + \mathbf{M}_4$ (where $\mathbf{M}_i$ are the magnetizations of four sublattices) can be used as the magnetic order parameter. In this case, the expression for the total densities of thermodynamic potentials of the magnetic subsystem Φ_m and the interaction of magnetic characteristics with the structural distortions $\Phi_{m\varphi}$ takes the form

$$\Phi_m = \frac{1}{2}\alpha_m(\partial\mathbf{m}/\partial x_i)^2 + \frac{1}{2}a_m\mathbf{m}^2 - \frac{1}{4}b_m\mathbf{m}^4 + \frac{1}{6}d\mathbf{m}^6 + \frac{1}{2}\alpha_1(\partial\mathbf{l}/\partial x_i)^2 + \delta_1\mathbf{l} + \mathbf{mH}, \quad (2)$$

$$\Phi_{m\varphi} = \rho\varphi[\mathbf{m}(\partial\mathbf{l}/\partial x_i) + \mathbf{l}(\partial\mathbf{m}/\partial x_i)] + \frac{1}{2}\delta''\mathbf{m}^2\varphi^2. \quad (3)$$

[The gradient terms with respect to **m** and **l** are introduced for the same reasons as in Eq. (1)]. All the phenomenological constants in Eqs. (2) and (3) have the exchange origin: a_m, b_m, d, α_m, δ_1, and δ'' are positive, and the sign of the parameter ρ is insignificant. The last term in Eq. (2) determines the Zeeman energy (H is the external magnetic field strength, and the demagnetizing fields are ignored.)

In the general case, the expression for the total density of the nonequilibrium thermodynamic potential Φ_{tot} of the MnAs system should also include the density of elastic energy Φ_u, the term $\Phi_{u\varphi}$ accounting for the relation of elastic deformations to the structural distortions, and the density of the magnetostriction energy Φ_{mu}. The term Φ_u takes the form

$$\Phi_u = \frac{1}{2}k_0u_{11}^2 + \frac{1}{2}k_zu_{zz}^2 + \frac{1}{2}k_1(u_{xx} - u_{yy})^2 + k_{0z}u_{11}u_{zz} + Pu_{11} - T(\nu_0u_{11} + \nu_2u_{zz}). \quad (4)$$

Here, u_{ik} are the components of the elastic deformation tensor of the lattice; k_0, k_z, k_1, and k_{0z} are the elastic moduli; and P is the external hydrostatic pressure. The last term characterizes thermal expansion.

The term $\Phi_{u\varphi}$ can be constructed from the so-called mixed invariants, which contain φ and the u_{ik} components

$$\Phi_{u\varphi} = \varphi^2[\Lambda_0u_{11} + \Lambda_zu_{zz} + \Lambda_1(u_{xx} - u_{yy})]. \quad (5)$$

Here, Λ_0, Λ_1, and Λ_z are the parameters characterizing the relation of elastic deformations to the structural distortions.

Finally, the density of the magnetostriction energy is written as

$$\Phi_{mu} = \mathbf{m}^2(\lambda_0u_{11} + \lambda_zu_{zz}), \quad (6)$$

where λ_0 and λ_z are the magnetostriction constants composed of the mixed invariants describing the relation between the magnetic subsystem and the crystal lattice.

Therefore, the relationship

$$\Phi_{tot} = \Phi_\varphi + \Phi_m + \Phi_{m\varphi} + \Phi_u + \Phi_{mu} + \Phi_{u\varphi} \quad (7)$$

represents the total density of the nonequilibrium thermodynamic potential, which allows descriptions of all the possible phase states in the MnAs system and the phase transitions between these states.

Since the temperatures of the $PM(B8_1) \longrightarrow PM(B31)$ structural phase transition (T_t = 400 K) and the $PM(B31) \longrightarrow FM(B8_1)$ structural–magnetic phase transition (T_c = 303 K) differ considerably, the question arises as to the legitimacy of expanding Φ_{tot} simultaneously in terms of **m** and φ in the vicinity of T_c, where the φ parameter can often be rather large. The experimental data on the temperature dependence of the inverse magnetic susceptibility $\chi^{-1}(T)$ for MnAs indicate a linear function. According to [9], $\chi^{-1} \sim a_m + \delta\varphi^2$;

therefore, the coefficient a_m and the quantity φ^2 linearly depend on temperature. This implies that $\varphi^2 \ll 1$, because, otherwise, the higher-order terms in the expansion in terms of φ should play a leading part, which would lead to a nonlinear temperature dependence of φ^2. Since $\varphi^2 \sim |a_\varphi|/(b\varphi)$, the smallness of φ^2 suggests the smallness of the $|a_\varphi|$ coefficient over the entire temperature range from T_t to T_c. Physically, this result can be explained by the structural changes in MnAs being governed by the electronic structure of the crystal (the geometry of the Fermi surface), which varies rather slowly at these temperatures.

The generalized model of structural and magnetic equilibrium states and the corresponding phase transitions should account for the presence of the modulated magnetic structures. In order to construct this model, we use the thermodynamic potential represented by expression (7). As mentioned above, the inhomogeneous structural distortions arise from the separation of the crystal into crystallographic domains upon the lowering of the lattice symmetry $P6_3/mmc \longrightarrow P_{nma}$. These distortions are localized within the domain boundaries. It is clear that the domain boundaries virtually do not affect the equilibrium phase states within domains, and, hence, the terms containing $\partial\varphi/\partial x_i$ can be omitted in analyzing Eq. (7). For the equilibrium u_{ik} values, we rewrite Eq. (7) in the following form:

$$\begin{aligned}\Phi_{\text{tot}} &= \Phi_0 + a'_\varphi(T, P)\varphi^2 + b'_\varphi\varphi^4 + \alpha_m(\partial\mathbf{m}/\partial x_i)^2 \\ &+ \frac{1}{2}a_m(T, P)\mathbf{m}^2 - \frac{1}{4}b_m\mathbf{m}^4 + \frac{1}{6}d_m\mathbf{m}^6 + \delta_1\mathbf{l}^2 \\ &+ \alpha_1(\partial\mathbf{l}/x_i)^2 + \frac{1}{2}\delta'\varphi^2\mathbf{m}^2 \\ &+ \rho\varphi[\mathbf{m}(\partial\mathbf{l}/\partial x_i) - \mathbf{l}(\partial\mathbf{m}/\partial x_i)].\end{aligned} \tag{8}$$

The phenomenological coefficients a'_φ, b'_φ, α_1, α_m, a_m, b_m, d_m, δ_1, δ', and ρ in relationship (8) result from the renormalization of the corresponding coefficients entering into Eqs. (1)–(6). The Φ_0 value is the reference point for the thermodynamic potential. The *x*, *y*, and *z* axes of the Cartesian coordinate system coincide with the *a*, *b*, and *c* orthorhombic axes, respectively.

Now, we consider the last term in expression (8). As will be shown below, the invariants linear in the first spatial derivatives of the irreducible magnetic vectors of the system and their competition with the quadratic invariants at certain ratios between the phenomenological parameters of the theory lead to the formation of modulated magnetic structures with the crystal symmetry P_{nma} (the so-called double helix) with the structure wavevector q along the *a* axis.

The solution to the problem on the structural and magnetic equilibrium states of the potential described by Eq. (8) is sought in the form

$$\varphi = \text{const}, \tag{9}$$

$$\begin{aligned}m_y &= m\sin(qx); \quad m_z = m\cos(qx); \\ l_y &= l\sin(qx - \psi); \quad l_z = l\cos(qx - \psi); \quad \psi = \text{const}.\end{aligned} \tag{10}$$

The above invariant in Eq. (8) with allowance made for relationships (10) leads to the formation of modulated magnetic structures of the simple double helix type and also specifies the mutual orthogonality of *m* and *l* (i.e., $\psi = \pm\pi/2$), which is the consequence of the exchange approximation we used.

By introducing the new variables

$$Q^2 = q^2(\alpha_1/\delta_1), \quad \tau^2 = \varphi^2\rho^2/(\alpha_m\delta_1) \tag{11}$$

and minimizing with respect to the incidental parameter *l* at $Q^2 \ll 1$ (recall that we consider only the case of small-scale spatial inhomogeneities), we obtain the following final expression for the density of the nonequilibrium thermodynamic potential in the MnAs system:

$$\begin{aligned}\Phi &= \frac{1}{2}a_\varphi(T, P)\tau^2 + \frac{1}{4}b_\varphi\tau^4 + \frac{1}{2}a_m(T, P)\mathbf{m}^2 - \frac{1}{4}b_m\mathbf{m}^4 \\ &+ \frac{1}{6}d_m\mathbf{m}^6 + \frac{1}{2}\delta\tau^2\mathbf{m}^2 + \frac{1}{2}\beta Q^2\mathbf{m}^2[1 - \tau^2(1 - Q^2)].\end{aligned} \tag{12}$$

Here, the phenomenological parameters $a_\varphi(T, P)$, b_φ, δ, and β are combinations of the parameters of the initial potential (8), that is,

$$\begin{aligned}a_\varphi(T, P) &= a'_\varphi(T, P)\alpha_m\delta_1/\rho^2, \quad b_\varphi = b'_\varphi(\alpha_m\delta_1/\rho^2)^2, \\ \delta &= \delta'(\alpha_m\delta_1/\rho^2), \quad \beta = 2(\alpha_m\delta_1/\alpha_1).\end{aligned} \tag{13}$$

The conventional treatment of the thermodynamic potential defined by Eq. (12) with the aim of determining its equilibrium states and regions of their stability demonstrates that only five types of states are realized in the system with the following combinations of the *m*, φ, and *Q* parameters:

$$\begin{aligned}&m = 0; \quad \varphi = 0; \quad Q = 0. \\ &m = 0; \quad \varphi \neq 0; \quad Q = 0. \\ &m \neq 0; \quad \varphi = 0; \quad Q = 0. \\ &m \neq 0; \quad \varphi \neq 0; \quad Q = 0. \\ &m \neq 0; \quad \varphi \neq 0; \quad Q \neq 0.\end{aligned} \tag{14}$$

It is evident that the first, second, third, fourth, and fifth types of states correspond to the $PM(B8_1)$, $PM(B31)$, $FM(B8_1)$, $FM(B31)$, and $MMS(B31)$ phases, respectively. The mutual arrangement of states in the phase diagram on the a_φ–a_m coordinates for the MnAs system is displayed in Fig. 2.

It should be emphasized that the $MMS(B31)$ phase can occur only at the structural distortions $\varphi^2 \geq 1$, whereas the $PM(B31)$ phase exists at any φ of the initial

phase, and the $FM(B31)$ phase is observed in the range $0 \le \varphi^2 \le 1$.

From the phase diagram (Fig. 2), we can draw the conclusions concerning the possible phase transitions in the MnAs system and their character.

The 1–2 phase transition, i.e., $PM(B8_1)$–$PM(B31)$, occurs along the line $a_\varphi = 0$ at $a_m \ge 3/16(b_m^2/d_m)$ in the region beginning at the point K and represents the second-order phase transition.

The 1–3 phase transition, i.e., $PM(B8_1)$–$FM(B8_1)$, takes place along the line $a_\varphi \ge 0$ at $a_m = 3/16(b_m^2/d_m)$ in the region beginning at the point K and represents the first-order phase transition.

The 1–4 phase transition, i.e., $PM(B8_1)$–$FM(B31)$, and the 1–5 phase transition, i.e., $PM(B8_1)$–$MMS(B31)$, are not observed.

The 2–3 phase transition, i.e., $PM(B31)$–$FM(B8_1)$, occurs along the line $3a_\varphi^2 = b_m m_3^2(b_m m_3^2 - 4a_m)$ in the region between points K and F and represents the first-order phase transition. Here, $m_3 = \{(1/2d_m)[b_m + (b_m^2 - 4a_m d_m)^{1/2}]\}^{1/2}$ is the equilibrium magnetic order parameter for the $FM(B8_1)$ phase.

The 2–4 phase transition, i.e., $PM(B31)$–$FM(B31)$, is observed along the line $a_m = \gamma a_\varphi + 3b_m^2(1 + \gamma^2 b_\varphi/b_m)^2 16d_m$ in the region between points F and G and represents the first-order phase transition. Here, $\gamma = \delta/b_\varphi$.

The 2–5 phase transition, i.e., $PM(B31)$–$MMS(B31)$, takes place along the line $a_m = \gamma a_\varphi + 3b_m^2(1 + \gamma^2 2b_\varphi/b_m)^2 16d_m$ in the region beginning at the point G and is the first-order phase transition.

The 3–4 phase transition, i.e., $FM(B8_1)$–$FM(B31)$, occurs along the line $a_m = -\gamma b_\varphi m_3^2$ in the region below point F and represents the second-order phase transition.

The 3–5 phase transition, i.e., $FM(B8_1)$–$MMS(B31)$, is absent.

The 4–5 phase transition, i.e., $FM(B31)$–$MMS(B31)$, takes place along the line $a_\varphi = -b_\varphi\{1 + (1/2d_m)\gamma[b_m + (b_m^2 - 4d_m a_m + 4d_m a_\varphi \gamma)^{1/2}]\}$ in the region below point D and represents the second-order phase transition.

Among all the above results, the inference that the $MMS(B31)$ and $FM(B8_1)$ states have no common boundary is inconsistent with the available experimental data. At first glance, the theoretical prediction that the boundary is absent contradicts the experimental P–T diagram for MnAs, according to which the $MMS(B31) \longrightarrow FM(B8_1)$ phase transition is observed along the df line (Fig. 1). However, it should kept in mind that the theoretical P–T diagram was constructed without regard for the constraint $\varphi \ne$ const in the crystallographic domain boundaries, which is quite justified in the treatment of equilibrium phase states (if for no other reason than the small volume occupied by the domain boundaries in the crystal) and cannot be tolerated in analyzing mechanisms of phase transitions. It turned out that even the qualitative consideration of the domain boundaries in the above theoretical treatment led to the consistent scheme of phase transitions, which accounts for both the $MMS(B31)$–$FM(B8_1)$ phase transition and the suppression of the $FM(B8_1)$ state.

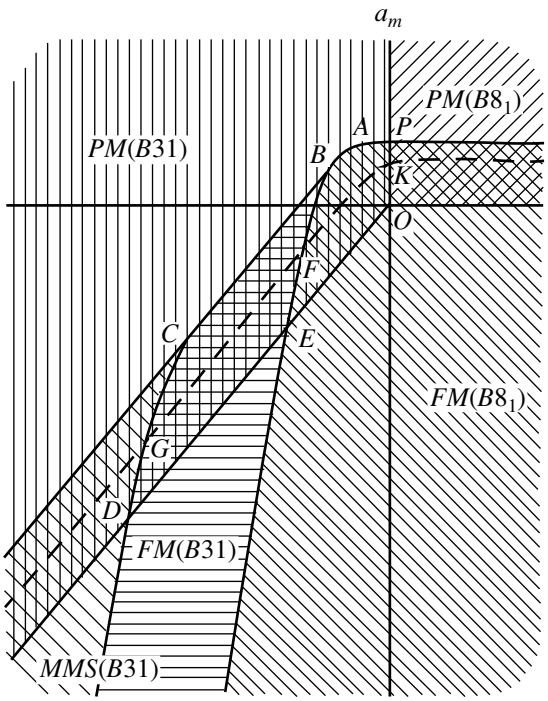

Fig. 2. Generalized theoretical phase diagram of magnetic and structural states for manganese arsenide.

According to this scheme, the $MMS(B31) \longrightarrow FM(B8_1)$ phase transition along the df line in the P–T diagram (Fig. 1) occurs through the intermediate state $PM(B31)$, which, in this region of the P–T diagram, is metastable with respect to the $FM(B8_1)$ phase. The bulk of the sample is penetrated by a network of twin boundaries in which the structure parameter φ is equal to zero. It is these domain boundaries that are crystal nuclei of the $FM(B8_1)$ phase [11]. Therefore, the interaction between nuclei of the $FM(B8_1)$ phase and the $PM(B31)$ matrix results either in the suppression of the nucleus growth, or in the formation of the magnetic (as more stable) phase throughout the crystal bulk.

3. EXPERIMENTAL RESULTS AND DISCUSSION

Let us consider the case when the $PM(B31)$ state is retained as metastable; i.e., the $FM(B8_1)$ state is sup-

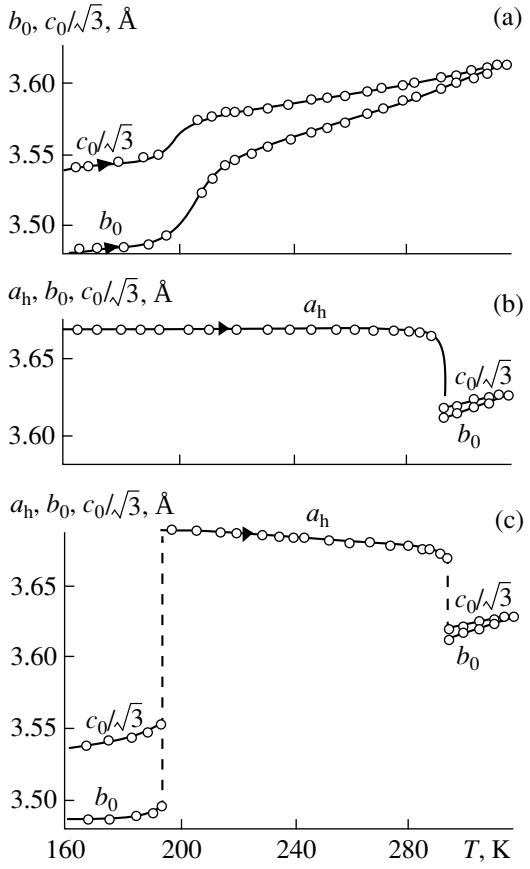

Fig. 3. Temperature dependences of the unit cell parameters for the $Mn_{0.99}Fe_{0.01}As$ alloy at different treatment stages.

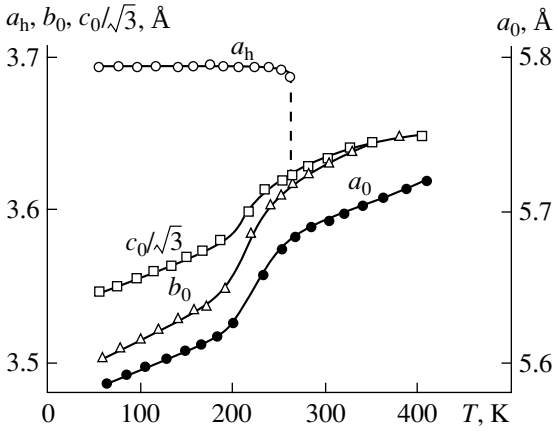

Fig. 4. Temperature dependences of the unit cell parameters for the $Mn_{0.95}Ni_{0.05}As$ alloy.

pressed. This phenomenon can be illustrated by the experimental temperature dependence of the unit cell parameters for the $Mn_{0.99}Fe_{0.01}As$ compound (Fig. 3a). It is known that, in manganese arsenide, the replacement of Mn atoms by Fe or Ni atoms in small amounts does not bring about a qualitative change in the *P–T* phase diagram of the initial sample, but only leads to a shift of the phase boundaries toward the low-pressure region [14, 15] and, thus, simplifies the technical problem of reaching the line of the *MMS*(*B*31) $\longrightarrow$ *FM*(*B*8$_1$) phase transition.

At the first experimental stage, the $Mn_{0.99}Fe_{0.01}As$ single-crystal sample at T = 300 K was subjected to hydrostatic compression up to $P > P_{cr}$ = 0.1 kbar [P_{cr} is the critical pressure above which the *FM*(*B*8$_1$) modification is not formed upon subsequent cooling of the sample] and, then, was cooled down to T = 160 K at constant pressure. After releasing the pressure under isothermal conditions, the single crystal appeared in the initial state in the *MMS*(*B*31) phase (the scheme of transformation is similar to that shown by the *ABCD* line in Fig. 1). As follows from the unit cell parameters measured upon subsequent heating of the sample at atmospheric pressure, the crystal over the entire temperature range remains in the orthorhombic modification ($c_0/\sqrt{3} \neq b_0$); i.e., the *FM*(*B*8$_1$) state is not formed (Fig. 3a). Anomalies in the curves $b_0(T)$ and $c_0/\sqrt{3}\,(T)$ at about T = 190 K indicate that only the *MMS*(*B*31) $\longrightarrow$ *PM*(*B*31) phase transition occurs in the crystal.

For the *MMS*(*B*31) $\longrightarrow$ *PM*(*B*31) phase transition to change to the *PM*(*B*31) $\longrightarrow$ *FM*(*B*8$_1$) phase transition and the ferromagnetic phase to be formed near the temperature of the initial *MMS*(*B*31) $\longrightarrow$ *PM*(*B*31) transition, the studied sample should be preliminarily transformed, at least once, into the *FM*(*B*8$_1$) state (for example, by cooling at P = 0 and then by heating to room temperature). Upon heating, the hexagonal symmetry is retained up to 290 K and then, upon the first-order phase transition, changes to the orthorhombic symmetry, which is typical of the *PM*(*B*31) state (Fig. 3b). After repeating the first experimental stage, i.e., the transformation of the sample into the *MMS*(*B*31) state along the trajectory similar to the *ABCD* line in Fig. 1, the temperature was increased, and two structural first-order phase transitions *MMS*(*B*31) $\longrightarrow$ *FM*(*B*8$_1$) and *FM*(*B*8$_1$) $\longrightarrow$ *PM*(*B*31) were observed at 190 and 290 K, respectively. The temperature dependences of the unit cell parameters upon these transformations are depicted in Fig. 3c. Therefore, the known *P–T* diagram for $Mn_{0.99}Fe_{0.01}As$ [14] is in agreement with the results obtained for the sample which at least once intersected the line of the *PM*(*B*31) $\longrightarrow$ *FM*(*B*8$_1$) phase transition in the high-temperature range. Otherwise, the *FM*(*B*8$_1$) phase is suppressed, the ferromagnetic state is not formed, and the *MMS*(*B*31) $\longrightarrow$ *PM*(*B*31) phase transition occurs at T = 190 K.

The suppression of the *FM*(*B*8$_1$) state more clearly manifests itself in the $Mn_{0.95}Ni_{0.05}As$ compound. In this case, the *PM*(*B*31) $\rightleftharpoons$ *MMS*(*B*31) phase transition is observed even at atmospheric pressure, and the ferromagnetic ordering is not realized at all [15]. An analysis of the temperature dependences of the unit cell parameters (Fig. 4, curves a_0, b_0, $c_0/\sqrt{3}$) and $\chi^{-1}(T)$ (Fig. 5)

for this alloy shows that the crystal lattice remains orthorhombic over the entire temperature range covered, and the $PM \rightleftharpoons MMS$ magnetic phase transition occurs near the temperature $T = 190$ K, at which the dependence of the unit cell parameters exhibits anomalous behavior.

The $FM(B8_1)$ state in $Mn_{0.95}Ni_{0.05}As$ can be induced by the magnetic field H, which exceeds the critical value H_{cr}. The effect of the magnetic field is most pronounced near the $PM(B31) \rightleftharpoons MMS(B31)$ phase transition point. This is confirmed by a sharp minimum in the $H_{cr}(T)$ curve (Fig. 6). The transition observed in the magnetic field is characterized by the ferromagnetic ordering with the saturation moment $\mu = 2.8\mu_B$ at $T = 195$ K (Fig. 5, curve M), an abrupt volume jump resulting in the fracture of the initial monolithic crystal, and a change in the crystal structure from orthorhombic to hexagonal (Fig. 4, curve a_h). The induced $FM(B8_1)$ phase is irreversible, because it persists after removal of the magnetic field. However, upon heating the sample above the $FM(B8_1) \longrightarrow PM(B31)$ phase transition temperature, the $FM(B8_1)$ state disappears through the first-order phase transition and does not arise at $H < H_{cr}$. It should be noted that the critical fields of inducing the ferromagnetic phase decrease in subsequent magnetization cycles. The boundaries of the existence of the $FM(B8_1)$ phase (metastable for this compound) on the P–T coordinates were determined by extrapolating the isothermal dependences $H_{cr}(P)$ to zero field [16]. It was found that the boundary of the spontaneous appearance of the magnetically ordered state is located in the region of "negative" pressures, whereas the boundary of the disappearance of this state lies in the region of positive pressures.

With the aim of revealing the reasons for the priority of either of the two above mechanisms of the $MMS(B31) \longrightarrow PM(B31)$ phase transition, let us analyze the interaction between the $FM(B8_1)$ crystal nuclei and the $PM(B31)$ matrix. This interaction is governed by a number of factors whose combination determines the final result of the phase transitions under consideration.

3.1. Factor of striction suppression of nuclei [17]. Upon the first-order phase transition, the crystal nucleation is attended by the appearance of inhomogeneous deformations due to the difference in the parameters and the symmetry of crystal lattices of the initial and final phases. An increase in the elastic energy of the crystal leads to the fact that the energy of the initial phase remains less than that of the sample containing crystal nuclei of energetically more favorable phase. Therefore, depending on the properties of the crystal, the nuclei of a new phase either arise at a considerable distance from the energy equilibrium of the phases or do not appear at all (i.e., remain suppressed).

3.2. Factor of dislocation unlocking of nuclei [18]. In real crystals, the stresses arisen upon nucleation partially relax through the dislocation motion. The dislocations decrease the elastic energy of the mixed state, moderate the striction effects, and, thus, narrow the range of locking the nuclei.

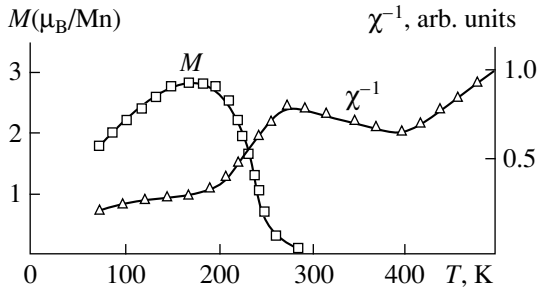

Fig. 5. Temperature dependence of the inverse magnetic susceptibility χ^{-1} in the initial state and the temperature dependence of the magnetization M in the induced state of the $Mn_{0.95}Ni_{0.05}As$ alloy.

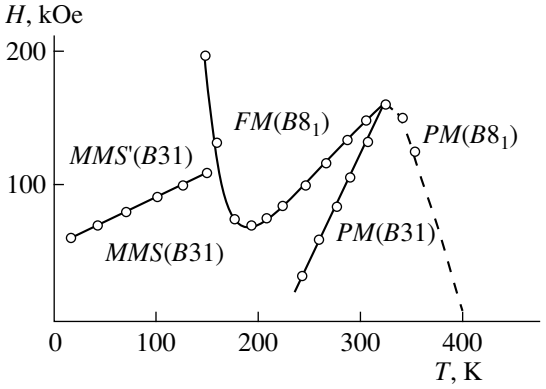

Fig. 6. Experimental H–T phase diagram of magnetic and structural states for the $Mn_{0.95}Ni_{0.05}As$ alloy.

3.3. Factor of dislocation immobilization. The appearance of crystal nuclei of the new phase brings about the motion of dislocations. These dislocations pile up near nuclei due to their pinning at crystal inhomogeneities. The interaction of dislocations at points of their pile-up leads to a strengthening of the material (a peculiar kind of "self-hardening"). The formation of a locking layer of dislocations around nuclei prevents their further motion. As a first approximation, it is reasonable to assume that the piled-up dislocations form a spherical frustum of diameter d_c. The degree of stress relaxation depends on the ratio between d_c and the linear sizes d of the sample. At $d > d_c$, the stresses around a nucleus partially relax, and the mechanism of nucleus locking is predominant in these samples. At $d < d_c$, the dislocations leave the sample without formation of a locking layer. The initial size d of the $Mn_{0.99}Fe_{0.01}As$ sample was equal to approximately 2 mm, which apparently exceeded the diameter of the locking layer of piled-up dislocations. As a result, the growth of the $FM(B8_1)$ crystal nuclei in this sample was hindered at

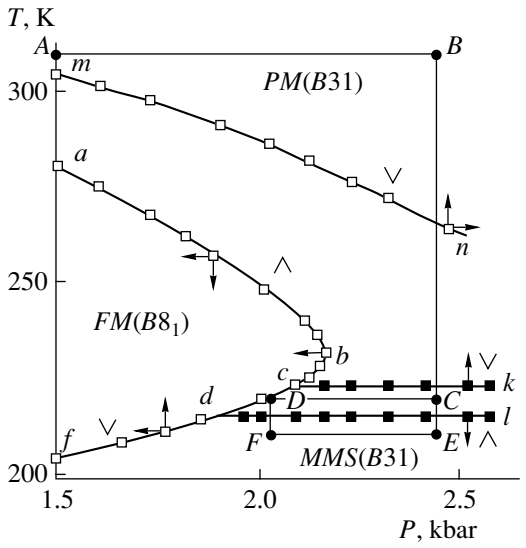

Fig. 7. A fragment of the experimental *P–T* phase diagram for manganese arsenide.

the first experimental stage. In the case when the sample in the $FM(B8_1)$ state is cooled at least once, or this state is induced by the magnetic field, the subsequent transition to the hexagonal phase is accompanied by a jumpwise change in both the symmetry and the specific volume of the crystal lattice. The mechanical stresses thus arisen bring about the fracture of the sample into fragments whose sizes are likely less than the characteristic size of the locking dislocation layer. These fragments are characterized by dislocation unlocking of nuclei. Therefore, the dislocation locking of the $FM(B8_1)$ crystal nuclei is absent in the subsequent experimental cycles.

The x-ray diffraction investigations demonstrate that the above transition occurs through the first-order phase transition close to the second-order transition. This is confirmed by a jumpwise change in the unit cell parameters (Fig. 3a) and also by the coexistence of diffraction maxima for both phases near the phase transition temperature, which was observed in the x-ray diffraction patterns of the (440) planes. Since the specific volume of the $PM(B31)$ phase is larger than that of the $MMS(B31)$ phase, the transition between these phases is associated with the manifestation of the following factor.

3.4. Factor of asymmetric change in crystal strength. Essentially, this factor is as follows. Upon the $MMS(B31) \longrightarrow PM(B31)$ phase transition, the growth of the $PM(B31)$ crystal nuclei with a larger specific volume brings about the strengthening of the sample due to the dislocation immobilization. Upon the reverse transition, the nuclei of the $MMS(B31)$ phase with a smaller specific volume separate from the matrix, which results in an increase in the dislocation concentration and a "softening" of the sample. As was noted in [18], this factor should lead to a radical difference between the direct and reverse transitions. Consequently, this factor prevents the growth of the $FM(B8_1)$ crystal nuclei in the vicinity of the $MMS(B31) \longrightarrow PM(B31)$ phase transition and, vice versa, favors their growth upon reverse transition.

The x-ray diffraction patterns recorded along the hexagonal basis of the $Mn_{0.95}Ni_{0.05}As$ crystal show that, at temperatures of the $MMS(B31) \longrightarrow PM(B31)$ phase transition, the contrast of the $(040)_0$ and $(026)_0$ diffraction lines disappears owing to their broadening. This indicates a nonuniform distribution of deformations in the crystal. As already mentioned, the deformations primarily accumulate in the boundaries between crystallographic domains. In this case, the sizes of inhomogeneities can be as large as those of orthorhombic distortions. The high contrast of the $(040)_0$ and $(026)_0$ diffraction lines well apart from the temperature of this phase transition shows that the inhomogeneous deformations comparable in magnitude to the orthorhombic distortions, if any, are localized in the small volume of the crystal. The loss of contrast in the x-ray diffraction patterns near the phase transition temperature indicates that these deformations occur throughout the bulk of the crystal. Note that the sample volume with zero structural order parameter increases, and, hence, the probability of the formation of the $FM(B8_1)$ crystal nuclei in the $PM(B31)$ matrix increases drastically. This feature of the $MMS(B31) \longrightarrow PM(B31)$ phase transition is a further contributing factor for the $MMS(B31) \longrightarrow FM(B8_1)$ phase transition.

Thus, we considered several factors, which, in our opinion, determine the directions of the processes of formation and growth of the $FM(B8_1)$ crystal nuclei in the $PM(B31)$ matrix in the vicinity of the $MMS(B31) \longrightarrow PM(B31)$ phase transition. Unfortunately, the combined effect of the aforementioned factors cannot be quantitatively evaluated because of the complexity of the appropriate mathematical apparatus and the lack of experimental data.

In this respect, the MnAs compound was further investigated by differential thermal analysis (DTA). The DTA data confirmed the possibility of the $MMS(B31) \longrightarrow FM(B8_1)$ phase transition occurring through the intermediate $PM(B31)$ state. For clarity, the experimental data are shown in the *P–T* diagram at $P \geq 1.5$ kbar (Fig. 7). In this figure, the points of thermal anomalies are denoted by open and closed squares, and the arrows near the squares indicate the directions of the change in *T* or *P*, at which the anomalies were observed. The symbols $\wedge$ and $\vee$ designate that the phase transformation occurs either with heat release or with heat absorption, respectively.

First and foremost, we note that the phase transition $PM(B31) \rightleftharpoons MMS(B31)$ is the first-order phase transition with a temperature hysteresis of ~7 K. The transition temperature, at least below $P = 2.6$ kbar, is virtually independent of pressure. As can be seen, the phase transition is accompanied by the heat release upon

cooling (line *dl*) and the heat absorption upon heating (line *ck*). The experimental amplitudes of the peaks associated with the heat release and the heat absorption are equal in magnitude and slightly decrease with an increase in P in the pressure range studied.

The $PM(B31) \longrightarrow FM(B8_1)$ phase transition occurring in the *abc* portion of the P–T diagram is universally accompanied by the heat release without regard to the sequence of changes in the thermodynamic parameters P and T in the course of the experiment. The heat absorption is observed upon the $MMS(B31) \longrightarrow FM(B8_1)$ phase transition, which takes place in the *df* portion of the phase diagram. Finally, both the $PM(B31) \longrightarrow FM(B8_1)$ and $MMS(B31) \longrightarrow FM(B8_1)$ phase transitions can occur in the *dc* portion, depending on the particular thermodynamic trajectory along which the sample is transformed into the $FM(B8_1)$ state. For example, when passing along the *ABCD* trajectory, the $PM(B31) \longrightarrow FM(B8_1)$ phase transition attended by the heat release is observed at point *D*. At the same time, the $MMS(B31) \longrightarrow FM(B8_1)$ transition with the heat absorption is realized when going to the same point *D* along the *ABCEFD* trajectory. Therefore, the triple point of the first-order phase transitions is located at about $T \approx 215$ K and $P \approx 2.0$ kbar.

Let us now elucidate how the pressure affects the amplitude of thermal effects observed upon phase transformations in MnAs. An increase in the pressure leads to a decrease in the amplitude of the exothermic peaks upon the $PM(B31) \longrightarrow FM(B8_1)$ phase transition in the *abcd* portion of the P–T diagram. This is a typical phenomenon; it is explained by an increase in the rate of thermal energy dissipation due to an increase in the density of a pressure transmitting medium. However, the amplitude of the endothermic peaks for the $MMS(B31) \longrightarrow FM(B8_1)$ phase transition increases with an increase in the pressure. Note that, near the triple point (at which P and T for all the phase transformations are virtually identical), the amplitudes of the peaks for the $PM(B31) \longrightarrow MMS(B31)$ phase transition only slightly exceed those for the $MMS(B31) \longrightarrow FM(B8_1)$ phase transition, whereas the amplitudes of the peaks for the $PM(B31) \longrightarrow FM(B8_1)$ phase transition are approximately three times smaller than the former amplitudes.

An anomalous increase in the amplitude of the endothermic peaks upon the $MMS(B31) \longrightarrow FM(B8_1)$ phase transition with an increase in P can be explained under the assumption that this transition occurs through the intermediate $PM(B31)$ state. This can be schematically represented in the following way. The $MMS(B31) \longrightarrow PM(B31)$ phase transition accompanied by the heat absorption occurs at the first stage. Then, the $PM(B31)$ phase transforms to the $FM(B8_1)$ phase with the heat release. Therefore, the combined effect of these thermal processes is recorded in the experimental DTA curves. Since the amplitudes of the peaks differ in magnitude and sign, and, moreover, the thermal effects are likely also different in the rates of energy dissipation, the observed anomalous situation can arise when the amplitude of the combined thermal effect decreases upon the two-stage phase transition $MMS(B31) \longrightarrow PM(B31) \longrightarrow FM(B8_1)$ with a decrease in the pressure.

4. CONCLUSION

Thus, an attempt was made to represent the specific features of the phase transitions in manganese arsenide and alloys on its base as the result of interaction between the magnetic and structure parameters. We proposed the new model for nucleation of the $FM(B8_1)$ phase upon the $PM(B31) \longrightarrow FM(B8_1)$ first-order phase transition when the $PM(B31)$ state is metastable. It was demonstrated that the nucleation of the $FM(B8_1)$ phase within the boundaries separating the crystallographic domains is thermodynamically favorable.

Within these boundaries, which are formed upon lowering the symmetry of crystal lattice from $B8_1$ to $B31$, the structural order parameter becomes zero and does not affect the magnetic processes, including the formation of the ferromagnetic state. Not all of the inferences and statements of our concepts were proven conclusively. In particular, the energy aspects of the $MMS(B31) \longrightarrow FM(B8_1)$ two-stage phase transition remain unclear. However, the general conclusion drawn in this work is beyond question: there is a close correlation between the magnetic and structural properties. In many respects, this relation determines the quantitative characteristics of the material and also brings about qualitatively new properties and phenomena, which cannot be manifestations either only of the magnetic or only of the structural subsystem. This is the main result obtained in our work. Note also that the consistent inclusion of interactions between the magnetic and structural subsystems is an important and fruitful direction in the development of the phase transition concepts in solids.

Owing to the specific features of manganese arsenide and alloys on its base, the structural properties substantially affect the phase transformations. However, there is no need to prove the universal character of this effect and the necessity of its inclusion in the treatment of a large number of phenomena outside the province of magnetism.

REFERENCES

1. A. T. Serres, J. Phys. Radium **8** (2), 146 (1947).
2. G. I. Gulliond, J. Phys. Radium **12** (3), 223 (1951).
3. R. H. Wilson and Y. S. Kasper, Acta Crystallogr. **17**, 95 (1964).
4. J. B. Goodenough and J. A. Kafalas, Phys. Rev. **157** (2), 389 (1967).

5. N. Menyuk, J. A. Kafalas, K. D. Wight, and J. B. Goodenough, Phys. Rev. **177** (2), 942 (1969).
6. C. Kittel, Phys. Rev. **120**, 335 (1960).
7. C. P. Bean and I. S. Rodbell, Phys. Rev. **126** (1), 104 (1962).
8. M. Blume, Phys. Rev. **141**, 517 (1966).
9. I. M. Vitebskiĭ, V. I. Kamenev, and D. A. Yablonskiĭ, Fiz. Tverd. Tela (Leningrad) **23** (1), 215 (1981) [Sov. Phys. Solid State **23**, 121 (1981)].
10. E. G. Galkina, É. A. Zavadskiĭ, V. I. Kamenev, and D. A. Yablonskiĭ, Fiz. Tverd. Tela (Leningrad) **25** (1), 79 (1983) [Sov. Phys. Solid State **25**, 43 (1983)].
11. E. G. Galkina, É. A. Zavadskiĭ, V. I. Kamenev, *et al.*, Fiz. Tverd. Tela (Leningrad) **28** (6), 1723 (1986) [Sov. Phys. Solid State **28**, 954 (1986)].
12. F. H. Franzen, C. Haas, and F. Jelinek, Phys. Rev. B **10** (4), 1248 (1974).
13. O. V. Kovalev, *Irreducible Representations of the Space Groups* (Akad. Nauk Ukr. SSR, Kiev, 1961; Gordon and Breach, New York, 1965).
14. V. I. Val'kov, E. G. Galkina, É. A. Zavadskiĭ, *et al.*, Fiz. Tverd. Tela (Leningrad) **23** (7), 2209 (1981) [Sov. Phys. Solid State **23**, 1295 (1981)].
15. B. M. Todris, in *Proceedings of the Conference on Physics of Magnetic Phenomena, Donetsk, 1977*, Donetsk, 1977, Part 2, p. 139.
16. A. A. Galkin, É. A. Zavadskiĭ, V. M. Smirnov, and V. I. Val'kov, Pis'ma Zh. Éksp. Teor. Fiz. **20** (4), 253 (1974) [JETP Lett. **20**, 111 (1974)].
17. V. G. Bar'yakhtar, I. M. Vitebskiĭ, and D. A. Yablonskiĭ, Fiz. Tverd. Tela (Leningrad) **19** (2), 347 (1977) [Sov. Phys. Solid State **19**, 200 (1977)].
18. I. M. Kaganova and A. L. Roĭtburd, Fiz. Tverd. Tela (Leningrad) **31** (4), 1 (1989) [Sov. Phys. Solid State **31**, 545 (1989)].

Translated by O. Borovik-Romanova

Physics of the Solid State, Vol. 42, No. 9, 2000, pp. 1705–1711. Translated from Fizika Tverdogo Tela, Vol. 42, No. 9, 2000, pp. 1657–1663.

MAGNETISM AND FERROELECTRICITY

Effect of the Substrate Crystalline Structure on the Magnetic, Electrical, and Crystallographic Characteristics of $La_{0.35}Nd_{0.35}Sr_{0.3}MnO_3$ Epitaxial Films

A. I. Abramovich*, O. Yu. Gorbenko*, A. R. Kaul*, L. I. Koroleva*, A. V. Michurin*, R. Szymczak, and S. Deev****

** Moscow State University, Vorob'evy gory, Moscow, 119899 Russia*
e-mail: koroleva@ofef343.phys.msu.su

*** Institute of Physics, Polish Academy of Sciences, 02-668 Warsaw, Poland*

Received February 11, 2000; in final form, February 29, 2000

Abstract—A study has been made of the electrical resistivity ρ, magnetoresistance Δρ/ρ, and magnetization of $La_{0.35}Nd_{0.35}Sr_{0.3}MnO_3$ epitaxial films on $ZrO_2(Y_2O_3)$, $SrTiO_3$, $LaAlO_3$, and MgO substrates. The first film can exist in four equivalent crystallographic orientations in the sample plane, while the other three have only one orientation. The maxima of ρ and Δρ/ρ of the first film are broadened considerably in the vicinity of the Curie point T_C compared to the three others, the magnitude of ρ itself being larger by 1.5 orders of magnitude, and a large negative magnetoresistance ($|\Delta\rho/\rho| \sim 10\%$ in a field of 8.4 kOe) is observed at temperatures $80 \le T \le 200$ K. In all films, the magnetic moment per molecule at 5 K is ~46% smaller than the pure spin value, due to the existence of magnetically disordered regions. The larger value of ρ of the film deposited on $ZrO_2(Y_2O_3)$ is due to the electrical resistance of the boundaries separating regions with different crystallographic orientations, and the magnetoresistance is associated with polarized carriers tunneling through the boundaries coinciding with domain walls. The low-temperature magnetoresistance in fields above technical saturation is caused by the strong *p–d* exchange coupling within spin-ordered regions. © *2000 MAIK "Nauka/Interperiodica".*

Although manganites with a perovskite structure have long been known [1, 2], interest in them has been growing since 1995. It is due to the discovery of a colossal room-temperature magnetoresistance (MR) in thin films of some compositions, an extremely important finding for device applications. The colossal MR is observed in these compounds near the Curie point T_C within a narrow temperature interval and lies mostly in the suppression of the resistivity peak in the region of T_C. Increasing the temperature range where colossal MR exists would be important from an application standpoint.

The highest Curie point of 370 K was observed for the $La_{0.35}Nd_{0.35}Sr_{0.3}MnO_3$ composition [1], but it has a metallic conduction, and its MR is much lower than that of the semiconducting manganites. It is of interest to find out how a partial replacement of La by other rare-earth ions in this composition would affect the Curie temperature and the magnitude of MR.

The aim of this work is to study the effect of a partial substitution of Nd for La on the electrical and magnetic properties of the above composition and to broaden the temperature region of existence of colossal MR by properly choosing the substrate. It was found earlier that $La_{0.85}Sr_{0.15}MnO_3$ films on (001)$ZrO_2(Y_2O_3)$ single-crystal substrates possess colossal MR within a broader temperature interval than those grown on (001)$LaAlO_3$ single-crystal plates [2, 3].

1. PREPARATION OF THIN FILMS AND EXPERIMENTAL TECHNIQUES

The films were prepared by the method of metal organic chemical deposition (MOCVD) with an aerosol source of metal-organic (La, Nd, Sr, and Mn dipivaloyl methanates) vapors [4].

The substrates were 1-mm thick plates cut from $ZrO_2(Y_2O_3)$, $LaAlO_3$, $SrTiO_3$, and MgO crystals so that their surface coincided with the (001) crystal plane.

The films were deposited in a vertical reactor on inductively heated substrates. After deposition, the films were additionally annealed in oxygen at the deposition temperature (750°C) for 0.5 h.

The x-ray diffraction analysis of the films, including the determination of the phase composition, orientation, and lattice parameters, was carried out on a Siemens D5000 four-circle diffractometer with a secondary graphite monochromator (CuK_α radiation). The film composition was determined by x-ray microprobe analysis (using a CASCAN scanning electron microscope equipped with the EDAX system).

The magnetization of thin films was determined with a SQUID magnetometer, and the electrical resistivity, by the four-probe method. The MR was measured in the film plane, with the current through the film parallel to the magnetic field **H**.

1063-7834/00/4209-1705$20.00 © 2000 MAIK "Nauka/Interperiodica"

Magnetic, electrical, and crystallographic characteristics of $La_{0.35}Nd_{0.35}Sr_{0.3}MnO_3$ films

Substrate	MgO	$LaAlO_3$	$SrTiO_3$	$ZrO_2(Y_2O_3)$
T_C, K (H = 10 Oe)	242	231	219	
T_C, K (H = 100 Oe)		241	223	245
Magnetic moment per formula unit, μ_B	1.7	1.6	2	1.9
Temperature of the maximum in ρ, T_m (K)	252	252	252	225
Temperature of the maximum in $\lvert\Delta\rho/\rho\rvert$, T_{max} (K) (H = 8.4 kOe)	228	223	213	225
Maximum value of ρ, ρ_{max} (Ω cm)	0.085	0.13	0.084	0.63
Value of ρ at 82 K, $\rho_{82\ K}$ (Ω cm)	0.0089	0.0059	0.0040	0.19
Maximum value of $\lvert\Delta\rho/\rho\rvert$, $\lvert\Delta\rho/\rho\rvert_{max}$, in a field H = 8.4 kOe	0.34	0.23	0.22	0.13
Value of $\lvert\Delta\rho/\rho\rvert$ at 82 K in a field H = 8.4 kOe, $\lvert\Delta\rho/\rho\rvert_{82\ K}$	0.04	0.03	0.03	0.11
Film thickness, Å	4100	5500	5500	5500
Interplanar parameter, Å	3.882 ± 0.001	3.880 ± 0.002	3.872 ± 0.001	3.874 ± 0.001
Intraplanar parameter, Å	3.876 ± 0.002	3.875 ± 0.002	3.878 ± 0.001	3.881 ± 0.002
Perovskite cell volume, $Å^3$	58.32 ± 0.08	58.26 ± 0.09	58.23 ± 0.05	58.25 ± 0.06

2. RESULTS OF THE EXPERIMENT AND THEIR DISCUSSION

2.1. Crystallographic Properties

The results of θ–2θ scanning showed that the films on $LaAlO_3$, $SrTiO_3$, and MgO have a (001) orientation, and that on $ZrO_2(Y_2O_3)$, a (110) orientation. The planar orientation was achieved by φ scanning. The films on $LaAlO_3$, $SrTiO_3$, and MgO were found to be in cube-on-cube epitaxial growth registry with the substrate.

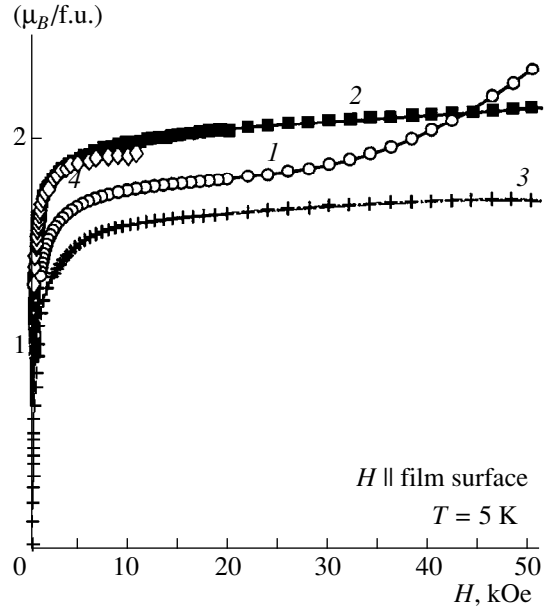

Fig. 1. Magnetization M (μ_B/f.u.) *vs* magnetic field H in $La_{0.35}Nd_{0.35}Sr_{0.3}MnO_3$ thin films on various substrates. The film composition in the subsequent figures is the same. Substrate: (*1*) MgO; (*2*) $SrTiO_3$; (*3*) $LaAlO_3$; and (*4*) $ZrO_2(Y_2O_3)$.

The film on $ZrO_2(Y_2O_3)$ also exhibits a planar orientation, but a more complex one. The body diagonals of its perovskite cubes are parallel to the fluorite cube-face diagonals of the $ZrO_2(Y_2O_3)$ structure, with four equivalent orientations available: (i) $[1–11]_f \parallel [110]_s$, $[–112]_f \parallel [–110]_s$, (ii) $[1–11]_f \parallel [110]_s$, $[–112]_f \parallel [–1–10]_s$, (iii) $[1–11]_f \parallel [–110]_s$, $[–112]_f \parallel [110]_s$, and (iv) $[1–11]_f \parallel [–110]_s$, $[–112]_f \parallel [–1–10]_s$, where the *f* and *s* subscripts denote the film and the substrate, respectively. As a result, angles of 19.5, 70.5, and 90° are formed in the Mn–O–Mn–O chains at the contacts of the above regions with different orientations. Such an orientation was observed earlier in $La_{1-x}Sr_xMnO_3$ films on the $ZrO_2(Y_2O_3)$ substrate [3].

It can be seen from the table presenting the lattice parameters of the films, they are close to the pseudocubic crystalline structure; indeed, their interplanar distance is close to the intraplanar parameter. These parameters are the same for films grown on different substrates. No reflections other than the ones characteristic of the simple perovskite structure were observed. This is due to the fact that the $La_{0.35}Nd_{0.35}Sr_{0.3}MnO_3$ composition under study here with the mean ionic radius of the *A* cation of 1.225 Å (a tolerance factor of 0.922) lies nearly at the morphotropic boundary between the orthorhombic *Pnma* and rhombohedral *R*3*c* structures. This is apparently why the distortions of the perovskite structure are so small as to be below the experimental accuracy. For this reason, the lattice stresses typical of manganite films obviously relax almost completely in the films under study.

2.2. Magnetic Properties

The film magnetization M was measured on an in-plane magnetic field, with corrections for the substrate magnetization being introduced properly. Figure 1 pre-

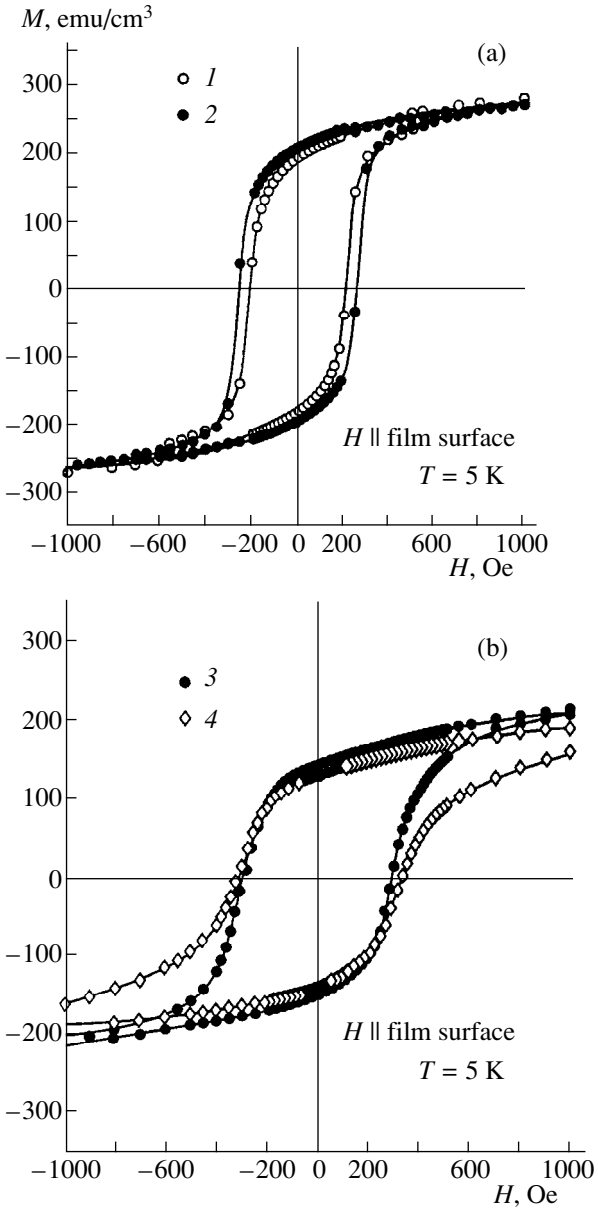

Fig. 2. Hysteresis loops for thin films deposited on various substrates: (a) (*1*) $SrTiO_3$, (*2*) $ZrO_2(Y_2O_3)$ and (b) (*3*) MgO and (*4*) $LaAlO_3$.

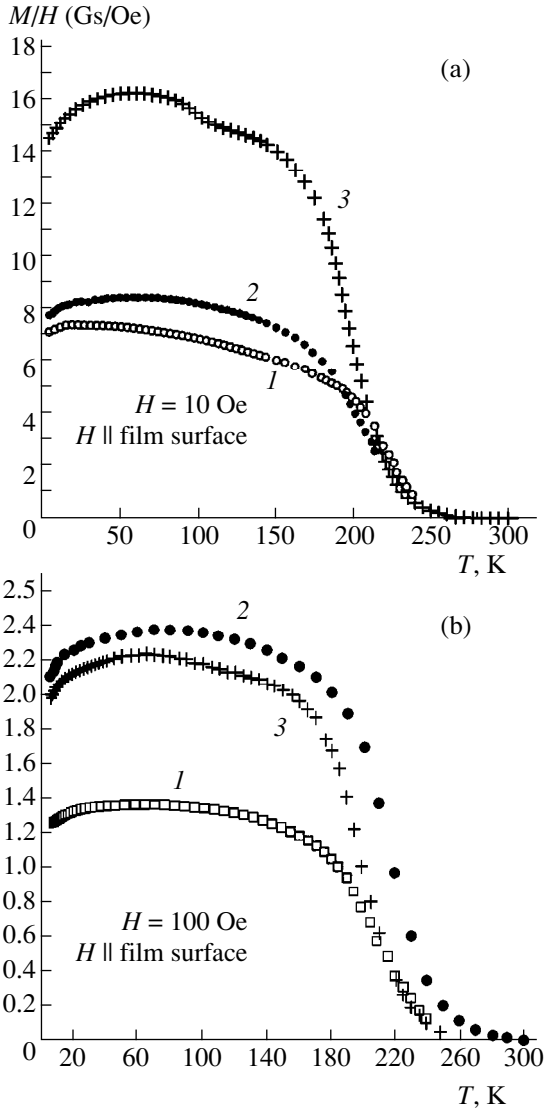

Fig. 3. Temperature dependence of the initial magnetic susceptibility of thin films on various substrates measured in fields *H*: (a) 10 and (b) 100 Oe. Substrates: (a) (*1*) MgO, (*2*) $LaAlO_3$, (*3*) $SrTiO_3$ and (b) (*1*) $LaAlO_3$, (*2*) $ZrO_2(Y_2O_3)$, and (*3*) $SrTiO_3$.

sents the $M(H)$ dependences for all the films obtained at $T = 5$ K. We readily see that the magnetization of all films, except that on MgO, saturates rapidly in a field of a few kOe. After saturation within the 7–25 kOe region, the film on MgO exhibits a close-to-linear growth of M as the field continues to increase (the maximum field used in the measurements was $H = 50$ kOe), with the magnetic moment per formula unit increasing from 1.9 μ_B to 2.6 μ_B.

Figure 2 shows the hysteresis loops of all the films studied, which were obtained at the maximum field of 1 kOe. As seen from the figure, the loops are fairly narrow, and the coercive force does not exceed 300 Oe. Displayed in Fig. 3 is the temperature dependence of the initial magnetic susceptibility of all the films. Their Curie points T_C listed in the table were determined by extrapolating the steepest part of the $M/H(T)$ curves to intersect with the temperature axis.

2.3. Electrical Properties

Figure 4 presents the temperature dependences of the electrical resistivity ρ of all the films studied, and Fig. 5, those of the MR, $\Delta\rho/\rho$, for films on $SrTiO_3$ and $ZrO_2(Y_2O_3)$. Here $\Delta\rho = \rho_H - \rho_{H=0}$. Figure 6 shows the $\Delta\rho/\rho(H)$ dependence obtained at several temperatures

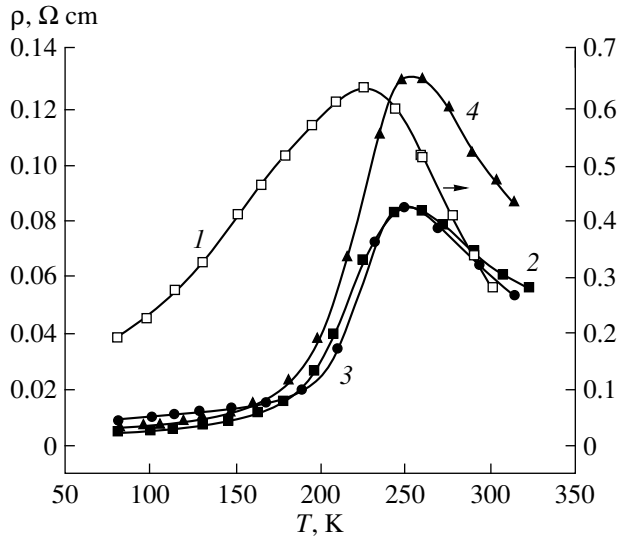

Fig. 4. Temperature dependence of electrical resistivity ρ of thin films on various substrates: (*1*) $ZrO_2(Y_2O_3)$, (*2*) $SrTiO_3$, (*3*) MgO, and (*4*) $LaAlO_3$.

on the same films. The $\Delta\rho/\rho(T)$ and $\Delta\rho/\rho(H)$ curves measured on films deposited on MgO and $LaAlO_3$ are similar to those presented in Figs. 5a and 6a for the film on $SrTiO_3$. The temperatures of the maxima in the $|\Delta\rho/\rho|(T)$ and $\rho(T)$ curves are listed in the table for all the films studied.

2.4. Discussion of Results

It can be seen from Fig. 4, the $\rho(T)$ curves have a maximum, its position T_m for the film on $ZrO_2(Y_2O_3)$ being lower than T_C by 20 K, and that for the films on $SrTiO_3$, MgO, and $LaAlO_3$, higher than T_C by about 20 K. The MR is negative, and the $|\Delta\rho/\rho|(T)$ curves also pass through a maximum near T_C (see Fig. 5). The MR isotherms do not saturate throughout the temperature region covered (see Fig. 6). The MR reaches as high as 34% at H = 8.4 kOe in the film on MgO, while for the other films it is lower: 23, 22, and 13% for the films on $LaAlO_3$, $SrTiO_3$, and $ZrO_2(Y_2O_3)$, respectively (see table). Thus, the films studied in this work exhibit colossal MR near T_C, just as this is observed in manganites of other compositions [5–7].

A comparison of the $\rho(T)$ curves of the film on $ZrO_2(Y_2O_3)$ with the three other films on the perovskite and MgO substrates (Fig. 4) shows the magnitude of ρ of the first film to be substantially larger than that of the others. It follows from the table that at 82 K it is larger by more than an order of magnitude, and at the maximum in ρ, by a factor of four–eight. The shapes of the curves are different as well. For instance, the strong

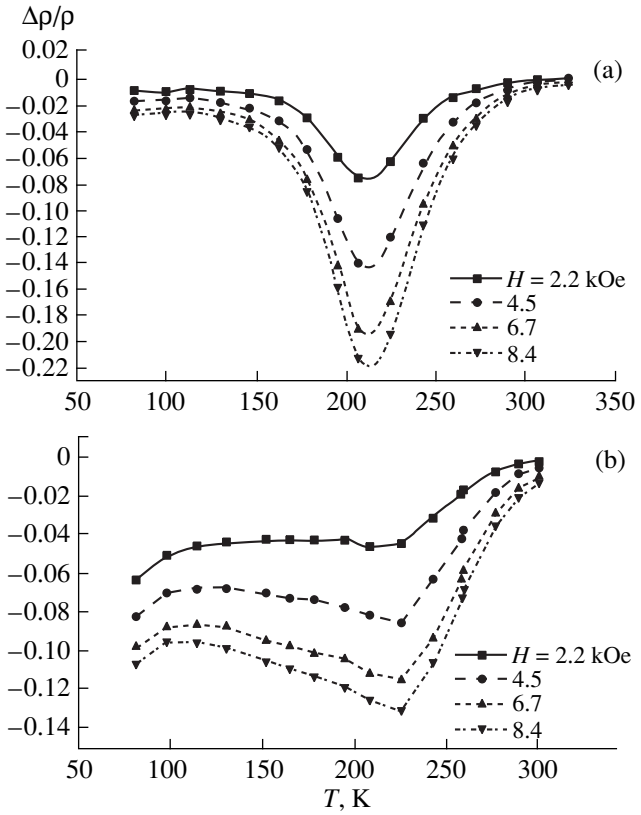

Fig. 5. Temperature dependence of magnetoresistance $\Delta\rho/\rho$: (a) thin film on the (001) $SrTiO_3$ substrate; (b) thin film on the (001) $ZrO_2(Y_2O_3)$ substrate.

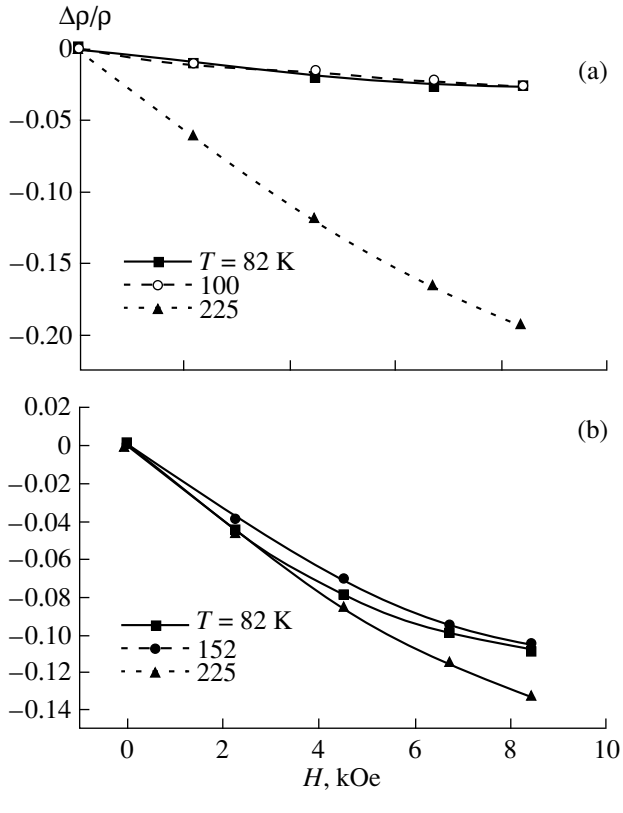

Fig. 6. Isotherms of magnetoresistance $\Delta\rho/\rho$: (a) thin film on the (001) $SrTiO_3$ substrate; (b) thin film on the (001) $ZrO_2(Y_2O_3)$ substrate.

growth of ρ with increasing temperature in films on $SrTiO_3$, $LaAlO_3$, and MgO starts at $T \sim 180$ K, whereas ρ of the film on $ZrO_2(Y_2O_3)$ already starts to increase monotonically at 80 K, which is the lowest measurement temperature, i.e., the maximum in the $\rho(T)$ curve is broadened considerably. The difference between the $|\Delta\rho/\rho|(T)$ curves is larger still; indeed, the first three films exhibit a sharp maximum at the temperature T_{max} which is slightly lower than T_C, while in the film on $ZrO_2(Y_2O_3)$ this peak, which also lies slightly below T_C, is diffuse and barely noticeable on the low-temperature side (Fig. 5). The latter film has a high $|\Delta\rho/\rho|$ at low temperatures; namely, it reaches ~10% in a field of 8.4 kOe and grows slowly starting from 100 K as the temperature is further lowered. The $|\Delta\rho/\rho|(H)$ curves of the first three films and of the last one also differ strongly (see Fig. 6); indeed, the first three exhibit a nearly linear increase in $|\Delta\rho/\rho|$ with the field at temperatures below that corresponding to the maximum on the $|\Delta\rho/\rho|(T)$ curve, whereas the latter film reveals a sharp growth of $|\Delta\rho/\rho|$ in weak fields up to ~ 2 kOe, which is replaced by a close-to-linear increase of $|\Delta\rho/\rho|$ at higher fields.

Behavior of ρ and $\Delta\rho/\rho$ similar to that observed in the film on $ZrO_2(Y_2O_3)$ was seen earlier in the polycrystalline bulk and in thin-film samples of manganites [8–22]. At the same time, the variation of ρ and $\Delta\rho/\rho$ in single-crystal samples of the same composition resembled that observed by us in films on $SrTiO_3$, $LaAlO_3$, and MgO. It was assigned to spin-polarized tunneling among grains [14], or to carrier scattering within domain walls, which coincide, as a rule, with grain boundaries [9]. It was shown [23] that NMR data obtained on a $La_{0.67}Ca_{0.33}MnO_3$ film indicate the hole concentration to be lower inside domains.

However, all the films studied in this work are single crystals, including the film on $ZrO_2(Y_2O_3)$. The latter differs from the other films investigated here in that it consists, as pointed out in 2.1, of microregions with four different crystallographic orientations. This results in the existence in it of magnetic domains having at least four different easy-magnetization axes, whose boundaries make different angles with the magnetization directions in the domains. The easy-magnetization axes in different parts of the films on the perovskite and MgO substrates are parallel to one another, and such films should therefore be largely made up of 180° magnetic domains.

The magnitude of ρ of the films on the perovskite and MgO substrates measured at $T < T_C$ (see table) indicates that their conduction is metallic. It follows that the carrier-mediated exchange coupling is dominant in this compound. The Curie temperature is given in this case by [24]

$$T_C \sim zt\nu, \qquad (1)$$

where t is the transfer integral (the conduction-band width W is proportional to t), z is the coordination number of the magnetic ion (Mn in the present case), and ν is the number of carriers per magnetic ion. As seen from the table, the film on $ZrO_2(Y_2O_3)$ has approximately the same Curie temperature as the three others. This means that the exchange interaction in this film is likewise mediated by carriers, and that the increase of its electrical resistivity by more than an order of magnitude compared to the three other films is due to the boundaries separating regions with different crystallographic orientations. It was already pointed out that there are no such boundaries in the other three films studied in this work. Obviously enough, the electrical resistivity of a film on $ZrO_2(Y_2O_3)$, as that of polycrystalline samples, consists of two parts, more specifically, of the resistivity ρ_1 inside the crystallographic regions with an average linear size L described in Section 2.1 (or the resistivity inside individual grains in the case of a polycrystal), i.e., the intrinsic electrical resistivity of the material, and of the electrical resistivity ρ_2 inside the boundaries separating regions with different crystallographic orientations, which have an average thickness L' (or the electrical resistivity of the grain boundaries). The quantity ρ can be written in the form [25]

$$\rho \cong \rho_1 + (L'/L)\rho_2 . \qquad (2)$$

Regions with different crystallographic orientations in a film on $ZrO_2(Y_2O_3)$ are separated by special large-angle boundaries (9.5, 70.5, and 90°). This means that the angles θ in the –Mn–O–Mn–O–Mn– chains between the lines connecting two manganese ions with the oxygen ion, which are close to 180° within the crystallographic regions, abruptly change to the above values inside the boundaries separating these regions.

It is known that the width of the conduction band in manganites (in the one-electron approximation) is proportional to $\cos^2\theta$ [7], and the sharp change of θ inside a boundary separating regions with different crystallographic orientations thus leads to a strong decrease of the conductivity inside it. It is shown by an electron microscope image of this film that the thickness of the boundary is close to the lattice constant [26]. At the same time, all regions of the films on $SrTiO_3$, $LaAlO_3$, and MgO have the same crystallographic orientation, and they have no such boundaries. Therefore, the higher value of ρ or the film on $ZrO_2(Y_2O_3)$ is only due to the second term in (2). Assuming ρ_1 to have the same magnitude in all four films and to be approximately 6×10^{-3} Ω cm (see table), and substituting this value, as well as the values $L' \cong 4$ Å and $L \cong 400$ Å [26] into (2), we obtain $\rho_2 \cong 18.4$ Ω cm at 82 K. Thus, the electrical resistivity within a boundary separating microregions with different crystallographic orientations is more than three times that in these microregions and, in order of magnitude, is of the semiconducting nature.

The small thickness of this layer and the large magnitude of ρ_2 suggest that the conduction is realized here by tunneling through such a boundary. As will be shown below, part of these boundaries coincide with the

domain walls. In this case, tunneling follows a specific pattern associated with the fact that the tunneling electrons are almost fully spin-polarized. This situation was described for polycrystalline bulk manganite samples [14]. In the case when the electron spins are conserved during tunneling, and when the magnetic moments of neighboring grains are not parallel to one another, the following expression was derived for the MR [14]:

$$\Delta\rho/\rho = -JP(4k_BT)[m^2(H, T) - m^2(0, T)], \quad (3)$$

where J is the intergranular exchange-coupling constant, P is the electron polarization, and m is the magnetization normalized to the saturation value. This expression can apparently be applied to the film on $ZrO_2(Y_2O_3)$ as well. As seen from (3), after reaching technical saturation of magnetization, the absolute magnitude of MR saturates too.

Figure 6 shows, however, that the MR isotherms of the film on $ZrO_2(Y_2O_3)$ do not exhibit saturation in the low-temperature domain, although the magnetization has already saturated (Fig. 1). It can be seen from Fig. 6 that the MR isotherms first reveal a strong growth of $|\Delta\rho/\rho|$ in fields of up to 2 kOe at low temperatures, followed by a slower, nearly linear-in-field increase as H continues to grow. It can therefore be conjectured that the low-temperature MR above the technical saturation field is accounted for, in addition to the above-mentioned spin-polarized tunneling, by some other processes as well.

It was mentioned above that the high low-temperature electrical resistivity and the MR in polycrystalline samples was also related to carrier scattering from spin system disorders within domain walls. This explanation is, however, hardly applicable to the manganites, which are characterized by a strong *p–d* exchange coupling and thick domain walls. It is well known that manganites are magnetically soft materials, because the magnetocrystalline anisotropy energy in them does not exceed 2×10^4 erg/cm^3 [27], and therefore, the domain-wall thickness is here large; estimates [28] suggest that it may be as high as 10^3 lattice constants a in bulk samples. In thin-film samples, where the film thickness is of the order of the domain wall thickness specified for a bulk sample (the films considered in this work are ~5500 Å thick), the domain structure is more complex. No consensus has yet emerged about it [28]. Therefore, as a rough approximation, one can consider the domain wall thickness in thin films to be the same as in a bulk sample. As mentioned above, the size of the crystallographic microregions in a film on $ZrO_2(Y_2O_3)$ ~ 400 Å, or $a \times 10^2$, which is an order of magnitude less than the possible domain wall thickness. Since this film preserves the long-range magnetic order, each domain should contain more than ten crystallographic microregions. In some regions of the film, however, the domain wall thickness is greater than the size of the crystallographic microregions and of the order of the film thickness; thus, there might not be long-range magnetic order. Indeed, as seen from Fig. 1 and the table, the magnetic moment per formula unit in this film is substantially less than that expected under complete ferromagnetic ordering of all ions (including the magnetic sublattice of the Nd^{3+} ions), and this constitutes ~54% of the latter. Within such a wide domain wall, the spins rotate gradually, and because of the strong *p–d* exchange coupling, the carrier spin is aligned parallel to the spin of the ion at which the carrier is at the given instant, a situation in which no carrier scattering occurs at all [24].

As seen from Fig. 5, the $|\Delta\rho/\rho|(T)$ curves have a maximum near T_C for all four films studied. The value of $|\Delta\rho/\rho|_{max}$ is large, 34% for the film on MgO, and 13% for the film on $ZrO_2(Y_2O_3)$; for the two remaining films, it is 22.5% in a field of 8.4 kOe (see table). We recall for comparison that in conventional magnets, for instance, in ferrites, $|\Delta\rho/\rho|_{max}$ near T_C is lower by two to three orders of magnitude. $La_{0.35}Nd_{0.35}Sr_{0.3}MnO_3$ is an antiferromagnetic semiconductor $La_{0.35}Nd_{0.35}MnO_3$ doped heavily with strontium, which exhibits metallic conduction below T_C, and a transition to semiconducting behavior near T_C (see Fig. 4). It was shown [29] that in such manganites with a strong *p–d* exchange interaction, there are two mechanisms by which impurity-induced magnetic interaction affects resistance: namely, the scattering of carriers, which reduces their mobility, and band tailing that involves localized states. In the vicinity of T_C, the mobility of carriers drops sharply, and they are localized partially in the band tail. The magnetic field reduces the impurity-induced carrier scattering, and the carriers delocalize from the band tail.

It can be seen from Fig. 4 that the value of ρ for the film on $ZrO_2(Y_2O_3)$ increases monotonically starting from the lowest measurement temperature, whereas the film on $SrTiO_3$, as well as those on $LaAlO_3$ and MgO, exhibit a substantially more pronounced growth starting from $T \cong 200$ K. The MR behaves in an identical manner, the only difference being that the sharp increase of $|\Delta\rho/\rho|$ for the film on $SrTiO_3$ starts from $T \cong 160$ K, whereas the maximum of $|\Delta\rho/\rho|$ lies here at a lower temperature than for ρ. At the same time, the peak of $|\Delta\rho/\rho|(T)$ for the film on $ZrO_2(Y_2O_3)$ is barely discernible, and the magnitude of $|\Delta\rho/\rho|$ in the low-temperature region is only 2–3% lower than that in the vicinity of T_C. This suggests that the MR at low temperatures occurring in fields above those producing technical saturation has the same origin as near T_C (see above). At low temperatures, the carriers in spin-disordered microregions, which, as was mentioned above, occupy ~54% of the film area, are roughly in the same conditions as near T_C, namely, the spins are strongly disordered, and a strong *p–d* exchange coupling prevails. This is only possible, however, when the spin-disordered regions exist in fields above technical saturation. In the same manner, one can explain the low-temperature MR above technical-saturation fields in films on $SrTiO_3$, $LaAlO_3$, and MgO, because they also apparently contain spin-disordered microregions. This is indicated by a lower level of magnetization in films on

$SrTiO_3$, $LaAlO_3$, and MgO as compared to the pure spin value for ferromagnetic ordering of all ions (see table and Fig. 1). It can be seen from Fig. 1 that after saturation in fields from 10 to 25 kOe, the film on MgO again exhibits a nearly linear-in-field increase in the magnetic moment.

It is known that the stresses created in manganite films by the lattice mismatch between the material and the substrate increase the magnetic anisotropy. However, the stresses in films on MgO substrates relax rapidly. It was pointed out in Section 2.1 that the stresses in films of the composition used here are very small because this composition is close to the morphotropic boundary separating the orthorhombic from the rhombohedral structure, which further enhances the relaxation in films on MgO. This film is apparently the least stressed of all those studied here, and this accounts for the spin ordering in magnetically disordered microregions that we observed.

By substituting La for Nd in $Nd_{0.7}Sr_{0.3}MnO_3$, we wanted to increase the Curie temperature of the films. The considerations are as follows. It is known that the Mn–O–Mn bond angle in an undistorted perovskite structure is 180°. Replacement of Nd ions by the smaller Sr ions results in a lattice distortion. It could be expected that a partial replacement of Nd ions by the larger La ions would bring the bond angle closer to 180°, as a result of which the conduction band would become wider, and therefore, the transfer integral t would increase, and the carrier-mediated exchange coupling would become stronger. In accordance with (1), this would also bring about an increase of the Curie temperature. As seen from the table, however, the replacement of half of the Nd ions by La did not produce the expected result; indeed, T_C, which is 240 K for $Nd_{0.7}Sr_{0.3}MnO_3$ [30], did not change for the $La_{0.35}Nd_{0.35}Sr_{0.3}MnO_3$ composition. This is apparently accounted for by crystallographic disordering of the A sites in the ABO_3 perovskite, which is described, for example, in [31]. Due to this disorder, the orthorhombic distortion of the perovskite lattice in the latter composition is the same as in the former one. Thus the transfer integrals t in both compositions are equal, as a result of which their Curie points are also equal, in accordance with (1).

ACKNOWLEDGMENTS

Support of the INTAS program (grant nos. 97-open-30253 and 97-0963) is gratefully acknowledged.

REFERENCES

1. G. H. Jonker and J. H. van Santen, Physica (Amsterdam) **16** (3), 337 (1950).
2. C. Searle and S. Wang, Can. J. Phys. **48** (17), 2023 (1970).
3. O. Yu. Gorbenko, R. V. Demin, A. R. Kaul, *et al.*, Fiz. Tverd. Tela (St. Petersburg) **40** (2), 290 (1998) [Phys. Solid State **40**, 263 (1998)].
4. O. Yu. Gorbenko, A. R. Kaul, N. A. Babushkina, and L. M. Belova, J. Mater. Chem. **7** (5), 747 (1997).
5. É. L. Nagaev, Usp. Fiz. Nauk **166** (8), 833 (1996) [Phys. Usp. **39**, 781 (1996)].
6. A. P. Ramirez, J. Phys.: Condens. Matter **9** (7), 8171 (1997).
7. Y. Tokura and Y. Tomioka, J. Magn. Magn. Mater. **200** (1), 1 (1999).
8. H. L. Ju, J. Gopalakrishnan, J. L. Peng, *et al.*, Phys. Rev. B **51** (9), 6143 (1995).
9. P. Schiffer, A. P. Ramirez, W. Bao, and S.-W. Cheong, Phys. Rev. Lett. **75** (18), 3336 (1995).
10. A. Gupta, G. Q. Gong, G. Xiao, *et al.*, Phys. Rev. B **54** (22), R15629 (1996).
11. H. Y. Hwang, S.-W. Cheong, N. P. Ong, and B. Batlogg, Phys. Rev. Lett. **77** (10), 2041 (1996).
12. R. Shreekala, M. Rajeswari, K. Ghosh, *et al.*, Appl. Phys. Lett. **71** (2), 282 (1997).
13. R. Mahesh, R. Mahendiran, A. K. Raychaudhuri, and C. N. R. Rao, Appl. Phys. Lett. **68** (16), 2291 (1996).
14. J.-H. Park, C. T. Chen, S.-W. Cheong, *et al.*, Phys. Rev. Lett. **76** (22), 4215 (1996).
15. P. Raychaudhuri, T. K. Nath, A. K. Nigam, and R. Pinto, J. Appl. Phys. **84** (4), 2048 (1998).
16. E. S. Vlakhov, R. A. Chakalov, R. I. Chakalova, *et al.*, J. Appl. Phys. **83** (4), 2152 (1998).
17. D. K. Petrov, A. Gupta, J. R. Kirtley, *et al.*, J. Appl. Phys. **83** (11), 7061 (1998).
18. A. K. M. Akter Hossain, L. F. Cohen, F. Damay, *et al.*, J. Magn. Magn. Mater. **192** (2), 263 (1999).
19. T. Walter, K. Dorr, K.-H. Muller, *et al.*, Appl. Phys. Lett. **74** (15), 2218 (1999).
20. V. G. Bar'yakhtar, A. N. Pogorilyi, N. A. Belous, and A. I. Tovstolytkin, J. Magn. Magn. Mater. **207** (1), 118 (1999).
21. M. Ziese, S. P. Sena, and H. J. Blythe, J. Magn. Magn. Mater. **202** (2), 292 (1999).
22. Y. Fu and C. K. Ong, J. Magn. Magn. Mater. **208** (1), 69 (2000).
23. G. Papavassiliou, M. Fardis, F. Milia, *et al.*, Phys. Rev. B **58** (18), 12237 (1998).
24. É. L. Nagaev, *Physics of Magnetic Semiconductors* (Nauka, Moscow, 1979).
25. H. Berger, Phys. Status Solidi **1** (2), 739 (1961).
26. M. Bibes, O. Gorbenko, B. Martinez, *et al.*, J. Magn. Magn. Mater. **209** (2000) (in press).
27. Y. Suzuki, H. Y. Hwang, S.-W. Cheong, *et al.*, J. Appl. Phys. **83** (11), 7064 (1998).
28. A. Hubert, *Theorie der Domanenwande in Geordneten Medien* (Springer-Verlag, Berlin, 1974; Mir, Moscow, 1977).
29. E. L. Nagaev, Phys. Lett. A **211** (5), 313 (1996).
30. L. M. Rodriguez-Martinez and J. P. Attfield, Phys. Rev. B **58** (5), 2426 (1998).
31. V. A. Bokov, N. A. Grigoryan, M. F. Bryzhina, and V. V. Tikhonov, Phys. Status Solidi **28** (2), 835 (1998).

Translated by G. Skrebtsov

Physics of the Solid State, Vol. 42, No. 9, 2000, pp. 1712–1715. Translated from Fizika Tverdogo Tela, Vol. 42, No. 9, 2000, pp. 1664–1667.

MAGNETISM AND FERROELECTRICITY

Optical Study of the Spontaneous Ferroelectric Phase Transition in Lead Scandoniobate Single Crystals

L. S. Kamzina and N. N. Kraĭnik

Ioffe Physicotechnical Institute, Russian Academy of Sciences, Politekhnicheskaya ul. 26, St. Petersburg, 194021 Russia

Received February 3, 2000

Abstract—A study is reported of the optical transmission and small-angle light scattering (SAS) in ordered and disordered stoichiometric single crystals of lead scandoniobate (PSN) with a zero and a dc electric field applied. It is shown that the spontaneous phase transition occurring in both crystals is accompanied by a sharp peak in SAS intensity, which implies the percolation nature of this transition. A field–temperature phase diagram has been constructed for the PSN single crystals studied in the work. © *2000 MAIK "Nauka/Interperiodica".*

INTRODUCTION

Lead scandotantalate $PbSc_{1/2}Ta_{1/2}O_3$ (PST) and scandoniobate $PbSc_{1/2}Nb_{1/2}O_3$ (PSN) occupy a specific place among the large class of relaxor materials. In contrast to such a classical relaxor as lead magnoniobate (PMN) and similar ferroelectric relaxors, which do not exhibit ferroelectric behavior in the absence of an electric field, these compounds, besides revealing relaxor properties within a certain temperature interval, undergo a spontaneous phase transition to a ferroelectric phase even with no electric field applied [1–3]. These materials are a very good subject not only for investigating the spontaneous ferroelectric phase transition, but also for studying the relaxor properties. As a result of a high-temperature order–disorder transition in the distribution of different ions in crystallographic positions of the same type [4], the order (or disorder) in the arrangement of the B' and B" cations can be different, depending on the heat treatment that a sample was subjected to. By varying the extent of ion ordering and monitoring it by x-ray diffraction, one can vary the relaxor properties of a material and study the relation between the relaxor and normal ferroelectric behavior in the same material. Before the discovery of these materials, the relation between the ferroelectric and relaxor properties could only be studied experimentally on different samples.

Despite a number of common features in the behavior of the PST and PSN compounds, there are, however, substantial differences. Indeed, the ferroelectric phase-transition temperature of ordered PST crystals ($T \sim 40$°C) is higher than that of disordered ones ($T \sim 0$°C), whereas for the PSN crystals the reverse is true. The change in the unit-cell volume at the ferroelectric–paraelectric phase transition in these compounds likewise has opposite signs. The reasons for these differences remain unclear. One possible reason could perhaps be the different order–disorder transition temperatures (T_{ord}). In PST crystals, this quantity is higher ($T_{ord} \sim 1450$°C) than in PSN ($T_{ord} \sim 1280$°C). At the same time, the sintering temperature of ceramic samples and the growth temperature of PST single crystals is always lower than T_{ord}, and the extent of order in as-grown PST compounds is therefore close to unity. The synthesis temperature of PSN ceramics and single crystals ~1100–1300°C; i.e., it is close to or higher than T_{ord}, and the extent of order in as-grown samples is, as a rule, close to zero. It was suggested [5, 6] that the nature of the difference in the relation between the ferroelectric phase-transition temperatures in ordered and disordered samples of PST and PSN could be associated with the larger nonlinearity of the Nb–O than Ta–O octahedra and with the smaller size of ordered regions in PSN compared to PST compounds. These effects were shown to shift the temperature of the maximum in ε to higher temperatures in disordered PSN samples.

Heat treatment, which is usually employed to change the extent of ordering in a sample [7] results in a lowering of the extent of ionic order *s* in PST, but in its increase in PSN. In both cases, however, the ferroelectric phase-transition temperature decreases. At the same time, annealing of a sample may give rise not only to a change in the extent of ion ordering, but also in lead losses. It is known [3, 8–10] that a large lead loss shifts the ferroelectric phase-transition point toward lower temperatures and hinders the spontaneous ferroelectric transition, making the material a conventional relaxor. At the same time, mere disorder in the ion arrangement is not a serious obstacle to a spontaneous ferroelectric transition in these materials. Thus, a straightforward comparison of the physical properties of PST and PSN compounds is impossible because of different initial conditions of ordering.

Application of a dc electric field should differently affect the relaxor properties and the character of the

1063-7834/00/4209-1712$20.00

spontaneous ferroelectric phase transition. The effect of an external field on the dielectric properties of PST ceramics with a different extent of ion ordering was studied comprehensively in [2]. However, optical methods, more specifically, optical transmission and small-angle light scattering (SAS), possess a higher sensitivity to the variation of inhomogeneities in size at phase transitions [11, 12]. If a phase transition is of the percolation type, the average size of a new-phase cluster at the percolation threshold tends to the size of the sample, a large-scale inhomogeneous structure forms, and the phase transition should be accompanied by the formation of anomalously narrow SAS intensity peaks and, hence, by a minimum in optical transmission. We showed by SAS measurements that the spontaneous phase transition occurring in PST single crystals with a different extent of ion ordering is of the first order, of a percolation nature, and accompanied by the appearance of an anomalously narrow peak in SAS intensity [12–15]. An external electric field reduces the region of existence of the relaxor phase and increases the stability of the ferroelectric phase.

No study on the effect of an electric field on the behavior of the relaxor and normal ferroelectric states in PSN crystals has been made before this experiment. This problem is of interest in itself, because a direct comparison of the effect of an electric field on the dielectric and optical properties of PST and PSN crystals is impossible to carry out due to the different initial conditions of ordering.

Thus, this work aimed to study the effect of an electric field on the spontaneous and relaxor phase transitions in ordered and disordered stoichiometric PSN single crystals by means of optical and dielectric measurements.

1. GROWTH OF SINGLE CRYSTALS AND EXPERIMENTAL TECHNIQUES

Before the initiation of this work, information on the properties of stoichiometrically ordered PSN compounds was lacking, with the exception of structural studies [10] and our publications [12–15]. Using the method proposed in [16], we succeeded in growing both disordered and ordered stoichiometric PSN single crystals. The different extent of ordering was reached by properly varying the sample preparation temperature, because heat treatment, usually employed for this purpose, entails lead losses and optical degradation of samples. The grown ordered crystals measured $3 \times 2 \times 2$ mm and were practically colorless, while the disordered ones were brownish and measured $2 \times 1 \times 1$ mm. The temperature of the maximum in ε was 80°C for the ordered samples and +112°C for the disordered ones, which agrees with [4].

We studied optical transmission and SAS measured in the transmission geometry [17]. A He–Ne laser was used for optical measurements. The electric field was applied along the [001] direction at room temperature, and the light was propagated along [100]. The dielectric measurements were carried out at a frequency of 1 kHz. The rate of sample temperature variation was varied from 1.5 to 4.5°C/min. On application of an electric field, the samples were depolarized before each measurement by heating them above $T_{\max \varepsilon}$.

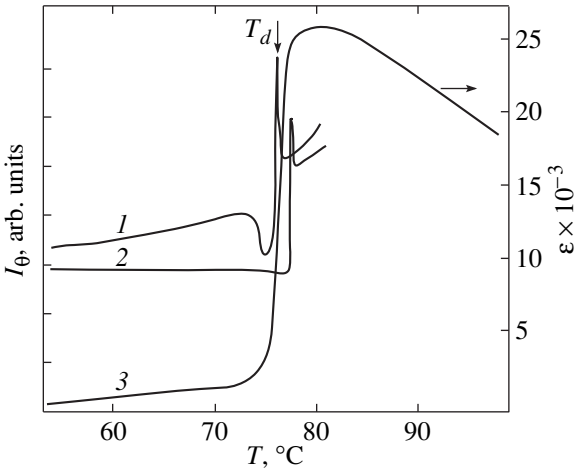

Fig. 1. Temperature dependences of SAS intensity with (*1*) no and (*2*) a 3-kV/cm electric field applied, and of (*3*) dielectric permittivity obtained on an ordered PSN crystal.

2. EXPERIMENTAL RESULTS AND DISCUSSION

Figure 1 presents the temperature dependences of the SAS intensity measured in a heating run in zero field (curve *1*) and a dc electric field applied (curve *2*), as well as of the dielectric permittivity (curve *3*) of an ordered PSN crystal. One clearly sees an SAS peak at the temperature T_d, which confirms the existence of a percolation-type spontaneous transition, whereas the ε curve exhibits only a quick rise of ε at this temperature. The nonrelaxation character of this spontaneous transition is corroborated by the coincidence in temperature of the SAS intensity peak measured at a zero field frequency, with the anomaly in the permittivity curve taken at 1 kHz. The maximum in ε lies ~2°C above the transition temperature T_d, which implies that a very small part of the crystal volume is occupied by the disordered phase. As the electric field increases, the T_d temperature also increases.

Figure 2 displays the temperature dependences of the dielectric permittivity (curve *1*) and of the optical transmission obtained in a heating (curve *2*) and a cooling (curve *3*) run on a disordered PSN crystal. The minimum in the optical transmission curve observed at ~100°C agrees in position with the SAS intensity maximum (see the inset in Fig. 2) and coincides with the T_d temperature derived from curve *1*. As seen from the transmission curves obtained in the heating and cooling runs (curves *2* and *3*, respectively), the difference in position between the optical transmission minima is

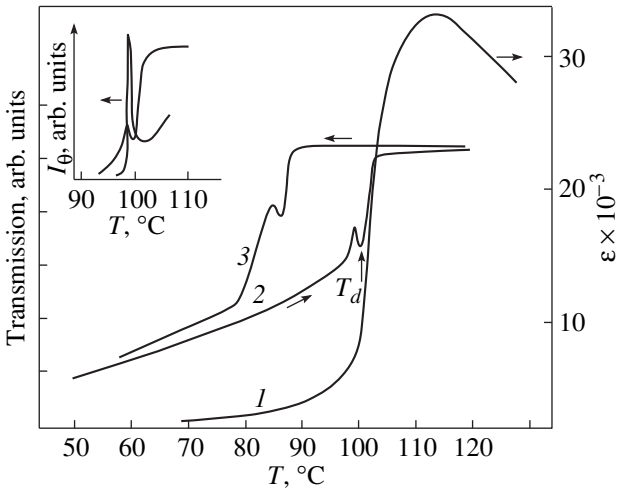

Fig. 2. Temperature dependences of dielectric permittivity (*1*) and optical transmission obtained in a heating (*2*) and cooling (*3*) runs on a disordered PSN crystal. Inset: SAS intensity (I_θ) and optical transmission at T_d.

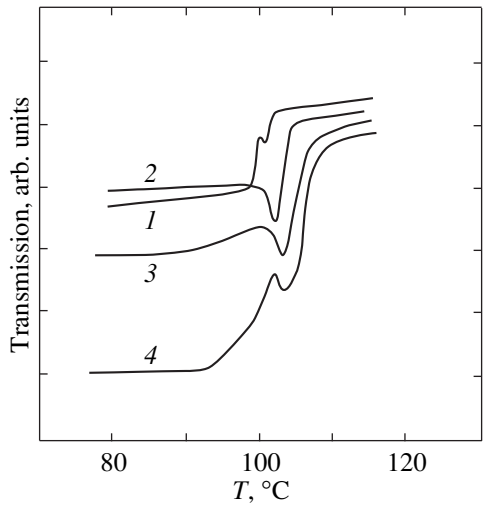

Fig. 3. Temperature dependence of optical transmission obtained on a disordered PSN crystal at different electric fields E (kV/cm): (*1*) 0, (*2*) 1, (*3*) 2, and (*4*) 4.

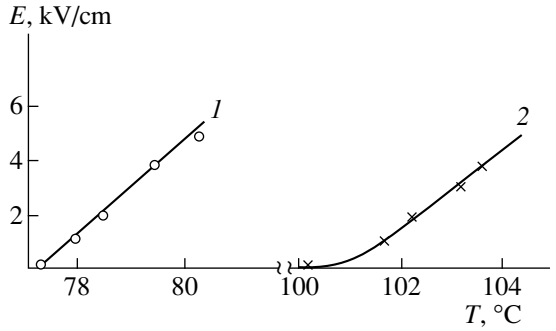

Fig. 4. Electric-field dependence of the temperature of the spontaneous ferroelectric phase transition obtained on (*1*) an ordered and (*2*) a disordered PSN crystal.

~13°C. The existence of a temperature hysteresis is a major signature of a first-order phase transition. Applying an electric field to the disordered sample shifts the spontaneous ferroelectric transition point toward higher temperatures (Fig. 3), as is also the case with the ordered sample (curve *2* in Fig. 1).

The measurements of the SAS intensity and of the optical transmission made on the ordered and disordered PSN samples under the application of dc electric fields were used to construct the electric-field dependences of the spontaneous ferroelectric phase transition temperature (curves *1* and *2* in Fig. 4). In a practically ordered crystal, the T_d temperature depends linearly on the electric field, which is typical of a first-order phase transition (curve *1* in Fig. 4). In a disordered crystal, this dependence differs slightly from a linear relation (curve *2* in Fig. 4), although the presence of a SAS peak and the observed temperature hysteresis suggest a first-order phase transition. This may be due to the existence of locally polarized regions in the disordered crystal above T_d.

The above data on the effect of an electric field on the behavior of the spontaneous ferroelectric transition in disordered and ordered PSN crystals agree with the results of [2] obtained on ceramic PST samples and with our data on PST single crystals [14].

CONCLUSION

Thus, we have succeeded in growing both ordered and disordered stoichiometric PSN single crystals. It has been shown that, despite the different initial conditions of ordering in PSN and PST crystals, an electric field acts on the spontaneous phase transition in the same way in both crystals, namely, the transition temperature grows with increasing field; the growth is linear in ordered crystals, while deviating from the linear relation in disordered ones. Similar to PST crystals, the spontaneous phase transition in ordered and disordered stoichiometric PSN crystals is of the first order, of a percolation nature, and accompanied by the formation of an anomalously narrow SAS peak. Applying an electric field to the sample reduces the temperature interval of existence of the relaxor phase.

REFERENCES

1. F. Chu, N. Setter, and A. K. Tagantsev, J. Appl. Phys. **74** (8), 5129 (1993).
2. F. Chu, G. R. Fox, and N. Setter, J. Am. Ceram. Soc. **81** (6), 1577 (1998).
3. F. Chu, I. M. Reaney, and N. Setter, J. Appl. Phys. **77** (4), 1671 (1995).
4. C. G. Stenger and A. J. Burggraaf, Phys. Status Solidi A **61** (1), 275 (1980).
5. M. Glinchuk and R. Farhi, J. Phys.: Condens. Matter **8**, 6985 (1996).

6. C. Caranoni, N. Menguy, B. Hilczer, *et al.*, in *Abstracts of 9th European Meeting on Ferroelectricity, Prague, 1999*, p. 219.
7. N. Setter and L. E. Cross, J. Appl. Phys. **51** (8), 4356 (1980).
8. F. Chu, I. M. Reaney, and N. Setter, J. Am. Ceram. Soc. **78** (7), 1947 (1995).
9. A. Sternberg, L. Shebanovs, E. Birks, *et al.*, Ferroelectrics **217**, 307 (1998).
10. C. Malibert, B. Dkhil, J. M. Kiat, *et al.*, J. Phys.: Condens. Matter **9**, 7485 (1997).
11. A. Krumins, T. Shiosaki, and S. Koizumi, Jpn. J. Appl. Phys., Part 1 **33** (9A), 4946 (1994).
12. L. S. Kamzina and A. L. Korzhenevskiĭ, Pis'ma Zh. Éksp. Teor. Fiz. **50** (3), 146 (1989) [JETP Lett. **50**, 163 (1989)].
13. L. S. Kamzina and A. L. Korzhenevskiĭ, Fiz. Tverd. Tela (St. Petersburg) **34** (6), 1795 (1992) [Sov. Phys. Solid State **34**, 957 (1992)].
14. L. S. Kamzina and N. N. Kraĭnik, Fiz. Tverd. Tela (St. Petersburg) **42** (1), 136 (2000) [Phys. Solid State **42**, 142 (2000)].
15. L. S. Kamzina and A. L. Korzhenevskiĭ, Ferroelectrics **131**, 91 (1992).
16. V. G. Smotrakov, I. P. Raevskiĭ, M. A. Malitskaya, *et al.*, Izv. Akad. Nauk SSSR, Neorg. Mater. **19** (1), 123 (1983).
17. L. S. Kamzina, A. L. Korzhenevskiĭ, and O. Yu. Korshunov, Fiz. Tverd. Tela (St. Petersburg) **36** (2), 479 (1994) [Phys. Solid State **36**, 264 (1994)].

Translated by G. Skrebtsov

Physics of the Solid State, Vol. 42, No. 9, 2000, pp. 1716–1721. Translated from Fizika Tverdogo Tela, Vol. 42, No. 9, 2000, pp. 1668–1672.

MAGNETISM AND FERROELECTRICITY

Atomic Structure of $Sr_{0.75}Ba_{0.25}Nb_2O_6$ Single Crystal and Composition–Structure–Property Relation in $(Sr,Ba)Nb_2O_6$ Solid Solutions

T. S. Chernaya*, B. A. Maksimov*, T. R. Volk*, L. I. Ivleva, and V. I. Simonov***

** Shubnikov Institute of Crystallography, Russian Academy of Sciences, Leninskiĭ pr. 59, Moscow, 117333 Russia*

*** Institute of General Physics, Russian Academy of Sciences, ul. Vavilova 38, Moscow, 117942 Russia*

e-mail: volk@ns.crys.ras.ru

Received February 8, 2000

Abstract—The structure of the $Sr_{0.75}Ba_{0.25}Nb_2O_6$ single crystal has been investigated by x-ray diffraction. The occupancies of the Ba and Sr sites in two structural channels are determined. It is found that these sites are split in the large (pentagonal) channel. A qualitative correlation is revealed between the smearing of the phase transition and the displacement of the Sr atom from the *m* symmetry plane in the pentagonal channel at different [Sr]/[Ba] ratios. The degree of acentricity of the NbO_6 octahedra is analyzed as a function of the [Sr]/[Ba] ratio.

1. INTRODUCTION

Ferroelectric crystals of $Sr_xBa_{1-x}Nb_2O_6$ (SBN-*x*) solid solutions have unique properties from the viewpoint of practical (pyroelectric, piezoelectric, electrooptical, and holographic [1, 2]) applications and basic investigations. These materials belong to the extensively studied class of relaxor ferroelectrics [3, 4], for which the characteristics of the ferroelectric phase transition (its smearing and temperature) and, hence, all the parameters are governed by the composition, i.e., the [Sr]/[Ba] concentration ratio. The SBN compounds have a structure of the unfilled tungsten bronze type [5–8] and exhibit a random disordering of Sr and Ba cations over two crystallographic positions. In this respect, it is of interest to trace a qualitative correlation between the characteristics of the phase transition in crystals of different compositions and the change in the structural disordering that accompanies the change in the composition. The revelation of this correlation is one of the purposes of the present work.

The structure of SBN crystals was investigated in a number of works [5–8]. Figure 1 shows the projection of the SBN model atomic structure onto the *ab* plane, which was proposed by Jamieson *et al.* [5]. The SBN structure is built up of two types of crystallographically independent NbO_6 octahedra joined via oxygen corners into a three-dimensional network. In this network, there are three types of structural channels running along the polar *c* axis. As follows from all the structural investigations [5–8], in the SBN structure, the narrowest channels with a triangle cross-section (channels *C* in terms of [5]) are empty, the tetragonal channels *A*1 with an intermediate diameter are occupied only by the Sr atoms, and the largest channels *A*2 with a pentagonal cross-section are filled by Ba and Sr atoms. All the channels are occupied in a random way.

Before proceeding to the discussion of our results, let us briefly summarize the findings of investigations into the SBN structure of different compositions [5–8].

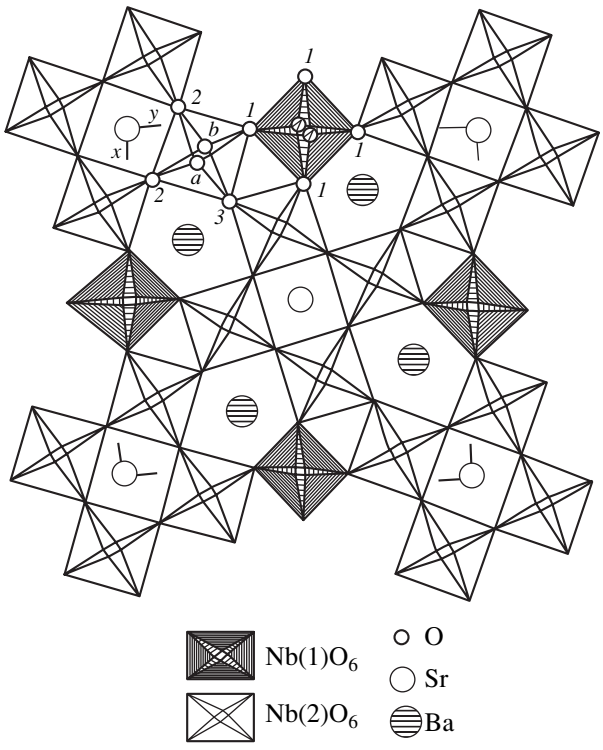

Fig. 1. Projection of the $(Sr,Ba)Nb_2O_6$ structure onto the *ab* coordinate plane.

Table 1. Coordinates and effective isotropic thermal parameters of the basis atoms in the $Sr_{0.746}Ba_{0.247}Nb_2O_6$ structure

Atom	Site multiplicity	Site occupancy, %	Symmetry	*x*/*a*	*y*/*b*	*z*/*c*	B_{eff}, Å^2
Nb(1)	2	100	mm	0	0.5	0.0	1.49
Nb(2)	8	100	1	0.0746(1)	0.2114(1)	0.0029(8)	1.11
Sr(1)	2	71.5(2)	4	0	0	0.5023(10)	0.81
Sr(2)	8	28.6(2)	1	0.1558(3)	0.6848(5)	0.5026(13)	1.73
Ba	4	30.9(3)	m	0.1738(3)	0.6738(3)	0.4992(14)	1.47
O(1)	8	100	1	0.3438(2)	0.0055(2)	0.0567(13)	2.22
O(2)	8	100	1	0.1396(2)	0.0682(2)	0.0397(22)	2.52
O(3)	4	100	m	0.2805(2)	0.7805(2)	0.0257(33)	2.01
O(4)	4	50	m	0.0165(4)	0.5165(4)	0.5166(32)	3.49
O(5A)	8	50	1	0.3072(3)	0.4012(3)	0.4995(35)	1.59
O(5B)	8	50	1	0.2830(4)	0.4458(4)	0.4812(36)	1.94

According to the phase diagram [9] and the data obtained in [5–8], the SBN crystals of the structural type under consideration exist in the composition region from $Sr_{0.2}Ba_{0.8}Nb_2O_6$ to $Sr_{0.8}Ba_{0.2}Nb_2O_6$ and show a tetragonal symmetry with the space group *P*4*bm*. The pioneering work by Jamieson *et al.* [5] was devoted to the structural analysis of the $Sr_{0.75}Ba_{0.27}Nb_2O_{5.78}$ compound. It was demonstrated that the Ba atoms located only in large channels occupy their own fourfold sites with an occupancy factor of 34.4%. The same sites are 50.3% filled by the Sr atoms. Therefore, each of these crystallographic sites is randomly occupied by the Ba and Sr atoms with a total occupancy factor of 84.7%. The remaining Sr atoms occupy twofold sites in the tetragonal channels with an occupancy of 82.2%. Considering the joint occupation of the general crystallographic position by the Ba and Sr atoms in the pentagonal channels, the authors of [5] proposed the model according to which the coordinates of the Ba and Sr atoms coincide and lie in the *m* mirror plane. It should be noted that these authors considered the possibility of splitting the barium–strontium site; however, they preferred the model with the general position of the Ba and Sr atoms and a substantial anisotropy of their thermal motion [5].

More recently, Andreĭchuk *et al.* [6] carried out the x-ray structure investigation of the SBN-0.33 compound, which is close to the limiting composition for the tetragonal structure [9]. The radical difference between this structure and the structure described above resides in the fact that the Ba and Sr atoms occupy different sites. All the Ba atoms occupy their sites only in large channels with an occupancy factor of 84.0%, and all the Sr atoms are located in the medium-sized channels with a site occupancy of 70.5%.

In our earlier work [7], we studied the structure of the SBN-0.61 compound whose composition corresponded to the congruent melt.[1] In the medium-sized channels of the structure, the Sr atoms occupy their twofold sites with an occupancy of 72.5%. The remaining Sr atoms and the Ba atoms are located in large channels in the structure. The Ba atoms occupy fourfold sites in the *m* mirror plane with an occupancy of 48.7%. The Sr atoms located in the same channels are displaced from the symmetry planes to the eightfold general positions by 0.292(1) Å. These positions are 20.2% filled by the Sr atoms on either side of the plane. In this case, the Ba–Sr distances are equal to 0.305(1) Å. The total occupancy factor for the Sr sites above and below the plane and the Ba sites in the plane is 89.1%. Thus, the fundamental difference between these results and those considered above lies in the splitting of the Sr and Ba sites in the pentagonal channels.

Trubelja *et al.* [8] investigated the crystal structure of the SBN-0.71, SBN-0.61, and SBN-0.51 compounds by x-ray powder diffraction. Methodically, this work casts some doubt. The distributions determined for the atomic site occupancies in [8] considerably differ from the results of other structural investigations. However, these authors obtained the important result that can be considered methodically reliable: relatively soft thermal annealing of the SBN-0.51 powder brought about a substantial redistribution of the Sr atoms over the sites. After the annealing, the occupancy factor for the Sr sites increased from 54.1 to 61.9% in the tetragonal channels and decreased from 36.5 to 32.6% in the pentagonal channels. The occupancy of the large channels by the Ba atoms remained unchanged upon annealing. This suggests that the frequently observed irreproducibility of the properties of SBN crystals having the

[1] The compound was doped by cerium at very small concentration (0.1 at. %), which did not substantially affect the structure parameters.

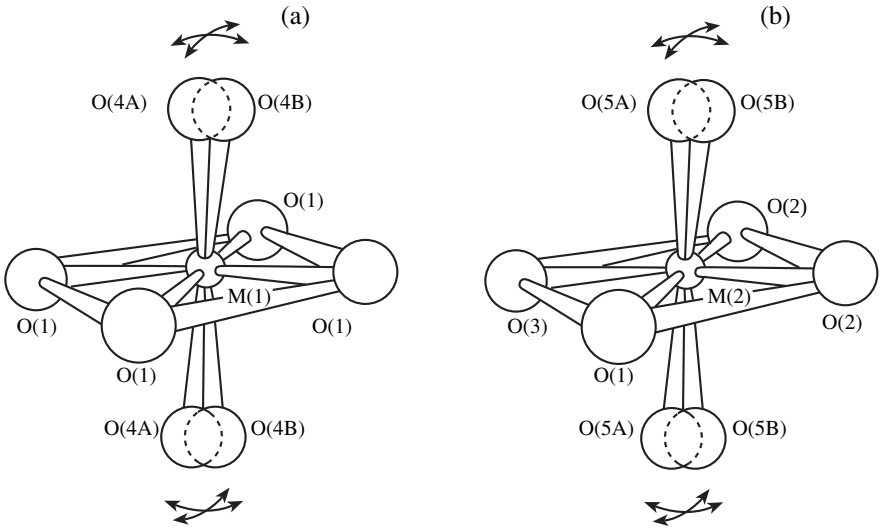

Fig. 2. Oxygen environment of (a) Nb(1) and (b) Nb(2) atoms in the (Sr,Ba)Nb_2O_6 structure. Disordering in the O(4) and O(5) sites is shown.

same composition is caused by different distributions of the Sr atoms over the sites, depending on the sample prehistory: the growth conditions and subsequent heat treatment.

2. EXPERIMENTAL TECHNIQUE

The SBN-0.75 single crystals to be studied were grown by the Czochralski method. Their composition was determined with a Camebax microanalyzer and agreed well with the composition of the initial batch. A spherical sample 0.22(1) mm in diameter was prepared for the x-ray diffraction experiment. The integrated intensities of x-ray diffraction reflections were collected on an Enraf–Nonius CAD 4F diffractometer (MoK_α radiation, ω scan mode, $\lambda = 0.7106$ Å, graphite monochromator) within a full sphere of the reciprocal space at $\sin\Theta/\lambda \le 1.2$ Å^{-1}. A total of 14 008 reflections were measured. After the rejection of weak reflections with $I < 4\sigma_1$ and the averaging over symmetrically equivalent reflections (R_{aver} = 2.5%), the data set included 1891 unique reflections. The unit cell parameters were refined by the least-squares procedure: a = 12.445(4) Å and c = 3.935(2) Å. Analysis of the structure amplitude array confirmed the tetragonal space group *P4bm* of the crystal. The absence of symmetry center is ensured by the properties of these crystals. All the calculations were performed according to the PROMETHEUS software package [10]. The x-ray scattering curves for neutral atoms were used in the calculations [11]. The structural model was refined by the full-matrix least-squares method to a discrepancy of 1.82% (between the experimental structure amplitude magnitudes and those calculated from the model).

Table 2. Selected interatomic distances in the structures $Sr_{0.282}Ba_{0.672}Nb_2O_6$ [6], $Sr_{0.613}Ba_{0.39}Nb_2O_6$ [7], $Sr_{0.75}Ba_{0.27}Nb_2O_{5.78}$ [5], and $Sr_{0.746}Ba_{0.247}Nb_2O_6$ (this work)

Nb(1) octahedron	Sr_{282}	Sr_{613}	$Sr_{0.75}$	Sr_{746}
–O(4) × 1/2	1.82(2)	1.83(1)	1.92(3)	1.92(1)
–O(4) × 1/2	1.82(2)	1.83(1)	1.92(3)	1.92(1)
–O(1) × 4	1.96(2)	1.95(1)	1.95(8)	1.96(1)
–O(4) × 1/2	2.17(2)	2.13(1)	2.03(4)	2.05(1)
–O(4) × 1/2	2.17(2)	2.13(1)	2.03(4)	2.05(1)
Nb(2) octahedron				
Nb(2)–O(5A) × 1/2	1.87(2)	1.90(1)	1.93(2)	1.99(1)
–O(5B) × 1/2	1.87(2)	1.89(1)	1.88(3)	1.90(1)
–O(1)	1.945(5)	1.93(1)	1.949(9)	1.94(1)
–O(2)	1.961(5)	1.96(1)	1.958(8)	1.96(1)
–O(3)	1.99(1)	2.00(1)	2.004(8)	2.00(1)
–O(2)	2.016(5)	2.00(1)	2.013(8)	2.00(1)
–O(5B) × 1/2	2.13(2)	2.09(1)	2.11(3)	2.07(1)
–O(5A) × 1/2	2.16(2)	2.08(1)	2.00(3)	2.02(1)

3. RESULTS

Table 1 lists the basis atoms in the structure, multiplicities of their sites, occupancy factors, symmetries, atomic coordinates, and the effective thermal parameters. It is evident from Table 1 that the chemical formula obtained from the x-ray diffraction data on the atomic site occupancies is in reasonable agreement with the initial formula.

The structure of crystals with the composition under study can be characterized as follows. All the Ba atoms are located in large channels with an occupancy factor of 30.9%, which agrees with the results reported in [5–8]. The Sr atoms in the large channels deviate from the

Table 3. Acentric distortions of Nb(1) and Nb(2) octahedra and the optical properties at different SBN compositions

Composition	Δ[Nb(1)–O], Å	Δ[Nb(2)–O], Å	d_{33}, 10^9, CGSE	n_e	Δn
SBN-0.33	0.35	0.28	38	2.303	0.54
SBN-0.61	0.3	0.19	22	2.324	0.3
SBN-0.75	0.13	0.1	17	2.343	0.13
SBN-0.73 [5]	0.11	0.15			

Note: d_{33} is the component of the quadratic optical susceptibility tensor for the SHG radiation at 1.06 μm, n_e and Δn are the extraordinary refractive index and the birefringence at λ = 0.53 μm. The values of d_{33}, n_e, and Δn are taken from [6].

m symmetry plane by 0.255(1) Å and occupy each site above and below the plane with an occupancy of 28.6%. The other Sr atoms are located in the medium-sized channels with a site occupancy of 71.5%. The crystal studied in the present work is very close in chemical composition to the material described in [5]. The new result obtained in our work is that the Sr atoms in the large channels in the SBN-0.75 crystals, as in the SBN-0.61 compound [7], are shifted relative to the Ba atoms, and the point symmetries of the Sr sites differ.

Based on the results of this work and the data obtained in [5–7], we elucidated how the chemical composition of solid solutions affects the acentric distortion of the NbO_6 octahedra comprising a three-dimensional network of the SBN structure; moreover, we evaluated the deviations of the Nb sites from the center of oxygen coordination octahedra for compounds of different compositions. Recall that the SBN structure involves two types of chains running along the crystal axis *c*, which are formed by two crystallographically independent octahedra Nb(1) and Nb(2) (Fig. 1). In the solid solutions of all compositions, the O(4) and O(5) atoms that join respectively the Nb(1) and Nb(2) octahedra into the chains running along the *c* axis are disordered. Each oxygen atom occupies two sites with an occupancy of 50 % (Fig. 2). The Nb–O distances in the Nb(1) and Nb(2) octahedra in the SBN structures of different compositions are given in Table 2. The Nb(1) atoms are located in the line of intersection of the *m* symmetry planes, and their four equatorial (with respect to the *c* axis) oxygen atoms $O(1)_{equat}$ occupy the general positions and are related by the symmetry planes, which provides the equality of the Nb(1)–$O(1)_{equat}$ distances. The distances from the Nb(1) atom to the upper and lower oxygen atoms along the *c* axis in the chain differ from each other.

A different situation arises with the Nb(2) atoms. These atoms occupy the general positions, and their distances to all the surrounding O atoms are crystallographically independent. In order to simplify our analysis, the Nb(2)–O(5) distances to the splitting of oxygen positions and also the distances to four equatorial atoms O_{equat} in the Nb(2) octahedra can be replaced by the mean distances.

As can be seen from Table 2, the Nb(1)–O_{equat} distances to four equatorial oxygen atoms in the more symmetric Nb(1) octahedra virtually coincide for all the SBN compositions and fall in the range 1.95–1.96 Å. The Nb(1)–O distances to the upper and lower O(4) atoms, which form the chains running parallel to the *c* axis, differ considerably for different compositions and lie in the range 1.82–2.17 Å. In the Nb(2) octahedra, whose structure has no symmetry constraints, the corresponding distances are somewhat different. The Nb(2)–O_{equat} equatorial (mean) distances fall in the range 1.97–1.98 Å (Table 2), even though the particular Nb(2)–O_{equat} distances in all the structures range from 1.93 to 2.02 Å. The distances in the Nb(2)–O chains, as in the Nb(1)–O chains, vary substantially and fall in the range 1.87–2.15 Å.

The displacement of the Nb atom from the center of an octahedron (acentric distortion of the octahedron) is characterized by the difference in the Nb–O distances to the upper and lower oxygen atoms forming the chain. These quantities for the Nb(1)–O and Nb(2)–O distances in different SBN structures are presented in Table 3. The important conclusion is that the acentric distortion of both octahedra decreases with an increase in the strontium content in the solid solution. The observed regularities characterize variations in the chemical bonds in crystals and reflect the transformation of the electronic structure in single crystals of the solid solutions under study.

4. DISCUSSION

Let us now analyze the correlation between the composition, structure, and physical properties of crystals on the basis of our results and the data available in the literature. (Here, we do not present the large tables containing interatomic distances in the Sr and Ba polyhedra. These data are available from the authors of this work or can be easily calculated from the atomic coordinates and the unit cell parameters given in Table 1 and the tables from [5–7].)

First, we compare our results with the data obtained by Jamieson *et al.* [5], who studied single crystals with the very close composition $Sr_{0.75}Ba_{0.27}Nb_2O_{5.78}$. The site occupancies of the barium atoms in pentagonal channels are close to 30.9% (this work) and 34.4% [5]. However, our data on the distribution of the Sr atoms over two structural channels substantially differ from

those found in [5]. It should be emphasized once again that, unlike the data [5], the strontium atoms in large channels in our case are displaced from the *m* symmetry planes by 0.255(1) Å. In our work, the total occupancy factor for two Sr sites (above and below the *m* plane) in large channels is equal to 57.2%, and the site occupancy of the Sr atoms in the medium-sized channels is 71.5%. According to [5], the site occupancy of the Sr atoms in the large and medium-sized channels are equal to 50.3 and 82.2%, respectively. The reliability of our results and the data obtained in [5] is beyond question. The inferences made by Trubelja *et al.* [8] suggest that the difference in the distributions of the Sr atoms over structural channels of two types can stem from different prehistory of samples due to different annealing conditions upon crystal growth or effects of the external field used in [5] for preparing single-domain samples. This is supported by the following fact. The phase transition temperature T_c found in [5] for the $Sr_{0.75}Ba_{0.27}Nb_2O_{5.78}$ compound is equal to 348 ± 5 K. This value is considerably higher than the phase transition temperature of our crystal $T_c \approx 320$ K, which agrees well with the available data for this composition $T_c \approx 315$–330 K [1–4, 12].

In analysis of the relation between the properties of the SBN crystals and their atomic structure, we have restricted ourselves to comparison of the results obtained in the present work and the data taken from [6, 7], because the single crystals studied in all these works were grown under identical conditions. The regularities observed for these compounds can be reliably related to the structure of the corresponding solid solutions without regard for the redistribution of the Sr atoms due to the prehistory of samples.

Now, we compare the results obtained in the study of the SBN-0.33 [6], SBN-0.61 [7], and SBN-0.75 (this work) solid solutions. The most important result of the variation in the composition is the change in the splitting of the Ba and Sr sites in the large channels (Table 1). The displacement of Sr atoms from the *m* symmetry plane is equal to 0.255(1) Å in SBN-0.75 and 0.292(1) Å in SBN-0.61. The "limiting nonequivalence" of the Ba and Sr sites is observed in SBN-0.33, because the pentagonal channel is occupied only by the Ba atoms and the tetragonal channel is filled only by the Sr atoms. A decrease in the Sr concentration in the crystals is accompanied by changes in the site occupancy of the large channel (an increase in the occupancy of the Ba sites and a decrease in the occupancy of the Sr sites), whereas the occupancy of the medium-sized channel by the Sr atoms remains virtually unchanged.

The change in the SBN composition in the same order (an increase in the [Sr]/[Ba] ratio) is attended by a decrease in the temperature of the phase transition and its smearing; the relaxor properties become more pronounced [1–4]. As is known, the relaxor properties are associated with the microscopic structural disordering, which for the SBN crystals was attributed to the disordering of the Sr and Ba cations over two crystallographic positions [3, 4]. However, as follows from our analysis, the site occupancy of the medium-sized channel by Sr atoms only slightly depends on the composition. Therefore, we can assume that the relaxor properties of the SBN crystals are primarily determined by the character of site occupation of the large (pentagonal) channels by the Ba and Sr atoms. A decrease in the Sr concentration leads to an increase in the splitting of the Ba and Sr sites (i.e., in their nonequivalence); in other words, the ordering increases, which qualitatively correlates with the composition dependence of the relaxor properties and a decrease in the smearing of the phase transition.

Let us now discuss the qualitative relation between the properties of the SBN crystals and the degree of acentricity of the NbO_6 octahedra, which depends on the composition (Table 3). It is known that the optical properties of ABO_6 perovskite-type crystals are governed by the parameters of BO_6 octahedra [13]. In this case, it is expedient, in our opinion, to use the data obtained in [5], since the structural unit BO_6 is stable and does not depend on external effects in contrast with a random occupation of sites in the large and medium-sized channels. Indeed, the calculated acentric distortions of the Nb(1) and Nb(2) octahedra in the $Sr_{0.746}Ba_{0.247}Nb_2O_6$ compound (this work) are close to those for the $Sr_{0.75}Ba_{0.27}Nb_2O_{5.78}$ compound studied in [5] (Table 3), even with the difference in the occupancies of cationic sites. It is seen from Table 3 that the distortions of the Nb(1) and Nb(2) octahedra are close to each other for different compositions.

Within the approximation of polarized Nb–O bond model for niobates [14], Andreĭchuk *et al.* [6] evaluated the components of the quadratic optical susceptibility tensor d_{ij} and, in particular, showed that the d_{33} component is determined by the difference in the Nb–O distances to the upper and lower oxygen atoms in the NbO_6 octahedra. As can be seen from Table 3, there is a qualitative correlation between the dependence of the acentric distortion of the Nb(1) and Nb(2) octahedra and the dependence of the d_{33} component on the SBN composition. A similar situation was observed for solid solutions with the $KTiOPO_4$-type structure [15]. The isomorphous substitution leads to a change in the degree of deviation of the TiO_6 octahedra from centrosymmetry, which brings about considerable variations in the nonlinear susceptibility.

5. CONCLUSION

Thus, we carried out the x-ray structure investigation of the $Sr_{0.75}Ba_{0.25}Nb_2O_6$ (SBN-0.75) single crystals. The composition–structure–property relation for several SBN compositions was analyzed using our results and the data available in the literature. It was demonstrated that the change in the SBN composition brings about structural effects of the following two

types: (1) A decrease in the [Sr]/[Ba] ratio leads to a decrease in the occupancy of only large (pentagonal) structural channels and an increase in the splitting of the Ba and Sr sites in these channels. It is believed that this ordering in the arrangement of the Ba and Sr atoms is responsible for the observed decrease in the smearing of the phase transition and a weakening in the relaxor properties of the SBN compounds. (2) A decrease in the [Sr]/[Ba] ratio results in an increase in the acentric distortion of the $Nb(1)O_6$ and $Nb(2)O_6$ octahedra; i.e., the displacement of the Nb ions from the octahedron centers increases, which is likely responsible for the observed increase in the quadratic optical susceptibility d_{33}.

REFERENCES

1. M. E. Lines and A. M. Glass, *Principles and Applications of Ferroelectrics and Related Materials* (Oxford Univ. Press, Oxford, 1977; Mir, Moscow, 1981).
2. Yu. S. Kuz'minov, *Ferroelectric Crystals for Control of Laser Radiation* (Nauka, Moscow, 1982).
3. L. E. Cross, Ferroelectrics **76**, 241 (1987).
4. J. R. Oliver, R. R. Neurgaonkar, and L. E. Cross, J. Appl. Phys. **64**, 37 (1988).
5. P. B. Jamieson, S. C. Abrahams, and J. L. Bernstein, J. Chem. Phys. **48**, 5048 (1968).
6. A. E. Andreĭchuk, L. M. Dorozhkin, Yu. S. Kuz'minov, *et al.*, Kristallografiya **29** (6), 1094 (1984) [Sov. Phys. Crystallogr. **29**, 641 (1984)].
7. T. S. Chernaya, B. A. Maksimov, I. A. Verin, *et al.*, Kristallografiya **42** (3), 421 (1997) [Crystallogr. Rep. **42**, 375 (1997)].
8. M. P. Trubelja, E. Ryba, and D. K. Smith, J. Mater. Sci. **31**, 1435 (1996).
9. J. R. Carruthers and M. Grasso, J. Electrochem. Soc. **117**, 1426 (1970).
10. U. Zuker, K. Perenthalter, W. F. Kuhs, *et al.*, J. Appl. Crystallogr. **16** (3), 358 (1983).
11. *International Tables for X-ray Crystallography* (Kynoch, Birmingham, 1974), Vol. IV, p. 366.
12. L. A. Bursill and Peng Jin Lin, Philos. Mag. B **54** (2), 157 (1986).
13. M. DiDomenico and S. H. Wemple, J. Appl. Phys. **40** (2), 720 (1969).
14. C. R. Jeggo and G. D. Boyd, J. Appl. Phys. **41**, 2741 (1970).
15. N. I. Sorokina, V. I. Voronkova, V. K. Yanovskiĭ, *et al.*, Kristallografiya **41** (3), 457 (1996) [Crystallogr. Rep. **41**, 432 (1996)].

Translated by O. Borovik-Romanova

Physics of the Solid State, Vol. 42, No. 9, 2000, pp. 1722–1726. Translated from Fizika Tverdogo Tela, Vol. 42, No. 9, 2000, pp. 1673–1677.

MAGNETISM AND FERROELECTRICITY

Calculation of Electronic Ion Polarizability and Parameters of Interionic Repulsion in $LiNbO_3$ Crystals

A. V. Yatsenko

Simferopol State University, Yaltinskaya ul. 4, Simferopol, 95007 Ukraine

e-mail: roton@ccssu.crimea.ua

Received February 24, 2000

Abstract—A method for calculating the anisotropy of the electronic polarizability of O^{2-} ions in oxygen octahedral ferroelectrics has been proposed. It is shown that, in the case of mixed ion-covalent bonds in the crystal, the calculation of the polarizability within the approximation of isolated ions gives incorrect results. The principal components of the polarizability tensor for the O^{2-} ions and the electronic polarizability of the Nb^{5+} ions are calculated for the $LiNbO_3$ ferroelectric. Analysis of the stability of the $LiNbO_3$ structure confirms the results obtained. © *2000 MAIK "Nauka/Interperiodica".*

1. INTRODUCTION

At present, computer simulation of the structure and physical properties of single-crystal materials on the basis of the electrostatic interactions has found wide application [1]. This method is efficient only with complete information on the effective charges of ions, their electronic polarizability, and the parameters of interionic repulsion due to the overlap of electron shells. The correctness of these data is especially important in the study of materials with partially covalent bonds, for example, displacement-type ferroelectrics. The classical representative of these materials is lithium niobate $LiNbO_3$.

Ramesh and Ethiraj [2] calculated the polarizabilities of Li^+ ions and $(NbO_3)^-$ clusters in the $LiNbO_3$ crystals. More recently, Kinase *et al.* [3] determined the polarizabilities of all ions in the $LiNbO_3$ structure: $\alpha_{Li} = 0.03 \times 10^{-3}$ nm^3, $\alpha_{Nb} = 0.945 \times 10^{-3}$ nm^3, and $\alpha_O = 1.976 \times 10^{-3}$ nm^3. The calculations were performed within the approximation of isotropic ion polarizability. However, it is known that the polarizability of the Nb–O bonds in lithium niobate single crystals (in the optical range) is nonlinear [4]. The electron shells of the Nb^{5+} ions and their nearest neighbors O^{2-} overlap considerably, which results in a nonspherical symmetry of the outer electron shells of the O^{2-} ions. Consequently, the electronic polarizability of the O^{2-} ions should be described by the second-rank tensor. Below, we will consider the technique for calculating the anisotropy of the electronic ion polarizability in single-crystal compounds and analyze the stability of the $LiNbO_3$ crystal structure.

2. COMPUTATIONAL TECHNIQUE

Let us consider the effect of a linearly polarized electromagnetic wave in the optical range on a ferroelectric crystal. If the amplitude of the electric component is sufficiently small, the relation between the electric field strength **E** of the optical wave and the polarization increment $\Delta\mathbf{P}$ of the crystal is defined by the linear approximation

$$\Delta P_k = \varepsilon_0(\varepsilon_k - 1)E_k, \tag{1}$$

where E_k and P_k are the components of the corresponding vectors along the direction **k**, and ε_k is the permittivity of the crystal. On the other hand, the polarization increment can be written as

$$\Delta\mathbf{P} = \sum_{i=1}^{S} N_i \Delta\mathbf{p}_i, \tag{2}$$

where S is the number of sorts of structurally nonequivalent ions, N_i is the volume concentration of ions of the ith sort, and $\Delta\mathbf{p}_i$ is the light-induced change in the electric dipole moment of the ion of the ith sort.

The induced dipole moments of ions in the crystal lattice are usually calculated by an iteration method. The equation of the first iteration for the isotropic ion polarizability has the form

$$\Delta\mathbf{p}_i = \alpha_1\left[\mathbf{E}' + \sum_{j=1}^{S} \mathbf{E}_{ij}(\alpha_j\mathbf{E}')\right], \tag{3}$$

where $\mathbf{E}' = \mathbf{E} + \Delta\mathbf{P}/3\varepsilon_0$ is the strength of the macroscopic component of the crystal field induced by the optical wave, α_i is the polarizability of the ion of the ith sort, and $\mathbf{E}_{ij}$ is the local field induced at the ion of the

1063-7834/00/4209-1722$20.00 © 2000 MAIK "Nauka/Interperiodica"

*i*th sort by the *j*th dipole subsystem. For the ions located on a threefold axis of symmetry, $\mathbf{E}' \parallel \mathbf{E}_{ij}$, and the $\mathbf{E}_{ij}$ components in the Cartesian coordinate system can be represented as

$$E_{ijk} = \frac{\alpha_j E'_k}{4\pi\varepsilon_0}\sum_{m=1}^{M_j}\frac{3K_{ijm}^2 - R_{ijm}^2}{R_{ijm}^5} = \alpha_j E_k D_{ijk}, \qquad (4)$$

where $k = x, y, z$; R_{ijm} is the distance between the chosen ion of the *i*th sort and the *m*th ion of the *j*th sort; K_{ijm} is the *k*th component of R_{ijm}; M_j is the number of ions of the *j*th sort in the chosen region of summation; and D_{ijk} is the corresponding structure sum.

In the case when the calculation of Δp_i is restricted to the first iteration, it is possible to divide each term of Eq. (3) by E'_k and to derive the expression for the effective polarizabilities $(\alpha_{\text{eff}})_{ik}$ of the ion of the *i*th sort with allowance made for the local environment, that is,

$$(\alpha_{\text{eff}})_{ik} = \frac{\Delta p_{ik}}{E'_k} = \alpha_i\left[1 + \sum_{j=1}^{S}\alpha_j D_{ijk}\right]\alpha_i b_{ik}. \qquad (5)$$

By combining Eqs. (1)–(5), we obtain the Lorentz–Lorenz formula with the correction for the nearest dipole environment

$$\frac{n_k^2 - 1}{n_k^2 + 2} = \frac{1}{3\varepsilon_0}\sum_{i=1}^{S} N_i b_{ik}\alpha_i, \qquad (6)$$

where n_k is the refractive index of the crystal at $\mathbf{E} \parallel \mathbf{K}$. A similar approach to the calculation of the polarizability was used in [2].

For the anisotropic polarizability of ions of the *j*th sort, the components of the contribution from the *j*th dipole subsystem to the local field at the ion of the *i*th sort (the external field **E** is directed along the *x* axis) are written as follows:

$$(E_{ijx})_x = E'_x\left[\sum_{l=1}^{3}\sum_{f}(\alpha_{ll})_j\cos\theta_{lxj}\cos\theta_{lfj}D_{ijxf}\right] = E'_x(T_{ijx})_x,$$

$$(E_{ijx})_y = E'_x\left[\sum_{l=1}^{3}\sum_{f}(\alpha_{ll})_j\cos\theta_{lxj}\cos\theta_{lfj}D_{ijyf}\right] = E'_x(T_{ijx})_y,$$

$$(E_{ijx})_z = E'_x\left[\sum_{l=1}^{3}\sum_{f}(\alpha_{ll})_j\cos\theta_{lxj}\cos\theta_{lfj}D_{ijzf}\right] = E'_x(T_{ijx})_z,$$

where θ_{lfj} are the angles between the *l*th principal axis of the polarizability tensor and the **f** direction; $(\alpha_{ll})_j$ are the polarizability tensor components for the ions of the *j*th sort in the system of proper axes; and $f = x, y$, and *z*. The structure sums D_{ijkf} and D_{ijkk} can be obtained in the form

$$D_{ijkf} = \frac{1}{4\pi\varepsilon_0}\sum_{m=1}^{M_j}\frac{3K_{ijm}F_{ijm} - \delta_{kf}R_{ijm}^2}{R_{ijm}^5}, \qquad (7)$$

where F_{ijm} is determined in the same manner as K_{ijm}, and δ_{kf} is the Kronecker symbol.

In the general case, the local field differs from **E** in direction; hence, the general relationship for the effective polarizability of ions of the *i*th sort takes the following form:

$$\begin{aligned}(\alpha_{\text{eff}})_{ix} = {} & \sum_{l=1}^{3}(\alpha_{ll})_i\cos^2\theta_{lxi}\left[1 + \sum_{j=1}^{S}(T_{ijx})_x\right] \\ & + \sum_{l=1}^{3}(\alpha_{ll})_i\cos\theta_{lxi}\cos\theta_{lyi}\sum_{j=1}^{S}(T_{ijx})_y \\ & + \sum_{l=1}^{3}(\alpha_{ll})_i\cos\theta_{lxi}\cos\theta_{lzi}\sum_{j=1}^{S}(T_{ijx})_z.\end{aligned} \qquad (8)$$

A similar expression for $(\alpha_{\text{eff}})_{iz}$ (the **E** vector is directed along the *z* axis) can be obtained from Eq. (8) by the permutation of subscripts ($x \longleftrightarrow z$). Thus, the substitution of the obtained relationships into Eq. (6) makes it possible to extend the applicability of the Lorentz–Lorenz formula to the case of the anisotropic electronic polarizability of ions involved in the crystal composition.

3. CALCULATION OF POLARIZABILITY OF O^{2-} IONS IN $LiNbO_3$ CRYSTAL

It should be noted that the approaches used in [2, 3] to the calculation of the polarizability differ essentially. According to Kinase *et al.* [3], all ions in the structure are considered to be independent, and the overlap between the electron shells of O^{2-} and Nb^{5+} ions is ignored. Ramesh and Ethiraj [2] calculated the polarizability of the $(NbO_3)^-$ cluster, which was treated as a point charge. The latter approach is likely to be more correct, but is less informative. Alternatively, the polarizability of short Nb–O bonds (0.1878 nm) can be considered the sum of the polarizabilities of Nb^{5+} and O^{2-} ions, which are determined independently from one another. Of fundamental importance in this case is that the dipole–dipole interactions between the ions in the short Nb–O bonds should be disregarded in the calculation of the structure sums.

In the subsequent calculations, it was assumed that the polarizability of the Li^+ ions is isotropic and equal to 0.032×10^{-3} nm^3 [2]. The polarizability α_{Nb} of the Nb^{5+} ions was also taken to be isotropic and varied over

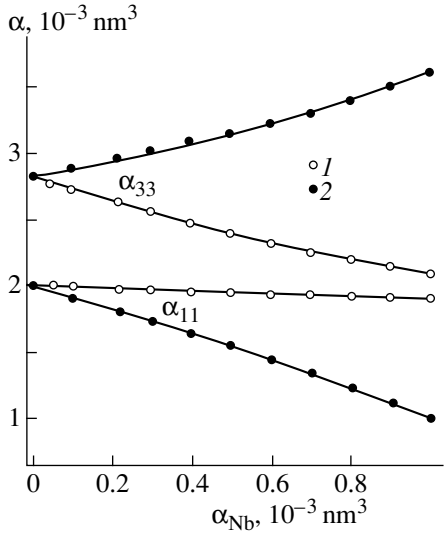

Fig. 1. Dependences of the principal components α_{11} and α_{33} of the electronic polarizability tensor for O^{2-} ions on the polarizability α_{Nb} of the Nb^{5+} ions in the $LiNbO_3$ structure. Calculations are performed in (*1*) the isolated ion polarizability and (*2*) bond polarizability approximations.

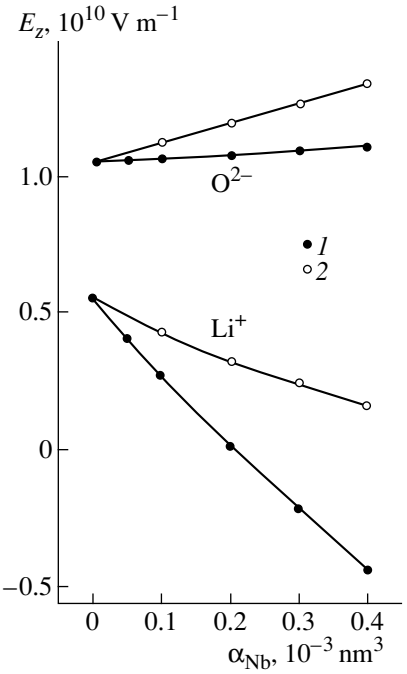

Fig. 2. Dependences of the *z* component of the local electric field E_z at the Li^+ and O^{2-} ions on α_{Nb}. Calculations are performed in (*1*) the isolated ion polarizability and (*2*) bond polarizability approximations.

a wide range with respect to the tabulated value of 0.22×10^{-3} nm^3 [5].

From symmetry considerations, it is clear that one of the principal axes of the polarizability tensor for the O^{2-} ions (*3*) should coincide with the direction of the Nb–O bond, and the polarizability tensor likely has an axial symmetry, so that $\alpha_{11} = \alpha_{22} \neq \alpha_{33}$. Hence, it is assumed that the second principal axis (*2*) lie in the oxygen plane. All the further calculations were performed using the structural data obtained by Iyi *et al.* [6] for the $LiNbO_3$ crystals of stoichiometric composition. The structure sums (6) were calculated with due regard for the dipole moments in a sphere of radius 12 nm with the center at the point occupied by the ion under consideration, which provided the convergence with an accuracy better than 1%.

The calculations were performed with the refractive indices for the $LiNbO_3$ crystals of stoichiometric composition in the far-IR range: $n_x = 2.2032$ and $n_z = 2.1187$ [7]. Figure 1 depicts the dependences of the principal components $\alpha_{11} = \alpha_{22}$ and α_{33} of the electronic polarizability tensor for the O^{2-} ions on the polarizability α_{Nb}. The dependences were calculated within the isolated ion polarizability and bond polarizability approximations. As can be seen from Fig. 1, the anisotropic polarizability of the O^{2-} ions is observed for both approximations. However, the results obtained differ substantially and call further analysis.

4. ANALYSIS OF STABILITY OF $LiNbO_3$ STRUCTURE

A possible method for verifying these results is to use the obtained data in the calculation of the local electric fields $\mathbf{E}_{loc}$ at the structurally nonequivalent ions in the $LiNbO_3$ lattice and to analyze the stability of the structure.

In addition to the $\alpha_{11}(\alpha_{Nb})$ and $\alpha_{33}(\alpha_{Nb})$ dependences, the local fields $\mathbf{E}_{loc}$ were determined using the following effective charges of the ions in the lattice: $q_{Li} = 0.98|e|$, $q_{Nb} = 3.67|e|$, and $q_O = -1.55|e|$ ($|e|$ is the magnitude of the electron charge), which were obtained by the LCAO method in [8]. The dipole contribution to $\mathbf{E}_{loc}$ was calculated by the iteration method (four iterations), and the ion contribution was determined by the procedure proposed in [9].

Figures 2 and 3 demonstrate the dependences of the *z* component of the local electric field E_z at the O^{2-}, Li^+, and Nb^{5+} ions and the component of the electric field gradient tensor $V_{zz}(Nb)$ at the Nb^{5+} ion on the polarizability α_{Nb}.

Since the Nb^{5+} ion, to a first approximation, can be treated as spherically symmetric, the force balance equation for this ion is written as

$$q_{Nb}E_z(Nb) + p_z(Nb)V_{zz}(Nb) + F_z(Nb) = 0, \qquad (9)$$

where $E_z(Nb)$ is the *z* component of $\mathbf{E}_{loc}$ at the Nb^{5+} ion, $p_z(Nb)$ is the *z* component of its dipole moment, and $F_z(Nb)$ is the resultant repulsive force in the NbO_6 octahedron. The force balance equation for the Li^+ ion has a similar form.

When calculating the stability of the crystal structure, it is usually assumed that the repulsive force

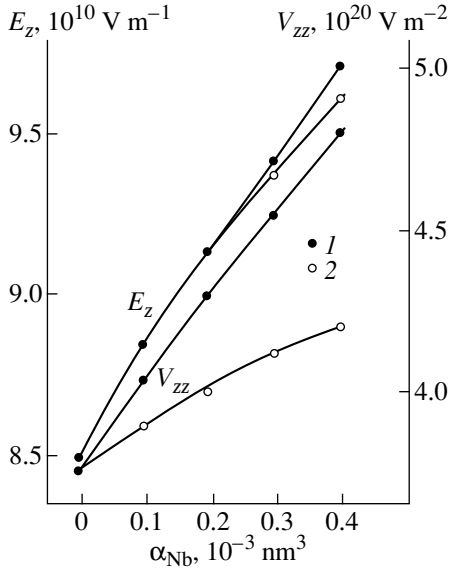

Fig. 3. Dependences of the *z* component of the local electric field E_z at the Nb^{5+} ions and the V_{zz}(Nb) component on α_{Nb}. Calculations are performed in (*1*) the isolated ion polarizability and (*2*) bond polarizability approximations.

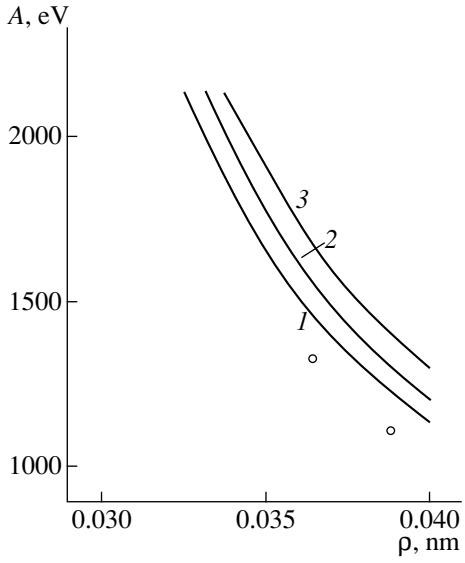

Fig. 4. Calculated dependences $A(\rho)$ for the Nb^{5+}–O^{2-} interaction at α_{Nb} = (*1*) 0, (*2*) 0.10, and (*3*) 0.20×10^{-3} nm^3 in the isolated ion polarizability approximation. The dependences calculated within the bond polarizability approximation at $\alpha_{Nb} = 0.05$ and 0.10×10^{-3} nm^3 are identical to curve *1*. Open circles indicate the tabulated data.

caused by the distortion and the overlap of electron shells of two ions is described by the Born–Mayer potential

$$F_r = -A\rho^{-1}\exp(-r\rho^{-1}), \qquad (10)$$

where A and ρ are the parameters characterizing the given interaction, and r is the distance between the ions. Equations (9) and (10) furnishes a means for determining the relation between the parameters A and ρ for the Nb^{5+}–O^{2-} and Li^+–O^{2-} interactions at different α_{Nb} values. The known parameters of the pair interactions under consideration are listed in the table.

The dependences $A(\rho)$ for the Nb^{5+}–O^{2-} and Li^+–O^{2-} interactions were calculated according to the described scheme with the obtained data on $\mathbf{E}_{loc}$. It was found that the A parameters determined for any above sets of polarizabilities (α_{Nb}, α_{11}, and α_{33}) are anomalously large compared to the parameters given in the table. It should be emphasized that the induced electric dipole moment $\mathbf{p}_O$ of oxygen ions in the $LiNbO_3$ structure is rather large ($|p_O| \cong 0.11|e|$ nm). Since the moment $\mathbf{p}_O$ is primarily determined by the shift in the center of the outer electron shells of the O^{2-} ion with respect to the nucleus center, this shift for a dipole-forming charge of $6|e|$ is equal to 0.018 nm, i.e., 0.1 of the short Nb^{5+}–O^{2-} bond length. The repulsive force F_r is associated with the overlap of the outer electron shells of ions, and, hence, r in Eq. (10) should mean the distance between the center of the metal ion and the "center" of the outer electron shells of the O^{2-} ion.

Within this approximation, the $A(\rho)$ dependences for the Nb^{5+}–O^{2-} and Li^+–O^{2-} interactions were recalculated at different α_{Nb} values. The calculated dependences, together with the tabulated data, are displayed in Figs. 4 and 5. Despite the fact that the above approach is rather simplified, the calculation at $\alpha_{Nb} = 0.05 \times 10^{-3}$ nm^3 in the bond polarizability approximation is in reasonable agreement with the parameters determined from first principles [10, 11].

Parameters of repulsive potentials

Interaction	A, eV			ρ, nm		
	I	II	III	I	II	III
Li^+–O^{2-}	262	862		0.0347	0.0260	
Nb^{5+}–O^{2-}	1796	1113	1333	0.0346	0.0388	0.0364
O^{2-}–O^{2-}	22 764	22 764	22 764	0.0149	0.0149	0.0149

Note: Columns I refer to the empirical calculations in the Li_2O and Nb_2O_5 structures [10]; columns II, to the "*ab initio*" calculations in the $LiNbO_3$ structure [10]; and columns III contain the results of the "*ab initio*" calculations in the $KNbO_3$ structure [1].

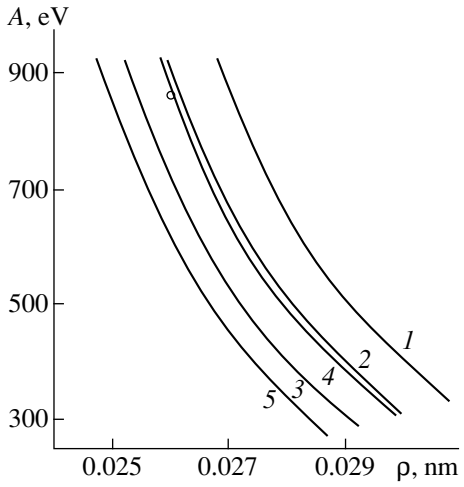

Fig. 5. Calculated dependences $A(\rho)$ for the Li^+–O^{2-} interaction at α_{Nb} = (*1*) 0, (*2*) 0.10, and (*3*) 0.20×10^{-3} nm^3 in the isolated ion polarizability approximation and at α_{Nb} = (*4*) 0.05 and (*5*) 0.10×10^{-3} nm^3 in the bond polarizability approximation. Open circles indicate the tabulated data.

For the O^{2-}–O^{2-} interaction, similar calculations cannot be carried out, because the outer electron shells of the O^{2-} ions are not spherically symmetric.

Note that the spontaneous polarization P_s calculated with the use of the data obtained within the bond polarizability approximation at $\alpha_{Nb} = 0.05 \times 10^{-3}$ nm^3 is equal to 0.77 C m^{-2}, which is close to the experimental value of P_s for the $LiNbO_3$ crystal.

Therefore, the electronic polarizability of the O^{2-} ions in the oxygen octahedral ferroelectrics should be calculated with due regard for the character of the metal–oxygen bonds and, as a consequence, the possible anisotropy of the polarizability.

From the above results, it can be concluded that the electronic polarizability of the Nb^{5+} ions in the $LiNbO_3$ structure is equal to 0.05×10^{-3} nm^3, and the components of the electronic polarizability tensor for the O^{2-} ions are $\alpha_{11} = \alpha_{22} = 1.97 \times 10^{-3}$ nm^3 and $\alpha_{33} = 2.86 \times 10^{-3}$ nm^3.

In closing, it should be noted that the components of the electronic polarizability tensor for the O^{2-} ions can be refined taking into account the possible anisotropy of the polarizability of the Nb^{5+} ions and the next iterations in the calculation of the field induced by the optical wave.

REFERENCES

1. B. A. Luty, I. G. Tironi, and W. F. van Gunsteren, J. Chem. Phys. **103**, 3014 (1995).
2. N. Ramesh and R. Ethiraj, J. Mater. Sci. Lett. **13**, 757 (1994).
3. W. Kinase, K. Harada, H. Yagi, *et al.*, J. Korean Phys. Soc. **32**, S137 (1998).
4. M. E. Lines and A. M. Glass, *Principles and Applications of Ferroelectrics and Related Materials* (Oxford Univ. Press, Oxford, 1977; Mir, Moscow, 1981).
5. M. Levaloic and G. Allais, Phys. Status Solidi A **40**, 181 (1977).
6. N. Iyi, K. Kitamura, F. Isumi, *et al.*, J. Solid. State Chem. **101**, 340 (1992).
7. U. Schlarb and K. Betzler, J. Appl. Phys. **73** (7), 3472 (1993).
8. W. Y. Ching, Zong-Quan Gu, and Yong-Nian Xu, Phys. Rev. B **50** (3), 1992 (1994).
9. O. V. Yatsenko, Ukr. Fiz. Zh. (Ukr. ed.) **44** (3), 381 (1999).
10. H. Donnerberg, S. M. Tomlinson, C. R. A. Catlow, and O. F. Shirmer, Phys. Rev. B **40** (17), 11909 (1989).
11. H. Donnerberg, Phys. Rev. B **50** (13), 9053 (1994).

Translated by O. Borovik-Romanova

Physics of the Solid State, Vol. 42, No. 9, 2000, pp. 1727–1730. Translated from Fizika Tverdogo Tela, Vol. 42, No. 9, 2000, pp. 1678–1681.

MAGNETISM AND FERROELECTRICITY

Periodic Domain Structure in Czochralski-Grown $LiNbO_3$: Y Crystals

N. F. Evlanova, I. I. Naumova, T. O. Chaplina, S. V. Lavrishchev, and S. A. Blokhin

Moscow State University, Physical Department, Vorob'evy gory, Moscow, 119899 Russia

e-mail: inna@crystal.phys.msu.su

Received March 9, 2000

Abstract—A study is reported of the correlation between the impurity distribution and the ferroelectric domain structure in a periodically polarized $LiNbO_3$: Y crystal grown by the Czochralski method. The domain walls forming near the impurity concentration modulation extrema are shown to be shifted by the temperature gradient below the Curie point. A new positive domain was observed to form near the trace of an electron beam scanning the $\{01\bar{1}0\}$ crystal surface in the course of x-ray microprobe analysis. © *2000 MAIK "Nauka/Interperiodica".*

1. Periodically polarized $LiNbO_3$: Y bulk ferroelectric crystals are a promising material for application in nonlinear optics making use of quasi-phase matching [1]. The periodic reversals of the spontaneous polarization P_s in neighboring domains correlate with those of the sign of the nonlinear coefficient (optical nonlinear superlattice).

The regular domain structure (RDS) in Czochralski-grown lithium niobate single crystals is related to the growth bands induced by crystal rotation [2]. The periodic temperature oscillations at the crystal–melt interface give rise to a modulation of the instantaneous growth rate, and the dependence of the effective impurity-distribution coefficient ($k_{\text{eff}} \neq 1$) on the growth rate governs the impurity concentration modulation along the growth direction. It is these rotation bands that account for the formation of periodic antiparallel ferroelectric domains with a period determined by the pulling-to-rotation rate ratio ($\Lambda = V_{\text{pull}}/V_{\text{rot}}$).

We observed, however, that domains of opposite sign present in periodically polarized lithium niobate crystals within one period λ were sometimes of unequal thickness, with this inequality increasing from the bottom to the top end of the crystal. The difference in thickness between domains of the same period results in a reduced efficiency of nonlinear optical transformations in the crystal.

2. This work was aimed at studying the correlation between the impurity distribution and the ferroelectric domain structure in an $LiNbO_3$: Y crystal, as well as at revealing the reasons for the unequal thickness of the domains making up the RDS period.

A periodically polarized $LiNbO_3$: Y crystal was grown along the $\langle 2\bar{1}\bar{1}0\rangle$ crystallographic direction (the *X* axis) by the Czochralski method from a melt close to a congruent composition (Li/Nb = 0.942) with an Y_2O_3 impurity (1 wt.%). The V_{pull} = 10 mm/h and V_{rot} = 6 min^{-1} rates corresponded to the calculated period λ = 27.8 μm. On completion of the growth process, the crystal was raised rapidly out of the melt to be cooled subsequently in the growth setup with a rate of 60°C/h.

The yttrium impurity introduced in the crystal modulates the periodic domain structure in $LiNbO_3$: Y, while at the same time leaving the crystal optically transparent in the 0.35–4.5 μm region. The $\langle 2\bar{1}\bar{1}0\rangle$ growth direction was chosen as the most favorable for using (because of the largest nonlinear coefficient d_{33}) in quasi-phase-matched nonlinear optical converters.

3. The yttrium concentration in the crystal under study was measured by x-ray microprobe analysis in a scanning electron microscope (JSM-840), with the polished sample surface scanned across the domain boundaries, while Camebax SX-50 was employed to measure the impurity concentration. To shield the sample charge, the surface to be studied was coated with a thin (100-Å) gold film. The electron beam diameter did not exceed 0.1 μm, the current was 5000 nA, the scanning range was 2 μm, and the time per one analysis point was 20 s (100 points altogether, 200 μm). The x-ray microprobe analysis of the yttrium impurity was complicated by the overlap of the Y*Lα* and Nb*Ll* spectral lines (Fig. 1), which resulted in a decrease of the peak/background intensity ratio and an apparent decrease of the impurity-concentration modulation depth. The yttrium concentration was recorded by two spectrographs simultaneously to eliminate random errors of either instrument.

The ferroelectric domain structure on the $\{01\bar{1}0\}$ surface of the $LiNbO_3$: Y crystal was studied by selective chemical etching. The crystal was cut by a diamond saw, and the surface to be studied was ground and polished. The samples were etched with an 1 : 2 (by vol-

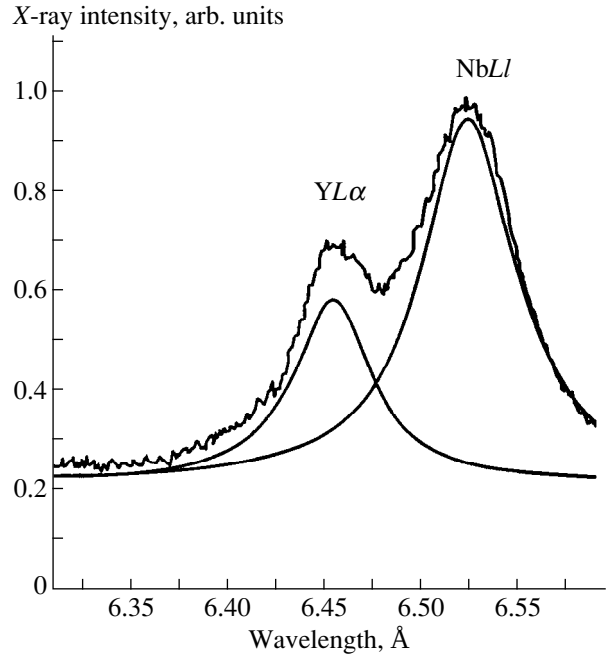

Fig. 1. Overlap of the Y*Lα* and Nb*Ll* spectral lines.

ume) HF + HNO_3 acid mixture in a platinum crucible for 20 min at the boiling temperature. Because the etching of the $(0\bar{1}10)$ surface proceeds faster than that of $(01\bar{1}0)$, it is possible to discriminate between the boundaries of domains of opposite sign.

4. The precise matching of domain walls to the measured impurity distribution curves is difficult. Direct x-ray microprobe investigation of a crystal surface with domain walls made visible by selective chemical etching is impossible, because the chemical composition of the surface varies under etching. Besides, the surface relief may distort the results of an analysis. In order to avoid inaccuracies in matching domain wall positions to the impurity distribution curves, the following sequence of operations was chosen:

(i) Chemical etching of the sample, observation of the domain structure in a metallurgical microscope, choosing regions free of growth defects, marking with a sapphire needle;

(ii) Polishing the sample, x-ray microprobe analysis, entering the impurity distribution curve and the image of persisting marks into the computer;

(iii) Re-etching, entering the electron-microscope image of the domain structure into the computer; and

(iv) Computer matching of the impurity concentration variation curves to the domain wall image using the marks and the electron beam trace.

Figures 2a and 2b present yttrium-impurity distribution curves on the $\{01\bar{1}0\}$ surface of the $LiNbO_3$: Y crystal. Because the electron beam was scanned not exactly perpendicular to the domain walls, the values of the impurity concentration are connected with the corresponding analysis spots by vertical lines. Two regions in the same main domain were chosen for x-ray microprobe analysis [3]. In the bottom part of the sample, two analyses were made (curves *1* and *2* in Fig. 2a). The upper and lower scans correspond to the upper (*1*) and lower (*2*) curves of the yttrium concentration distribution, respectively.

The measured RDS period in the lower part of the crystal (Λ = 28.4 μm) is larger than the calculated one (27.8 μm) because of the melt level lowering in the course of crystal growth. Figure 2b shows the impurity distribution in the top part of the crystal.

In both regions studied, domain walls are located near the extrema in the impurity distribution. While in the upper and lower parts of the crystal, the domain walls are located approximately in the same way relative to the maxima; the walls associated with the minima in the upper part are shifted with respect to the minima by a few microns as compared to their positions in the lower part of the crystal. This may be attributed to domain wall motion in the course of crystal growth and cooling. The motion of the domain walls associated with the concentration minima, i.e., of those least pinned by the impurity, is more pronounced. The domain wall motion is driven by an internal field *E* (thermopower) created by the temperature gradient, which is fairly large in the Czochralski method. When grown by this method along the $\langle 2\bar{1}\bar{1}0\rangle$ direction, the crystal breaks down in two antiparallel main domains and a series of internal domains [3]. We believe that the radial temperature gradient affects the formation of a domain structure in a crystal of such orientation not only near the Curie isotherm, but also at lower temperatures through motion of the walls of the internal domains, i.e., of the RDS domain walls in our case. This motion accounts for the unequal domain thicknesses within the same period and the observed increase in the margin of this inequality in the upper part of the crystal, which formed before the lower one and, hence, was acted upon by the temperature gradient for a longer time. One can estimate the domain-wall motion velocity from the crystal pulling rate, the distance between the regions under study, and the observed wall displacement.

The value thus obtained (≈5 μm/h) reflects the domain-wall velocity for the crystal regions under study. Generally speaking, the velocity should depend on the temperature, the temperature gradient, and the concentration of the wall-stabilizing impurities.

5. A study of the correlation between the yttrium distribution and the positions of the ferroelectric domain walls showed that the impurity concentration modulation period is in agreement with the RDS period. The maxima are typically broader than the minima and are asymmetric in shape. One domain wall forms near a maximum and another arises near a mini-

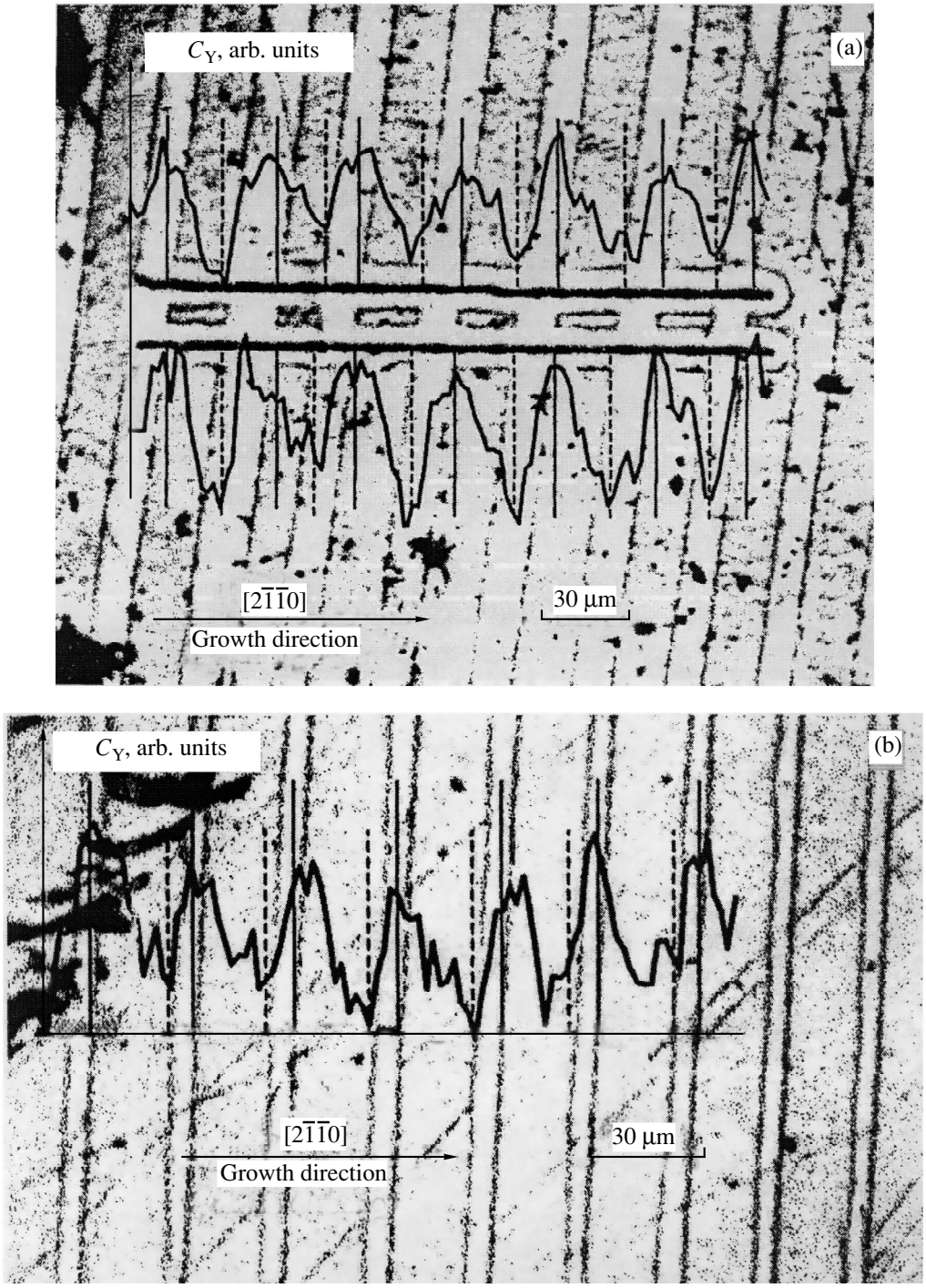

Fig. 2. Domain structure patterns matched to the curves of yttrium concentration distribution on the $LiNbO_3 : Y \{01\bar{1}0\}$ surface (a) in the lower part of the crystal and (b) in the upper crystal part.

mum of the yttrium concentration. A similar result was obtained by the present authors in a study of an $LiNbO_3 : Nd : Mg$ crystal [4–6]. The asymmetric shape of the Nd impurity distribution curve corresponded to the unequal thicknesses of the positive and negative domains within one RDS period.

Our results are comparable with those quoted in [2, 7, 8] where Czochralski-grown $LiNbO_3 : Y$ crystals (1–0.5 wt %) were investigated. The domain structure and the impurity distribution also had the same period determined by the actual growth parameters, and the narrow minima and broad maxima in the Y distribution

likewise were associated with domain wall positions. The impurity distribution curves obtained by us are less symmetrical; the more symmetric shape of these curves in [2, 7] is probably connected with the transmission electron microscope technique [8] used in the measurements.

In contrast to [7], however, we believe that the unequal domain widths within the same period cannot be accounted for solely in terms of the mechanism [7] of critical impurity concentration gradient and of the unequal widths of crystal layers grown during the half-periods of their rotation differing in temperature [8]. We followed the increase in domain width difference over the crystal and believe that domain walls move in the course of crystal growth. Nevertheless, a proper comparison with our results cannot be carried out, because the publication in question lacks the necessary information; in particular, the part of the crystal from which the sample was cut is not specified in [7].

6. Scanning of the $\{01\bar{1}0\}$ lithium niobate surface parallel to the P_s vector revealed for the first time the formation of a new positive domain around the electron beam trace.

It is known that an electron beam is capable of repolarizing the {0001} surface of an $LiNbO_3$ crystal perpendicular to P_s. The scanning electron beam was used to produce a periodic domain structure in lithium niobate at room temperature [9]. The authors attribute this effect to the polarization switching action of the local electric field along P_s. Illumination of the $\langle 2\bar{1}\bar{1}0\rangle$ and $\{01\bar{1}0\}$ surfaces and of *X* and *Y* cuts of $LiNbO_3$: Fe crystals created microdomain regions at a nonzero light intensity gradient [10]. The formation of the microdomains is attributed [10] to a generation of an internal, high-strength electric field as a result of spatial charge separation in the photogalvanic effect. Besides, local polarization switching in the surface layer of a lithium niobate crystal with the *Z* axis parallel to the surface was observed to occur during the motion of a pointed electrode to which an electric potential was applied [11].

We attribute the formation of a new domain of opposite sign on the $\{01\bar{1}0\}$ surface to the formation near the crystal surface of a space charge gradient as the surface is scanned by an electron beam. Besides, we believe that a local temperature gradient may also affect P_s, because the electron beam heats the crystal fairly strongly and leaves an indented trace on the polished crystal surface.

While the x-ray microprobe analyses (Figs. 2a and 2b) were performed in identical conditions, in one case (Fig. 2a), where a new positive domain formed, the electron beam was focused to a smaller spot.

7. To sum up:

(i) We have developed a new method of studying the correlation between the impurity distribution and the domain wall positions in a periodically polarized lithium-niobate crystal. The domain wall images revealed by selective chemical etching were matched to the impurity distribution curves by means of marks and x-ray microprobe analysis traces on the $LiNbO_3$: Y $\{01\bar{1}0\}$ surface. The ferroelectric domain boundaries were found to coincide with the impurity modulation extrema;

(ii) We have shown for the first time that, below the Curie temperature, domain walls displace with respect to the corresponding yttrium concentration minima (by 5 μm/h) in the course of lithium-niobate crystal growth; and

(iii) A new positive domain has been observed to form around the electron beam trace on the $\{01\bar{1}0\}$ surface of the $LiNbO_3$: Y crystal. This opens new possibilities for RDS generation.

ACKNOWLEDGMENTS

Support of the INTAS program (Grant no. 97-31275) is gratefully acknowledged.

REFERENCES

1. J. A. Armstrong, N. Bloembergen, J. Ducuing, and P. S. Pershan, Phys. Rev. **127**, 1918 (1962).
2. N. B. Ming, J. F. Hong, and D. Feng, J. Mater Sci. **17**, 1663 (1982).
3. N. V. Evlanova and L. N. Rashkovich, Fiz. Tverd. Tela (Leningrad) **13** (1), 282 (1971) [Sov. Phys. Solid State **13**, 223 (1971)].
4. I. I. Naumova, N. F. Evlanova, O. A. Gliko, and S. V. Lavrishchev, Ferroelectrics **190**, 107 (1997).
5. I. I. Naumova, N. F. Evlanova, O. A. Gliko, and S. V. Lavrishchev, J. Cryst. Growth **181**, 160 (1997).
6. I. I. Naumova, N. F. Evlanova, S. A. Blokhin, and S. V. Lavrishchev, J. Cryst. Growth **187**, 102 (1998).
7. Ya-lin Lu, Yan-qing Lu, X. Cheng, *et al.*, Appl. Phys. Lett. **68**, 2642 (1996).
8. J. Chen, Q. Zhou, J. F. Hong, *et al.*, J. Appl. Phys. **66** (1), 336 (1989).
9. H. Ito, C. Takyu, and H. Inaba, Electron. Lett. **27**, 1221 (1991).
10. V. V. Lemeshko, V. V. Obukhovskiĭ, and A. V. Stoyanov, Fiz. Tverd. Tela (St. Petersburg) **34** (6), 1833 (1992) [Sov. Phys. Solid State **34**, 977 (1992)].
11. S. O. Fregatov and A. B. Sherman, Pis'ma Zh. Tekh. Fiz. **23** (11), 54 (1997) [Tech. Phys. Lett. **23**, 438 (1997)].

Translated by G. Skrebtsov

Physics of the Solid State, Vol. 42, No. 9, 2000, pp. 1731–1733. Translated from Fizika Tverdogo Tela, Vol. 42, No. 9, 2000, pp. 1682–1684.

MAGNETISM AND FERROELECTRICITY

Low-Temperature X-ray Diffraction Studies of the Crystallographic Parameters and Thermal Expansion of $(CH_3)_2NH_2Al(SO_4)_2 \cdot 6H_2O$ Crystals

A. U. Sheleg, E. M. Zub, and K. N. Semenov

Institute of Solid-State and Semiconductor Physics, Belarussian Academy of Sciences, ul. Brovki 17, Minsk, 220072 Belarus
e-mail: sheleg@ifttp.bas-net.by

Received January 13, 2000

Abstract—The *a*, *b*, *c*, and β crystallographic parameters of the $(CH_3)_2NH_2Al(SO_4)_2 \cdot 6H_2O$ crystal (DMAAS) have been measured by x-ray diffraction in the 90–300-K temperature range. The thermal expansion coefficients along the principal crystallographic axes α_a, α_b, and α_c have been determined. It was shown that, as the temperature is increased, the parameter α decreases and *b* increases, whereas *c* decreases for $T < T_c$ (where T_c is the transition temperature) and increases for $T > T_c$, so that one observes a minimum in the $c = f(T)$ curve in the region of the phase transition (PT) temperature $T_c \sim 152$ K. The thermal expansion coefficients α_a, α_b, and α_c vary in a complicated manner with increasing temperature, more specifically, α_a and α_c assume negative values at low temperatures, and the $\alpha_a = f(T)$, $\alpha_b = f(T)$, and $\alpha_c = f(T)$ curves exhibit anomalies at the PT point. The crystal has been found to be substantially anisotropic in thermal expansion. © *2000 MAIK "Nauka/Interperiodica".*

Dimethylammonium-aluminum sulfate (DMAAS) $(CH_3)_2NH_2Al(SO_4)_2 \cdot 6H_2O$ crystals have been synthesized fairly recently [1] and, similar to their gallium-containing analog DMAGS, belong to a new class of ferroelectrics–ferroelastics. DMAAS crystallizes in a monoclinic structure of a space group $P2_1/n$ with room-temperature unit-cell parameters $a = 6.403$ Å, $b = 10.747$ Å, $c = 11.128$ Å, and $\beta = 100.47°$ [2]. The paraelectric phase of DMAAS exhibits ferroelastic properties, and when cooled to $T_c \sim 152$ K, the crystal undergoes a proper second-order transition from the ferroelastic to ferroelectric phase involving a change in symmetry $2m \longrightarrow m$ [1]. Measurements of the optical and electrooptical properties [3, 4] do not exclude the possibility of a phase transition (PT) in DMAAS at $T \sim 110.5$ and 390 K. A study of the plastic properties of DMAAS crystals [5] revealed a break in the $\sigma_{0.2} = f(T)$ curve at $T = 110$ K. Besides, a low-temperature phase transition was observed in the region of $T \sim 75$ K [6, 7], whose nature remains unclear, with the symmetry of the low-temperature phase being unknown.

This work reports an x-ray diffraction study of the lattice parameters *a*, *b*, *c*, and β and of thermal expansion of DMAAS crystals made in the temperature range from 90 to 300 K.

1. EXPERIMENTAL TECHNIQUES AND RESULTS OF THE STUDY

The x-ray diffraction studies were carried out on a diffractometer with CuK_α radiation using a Rigaku low-temperature x-ray camera. The subjects for the study were single-crystal plates $4 \times 4 \times 2$ mm in size, whose surfaces were set parallel to the (*h*00), (0*k*0), and (001) crystallographic planes to within ~3–5′. Besides, the angles of some reflections were also measured on powder samples in the same temperature range. The diffraction spectra were obtained by $\theta = 2\theta$ scanning, with the reflection intensity profile recorded on perforated tape. The sample temperature was set by a control unit based on a VRT-3 temperature controller. The temperature was monitored with a copper–constantan thermocouple. This system permitted one to set and maintain a temperature to 0.1 K within the 90–300-K range covered. Before each exposure, the sample was kept at the given temperature for 10–15 min. The diffraction angles were measured in 2–4 K steps. The accuracy of determination of the parameters was ±0.0004 Å. The room-temperature crystallographic parameters of DMAAS were found to be $a = 6.3939 \pm (4)$ Å, $b = 10.7450 \pm (4)$ Å, $c = 11.0686 \pm (4)$ Å, and $\beta = 99.53°$.

Figure 1 presents temperature dependences of the lattice parameters *a*, *b*, and *c* of single-crystal DMAAS. One readily sees that the *a* parameter decreases with increasing temperature, to increase slightly only in the 270–300 K region. Near the PT temperature ($T_c \sim 152$ K), the $a = f(T)$ curve changes slope. The *b* parameter grows with increasing temperature throughout the 90–300 K range covered, and only in the PT region (150–155 K) the $b = f(T)$ curve exhibits an anomaly in the form of a plateau (the invar effect). Parameter *c* decreases with increasing temperature for $T < T_c$ and increases for $T > T_c$; that is, at the PT point, the $c = f(T)$ curve passes through a minimum. The tem-

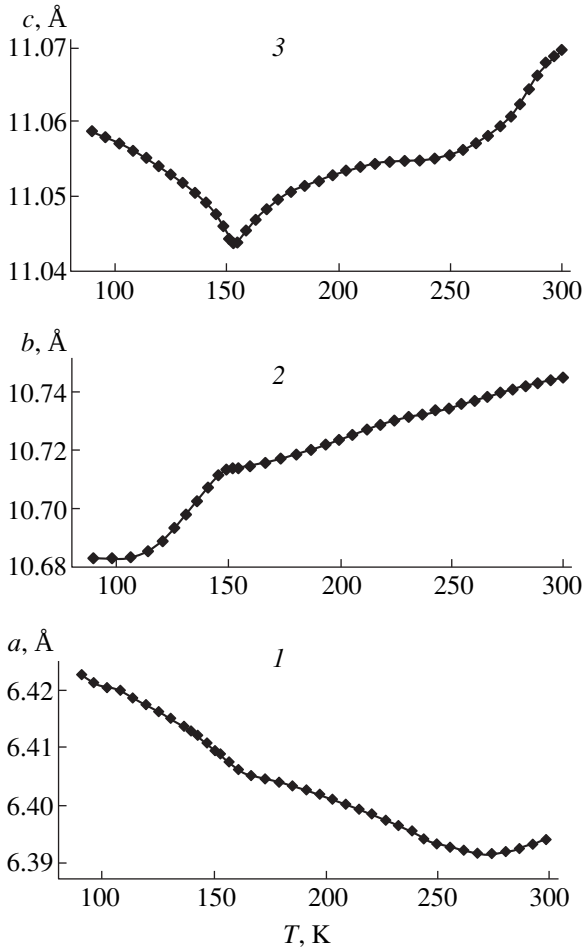

Fig. 1. Temperature dependences of the lattice parameters (*1*) *a*, (*2*) *b*, and (*3*) *c* of a DMAAS crystal.

perature dependence of the β angle calculated from interplanar distances $d_{600} = f(T)$, $d_{080} = f(T)$, $d_{0012} = f(T)$, and $d_{132} = f(T)$ is displayed in Fig. 2 (curve *1*). One readily sees that, as the temperature increases, the β angle remains nearly unchanged in the 100–150-K region, to grow slightly afterwards. In the vicinity of the PT point ($T_c \sim 152$ K), a sharp increase of the β angle is observed to occur. The same figure (curve *2*) shows the variation of the unit-cell volume *V* of the DMAAS crystal with temperature. We see that, as the temperature approaches the PT point, *V* increases only slightly, but near the PT point at $T = 152$ K the volume *V* drops sharply. As the temperature continues to increase, *V* changes insignificantly, and only at $T = 260$ K, the volume *V* increases rapidly.

Temperature dependences of the crystallographic parameters of DDMAAS, i.e., deuterated DMAAS, can be found in [8]. Note that the temperature behavior of the crystallographic parameters of DDMAAS and of our data on DMAAS follows the same pattern. A detailed comparison is, however, impossible to make because the measurements in [8] were performed with a larger temperature step.

Figure 3 presents the temperature dependences of the thermal expansion coefficients (TEC) α_a, α_b, and α_c along the principal crystallographic axes of the DMAAS crystal. The values of α_a are negative in the 90–270 K region, and in the PT region ($T_c \sim 152$ K) the $\alpha_a = f(T)$ curve passes through a minimum. The sign of the $\alpha_b = f(T)$ TEC remains positive throughout the temperature range covered, while at the PT point ($T_c \sim 152$ K) $\alpha_b = 0$. The α_c TEC is negative at temperatures from 90 to 152 K, with $\alpha_c = f(T)$ reversing sign at the PT point. The complex pattern of the temperature behavior of the crystallographic parameters and the significant anisotropy of thermal expansion are due to the specific features of the structure of this crystal.

2. RESULTS AND DISCUSSION

The crystal structure of DMAAS has a complex system of hydrogen bonds, which play a decisive role in the formation of the three-dimensional lattice framework. X-ray and neutron diffraction studies [2, 9–12] showed the DMAAS structure to be made up of nearly

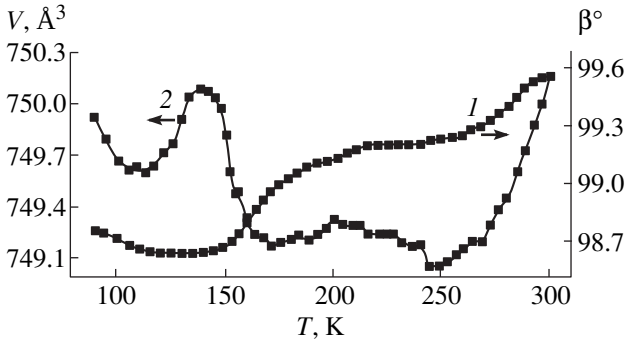

Fig. 2. Temperature dependences of the β angle (*1*) and unit-cell volume *V* (*2*) of the DMAAS crystal.

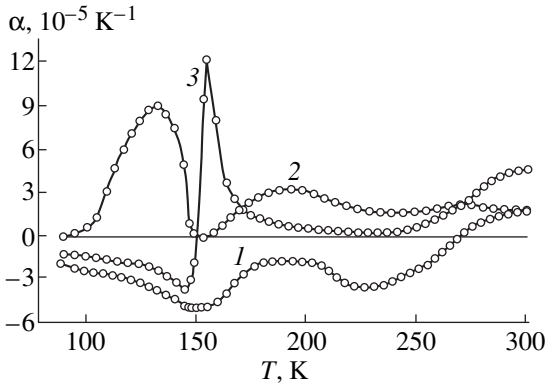

Fig. 3. Temperature dependences of the thermal expansion coefficients along the principal crystallographic axes *a*, *b*, and *c*: (*1*) α_a (*2*) α_b, and (*3*) α_c of the DMAAS crystal.

regular $(SO_4)^{2-}$ tetrahedra connected by strong hydrogen bonds O–…–H–O with water molecules contained in the $(Al(H_2O)_6]^{3+}$ complex cation. This system constitutes a rigid three-dimensional framework. The molecular cations of dimethylammonium (DMA) $[(CH_3)_2NH_2]^+$ occupy large voids in this framework and play a decisive role in the mechanism of the ferroelectric PT at T_c = 152 K. The PT is considered [9–14] to be associated with the ordering of the DMA molecular cations with decreasing temperature, because orientational ordering of these cations results in a loss of the inversion center at the ferroelectric transition and the dipole-moment formation. There is, however, another viewpoint, which is that the PT at T_c = 152 K is caused by orientational ordering of H_2O molecules at the Al–OH–…–OS bonds [15]. The $[Al(H_2O)_6]^{3+}$ and DMA complex cations lie in layers parallel to the (100) plane, which sandwich an $(SO_4)^{2-}$ anion layer. The $[Al(H_2O)_6]^{3+}$ and DMA complexes form arrays parallel to the *c* axis and alternating in the *b* direction within the same cation layer [9]. A change in the temperature brings about not only a change in the distance between the complexes, but their rotation as well. This is why one observes such a complex pattern of crystal-lattice parameter and TEC variation along the principal crystallographic directions. It should be pointed out that this involves not a rupture of interatomic chemical bonds, but only their deformation, which is evidenced by the absence of a jump in the unit-cell volume *V* in the PT region; only a strong decrease in *V* is observed with increasing temperature, so that the crystal does not break down under repeated thermal cycling through the PT, unlike the DMAGS, where one observes a jump in *V* at the low-temperature PT (T_{c2}) to result in crystal breakdown [16]. The three-dimensional framework of the DMAAS structure formed by the rigid $[Al(H_2O)_6]^{3+}$ and $(SO_4)^{2-}$ complexes changes little with temperature. The PT at *T* = 152 K is a result of the response of the framework to orientational ordering of the DMA complex dipoles. By [16], the DMA ions can be conceived as rigid molecular dipoles with a certain dipole moment $\boldsymbol{\mu}$. The major part of the structural evolution occurring with variation of temperature and, in particular, in the vicinity of the PT, is associated with a reorientation of the $\boldsymbol{\mu}$ vector in the plane where the $\mathbf{P}_s$ polarization vector and the *b* axis lie. The compression of the DMAAS cell in the ferroelectric phase induced by decreasing temperature deforms the main void occupied by the DMA ions. Similar to DMAGS [16], DMAAS undergoes orientational ordering of the DMA cations at the PT, and the dipole-moment vectors $\boldsymbol{\mu}$ tend to assume an orientation close to the [101] direction [16], i.e., nearly perpendicular to [010]. Thus, as the temperature is decreased below T_c, the voids occupied by DMA cations in the crystal will most likely be compressed along the [010] crystallographic direction, whereas the lack of free volume along [100] and [001] also allows expansion, exactly what is observed experimentally. Besides, the character of variation of the β angle also plays its part in the lattice distortion.

ACKNOWLEDGMENTS

Support of the Belarus Foundation for Basic Research is gratefully acknowledged.

REFERENCES

1. L. F. Kirpichnikova, E. F. Andreev, N. R. Ivanov, *et al.*, Kristallografiya **33** (6), 1437 (1988) [Sov. Phys. Crystallogr. **33**, 855 (1988)].
2. A. Pietraszko, K. Lukaszewicz, and L. F. Kirpichnikova, Pol. J. Chem. **67**, 1877 (1993).
3. O. G. Vlokh, V. B. Kapustyanykh, I. I. Polovinko, *et al.*, Izv. Akad. Nauk SSSR, Ser. Fiz. **54** (6), 1143 (1990).
4. O. G. Vlokh, V. B. Kapustyanykh, I. I. Polovinko, *et al.*, Kristallografiya **36** (4), 919 (1991) [Sov. Phys. Crystallogr. **36**, 516 (1991)].
5. L. F. Kirpichnikova, A. L. Urusovskaya, V. I. Mozgovoĭ, *et al.*, Kristallografiya **36** (6), 1516 (1991) [Sov. Phys. Crystallogr. **36**, 859 (1991)].
6. A. Petrashko, L. F. Kirpichnikova, and L. A. Shuvalov, Kristallografiya **40** (3), 569 (1995) [Crystallogr. Rep. **40**, 523 (1995)].
7. L. F. Kirpichnikova, W. Bednarskyi, S. Waplak, *et al.*, Kristallografiya **44** (1), 111 (1999) [Crystallogr. Rep. **44**, 106 (1999)].
8. L. F. Kirpichnikova, A. Petrashko, K. Lukashevich, *et al.*, Kristallografiya **39** (6), 1078 (1994) [Crystallogr. Rep. **39**, 990 (1994)].
9. G. A. Kiosse, I. M. Razdobreev, L. F. Kirpichnikova, *et al.*, Kristallografiya **39** (1), 34 (1994) [Crystallogr. Rep. **39**, 27 (1994)].
10. V. Yu. Kazimirov, E. É. Rider, V. A. Sarin, *et al.*, Kristallografiya **43** (2), 228 (1998) [Crystallogr. Rep. **43**, 193 (1998)].
11. V. Yu. Kazimirov, V. A. Sarin, C. Ritter, and L. A. Shuvalov, Kristallografiya **44** (1), 61 (1999) [Crystallogr. Rep. **44**, 56 (1999)].
12. G. A. Kiosse, I. M. Razdobreev, and L. F. Kirpichnikova, Izv. Akad. Nauk SSSR, Ser. Fiz. **54** (4), 749 (1990).
13. R. Sobiestianskas, J. Grigas, and E. F. Andreev, Izv. Akad. Nauk SSSR, Ser. Fiz. **55** (3), 548 (1991).
14. J. Dolinšek, M. Klanjšek, D. Arcoň, *et al.*, Phys. Rev. B **59** (5), 3460 (1999).
15. V. I. Torgashev, Yu. M. Yuzyuk, L. F. Kirpichnikova, *et al.*, Kristallografiya **36** (3), 677 (1991) [Sov. Phys. Crystallogr. **36**, 376 (1991)].
16. L. F. Kirpichnikova, A. Petrashko, M. Polomska, *et al.*, Kristallografiya **41** (4), 722 (1996) [Crystallogr. Rep. **41**, 685 (1996)].

Translated by G. Skrebtsov

Physics of the Solid State, Vol. 42, No. 9, 2000, pp. 1734–1737. Translated from Fizika Tverdogo Tela, Vol. 42, No. 9, 2000, pp. 1685–1688.

LOW-DIMENSIONAL SYSTEMS AND SURFACE PHYSICS

Electrically Induced Luminescence in Parabolic Quantum Wells in a Magnetic Field

É. P. Sinyavskiĭ and S. M. Sokovnich

Institute of Applied Physics, Academy of Sciences of Moldova, Chisinau, 2028-MD Moldova

Received August 19, 1999

Abstract—Interband luminescence in a parabolic quantum well is studied in applied electric and magnetic fields. It is shown that the luminescence peak is displaced towards higher frequencies with increasing magnetic field strength, while an increase in the electric field strength causes a displacement of the emission peak towards the long-wave region and a decrease in its amplitude. The theoretical results are compared with the experimental data. The existence of a new electromagnetic-wave emission channel (electrically induced luminescence) associated with indirect optical transitions is predicted. The frequency dependence of the electrically induced radiation is computed, taking into account the interaction of an electron with acoustic and optical phonons. It is found that the half-width of the luminescence peak increases with the electric field strength. © *2000 MAIK "Nauka/Interperiodica".*

1. Modern technology using computer control of the molecular beam shutters makes it possible to obtain various profiles of the quantum well (QW) potential. Gossard [1] was the first to obtain an artificial parabolic quantum well in a small-size structure GaAs–$Al_xGa_{1-x}As$. Luminescence in parabolic quantum wells from high size-quantized levels was clearly observed by Wang *et al.* [2]. The size-quantized levels are formed in relatively wide quantum wells with $d >$ 1000 Å (d is the width of the small-size system). It is this circumstance that makes such systems promising for application in optoelectronic instruments. For typical parameters of the parabolic quantum well in GaAs–$Al_xGa_{1-x}As$, the space quantization step $\hbar\omega$ (eV) for electrons is equal to 14.6/d (Å), i.e., $\hbar\omega$ = 14.6 meV for d = 1000 Å. Consequently, for $T <$ 100 K, the size-quantized levels can determine the kinetic properties of such systems to a considerable extent. Hence, it is not surprising that the optical properties of parabolic QW (e.g., interband luminescence [3, 4] and inelastic resonance scattering of light [5]) are studied for $d >$ 1000 Å.

If the magnetic field **H** is directed parallel to the surface of a parabolic QW and the electric field **F** is directed along the space quantization axis, the wave functions and eigenvalues for the electron are known [6]. In particular, the electron energies E_i in the conduction band and E_f in the valence band are defined by the relations

$$E_i = \frac{\hbar^2 K_x^2}{2m_c} + \frac{\hbar^2}{2m_c}\left(\frac{\omega}{\omega_0}\right)^2 (K_y - K_y^0)^2 + \hbar\omega_0\left(n + \frac{1}{2}\right) - \Delta_c,$$

$$E_f = -E_g - \frac{\hbar^2 K_x^2}{2m_v} - \frac{\hbar^2}{2m_v}\left(\frac{\Omega}{\Omega_0}\right)^2 \quad (1)$$

$$\times (K_y + P_y^0)^2 - \hbar\Omega_0\left(n + \frac{1}{2}\right) + \Delta_v.$$

Here, we have used the notation

$$\Delta_c = \frac{e^2F^2}{2m_c\omega^2}; \quad \Delta_v = \frac{e^2F^2}{2m_v\Omega^2}; \quad K_y^0 = \frac{eF\omega_c}{\hbar\omega^2};$$

$$P_y^0 = \frac{eF\Omega_c}{\hbar\Omega^2}; \quad \omega_0^2 = \omega_c^2 + \omega^2; \quad \Omega_0^2 = \Omega_c^2 + \Omega^2,$$

ω_c and Ω_c are the cyclotron frequencies for an electron with an effective mass m_c and a hole with an effective mass m_v, respectively; E_g is the band gap; K_x and K_y are the components of the wave vector of a charged particle; and $\hbar\Omega$ is the space quantization energy in the valence band.

It follows directly from Eq. (1) that the dispersion relation for band carriers changes significantly in external fields. While the dependence of the energy on K_y in a zero electric field (F = 0) is described by a quadratic relation (dashed curves in Fig. 1), the band extrema are displaced towards the forbidden energy region for $F \neq 0$ (solid curves in Fig. 1). Consequently, direct optical transitions I for $F \neq 0$ are supplemented by additional luminescence channels associated with indirect optical transitions (transition *II* in Fig. 1). Thus, indirect-band quantum systems can be created in external fields of the configuration under consideration (**H** ⊥ **F**). Techniques for producing indirect-band quasi-two-dimensional systems have been developed in recent years. For example, it was shown [7] that a considerable enhancement of radiative recombination is observed in a quantum well of $Ga_xIn_{1-x}As$–InP for $x > x_0$ (x_0 = 0.52 for a QW width of 60 Å). This is due to the fact that the valence band top of GaInAs is displaced in K space and the system becomes an indirect-band system. The energy of an optical phonon could be determined from the experimental data on photoluminescence [7]. Mag-

netically induced optical transitions in the system $Al_{0.23}Ga_{0.77}As$–$In_{0.11}Ga_{0.89}As$–GaAs were studied by Whittaker *et al.* [8]. In the complex system under consideration, the bottom of the conduction band is displaced in K_y-space in the presence of a magnetic field in the QW plane and an indirect-band quantum system is created.

2. In the following analysis, we shall disregard exciton effects while studying band-to-band luminescence processes. This approximation is quite justified, as we are considering strong magnetic fields, in which the Coulomb interaction of an electron with a hole is small compared to the separation between size-quantized states [9]. The overlapping of the electron and hole wave functions decreases in an electric field, and therefore, the exciton effects are considerably suppressed [10]. The spectral intensity of radiation associated with a transition of an electron from the initial state i to a final state f is simply connected with the transition probability per unit time [11] and is defined by the relation

$$\Phi(\nu) = \frac{4\nu^2\sqrt{\varepsilon_0}e^2}{Vc^3}\left|\frac{\mathbf{P}_{c\nu}\mathbf{e}_0}{m_0}\right|^2\sum_{i,f} f_i^{(c)} f_f^{(\nu)} \times\left|\int\Phi_i^*(\mathbf{r})\Phi_f(\mathbf{r})d\mathbf{r}\right|^2\delta\{E_i - E_f - \hbar\nu\}, \quad (2)$$

where V stands for the volume of the small-size system, m_0 is the mass of a free electron having a charge e, $\mathbf{P}_{c\nu}$ is the matrix element of the momentum operator involving the Bloch amplitudes of band carriers, ν is the frequency of the emitted electromagnetic wave of polarization $\mathbf{e}_0$, ε_0 is the dielectric constant of the quantum system, and $f_i^{(c)}$ is the electron distribution function in the conduction band, which can be presented in the form

$$f_i^{(c)} = \frac{2\pi d\beta\hbar^2\omega}{m_c\omega_0}\sinh\left(\frac{\beta\hbar\omega_0}{2}\right) \times n_e\exp\{-\beta E_i\}\exp\{\beta\Delta_c\}$$

for a nondegenerate semiconductor, and n_e is the number density of electrons. The hole distribution function $f_f^{(\nu)}$ in the valence band can be expressed in an analogous form.

In the following, we shall consider the luminescence processes associated with a transition of an electron from the lowest size-quantized conduction band ($n = 0$) to the zeroth size-quantized state in the valence band (transition I in Fig. 1). This is fully justified if we consider that all electrons occupy the lowest conduction band for $\hbar\omega \gg k_0T$. As a result, the final expression for the spectral intensity of radiation assumes the form

$$\Phi(\nu) = \frac{8\nu^2\sqrt{\varepsilon_0}e^2\pi d\beta^2\hbar^2}{c^3 m_c m_\nu}\left(\frac{\omega\Omega}{\Omega_0\omega_0}\right)\sqrt{\mu\mu^*}\frac{\sqrt{\lambda_c\lambda_\nu}}{\lambda_c+\lambda_\nu} \times\left|\frac{\mathbf{P}_{c\nu}\mathbf{e}_0}{m_0}\right|^2 n_e n_h\exp(-\beta\Delta)\exp(-u\alpha^2)\exp\left(-\frac{u\beta_0^2}{2}\right) \times\sum_k I_k\left(\frac{u\beta_0^2}{2}\right)I_{2k}(2\alpha\beta_0 u)(-1)^k. \quad (3)$$

Here, we have used the notation

$$\lambda_c = \frac{m_c\omega_0}{\hbar},\quad \lambda_\nu = \frac{m_\nu\Omega_0}{\hbar},\quad \mu = \frac{m_c m_\nu}{m_c+m_\nu},$$

$$\mu^* = \frac{m_c^* m_\nu^*}{m_c^*+m_\nu^*},\quad m_c^* = m_c\left(\frac{\omega_0}{\omega}\right)^2,$$

$$m_\nu^* = \left(\frac{\Omega_0}{\Omega}\right)^2,\quad u = \frac{\lambda_c\lambda_\nu}{\lambda_c+\lambda_\nu},$$

$$\alpha = -eF\left\{\frac{1}{m_c\omega_0^2}+\frac{1}{m_\nu\Omega_0^2}\right\}+\frac{1}{\lambda M^*}\{m_\nu^* K_y^0 + m_c^* P_y^0\},$$

$$M^* = m_c^* + m_\nu^*,$$

$$\frac{1}{\lambda} = \frac{1}{\lambda_\nu}\left(\frac{\Omega_c}{\Omega_0}\right)-\frac{1}{\lambda_c}\left(\frac{\omega_c}{\omega_0}\right),$$

$$\beta_0 = \frac{1}{\lambda}\left[\frac{2\mu^*}{\hbar^2}\left(\Delta-\frac{\hbar^2}{2M^*}(\Delta K)^2\right)\right]^{1/2},$$

$$\Delta K = K_y^2 + P_y^0,$$

$$\Delta = \hbar\nu - E_g + \Delta_c + \Delta_\nu - \frac{1}{2}(\hbar\omega_0 + \hbar\Omega_0) \geq 0,$$

$I_p(z)$ is the modified Bessel function of the pth order, and n_h is the hole concentration.

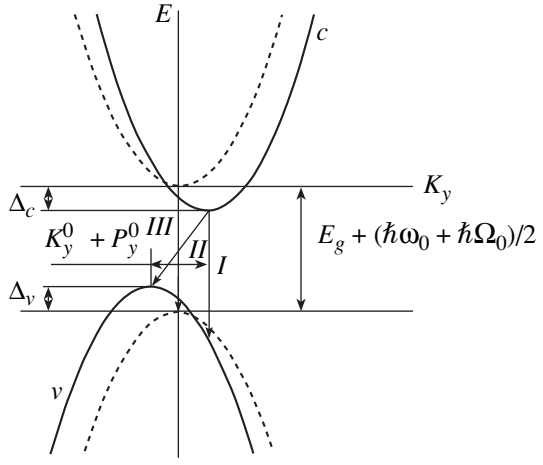

Fig. 1. Band-to-band radiative transitions in a solitary parabolic quantum well in the presence of uniform external electric and magnetic fields.

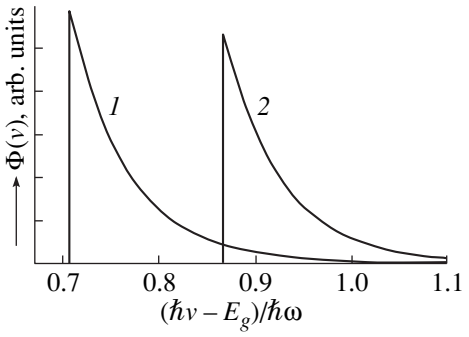

Fig. 2. Frequency dependence of the spectral intensity of radiation for direct optical transitions in relative units in a zero electric field. Curve *1* corresponds to $\delta = 1$, and curve *2* to $\delta = 2$.

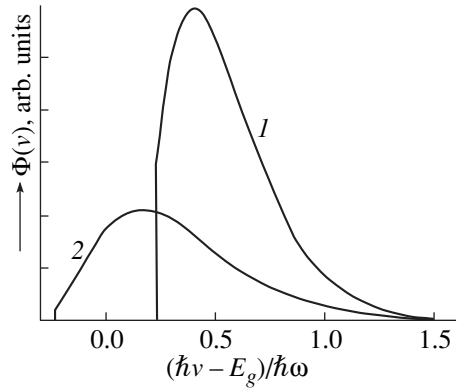

Fig. 3. Frequency dependence of the spectral intensity of radiation for direct optical transitions in relative units in a constant magnetic field ($\delta = 1$). Curve *1* corresponds to $F_0 = 0.5$ and curve *2* to $F_0 = 1$.

In the absence of a magnetic field, Eq. (3) coincides exactly with the results of investigations carried out by Hou *et al.* [12], who studied the effect of an electric field on the optical properties of parabolic QWs. In the case of zero electric field ($F = 0$), Eq. (3) directly leads to the expression

$$\Phi(\nu) = \frac{8\nu^2\sqrt{\varepsilon_0}e^2\pi\beta^2 d\hbar^2}{c^3 m_c m_\nu}\left(\frac{\omega\Omega}{\Omega_0\omega_0}\right)n_e n_h\left|\frac{\mathbf{P}_{c\nu}\mathbf{e}_0}{m_0}\right|^2\sqrt{\mu\mu^*}$$

$$\times\frac{\sqrt{\lambda_c\lambda_\nu}}{\lambda_c+\lambda_\nu}\exp(-\beta\Delta_0)\exp(-u\tau^2/2)I_0(-u\tau^2/2), \quad (4)$$

$$\tau = \frac{1}{\lambda}\left[\frac{2\mu^*}{\hbar^2}\Delta_0\right]^{1/2},$$

$$\Delta_0 = \hbar\nu - E_g - \frac{1}{2}(\hbar\omega_0 + \hbar\Omega_0) \geq 0.$$

This expression describes the frequency dependence of the spectral intensity of radiation (transition *III* in Fig. 1) in parabolic QWs in the presence of a magnetic field directed along the surface of the size-confined system.

Figure 2 shows the frequency dependence of the spectral intensity of radiation in relative units. Calculations were made for typical QWs of GaAs–AlGaAs with $m_c = 0.06m_0$ and $m_\nu = 0.4m_0$ for $d = 1000$ Å and $\lambda_c^{(0)} = m_c\omega/\hbar = 1.4\times10^{12}$ (cm^{-2}). Curve *1* was obtained for $\delta = (\omega_c/\omega)^2 = 1$, while curve *2* corresponds to $\delta = 2$. The half-width δ_0 of the luminescence peak is ≈ 0.7 meV and increases with decreasing QW thickness ($\delta_0 \approx 7$ meV for $d = 100$ Å). It can be seen from Fig. 2 that the peak of the luminescence line is displaced towards higher frequencies upon an increase in the magnetic field strength. This is due to an increase in the width of the band gap as a result of quantization in the magnetic field. Hou *et al.* [12] experimentally studied the photoluminescence in narrow ($d = 30$ Å) rectangular QWs in InGaAs–GaAs and showed that the luminescence peak is displaced towards the short-wave region, the peak half-width being $\delta_0 \approx 8$ meV. Since the shape of the emission line peaks is not very sensitive to the form of the potential well (for wells of nearly identical width), the theoretical results obtained are in qualitative agreement with the experiment.

Figure 3 shows the dependence of the spectral intensity of radiation in relative units for $\delta = 1$, calculated by using Eq. (3). The first peak was calculated for $F_0 = \frac{e^2F^2}{m_c\omega^2}\frac{1}{\hbar\omega} = 0.5$, and the second for $F_0 = 1$. Consequently, the luminescence peak is displaced towards the long-wave region for a fixed value of the magnetic field and its intensity decreases. This is due to the fact that the band gap decreases by an amount $\Delta_c + \Delta_\nu$, and the overlapping of the wave functions of band carriers decreases. Such a behavior of the luminescence intensity is typical of small-size systems and is confirmed experimentally (in zero magnetic field) for both square [13–15] and parabolic QWs [16], as well as for inversion parabolic QW [17].

A distinguishing feature of the system under consideration is the dependence of the half-width of the luminescence peak on the electric field strength. The half-width increases with an increasing field.

3. Let us now consider the electrically induced luminescence (transition *II* in Fig. 1), which is determined by the interaction of electrons with phonons. Subsequent calculations for indirect optical transitions are carried out in the conventional manner as described in [18]. Considering the scattering of electrons by acoustic vibrations in the elastic scattering approximation and for $N_q \approx \frac{k_0T}{\hbar wq} > 1$ (N_q is the equilibrium distribution of phonons with the energy $\hbar wq$ and the wave vec-

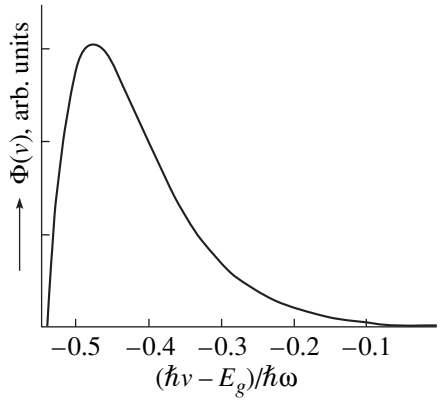

Fig. 4. Frequency dependence (in relative units) of the spectral intensity of radiation, taking into account the interaction of an electron with acoustic vibrations ($F_0 = 0.5$, $\delta = 1$).

tor **q**), we can define the spectral intensity of radiation at the emission band edge as follows:

$$\Phi_{ac}(\nu) = \frac{B_a \exp(-u\alpha^2)\Delta \exp(-\beta\hbar\omega\Delta)}{\left[\Delta - \left(\frac{\omega}{\omega_0}\frac{(\Delta K)^2}{2\lambda_c}\right)\right]^2}. \qquad (5)$$

Here, we have used the notation

$$B_a = \frac{\nu^2\sqrt{\varepsilon_0}e^2}{\pi c^3}\left|\frac{\mathbf{P}_{cv}\mathbf{e}_0}{m_0}\right|^2 \frac{d\beta n_e n_h}{\lambda_c + \lambda_\nu}\frac{E_1^2\lambda_c}{\rho w^2}\frac{1}{\hbar\omega}\sqrt{2\pi\lambda_\nu},$$

E_1 is deformation potential constant for electrons, ρ is the matter density of the small-size systems, and w is the velocity of sound in the medium.

The spectral intensity of radiation taking into consideration an optical phonon with energy $\hbar\omega_{op}$ can be calculated in a similar manner:

$$\Phi_{op} = \frac{B_0 \exp(-u\alpha^2)\tilde{\Delta}\exp(-\beta\hbar\omega\tilde{\Delta})^2}{\left[\tilde{\Delta} - \frac{\hbar(\Delta K)^2}{2m_c^*\omega}\right]}, \qquad (6)$$

where

$$B_0 = \frac{4\nu^2\sqrt{2\pi\lambda_\nu}\lambda_c\sqrt{\varepsilon_0}e^2}{c^3\omega(\Delta K)^2(\lambda_\nu + \lambda_c)}\left|\frac{\mathbf{P}_{cv}\mathbf{e}_0}{m_0}\right|^2 d\beta^2 n_e n_h e^2\omega_{op}c_0,$$

$$\hbar\omega\tilde{\Delta} = \Delta + \hbar\omega_{op}, \quad c_0 = \frac{1}{n} - \frac{1}{\varepsilon_0},$$

n is the refractive index, and ε_0 is the dielectric constant.

The frequency dependence of the spectral intensity of radiation taking into account the interaction of an electron with acoustic vibrations (in relative units) is shown in Fig. 4. The shape of the emission line is described by a curve whose peak is displaced relative to the edge of the optical transition (transition *I* in Fig. 1) towards lower frequencies by an amount $\Delta\nu = \frac{\hbar(\Delta K)^2}{2m_c}$ and moves towards the long-wave region with increasing electric field strength. If the half-width of the luminescence curve $\delta_1 > \hbar\Delta\nu$, electrically induced luminescence must be observed in the long-wave spectral region. This luminescence is manifested most clearly in the case of electron interaction with optical vibrations. This is due to the fact that, first and foremost, the interaction of an electron with optical phonons in typical parabolic QWs in GaAs–AlGaAs is stronger than with acoustic phonons. Second, the electrically induced luminescence peak is additionally displaced towards the long-wave region by an amount $\hbar\omega_{op}/\hbar\omega$. While deriving Eqs. (5) and (6), we took into account the fact that an indirect optical transition initially involves the scattering of an electron from phonons followed by the emission of a photon. This process has a higher probability than the process of photon emission, followed by the scattering of carriers from photons.

REFERENCES

1. A. S. Gossard, Conf. Ser.–Inst. Phys. **69**, 1 (1983).
2. S. H. Wang, G. Treideris, W. Q. Chen, and T. G. Andersson, Appl. Phys. Lett. **62**, 61 (1993).
3. J. H. Burnett, H. M. Cheog, W. Paul, *et al.*, Phys. Rev. B **48**, 7940 (1993).
4. M. Fritze, W. Chen, A.V. Nurmikko, *et al.*, Phys. Rev. B **48**, 15103 (1993).
5. I. H. Burnett, H. M. Cheong, R. M. Westerwelt, *et al.*, Phys. Rev. B **43**, 12033 (1991).
6. E. P. Sinyavskii, S. M. Sokovnich, and F. I. Pasechnik, Phys. Status Solidi B **209**, 55 (1998).
7. P. Michler, A. Hangleiter, A. Moritz, *et al.*, Phys. Rev. B **48**, 11991 (1993).
8. D. M. Whittaker, T. A. Fisher, P. E. Simmonds, *et al.*, Phys. Rev. Lett. **67**, 887 (1991).
9. I. V. Lerner and Yu. E. Lozovik, Zh. Éksp. Teor. Fiz. **78**, 1167 (1980) [Sov. Phys. JETP **51**, 588 (1980)].
10. T. Yamanaka, K. Wakita, and K. Yakoyama, Appl. Phys. Lett. **65**, 1540 (1994).
11. A. P. Levanyuk and V. V. Osipov, Usp. Fiz. Nauk **133**, 427 (1981) [Sov. Phys. Usp. **24**, 187 (1981)].
12. H. Q. Hou, W. Staguhn, N. Miura, *et al.*, Solid State Commun. **74**, 687 (1990).
13. M. Yamanishi, Y. Usami, Y. Kan, and I. Suemune, Jpn. J. Appl. Phys. **24** (8), L585 (1985).
14. Y. Kan, M. Yamanishi, I. Suemune, *et al.*, Jpn. J. Appl. Phys. **24** (8), L589 (1985).
15. E. E. Mendez, G. Bastard, L. L. Chang, *et al.*, Phys. Rev. B **26**, 7101 (1982).
16. T. Ishikowa, S. Nashimura, and K. Tada, Jpn. J. Appl. Phys. **29**, 1466 (1990).
17. W. Chen, T. G. Andersson, and S. Wang, Jpn. J. Appl. Phys. **33**, 896 (1994).
18. A. I. Ansel'm, *Introduction to the Theory of Semiconductors* (Nauka, Moscow, 1977).

Translated by N. Wadhwa

Physics of the Solid State, Vol. 42, No. 9, 2000, pp. 1738–1743. Translated from Fizika Tverdogo Tela, Vol. 42, No. 9, 2000, pp. 1689–1694.

LOW-DIMENSIONAL SYSTEMS AND SURFACE PHYSICS

Energy Dispersion of Localized States in Light-Sensitive Nanocrystals

V. I. Leĭman

St. Petersburg Technological University of Plant Polymers, ul. Ivana Chernykh 4, St. Petersburg, 198095 Russia
e-mail: valeri_leiman@ip.com.ru

Received May 5, 1999; in final form, September 9, 1999

Abstract—The kinetics of the formation and thermal destruction of color centers in CuCl and AgCl nanocrystals (NCs) distributed in a glass matrix is described on the basis of the band model of an NC with colloidal color centers and with hole traps of one species. The possibility of experimentally determining the relative depth distribution of hole states in light-sensitive NCs in glass is demonstrated. The observed energy dispersion of localized hole states and its variation in NCs are associated, in accordance with Dexter's idea, with large-scale thermal fluctuations of the crystal field. The presence of an excess charge on a colloidal particle and its influence on localized hole states are presumed. © *2000 MAIK "Nauka/Interperiodica".*

Detailed studies of the relaxation kinetics of color centers in light-sensitive CuHal and AgHal nanocrystals (NCs) distributed in a glass matrix proved [1] that the kinetic curve of the absorption relaxation for Cu_n colloidal particles becomes linear in $\ln t$ coordinates (t is the time). The specific relaxation mechanism of color centers in these systems remains unclear. The diffusion models proposed earlier for the electron–hole recombination kinetics of such systems [2–4] are unable to explain the "termination" of the decay of color centers, which is observed in these systems [5–8]. We propose here a mechanism and a kinetic model of electron–hole processes occurring during the formation and destruction of color centers (copper Cu_n or silver Ag_n colloidal particles) that appear as a result of the optical excitation of CuHal and AgHal NCs.

1. KINETIC MODEL

Proceeding from the results obtained in [9–11], we can present the mechanism of formation (destruction) of Cu_n or Ag_n particles in the first approximation as the combination of processes demonstrated in the band model of CuCl NCs (Fig. 1) with colloidal particles and hole traps of the same species under conditions of UV excitation.

In the case of UV excitation, electron–hole pairs are formed in the region of fundamental absorption of the NC. In this scheme, two processes facilitate the growth of colloidal particles. Electrons trapped by interstitial cations Cu^+ facilitate the formation and growth of Cu_n particles, thereby leading to an increase in the optical absorption associated with these particles. Holes are captured at hole trapping centers, thus facilitating the stabilization of colloidal particles.

On the other hand, these two processes decrease the size of colloidal particles. The trapping of a hole by a colloidal particle, followed by the tearing of a Cu^+ cation from it, leads to the destruction of the colloidal particle and to a decrease in the observed optical absorption. On the other hand, the electrons formed as a result of UV excitation can recombine with a trapped hole, which decelerates the growth of colloidal particles. It turned out [9–11] that the limiting stage of all these processes is the capture of holes and their liberation from the traps.

The peculiarities of the kinetic regularities observed in such systems [1] can be explained by assuming the existence of dispersion over the depth of hole-trapping centers. The emergence of the energy dispersion of localized states in an NC can be due to energy fluctua-

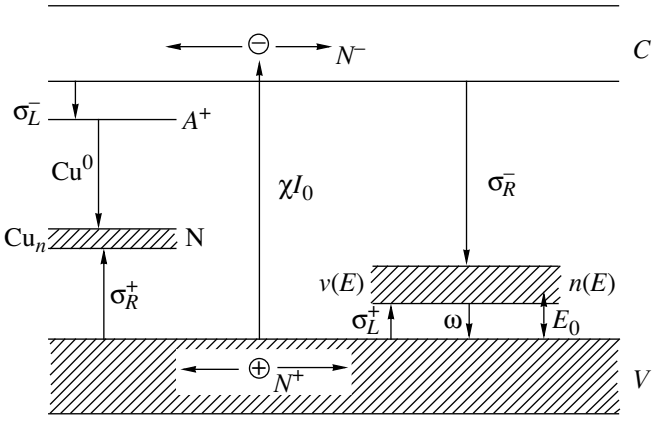

Fig. 1. Band model of a CuCl NC with Cu_n colloidal particles and hole traps of one species under UV excitation. The valence band is denoted by V and the conduction band by C. The rest of the notation is given in the text.

1063-7834/00/4209-1738$20.00 © 2000 MAIK "Nauka/Interperiodica"

tions of the crystal lattice in the surface layer of the NC [12, 13], in which the impurity atoms forming hole traps can be embedded.

This model of electron–hole processes using the concepts of the classical kinetic theory of crystals [14] not only provides a description for the kinetics of absorption relaxation (destruction) of colloidal particles in the systems under investigation, but also (which is equally important) allows us, for the first time, to describe the kinetics of formation of colloidal color centers.

In the first approximation, we can assume that the energy dispersion of hole traps has a normal Gaussian distribution

$$\nu = \frac{\nu_0}{\sqrt{2\pi}s}\exp\left(-\frac{(E_0 - E)^2}{2s^2}\right), \quad (1)$$

where ν_0 is the total number of hole traps in all NCs being excited; E and E_0 are the energy depth of a trap and the energy of the distribution peak, respectively; and s is the distribution width. The probability of thermally activated expulsion from a trap is determined by its depth E and temperature T:

$$\omega = p\exp\left(-\frac{E}{kT}\right), \quad (2)$$

where p is the rate factor. In accordance with the proposed model, the time-dependent total number $n(t)$ of holes trapped in all NCs is equal to the total number $N(t)$ of atoms in the colloidal particles of all NCs:

$$n(t) = N(t). \quad (3)$$

In this case, the process of formation and destruction of colloidal particles determining the optical absorption can be described by kinetic equations specifying the time variation of hole distribution among traps:

$$\frac{d}{dt}n(E, t) = -\omega(E)n(E, t) - \sigma_R^- n(E, t)u^- N^- + \sigma_L^+(\nu(E) - n(E, t))u^+ N^+, \quad (4)$$

$$u^- N^- = \frac{\chi I_0}{\sigma_R^- n(t) + \sigma_L^- A^+}, \quad (5)$$

$$u^+ N^+ = \frac{\int_0^\infty \omega(E)n(E, t)dE + \chi I_0}{\sigma_L^+\int_0^\infty(\nu(E) - n(E, t))dE + \sigma_R^+ n(t)}, \quad (6)$$

where σ_L^-, σ_R^-, σ_L^+, and σ_R^+ are the effective cross sections of localization and recombination for an electron and a hole, respectively; u^- and u^+ are the average electron and hole velocities; N^- and N^+ are the numbers of free electrons and holes, respectively; χ is the optical absorption at the UV radiation wavelength; I_0 is the intensity of excitation; and A^+ is the number of interstitial Cu^+ cations contained in all the crystals. The value of A^+ is generally a function of temperature [15].

The first term on the right-hand side of Eq. (4) determines the decrease in the number of holes at traps with the energy E due to thermally activated expulsion, while the second term determines the decrease in the number of trapped holes as a result of recombination with free electrons. The third term determines the capture of holes by empty traps with energy E. (A detailed substantiation of these relations is given in [14].)

The kinetics of variation of the total number of holes in traps can be determined from Eq. (4) by the numerical calculation of $n(E, t)$ and by the integration with respect to dE:

$$n(t) = \int_0^\infty n(E, t)dE. \quad (7)$$

According to Eq. (3), the optical absorption $D(t)$ is proportional to $n(t)$:

$$D(t) = \gamma n(t), \quad (8)$$

where γ is the effective oscillator strength determining the optical absorption of atoms in colloidal particles.

2. EXPERIMENTAL RESULTS

Figure 2 shows the results of experiments on recording the buildup of absorption of Cu_n centers under UV excitation, as well as the absorption relaxation after the termination of excitation, for CuCl NCs with an average radius of 2 to 8 nm. The experiments were made on a glass sample with a continuous variation of the average radius of CuCl NCs along the sample, which was investigated earlier in [12, 13]. Figure 2b separately shows the relaxation segments of the curves describing the variation of absorption $D_r(t)$ in $\ln[(t + a_1)/b_1]$ coordinates. Most of the relaxation curves are straightened for $a_1 = 0.05$ and $b_1 = 10$. The small value of a_1 corresponds to a strong excitation [1].

Figure 2 shows the theoretical curves describing the kinetics of the absorption variation for NCs with an average radius of 8 and 2 nm (curves *1'*, *5'*). The value of $D(t)$ was calculated after analyzing the distribution $n(E, t)$ in accordance with Eqs. (3)–(8). The complete coincidence of the theoretical curve *1'* with the experimental curve *1* for the NC of radius 8 nm was attained for a rate factor $p = 10^6$, energy $E_0 = 0.47$ eV, and distribution width $s = 0.23$ eV. The kinetic parameters were $\sigma_R^-\nu_0/\sigma_L^- A^+ = 0.05$ and $\sigma_L^+/\sigma_R^+ = 0.06$. The relative intensity of UV excitation was $\chi I_0/\nu_0 = 0.04$. The product $\gamma\nu_0$ was 0.46. While choosing the parame-

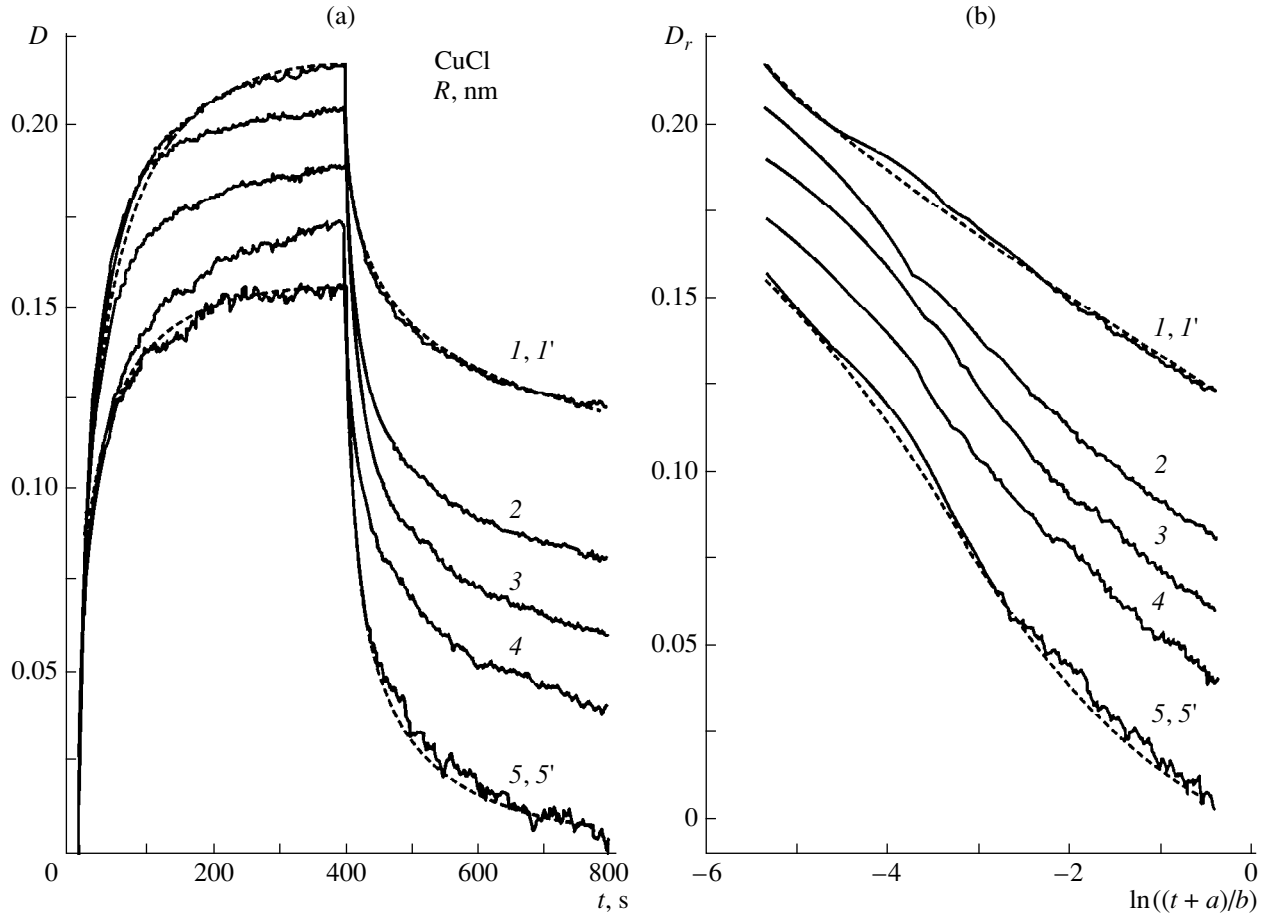

Fig. 2. Kinetics of Cu_n center absorption build-up during UV excitation and the absorption relaxation after the termination of excitation for CuCl NCs of different size in glass: (a) absorption build-up and relaxation and (b) absorption relaxation; the NC radius *R*, nm: (*1*) 8.3, (*2*) 6.2, (*3*) 4.5, (*4*) 3.2, and (*5*) 2.1; curves *1′* and *5′* are calculated by Eqs. (3)–(8).

ters for our calculations, we found that the UV excitation heats the NCs by 20–30 K, and the temperature immediately returns to room temperature $T = 300$ K after the termination of excitation. The parameters of the theoretical curve describing the buildup of absorption and its relaxation (after the termination of UV excitation) coincide only under this condition.

An analysis of the obtained parameters of the kinetics shows that the probability $\sigma_L^- A^+$ of electron localization at interstitial ions is much higher than the probability $\sigma_R^- \nu_0$ of recombination with localized holes (in the case of their complete filling), and the effective cross section σ_R^+ of hole trapping by a colloidal particle is 17 times as large as the cross section σ_L^+ of hole localization at a trap. Such a ratio of cross sections is possible if the size of the impurity center forming the hole trap equals the lattice constant, and a colloidal particle in the ground state carries a certain negative charge.

For a 2 nm-long NC (curves *5* and *5′*), the theoretical half-width of the distribution decreases to $s = 0.045$ (almost by a factor of 5), while $E_0 = 0.45$ eV (if we assume that the rate factor remains unchanged) and $\chi I_0/\nu_0 = 0.03$. The remaining parameters are the same.

It was found that the slope of the absorption relaxation curves $D_r(t)$ in the $\ln(t)$ coordinates in Fig. 2b is mainly determined by the distribution width *s* and by the ratio σ_L^+/σ_R^+. A decrease in the intensity of UV excitation complicates the curve describing the increase in the absorption of colloidal particles, which can be due to the possible formation of UV-induced radiation defects facilitating the formation of new hole traps in NCs and the possible superimposition of the effect of optical sensitization [16] facilitating the formation of additional electron–hole pairs during the optical excitation of the Cu_n colloidal particles themselves.

Carrying out the change of the variables $dT = cdt$ (*c* is the heating rate) in Eqs. (3)–(8), we can derive the temperature dependence $n(E, T)$ of the hole distribution over the traps and, accordingly, the optical absorption

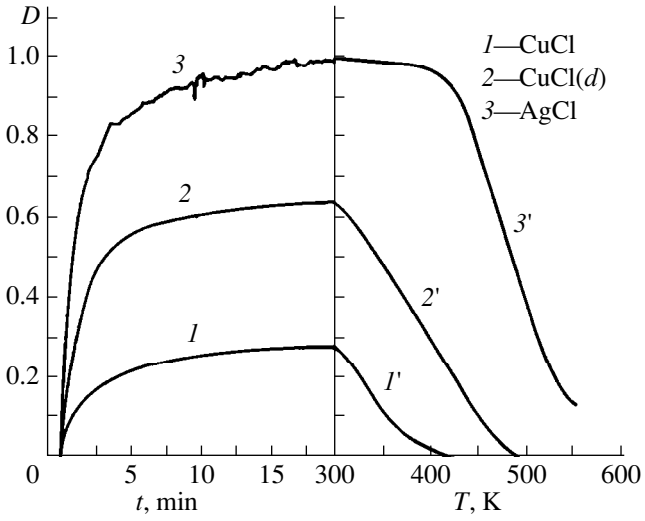

Fig. 3. Curves $D(t, T)$ describing the build-up of absorption of Cu_n and Ag_n centers during the excitation of CuCl and AgCl NCs to saturation, followed by a linear heating under the excitation. Curves *1* and *1′* correspond to CuCl NCs free of defects (annealed for 30 min at 300°C), curves *2* and *2′* correspond to CuCl NCs with frozen intrinsic defects, curves *3* and *3′*, to AgCl NCs; the heating rate c = 5 K/min.

$D(T)$. According to calculations, the derivative $dD(T)/dT$ in the case of UV excitation to the equilibrium state gives the curve proportional to the energy density distribution $\nu(E)$ for traps. Presenting the theoretical curve in the $dD(T)/dT$ and $E_T = kl$, kT coordinates (the parameter kl is slightly larger than the value of $\ln(p)$), we find that it perfectly coincides with the distribution curve of Eq. (1). Consequently, the $D(T)$ curve that can be obtained during the heating of a sample excited to saturation presents the energy scanning of the distribution of hole traps in energy E_T in a real experiment. The derivative $dD(T)/dT$ is proportional to the distribution $\nu(E)$ only if other temperature-dependent mechanisms disregarded in the calculations are not activated during the sample heating.

The results of such an experiment are presented in Figs. 3 and 4. Figure 3 shows the increase in the absorption $D(t)$ (curve *1*) under UV excitation and the decrease in absorption $D(T)$ due to the increasing temperature of a sample with CuCl NCs of radius 10 nm in the presence of excitation (curve *1′*). Curves *2* and *2′* correspond to $D(t)$ and $D(T)$ for quenched CuCl NCs in the same sample. The quenching of NCs was carried out during the short-term holding of the sample at 500°C, followed by rapid cooling to room temperature. A similar experiment was carried out for AgCl NCs in glass (curves *3* and *3′*).

Curves *1–3* in Fig. 4 correspond to the derivatives $dD(T)/dT$ obtained from the data presented in Fig. 3 (curves *1′–3′*); their approximation is also carried out. The temperature scale is presented in the energy units E_T = 18.5 kT.

Curve *1* in Fig. 4 for CuCl NCs is approximated by the descending wing of the Gaussian distribution having a peak at E_T = 0.5 and a width 0.095 eV. The energy E_T is close to the energy E_0 obtained from the analysis of the kinetics for NCs of radius 8 nm (see above), but the experimental width of the distribution is twice as small as the theoretical value (s = 0.23 eV). This indicates a stronger temperature dependence of the kinetics of the NCs under investigation than that predicted by Eq. (2). Further investigations are required to clarify this situation.

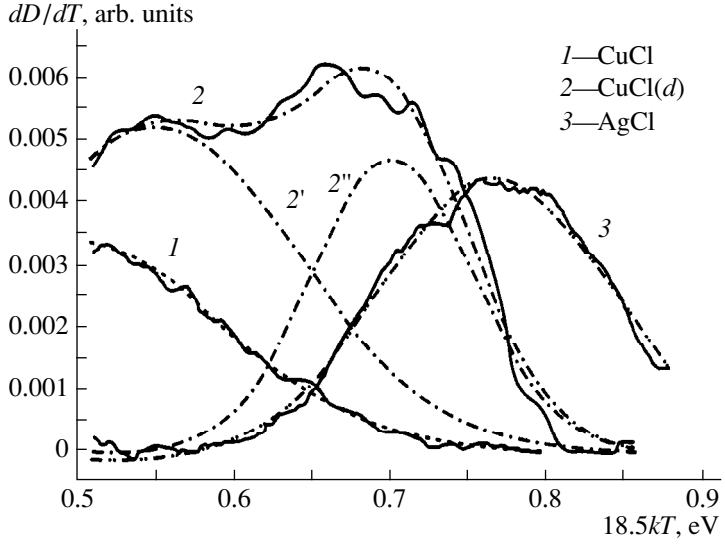

Fig. 4. Derivatives $dD(T)/dT$ for the corresponding temperature regions of $D(T)$ curves (from Fig. 3), reflecting the relative energy distribution of localized hole states for CuCl and AgCl NCs in glass and their interpolation by Gaussians. Curve *1* corresponds to a CuCl NC without defects, curves *2*, *2′*, and *2″*, to NCs with frozen intrinsic defects; and curve *3* corresponds to AgCl NCs.

For quenched CuCl NCs, the $dD(T)/dT$ curve has a more intricate shape (curve *2* in Fig. 4). Its decomposition proved that the quenching of NCs increases the number of hole traps of the second type (stabilized, thermally activated defects, viz., cation vacancies or their aggregates) with the distribution peak in the energy range $E_T = 0.70$ eV and the distribution width 0.055 eV. Consequently, the efficiency of the formation of colloidal particles is twice as high (cf. curves *1* and *2* in Fig. 3).

The energy scanning of glass samples with light-sensitive AgCl NCs gives a peak on the $dD(T)/dT$ curve (curve *3* in Fig. 4) for a still higher energy $E_T = 0.77$ eV for a distribution width of 0.073 eV. The large depth of the hole center in an AgCl NC is responsible for the weak relaxation of absorption of Ag_n particles at room temperature, which is observed in experiments.

Thus, the regularities in the kinetics of formation and destruction of colloidal particles of copper and silver in light-sensitive CuHal or AgHal NCs are associated with the energy dispersion of localized hole states. The decrease in the NC radius from 8 to 2 nm leads to a decrease in the depth of hole centers and to a gradual, but significant decrease in the width of the energy distribution for hole traps.

3. DISCUSSION OF RESULTS

The energy dispersion of localized states in NCs can be explained using, in the first place, Dexter's idea [17] concerning the presence of large-scale crystal-field fluctuations emerging due to thermal vibrations of the lattice. As a result of lattice deformation Δ, the energy of the localized state changes:

$$E(\Delta) = E_0 - E_1\Delta. \tag{9}$$

The width of the dispersion of the localized state is determined by the random quantity $P(\Delta) = \text{const} \times \exp(-B\Delta^2/2kT)$, which is equal to the probability of the emergence of deformation Δ in NCs (B is a certain average value of the elastic constant).

We can calculate the elastic constant from the data on the Young modulus for CuCl [18] and assume that its average value is $B = 1.0$ (at $T = 300$ K). Then distribution curve *1* in Fig. 4 corresponds to the coefficient $E_1 = 0.6$ eV, which determines the amplitude of crystal field oscillations. For distribution curve *2″* in Fig. 4, which is connected with the thermally activated Frenkel defects in CuCl NCs, the value of B is equal to 3. Thus, the elastic constant in the vicinity of thermally activated defects is higher (if we assume that the value of E_1 remains unchanged), and the crystal field fluctuations decrease. As the radius of CuCl NC falls to 2 nm, the dispersion width for hole states decreases to 0.045 eV, which corresponds to $B = 4.5$. The considerable decrease in the elastic constant is probably associated with the cutoff of the phonon spectrum on the side of long wavelengths, which cannot exceed the size of NCs.

The dispersion width of localized hole states in AgCl NCs amounts to 0.077 eV (see distribution curve *3* in Fig. 4), which corresponds to $B = 1.7$ (for the constant $E_1 = 0.6$ eV).

Due to the presence of an excess negative charge at a colloidal particle (see above), we must take into account the possible effect of an electric field on photoelectronic processes in the NCs under investigation. The mechanisms of the effect of the external electric field on photoelectronic processes are considered in detail in [19–21] for activated KCl–In ionic crystals. The probability of the decay of an excited state of an impurity increases in an electric field [19]. As applied to the NCs under investigation, the field of a charged Cu_n center may increase the probability of exciton decay under UV excitation in the vicinity of this center. In this connection, the localization of a hole can take place close to the site of exciton decay in the range of action of the electric field of a Cu_n center. Under the action of the field, not only the depth of a hole trap, but also the rate factor can decrease [20]. If the localization of holes is characterized by a certain distribution $P(r)$ in a distance to a charged center, the depth $E(r)$ of hole traps has a dispersion due to different values of the electric field strength $F(r)$ and is determined by the relation [20]

$$E(r) = E_0 - bF(r)^{0.5}, \tag{10}$$

where E_0 is the depth of a localized state in a zero field and b is the proportionality factor ($b = 3.4 \times 10^{-6}$ eV m V^{-1} in the case of a Coulomb center [20]).

If a hole is captured at traps nearest to a Cu_n center, the $P(r)$ distribution corresponds to the probability of capture at the nearest trap [21]:

$$P(r)dr = 4\pi r^2 N \exp\left(-\frac{4}{3}\pi r^3 N\right)dr, \tag{11}$$

where N is the concentration of traps.

Indeed, the dispersion of the depth of electron states localized near a charged center was observed earlier by the thermoluminescence method [22]. The average distance to the nearest trap is defined from Eq. (11) as $r_c = 0.55N^{-1/3}$, which amounts to 3.2 nm for the concentration indicated in [22].

For the field of a Cu_n center to be responsible for a dispersion width 0.1 eV of localized states (distribution curve *1* in Fig. 4), holes must be trapped at a distance r_c, where the field must be equal to 6×10^7 V/m in accordance with Eq. (10). This distance $r_c^- = 1.13$ nm for an excess charge $q = 0.5e$ at a colloidal particle (e is the electron charge) and for the permittivity $\varepsilon = 10$ (for CuCl). Such a short-range trapping of holes is possible only for a very large concentration of traps, which is highly improbable.

In all probability, the energy dispersion of localized states is due to thermal fluctuations of the crystal field, and the field of a charged center shifts the entire distribution towards lower energies upon a decrease in the size of NCs. The experimentally observed decrease in E_0 by 0.02 eV upon a decrease in the NC radius from 8 to 2 nm is possible if, in accordance with Eq. (10), the field strength amounts to 4×10^5 V/m. Such a field may create a charge $q = 0.07e$ on a Cu_n center at a distance of 4 nm (the distance along the particle diameter).

The total number of atoms in a CuCl NC of radius 2 nm is approximately equal to 1500, and only 7 lattice constants a can be accommodated in the diameter (a = 0.54 nm for CuCl with the lattice of a zinc blende). It is impossible to determine the fraction of Cu atoms involved in the formation of a Cu_n colloidal particle, since the existing theoretical calculations based on the Mie theory [23, 24] were made for Cu_n particles having a size comparable with that of the entire NC. Carrying out gauge measurements of the absorbed energy of UV radiation and evaluating the number of NCs in the sample under investigation, we can determine the number of traps in an individual crystal and the number of atoms in a colloidal particle from the kinetics parameters. Such studies will be carried out in the future.

The magnitude of the effective excess charge on a Cu_n colloidal particle in a mobile Cu^+ cation (which moves mainly over tetrahedral voids of the NC lattice [25]) and the configuration of the potential of localized hole states remain unclear. When the model of formation of colloidal particles is constructed for small crystals, the possible manifestation of tunnel capture effects and charge localization at low temperatures should also be taken into account [21].

In accordance with Eq. (8), the number of atoms in a Cu_n particle in the CuCl crystal can be determined experimentally if we find the total number ν_0 of hole traps from the data on the kinetics parameter and then determine the number of hole traps corresponding to an individual NC. For this purpose, we must carry out gauge measurements of the absorbed energy of UV radiation and determine the number of NCs of a particular size in the sample under investigation. Such measurements will be made at a later stage.

REFERENCES

1. A. A. Anikin, V. K. Malinovskiĭ, and A. A. Sokolov, Fiz. Khim. Stekla **13** (2), 209 (1987).
2. R. J. Araujo and N. F. Borrelli, J. Appl. Phys. **47** (4), 1370 (1976).
3. R. J. Araujo, N. F. Borrelli, and D. A. Nolan, Philos. Mag. B **40** (4), 279 (1979).
4. W. Moller and E. Sutter, Optik (Stuttgart) **75** (1), 37 (1986).
5. T. Flohr and R. Helbig, Glastech. Ber. **59** (10), 292 (1986).
6. S. K. Chandhuri, N. Biswas, and S. Thiagarajan, Indian Ceram. Soc. (Transl.) **48** (1), 1 (1989).
7. L. V. Gracheva and V. A. Tsekhomskiĭ, Fiz. Khim. Stekla **4** (2), 192 (1978).
8. A. V. Dotsenko and V. K. Zakharov, Fiz. Khim. Stekla **6** (2), 224 (1980).
9. L. V. Gracheva, V. I. Leĭman, and V. A. Tsekhomskiĭ, Fiz. Khim. Stekla **5** (3), 380 (1980).
10. L. V. Gracheva and V. I. Leĭman, Fiz. Khim. Stekla **13** (2), 280 (1987).
11. P. M. Valov, L. V. Gracheva, V. I. Leĭman, and T. V. Negovorova, Fiz. Khim. Stekla **19** (4), 578 (1993).
12. P. M. Valov and V. I. Leĭman, Pis'ma Zh. Éksp. Teor. Fiz. **66** (7), 481 (1997) [JETP Lett. **66**, 510 (1997)].
13. P. M. Valov and V. I. Leĭman, Fiz. Tverd. Tela (St. Petersburg) **41** (2), 310 (1999) [Phys. Solid State **41**, 278 (1999)].
14. V. V. Antonov-Romanovskiĭ, *Photoluminescence Kinetics of Phosphor Crystals* (Nauka, Moscow, 1966).
15. J. Frenkel, *Collection of Selected Works*, Vol. 3: *Kinetic Theory of Liquids* (Akad. Nauk SSSR, Moscow, 1959; Clarendon Press, Oxford, 1946).
16. A. A. Ashkalunin, P. M. Valov, V. I. Leĭman, and V. A. Tsekhomskiĭ, Fiz. Khim. Stekla **10** (3), 325 (1984).
17. L. D. Dexter, Nuovo Cimento Suppl. **7**, 245 (1958).
18. K. Kune, M. Balkanski, and M. A. Nucimovici, Phys. Status Solidi B **72** (2), 229 (1975).
19. V. P. Denks and V. I. Leĭman, Tr. Inst. Fiz. Astron., Akad. Nauk Ést. SSR **42**, 109 (1974).
20. V. I. Leĭman, V. P. Denks, and A. É. Dudel'zak, Fiz. Tverd. Tela (Leningrad) **15** (8), 2454 (1973) [Sov. Phys. Solid State **15**, 1630 (1973)].
21. V. I. Leĭman, Fiz. Tverd. Tela (Leningrad) **14** (12), 3650 (1972) [Sov. Phys. Solid State **14**, 3057 (1972)].
22. V. I. Leĭman, Fiz. Tverd. Tela (Leningrad) **15** (2), 503 (1973) [Sov. Phys. Solid State **15**, 351 (1973)].
23. A. V. Dotsenko, V. K. Zakharov, S. A. Kuchinskiĭ, and T. E. Chebotarev, Zh. Prikl. Spektrosk. **39** (5), 795 (1983).
24. R. Ruppin, J. Appl. Phys. **59** (4), 1355 (1986).
25. J. B. Boyce, T. M. Hayes, and J. C. Mikkelsen, Phys. Rev. B **23** (6), 2876 (1981).

Translated by N. Wadhwa

Physics of the Solid State, Vol. 42, No. 9, 2000, pp. 1744–1748. Translated from Fizika Tverdogo Tela, Vol. 42, No. 9, 2000, pp. 1695–1699.

LOW-DIMENSIONAL SYSTEMS AND SURFACE PHYSICS

Optical Properties of Doped Quasi-Two-Dimensional Systems

É. P. Sinyavskiĭ and S. M. Sokovnich

Pridnestrovskiĭ State University, Tiraspol', MD-3300 Moldova

Received October 22, 1999

Abstract—A wide class of experimental data on luminescence in doped two-dimensional systems is explained in terms of multiphonon optical transitions. A zero-radius-potential model is employed to describe localized states in square quantum wells. Specifically, it is shown that the luminescence intensity varies nonmonotonically with the acceptor-impurity position, whereas the half-width of the luminescence peak decreases with the impurity distance from the center of the size-confined system. The features of luminescence in a longitudinal magnetic field are investigated. © *2000 MAIK "Nauka/Interperiodica".*

INTRODUCTION

In recent years, considerable study has been devoted to the processes of luminescence caused by electron transitions from the lowest size-quantized conduction band to bound states in size-confined structures (heterostructures, solitary quantum wells, and superlattices). Band-to-band transitions are characterized by narrow photoluminescence (PL) lines observed at low temperatures. For example, in GaAs–$Al_xGa_{1-x}As$ at $T = 2$ K (the quantum-well thickness is $a = 20$ Å), the half-width of PL lines Δ_0 is about 7 meV [1], and at $T = 4$ K ($a = 50$ Å), $\Delta_0 \approx 2.7$ meV [2]; in In_xGaAs–GaAs at 5 K ($a = 37$ Å), $\Delta_0 \approx 1.4$ meV [3].

In doped size-confined systems, radiative electron transitions to acceptor states can occur. In GaAs–AlGaAs solitary quantum wells (QWs), broad PL lines were observed at high temperatures ($\Delta_0 \approx 70$ meV [1] at $T = 180$ K); these lines are broadened and their intensity decreases with the increasing temperature. A similar picture was observed for PL lines from $Ga_{0.47}In_{0.53}As$–$Al_{0.48}In_{0.52}As$ quantum wells [4] (acceptor atoms of Be were located at the centers of QWs; the half-width of emission lines was $\Delta_0 \approx 96$ meV at $T = 110$ K). These features of PL lines suggest that optical transitions involve many vibrational quanta. Possible multiphonon optical electron transitions from the conduction band to acceptor states in GaAs–$Al_xGa_{1-x}As$ quantum wells (with $a \cong 30$ Å and C atoms as acceptors) were discussed in [5]. Luminescence associated with an electron gas of a high density and acceptor states of Si in GaAs–$Al_{0.3}Ga_{0.7}As$ (the Fermi energy $E_F = 37.5$ meV, $a = 200$ Å) was studied in [6]. It was found that PL peaks decrease in intensity and become broader with increasing temperature in a range of $T = 4.2$–110 K. Detailed experimental investigations of the radiative recombination on acceptors of a two-dimensional electron gas were performed in [7–10] for simple GaAs–$Al_xGa_{1-x}As$ heterostructures, in [11–15] for structures with QW clusters, and in [15] for doped InGaAs–GaAs solitary QWs. Theoretical investigations of PL involving acceptor states in QWs were performed in [16–18] under the assumption that hydrogenlike acceptor impurities are distributed uniformly over the size-confined system. At the present time, advanced technology allows detailed investigations to be made of the dependence of optical transitions to bound states on the distance of the impurity center from the surface of the size-quantized system. It was shown in [7] that the variation of the PL intensity with the distance of zero-radius (δ-) acceptor impurity centers from the surface is highly nonmonotonic. The half-width of emission lines associated with electron transitions from higher energy bands of the size-quantized system to acceptor states decreases as the impurity approaches the boundary of the heterostructure. Radiative recombination becomes more intense in QWs when acceptor impurity atoms are located at their centers [19]. The optical properties associated with impurity states were investigated in promising GaN–AlGaN quantum wells in [20]. These quantum systems are of interest for optical instruments operating in the blue and ultraviolet region. In particular, it was shown in [20] that the half-width of impurity luminescence lines due to electron transitions from a donor state to the valence band Δ_0 (equal to about 44 meV at $T = 10$ K, $a = 50$ Å) and the radiation intensity decrease with increasing temperature and the luminescence virtually disappears at $T = 200$ K. The last circumstance suggests that nonradiative (multiphonon) transitions become important at high temperatures.

The effect of an external magnetic field on optical characteristics of doped QWs is of critical importance. The point is that the energy of a free electron is completely quantized when a magnetic field is perpendicular to the QW surface. Therefore, the absorption and emission of electromagnetic radiation involve transitions of carriers between bound states and discrete states of the quantum system. Experimental investigations of luminescence associated with electron transitions to localized states in the case where the quantum

1063-7834/00/4209-1744$20.00

system is placed in an external magnetic field showed that, as the magnetic field is increased, the luminescence peak shifts to higher frequencies (in simple heterostructures [21] and superlattices [22, 23]) and its half-width is $\Delta_0 \approx 2.7$ meV [7] at low temperatures.

In this paper, we provide an interpretation of some experimental data on optical properties of doped size-confined systems in terms of multiphonon optical transitions.

1. STATEMENT OF THE PROBLEM AND BASIC EQUATIONS

Let us consider a square QW with infinitely high walls, doped with an acceptor of a binding energy E_A, which is measured from the top of the valence band of the three-dimensional (bulk) material. The wave function and energy eigenvalues of an electron moving in a magnetic field **H** applied along the size-quantization axis z are

$$\Psi_\alpha(\mathbf{r}) = [L_x a R\sqrt{\pi} N! 2^{N-1}]^{-1/2} \sin\left(\frac{\pi \nu z}{a}\right)\exp(iK_x x)$$
$$\times \exp\left[-\frac{1}{2R^2}(y + R^2K_x)^2\right] H_N\left[\frac{y + R^2K_x}{R}\right], \quad (1)$$
$$E_\alpha = \hbar\omega_c(N + 1/2) + \varepsilon_0\nu^2,$$
$$\varepsilon_0 = \frac{\pi^2\hbar^2}{2m_e a^2}, \quad R^2 = \frac{\hbar}{m_c\omega_c}.$$

Here, L_x is the length of the QW along the x axis, K_x is the component of the electron wave vector, $\alpha = (N, \nu, K_x)$ are the quantum numbers specifying the electron state, ω_c is the electron cyclotron frequency, ε_0 is the spacing between space-quantized energy levels, a is the QW thickness, m_e is the effective mass of an electron, and $H_N(z)$ are the Hermite polynomials.

The normalized wave function of an electron localized on the acceptor is given by the following expression in the zero-radius-potential model [24]:

$$\Psi_A(\mathbf{r}) = A\sum_\alpha \frac{\Psi_\alpha(\mathbf{r})\Psi^*_\alpha(z_0)}{E_A + \hbar\omega_\nu(N + 1/2) + \varepsilon\nu^2}, \quad (2)$$
$$\varepsilon = \frac{\pi^2\hbar^2}{2m_\nu a^2},$$

where m_ν is the effective mass of a hole and ω_ν is the hole cyclotron mass.

In Eq. (2), it is assumed that the impurity is localized at the point $\mathbf{r}_0(0, 0, z_0)$. We will consider deep acceptor states, $\hbar\omega_\nu/F_A < 1$, in what follows. In this case,

$$A^2 = \frac{2\pi\hbar^4 K_0}{m_\nu^2}\frac{\sinh(K_0 a)}{\sinh[(K_0 a)(1 - (z_0/a))]\sinh(K_0 z_0)},$$
$$E_A + (\hbar\omega_4/2) \equiv \frac{\hbar^2 K_0}{2m_\nu}.$$

The spectral radiation intensity associated with a transition of an electron from a state of Eq. (1) to the acceptor level is related to the transition probability rate [25] and can be written as

$$\Phi(\Omega) = \frac{4\Omega^2 n_0}{Vc^3}\left|\frac{\mathbf{P}_{c\nu}\mathbf{e}_0}{m_0}\right| e^2 \sum_{S,\alpha} n_\alpha |I_{S,\alpha}|^2 \quad (3)$$
$$\times \delta\{\hbar\omega_c(N + 1/2) + \varepsilon_0\nu^2 + E_g - E_A - \hbar\Omega\}.$$

Here, $\mathbf{P}_{c\nu}$ is the matrix element of the momentum operator involving the Bloch amplitudes, $\mathbf{e}_0$ is the polarization vector of the emitted electromagnetic wave of a frequency Ω, V is the QW volume, m_0 is the mass of a free electron, c is the velocity of light, E_g is the band gap width of the size-confined system, n_0 is the refractive index, and n_α is the electron distribution function. For a nondegenerate gas, we have

$$n_\alpha = 4\pi a R^2 \sinh(\beta\hbar\omega_c/2)$$
$$\times \exp\{-\beta[\hbar\omega_c(N + (1/2)) + \varepsilon_0\nu^2]\} D^{-1}, \quad (4)$$
$$D = \sum_{\nu=1}^{\infty} \exp\{-\beta\varepsilon_0\nu^2\},$$

where n_e is the electron concentration.

The overlap integral for the initial state of Eq. (1) and the final state of Eq. (2) is easily calculated and has the form

$$I_{S,\alpha} = \int \Psi^*_A(\mathbf{r})\Psi_\alpha(\mathbf{r}) = A\left[\frac{2}{L_x a R\sqrt{\pi}}\right]^{1/2}$$
$$\times \frac{\sin\left(\frac{\pi z_0}{a}\nu\right)\exp\left[-\frac{1}{2}(RK_x)^2\right] H_N(RK_x)}{\left[E_A + \hbar\omega_\nu\left(N + \frac{1}{2}\right) + \varepsilon\nu^2\right]}. \quad (5)$$

According to the theory of multiphonon optical transitions [26, 27], the spectral radiation intensity, with allowance made for lattice vibrations, can be obtained from Eq. (3) by replacing

$$\delta\{\hbar\omega_c(N + 1.2) + \varepsilon_0\nu^2 + E_g - E_A - \hbar\Omega\} \longrightarrow \frac{1}{2\pi\hbar} \quad (6)$$
$$\times \int_{-\infty}^{\infty} dt \exp\left\{\frac{it}{\hbar}[\hbar\omega_c(N + (1/2)) + E_g - E_A - \hbar\Omega] - g(t)\right\},$$

$$g(t) = \frac{it}{\hbar}\sum_{\mathbf{q}}\frac{|V_{qss}|^2}{\hbar\omega_q} + \sum_{\mathbf{q}}\frac{|V_{qss}|^2}{(\hbar\omega_q)^2}$$

$$\times[(2N_q+1) + i\sin(\omega_q t) - (2N_q+1)\cos(\omega_q t)],$$

$$V_{qss} = C_q\int|\Psi_A(\mathbf{r})|^2\exp(i\mathbf{qr})d\mathbf{r}, \quad (7)$$

$$N_q = [\exp(\beta\hbar\omega_q - 1)]^{-1}, \quad \beta = 1/(k_0T),$$

where C_q is the coefficient of the electron–phonon interaction and $\hbar\omega_q$ is the energy of a phonon with a wave vector $\mathbf{q}$. We consider the temperature range for which $4\varepsilon_0 \gg k_0T$; in this case, optical transitions from the lowest size-quantized level ($\nu = 1$) are dominant. With Eqs. (4)–(6), the spectral radiation intensity of Eq. (3) becomes

$$\Phi(\Omega) = F(z_0)\Phi_0\sum_N\left(\frac{\hbar\Omega}{E_A + \hbar\omega_\nu(N + (1/2)) + \varepsilon}\right)^2 \times \exp[-\beta\hbar\omega_c(N + (1/2))]I(\Omega, N). \quad (8)$$

Here, $I(\Omega, N)$ is a characteristic function, which occurs in the theory of optical multiphonon transitions,

$$I(\Omega, N) = \int_{-\infty}^{\infty}dt\exp\left\{\frac{it}{\hbar}[\hbar\omega_c(N + (1/2)) + \varepsilon_0 + E_g - E_A - \hbar\Omega] - g(t)\right\},$$

$$\Phi_0 = \frac{2^4\hbar n_0e^2n_An_e}{c^3am_\nu^2}\left|\frac{\mathbf{P}_{c\nu}\mathbf{e}_0}{m_0}\right|^2\sinh(\beta\hbar\omega_c/2), \quad (9)$$

$$F(z_0) = \frac{\sin^2(\pi z_0/a)\sinh(K_0a)K_0a}{\sinh[(1 - z_0/a)K_0a]\sinh(K_0z_0)},$$

and n_A is the concentration of acceptors in the QW.

In the absence of a magnetic field, we obtain the following expression for the spectral radiation intensity in the case of multiphonon transitions:

$$\Phi^{(0)}(\Omega) = F(z_0)\Phi^{(0)}I(\Omega, 0),$$

$$\Phi^{(0)} = \frac{2n_0e^2\hbar n_en_A}{c^3am_\nu^2}\left|\frac{\mathbf{P}_{c\nu}\mathbf{e}_0}{m_0}\right|^2\left(\frac{\hbar\Omega}{E_A}\right)^2. \quad (10)$$

Here, $I(\Omega, 0)$ is given by Eq. (9) with $\hbar\omega_c = 0$. Equation (10) has been derived under the assumption that $E_A \gg k_0T$ and that the electron transitions to bound states occur from the lowest size-quantized level of the conduction band ($\nu = 1$).

2. DISCUSSION AND COMPARISON WITH THE EXPERIMENT

In the case of the interaction of a localized electron with optical lattice vibrations with the energy $\hbar\omega_0$ (ω_0 is the limiting optical-phonon frequency), Eq. (7) takes the form

$$g_{op}(t) = it\omega_0a_0 + z\cos(\omega_0t + \varphi) + a_0(2N + 1),$$

$$a_0 = \sum_{\mathbf{q}}\frac{|V_{qss}|^2}{(\hbar\omega_0)^2}, \quad z = 2a_0\sqrt{N(N+1)}, \quad \tan\varphi = \frac{-i}{2N+1}, \quad (11)$$

where N is the equilibrium distribution function of optical phonons. Using the relation [28]

$$\exp(z\cos\alpha) = \sum_{n=-\infty}^{\infty}I_n(z)\exp(in\alpha),$$

[$I_n(z)$ is the modified Bessel function] and Eq. (11), the spectral radiation intensity of Eq. (10) can be written as

$$\Phi^{(0)}(\Omega) = F(z_0)\Phi^{(0)}\frac{\hbar}{\omega_0}\sum_n I_n(z)\exp[-a_0(2N+1)] \times \exp(\beta\hbar\omega n/2)\delta(\Delta - n\hbar\omega_0),$$

$$\Delta = \varepsilon_0 + E_g - \hbar\omega_0a_0 - E_A - \hbar\Omega \geq 0. \quad (12)$$

From Eq. (12), it immediately follows that the frequency dependence of $\Phi^{(0)}$ is a set of sharp δ-shaped peaks (at $z < 1$), the spacing between them beeng equal to the limiting optical-phonon energy.

Let us now take into account the interaction of an electron with acoustic phonons and use the quasi-classical description of long-wavelength vibrations (the corresponding criteria are discussed in detail in [29]). Expanding $g(t)$ in a power series in t and keeping only quadratic terms, we obtain

$$g(t) = \frac{1}{2\hbar^2}\sum_{\mathbf{q}}|V_{qss}|^2(2N_q+1)t^2 \equiv Bt^2. \quad (13)$$

Substituting Eq. (13) to Eq. (10) leads to the following expression for the spectral radiation intensity:

$$\Phi^{(0)}(\Omega) = F(z_0)\Phi^{(0)} \times\sqrt{\frac{\pi}{B}}\exp\left\{\frac{(\varepsilon_0 + E_g - E_A - \hbar\Omega)^2}{4\hbar^2B}\right\}. \quad (14)$$

From Eq. (14), it is seen that the frequency dependence of $\Phi^{(0)}(\Omega)$ is described by a Gaussian curve with a half-width of

$$\Delta_0 = 4\hbar\sqrt{B\ln 2}. \quad (15)$$

Thus, in the case of electron transitions involving many optical and acoustic phonons, as is seen from Eqs. (12) and (14) at $z \le 1$, the radiation intensity as a function of frequency is described by a set of Gaussian curves with the half-width Δ_0. The spacing between the peaks of these curves equals the limiting optical-phonon energy $\hbar\omega_0$. Such phonon satellites were observed [20] in GaN–AlGaN quantum wells (a = 25 Å).

In order to estimate the half-width Δ_0, we employ the model of a zero-radius potential [24] (widely used in current calculations in the solid state physics) for deep acceptor states. In the model of a square QW with infinitely high walls, the wave function of a bound state has the form

$$\Psi_A(\mathbf{r}) = \frac{2}{a}\frac{1}{L_x L_y}C \times \sum_{\nu} \frac{\exp[i(\mathbf{K}_\perp\boldsymbol{\rho})]\sin(\pi z\nu/a)\sin(\pi z_0\nu/a)}{E_A + \dfrac{\hbar^2 K_\perp^2}{2m_\nu} + \varepsilon\nu^2}, \quad (16)$$

$$K_\perp^2 = K_x^2 + K_y^2, \quad (\mathbf{K}_\perp\boldsymbol{\rho}) = K_x x + K_y y.$$

This expression corresponds to the case where the impurity center is situated at the point $\mathbf{r}(0, 0, z_0)$. Performing the summation over $\mathbf{K}_\perp$, we obtain

$$\Psi_A(\mathbf{r}) = \frac{2}{a}\frac{cm_\nu}{a\hbar^2}\sum_{\nu=1}^{\infty}\sin(\pi z\nu/a)\sin(\pi z_0\nu/a) \times K_0\left[\boldsymbol{\rho}\sqrt{\frac{2m_\nu}{\hbar^2}(E_A + \varepsilon_0\nu^2)}\right].$$

In this expression, the argument of the Macdonald function $K_0(z)$ increases with increasing ν, meaning that we can restrict ourselves to the case of $\nu = 1$ for qualitative estimations. This last approximation is reasonable for narrow QWs, for which $E_A/\varepsilon_0 < 1$. When normalized, the wave function becomes

$$\Psi_A(\mathbf{r}) = \sqrt{\frac{2\pi^2\xi}{a^3}}\sin(\pi z/a)K_0\left[\frac{\pi\boldsymbol{\rho}}{a}\xi\right], \quad (17)$$

$$\xi = \sqrt{1 + E_A/\varepsilon_0}.$$

This wave function is the product of the wave function for one-dimensional motion along the size-quantization axis and the wave function of the bound state in the zero-radius potential of impurity centers in a two-dimensional system [30]. The function of Eq. (17) is close to the wave function for an acceptor center, which is commonly used to estimate the hot-electron scattering cross section by neutral acceptors in structures with QWs [31]. For temperatures at which $N_q \approx k_0 T/(\hbar wq) > 1$ ($\hbar wq$ is the energy of an acoustic phonon), the calculation of the constant B in Eq. (13) is straightforward. The result is

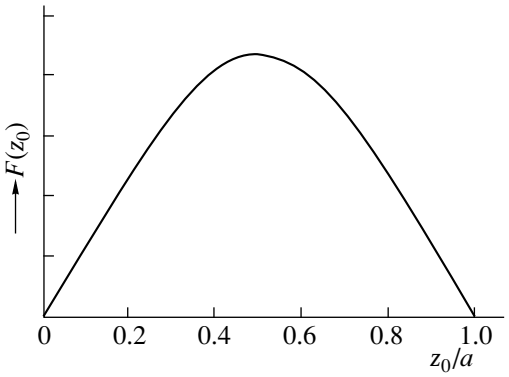

Dependence of $F(z_0)$ on the position of the impurity center in the quantum well.

$$B \approx \frac{3\pi}{2}\frac{k_0 T E_1^2}{\boldsymbol{\rho}_0 w^2 \hbar^2 a^3}\xi^2. \quad (18)$$

Here, E_1 is the deformation-potential constant for a hole, ρ_0 is the crystal density, and w is the velocity of sound. Thus, the spectral line half-width of Eq. (15) takes the form

$$\Delta_0 = 4\xi\sqrt{\frac{3\pi k_0 T E_1^2}{\boldsymbol{\rho}_0 w^2 a^3}}. \quad (19)$$

For typical GaAs–AlGaAs quantum wells (E_1 = 10 eV, ρ_0 = 5.4 g/cm^3, $w = 3\times10^5$ cm/s) with E_A = 60 meV and a = 20 Å ($\varepsilon_0 \approx$ 200 meV), we have $\Delta_0 \approx 5.3\sqrt{T}$. Therefore, at T = 180 K, we have $\Delta_0 \approx$ 70 meV, which is close to the experimental values presented in [1]. The half-width increases with temperature and, hence, the radiation intensity of Eq. (14) decreases, which is consistent with the experimental data [1, 2, 20]. The function $F(z_0)$ determines the dependence of the radiation intensity on the position of the δ-impurity center in the QW. A plot of $F(z_0)$ *versus* z_0/a is presented in the figure (for Ka = 1). The form of the $F(z_0)$ function varies only slightly with varying Ka over a wide range (from 1 to 0.1). From the figure, it is seen that the impurity radiation intensity peaks when the acceptor is at the QW center; as the acceptor approaches the boundary of the size-confined system, the radiation intensity decreases. This is because the overlap of the band-state and localized-state wave functions of the electron decreases with the increasing distance of the acceptor from the QW center. Such a nonmonotonic dependence of $\Phi^{(0)}(\Omega)$ on the position of the impurity was observed experimentally in simple heterostructures GaAs–$Al_xGa_{1-x}As$ with δ-acceptor impurities [7]. We note that, as the impurity nears the QW surface, E_A approaches the valence band top, which leads to a decrease in ξ and, hence, in Δ_0.

Such a dependence of the half-width of luminescence lines on z_0 was experimentally observed in [7] and, therefore, the multiphonon broadening of luminescence lines, considered in this paper, is a possible mechanism of this dependence.

In the presence of a longitudinal magnetic field, the spectral radiation intensity calculated from Eq. (8) in the quasi-classical approximation to crystal lattice vibrations has the form

$$\Phi(\Omega) = F(z_0)\Phi_0\sum_N\left(\frac{\hbar\Omega}{E_A+\hbar\omega_c(N+1/2)+\varepsilon_0}\right)^2 \times\exp[-\beta\hbar\omega_c(N+(1/2))]\sqrt{\frac{\pi}{B}} \times\exp\left\{-\frac{[\hbar\omega_c(N+1/2)+\varepsilon_0+E_g-E_A-\hbar\Omega]}{4B\hbar^2}\right\}. \quad (20)$$

Therefore, in the approximations considered above, the luminescence line is described by a Gaussian curve with the half-width given by Eq. (15). As the magnetic field increases, the position of the luminescence maximum is shifted to shorter wavelengths, which is due to the energy quantization in the magnetic field. This is observed in various quasi-two-dimensional systems [21–23].

REFERENCES

1. M. Haefner, L. Lehmann, R. Mitdank, *et al.*, Phys. Status Solidi A **122**, 683 (1990).
2. M. Gurioli, A. Vinattieri, and M. Colocci, Appl. Phys. Lett. **59**, 2150 (1991).
3. A. S. Ignat'ev, M. V. Karachevtseva, V. G. Makarov, *et al.*, Fiz. Tekh. Poluprovodn. (S.-Peterburg) **28**, 125 (1994) [Semiconductors **28**, 75 (1994)].
4. Y. H. Zhang, N. N. Ledentsov, and K. Ploog, Phys. Rev. B **44**, 1399 (1991).
5. J. A. Kash, E. E. Mendez, and H. Morkoc, Appl. Phys. Lett. **46**, 173 (1985).
6. D. W. Lui, X. M. Xu, and Y. F. Chen, Phys. Rev. B **49**, 4640 (1994).
7. I. V. Kukushkin, K. von Klitzing, K. Ploog, and V. B. Timofeev, Phys. Rev. B **40**, 7788 (1989).
8. A. F. Dite, K. von Klitzing, I. V. Kukushkin, *et al.*, Pis'ma Zh. Éksp. Teor. Fiz. **54**, 393 (1991) [JETP Lett. **54**, 389 (1991)].
9. J. L. Bradshaw, W. J. Choyke, R. P. Devaty, and R. L. Messham, J. Lumin. **47**, 249 (1991).
10. O. V. Volkov, I. V. Kukushkin, K. von Klitzing, and K. Eberl, Pis'ma Zh. Éksp. Teor. Fiz. **68**, 223 (1998) [JETP Lett. **68**, 236 (1998)].
11. R. G. Ulbrich, J. A. Kash, and J. C. Tsang, Phys. Rev. Lett. **62**, 949 (1989).
12. B. P. Zakharchenya, P. S. Kop'ev, D. N. Mirlin, *et al.*, Solid State Commun. **69**, 203 (1989).
13. B. J. Skromme, R. Bhat, M. A. Koza, *et al.*, Phys. Rev. Lett. **65**, 2050 (1990).
14. P. S. Kop'ev, D. N. Mirlin, D. G. Polyakov, *et al.*, Fiz. Tverd. Tela (Leningrad) **24**, 1200 (1990) [Sov. Phys. Solid State **24**, 678 (1982)].
15. L. V. Dao, M. Gal, G. Li, and C. Jagadish, Appl. Phys. Lett. **71**, 1849 (1997).
16. L. E. Oliveria and J. Lopez-Condor, Phys. Rev. B **41**, 3719 (1990).
17. Rosana B. Santiago, J. D'Albuquerqua e Castro, and Luiz E. Oliveira, Phys. Rev. B **48**, 4498 (1993).
18. A. A. Afonenko, V. K. Kanonenko, I. S. Manak, and V. A. Shevtsov, Fiz. Tekh. Poluprovodn. (S.-Peterburg) **31**, 1087 (1997) [Semiconductors **31**, 929 (1997)].
19. G. C. Rune, P. O. Holtz, M. Sudaram, *et al.*, Phys. Rev. B **44**, 4010 (1991).
20. K. C. Zeng, J. Y. Lin, H. X. Jiang, *et al.*, Appl. Phys. Lett. **71**, 1368 (1997).
21. A. S. Plant, I. V. Kukushkin, K. von Klitzing, and K. P. Ploog, Phys. Rev. B **42**, 5744 (1990).
22. B. J. Skromme, R. Bhat, and M. A. Koza, Solid State Commun. **66**, 543 (1988).
23. D. Gekhtman, J. A. Kash, E. Cohen, and Arza Ron, Phys. Rev. B **54**, 2756 (1996).
24. Yu. N. Demkov and V. N. Ostrovskiĭ, *Zero-Range Potentials and Their Applications in Atomic Physics* (Leningrad. Gos. Univ., Leningrad, 1975; Plenum, New York, 1988).
25. A. P. Levanyuk and V. V. Osipov, Usp. Fiz. Nauk **133**, 427 (1981) [Sov. Phys. Usp. **24**, 187 (1981)].
26. Yu. E. Perlin, Usp. Fiz. Nauk **80** (4), 553 (1963) [Sov. Phys. Usp. **6**, 542 (1964)].
27. V. A. Kovarskiĭ, *Multiquantum Transitions* (Shtiintsa, Kishinev, 1974).
28. I. S. Gradshteĭn and I. M. Ryzhik, *Table of Integrals, Series, and Products* (Nauka, Moscow, 1971; Academic, New York, 1980).
29. Yu. E. Perlin and B. S. Tsukerblat, *The Effects of Electron-Phonon Interaction in Optical Spectra of Paramagnetic Impurity Ions* (Shtiintsa, Kishinev, 1976).
30. É. P. Sinyavskiĭ, Izv. Akad. Nauk Resp. Mold., Ser. Fiz.-Tekh. **1** (7), 12 (1992).
31. D. N. Mirlin, V. I. Perel', and I. I. Reshina, Fiz. Tekh. Poluprovodn. (S.-Peterburg) **32**, 866 (1998) [Semiconductors **32**, 770 (1998)].

Translated by Yu. Epifanov

Physics of the Solid State, Vol. 42, No. 9, 2000, pp. 1749–1755. Translated from Fizika Tverdogo Tela, Vol. 42, No. 9, 2000, pp. 1700–1706.

LOW-DIMENSIONAL SYSTEMS AND SURFACE PHYSICS

Deformation States in Nanocrystals

V. V. Meshcheryakov

Moscow Institute of Steel and Alloys, Leninskiĭ pr. 4, Moscow, 117936 Russia

e-mail: Valery@Meshcheryakov.misa.ac.ru

Received November 22, 1999; in final form, December 28, 1999

Abstract—The limitations of the classical description of static deformations in crystals in nanometric regions are demonstrated. The problem is formulated on the basis of the phonon Hamiltonian supplemented with point force sources of the monopole and dipole types. It is found that the quantization of Fourier amplitudes of the total energy for steady deformation states leads to an energy spectrum with the Fermi-type energy level distribution and that the stationary response of nanocrystals to the force action is determined by the discreteness of variation in the number of displaced ions in the region of the force nonuniformity. The conditions for the generation of ionic displacement waves are determined, and the possibility of creating new solid-state elements for information storage and transmission by controlling the collective properties of deformation-induced excitations is envisaged. © *2000 MAIK "Nauka/Interperiodica".*

The response of the electron–ion system of a crystal to the action of an external static electric field is known to be in the form of a static deformation (e.g., in metals) or a static polarization (like in polar crystals). This effect has been studied in detail both experimentally and theoretically [1– 3]. However, the objects of application of the developed theoretical models for polarization or deformation phenomena are macroscopic-sized crystals, although these models have a microscopic substantiation. In the case of macrocrystals, the mechanisms of static polarization or deformation are more or less clear. On the contrary, numerous investigations [4, 5] indicate the existence of microstructural deformation-induced peculiarities in nanocrystals and nanocrystalline materials. The presence of such peculiarities was confirmed, among others, by experimental data on structural instability [6, 7], large elastic stresses [8, 9], local deformations of the lattice of crystallites near their boundaries [10], as well as anomalous strength [11, 12] and damping properties [8, 13]. This necessitates the formulation of the new problem on force action exerted on nanocrystals or individual nanocrystallites of compact materials.

It may not be possible to describe the force action on a small crystal using the classical concept of its monopole and dipole deformation. The monopole and dipole types of deformation in a macroscopic crystal are separated by a scale factor. A decrease in the crystal size, which removes this division, must lead to the emergence of new deformation states. This can be substantiated as follows.

In a finite-size crystal, the response to an external force must have the form of a bounded field of deformation. Such a situation can be described using cyclic boundary conditions. For this purpose, the space is divided into cells having a volume V corresponding to the size of the crystal, and a finite force is applied to each cell. Such a problem was solved for a finite crystal deformed by point defects (i.e., static force dipoles) by the method of lattice statics [14] in which atomic displacements are determined by combinations of normal modes with identical wave vectors. The boundedness of the deformation field in such a solution is manifested in the increment $\pm\Delta V$ of the volume of a $3D$ cell, which appears as a result of the displacement of the medium under the action of force. This means that the deformation field is bounded but extends to the crystal boundaries. The crystal size is not limited in the lattice statics method, and hence, it might have a macroscopic size, as well as the deformation field. As a result, the deformation field remains infinite, as in the problem on a continuous infinite medium, and the calculation of ΔV still leads to an estimate which can hardly be compared to the experimental data and (which is most important), has nothing in common with the quantum properties of the material. The situation remains essentially the same when atomic interaction potentials calculated from first principles are used to estimate the value of ΔV.

On the contrary, the quantization of atomic vibrations in a crystal deformed by the superposition of the monopole and dipole forces leads to the occupation of a region with a characteristic size in the nanometer range by the deformation field in the vicinity of the point of application of an extraneous point force [15]. As a result of such a boundedness of the deformation field, the sizes of the 3 D cells describing the deformed crystals become smaller than the period of the cells in a perfect crystal, and the vibrations at a frequency that is lower than a certain threshold frequency determined by the parameters of the force source become forbidden in the crystal. This is associated with the cutoff of long-wavelength harmonics of zero-point vibrations, determining the region ΔV of force nonuniformity in the

crystal. The mode of harmonics cutoff leads to a value of ΔV which turns out to be independent of the sign of the deformation field (in contrast to the method of lattice statics) and differs only quantitatively for the sources of dipole and monopole types (the latter is disregarded in statics). The results correspond to the case when the crystal temperature $T = 0$. It can be easily assumed further that the initiation of thermal vibrations of the lattice may transform the forbidden harmonics (i.e., those cut off by the field of force nonuniformity) into excited states, which can be observed in experiments.

The present work aims at demonstrating the possibility of emergence of dynamic objects associated with the structure of the deformation field in a statically deformed nanocrystal. For this purpose, we use a linearly elastic model of a homogeneous two-component system of charges. The explicit form of the Coulomb interaction or a screened Coulomb interaction is absent. For this reason, the dynamic stability of the electron–ion system under investigation, which is ensured by the Fermi type of the electron statistics, is postulated by defining its parameters. It should also be noted that since such a model is within the adiabatic approximation and does not permit the separation of purely acoustic vibrational branches from polarization branches, we will also use in the subsequent analysis the term "deformation" along with the term "polarization" in equivalent situations.

1. PHONON HAMILTONIAN WITH POINT-LIKE SOURCES

Let us find the mechanism of crystal response to the action of an external electrostatic source whose force field is specified by the electric field density vector with the component

$$E_\alpha(\mathbf{r}) = E_{1\alpha}\delta(\mathbf{r}) - E_{\alpha\beta}\frac{\partial}{\partial x_\beta}\delta(\mathbf{r}). \quad (1)$$

In this formula, the quantity $E_{1\alpha}$ defines the component of the external electric field strength vector leading to a unidirectional (i.e., monopole) deformation of the ionic lattice in the vicinity of the source under the action of the force $\mathbf{F}_1 = ne\mathbf{E}_1$ displacing n elementary charges e. The dipole deformation tensor

$$E_{\alpha\beta} = \begin{vmatrix} E_{2x}X & E_{2x}Y & E_{2x}Z \\ E_{2y}X & E_{2y}Y & E_{2y}Z \\ E_{2z}X & E_{2z}Y & E_{2z}Z \end{vmatrix} \quad (2)$$

is defined by the components $E_{2\alpha}$ of the external electric field strength vector, which lead to an oppositely directed (i.e., dipole) deformation of the lattice. In order to create an ionic inhomogeneity of this type, we must define the arm vector $\mathbf{R}(X, Y, Z)$ of the dipole force $\mathbf{F}_2 = ne\mathbf{E}_2$. Some features of the force action on the crystal described by a multipole decomposition of the type (1) are given in [15–17]. It should be noted here that a stable static deformation of the crystal requires that the values of forces F_1 and F_2 be bounded by atomic forces. This is attained for arbitrary static force actions on the crystal, excluding the diffusion transport of atoms, the structural transformations, or the plastic flow of the material. The force action described by the decomposition (1) can be realized in an elementary form in the monatomic contacts used, for example, in atomic-force microscopy.

In order to describe the behavior of a crystal in the field $E_\alpha(\mathbf{r})$, we will use the model of a continuous isotropic dynamic medium formed by a uniform distribution of positive and negative charges. In this connection, we will associate the mechanism of polarization or deformation of the medium with an arbitrary displacement of crystal charges, leading to a nonhomogeneous distribution. Introducing the polarization vector $\mathbf{P}(\mathbf{r}, t)$ characterizing the displacement of ne charges and specifying the density $\rho = m/\Omega$ of the medium, where m is the mass of an atomic cell of volume Ω, as well as the coupling constant χ, we can describe the motion of a linearly elastic charged medium under the action of an external field by the Lagrangian function of the form

$$L = \frac{1}{2}\sum_{\alpha = x,y,z}\int_0^{L_\alpha^3}\left\{\frac{\rho}{(ne)^2}\left[\frac{\partial P_\alpha(\mathbf{r}, t)}{\partial t}\right]^2 - \chi[\nabla P_\alpha(\mathbf{r}, t)]^2\right\}d\mathbf{r} + \sum_{\alpha = x,y,z}\int_0^{L_\alpha^3} E_\alpha(\mathbf{r}, t)P_\alpha(\mathbf{r}, t)d\mathbf{r}, \quad (3)$$

where L_α is the crystal length in the direction $\alpha = x, y, z$. The quadratic form for the potential energy appearing in the function L presumes the small value of polarization of a point of the medium relative to the charge density in a unit cell. Formally, this is associated with small displacements $\Delta q \approx \xi\Omega^{1/3}$ of the medium relative to the linear dimension $\Omega^{1/3}$ of an atomic cell. In this case, the polarization of the medium is $P \approx ne\Delta q \approx ne\Omega^{1/3}\xi$, where the small parameter $\xi \ll 1$. Thus, the Lagrangian function (3) presumes a phenomenological description of the variation in the polarization of the electron–ion system, which is associated with the action of the extraneous electrostatic field.

For the quantization of oscillations of the continuum, we use the Legendre transformation to go over from the function L to the Hamiltonian function

$$H = \frac{1}{2}\sum_{\alpha = x,y,z}\int_0^{L_\alpha^3}\left\{\frac{(ne)^2}{\rho}M_\alpha^2(\mathbf{r}, t) + \chi[\nabla P_\alpha(\mathbf{r}, t)]^2\right\}d\mathbf{r} - \sum_{\alpha = x,y,z}\int_0^{L_\alpha^3} E_\alpha(\mathbf{r}, t)P_\alpha(\mathbf{r}, t)d\mathbf{r}. \quad (4)$$

Defining the canonically conjugate variables in the form of expansions in plane monochromatic waves, we transform the Hamiltonian function (4) containing the force nonuniformity in the form (1), to the function

$$H = \sum_{\mathbf{k}\alpha} \frac{\hbar\omega_k}{2}(a_{\mathbf{k}\alpha}a^*_{\mathbf{k}\alpha} + a^*_{\mathbf{k}\alpha}a_{\mathbf{k}\alpha}) + \sum_{\mathbf{k}\alpha} \hbar\omega_{\mathbf{k}}[\gamma_{\mathbf{k}\alpha}(t)a^*_{\mathbf{k}\alpha} + \gamma^*_{\mathbf{k}\alpha}(t)a^*_{\mathbf{k}\alpha}] \quad (5)$$

in which the amplitudes

$$\gamma_{\mathbf{k}\alpha} = \left(\frac{1}{2M\hbar\omega_{\mathbf{k}}}\right)^{1/2}(M\omega_{\mathbf{k}}q_{0\mathbf{k}\alpha} + ip_{0\mathbf{k}\alpha})^{\exp(-i\omega_{\mathbf{k}}t)},$$

$$\gamma^*_{\mathbf{k}\alpha} = \left(\frac{1}{2M\hbar\omega_{\mathbf{k}}}\right)^{1/2}(M\omega_{\mathbf{k}}q_{0\mathbf{k}\alpha} - ip_{0\mathbf{k}\alpha})^{\exp(i\omega_{\mathbf{k}}t)}$$

are expressed in terms of the force variables

$$q_{0\mathbf{k}\alpha} = -neE_{1\alpha}/M\omega^2_{\mathbf{k}}, \quad p_{0\mathbf{k}\alpha} = -neE_{2\alpha}\mathbf{kR}/\omega_{\mathbf{k}},$$

the crystal mass $M = \rho V$, and the frequency of oscillations described by the dispersion equation

$$\nu^2\mathbf{k}^2 - \omega^2(\mathbf{k}) = 0,$$

where $\nu = ne(\chi/\rho)^{1/2}$ is the velocity of propagation of elastic displacements of the medium; $k_\alpha = 2\pi n_\alpha/L_\alpha$ is the wave vector component; and n_α is an integer.

The standard quantization procedure for Hamiltonian (5) leads to the total energy operator

$$\hat{H} = \sum_{\mathbf{k}\alpha}\hbar\omega_{\mathbf{k}}\left(\hat{\hat{b}}_{\mathbf{k}\alpha}\hat{\hat{b}}^+_{\mathbf{k}\alpha} + \frac{1}{2}\right) - \sum_{\mathbf{k}\alpha}\left(\frac{M\omega^2_{\mathbf{k}}q^2_{0\mathbf{k}\alpha}}{2} + \frac{p^2_{0\mathbf{k}\alpha}}{2M}\right), \quad (6)$$

where the first term describes the variation of the energy of normal modes of the harmonically vibrating lattice in the second-quantization representation. The application of permutation relations for the renormalized operators $\hat{\hat{b}}_{\mathbf{k}\alpha}$ and $\hat{\hat{b}}^+_{\mathbf{k}\alpha}$ makes it possible to construct the eigenstates and to find the energy eigenvalues

$$\varepsilon_{\mathbf{k}\alpha}(\omega, \theta) = \varepsilon_{f\alpha}(\omega) + \varepsilon_0(\omega) + \varepsilon_{1\alpha}(\omega) + \varepsilon_{2\alpha}(\theta), \quad (7)$$

where $\varepsilon_{f\alpha} = \hbar\omega_{\mathbf{k}}n_{\mathbf{k}\alpha}$ is the energy of $n_{\mathbf{k}\alpha}$ phonons in a state with the wave vector $\mathbf{k}$; $\varepsilon_0 = \hbar\omega_{\mathbf{k}}/2$ is the energy of the kth zero-point vibration,

$$\varepsilon_{1\alpha} = -n^2e^2E^2_{1\alpha}/2M\omega^2_{\mathbf{k}}$$

is the Fourier component of the energy of monopole deformation of the crystal and

$$\varepsilon_{2\alpha} = -n^2e^2E^2_{2\alpha}R^2\cos^2(\theta/2M\nu^2)$$

is the same for dipole deformation. While calculating $\varepsilon_{2\alpha}$ we took into account the dispersion equation and introduced the polar angle θ between the directions of the plane wave vector $\mathbf{k}$ and the arm $\mathbf{R}$ of the dipole force.

The second term of operator (6) is a numerical function defining the displacements of the phonon energy spectrum depending on the peculiarities of the force nonuniformity region formed by the applied field. A distinguishing feature of this function is that, as a result of application of the multipole expansion (1), it acquired a form that was similar to the Hamiltonian function of the superposition of classical harmonic oscillators. The condition that the displacements and momenta of the points of the medium are real-valued, which was imposed at the beginning with the help of a superposition of waves, requires positive definiteness of the squares of displacements and momenta; the functions $-q^2_{0\mathbf{k}\alpha}$ and $--p^2_{0\mathbf{k}\omega}$ do not satisfy this requirement. It is possible to find a transformation for which the given numerical function assumes the form of a superposition of harmonic oscillators. This will subsequently help in finding new peculiarities of the collective behavior of a deformed charged medium.

The above-mentioned transformation has the form

$$q^2_{\mathbf{k}\alpha} = a\hbar/M\omega_{\mathbf{k}} - n^2e^2E^2_{1\alpha}/M^2\omega^2_{\mathbf{k}},$$
$$p^2_{\mathbf{k}\alpha} = b\hbar\omega_{\mathbf{k}}M - n^2e^2E^2_{2\alpha}(\mathbf{kR})^2/\omega^2_{\mathbf{k}}, \quad (8)$$

where a and b are indeterminate constant coefficients satisfying the condition $a + b = 1$. Using relations (8), we transform (6) to the operator

$$\hat{H} = \sum_{\mathbf{k}\alpha}\hbar\omega_{\mathbf{k}}\hat{\hat{b}}_{\mathbf{k}\alpha}\hat{\hat{b}}^+_{\mathbf{k}\alpha} + \sum_{\mathbf{k}\alpha}\left(\frac{M\omega^2_{\mathbf{k}}q^2_{\mathbf{k}\alpha}}{2} + \frac{p^2_{0\mathbf{k}\alpha}}{2M}\right), \quad (9)$$

in which the second sum has the form of a superposition of noninteracting classical oscillators.

Transformations (8) do not change the eigenvalue spectrum (7) and hence, do not lead to any new results from the phonon problem view point. Nevertheless, the appearance in the Hamiltonian of a numerical function having the form of a sum over wave vectors and describing the system of oscillators make it possible to obtain a more comprehensive physical interpretation of the second term in Hamiltonian (9) than the well-known displacement of the phonon spectrum. The essence of this interpretation is that the oscillators presented by this term might correspond to new quantum states of the crystal lattice deformed by a static force field.

2. QUANTIZED DEFORMATION MODES IN A DISTORTED LATTICE

The second sum in operator (9) corresponds to the difference of the Fourier components of the energy of zero-point vibrations of the crystal and to the energy of formation of a force nonuniformity. The coordinates $q_{\mathbf{k}\alpha}$ and the momenta $p_{\mathbf{k}\alpha}$ determine the actual displace-

ments and momenta of points of the medium only if we take into consideration the zero-point energy of the crystal vibrations, which is of quantum origin. For $E_{1\alpha} = E_{2\alpha} = 0$, the product $p_{\mathbf{k}\alpha}k_{\mathbf{k}\alpha} = \hbar/2$ satisfies the uncertainty relation according to which the motion of the points of the medium for the **k**th vibrational mode cannot have definite values of the coordinate and the momentum simultaneously. This means that the stationary states of the force nonuniformity are basically related to the collective motion of the medium. This relation can be found as follows. Instead of the standard classification of the spectrum of operator (9) in the eigenvalues of the operators $b_{\mathbf{k}\alpha}$ and $b^{+}_{\mathbf{k}\alpha}$, we will proceed from the sum over wave vectors. Let us try to interpret each term of this sum as an energy eigenvalue not of the phonon Hamiltonian (9) describing excited states of the Bose type, but of another Hamiltonian. A method of correct construction of such a Hamiltonian can be established only after appropriate theoretical and experimental investigations. Proceeding from the eigenvalue spectrum (7) and assuming that the **k**th oscillation corresponds to the momentum $\mathbf{p} = \hbar\mathbf{k}$, we obtain a new spectrum

$$\varepsilon_\alpha(p, \theta) = \varepsilon_{f\alpha}(p) + \varepsilon_0(p) + \varepsilon_{1\alpha}(p) + \varepsilon_{2\alpha}(\theta), \quad (10)$$

where $\varepsilon_{f\alpha} = \nu p n_\alpha$ is the energy of n_α phonons; $\varepsilon_0 = \nu p/2$ is the zero-point energy; and $\varepsilon_{1\alpha} = -\alpha\nu\, p_{0\alpha}^3/2p^2$ is the momentum component of the energy of monopole deformation of the crystal, which is a function of the limiting momentum

$$p_{0\alpha} = (\hbar^2 n^2 e^2 E_{1\alpha}^2/aM\nu^3)^{1/3},$$

defined by the conditions of real-valuedness of the displacement field $q_{\mathbf{k}\alpha}^2 \geq 0$.

Spectrum (10) presumes the independence of the dipole term $\varepsilon_{2\alpha}$ of the momentum. Dipole steady-state displacements of ions in the crystal are manifested in the displacement of the phonon band without its distortion, which agrees with the known results [1].

The peculiarities in the phonon displacement by a monopole source can be determined if we assume that $a = 1$, which eliminates the dipole source, and express $p_{0\alpha}$ in terms of the crystal volume V, the number of atoms $N = V/\Omega$, and the Debye momentum $p_D = \pi\hbar/\Omega^{1/3}$. This gives $p_{0\alpha} = p_D(m_\alpha/N)^{1/3}$, where

$$m_\alpha = E_{1\alpha}^2/\pi^3\hbar\nu\chi \quad (11)$$

is the dimensionless quantity depending on the external force and the parameters of the medium. According to the definition of $p_{0\alpha}$, the quantity m_α by nature must be proportional to the number of monopole-shifted ions and must determine the volume of the nonuniformity region.

The displacements of the bottom of the phonon band can be found from the condition $n_\alpha = 0$. The region of monopole displacements of ions in this case is presented by a quasi-continuous set of harmonics with the wavelengths

$$\lambda < \lambda_{0\alpha} = \lambda_D(N/m_\alpha)^{1/3},$$

where α_D is the Debye wavelength. These are zero-point oscillations, i.e., the set of harmonics determined by spectrum (10), which form the field of steady-state variation of the charge density of the medium. The value of m_α determines the number of half-waves $\lambda_{0\alpha}$ that can be accommodated in the crystal length $L = (\Omega N)^{1/3}$. As the value of $E_{1\alpha}$ increases, the number of ions involved in the displacements of lattice sites becomes larger, while the wavelength $\lambda_{0\alpha}$ of the threshold wave decreases, which corresponds to the cutoff of long-wave harmonics.

The above arguments prove that for $n_\alpha = 0$, the function (10) describes states of the crystal with energies $\varepsilon_\alpha(p < p_{0\alpha}) < 0$, which characterize the stationary deformation field of the medium, as well as energies $\varepsilon_\alpha(p < p_{0\alpha}) > 0$, which may correspond to its collective motion. The values of $\varepsilon_\alpha(p > p_{0\alpha})$ can be described by the positive-definite component of spectrum (10),

$$\tilde{\varepsilon}_a(p) = \nu\left|p - m_\alpha p_D^3/2Np^2\right|, \quad (12)$$

which permits the emergence of excited states. The inclusion of phonons, which corresponds to the condition $n_\alpha \geq 1$, displaces the point $\tilde{p}_{0\alpha} = p_{0\alpha}/(2n_\alpha)^{1/3}$ defined by the condition $\tilde{\varepsilon}_\alpha(\tilde{p}_{0\alpha}) = 0$, towards smaller momenta. The condition $q_{\mathbf{k}\alpha}^2 \geq 0$ can be satisfied again for a certain occupancy of phonon states. This must lead to the emergence of a new (nonphonon) type of collective motion of the atomic lattice, whose excited states can be constructed by using the definition of $\tilde{p}_{0\alpha}$. For example, the wavelength of a new excitation for the excited phonon state $n_\alpha = 1$ is

$$\lambda_{\alpha l} = \lambda_D(2Nl/m_\alpha)^{1/3},$$

where $l = 1, 2, \ldots, m_\alpha/2$ are the integers whose upper value is defined by the condition $\lambda_{\alpha l_m}^3 = \lambda_L^2 = N\lambda_D^3$. It follows that the value of m_α must determine the number of vibrational states $\lambda_{\alpha l}$. Indeed, the definition of the boundary momentum $\tilde{p}_{0\alpha}$ leads to the expression

$$m_\alpha = 2\tilde{V}_{0\alpha}V/(2\pi\hbar)^3, \quad (13)$$

where $\tilde{V}_{0\alpha} = 8p_{0\alpha}^3$ is the volume of the cubic momentum space (due to quantization in the well), including the modes belonging to the admissible region $q_{\mathbf{k}\alpha}^2 \geq 0$ (the coefficient 8 appeared from the definition of momenta in spherical coordinates).

Relation (13) defines the number of states of particles with the Fermi type of energy level filling [18]. In

other words, in a crystal with a preset value of m_α, modes with groups of atomic states differing in number and direction have different energy values from the quasi-continuous set $\varepsilon(p)$, and hence, a deformed crystal cannot have two identical groups of displaced atomic states.

The number of states of the m_α mode must depend on the number N_α of monopole-displaced atoms in the region of force nonuniformity of the crystal. The computation of the energies of excited states for $\tilde{\varepsilon}_\alpha(p \le \tilde{p}_{0\alpha})$ and $\tilde{\varepsilon}_\alpha(p \ge \tilde{p}_{0\alpha})$ gives

$$\tilde{\varepsilon}_D = \varepsilon_D(1 - m_\alpha)/2N, \quad \tilde{\varepsilon}_L = \varepsilon_L(m_\alpha/2 - 1), \quad (14)$$

respectively. For $N_\alpha = m_\alpha/2 = 1$ and $N_\alpha = m_\alpha/2 = N$, which corresponds either to the absence of the ionic displacement field or to a complete covering of the crystal by the deformation field, the number of states of the m_α mode varies from 2 to $2N_\alpha$, leading to the values $\tilde{\varepsilon}_V = 0$ and $\tilde{\varepsilon}_A = 0$. This confirms the definition of the quantity m_α as the total number of various states and the quantity $N_\alpha = m_\alpha/2$ as the number of monopole-displaced ions.

Thus, the quantity $\varepsilon_F = 0$ plays the role of the Fermi energy of deformed oscillators. Deformed states with a negative energy must be manifested in experiments in the form of bounded regions of static displacements of ions from the points of a regular lattice. As the monopole force changes in the range

$$ne\sqrt{2\pi^3\hbar\nu\chi N_\alpha} \le F_{1\alpha} \le F_{\alpha c},$$

where $F_{\alpha c}$ is the upper critical value of the force, corresponding to the rupture of an atomic bond, the structure of the deformation field undergoes jumplike changes depending on N_α, reflecting the fact that the change in the number of displaced ions upon an increase in $F_{1\alpha}$ is of a discrete nature. In this case, the monopole force $F_{1\alpha}$ loses the initial representation in the form of a continuous quantity and acquires the form of a discrete quantity. Figure 1 shows the $F_\alpha(N_\alpha)$ dependence in a typical case. The jumps in the force indicate that, for arbitrary force interactions in discrete media, it is expedient to determine the value of force only to within the difference in the force amplitudes before and after a transition of an ion to a displaced state. The amplitude of the jumps decreases with increasing the number N_α of displaced ions. Assuming that the value of N_α changes by unity and defining the amplitude of the corresponding jump in force by the difference

$$\Delta F_{1\alpha}(N_\alpha - 1) = F_{1\alpha}(N_\alpha) - F_{1\alpha}(N_\alpha - 1),$$

we obtain

$$\Delta F_{1\alpha} = ne\sqrt{2\pi^3\hbar\nu\chi}(\sqrt{N_\alpha} - \sqrt{N_\alpha - 1}). \quad (15)$$

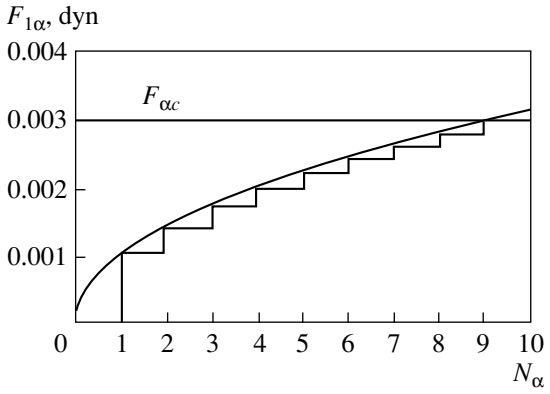

Fig. 1. Dependence of the amplitude of the monopole force on the number of displaced ions in the deformed region of the crystal. The quantity $F_{\alpha c}$ shows the upper critical value of the force corresponding to the rupture of an atomic bond.

For example, by assuming that the deformation region is formed by the number of ions N_α equal to 10, 10^3, and 10^5, we can estimate the amplitude of the last jump $\Delta F_{1\alpha}(N_\alpha)$ of the force relative to the force amplitude $F_{1\alpha}(1)$, bringing only one ion to a displaced state. The values of the force constants $n^2e^2\chi \approx 10^{12}$ dyn cm^{-2} and density $\rho \approx 10$ g/cm^3 typical of solids lead to the estimates

$$\Delta F_{1\alpha}(10) \approx 10^{-1}F_{1\alpha}(1), \quad \Delta F_{1\alpha}(10^3) \equiv 10^{-2}F_{1\alpha}(1),$$
$$\Delta F_{1\alpha}(10^5) \approx 10^{-3}F_{1\alpha}(1).$$

Thus, the discrete nature of force interaction becomes less and less pronounced with an increasing number of ions in the deformed region of the crystal. This agrees with the generally accepted ideas concerning the pointlike deformation of the crystal, and in particular, with the assumption that ionic displacement at large distances from the center of dipole perturbation must satisfy the continual limit [1].

The range of spectrum (12) is determined by the boundary values of the momenta p_L and p_D, and therefore, depends on the size of the crystal and an atomic cell. The nature of variation of the spectrum is determined by the boundary momentum $\tilde{p}_{0\alpha}$, and therefore, by the magnitude of the external force. Figure 2 shows possible versions of spectrum (12) for various numbers N of atoms in the crystal for the same number N_α of atoms in its deformed region. The curves in Figs. 2a–2f illustrate the emergence and vanishing of the spectrum of excited states upon a change in N from $N > N_\alpha^3$ to $N < N_\alpha^3$.

If we assume the parity of quasiparticles with a given energy, i.e., if we put that the number of particles is equal to the number of antiparticles, Eq. (14) implies that the momentum p_D on the branch of the particle spectrum must correspond to the momentum p_V on the

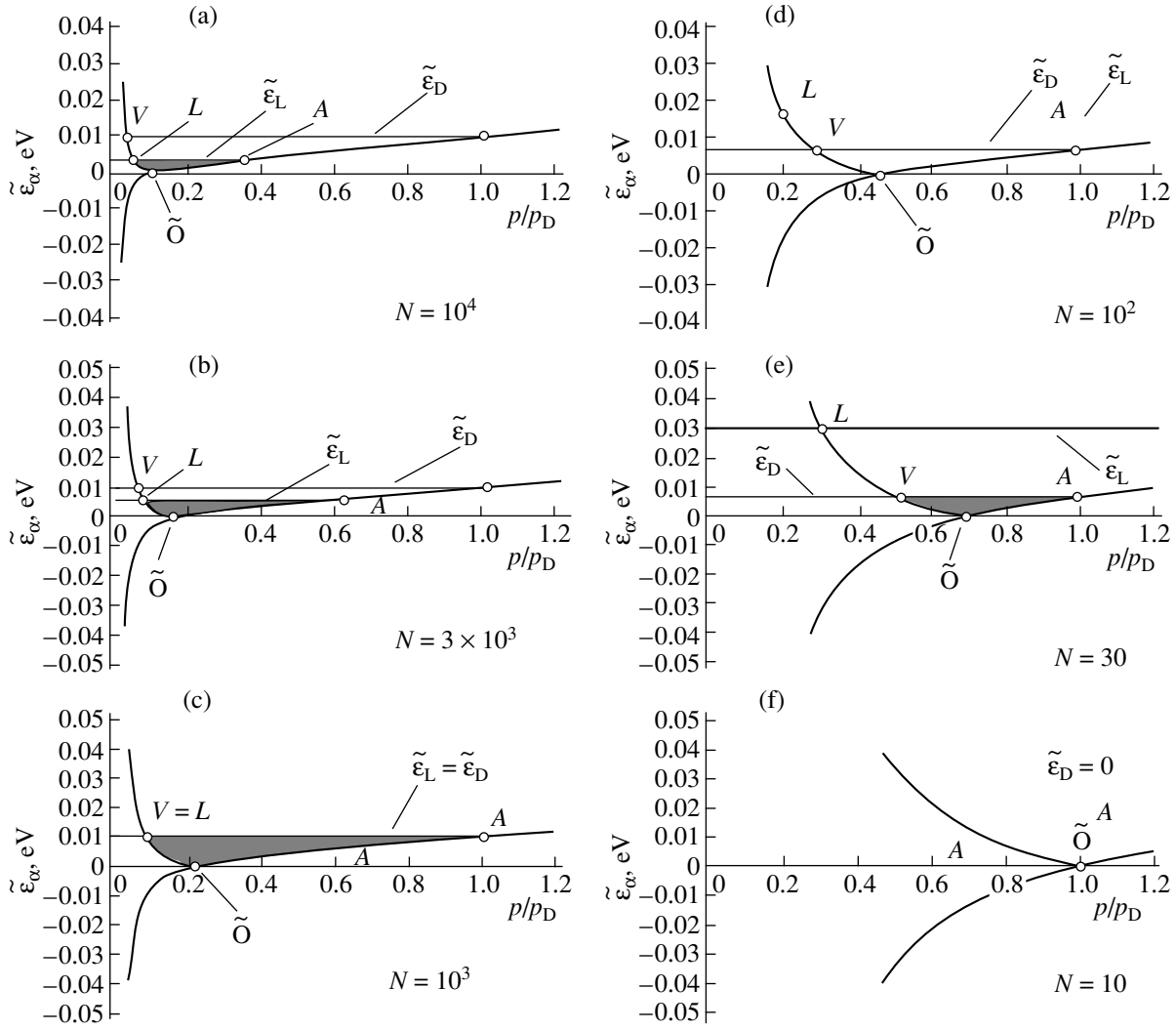

Fig. 2. Spectra of vibrational states of a deformed nanocrystal with the total number of ions N = var; the number of ion $N_\alpha = 10$ in the deformed region; and the Debye energy $\varepsilon_D = 10^{-2}$ eV. The shaded regions of the spectra show excited states. The characteristic points of the spectra correspond to the values of $L = p_L/p_D$, $V = p_V/p_D$, $A = p_A/p_D$; and $\tilde{O} = \tilde{p}_{0\alpha}/p_D$. As the crystal size decreases, i.e., as the point $\tilde{O}$ shifts to the right, the energy of the uppermost excited state is determined by the value of $\tilde{\varepsilon}_L$ which increases (a, b) and attains its peak value equal to $\tilde{\varepsilon}_D$ (c). As the point $\tilde{O}$ is further displaced to the right, the energy of the uppermost excited state is determined by the value of $\tilde{\varepsilon}_D$ which decreases (d, e) and vanishes (f) for $\tilde{O} = 1$, which corresponds to the disappearance of excited states.

quasiparticle branch, which is a solution of the cubic equation

$$p_V^3 + \left(1 - \frac{N_\alpha}{N}\right) p_D p_V^2 - \frac{N_\alpha}{N} p_D^3 = 0.$$

For $p_A < p_D$, which corresponds to the condition $N > N_\alpha^3$ (see Fig. 2b), the uppermost excited state of a mode is determined by the value of $\tilde{\varepsilon}_L$, while for $p_V > p_L$ ($N < N_\alpha^3$, Figs. 2d and 2e), it is determined by the value of $\tilde{\varepsilon}_D$. For $p_V = p_L$ and $p_A = p_D$ (see Fig. 2c), the quasiparticle energy becomes equal to the energy of a Debye phonon ($\tilde{\varepsilon}_D = \tilde{\varepsilon}_L \approx \varepsilon_D$, and, according to Eq. (14), the number of particle–antiparticle pairs (the number of monopole-displaced ions) is given by

$$N_\alpha = (N + N^{2/3})/(1 + N^{2/3}) \approx N^{1/3}.$$

For $\tilde{p}_{0\alpha} = p_D$ (Fig. 2f), when all the atoms of the crystal are involved in steady-state displacements from the points of the perfect lattice, the energy of the excited

state $\tilde{\varepsilon}_D \longrightarrow 0$, i.e., deformation-induced excitations do not emerge in a completely distorted lattice.

Deformation-induced excitations in a distorted lattice can be sought in two directions. One of them is associated with the attempt to detect a mode of natural origin, i.e., natural deformation-induced vibrations, e.g., in individual crystallites of nanocrystalline materials. The other direction is dictated by the possibility to obtain an artificially generated deformation mode, e.g., with the help of an atomic-force microscope. In any case, the size of the crystal or of its individual crystallite in which deformation-induced vibrations can be generated must be in the limits

$$(N_\alpha)\Omega^{1/3} < L < N_\alpha\Omega^{1/3}.$$

While choosing an external radiation with a wavelength $\lambda_D < \lambda < N_\alpha^{2/3}\lambda_D$, the mode should be manifested in the absorption in the emission spectrum.

However, the model (3) used in the above analysis does not allow us to judge on the charge state of nanocrystal vibrations under the action of an external static force or on the charge structure of the corresponding quasiparticle excitations. Consequently, the type of external radiation remains indeterminate. Nevertheless, by assuming a certain type of atomic interactions in a nanocrystal, we can envisage the corresponding structure of excitations. For example, for small metallic particles under the conditions when longitudinal branches of ionic plasma oscillations become acoustic due to electron shielding, excitations must also be of the acoustic type. In ionic crystals in which the displacements of ions from their equilibrium positions lead to the emergence of electric dipole moments, these excitations can be in the form of electric multipoles. The same applies to crystals with a strongly manifested nonadiabaticity of oscillations in the electron–ion system, e.g., in narrow-band semiconductors or in substances with strong electron correlations. In this case, the retardation of electron coordinates during ionic vibrations, and therefore, for oscillations and translation of displaced ionic states over the crystal, might also generate a certain charge structure of a deformation-induced excitation. Consequently, while selecting the external radiation, we must bear in mind that deformation-induced excitations of acoustic origin must effectively interact with superhyperacoustic elastic vibrations, while polarization-induced excitation of the multipole type must interact with an external electromagnetic field.

The above analysis suggests the possibility of creating solid-state elements for the storage and transmission of information on a basically new foundation. The Fermi nature of excitations in the distorted lattice of a nanocrystal makes it possible to control the dynamics of acoustic or electric multipoles with the help of an external elastic or electromagnetic field and their gradients. This forms the basis for constructing closed circuits conducting ordered force actions or electric multipole moments, and therefore, permits the development of devices and appliances of the new type.

ACKNOWLEDGMENTS

The author is grateful to A.G. Lyapin, O.A. Kazakov, A.E. Krasnopol'skiĭ, and G.D. Kuznetsov for encouragement and for numerous critical remarks concerning the manuscript.

REFERENCES

1. A. M. Stoneham, in *Theory of Defects in Solids: the Electronic Structure of Defects in Insulators and Semiconductors* (Clarendon, Oxford, 1975; Mir, Moscow, 1978), Vol. 1.
2. G. Leibfried and N. Brauer, *Point Defects in Metals. Introduction to the Theory* (Springer, Heidelberg, 1978; Mir, Moscow, 1981).
3. H. Bottger, *Principles of the Theory of Lattice Dynamics* (Physik, Weinheim, 1983; Mir, Moscow, 1986).
4. É. L. Nagaev, Usp. Fiz. Nauk **162** (9), 49 (1992) [Sov. Phys. Usp. **35**, 747 (1992)].
5. A. I. Gusev, Usp. Fiz. Nauk **168** (1), 55 (1998) [Phys. Usp. **41**, 49 (1998)].
6. S. Iijima and T. Ichihashi, Phys. Rev. Lett. **56** (6), 616 (1986).
7. D. M. Farkas, T. Yamashita, and J. Perkins, Acta Metall. Mater. **38** (10), 1883 (1990).
8. R. Z. Valiev, A. V. Korznikov, and R. R. Mulyukov, Mater. Sci. Eng., A **168**, 141 (1993).
9. A. A. Rempel and A. I. Gusev, Phys. Status Solidi B **196** (1), 251 (1996).
10. W. Wunderlich, Y. Ishida, and R. Maurer, Scr. Metall. Mater. **24** (2), 403 (1990).
11. R. Z. Valiev, N. A. Krasilnikov, and N. K. Tsenev, Mater. Sci. Eng., A **137**, 35 (1991).
12. R. W. Siegel and G. E. Fougere, Nanostruct. Mater. **6** (1–4), 205 (1995).
13. R. R. Mulyukov *et al.*, Nanostruct. Mater. **6** (5–8), 577 (1995).
14. H. Kanzaki, J. Phys. Chem. Solids **2**, 24 (1957).
15. V. V. Meshcheryakov, Zh. Éksp. Teor. Fiz. **111** (5), 1845 (1997) [JETP **84**, 1010 (1997)].
16. V. V. Meshcheryakov, Fiz. Tverd. Tela (St. Petersburg) **37** (1), 43 (1995) [Phys. Solid State **37**, 20 (1995)].
17. V. V. Meshcheryakov, G. D. Kuznetsov, and A. A. Yuldashev, Zh. Éksp. Teor. Fiz. **116** (1), 157 (1999) [JETP **89**, 86 (1999)].
18. A. A. Abrikosov, A. P. Gor'kov, and I. E. Dzyaloshinskiĭ, *Methods of Quantum Field Theory in Statistical Physics* (Fizmatgiz, Moscow, 1962; Prentice-Hall, Englewood Cliffs, 1963).

Translated by N. Wadhwa

Physics of the Solid State, Vol. 42, No. 9, 2000, pp. 1756–1765. From Fizika Tverdogo Tela, Vol. 42, No. 9, 2000, pp. 1707–1715.

LOW-DIMENSIONAL SYSTEMS AND SURFACE PHYSICS

Exciton Polaritons in Quantum-Dot Photonic Crystals[1]

E. L. Ivchenko*, Y. Fu, and M. Willander****

** Ioffe Physicotechnical Institute, Russian Academy of Sciences, Politekhnicheskaya ul. 26, St. Petersburg, 194021 Russia*

*** Laboratory of Physical Electronics and Photonics, MC2, Department of Physics, University of Gothenburg and Chalmers University of Technology, Fysikgränd 3, S-412 96, Gothenburg, Sweden*

Received March 2, 2000

Abstract—We present a theory of the photonic band structure of three-dimensional arrays of quantum dots (QDs). A system of Maxwell's and material equations is solved and the dispersion equation for exciton–polaritons is derived making allowance for a nonlocal dielectric response of quasi-zero-dimensional excitons confined in QDs. The reflection and transmission coefficients are calculated for a single plane, a pair of planes and a stack of equidistant planes of QDs. Two different approaches are proposed to perform a calculation. One of them is based on recurrent equations relating the reflection coefficients for $N + 1$ and N planes, while in the other approach the Bloch solutions for an infinite QD lattice are used. *© 2000 MAIK "Nauka/Interperiodica".*

I. INTRODUCTION

In bulk crystals, a photon and an exciton mix in the dispersion-crossover region, losing their identity in a combined quasi-particle called the exciton–polariton. Exciton–polaritons were intensively studied in the 1960s and 1970s, their manifestation in various optical phenomena, including light reflection and transmission, photoluminescence and resonant light scattering, are well established and documented (see, e.g., the contributed volume [1] and references therein). Renewed interest and recent important developments in this field [2–7] were stimulated by technological achievements in the fabrication of high-quality multi-layered heterostructures, multiple quantum wells (MQWs) and superlattices (SLs). Moreover, the concept of exciton–polariton has undergone a substantial modification, in particular with respect to long-period MQW structures containing a finite number of wells [8–18]. The present paper outlines the framework for similar studies of structures containing regular arrays of quantum dots (QDs). The shift from long-period MQWs to 3D lattices of quantum dots allows to bridge the gap between multilayered structures and photonic crystals. The latter are defined as periodic dielectric structures with the period being comparable to the wavelength of the visible-range electromagnetic waves. In the simplest realization, a photonic crystal is thought of as a periodic lattice of dielectric spheres of dielectric constant ε_a embedded in a uniform dielectric background ε_b (see reviews [19, 20]). Other potential realizations are a three-dimensional (3D) lattice of resonant two-level atoms [21] or semiconductor microcrystals embedded into the pores of periodic porous materials [22] (see also [23]).

[1] This article was submitted by the authors in English.

Here, we study the photonic (or, more precisely, exciton–polaritonic) band structure of 3D periodic arrays of QDs or simply QD lattices and the light reflection from a finite number of QD planes. The excitonic states in a single QD are quasi-zero-dimensional due to the quantum-confinement effect and we consider a narrow frequency region near a particular exciton size-quantization level. In the resonant frequency region, the dielectric response to an electromagnetic wave is nonlocal and the main goal of the work is to develop a theory which makes allowance for such a nonlocality.

In Section II, we derive the dispersion equation for exciton–polaritons in a 3D QD lattice. The reflection from and transmission through a single plane containing square QD lattice are considered in Section III. The relation between the exciton–polariton dispersion equation and single-plane reflection and transmission coefficients is established in Section IV. The reflection from a pair of QD planes and from a stack of QD planes is considered in Sections V and VI, respectively. The derived theory can also be used for the description of nuclear resonant scattering of γ quanta by artificial nuclear multilayers (see [24–26]).

II. BLOCH SOLUTIONS IN THREE-DIMENSIONAL QUANTUM-DOT LATTICES

We start from the Maxwell equations

$$\Delta\mathbf{E} - \mathrm{grad}\,\mathrm{div}\mathbf{E} = -\left(\frac{\omega}{c}\right)^2\mathbf{D}, \qquad \mathrm{div}\mathbf{D} = 0 \tag{1}$$

for the electric field $\mathbf{E}$ and the displacement vector $\mathbf{D}$. The nonlocal material equation relating $\mathbf{D}$ and $\mathbf{E}$ is

1063-7834/00/4209-1756$20.00 © 2000 MAIK "Nauka/Interperiodica"

taken in the form (see [27])

$$\mathbf{D}(\mathbf{r}) = \varepsilon_b \mathbf{E}(\mathbf{r}) + 4\pi \mathbf{P}_{exc}(\mathbf{r}), \quad (2)$$

$$4\pi \mathbf{P}_{exc}(\mathbf{r}) = T(\omega) \sum_{\mathbf{a}} \Phi_{\mathbf{a}}(\mathbf{r}) \int \Phi_{\mathbf{a}}(\mathbf{r}') \mathbf{E}(\mathbf{r}') d\mathbf{r}'. \quad (3)$$

Here, $\mathbf{a}$ are the lattice translation vectors enumerating quantum dots, $\Phi_{\mathbf{a}}(\mathbf{r}) = \Phi_0(\mathbf{r} - \mathbf{a})$ is the envelope function $\Psi_{exc}(\mathbf{r}_e - \mathbf{a}, \mathbf{r}_h - \mathbf{a})$ of an exciton excited in the $\mathbf{a}$th QD at coinciding electron and hole coordinates: $\Phi_{\mathbf{a}}(\mathbf{r}) = \Psi_{exc,\,\mathbf{a}}(\mathbf{r}, \mathbf{r})$. The other notations are

$$T(\omega) = 2\pi \frac{\varepsilon_b \omega_{LT} \omega_0 a_B^3}{\omega_0^2 - \omega^2} \approx \frac{\varepsilon_b \omega_{LT} \pi a_B^3}{\omega_0 - \omega}, \quad (4)$$

ω_{LT} and a_B are the exciton longitudinal–transverse splitting and Bohr radius, respectively, in the corresponding bulk semiconductor; ω_0 is the QD-exciton resonance frequency; and ε_b is the background dielectric constant, which is assumed to coincide with the dielectric constant of the barrier material. In the following, we neglect the overlap of exciton envelope functions $\Psi_{\mathbf{a}}$ and $\Psi_{\mathbf{a}'}$ with $\mathbf{a} \neq \mathbf{a}'$, so that excitons excited in different dots are assumed to be coupled only via electromagnetic field.

It follows from Eq. (2) that $\mathrm{div}\mathbf{E} = -(4\pi/\varepsilon_b)\mathrm{div}\mathbf{P}_{exc}$, which allows one to rewrite the first of Eqs. (1) as

$$\Delta \mathbf{E}(\mathbf{r}) + k^2 \mathbf{E}(\mathbf{r}) = -4\pi k_0^2 (1 + k^2 \mathrm{graddiv}) \mathbf{P}_{exc}(\mathbf{r}), \quad (5)$$

where $k_0 = \omega/c$, $k = k_0 n_b = \omega n_b/c$, and $n_b = \sqrt{\varepsilon_b}$. We seek for Bloch-like solutions of Eq. (8) satisfying the translational symmetry

$$\begin{aligned} \mathbf{E}_{\mathbf{q}}(\mathbf{r} + \mathbf{a}) &= \exp(i\mathbf{q}\mathbf{a}) \mathbf{E}_{\mathbf{q}}(\mathbf{r}), \\ \mathbf{P}_{exc,\,\mathbf{q}}(\mathbf{r} + \mathbf{a}) &= \exp(i\mathbf{q}\mathbf{a}) \mathbf{P}_{exc,\,\mathbf{q}}(\mathbf{r}), \end{aligned} \quad (6)$$

where the wave vector $\mathbf{q}$ is defined within the first Brillouin zone. The exciton–polariton dispersion $\omega(\mathbf{q})$ can be shown to satisfy the equation

$$\mathrm{Det} \| \delta_{\alpha\beta} - R_{\alpha\beta}(\omega, \mathbf{q}) \| = 0, \quad (7)$$

where $\alpha, \beta = x, y, z$; $\delta_{\alpha\beta}$ is the Kronecker symbol; and, for QD lattices,

$$R_{\alpha\beta}(\omega, \mathbf{q}) = \frac{k_0^2 T(\omega)}{V_0} \sum_{\mathbf{g}} \frac{I_{\mathbf{q}+\mathbf{g}}^2 S_{\alpha\beta}(\mathbf{q} + \mathbf{g})}{(\mathbf{q} + \mathbf{g})^2 - \mathbf{k}^2}, \quad (8)$$

$$I_{\mathbf{Q}} = \int \Phi_0(\mathbf{r}) e^{i\mathbf{Q}\mathbf{r}} d\mathbf{r}, \quad S_{\alpha\beta} = \delta_{\alpha\beta} - \frac{Q_\alpha Q_\beta}{k^2}, \quad (9)$$

$\mathbf{g}$ are the reciprocal lattice vectors and $V_0(\mathbf{r})$ is the volume of the lattice primitive cell.

Equations (7) and (8) can be derived by using the two equivalent approaches: (a) to express the exciton dielectric polarization $\Phi_0(\mathbf{r})$ in terms of the electric field, $\mathbf{E}(\mathbf{r})$, and find solutions to the wave equation for $\mathbf{E}(\mathbf{r})$; or, (b) by using the Green's function of the wave equation, to express the electric field in terms of the exciton polarization and write a system of self-consistent equations describing electric-field-mediated coupling between the excitons excited in different quantum dots. In the first approach, we substitute Eq. (3) into Eq. (5) and expand the vector function $\mathbf{E}_{\mathbf{q}}(\mathbf{r})$ in the Fourier series as follows:

$$\mathbf{E}_{\mathbf{q}}(\mathbf{r}) = \sum_{\mathbf{g}} e^{i(\mathbf{q}+\mathbf{g})\mathbf{r}} \mathbf{E}_{\mathbf{q}+\mathbf{g}}. \quad (10)$$

The integral in Eq. (2) can be transformed into

$$\int \Phi_{\mathbf{a}}(\mathbf{r}) \mathbf{E}(\mathbf{r}) d\mathbf{r} = e^{i\mathbf{q}\mathbf{a}} \sum_{\mathbf{g}} I_{\mathbf{q}+\mathbf{g}} \mathbf{E}_{\mathbf{q}+\mathbf{g}} \equiv e^{i\mathbf{q}\mathbf{a}} \mathbf{\Lambda}. \quad (11)$$

The sum $\sum_{\mathbf{a}} \Phi_{\mathbf{a}}(\mathbf{r})\, e^{i\mathbf{q}\mathbf{a}}$ satisfies the translational symmetry similar to Eq. (6) and can be presented as

$$\sum_{\mathbf{a}} \Phi_{\mathbf{a}}(\mathbf{r}) e^{i\mathbf{q}\mathbf{a}} = \sum_{\mathbf{g}} e^{i(\mathbf{q}+\mathbf{g})\mathbf{r}} \frac{I_{\mathbf{q}+\mathbf{g}}^*}{V_0}. \quad (12)$$

The system of linear equations for the space harmonics $\mathbf{E}_{\mathbf{q}+\mathbf{g}}$ can be written in the form

$$[(\mathbf{q} + \mathbf{g})^2 - k^2] \mathbf{E}_{\mathbf{q}+\mathbf{g}} = T(\omega) k_0^2 \frac{I_{\mathbf{q}+\mathbf{g}}^*}{V_0} \hat{S}(\mathbf{q} + \mathbf{g}) \mathbf{\Lambda}, \quad (13)$$

where the vector $\mathbf{\Lambda}$ is introduced in Eq. (11) and $\hat{S}(\mathbf{Q})\mathbf{\Lambda}$ is a vector with components $S_{\alpha\beta}(\mathbf{Q})\Lambda_\beta$. Dividing both parts of Eq. (13) by $(\mathbf{q} + \mathbf{g})^2 - k^2$, multiplying them by $I_{\mathbf{q}+\mathbf{g}}$, and summing over $\mathbf{g}$, we arrive at a vector equation $\mathbf{\Lambda} = \hat{R}(\omega, \mathbf{q})\mathbf{\Lambda}$, where the matrix $\hat{R}$ is defined by Eq. (8), and therefore, at the dispersion equation (7).

In the second approach, we use the Green's function

$$\begin{aligned} G(\mathbf{r} - \mathbf{r}') &= \frac{\exp(ik|\mathbf{r} - \mathbf{r}'|)}{4\pi|\mathbf{r} - \mathbf{r}'|} \\ &= \frac{1}{V} \sum_{\mathbf{Q}} \frac{\exp[i\mathbf{Q}(\mathbf{r} - \mathbf{r}')]}{\mathbf{Q}^2 - k^2}, \end{aligned} \quad (14)$$

satisfying the differential equation

$$(\Delta + k^2) G(\mathbf{r} - \mathbf{r}') = -\delta(\mathbf{r} - \mathbf{r}'). \quad (15)$$

Here, V is the lattice volume. The Green's function allows one to express $\mathbf{E}(\mathbf{r})$ via the polarization as

$$\begin{aligned} \mathbf{E}(\mathbf{r}) &= 4\pi k_0^2 T(\omega) \\ &\times \int d\mathbf{r}' G(\mathbf{r} - \mathbf{r}')(1 + k^{-2}\mathrm{graddiv}) \mathbf{P}_{exc}(\mathbf{r}'). \end{aligned} \quad (16)$$

Dispersion equations written in terms of $R_{\alpha\beta}$ for different **K** points in the Brillouin zone of a face-centered-cubic QD lattice

K ($2\pi/a$)	Nonzero components of $R_{\alpha\beta}$	Dispersion equations
Γ (0, 0, 0)	$R_{xx} = R_{yy} = R_{zz}$	$R_{xx} = 1$
X (0, 0, 1)	$R_{xx} = R_{yy}$, R_{zz}	$R_{xx} = 1$, $R_{zz} = 1$
L (1/2, 1/2, 1/2)	$R_{\alpha\alpha} = R_{xx}$, $R_{\alpha\beta} = R_{xy} (\alpha \neq \beta)$	$R_{xx} - R_{xy} = 1$, $R_{xx} + 2R_{xy} = 1$
W (1/2, 0, 1)	R_{xx}, $R_{yy} = R_{zz}$	$R_{xx} = 1$, $R_{yy} = 1$
K (3/4, 0, 3/4)	$R_{xx} = R_{zz}$, R_{yy}, $R_{xz} = R_{zx}$	$R_{xx} \pm R_{xz} = 1$, $R_{yy} = 1$
U (1/4, 1/4, 1)	$R_{xx} = R_{yy}$, R_{zz}, $R_{xy} = R_{yx}$	$R_{xx} \pm R_{xy} = 1$, $R_{zz} = 1$

Now, Eq. (3) is presented in the form

$$4\pi \mathbf{P}_{\text{exc}}(\mathbf{r}) = \sum_{\mathbf{a}} \mathbf{p}_{\mathbf{a}} \Phi_{\mathbf{a}}(\mathbf{r}), \tag{17}$$

where

$$\mathbf{p}_{\mathbf{a}} = T(\omega) \int \Phi_{\mathbf{a}}(\mathbf{r}') \mathbf{E}(\mathbf{r}') d\mathbf{r}'. \tag{18}$$

For the Bloch solutions (6) one has $\mathbf{p}_{\mathbf{a}} = e^{i\mathbf{q}\mathbf{a}} \mathbf{p}_0$. Taking $\mathbf{a} = 0$ in Eq. (18) and using Eqs. (16) and (17) we obtain

$$\begin{aligned} \mathbf{p}_0 &= T(\omega) \int d\mathbf{r}' \Phi_0(\mathbf{r}') \\ &\times \int d\mathbf{r} G(\mathbf{r}' - \mathbf{r}) (1 + k^{-2} \text{graddiv}) \sum_{\mathbf{a}'} \mathbf{p}_0 \Phi_{\mathbf{a}'}(\mathbf{r}) e^{i\mathbf{q}\mathbf{a}'}. \end{aligned} \tag{19}$$

If we now use Eqs. (9) and (12) and the integral presentation of the Green's function, we will finally come to the equation $\mathbf{p}_0 = \hat{R}(\omega, \mathbf{q})\mathbf{p}_0$ and re-derive Eq. (7).

A numerical calculation is performed for spherical QDs with the radius R exceeding the Bohr radius a_B, in which case we have

$$I_{\mathbf{Q}} = \pi \left(\frac{2R}{a_B}\right)^{3/2} \frac{\sin QR}{QR[\pi^2 - (QR)^2]}. \tag{20}$$

Then, Eq. (8) can be transformed into

$$R_{\alpha\beta}(\Omega, \mathbf{K}) = \xi \frac{\Omega^2}{\Omega^2 - 1} \sigma_{\alpha\beta}(\Omega, \mathbf{K}), \tag{21}$$

$$\sigma_{\alpha\beta}(\Omega, \mathbf{K}) = \sum_{\mathbf{b}} \frac{f(|\mathbf{K} + \mathbf{b}|R) S_{\alpha\beta}(\mathbf{K} + \mathbf{b})}{\Omega^2 - \Omega^2(\mathbf{K} + \mathbf{b})}, \tag{22}$$

$$\begin{aligned} \Omega &= \frac{\omega}{\omega_0}, \quad \xi = \frac{64}{\pi} \frac{\omega_{LT}}{\omega_0} \left(\frac{R}{a}\right)^3, \\ f(x) &= \left[\frac{\pi^2 \sin x}{x(\pi^2 - x^2)}\right]^2, \end{aligned} \tag{23}$$

$\Omega(\mathbf{Q}) = cQ/\omega_0 n_b$. Equation (7) is equivalent to the three separate equations $R_j(\Omega, \mathbf{K}) = 1$, where R_j ($j = 1, 2, 3$) are eigenvalues of the matrix $R_{\alpha\beta}$. Further simplification follows taking into account a small value of the parameter ξ in Eq. (21) since, in semiconductors, the

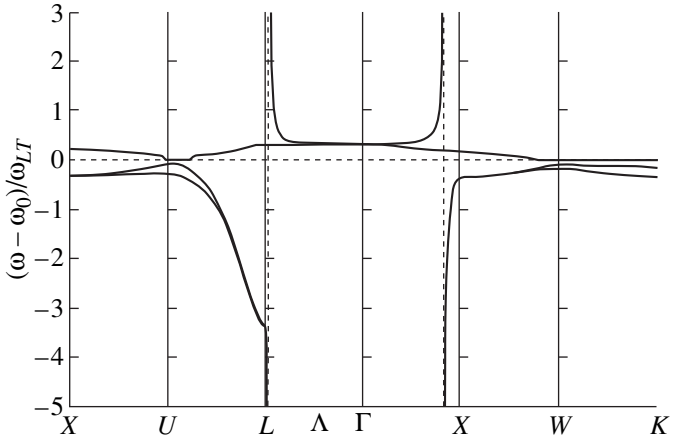

Fig. 1. Exciton–polariton dispersion near the exciton resonance frequency ω_0 in a face-centered-cubic lattice of spherical QDs characterized by the following set of parameters: $P = 1.1$, $R/a = 1/4$, and $\omega_{LT}/\omega_0 = 5 \times 10^{-4}$. The dashed lines show the photon dispersion in the empty lattice, i.e., for $\omega_{LT} = 0$, the dotted horizontal line indicates the value $\omega = \omega_0$.

ratio ω_{LT}/ω_0 typically lies between 10^{-4} and 10^{-3}. Then one can change the factor $\Omega/(\Omega + 1)$ in Eq. (21) by 1/2.

Figure 1 shows the photonic band structure for face-centered-cubic QD lattices with the radius $R = a/4$, $\omega_{LT}/\omega_0 = 5 \times 10^{-4}$, and $P = (\pi\sqrt{3}\, c/a\omega_0 n_b)^3 = 1.1$.

Note that, in this case, the lattice constant a and the unit-cell volume v_0 are related by $v_0 = a^3/4$. For high-symmetry points of the Brillouin zone, the symmetry imposes certain relations between the $R_{\alpha\beta}$ components and the eigenvalues R_j can be readily expressed via these components as illustrated in the Table 1 for the points Γ, X, L, W, K, and U. According to Fig. 1, the dispersion on the Λ line is characterized by a giant anticrossing between the branches of bare transverse photon and exciton modes. At the X point, the gap is determined by the separation between the longitudinal and lower transverse branches, it is still remarkable and exceeds $0.5\omega_{LT}$. However, near the points U and W, the exciton-polariton branches converge and the gap almost disappears. Note that the anticrossing can be described with a high accuracy by retaining in the sum over $\mathbf{b}$ in Eq. (22) the two terms due to $\mathbf{b} = 0$ and $-(4\pi/a)(0, 0, 1)$ for the Δ points and $\mathbf{b} = 0$ and $-(2\pi/a)(1, 1, 1)$ for the Λ points.

III. REFLECTION FROM AND TRANSMISSION THROUGH A PLANAR ARRAY OF QUANTUM DOTS

We start analysis of the resonant light reflection from an array of dots regularly packed in one plane. For simplicity, we consider here a square lattice of spherical or cubic quantum dots and normal incidence of light. In this case, the integral of Eq. (9) can be reduced to

$$\begin{aligned} I_{\mathbf{Q}} &= \int \Phi_0(\mathbf{r}) \cos \mathbf{Q}\mathbf{r}\, d\mathbf{r} \\ &= \int \Phi_0(\mathbf{r}) \cos Q_x x \cos Q_y y \cos Q_z z\, d\mathbf{r}; \end{aligned} \tag{24}$$

it is real if $\mathbf{Q}$ is a purely real or a pure imaginary vector. First, we consider the normal incidence of light on a planar array of quantum dots. The electric field can be written in the form

$$\mathbf{E}(\mathbf{r}) = \sum_{\mathbf{b}} \mathbf{E}_{\mathbf{b}}(z) \exp(i\mathbf{b}\boldsymbol{\rho}), \tag{25}$$

where $\mathbf{b} = l\mathbf{b}_1 + m\mathbf{b}_2$ are the two-dimensional reciprocal-lattice vectors.

The integral in Eq. (3) can be transformed into

$$\begin{aligned} \int \Phi_{\mathbf{a}}(\mathbf{r}) \mathbf{E}(\mathbf{r})\, d\mathbf{r} &= \sum_{\mathbf{b}} e^{i\mathbf{b}\mathbf{a}} \int \mathbf{E}_{\mathbf{b}}(z) \Phi(\boldsymbol{\rho}, z) \exp(i\mathbf{b}\boldsymbol{\rho})\, d\boldsymbol{\rho}\, dz \\ &= \sum_{\mathbf{b}} \int \varphi_{\mathbf{b}}(z) \mathbf{E}_{\mathbf{b}}(z)\, dz \equiv \boldsymbol{\Lambda}_1, \end{aligned} \tag{26}$$

where

$$\varphi_{\mathbf{b}}(z) = \int \Phi(\boldsymbol{\rho}, z) \exp(i\mathbf{b}\boldsymbol{\rho})\, d\boldsymbol{\rho} \tag{27}$$

and we have used the identity $\exp(i\mathbf{b}\mathbf{a}) = 1$. We will also use the expansion

$$\sum_{\mathbf{a}} \Phi_{\mathbf{a}}(\mathbf{r}) = \frac{1}{a^2} \sum_{\mathbf{b}} \varphi_{\mathbf{b}}(z) \exp(i\mathbf{b}\boldsymbol{\rho}), \tag{28}$$

where a^2 is the unit-cell area.

The function $\mathbf{E}_{\mathbf{b}}(z)$ satisfies the equation

$$\begin{aligned} &\left(\frac{d^2}{dz^2} + k_{\mathbf{b}}^2\right) \mathbf{E}_{\mathbf{b}}(z) \\ &= -\frac{k_0^2}{a^2} T(\omega)(1 + k^{-2}\mathrm{graddiv})_{\mathbf{b}} \varphi_{\mathbf{b}}(z) \boldsymbol{\Lambda}_1, \end{aligned} \tag{29}$$

where

$$\begin{aligned} k_{\mathbf{b}} &= \sqrt{k^2 - \mathbf{b}^2}, \quad \left(\frac{\partial^2}{\partial r_\alpha \partial r_\beta}\right)_{\mathbf{b}} = -K_\alpha K_\beta, \\ K_x &= b_x, \quad K_y = b_y, \quad K_z = -i\frac{\partial}{\partial z}. \end{aligned} \tag{30}$$

A solution can be presented as

$$\begin{aligned} \mathbf{E}_{\mathbf{b}}(z) &= \mathbf{E}^{(0)} e^{ikz} \delta_{\mathbf{b},0} + \frac{ik_0^2}{2k_{\mathbf{b}} a^2} T(\omega) \\ &\times \int dz' e^{ik_{\mathbf{b}}|z - z'|} (1 + k^{-2}\mathrm{graddiv})_{\mathbf{b}} \varphi_{\mathbf{b}}(z') \boldsymbol{\Lambda}_1, \end{aligned} \tag{31}$$

where $\mathbf{E}^{(0)}$ is the amplitude of the initial wave. Multiplying both parts of Eq. (31) by $\varphi_{\mathbf{b}}(z)$ and integrating over z, we obtain

$$\begin{aligned} \boldsymbol{\Lambda}_1 &= \boldsymbol{\Lambda}_1^0 + \sum_{\mathbf{b}} \frac{ik_0^2}{2k_{\mathbf{b}} a^2} T(\omega) \int dz\, dz' e^{ik_{\mathbf{b}}|z - z'|} \varphi_{\mathbf{b}}(z) \\ &\times (1 + k^{-2}\mathrm{graddiv})_{\mathbf{b}} \varphi_{\mathbf{b}}(z') \boldsymbol{\Lambda}_1, \end{aligned} \tag{32}$$

where

$$\boldsymbol{\Lambda}_1^0 = \mathbf{E}^{(0)} \int \varphi_0(z) e^{ikz} dz = \mathbf{E}^{(0)} \int \varphi_0(z) \cos kz\, dz. \tag{33}$$

Let us denote by β the star of the vector $\mathbf{b}$. If $\mathbf{b} = l\mathbf{b}_1 + m\mathbf{b}_2$, the star β contains the vectors $\pm l\mathbf{b}_1 \pm m\mathbf{b}_2$, $\pm m\mathbf{b}_1 \pm l\mathbf{b}_2$ of equal moduli. For $l \neq m \neq 0$, the star consists of eight vectors, otherwise, it has four vectors ($l = m \neq 0$ or $l = 0$,

$m \neq 0$ or $l \neq 0$, $m = 0$), or one vector in the particular case $l = m = 0$. Then, the second term in the right-hand side of Eq. (32) can be rewritten as

$$T(\omega)\sum_{\beta}\frac{ik_0^2 n_\beta}{2k_\beta a^2}\iint dz dz' e^{ik_\beta|z-z'|}\varphi_\beta(z) \times\left[\left(1-\frac{\beta^2}{2k^2}\right)\mathbf{\Lambda}_{1,\parallel}+\left(1-\frac{1}{k^2}\frac{\partial^2}{\partial z'^2}\right)\mathbf{\Lambda}_{1,\perp}\right]\varphi_\beta(z'),$$

where $\mathbf{\Lambda}_{1,\parallel}$ and $\mathbf{\Lambda}_{1,\perp}$ are vectors with components $(\Lambda_{1,x}, \Lambda_{1,y}, 0)$ and $(0, 0, \Lambda_{1,z})$, respectively; n_β is the number of vectors in the star β; and $\beta^2 = |\mathbf{b}|^2$. Taking into account that $\mathbf{\Lambda}_1^0 = (\Lambda_{1,x}^0, \Lambda_{1,y}^0, 0)$, we obtain

$$\begin{aligned}\mathbf{\Lambda}_1 &= \mathbf{\Lambda}_1^0\left[1-T(\omega)\sum_\beta\frac{ik_0^2 n_\beta}{2k_\beta a^2}\left(1-\frac{\beta^2}{2k^2}\right)\right.\\ &\left.\times\int dz dz' e^{ik_\beta|z-z'|}\varphi_\beta(z)\varphi_\beta(z')\right]^{-1}\\ &= \mathbf{\Lambda}_1^0\frac{\omega_0-\omega-i\Gamma}{\tilde{\omega}_0-\omega-i(\Gamma+\Gamma_0)}.\end{aligned} \tag{34}$$

Here, $\tilde{\omega}_0$ is the normalized exciton resonance frequency, the difference between $\tilde{\omega}_0$ and ω_0 consists of two terms

$$\begin{aligned}\delta\omega_1 &= \omega_{LT}\frac{k^2\pi a_B^3}{2a^2}\sum_{\beta\in B_1}\frac{n_\beta}{k_\beta}\left(1-\frac{\beta^2}{2k^2}\right)\\ &\times\int dz dz' \sin k_\beta|z-z'|\varphi_\beta(z)\varphi_\beta(z'),\\ \delta\omega_2 &= -\omega_{LT}\frac{k^2\pi a_B^3}{2a^2}\sum_{\beta\in B_2}\frac{n_\beta}{\kappa_\beta}\left(1-\frac{\beta^2}{2k^2}\right)\\ &\times\int dz dz' e^{-\kappa_\beta|z-z'|}\varphi_\beta(z)\varphi_\beta(z'),\end{aligned} \tag{35}$$

B_1 and B_2 represent stars β with real and imaginary k_β, respectively; and $\kappa_\beta = \mathrm{Im}k_\beta$. The exciton radiative damping rate is given by

$$\Gamma_0 = \omega_{LT}\frac{k^2\pi a_B^2}{2a^2}\sum_{\beta\in B_1}\frac{n_\beta}{k_\beta}\left(1-\frac{\beta^2}{2k^2}\right)\lambda_\beta^2, \tag{36}$$

$$\begin{aligned}\lambda_\beta &= \int\varphi_\beta(z)\cos k_\beta z dz\\ &= \int\Phi_0(\mathbf{r})\cos(\mathbf{b}\boldsymbol{\rho}+k_\beta z)d\mathbf{r}.\end{aligned} \tag{37}$$

The reflected and transmitted light waves are written as

$$\sum_{\mathbf{b}}\mathbf{E}_{\mathbf{b}}^{(r)}\exp[i(\mathbf{b}\boldsymbol{\rho}-k_{\mathbf{b}}z)] \quad \text{and} \quad \sum_{\mathbf{b}}\mathbf{E}_{\mathbf{b}}^{(t)}\exp[i(\mathbf{b}\boldsymbol{\rho}+k_{\mathbf{b}}z)]. \tag{38}$$

The amplitudes $\mathbf{E}_{\mathbf{b}}^{(r)}$, $\mathbf{E}_{\mathbf{b}}^{(t)}$ are given by

$$\begin{aligned}\mathbf{E}_{\mathbf{b}}^{(r)} &= i\frac{k^2\pi a_B^3}{2k_{\mathbf{b}}a^2}\frac{\omega_{LT}\lambda_{\mathbf{b}}\lambda_0}{\tilde{\omega}_0-\omega-i(\Gamma+\Gamma_0)}\left(1-\frac{\mathbf{K}_r^\wedge\mathbf{K}_r}{k^2}\right)\mathbf{E}^{(0)},\\ \mathbf{E}_{\mathbf{b}}^{(t)} &= \left[\delta_{\mathbf{b},0}+i\frac{k^2\pi a_B^3}{2k_{\mathbf{b}}a^2}\frac{\omega_{LT}\lambda_{\mathbf{b}}\lambda_0}{\tilde{\omega}_0-\omega-i(\Gamma+\Gamma_0)}\right.\\ &\left.\times\left(1-\frac{\mathbf{K}_t^\wedge\mathbf{K}_t}{k^2}\right)\right]\mathbf{E}^{(0)},\end{aligned} \tag{39}$$

where $(\mathbf{K}^\wedge\mathbf{K}\mathbf{E})_i = K_i\Sigma_j K_j E_j$, $\mathbf{K}_r = (b_x, b_y, -k_{\mathbf{b}})$, and $\mathbf{K}_t = (b_x, b_y, k_{\mathbf{b}})$. While deriving Eq. (39), we took into account that $\Lambda_z^{(0)} = 0$ and

$$\begin{aligned}&\int e^{ik_{\mathbf{b}}z}(-id/dz)\varphi_{\mathbf{b}}(z)dz\\ &= -k_{\mathbf{b}}\int e^{ik_{\mathbf{b}}z}\varphi_{\mathbf{b}}(z)dz = -k_{\mathbf{b}}\lambda_{\mathbf{b}}.\end{aligned}$$

One can check that Eq. (39) satisfies the energy-flux conservation law. Indeed, for zero dissipation, i.e., for $\Gamma = 0$, we have

$$\sum_{\mathbf{b}\in B_1}k_{\mathbf{b}}\left[\left|\mathbf{E}_{\mathbf{b}}^{(r)}\right|^2+\left|\mathbf{E}_{\mathbf{b}}^{(t)}\right|^2\right] = k\left|\mathbf{E}^{(0)}\right|^2. \tag{40}$$

Equations (35)–(39) are original; previously, analytical results for the reflectivity of a planar QD array were obtained only for particular limiting cases [27].

Note that

$$\mathbf{E}_\beta^{(r,t)} = \sum_{\mathbf{b}\in\beta}\mathbf{E}_{\mathbf{b}}^{(r,t)} \parallel \mathbf{E}^{(0)} \perp z.$$

It follows then that, in a more general case $\mathbf{E}_{\mathbf{b}}^{(0)} \neq 0$ for $\mathbf{b} \neq 0$ but

$$\mathbf{E}_\beta^{(0)} = \sum_{\mathbf{b}\in\beta}\mathbf{E}_{\mathbf{b}}^{(0)} \parallel \mathbf{E}^{(0)} \equiv \mathbf{E}_0^{(0)},$$

the vector

$$\mathbf{\Lambda}_1^0 = \sum_\beta\lambda_\beta\mathbf{E}_\beta^{(0)} \tag{41}$$

is oriented along $\mathbf{E}^{(0)}$ and Eq. (34) is also valid. As a result, we obtain

$$\mathbf{E}_\beta^{(r)} = \sum_{\beta'} r_{\beta\beta'}\mathbf{E}_{\beta'}^{(0)}, \quad \mathbf{E}_\beta^{(t)} = \sum_{\beta'} t_{\beta\beta'}\mathbf{E}_{\beta'}^{(0)} \tag{42}$$

with

$$r_{\beta\beta'} = i\frac{k^2\pi a_B^3 n_\beta}{2k_\beta a^2}\frac{\omega_{LT}\lambda_\beta\lambda_{\beta'}}{\tilde{\omega}_0 - \omega - i(\Gamma + \Gamma_0)}\left(1 - \frac{\beta^2}{2k^2}\right), \tag{43}$$
$$t_{\beta\beta'} = \delta_{\beta\beta'} + r_{\beta\beta'}.$$

Since $\mathbf{E}_\beta^{(0)}$, $\mathbf{E}_\beta^{(r)}$, and $\mathbf{E}_\beta^{(0)}$ are parallel to $\mathbf{E}^{(0)}$, one can omit the vector notation for these quantities.

In the following, it is convenient to have the reflection and transmission referred to the planes shifted by some distance $d/2$ to the left and to the right with respect to the quantum-dot plane, i.e., the field on the left-hand side is written as $E_{\beta,+}\exp[ik_\beta(z + d/2)] + E_{\beta,-}\exp[-ik_\beta(z + d/2)]$ and the field on the right-hand side is written as $E'_{\beta,+}\exp[ik_\beta(z - d/2)] + E'_{\beta,-}\exp[-ik_\beta(z - d/2)]$. The corresponding reflection and transmission coefficients are related to Eq. (43) by

$$\tilde{r}_{\beta\beta'} = s_\beta s_{\beta'} r_{\beta\beta'}, \quad \tilde{t}_{\beta\beta'} = s_\beta s_{\beta'} t_{\beta\beta'}, \quad s_\beta = \exp(ik_\beta d/2). \tag{44}$$

IV. EXCITON–POLARITON DISPERSION IN TERMS OF $\tilde{r}_{\beta\beta'}$ AND $\tilde{t}_{\beta\beta'}$

We show here that the dispersion equation (7) for exciton–polaritons with $\mathbf{q} = (0, 0, q)$ can be derived independently by using the reflection and transmission coefficients for a single plane of quantum dots. Taking into account that, for polaritons in an infinite primitive cubic (PC) lattice, the amplitudes $E_{\beta,\pm}$ and $E'_{\beta,\pm}$ at the planes $z = -a/2$ and $z = a/2$ are related by the Bloch condition $E'_{\beta,\pm} = \exp(iqa)E_{\beta,\pm}$ and using the definition of $\tilde{r}_{\beta\beta'}$ and $\tilde{t}_{\beta\beta'}$, for $d = a$ we can write

$$E_{\beta,-} = \tilde{r}_{\beta\beta'}E_{\beta',+} + (s_\beta^2\delta_{\beta\beta'} + \tilde{r}_{\beta\beta'})e^{iqa}E_{\beta',-},$$
$$e^{iqa}E_{\beta,+} = (s_\beta^2\delta_{\beta\beta'} + \tilde{r}_{\beta\beta'})E_{\beta',+} + \tilde{r}_{\beta\beta'}e^{iqa}E_{\beta',-}. \tag{45}$$

The latter equations can be rewritten as

$$(1 - e^{iqa}s_\beta^2)E_{\beta,-} = (e^{iqa} - s_\beta^2)E_{\beta,+} = \tilde{r}_{\beta\beta'}(E_{\beta',+} + e^{iqa}E_{\beta',-})$$

or

$$E_{\beta,+} + e^{iqa}E_{\beta,-} = \eta_\beta\tilde{r}_{\beta\beta'}(E_{\beta',+} + e^{iqa}E_{\beta',-}), \tag{46}$$

where

$$\eta_\beta = \frac{1}{e^{iqa} - s_\beta^2} + \frac{1}{e^{-iqa} - s_\beta^2}.$$

Note that the β' dependence of $\tilde{r}_{\beta\beta'}$ is governed by the product $\lambda_{\beta'}s_{\beta'}$ and one can present this amplitude coefficient in the form

$$\tilde{r}_{\beta\beta'} = U_\beta\lambda_{\beta'}s_{\beta'}, \tag{47}$$

where U_β is β'-independent. Now, we multiply Eq. (46) by $\lambda_\beta s_\beta$, sum over β, and eventually come to the equation

$$\left(1 - \sum_\beta U_\beta\eta_\beta\lambda_\beta s_\beta\right) \times \sum_{\beta'}\lambda_{\beta'}s_{\beta'}(E_{\beta',+} + e^{iqa}E_{\beta',-}) = 0,$$

which can be reduced to

$$\tilde{\omega}_0 - \omega - i(\Gamma + \Gamma_0) = i\frac{k^2\omega_{LT}\pi a_B^3}{2a^2}\sum_\beta\frac{n_\beta\lambda_\beta^2}{k_\beta}\left(1 - \frac{\beta^2}{2k^2}\right)s_\beta^2\eta_\beta. \tag{48}$$

The equivalence between Eqs. (7) and (48) follows immediately if we observe that

$$s_\beta^2\eta_\beta = \frac{\cos qa - e^{ik_\beta a}}{\cos k_\beta a - \cos qa} = -1 - \frac{i\sin k_\beta a}{\cos k_\beta a - \cos qa} \tag{49}$$

and, for a PC lattice and for $\mathbf{q} \parallel [001]$,

$$\sum_{\mathbf{g}}\frac{I_{\mathbf{q}+\mathbf{g}}^2 S_{xx}(\mathbf{q}+\mathbf{g})}{(\mathbf{q}+\mathbf{g})^2 - k^2} = \iint d\mathbf{r}d\mathbf{r}'\Phi_0(\mathbf{r})\Phi_0(\mathbf{r}') \times \sum_{\mathbf{g}}\frac{e^{i(\mathbf{q}+\mathbf{g})(\mathbf{r}-\mathbf{r}')}}{(\mathbf{q}+\mathbf{g})^2 - k^2}S_{xx}(\mathbf{q}+\mathbf{g}) = \sum_\beta n_\beta\left(1 - \frac{\beta^2}{2k^2}\right) \times \iint dzdz'\varphi_\beta(z)\varphi_\beta(z')F(z - z', q, k_\beta), \tag{50}$$

where

$$F(\zeta, q, K) = \frac{a}{2K} \times \left[-\sin K|\zeta| + \frac{\sin Ka}{\cos Ka - \cos qa}\left(\cos K\zeta + i\frac{\sin qa}{\sin Ka}K\zeta\right)\right]. \tag{51}$$

V. OPTICAL REFLECTION FROM A PAIR OF (001) QUANTUM-DOT PLANES

For two d-spaced quantum-dot planes (001), the normal-incidence reflection coefficient can be expanded as follows:

$$\tilde{r}_{\beta'\beta}^{(2)} = \tilde{r}_{\beta'\beta} + \tilde{t}_{\beta'\beta_2}\tilde{r}_{\beta_2\beta_1}\tilde{t}_{\beta_1\beta} + \tilde{t}_{\beta'\beta_4}\tilde{r}_{\beta_4\beta_3}\tilde{r}_{\beta_3\beta_2}\tilde{r}_{\beta_2\beta_1}\tilde{t}_{\beta_1\beta} + \ldots. \tag{52}$$

Taking into account the representation (47), we obtain

$$\tilde{r}_{\beta_4\beta_3}\tilde{r}_{\beta_3\beta_2}\tilde{r}_{\beta_2\beta_1} = U_{\beta_4}\lambda_{\beta_3}s_{\beta_3}U_{\beta_3}\lambda_{\beta_2}s_{\beta_2}U_{\beta_2}\lambda_{\beta_1}s_{\beta_1} = \left(\sum_{\beta_3}\tilde{r}_{\beta_3\beta_3}\right)^2\tilde{r}_{\beta_4\beta_1}.$$

It follows then that

$$\tilde{r}^{(2)}_{\beta'\beta} = \tilde{r}_{\beta'\beta} + \frac{\tilde{t}_{\beta'\beta_2}\tilde{r}_{\beta_2\beta_1}\tilde{t}_{\beta_1\beta}}{1-\left(\sum_{\beta_3}\tilde{r}_{\beta_3\beta_3}\right)^2}. \quad (53)$$

In a similar way, one can show that

$$\begin{aligned}\tilde{t}_{\beta'\beta_2}\tilde{r}_{\beta_2\beta_1}\tilde{t}_{\beta_1\beta} &= (e^{ik_{\beta'}d}\delta_{\beta'\beta_2}+\tilde{r}_{\beta'\beta_2})\tilde{r}_{\beta_2\beta_1}(e^{ik_\beta d}\delta_{\beta_1\beta}+\tilde{r}_{\beta_1\beta})\\ &= e^{ik_\beta d}e^{ik_{\beta'}d}\tilde{r}_{\beta'\beta}+(e^{ik_{\beta'}d}+e^{ik_\beta d})\tilde{r}_{\beta'\beta_1}\tilde{r}_{\beta_1\beta}\\ &\quad +\tilde{r}_{\beta'\beta_2}\tilde{r}_{\beta_2\beta_1}\tilde{r}_{\beta_1\beta}\\ &= e^{i(k_\beta+k_{\beta'})d}\tilde{r}_{\beta'\beta}+(e^{ik_{\beta'}d}+e^{ik_\beta d})\tilde{r}_{\beta'\beta}V+\tilde{r}_{\beta'\beta}V^2,\end{aligned} \quad (54)$$

where $V=\sum_\beta \tilde{r}_{\beta\beta}$. Thus, we finally obtain

$$\tilde{r}^{(2)}_{\beta'\beta} = \tilde{r}_{\beta'\beta}\left[1+\frac{(e^{ik_\beta d}+V)(e^{ik_{\beta'}d}+V)}{1-V^2}\right]. \quad (55)$$

In particular, it follows then that

$$\begin{aligned}\tilde{r}^{(2)}_{00} &= \tilde{r}_{00}\left[1+\frac{(e^{ikd}+V)^2}{1-V^2}\right],\\ \tilde{r}_{00} &= e^{ikd}\frac{i\Gamma_0}{\tilde{\omega}_0-\omega-i(\Gamma+\Gamma_0)}.\end{aligned} \quad (56)$$

Hereafter, we use the parameter a_{Br} defined by the resonant Bragg condition

$$\frac{\pi}{a_{\mathrm{Br}}} = \frac{\omega_0}{c}n_b. \quad (57)$$

According to Eqs. (43) and (44), for $a < 2a_{\mathrm{Br}}$, we have

$$V = \frac{i\Gamma_0 e^{ikd}+A}{\tilde{\omega}_0-\omega-i(\Gamma+\Gamma_0)}, \quad (58)$$

where

$$A = \frac{k^2\omega_{LT}\pi a_B^3}{2a^2}\sum_{\beta\neq 0}\frac{n_\beta\lambda_\beta^2}{\kappa_\beta}\left(1-\frac{\beta^2}{2k^2}\right)e^{-\kappa_\beta d}$$

and $\kappa_\beta = \sqrt{\beta^2-k^2}$. From Eqs. (56) and (58), we obtain

$$\tilde{r}^{(2)}_{00} = e^{ikd}2i\Gamma_0 \times\frac{(\omega-\tilde{\omega}_0+i\Gamma)\cos kd+\Gamma_0\sin kd-A}{[\omega-\tilde{\omega}_0+i(\Gamma+\Gamma_0)]^2-(i\Gamma_0e^{ikd}+A)^2}. \quad (59)$$

For the resonant Bragg double-plane structure with $d = a = a_{\mathrm{Br}}$, this equation reduces to

$$\tilde{r}^{(2)}_{00}(d=a_{\mathrm{Br}}) = \frac{-2i\Gamma_0}{\tilde{\omega}_0-A-\omega-i(\Gamma+2\Gamma_0)}. \quad (60)$$

We see that the reflection coefficient $\tilde{r}^{(2)}_{00}$ $(d = a_{\mathrm{Br}})$ differs from that for the single-plane case by the replacement of Γ_0 by $2\Gamma_0$, similarly to the resonant Bragg double QWs [8], and of $\tilde{\omega}_0$ by $\tilde{\omega}_0 - A$.

VI. OPTICAL REFLECTION FROM A STACK OF QUANTUM-DOT PLANES

Here, we consider the reflection from a system of N parallel (001) planes, which is nothing more than a layer of the PC lattice of quantum dots. The first approach can be based on recurrent equations relating the reflection coefficients for $N + 1$ and N planes:

$$\tilde{r}^{(N+1)} = \tilde{r}+\tilde{t}P^{(N)}\tilde{t}, \quad (61)$$

where the matrix $P^{(N)}_{\beta'\beta}$ satisfies the equation

$$P^N = \tilde{r}^{(N)}(I+\tilde{r}P^{(N)}),$$

I is the unit matrix: $I_{\beta'\beta} = \delta_{\beta'\beta}$, and, for the sake of brevity, we omit the indices β, β'. The similar equations for a semiinfinite lattice can be presented in the form

$$\begin{aligned}\tilde{r}^{(\infty)} &= \tilde{r}+\tilde{t}P^{(\infty)}\tilde{t},\\ P^{(\infty)} &= (\tilde{r}+\tilde{t}P^{(\infty)}\tilde{t})(I+\tilde{r}P^{(\infty)}).\end{aligned} \quad (62)$$

In fact, this approach was used in the previous section to calculate the reflectivity from two QD planes.

In an alternative approach, we divide the space into the following three parts: (I) $z < z_L$, (II) $z_L < z < z_R$, and (III) $z_R < z$, where the planes $z = z_L = -a/2$ and $z = z_R = Na - a/2$ are shifted by the half-period from the leftmost and rightmost quantum dots, respectively. The secondary electric field appearing as a result of the diffraction from the quantum dot lattice allows the expansion

$$\begin{aligned}\mathbf{E}(\mathbf{r};\, z\le z_L) &= e^{ik(z-z_L)}\mathbf{E}_0+\sum_{\mathbf{g}_-}e^{i\mathbf{g}_-(\mathbf{r}-\mathbf{r}_L)}\mathbf{E}_{\mathbf{g}_-},\\ \mathbf{E}(\mathbf{r};\, z_L\le z\le z_R) &= \sum_{\mathbf{b}}\exp(i\mathbf{b}\boldsymbol{\rho})\mathbf{E}_{\mathbf{b}}(z),\\ \mathbf{E}(\mathbf{r};\, z\ge z_R) &= \sum_{\mathbf{g}_+}e^{i\mathbf{g}_+(\mathbf{r}-\mathbf{r}_R)}\mathbf{E}_{\mathbf{g}_+}.\end{aligned} \quad (63)$$

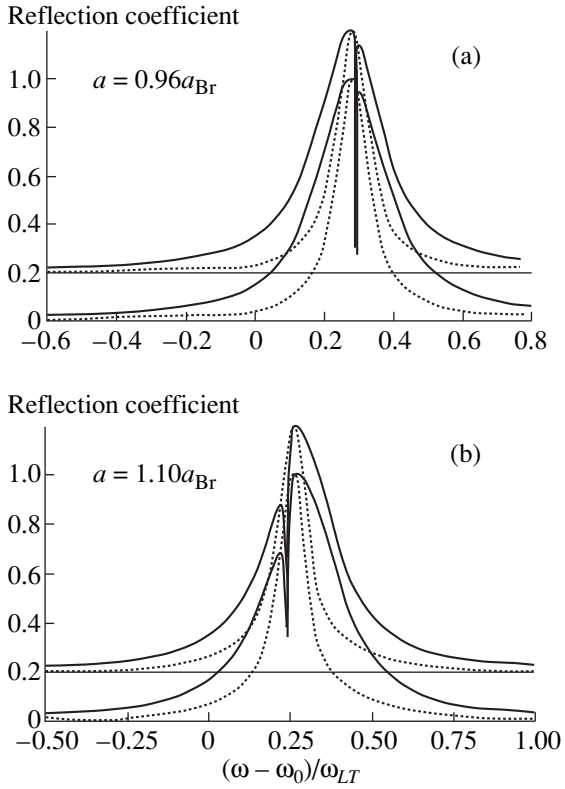

Fig. 2. The reflectance from single (dotted) and double, $d = a$, (solid) planes containing the square QD lattice with two different periods, $a = 0.96a_{Br}$ (a) and $a = 1.10a_{Br}$ (b). The spectra are calculated by using Eqs. (59) and (68). For the sake of convenience, the latter are vertically shifted by 0.2.

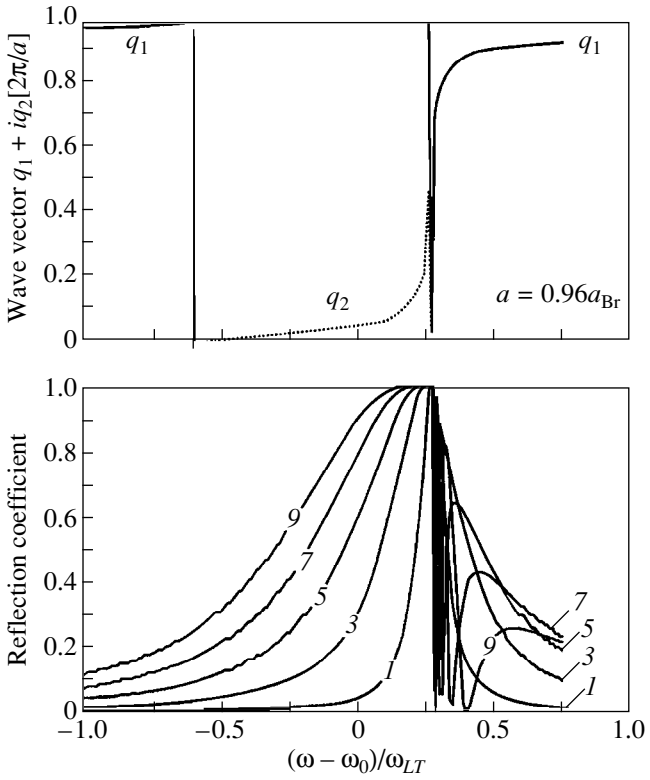

Fig. 3. The dispersion of exciton–polaritons propagating in the infinite QD lattice along the [001] direction (upper graph) and the reflectance from a stack of N QD planes with the spacing $d = a$ and the period $a = 0.96a_{Br}$ for $N = 1$, 3, 5, 7, and 9 (lower graph).

Here, $\mathbf{E}_0$ is the amplitude of the primary wave, $\mathbf{r}_L = (0, 0, z_L)$, $\mathbf{r}_R = (0, 0, z_R)$,

$$g_{\pm,x} = b_x = \frac{2\pi l}{a}, \quad g_{\pm,y} = b_y = \frac{2\pi m}{a},$$

$$g_{\pm,z} = \pm k_{\mathbf{b}} = \pm\sqrt{k^2 - b_x^2 - b_y^2}.$$

In region II, the field is a superposition of two Bloch solutions

$$\mathbf{E}(\mathbf{r};\, z_L \le z \le z_R) = \mathbf{E}_{\mathbf{q}}(\mathbf{r}) + \mathbf{E}_{-\mathbf{q}}(\mathbf{r}), \tag{64}$$

where $\mathbf{q} = (0, 0, q)$ satisfies the dispersion equation (7). In region I, in addition to the primary wave, $\mathbf{E}_0$, and specularly reflected wave, $\mathbf{E}_r = \mathbf{E}_{\mathbf{g}_-}$ with $\mathbf{g}_- = (0, 0, -k)$, there are space harmonics oscillating in the (x, y) plane. Among the latter, those which satisfy the condition $k > (2\pi/a)\sqrt{l^2 + m^2}$ are diffracted waves propagating in region I without decay. The harmonics with $k < (2\pi/a)\sqrt{l^2 + m^2}$ decay with increasing distance from the left-hand side interface. In region III, in addition to the transmitted wave $\mathbf{E}_t$ with $\mathbf{g}_+ = (0, 0, k)$, there exist free and decaying diffracted waves with $l^2 + m^2 \ne 0$. From the field continuity at $z = z_L$ and $z = z_R$, we obtain the boundary conditions

$$\Pi_{0,+}\mathbf{E}_{\mathbf{b}=0}(z_L) = \mathbf{E}_0, \quad \Pi_{\mathbf{b},-}\mathbf{E}_{\mathbf{b}}(z_L) = \mathbf{E}_{\mathbf{g}_-},$$
$$\Pi_{\mathbf{b},+}\mathbf{E}_{\mathbf{b}}(z_R) = \mathbf{E}_{\mathbf{g}_+}, \tag{65}$$

$$\Pi_{\mathbf{b},+}\mathbf{E}_{\mathbf{b}\ne 0}(z_L) = 0, \quad \Pi_{\mathbf{b},-}\mathbf{E}_{\mathbf{b}}(z_R) = 0, \tag{66}$$

where we have introduced the projection operators

$$\Pi_{\mathbf{b},\pm} = \frac{1}{2}\left(1 \pm \frac{1}{ik_{\mathbf{b}}}\frac{d}{dz}\right).$$

Note that Eqs. (66) mean that, under the normal incidence, there are no incoming waves with $\mathbf{b} \ne 0$.

We expand $\mathbf{E}_{\mathbf{q}}(\mathbf{r})$, $\mathbf{E}_{-\mathbf{q}}(\mathbf{r})$ in the Fourier series (10) and take into account the boundary conditions (65) and (66) for $\mathbf{b} = 0$. The latter can be rearranged and written as

$$E_0 + E_r = \sum_n [E_{q+b_n} e^{i(q+b_n)z_L} + E_{-q+b_n} e^{i(-q-b_n)z_L}],$$

$$E_0 - E_r = \sum_{n,\pm} \frac{\pm q + b_n}{k} E_{\pm q + b_n} e^{i(\pm q + b_n)z_L},$$

$$E_t = \sum_{n,\pm} E_{\pm q + b_n} e^{i(\pm q + b_n)z_R} \tag{67}$$

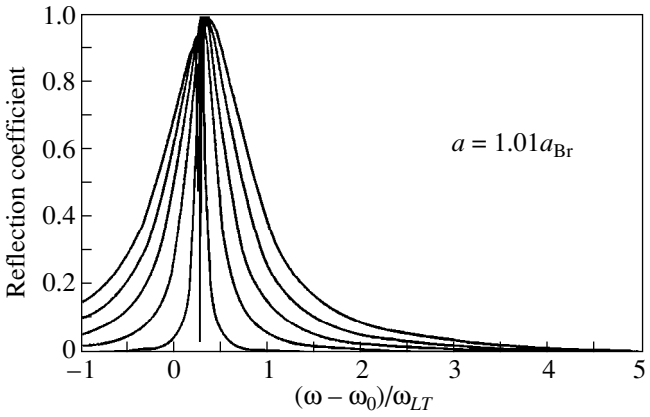

Fig. 4. The reflectance from a stack of N QD planes with the spacing $d = a$ and the period $a = 1.01a_{Br}$ for $N = 1$, 3, 5, 7, and 9.

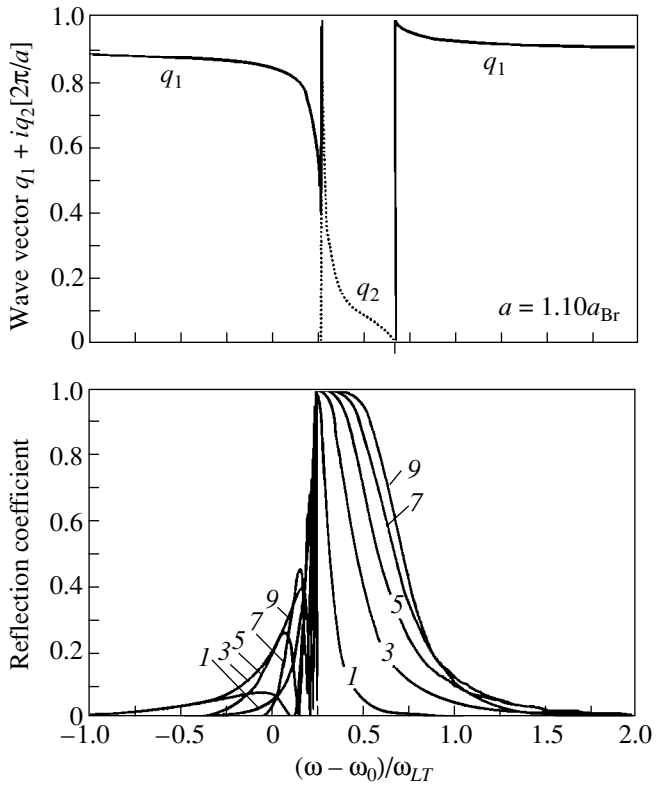

Fig. 5. The same as Fig. 3 but for the period $a = 1.10a_{Br}$.

$$= \sum_{n,\pm} \frac{\pm q + b_n}{k} E_{\pm q + b_n} e^{i(\pm q + b_n) z_R},$$

where $b_n = 2\pi n/a$ and, for $\mathbf{b} = 0$, one can use the scalar form for representing the field amplitudes. Solving Eqs. (67), we come to

$$\tilde{r}^{(N)} = \frac{A_+ A_- (1 - e^{i2Nqa})}{A_+^2 - A_-^2 e^{i2Nqa}}, \quad \tilde{t}^{(N)} = \frac{(A_+^2 - A_-^2) e^{iNqa}}{A_+^2 - A_-^2 e^{i2Nqa}}, \quad (68)$$

where

$$A_\pm = F\left(-\frac{a}{2}, q, k\right) \pm \frac{1}{ik} F'\left(-\frac{a}{2}, q, k\right)$$

and the function $F(\zeta, q, k)$ is defined by Eq. (51). One can show in a straightforward manner that

$$\frac{ikF(-a/2, q, k)}{F'(-a/2, q, k)} = \tan\frac{qa}{2} \cot\frac{ka}{2}.$$

Efficiency of the both approaches is demonstrated in Fig. 2, which shows reflection spectra from a single plane and double planes containing a square lattice of spherical QDs. In the case of the double-plane structures, the interplane spacing, d, is taken to coincide with the in-plane period $a = 0.96a_{Br}$ (Fig. 2a) and $a = 1.10a_{Br}$ (Fig. 2b). The chosen values of the QD radius and the bulk longitudinal–transverse splitting are $R = a/4.001$ and $\omega_{LT}/\omega_0 = 5 \times 10^{-4}$, respectively; and the nonradiative exciton damping is neglected: $\Gamma = 0$. For convenience, the spectra calculated by using Eqs. (59) and (68) are shifted by 0.2 along the vertical axis. One can see that the two approaches give identical results. The spectral dips reflect the fact that the numerator in Eq. (59) vanishes at the frequency $\omega = \tilde{\omega}_0 + A - \Gamma_0 \sin kd$.

Figures 3, 4, and 5 show the dependence of the reflection spectra on the N number of QD planes. The parameters R and ω_{LT}/ω_0 are the same as in Fig. 2, the interface spacing d equals the in-plane period $a = 0.96a_{Br}$, $1.01a_{Br}$, and $1.10a_{Br}$, respectively. The upper panels of Figs. 3 and 5 present the dispersion curves of exciton polaritons propagating along the [001] principal axis of the corresponding 3D primitive-cubic QD lattice. Note that, within forbidden gap, the polariton wavevector is imaginary, $q_1 = 0$, $q_2 \neq 0$. The period $d = a = 1.01a_{Br}$ is almost satisfying the Bragg condition at the exciton resonance frequency ω_0. One can see from Fig. 4 that, in this case, the half-width of the reflection spectrum is almost linearly increasing as a function of N, similarly to the enhancement by a factor of N of the radiative damping of the superradiant mode in resonant Bragg MQW structures [8].

VII. CONCLUSION

In conclusion, we have developed a theory of exciton polaritons in QD regular structures and calculated the resonant reflection spectra from a stack of N planes containing quadratic-lattice arrays of spherical QDs. The theory fills the gap existing between long-period multiple quantum well structures and photonic crystals. It can also be used to generalize the theory of resonant diffraction of γ radiation by nuclei from bulk crystals [28] to synthesized multilayers like the nuclear multilayer [^{57}Fe(22 Å)/Sc(11 Å)/Fe(22 Å)/Sc(11 Å)] × 25 studied by Chumakov *et al.* [26].

The developed theory takes into account a contribution of only one confined-exciton resonance which is

valid if the separation between the exciton size-quantization levels is much larger than the bulk value of the exciton longitudinal–transverse splitting, ω_{LT}. In the opposite limit of extremely large bulk-exciton translational effective mass, one can use the local material relation $\mathbf{D}(\mathbf{r}) = \varepsilon(\mathbf{r}, \omega)\mathbf{E}(\mathbf{r})$ as it was done by Sigalas *et al.* [29] for phonon–polaritons in a two-dimensional lattice consisting of semiconductor cylinders.

ACKNOWLEDGMENTS

We are grateful to S.V. Goupalov and M.M. Voronov for useful discussions.

E.L.I. would like to thank the program "Nanostructures" (Russian Ministry of Science) and Russian Foundation for Basic Research for financial support.

REFERENCES

1. *Excitons*, ed. by M. D. Sturge and E. I. Rashba (North-Holland, Amsterdam, 1982).
2. E. L. Ivchenko, V. P. Kochereshko, P. S. Kop'ev, *et al.*, Solid State Commun. **70**, 529 (1989).
3. E. L. Ivchenko, Fiz. Tverd. Tela (Leningrad) **33**, 2388 (1991) [Sov. Phys. Solid State **33**, 1344 (1991)].
4. V. A. Kosobukin, Fiz. Tverd. Tela (S.-Peterburg) **33**, 3107 (1992) [Sov. Phys. Solid State **34**, 1662 (1992)].
5. E. L. Ivchenko, A. V. Kavokin, V. P. Kochereshko, *et al.*, Phys. Rev. B **46**, 7713 (1992).
6. D. S. Citrin, Solid State Commun. **89**, 139 (1994).
7. L. C. Andreani, Phys. Lett. A **192**, 99 (1994); Phys. Status Solidi B **188**, 29 (1995).
8. E. L. Ivchenko, A. I. Nesvizhskiĭ, and S. Jorda, Fiz. Tverd. Tela (S.-Peterburg) **36**, 2118 (1994) [Phys. Solid State **36**, 1156 (1994)].
9. V. P. Kochereshko, G. R. Pozina, E. L. Ivchenko, *et al.*, Superlattices Microstruct. **15**, 471 (1994).
10. V. A. Kosobukin and M. M. Moiseeva, Fiz. Tverd. Tela (S.-Peterburg) **37**, 3694 (1995) [Phys. Solid State **37**, 2036 (1995)].
11. Y. Merle d'Aubigne, A. Wasiela, H. Mariette, and T. Dietl, Phys. Rev. B **54**, 14003 (1996).
12. T. Stroucken, A. Knorr, P. Thomas, and S. W. Koch, Phys. Rev. B **53**, 2026 (1996).
13. E. L. Ivchenko, V. P. Kochereshko, A. V. Platonov, *et al.*, Fiz. Tverd. Tela (S.-Peterburg) **39**, 2071 (1997) [Phys. Solid State **39**, 1852 (1997)].
14. M. R. Vladimirova, E. L. Ivchenko, and A. V. Kavokin, Fiz. Tekh. Poluprovodn. (S.-Peterburg) **32**, 101 (1998) [Semiconductors **32**, 90 (1998)].
15. J. Sadowski, H. Mariette, A. Wasiela, *et al.*, Phys. Rev. B **56**, 1664 (1997).
16. C. Ell, J. Prineas, T. R. Nelson, *et al.*, Phys. Rev. Lett. **80**, 4795 (1998).
17. S. Haas, T. Stroucken, M. Hübner, *et al.*, Phys. Rev. B **57**, 14860 (1998).
18. M. Hübner, J. Kuhl, T. Stroucken, *et al.*, Phys. Rev. Lett. **76**, 4199 (1996).
19. *Photonic Band Gaps and Localization*, ed. by C. M. Soukoulis (Plenum, New York, 1993), Proc. of the NATO Adv. Sci. Inst. Ser.
20. *Photonic Band Gaps Materials*, ed. by C. M. Soukoulis (Kluwer, Dordrecht, 1996), NATO Adv. Study Inst. Ser., Ser. E **315** (1996).
21. D. V. van Coevorden, R. Sprik, A. Tip, and A. Lagendijk, Phys. Rev. Lett. **77**, 2412 (1996).
22. Yu. A. Vlasov, V. N. Astratov, O. Z. Karimov, *et al.*, Phys. Rev. B **55**, 13357 (1997).
23. Yu. A. Vlasov, Nan Yao, and D. J. Norris, Adv. Mater. **11**, 165 (1999).
24. U. van Bürck, R.L. Mössbauer, E. Gerdau, *et al.*, Phys. Rev. Lett. **59**, 355 (1987).
25. A. I. Chumakov, G. V. Smirnov, A. Q. R. Baron, *et al.*, Phys. Rev. Lett. **71**, 2489 (1993).
26. G. V. Smirnov, Hyperfine Interact. **97/98**, 551 (1996).
27. E. L. Ivchenko and A. V. Kavokin, Fiz. Tverd. Tela (S.-Peterburg) **34**, 1815 (1992) [Sov. Phys. Solid State **34**, 968 (1992)].
28. Yu. Kagan, A. M. Afanas'ev, and I. P. Pertsev, Zh. Éksp. Teor. Fiz. **54**, 1530 (1968) [Sov. Phys. JETP **27**, 819 (1969)].
29. M. M. Sigalas, C. M. Soukoulis, C. T. Chan, and K. M. Ho, Phys. Rev. B **49**, 11080 (1994).

Physics of the Solid State, Vol. 42, No. 9, 2000, pp. 1766–1770. Translated from Fizika Tverdogo Tela, Vol. 42, No. 9, 2000, pp. 1716–1720.

FULLERENES AND ATOMIC CLUSTERS

Kinetics of "Quenching" Effect in C_{60} Crystals

V. M. Egorov*, R. K. Nikolaev, B. I. Smirnov*, and V. V. Shpeĭzman***

** Ioffe Physicotechnical Institute, Russian Academy of Sciences, Politekhnicheskaya ul. 26, St. Petersburg, 194021 Russia*

*** Institute of Solid-State Physics, Russian Academy of Sciences, Chernogolovka, Moscow oblast, 142432 Russia*

e-mail: shpeizm.v@pop.ioffe.rssi.ru

Received March 3, 2000

Abstract—The thermodynamic transition in the C_{60} crystals subjected to uniaxial compression at different temperatures and heat treatment has been investigated by differential scanning calorimetry (DSC). The kinetic parameters of the irreversible endothermic "quenching" effect are determined. It is revealed that the process is accompanied by the cooperative molecular motion, which is characteristic of the high-elasticity state of organic glasses. © *2000 MAIK "Nauka/Interperiodica".*

1. INTRODUCTION

Earlier [1], we studied C_{60} crystals by the calorimetric technique and found the change in the characteristics of the orientational phase transition (at temperatures of 250–260 K) under mechanical action. It was revealed that the distortions observed in λ-shaped endothermic peaks in the differential scanning calorimetric (DSC) curves of strained crystals substantially depend on the temperature of mechanical loading. In particular, the deformation at room temperature suppressed the peak, whereas the changes in the intensity and the temperature location of the peak turned out to be insignificant upon deformation at a temperature of 77 K at which the C_{60} crystals occur in the state of orientational glass [2]. In the latter case, the DSC curves showed an additional endothermic effect in the form of a low-temperature shoulder or a smeared peak against the background of the main λ peak. More recently, it was shown that this effect is metastable and is directly unrelated to the deformation, but depends on the cooling kinetics or holding at low temperatures [3]. This means that the nonequilibrium state in the C_{60} crystals stems from the thermal effect rather than from the mechanical action.

The "quenching" effect is associated with the presence of a nonequilibrium orientational order in the quenched fullerene crystals [3]. As is known [4–6], the orientational order in the equilibrium state is characterized by a specific ratio between the concentrations of C_{60} molecules with two different (pentagonal and hexagonal) orientations in tetrahedral formations. Upon rapid cooling (quenching) down to a low temperature, the nonequilibrium state that corresponds to a higher temperature becomes frozen, so that the ratio (balance) between the pentagonal and hexagonal configurations is disturbed toward the high-energy hexagonal configurations.

The purpose of the present work was to investigate the kinetics of the quenching effect in the fullerene crystals preliminarily subjected to thermal and mechanical action.

2. EXPERIMENTAL TECHNIQUE

Single crystals of C_{60} were prepared according to the procedure described in [3].

The calorimetric measurements were performed on a Perkin–Elmer DSC-2 differential scanning calorimeter according to the technique given in [7, 8]. The DSC data on the mechanical action at temperatures of 77 and 293 K were taken from our earlier work [3]. The fullerene samples were rapidly cooled (quenched) from room temperature in liquid nitrogen. Then, the samples in a vessel with liquid nitrogen were carried into a calorimeter cell (preliminarily cooled down to 100 K) and were heated up to 300 K, during which the DSC curves with thermal effects were recorded. The heating rate was varied from 0.6 to 20 K/min.

3. RESULTS AND DISCUSSION

Figure 1 depicts the DSC curves for the quenched and strained samples. It is seen that the quenching peak disappears upon repeat heating (dashed lines) for both unstrained (curve *1*) and strained (curve *2*) C_{60} samples. With the relatively simple DSC technique [9], it is possible to determine the activation energy of heat absorption from the shift of the temperature T_{max} at a maximum of the peak in the DSC curve (Fig. 1) at different heating rates *V.* In this work, we measured a series of the identically prepared (quenched) C_{60} crystal samples. The experimental data on T_{max} obtained for both peaks (main and quenching) were used to construct the dependences on a semilog scale (Fig. 2). As can be seen from Fig. 2, these dependences are nearly linear, which allows one to determine the activation energies of processes from the relationship $Q = -Rd\ln V/d(1/T_{max})$ (where R is the gas constant) [9]. Note that the dependence $\ln V(1/T_{max})$ for the main peak is close to a vertical line, which corresponds to the activation energy of the equilibrium thermodynamic transition $Q \longrightarrow \infty$. Now, we take into account the systematic error ΔT in

the determination of temperature, which arises from the thermal lag of an operating cell of the calorimeter [10], and subtract ΔT from the experimental values of T_{max} (the experimental values of ΔT for the C_{60} fullerene crystals at each heating rate were obtained in [7]). As a result, the dependence $\ln V(1/T_{max})$ for the main peak becomes vertical to within the other systematic errors, and the slope of the straight line for the quenching peak changes only slightly. The activation energy is determined from this slope as $Q = 0.6 \pm 0.2$ eV.

The nature of the above effect was explained in [3] by the annealing of quenching defects in the C_{60} crystals, in which the ratio between the equilibrium concentrations of the pentagonal (n_p) and hexagonal (n_h) configurations of C_{60} molecules is disturbed. In this case, the quenching defects were differentiated from the deformation defects. Note that the quenching defects occur in a primitive cubic lattice of fullerene and are annealed even below the temperature of the transition to the face-centered cubic lattice, whereas the deformation defects predominantly arise in the face-centered cubic lattice and bring about a smooth smearing of the λ peak. According to [11, 12], the structure of the latter defects can be associated with the formation of dimers and more complex polymerized structures.

In the quenched crystals, a C_{60} molecule changed from one metastable orientation to another one (hexagonal or pentagonal) due to an abrupt temperature drop upon quenching can be treated as the simplest defective structure. However, according to [4, 5, 13], the activation energy for transition from one configurational modification of C_{60} molecules to another modification is equal to 0.3 eV. Moreover, the period of librations or the time for which the molecule occurs at each equilibrium position is equal to $\sim 4 \times 10^{-14}$ s. Therefore, the activation energy for the irreversible quenching process is more than twice as large as that for the elementary act of change in the orientation of one C_{60} molecule. This can be caused by a more complex cooperative process of redistributing the concentrations of the pentagonal (n_p) and hexagonal (n_h) configurations of C_{60} molecules in the quenched fullerene crystal. For example, Natsik *et al.* [14] noted that the orientation states and the transitions in a system of C_{60} molecules are cooperative in character. Nonetheless, the model, which treats one C_{60} molecules as an elementary kinetic unit, appears to be fruitful and, in the authors' opinion, provides an adequate description of a number of experimental properties of the primitive cubic phase in the C_{60} crystals. Apparently, the quenched crystal of fullerene can be characterized by both processes that involve kinetically simple quasi-independent acts of motion of kinetic units and obey the Arrhenius relation with the preexponential factor $A \sim 10^{13}$ and the concurrent process of annealing the quenching defects with the characteristic cooperative motion of kinetic units.

Similar processes are observed in organic and inorganic glasses in a specific aggregate state that exists in the range from the glass transition temperature T_g to the temperature of a transition to the liquid-flow state T_{lf} (or to the melting temperature of the crystalline phase for partially crystallized glasses). This state in organic glasses is referred to as the "high-elasticity" state. The kinetic parameters of relaxation processes (including the enthalpy relaxation) in this temperature range are not constant: the activation energy of cooperative

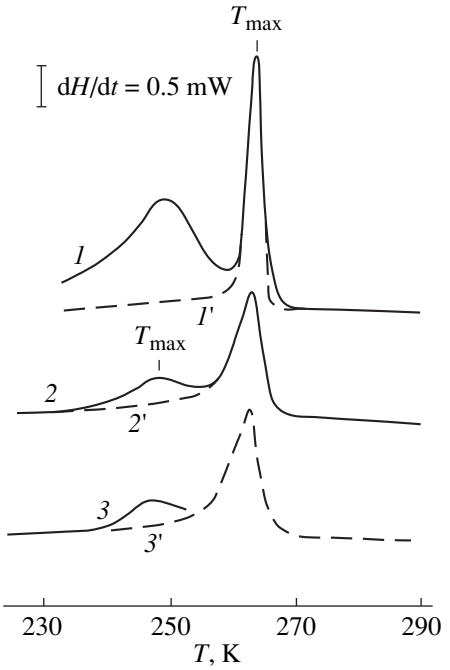

Fig. 1. DSC curves (changes in enthalpy per unit time dH/dt) for (*1*) the initial C_{60} sample and (*2*, *3*) the C_{60} samples subjected to uniaxial compression at $T = 77$ K and $\sigma = 460$ MPa after the preliminary quenching in liquid nitrogen. (*3*) Heating of the initial sample up to 253 K. Dashed lines *1'*–*3'* correspond to repeat heating after cooling down to 220 K. Heating rate is 5 K/min.

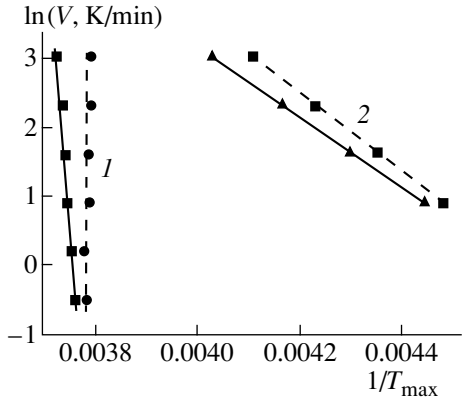

Fig. 2. Experimental (solid lines) and corrected (dashed lines) dependences of the cooling rate on T_{max} for the (*1*) main and (*2*) quenching endothermic effects in the C_{60} fullerene.

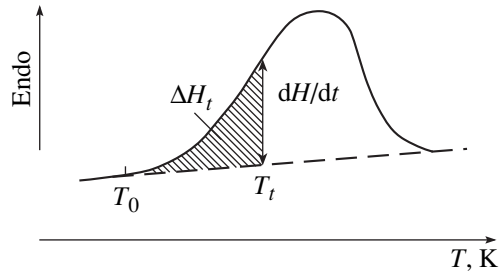

Fig. 3. Schematic representation of the DSC curve with the endothermic effect for calculation of the kinetic parameters for heat absorption [15].

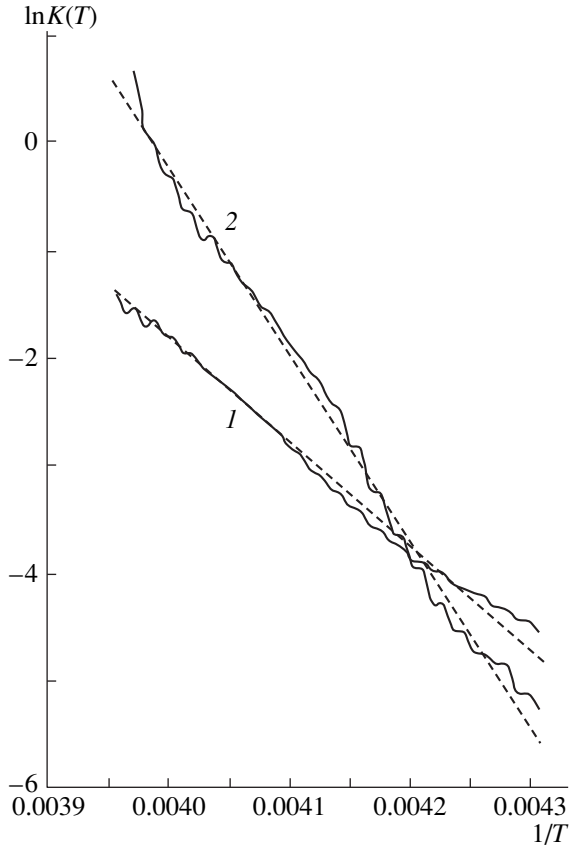

Fig. 4. Temperature dependences of the rate constant $K(T)$ for the irreversible quenching endothermic process in (*1*) unstrained and (*2*) strained quenched C_{60} fullerene crystals.

motion Q_{coop} increases many times as the temperature decreases from the temperature of the liquid-flow state (characterized by the Arrhenius activation energy Q) to the glass transition temperature. The relationship $Q_{coop}/Q = z = 4 \pm 1$ [where z is the so-called cooperativity factor (parameter)] holds true near the T_g temperature for a wide variety of glass-forming materials [15]. In a number of works [16–19], it was demonstrated that the high (non-Arrhenius) activation energies Q_{coop} correspond to the potential barriers to the motion of z molecules or segments (for organic glasses). The mechanism of a particular act of the cooperative motion is differently interpreted by different authors. In our opinion, the most descriptive model was proposed by Gotlib [17], who treated the overcoming of the potential barrier Q_{coop} as a correlated overcoming of several potential barriers Q.

The above technique for determining the activation energy gives no way of obtaining the other kinetic parameters of the relaxation process, which could clarify the physical nature of the quenching effect observed. A deeper insight into the nature of this effect can be gained with the technique used in analysis of a wide variety of kinetic phenomena, including the concurrent multistage thermal processes [15]. This technique makes it possible to determine the kinetic parameters for each of stages of the process provided that these stages can be separated experimentally or theoretically on the basis of particular model concepts. As follows from the data shown in Fig. 1 (curve *3*), in our case, the quenching and dominant λ-shaped endothermic effect can be separately observed in the C_{60} sample. It is seen that the heating up to a temperature of 253 K makes possible recording only the quenching effect, and the main λ peak alone is observed upon repeat heating of this sample (Fig. 1, solid curve *3* and dashed curve *3*').

The kinetic parameters of the two-stage endothermic process were determined from the DSC curve obtained at a heating rate of 5 K/min, when the overlapping of peaks is small. By analogy with the chemical reaction, the kinetic equation for the thermal process can be written in the general form as follows:

$$d\alpha/dt = K(T)(1-\alpha)^n, \quad (1)$$

where α is the degree of conversion, n is the order of reaction, and the $K(T)$ is the rate constant. The rate constant is defined by the Arrhenius equation

$$K(T) = A\exp(-Q/RT), \quad (2)$$

where A is the preexponential factor, Q is the activation energy of the process, and R is the gas constant.

In the case of DSC, the variable α is represented by the ratio $\Delta H_t/\Delta H_0$, where ΔH_t is the reaction heat evolved for time t in the temperature range from T_0 to T_t (which corresponds to the area of the hatched part of the peak in Fig. 3), and ΔH_0 is the total endothermic effect of the process (the area of the whole peak). The rate of conversion $d\alpha/dt$ in the kinetic equation (1) is equivalent to the heat flux dH/dt normalized to the overall heat of the process ΔH_0; that is,

$$(1/\Delta H_0)dH/dt = K(T)(1-\Delta H_t/\Delta H_0)^n. \quad (3)$$

By using the experimental DSC curve (the known dH/dt, ΔH_t, and ΔH_0 quantities) and fitting the n value, this relationship permits one to determine the dependence $K(T)$, which is linear on the Arrhenius coordinates ln$K$–1/T. Then, this dependence is used to calcu-

late the activation energy Q from the expression $Q = -Rd\ln K/d(1/T)$. In this case, the portion A is intercepted on the ordinate axis by the straight line $\ln K(1/T)$. The above technique for calculating the kinetic parameters is appropriate in the case of describing a multistage process whose stages each are governed by relationship (2).

It turns out that the endothermic effect of the λ peak observed for both strained and quenched C_{60} samples makes it impossible to obtain the parameter n at which the dependence $\ln K(1/T)$ would be linear over the entire temperature range of the thermal effect. This result agrees well with the above data, because the λ peak corresponds to the equilibrium thermodynamic transition. At the same time, in the case of the quenching effect (see Fig. 4), it has become possible to fit the corresponding parameters for the quenched unstrained ($n_1 = 1.26$) and strained ($n_2 = 1.12$) C_{60} samples, at which the dependences $\ln K(1/T)$ are linear over the entire temperature range of the thermal effects. The other parameters of these linear dependences are as follows: $\ln A_1 = 36.9$ and $Q_1 = 0.85$ eV for the quenched samples and $\ln A_2 = 68.9$ and $Q_2 = 1.52$ eV for the strained samples.

The activation energy $Q = 0.6 \pm 0.2$ eV (determined above with other experimental technique and computational procedure) is comparable with the activation energy Q_1 for the quenched sample but is considerably less than the activation energy Q_2 for the strained sample. The cooperativity factor z is equal to the ratio between the found activation energy and the activation energy of the Arrhenius process ($Q = 0.3$ eV): $z = 2$–2.8 for the quenched C_{60} sample and $z = 5$ for the strained sample. This result is in reasonable agreement with the above factor $z = 4 \pm 1$, which is typical of organic and inorganic glasses.

It is known that the order of reaction or the parameter n characterizes the mechanism of the chemical reaction or the process [20]. For example, the one-stage reaction of radioactive decay is the reaction with the order close to unity ($n \sim 1$). In more complex cases when the reaction or process involves several stages, the order of reaction can be close to unity if the initial stage is the first-order reaction. For the quenched and strained C_{60} samples, the order of reaction or the process of enthalpy relaxation is also close to unity ($n_1 = 1.26$ and $n_2 = 1.12$). In this case, the transition of the C_{60} molecule from one metastable equilibrium position to another metastable equilibrium, i.e., the hexagonal–pentagonal orientational transition, can be treated as the initial stage of the cooperative process. This elementary act leads to the next stages involving several orientational transitions of the adjacent molecules. The number of the events is determined by the cooperativity factor z.

The cooperativity factor is associated with structural formations in glasses. In organic and inorganic glasses, the factor z is governed by the coordination number of chain packing in the first coordination sphere of the intermolecular "lattice" and also by the size of short-range order regions [15]. In the fullerene crystals, each site in the primitive cubic lattice is matched by the tetrahedron formed by four C_{60} molecules with particular orientations [2, 21]. This implies that the cooperativity factor for C_{60} is close to the number of C_{60} molecules in the tetrahedron. This fact permits us to assume that the quenching defects represent local formations containing from three to five C_{60} molecules, which occur in the metastable orientation equilibrium state and belong to one or several contacting tetrahedra.

Thus, the data obtained in the present work led to the conclusion that the kinetics of the quenching effect is cooperative in character. The kinetic units involved in this cooperative process or quenching defects represent local formations comparable in size to the tetrahedra in the primitive cubic lattice of fullerene crystals.

ACKNOWLEDGMENTS

This work was supported by the Russian Scientific and Technical Program "Fullerenes and Atomic Clusters", project no. 98065 "Cluster".

REFERENCES

1. V. M. Egorov, B. I. Smirnov, V. V. Shpeĭzman, and R. K. Nikolaev, Fiz. Tverd. Tela (S.-Peterburg) **38** (7), 2214 (1996) [Phys. Solid State **38** (7), 1219 (1996)].
2. M. I. F. David, R. M. Ibberson, T. J. S. Dennis, *et al.*, Europhys. Lett. **18**, 219 (1992).
3. V. M. Egorov, V. I. Nikolaev, R. K. Nikolaev, *et al.*, Fiz. Tverd. Tela (S.-Peterburg) **41** (3), 550 (1999) [Phys. Solid State **41** (3), 494 (1999)].
4. W. Schranz, A. Fuith, P. Dolinar, *et al.*, Phys. Rev. Lett. **71** (10), 1561 (1993).
5. F. Gugenberger, R. Heid, C. Meingast, *et al.*, Phys. Rev. Lett. **69** (26), 3774 (1992).
6. J. D. Axe, S. C. Moss, and D. A. Neumann, in *Solid State Physics*, ed. by H. Ehrenreich and F. Spaepen (Academic, New York, 1994), Vol. 48, p. 150.
7. V. M. Egorov, V. V. Shpeĭzman, and I. N. Kremenskaya, Pis'ma Zh. Tekh. Fiz. **19** (19), 49 (1993) [Tech. Phys. Lett. **19**, 621 (1993)].
8. V. M. Egorov, I. N. Kremenskaya, B. I. Smirnov, and V. V. Shpeĭzman, Fiz. Tverd. Tela (S.-Peterburg) **37** (11), 3493 (1995) [Phys. Solid State **37** (11), 1919 (1995)].
9. C. Moinihan, A. Eastel, and J. Wilder, J. Phys. Chem. **78**, 2673 (1974).
10. K. Illers, Eur. Polym. J. **10**, 911 (1974).
11. A. M. Rao, P. C. Eklund, V. D. Venkateswaran, *et al.*, Appl. Phys. A **64** (2), 231 (1997).
12. A. L. Kolesnikova and A. E. Romanov, Fiz. Tverd. Tela (S.-Peterburg) **40** (6), 1178 (1998) [Phys. Solid State **40** (6), 1075 (1998)].

13. R. C. Yu, N. Tea, M. B. Salamon, *et al.*, Phys. Rev. Lett. **68** (13), 2050 (1992).
14. V. D. Natsik, S. V. Lubenets, and L. S. Fomenko, Fiz. Nizk. Temp. **22** (3), 337 (1996) [Low Temp. Phys. **22**, 264 (1996)].
15. V. A. Bershtein and V. M. Egorov, *Differential Scanning Calorimetry of Polymers* (Ellis Horwood, New York, 1993).
16. E. Bueche, J. Chem. Phys. **24** (2), 418 (1956).
17. Yu. Ya. Gotlib, Fiz. Tverd. Tela (Leningrad) **6** (10), 2938 (1964) [Sov. Phys. Solid State **6** (10), 2341 (1964)].
18. E. Donth, in *Glasubergang* (Akademie Verlag, Berlin, 1981), p. 202.
19. Yu. A. Emel'yanov and V. A. Bershteĭn, Fiz. Khim. Stekla **11** (4), 429 (1985).
20. L. Pauling, *General Chemistry* (Freeman, San Francisco, 1970; Moscow, Mir, 1974).
21. P. A. Heiney, J. E. Fischer, A. R. McGhie, *et al.*, Phys. Rev. Lett. **66**, 2911 (1991).

Translated by O. Borovik-Romanova

Physics of the Solid State, Vol. 42, No. 9, 2000, pp. 1771–1773. Translated from Fizika Tverdogo Tela, Vol. 42, No. 9, 2000, pp. 1721–1723.

FULLERENES AND ATOMIC CLUSTERS

Inelastic Deformation of C_{60} Single Crystals in the Temperature Range 80–300 K

V. V. Shpeĭzman*, N. N. Peschanskaya*, V. M. Egorov*, V. I. Nikolaev*, R. K. Nikolaev, and B. I. Smirnov***

**Ioffe Physicotechnical Institute, Russian Academy of Sciences, Politekhnicheskaya ul. 26, St. Petersburg, 194021 Russia*
***Institute of Solid-State Physics, Russian Academy of Sciences, Chernogolovka, Moscow oblast, 142432 Russia*
e-mail: shpeizm.v@pop.ioffe.rssi.ru
Received March 3, 2000

Abstract—The rate spectrum of small inelastic strains of the C_{60} single crystal in the temperature range 80–300 K has been obtained with a precision laser interferometer. It is revealed that the spectrum exhibits two large peaks in the glass formation (90–100 K) and phase transition (250–260 K) ranges. A small strain acceleration is also observed at ~220 and 240 K. The first two maxima are attributed to the changes in strain resistance upon transitions, and the strain acceleration at 220 and 240 K is associated with the annealing of the defects formed upon rapid cooling of the crystal. It is demonstrated that the peak at 250–260 K broadens with an increase in the stress. The spectrum of strain rates is compared with the calorimetric curve for the same single crystal. © *2000 MAIK "Nauka/Interperiodica".*

1. INTRODUCTION

A correlation between orientational transformations in the C_{60} crystals and their microplasticity has been observed in a number of works [1–6]. For example, the temperature dependence of the Vickers microhardness exhibits kinks at 150 K [1, 2] and in the range 240–260 K [1–3]. The presence of the kinks is explained by the glass transition, which supposedly proceeds from 150 [1, 2] to 85 K [7] during cooling the crystal, and also by the phase transition from the primitive cubic (pc) lattice to the face-centered cubic (fcc) lattice. The reverse effect—the influence of the mechanical action on the characteristics of the pc–fcc phase transition—is also known. It has been demonstrated that the compression of the C_{60} single crystals at temperatures above and below the transition point variously affects their energy characteristics, which were determined by differential scanning calorimetry (DSC) [4, 5]. The distortions observed in the peak upon deformation at 77 K are substantially smaller than those caused by the compression at room temperature when the peak is almost completely smeared even at relatively low pressures. Earlier [5], it was assumed that this effect is due to larger possibilities for local deformation (preceding the destruction) in the high-symmetry fcc lattice as compared to the pc lattice or the glassy state of the C_{60} fullerites. In [6], the microplasticity was found upon uniform loading (compression of the crystal). It was shown that the rate spectrum of small inelastic deformations, which was obtained for the C_{60} single crystal by the high-resolution laser interferometry, exhibited a peak at T = 250–260 K. The presence of this peak indicated the microstrain acceleration during the pc–fcc transition.

In the present work, we continued the investigations of the spectra of inelastic deformations for the C_{60} single crystals in an extended temperature range (80–300 K), which also covered the glass transition range. The laser interferometry was used for measuring the rates from small strain increments [6]. The spectra obtained were compared with the calorimetric curves for the same crystals.

2. EXPERIMENTAL TECHNIQUE

The C_{60} single crystals were grown from the vapor phase. Fine C_{60} crystals, which were preliminary purified by multistage vacuum sublimation [5, 7], served as the starting material. The preparation procedure of the starting material and single crystal growth were described in [5, 8]. The crystals were obtained at the following conditions: sublimation temperature, 873 K; crystallization temperature, 813 K; and crystal growth duration, 8–12 h. The well-faceted C_{60} single crystals prepared by this procedure weighed as much as 30 mg and reached several millimeters in size.

The interferometric technique of recording the deformation in time in the form of sequential oscillations [9, 10], which was used in the present work, enables one to measure the strain rate $\dot{\varepsilon}$ from small changes in the sample length with an error of no more than 5%. One oscillation in the interferogram is equal to the strain increment $|\Delta l_0|$ = 0.3 μm. In order to construct the rate spectrum, the strain interferogram was obtained after loading the sample in a creep mode for

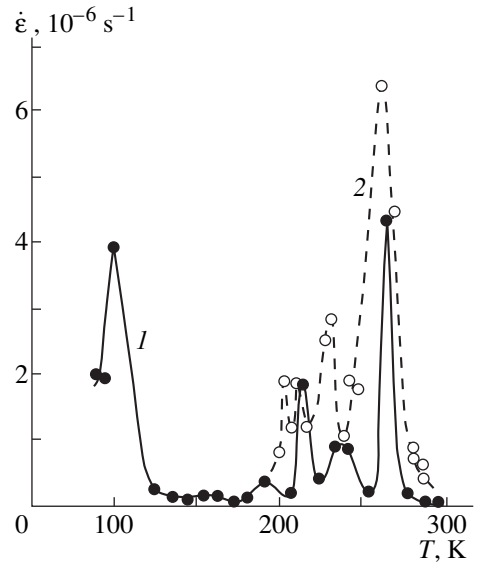

Fig. 1. Spectra of the rates of small inelastic strains $\dot{\varepsilon}$ for the C_{60} single crystals under loads of (*1*) 2 and (*2*) 20 N.

approximately 1 min; then, the sample was unloaded, heated by 3–10 K, loaded repeatedly, etc. The experiment was started at low temperatures, and the creep strain was several hundredth of percent. The rate measurements were carried out at the same stress and equal intervals after loading. To obtain the spectrum, the C_{60} single crystal was placed in a test chamber [9, 10] and rapidly cooled down to ~77 K. Then, the sample was slowly heated and loaded with a compressive force of 2 N at gradually increasing temperatures. The average heating rate was 1 K/min, and the isothermal loading pulse length was 2 min. The error in determining and controlling the temperature at the instant of loading was ±0.5 K, and the strain rate was measured at intervals of 1 min after the onset of loading at each temperature.

The DSC data were also used in analysis of the results. The calorimetric measurements were carried out on a Perkin–Elmer DSC-2 calorimeter according to the procedure described in [4–6]. In order to provide the similarity of temperature conditions for both methods, the C_{60} sample was preliminary rapidly cooled with liquid nitrogen and placed in a calorimeter chamber. Measurements were carried out at a heating rate of 5 K/min in the temperature range 170–300 K. The DSC curves showed the thermal effects, which were observed in the sample during the pc–fcc phase transition, and the "quenching" effects found earlier [4–6].

3. RESULTS AND DISCUSSION

The rate spectrum of the inelastic strain for the C_{60} single crystal under a load of 2 N in the temperature range 80–290 K is shown in Fig. 1. Two sharp peaks are clearly seen at ~100 and 260 K, i.e., in the region of structural phase transitions. Several small peaks are also observed in the range 150–240 K. It was demonstrated earlier for a large variety of materials [10] that the peaks, which were obtained at stresses far below the yield point and fracture stresses, correspond to the activation of a rapidly damping local deformation. No peak near the glass transition temperature was observed earlier when studying the mechanical properties of fullerites. In our opinion, its appearance in our experiments is caused by a very high sensitivity of the method and very small loads. On the one hand, this enables one to reveal the earliest stages of deformation, and on the other hand, to avoid the crystal fracture. It seems likely that a small peak at 150 K correlates with a kink in the temperature dependence of the microhardness of the C_{60} single crystals, which was found in [1]. However, a similar dependence for polycrystals has no specific features [11]. The difference in temperatures that correspond to the glassy state has also been revealed in [1]. This difference can stem either from the difference in stresses or from the specific features of the crystals.

For comparison, the spectrum for another C_{60} single crystal, which was grown by the same technique, is also shown in Fig. 1 [5]. This spectrum was recorded at a larger load (20 N) in the temperature range 200–300 K. It is seen that both spectra exhibit the same characteristic peaks that are attributed to the phase transition and the rapid cooling of the sample. These are the main peaks at 260 K and the so-called "quenching" peaks at 240 K, respectively. However, there are some differences. First, the strain rates are higher at a larger load. Second, the main peak is considerably broader in this case, and this broadening is conditioned primarily by its low-temperature branch. This means that the microdeformation is more sensitive to the phase transition at a larger load. The shift of the low-temperature branch of the peak at $\dot{\varepsilon} = (2\text{–}4) \times 10^{-6}$ s^{-1} is $\Delta T = 12$ K. If we consider the microdeformation as a thermally activated process and assign this shift exclusively to the load change, the efficient activation volume of deformation can be estimated as $V_{\text{eff}} = k(\ln\dot{\varepsilon}_0 - \ln\dot{\varepsilon})\Delta T/\Delta\sigma$, where k is the Boltzmann constant; $\dot{\varepsilon}_0 \approx 10^{13}$ s^{-1}; and $\Delta\sigma$ is calculated with the constraint that the mean cross-section of the single crystal is equal to ~3 mm^2. The calculations give $V_{\text{eff}} \approx 7 \times 10^{-22}$ cm^{-3}, which is close to the unit cell volume. If we consider the microdeformation as governed by the dislocation mechanism, the last circumstance indicates that the microdeformation in C_{60} in the pc–fcc phase transition region can be realized through very short segments of dislocations only.

Figure 2 depicts the calorimetric curves for two different C_{60} single crystals. The measurements were performed with small pieces of the samples subjected to compression in the above experiments at 2 and 20 N, respectively. As is seen from Fig. 2, the peak corresponding to the phase transition is virtually identical for two samples, while the small peaks at 220–250 K differ in both the magnitude and the location of the

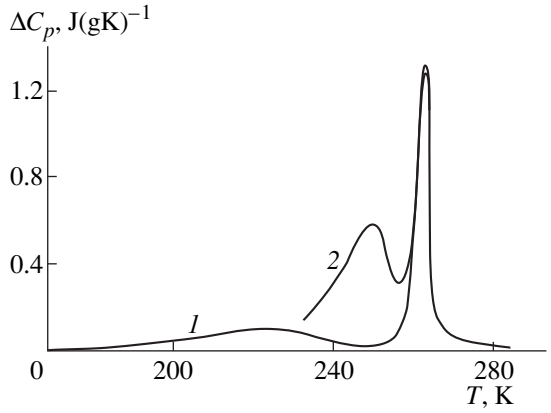

Fig. 2. DSC curves (changes in the specific heat capacity ΔC_p) for two quenched C_{60} single crystals. Heating rate is 5 K/min.

maximum. A comparison of Figs. 1 and 2 demonstrates that the calorimetric and deformation curves are similar in the temperature range covered. Unfortunately, we failed to perform the calorimetric measurements with a DSC-2 calorimeter at lower temperatures near the glass transition point. For this reason, the comparison between the calorimetric and deformation curves was made only in the range 170–300 K.

Note that the width of the strain maximum at small stresses approaches that of the calorimetric peak in the phase transition range. It can be assumed that large stresses can give rise to defects in the pc lattice, which promote the phase transition and bring about the broadening of the peak primarily at the sacrifice of its low-temperature branch.

One or several peaks of relatively small amplitude are observed in each curve (Figs. 1, 2) in the temperature range 190–250 K. These peaks were termed the "quenching" peaks [5], since they manifested themselves in the rapidly cooled samples. The "quenching" effect was associated with the presence of the nonequilibrium orientational order in the quenched fullerene crystals [5]. The orientational order is determined by the occupancy ratio for pentagonal (n_p) and hexagonal (n_h) configurations n_p/n_h, whose equilibrium value depends on temperature. For example, at room temperature, when the C_{60} molecules rotate almost freely, we can assume that $n_p/n_h \approx 1$. In the temperature range $85 < T < 260$ K, we have $n_p/n_h \approx 4$, while at $T < 85$ K, i.e., in the state of "orientational glass", $n_p/n_h \approx 5$ [7]. Upon rapid cooling (quenching), the low-temperature nonequilibrium state that corresponds to a higher temperature becomes frozen, so that the ratio n_p/n_h is violated toward the high-energy hexagonal (h) configuration. Thus, the quenching defects in the pc lattice of fullerene are annealed below the pc–fcc transition temperature. This is reflected in the DSC curves and in the deformation curve, which is sensitive to mobility of the defects during annealing. The presence of several maxima in the deformation spectra in the range 190–240 K can be attributed to multiple transitions, which are often observed in complex systems [12]. Positions and magnitudes of "quenching" maxima are governed by individual specific features of the crystal and its prehistory. The difference between calorimetric and deformation curves for two different crystals is apparently associated with these circumstances.

Thus, the rate spectrum of small inelastic deformations makes it possible to investigate the transition to the state of orientational glass, phase transition, and other structural transformations in the C_{60} single crystals reasoning from their correlation with microplasticity. This spectrum is similar to the DSC curve for the single crystal. Some differences are observed only in the range of annealing the quenching defects.

ACKNOWLEDGMENTS

This work was supported by the Russian Scientific and Technical Program "Fullerenes and Atomic Clusters", project no. 98065 "Cluster".

REFERENCES

1. V. D. Natsik, S. V. Lubenets, and L. S. Fomenko, Fiz. Nizk. Temp. **22** (3), 337 (1996) [Low Temp. Phys. **22**, 264 (1996)].
2. L. S. Fomenko, V. D. Natsik, S. V. Lubenets, *et al.*, Fiz. Nizk. Temp. **21** (4), 465 (1995) [Low Temp. Phys. **21**, 364 (1995)].
3. M. Tachibana, M. Michiyama, K. Kikuchi, *et al.*, Phys. Rev. B **49** (21), 14945 (1994).
4. V. M. Egorov, B. I. Smirnov, V. V. Shpeĭzman, and R. K. Nikolaev, Fiz. Tverd. Tela (S.-Peterburg) **38** (7), 2214 (1996) [Phys. Solid State **238**, 1219 (1996)].
5. V. M. Egorov, V. I. Nikolaev, R. K. Nikolaev, *et al.*, Fiz. Tverd. Tela (S.-Peterburg) **41** (3), 550 (1999) [Phys. Solid State **41**, 494 (1999)].
6. V. V. Shpeĭzman, N. N. Peschanskaya, V. M. Egorov, *et al.*, Fiz. Tverd. Tela (S.-Peterburg) **41** (6), 1115 (1999) [Phys. Solid State **41**, 1017 (1999)].
7. A. K. Soper, W. I. F. David, D. S. Sivia, *et al.*, J. Phys.: Condens. Matter **4** (28), 6087 (1992).
8. M. Tachibana, M. Michiyama, H. Sakuma, *et al.*, J. Cryst. Growth **166** (1–4), 883 (1996).
9. N. N. Peschanskaya, P. N. Yakushev, and V. A. Stepanov, Fiz. Tverd. Tela (Leningrad) **26** (4), 1202 (1984) [Sov. Phys. Solid State **26**, 729 (1984)].
10. N. N. Peschanskaya, A. B. Sinani, V. V. Shpeĭzman, and P. N. Yakushev, Izv. Ross. Akad. Nauk, Ser. Fiz. **63** (9), 882 (1999).
11. Yu. A. Ossipyan, V. S. Bobrov, Yu. S. Grushko, *et al.*, Appl. Phys. A **56**, 413 (1993).
12. N. N. Peschanskaya, P. N. Yakushev, and V. Yu. Surovova, Fiz. Tverd. Tela (S.-Peterburg) **37** (9), 2602 (1995) [Phys. Solid State **37**, 1429 (1995)].

Translated by N. Korovin